

Topics in Advanced Model Rocketry

Mandell, Caporaso, Bengen



TOPICS IN ADVANCED MODEL ROCKETRY



TOPICS IN ADVANCED MODEL ROCKETRY

Gordon K. Mandell

George J. Caporaso

William P. Bengen

The MIT Press

Cambridge, Massachusetts, and London, England

Copyright © 1973 by

The Massachusetts Institute of Technology

All rights reserved. No part of this book may be reproduced in any form or by any means, electronic or mechanical, including photocopying, recording, or by any information storage and retrieval system, without permission in writing from the publisher.

This book was printed on Fernwood Opaque
and bound in Columbia Milbank Vellum
by The Colonial Press, Inc.
in the United States of America.

Library of Congress Cataloging in Publication Data

Mandell, Gordon K
Topics in advanced model rocketry.

1. Rockets (Aeronautics)--Models. 2. Rockets
(Aeronautics)--Performance. I. Caporaso, George J.
II. Bengen, William P. III. Title.
TL844.M36 629.47'52 72-10386
ISBN 0-262-02096-3

HUNTER LIBRARY
WESTERN CAROLINA UNIVERSITY

TL
844

M36

To Orville H. Carlisle and G. Harry Stine,
without whom model rocketry could not have
begun; and to the advanced model rocketeers
of the world, without whom it could not
continue.

PUBLISHER'S FOREWORD

The aim of this format is to close the time gap between the preparation of a monographic work and its publication in book form. A large number of significant though specialized manuscripts make the transition to formal publication either after a considerable delay or not at all. The time and expense of detailed text editing and composition in print may act to prevent publication or so to delay it that currency of content is affected.

The text of this book has been photographed directly from the author's typescript. It is edited to a satisfactory level of completeness and comprehensibility though not necessarily to the standard of consistency of minor editorial detail present in typeset books issued under our imprint. A detailed table of contents is included.

The MIT Press

PREFACE

To some members of the rocket modeling community, this work may require justification. Perhaps these people fail to recognize the need for, or the value of, an advanced treatment of the subjects of model rocket stability and performance. Perhaps they resent the intrusion of the difficulty and complexity inevitably associated with higher mathematics, physics, and engineering analysis upon that sanctuary of the designer's unassisted intuition that has been, until recent years, the hobby of model rocketry. Why, they may ask, should model rocketry become so technical?

The answer becomes self-evident if one examines the state of the hobby over the past several years. In 1969 the twelve-year-old model rocket hobby was losing most of its older, better-educated participants because of a widespread misconception that model rocketry had nothing interesting or challenging enough to merit their attention. Since that time our retention rate of advanced modelers has measurably improved due to a number of programs and projects (of which this book is one) aimed at increasing the technical content of, and improving the lines of communication within, our avocation. The introduction of more technically-oriented kits, supplies, and literature by the model rocket industry; the proliferation of annual conventions sponsored by various Sections of the National Association

of Rocketry; the establishment of Model Rocketry magazine, the first independent monthly publication serving the rocket hobby exclusively -- all have done their part to help solve model rocketry's "senior problem", and thereby to help insure the stability and continuity of the hobby. These programs and projects, by making model rocketry an activity of interest to a broader cross-section of the public, have helped guard against our suffering the kind of "boom-and-bust" fad cycle that befell our sister hobby of slot-car racing in 1967.

The treatments presented herein were written by several college-level model rocketeers who found within the existing limits of our hobby a veritable goldmine of opportunity for scientific and engineering contributions. Most of the material has been taken from research performed by members of the Massachusetts Institute of Technology Model Rocket Society over a five-year period extending from 1965 through 1970 -- research founded, in part, upon the work of James S. Barrowman, Dr. Gerald M. Gregorek, Douglas J. Malewicki, and Mark Mercer. The resulting analytical philosophy of model rocket design represents the current state of our designer's art and establishes the current frontiers of engineering analysis within the model rocket hobby.

Though the various chapters of this volume have been written by different authors, the structure and purpose of the whole are unified so as to present a consistent and logical analysis of model rockets in flight from the viewpoints of static and dynamic stability, drag, and trajectory analysis. The results of the dynamic analyses of Chapter 2 are used in Chapter 4 to provide

estimates of the effects of pitching and yawing oscillations on altitude performance. The results of the drag analyses of Chapter 3 are then combined with the treatments of Chapters 2 and 4 to provide criteria that will enable an experienced modeler with good physical intuition and a working knowledge of algebra to design rocket models as nearly optimized from the standpoint of altitude performance as the current state of our knowledge permits.

The results of Chapter 2 have been experimentally verified by that chapter's author in wind tunnel tests conducted in the Aeronautical Projects Laboratory at the Massachusetts Institute of Technology. Data taken by various researchers such as G. Harry Stine, Mark Mercer, and Douglas Malewicki have generally tended to confirm the results of Chapter 3; there are, however, still some gaps in the current theory of drag design, and a fully sound theory of flight performance must await their elimination. It has not yet, for instance, been determined precisely what effect the rocket exhaust gases have on the thrusting-phase drag coefficient -- and some arguments suggest that the exhaust jet could lower that coefficient by as much as a factor of two. If the influence of the jet is as great as some suspect, a method must be found for estimating its magnitude before more accurate altitude predictions can become a reality. Chapter 4, unfortunately, has had little experimental verification due to deficiencies in accuracy and reliability inherent in present optical tracking systems and the relative paucity of experimentation in this area.

No preface to this volume would be complete without a

word of caution: this book is highly technical and it is not for everyone. We do not recommend it to anyone under sixteen years of age, to anyone whose schoolwork in science and mathematics has not been consistently above average, or to anyone who has had no previous exposure to model rocketry or its literature. We advise younger, less experienced, less technically oriented modelers to avail themselves of G. Harry Stine's Handbook of Model Rocketry and the excellent, elementary treatments of technical topics in rocketry available through some of the larger manufacturers (most notably Estes Industries and the Centuri Engineering Company).

If, on the other hand, you are technically inclined and feel capable of assimilating material written at a late high school or early college undergraduate level, we have written this volume for you. By means of this and similar projects we hope to show you that model rocketry is not just a pastime for children and early adolescents, but an activity that can be challenging and rewarding even for well-educated, technically proficient adults. You will find that the information contained herein can be put to good practical use in designing models which will possess good stability and maximum altitude capability. It is our hope, moreover, that some of you will find in this work a basis for further advanced research in the field and a foundation for the further refinement of those theories presently governing the design of model rocket vehicles.

George J. Caporaso
Gordon K. Mandell

Cambridge, Massachusetts
May, 1971

TABLE OF CONTENTS

CHAPTER 1

AN INTRODUCTION TO THE DYNAMICS OF MODEL ROCKET FLIGHT 1

George J. Caporaso
and
Gordon K. Mandell

1.	Definition of the Problem	6
1.1	Point-Mass and Rigid-Body Dynamics	8
1.2	Separation of the Differential Equations of Motion	11
2.	Description of the Flight Forces	12
2.1	Thrust	12
2.2	Weight	31
2.3	Drag and Side Force	34
3.	Description of the Perturbing Forces	43
3.1	Aerodynamic Disturbances	45
3.2	Mechanical Disturbances	47

CHAPTER 2

A UNIFIED APPROACH TO AERODYNAMIC STABILITY 53

Gordon K. Mandell

Introduction	63	
1.	The Dynamical Equations	67
1.1	Euler's Angles	67
1.2	Angular Velocity	69
1.3	Applied Moments, Angular Accelerations, and Moment of Inertia	74

1.4 Euler's Dynamical Equations	76
2. The Linearized Theory	81
2.1 Corrective and Damping Moment	81
2.2 The Linearization Approximations	84
2.3 Coupled and Decoupled Systems of Equations	89
2.4 Homogeneous, Particular, and Steady-State Solutions	90
3. Solutions to the Dynamical Equations for Particular Cases of Interest	92
3.1 Dynamical Behavior at Zero Roll Rate	93
3.1.1 Generalized Homogeneous Response	93
3.1.2 Complete Response to Step Input	109
3.1.3 Complete Response to Impulse Input	119
3.1.4 Steady State Response to Sinusoidal Forcing	130
3.2 Dynamical Behavior at a Constant, Nonzero Roll Rate	138
3.2.1 Generalized Homogeneous Response	138
3.2.2 Complete Response to Step Input	163
3.2.3 Complete Response to Impulse Input	167
3.2.4 Steady State Response to Sinusoidal Forcing at the Roll Rate	170
3.2.5 Roll Stabilization	178
4. Analytical Determination of the Dynamic Parameters	184
4.1 Normal Force Coefficients and Center of Pressure: the Barrowman Method	185
4.2 Locating the Center of Gravity	196
4.3 The Corrective Moment Coefficient	201
4.4 The Damping Moment Coefficient	203
4.5 The Longitudinal Moment of Inertia	205

4.6	The Radial Moment of Inertia	211
4.7	General Properties of the Parameters	213
5.	Experimental Determination of the Dynamic Parameters	216
5.1	Moments of Inertia: the Torsion-Wire Experiment	217
5.2	The Corrective Moment Coefficient	222
5.3	The Damping Moment Coefficient	229
6.	Model Rocket Design	234
6.1	Representative Parameters	235
6.2	Effects of Varying the Parameters	241
6.3	Rolling Rockets	249
6.4	Design Procedures and Criteria	254
6.4.1	Design Definition; Center of Gravity and Moments of Inertia	255
6.4.2	Static Stability Margin	255
6.4.3	Damping Ratio	255
6.4.4	Roll Rate	256
6.4.5	Construction and Testing	257

CHAPTER 3

THE AERODYNAMIC DRAG OF MODEL ROCKETS 261

William P. Bengen

Introduction 271

1.	Basic Considerations	276
2.	Basic Concepts Relating to the Study of Drag	280
2.1	Atmospheric Properties for Model Rocket Flight	280
2.1.1	Density	281

2.1.2 Viscosity and Kinematic Viscosity	286
2.2 Dimensionless Coefficients and Quantities	292
2.2.1 The Reynolds Number	292
2.2.2 The Drag Coefficient	299
2.2.3 The Coefficient of Pressure	302
2.3 Constituents of the Total Drag Coefficient	303
3. Viscous (Skin-Friction) Drag	308
3.1 The Importance of Viscosity in Real Fluid Flow	308
3.2 The Distinction Between Laminar and Turbulent Flow	313
3.3 The Laminar Boundary Layer on a Smooth, Flat Plate	316
3.4 The Turbulent Boundary Layer on a Smooth, Flat Plate	330
3.5 Boundary Layer Transition	342
3.5.1 Effects of Pressure Gradient and Reynolds Number	342
3.5.2 Effects of Surface Roughness	347
3.5.3 Skin-Friction Drag of Boundary Layers With Transition	355
3.6 Three-Dimensional Corrections to the Flat-Plate Skin-Friction Coefficients	357
3.6.1 Body Corrections	359
3.6.2 Fin Corrections	360
4. Pressure Drag	362
4.1 Introduction	362
4.2 Boundary-Layer Separation	363
4.3 Pressure Drag of the Forebody and Fins	376
4.3.1 Nosecone (Forebody) Pressure Drag	376
4.3.2 Fin Pressure Drag	387
4.3.3 Launch Lug Drag	388

4.4	Base Drag	391
5.	Other Contributions to Model Rocket Drag	400
5.1	Introduction	400
5.2	Drag at Small Angles of Attack	401
5.2.1	Body Drag at Angle of Attack	402
5.2.2	Fin Drag at Angle of Attack	412
5.2.3	Fin-Body Interference Drag at Angle of Attack	414
5.2.4	Total Drag Increase at Angle of Attack	417
5.3	Drag Due to Rotation	420
5.4	Drag Due to Surface Roughness in Turbulent Flow	424
6.	Calculation of the Zero-Lift Drag of Simple Model Rockets	429
6.1	The United States Air Force Stability and Control Datcom Method	429
6.1.1	Zero-Lift Drag Coefficient of the Fins	431
6.1.2	Zero-Lift Drag Coefficient of the Body	436
6.2	The Datcom Method Applied to the Javelin Rocket	443
6.3	General Analysis of the Datcom Method	453
6.3.1	The General Configuration Rocket (GCR)	454
6.3.2	Dependence of the Drag Coefficient on Reynolds Number for the General Configuration Rocket	460
6.3.3	Dependence of the Drag Force on Reynolds Number for the General Configuration Rocket	468
7.	Model Rocket Drag at Transonic and Supersonic Speeds	473
7.1	Limits on the Applicability of Incompressible Analysis	473
7.2	Drag Divergence	475
7.3	Semiempirical Determination of Transonic and Supersonic Drag Coefficients	478
8.	Experimental Determination of Drag Coefficients	484

8.1	Wind Tunnel and Balance System	485
8.2	Vertical Wind Tunnel	489
8.3	Vertical Drop Test	490
8.4	Conclusion	494

CHAPTER 4

ELEMENTS OF TRAJECTORY ANALYSIS 497

George J. Caporaso

Introduction 505

1.	The General Differential Equations of Motion	509
1.1	Mathematical Representation of the Flight Forces	514
1.2	Selection of the Coordinate System and Formation of the General Differential Equations of Motion	517
2.	The Non-Oscillating Rocket: Solutions for Vehicles Launched Vertically	520
2.1	The Specialized Differential Equation for the Vertical Case	520
2.1.1	Fehskens-Malewicki Solution	522
2.1.2	Caporaso-Bengen Solution	523
2.1.3	Caporaso-Riccati Solution	525
2.2	Extension of the Solutions to Multistaged Vehicles	528
2.2.1	Extended Caporaso-Bengen Solution	529
2.2.2	Extended Fehskens-Malewicki Solution	535
2.3	Solutions for a Non-Oscillating Rocket in the Coasting Phase	539
2.4	Numerical Methods for the Digital Computation of Altitude Performance	541
2.5	Validity of the Approximate Methods Compared to Numerical Solutions by the Interval Method	553

3.	The Non-Oscillating Rocket: Solutions for Vehicles Launched at Any Angle From the Vertical	564
3.1	The Differential Equations of Motion	564
3.2	Numerical Methods for the Digital Computation of Nonvertical Trajectories	564
3.3	Examples of Nonvertical Model Rocket Trajectories	568
4.	Coupling of Dynamic Oscillations to the Trajectory Equations	578
4.1	The Differential Equations of Motion With Perturbation Terms	579
4.2	A Numerical Method for the Digital Computation of Altitude Performance in Cases of Oscillating Rockets	582
4.3	Solutions for Standard Forcing Functions	585
4.3.1	Homogeneous Response for General Initial Conditions	586
4.3.2	Step Response	588
4.3.3	Impulse Response	590
4.3.4	Response to Sinusoidal Forcing	591
4.4	The Effect of Dynamic Oscillations on the Altitude Performance of a Typical Model Rocket	594
5.	Recapitulation and Qualitative Features of the Analytical Results	602
5.1	Bengen's Maxima	603
5.2	Model Rocket Design Optimization	606
5.2.1	Initial Design Definition	607
5.2.2	Drag Coefficient	607
5.2.3	Weight Optimization	608
5.2.4	Dynamic Stability Optimization	610
5.2.5	Reduction of Drag at Angle of Attack	611
5.2.6	Philosophy of Design and Flight	611

APPENDIX A

CORRESPONDENCE BETWEEN METRIC AND ENGLISH UNITS 617

APPENDIX B

PHYSICAL CONSTANTS AND PARAMETERS 618

APPENDIX C

CORRESPONDENCE BETWEEN SCIENTIFIC AND DECIMAL NOTATION 620

APPENDIX D

A WORD ABOUT THE NATIONAL ASSOCIATION OF ROCKETRY 621

FIGURE CREDITS 623

CHAPTER 1

AN INTRODUCTION TO THE DYNAMICS OF MODEL ROCKET FLIGHT

George J. Caporaso

and

Gordon K. Mandell

SYMBOLS

<u>Symbol</u>	<u>Meaning</u>
A	coefficient used in writing example of $F(t)$
A_r	reference area
C	constant of integration
c_D	drag coefficient
c_{D0}	coefficient of drag at zero angle of attack
c_n	normal force coefficient
D	drag
F	magnitude of thrust, whose direction is assumed to be forward along the vehicle centerline
\vec{F}	thrust
$F(t)$	thrust as a function of time
F_{av}	average thrust
F_1, \dots, F_8	thrust values used in computing total impulse by approximate summation method
I_{sp}	specific impulse
I_t	total impulse
L	characteristic length
N	normal force
R	radius measured from the center of the Earth
R_e	Reynolds number
R_o	radius of the Earth
S	side force
c	magnitude of exhaust velocity, whose direction is assumed to be rearward along the vehicle centerline

<u>Symbol</u>	<u>Meaning</u>
\vec{c}	exhaust velocity
$d(\)$	differential of ()
$d(\)/dt$	derivative of () with respect to time
$f(\)$	function of angle of attack
g	magnitude of acceleration of Earth's gravity
\vec{g}	acceleration of Earth's gravity
g_0	value of g at sea level
k	parameter of drag at zero angle of attack
m	mass
m_b	burnout mass
m_f	propellant mass
m_0	initial mass
\dot{m}	mass flow rate
Δm_e	increment of mass added to the exhaust stream
Δm_r	change in mass of rocket
n	exponent of t used in writing example of $F(t)$
t	time
t'	time at which a time-derivative is computed
Δt	interval of time
$\Delta t_1, \dots, \Delta t_8$	time intervals used in computing total impulse by approximate summation method
t_b	burn time
v	magnitude of velocity; <u>also</u> airspeed
\vec{w}	weight
w_f	weight of propellant charge
x	horizontal coordinate, range
y	vertical coordinate, altitude

<u>Symbol</u>	<u>Meaning</u>
$\Delta()$	increment of (), change in ()
$\Delta()$	sum of all ()
α	angle of attack
ϵ	parameter of drag due to angle of attack
μ	absolute viscosity
ν	kinematic viscosity
ρ	mass density
$\lim_{n \rightarrow \infty}$	limit as n approaches infinity
$\int [] d()$	integral of [] with respect to ()

AN INTRODUCTION TO THE DYNAMICS OF MODEL ROCKET FLIGHT

1. Definition of the Problem

There is probably not a single model rocketeer in the world who has not, at one time or another, found himself speculating on the subject of model rocket flight performance. How high, how fast will a rocket go? Will it fly straight and true or not? Will it "weathercock" -- that is, fly into the wind? Will it wobble on the way up? How high will it go if launched at an angle, and how far? Such questions as these are the most natural and common that come to mind when one is presented with a new rocket design. They are of interest to even the most casual sport flyer, and of course are the vital concerns of competition rocketeers and researchers. It is the purpose of this book to present information that will enable any interested model rocketeer with a reasonably complete educational background to answer them accurately and completely, using the most advanced and general methods available in our hobby to date.

The mathematical equations that would have to be solved to compute theoretically exact answers to the questions of model rocket flight performance are among the most difficult known to the physical sciences. Complete, exact, and unique solutions to these equations have never been obtained by anyone, whether model rocketeer or professional scientist.

As do professional scientists and engineers, therefore, we shall formulate the problems subject to certain simplifying approximations and assumptions that will permit them to be solved to a high order of accuracy. Such approximations make solutions possible but this still gives us no right to expect them to be easy, and indeed we invariably find that they are quite difficult to obtain in "closed form" -- that is, a form which can be expressed by a single algebraic formula; not, for instance, a graph, a table, or an infinite series. This is because the most liberal approximations that are possible without badly degrading the accuracy of the desired solution still cannot alter the fact that the equations describing the motion of a model rocket at any given instant during its flight are of a type called differential equations, and as such cannot be solved without the methods of differential and integral calculus. We have used these methods extensively in compiling the material used in this book and have used the various notations of calculus freely in describing the steps by which flight performance solutions are obtained, both for the interest of those advanced rocketeers who are familiar with calculus and because there is simply no other way of discussing these matters accurately. We know very well, however, that only a small fraction of our readers can be expected to have any knowledge of advanced mathematics, and we have adjusted our presentation accordingly. You should not, therefore, become discouraged if you cannot follow the various mathematical treatments describing how the solutions are obtained. As a practical model rocketeer you will be most

interested in the final results of these presentations -- the solutions themselves. And in every case you will find that these solutions can be worked out numerically using relatively simple numerical substitutions in the algebraic formulae which have been obtained, plus a handbook of mathematical tables.

In this chapter the general problem of computing model rocket flight performance will be considered, and the various techniques used to cast these problems into forms capable of closed-form, analytic solution will be discussed. The forces which influence the motion of model rockets will be briefly described and the methods by which the performance problems will be attacked in subsequent chapters will be introduced, while the presentation of the detailed solutions themselves will be left for the chapters reserved for them.

1.1 Point-Mass and Rigid-Body Dynamics

The problem of computing in detail the motion of a model rocket in flight is one of analytical dynamics and kinematics. By "kinematics" is meant the mathematical study of movement itself, while "dynamics" can, for the purposes of this book, be taken to mean the physical and mathematical study of the relationships between movement and the various forces and moments which produce it. In general, one can distinguish two classes of motion of which rigid, extended bodies are capable: the translational motion of the body considered as a point mass concentrated at its center of mass and the rotational motion described by the body about its center of mass. Since, for all purposes of interest to model rocketeers, the center of

mass of an object can be considered equivalent to its center of gravity, the notation C.G. will hereafter be used to refer to a model rocket's center of mass or center of gravity. The concepts of translation and rotation are illustrated by example in Figure 1.

In the absence of any physical interrelation between the motion of the C.G. itself and the rotation of the model about its C.G. the differential equations describing the rocket's motion would possess a certain very useful and valuable property: the equations describing the rigid-body rotations would be decoupled from those describing the point-mass motions. That is to say that, if the rotation of the model about its C.G. in flight did not affect the net forces acting on it, and if the translational motion of the rocket as a point mass did not affect the moments tending to rotate the model about its C.G., the equations of motion of the C.G. and the equations of motion for the rigid-body rotations could be solved independently of one another. The practical effect of such a state of affairs would be to greatly simplify the mathematics involved, since the translational motion could be solved while ignoring rotation and the rotational motion could be solved while ignoring translation.

For any extended body moving through the atmosphere in the Earth's gravitational field, however, there are external forces and moments which couple the rigid-body rotation to the C.G. translation. These external forces and moments arise from the various components of atmospheric resistance, or drag,

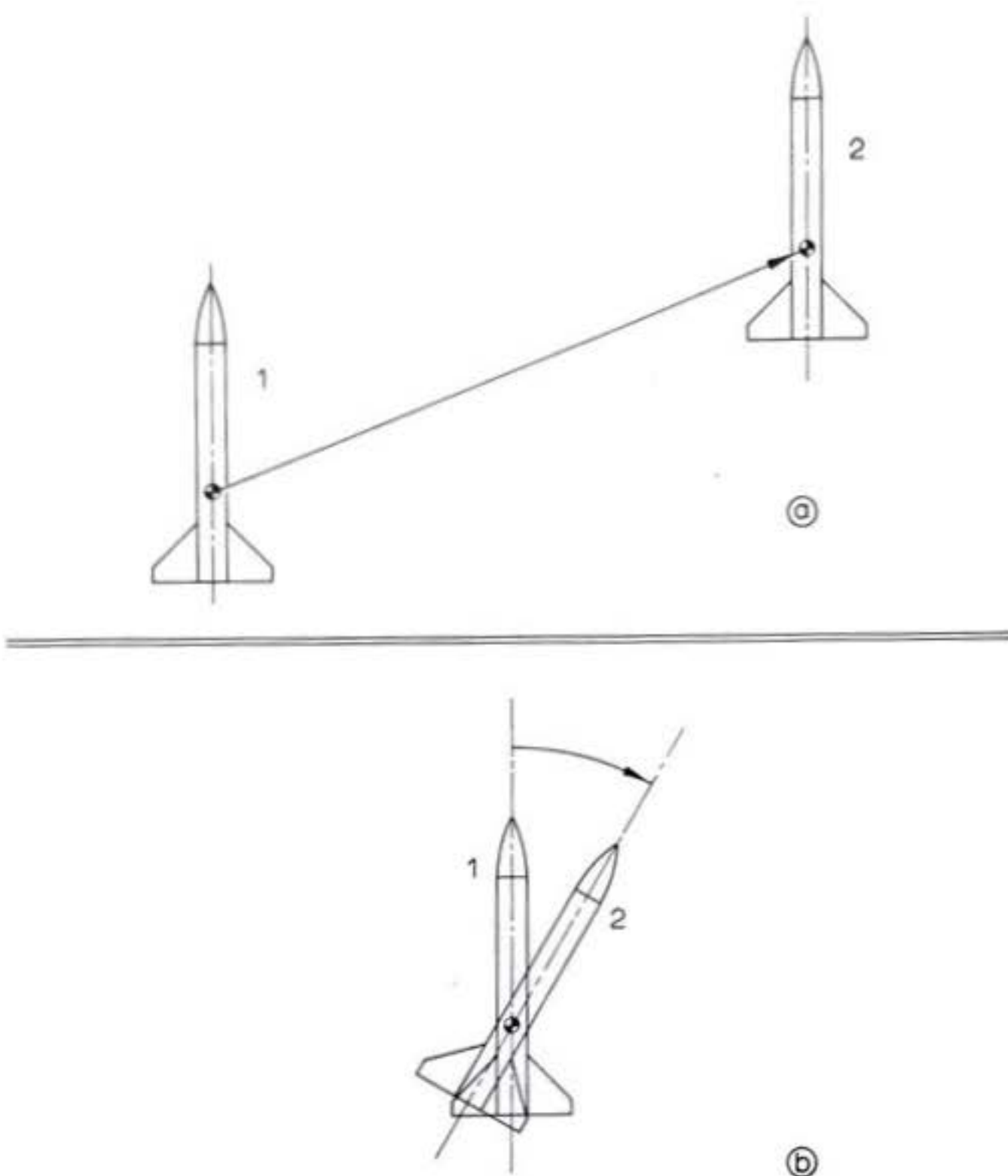


Figure 1: Translational and rotational motion. The center of gravity of the rocket in illustration (a) has translated from position 1 to position 2; the rocket has not rotated at all during the motion. The rocket of illustration (b) has rotated from position 1 to position 2 about its center of gravity without undergoing any translation.

acting on the body which affect both the C.G. motion and the rigid-body motion. If the model should undergo rigid-body motion due to aerodynamic or other forces, the changes in its angle to the incident airflow resulting from such motion will change the drag experienced by the vehicle, thus affecting the total force on it. In the presence of gravity, the rigid-body rotations will also change the angle of the thrust vector with respect to the local vertical and will therefore change the vertical and horizontal components of the force on the model due to the thrust. The point-mass motion also influences the rigid-body motion, since the magnitude of the drag components which act to rotate the vehicle vary strongly with the velocity of the C.G. The differential equations of motion of a model rocket travelling through the atmosphere under the influence of gravity are, therefore, a coupled set of equations.

1.2 Separation of the Differential Equations of Motion

Since, as we have remarked, it is generally much easier to solve a system of mutually independent equations than it is to solve a coupled set, the authors of the various chapters have followed the procedure generally used in full-scale science and engineering for problems of this type by adopting various simplifying approximations which permit the point-mass and rigid-body equations of motion to be decoupled (and also greatly simplify the solution of each of the decoupled sets). Such a separation cannot result in exact solutions; it will yield solutions of acceptable accuracy only if the coupling between the two types of motion is slight or "weak" in some sense.

The analyses of model rocket flight presented in this book will therefore be restricted to cases of weak coupling. As will be shown in Chapter 2, and later in Chapter 4, the coupling is in fact slight for all rockets that can be considered well-designed, so such a restriction is not unreasonable. One may therefore decouple the equations of motion under the assumption that the forces on the C.G. due to the rigid-body rotations are small compared to the other forces influencing the point-mass motion.

Once the separate solutions to the decoupled equations of motion have been obtained, approximate methods will be used to re-introduce coupling for the purpose of obtaining a "first-order" idea of the effect of rigid-body motions on the altitude capability of any given model rocket.

The remaining sections of this chapter will be devoted to brief discussions of each of the forces and moments which influence the rigid-body and point-mass motion of model rockets.

2. Description of the Flight Forces

This section will enumerate and consider the forces on the model which give rise to the motion of its center of mass. Such forces will hereafter be referred to as flight forces, as opposed to those forces encountered during the course of a model's flight whose moments give rise to rigid-body rotations. These latter forces will be referred to as perturbing forces.

2.1 Thrust

Thrust is the term applied to the force produced by a model rocket engine due to the rapid exit of exhaust gases

from its nozzle. The engine itself is no more than an enclosed furnace in which the fuel is burned to produce a hot gas which then exits under extreme pressure from a small nozzle specially shaped so as to produce the greatest possible velocity of the exhaust stream. A chemical rocket, however, is a highly specialized type of furnace in that the oxygen required for the combustion of the fuel is obtained not from the air, but from an oxygen-rich chemical, or oxidizer, carried along with the fuel in the rocket itself. For this reason a rocket will continue to burn in the vacuum of outer space, and hence chemical rockets are used in spaceflight. In the case of the solid-propellant model rocket engine the fuel and oxidizer are mixed together to form a homogeneous propellant grain.

To gain some understanding of how a rocket engine produces thrust, suppose we examine the hypothetical rocket of Figure 2, which is emitting gas at a constant exhaust velocity of magnitude c in the negative y direction. In some short interval of time, say Δt , a mass of exhaust gas Δm_e leaves the nozzle, so that the mass of the rocket engine changes by the amount $\Delta m_r = -\Delta m_e$. If the time interval is permitted to become so short as to be what mathematicians refer to as infinitesimal it may be denoted by dt , also referred to in the language of calculus as the differential of time. In this case the mass change experienced by the rocket will also become so small as to be considered a differential quantity, denoted by $-dm_e$. The instantaneous rate at which the mass of the rocket is changing is then given by the ratio of the differential mass change to the differential

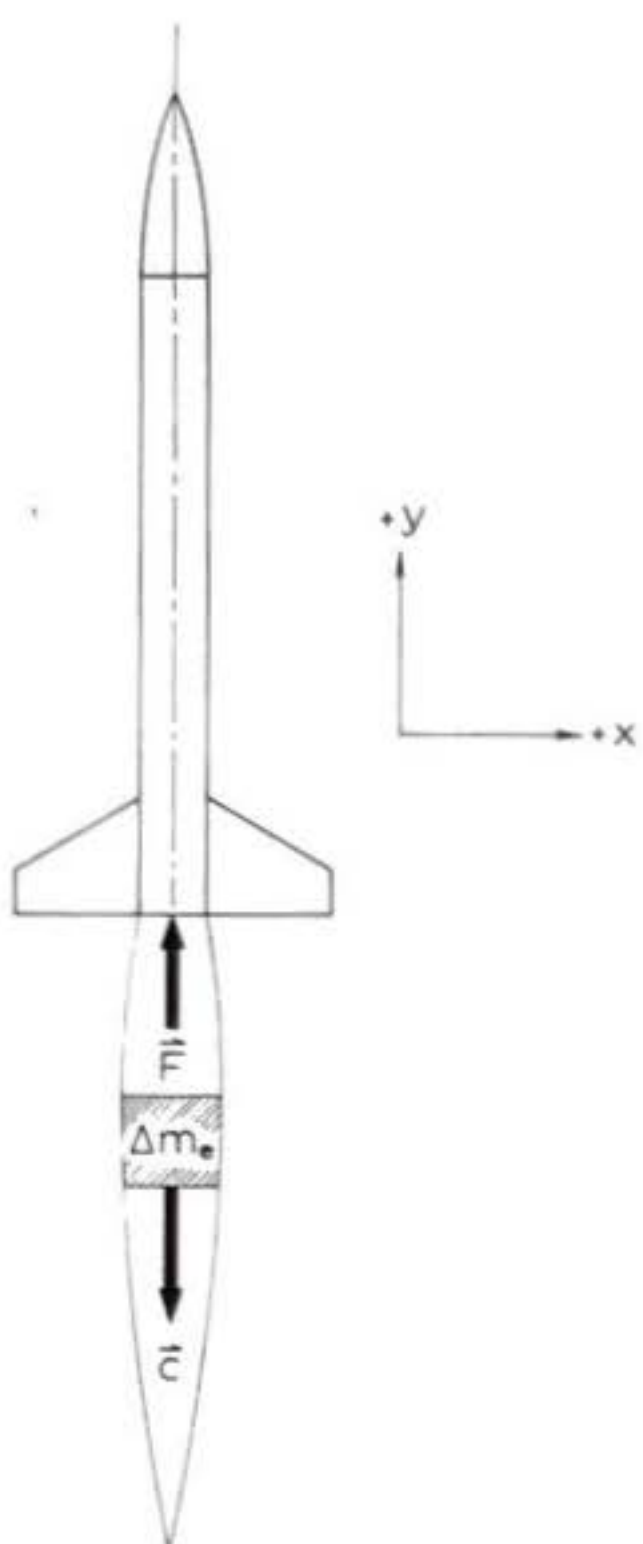


Figure 2: Origin of rocket thrust. In a time interval Δt the rocket expels the quantity of mass Δm_e at the exhaust velocity \vec{c} in the (-y) direction. "In the limit" as Δt becomes dt and Δm_e becomes dm_e the rate of mass expulsion -- or "mass flow rate" -- is dm_e/dt (also written \dot{m}). The thrust \vec{F} is given by the equation $\vec{F} = -\vec{c}(dm_e/dt)$ and thus acts in the (+y) direction.

time interval over which that change occurs. This ratio is also called the derivative of the rocket's mass with respect to time:

$$\text{rate of mass change} = \frac{-dm_e}{dt}$$

= derivative of mass with respect
to time

The above explanation of the derivative as a ratio of differentials is useful in forming a mental picture of what a derivative physically represents, but it provides no information about how derivatives are actually computed. They are not calculated by somehow finding each differential and taking the ratio of the two; they are, rather, done "all at once" by one of two possible methods. The first such method is usable when the dependent variable (in this case mass) is given as an analytic function of the independent variable (in this case time); that is, when the dependent variable is expressed as some algebraic formula in terms of the independent variable. In such cases the derivative is itself an algebraic formula which is computable from the original function by means of the limiting arguments used in differential calculus. You will not need to know how to perform any such calculations to understand this book; wherever the derivative of an algebraic expression is needed we will supply it already written out. The second method is an approximate one and is used when the function whose derivative is to be taken is supplied in graph or table form. In the case of a graph, the derivative at any given time t' is just the slope of the tangent line touching the graph at

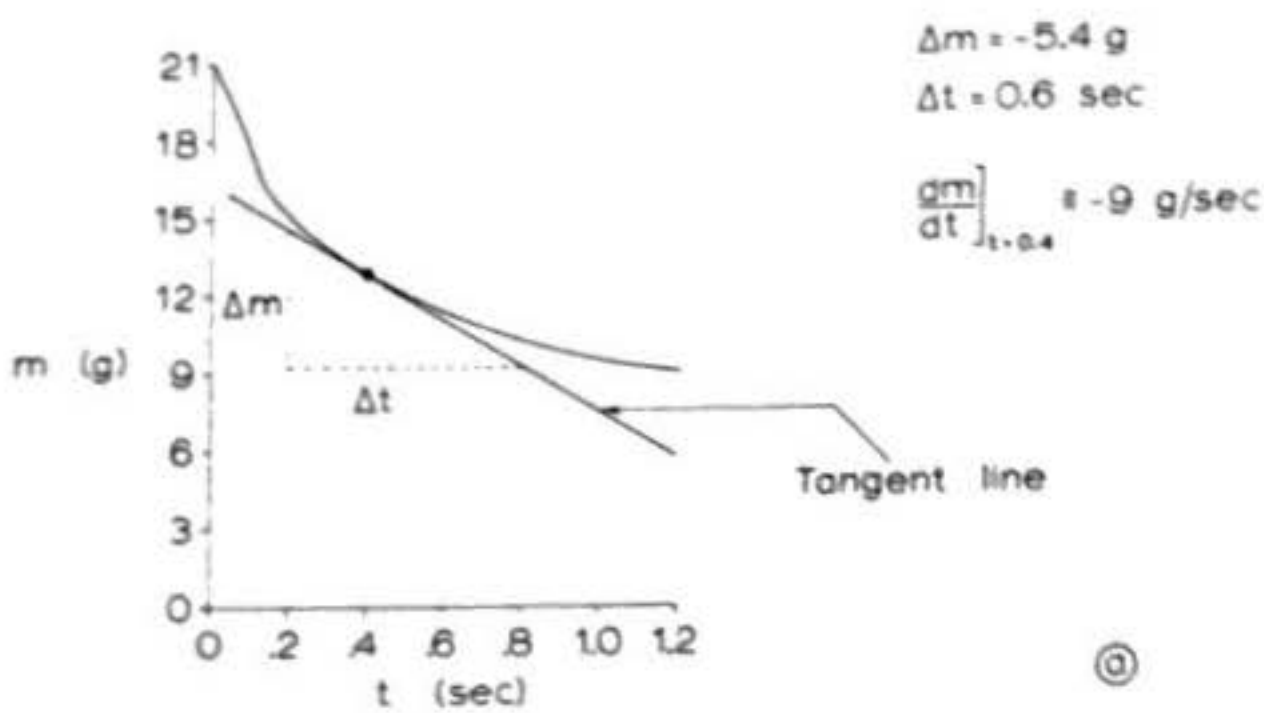
that value of time. The meaning of these terms is indicated by the example in Figure 3, which also describes the procedures for obtaining derivatives from graphs and tables.

Now the connection between the time derivative of a rocket's mass and the thrust of its engine lies in the fact that the thrust of a rocket motor is equal to the rate at which it is transferring momentum to the rocket in which it is mounted. Those of you who have had some exposure to elementary physics will be familiar with the concept of momentum; some of you, moreover, may already know that the rate of momentum transfer resulting from the expulsion of mass from a body depends upon two quantities: the rate at which mass is being expelled and the velocity with which it is being ejected. In Chapter 4 it will be shown by more detailed momentum considerations that the relationship involved is

$$(1) \quad \vec{F} = -\vec{c} \frac{dm_e}{dt}$$

where \vec{F} denotes the thrust produced by the motor and \vec{c} is the velocity of the exhaust gases as measured by an observer moving with the rocket. Both the thrust force and the exhaust velocity, students of physics will note, are vector quantities; that is, both their magnitudes and the directions in which they act must be specified to describe them completely. Mass (and its time derivative), on the other hand, is a scalar quantity; it can have only a magnitude.

In a properly designed and constructed model rocket whose engine is not suffering from any malfunction the exhaust stream



t (sec)	m (g)	$\Delta m = 11.3 - 15.1 = -3.8 \text{ g}$
0.0	21.0	$\Delta t = 0.6 - 0.2 = 0.4 \text{ sec}$
0.2	15.1	$\frac{dm}{dt} \Big _{t=0.4} = -9.5 \text{ g/sec}$
0.4	12.8	Δm
0.6	11.3	
0.8	10.2	
1.0	9.4	
1.2	9.0	

(b)

Figure 3: The concept of a derivative, as illustrated by the rate of mass change of a model rocket engine due to the expulsion of exhaust gases. Two approximate methods for the computation of derivatives are illustrated: graphical solution by the use of a "tangent" line (a) and numerical solution using a table (b). Note that Δm is negative because mass decreases as time increases. dm/dt as illustrated here is just the negative of dm_e/dt .

is directed dead astern. In such a case we can replace the full vector notation for force and velocity with a simpler, fore-and-aft sign convention in which vector quantities directed forward along the vehicle longitudinal axis are considered positive, while those directed rearward are considered negative. According to this convention.

$$\vec{c} \equiv -c$$

so that

$$(2) \quad F = C \frac{d m_e}{dt}$$

Professional rocket engineers refer to the derivative $d m_e / dt$ as the mass flow rate and sometimes write it as \dot{m} , the superscript dot denoting differentiation with respect to time (an alternate calculus notation for the time derivative which is sometimes used to save writing). Note that, since positive quantities only are involved in the right-hand side of equation (2), the thrust is a positive quantity also -- confirming what we as practical model rocketeers already know to be the case; namely that the thrust is directed forward along the rocket's centerline.

In theory, then, if you were given the exhaust velocity and mass flow rate of any given rocket motor as functions of time, you could compute the thrust of that motor as a function of time. It is also theoretically possible to calculate both the exhaust velocity and the mass flow rate from the combustion characteristics and thermodynamic properties of the propellant and the size and shape of the combustion chamber and the nozzle. In practice, however, rocket engineers generally compute the thrust directly from the propellant, casing and nozzle characteristics and obtain the exhaust velocity and mass flow rate as byproducts of this calculation. The thrusts of model rocket engines as functions of time are always supplied by the manufacturers in graphical form: the so-called thrust-time curves, which are derived from averaging a large number of traces recorded during static firings of engines of the same type. The thrust-time curves of individual model rocket motors may differ somewhat from the average for their type. This variation is not too severe, however, in motor types which have received Safety Certification or Contest Certification from the Standards and Testing Committee of the National Association of Rocketry.

In any one given engine, one generally finds that variations in thrust with time are due more to variations in the mass flow rate than variations in the exhaust velocity. In fact, it is almost always accurate enough for model rocketry purposes to assume the exhaust velocity to be constant during the entire burning period. The mass flow rate can then be easily computed from equation (2) if you are careful with units. Suppose, for

instance, that the thrust is given in newtons and the exhaust velocity in meters/second. Remembering that one newton is one kilogram-meter/(second²), one then obtains the mass flow rate in kilograms/second, which can easily be converted to grams/second by multiplying by a thousand. An easy method of calculating the average exhaust velocity will be described a little later on.

Model rocket engines come in a wide variety of sizes and configurations, permitting the modeler to choose any desired average thrust from as low as 3 newtons to as high as 100 newtons. A knowledge of the average thrust alone, however, is not sufficient to enable one to predict the overall effect of the engine on the rocket's performance. It is also necessary to know how the thrust varies as a function of time and the length of time for which the engine will burn. Knowing these the modeler can compute the total momentum change which the engine will impart to the rocket, also called the total impulse, according to the relation

$$(3) \quad I_t \equiv \int_0^{t_b} F(t) dt$$

where I_t is the total impulse, $F(t)$ is the calculus notation for "thrust as a function of time", and t_b is the total burning time (not counting the delay/tracking charge) of the engine. Equation (3) is the first we have encountered so far needing the techniques of integral calculus for its solution. The symbol \int is referred to as an integral sign. The quantity to be "integrated" (in this case $F(t)$) is called the integrand, and the variable with respect to which the integration is to be

performed; that is, the independent variable (in this case time, or t) is referred to as the variable of integration, or running variable. The differential of the running variable is always written after the integrand to identify the running variable; hence the "dt" after $F(t)$. The time values 0 and t_b are the limits of integration, and the integration is said to be performed between 0 and t_b , or from 0 to t_b .

As far as model rocketeers are concerned there are two ways in which an actual number for I_t can be obtained from equation (3). The first of these can be used only if $F(t)$ is given by some well-defined algebraic formula, in which case mathematicians have shown that there also exists an algebraic formula for $\int F(t)dt$ (the integral written without limits is called an "indefinite integral" and is used to refer to the general functional form of the integral as opposed to the integral written with limits, or "definite integral", which refers to the actual value of the integral taken between specific limits). The integrals of a great many specific functions have been tabulated and listed in such books as Burlington's Handbook of Mathematical Tables and Formulae and the CRC Standard Mathematical Tables, which are used as references by students of science and engineering. For instance, if the functional form of $F(t)$ is given by

$$F(t) = At^n$$

where A and n are constants, then

$$\int F(t)dt = \frac{A}{n+1} t^{(n+1)} + C$$

where C is a "constant of integration" which must generally be determined by physical considerations called the "initial conditions" of the problem. Of particular interest is the case $n = 0$, which describes a thrust that is constant over the burn time:

$$\begin{aligned}F(t) &= At^0 \\&= A\end{aligned}$$

Then

$$\int F(t)dt = At + C$$

It will be found that, in all problems of computing total impulse, C is zero. Now it is a basic rule of calculus that the value of a definite integral is equal to the value of the integral taken at the upper limit minus the value taken at the lower limit. That is, in this case,

$$\begin{aligned}\int_0^{t_b} F(t)dt &= At]_{t=0}^{t=t_b} - At]_{t=0} \\&= At_b - A \cdot 0 \\&= At_b\end{aligned}$$

So you can see that for the case of constant thrust the total impulse is just equal to the thrust multiplied by the burn time. In fact, the total impulse is always equal to the average thrust multiplied by the burn time, but for all cases other than that of constant thrust the average thrust itself must be calculated from the total impulse, which has been determined from (3), according to

$$(4) \quad F_{av} = I_t/t_b$$

You can also see that total impulse has units of (force x time). Since model rocket thrust is measured in newtons and time in seconds, total impulse is given in newton-seconds.

But suppose there is no simple algebraic formula that describes $F(t)$. Suppose there is either no known formula at all or one so complicated that its integral would literally cover pages. In such cases the total impulse can be computed numerically, without integral formulae. To see how this is done suppose we take as an example the thrust-time curve of Figure 4a, which is typical of many of the smaller classes of model rocket engines: there is an initial "spike" at ignition followed by a drop-off to a fairly constant thrust for the rest of the burn time. In Figure 4b the exact thrust-time curve has been approximated by a series of eight adjacent rectangles. There are many mathematically "fancier" and more precise ways to do this, but in Figure 4b it has been done "by eye" and indeed such an intuitive, physical approach will be found sufficiently accurate for virtually all model rocketry work. The total impulse according to this method is given approximately by

$$I_t \approx F_1\Delta t_1 + F_2\Delta t_2 + F_3\Delta t_3 + F_4\Delta t_4 + F_5\Delta t_5 + F_6\Delta t_6 + \\ F_7\Delta t_7 + F_8\Delta t_8$$

It is evident that more than eight rectangles can be used, and that the approximation will get better as the number of rectangles increases and they get narrower and narrower. "In the limit", as the rectangles get infinitesimally thin, the approximation will become exact -- and in fact this is just the definition of

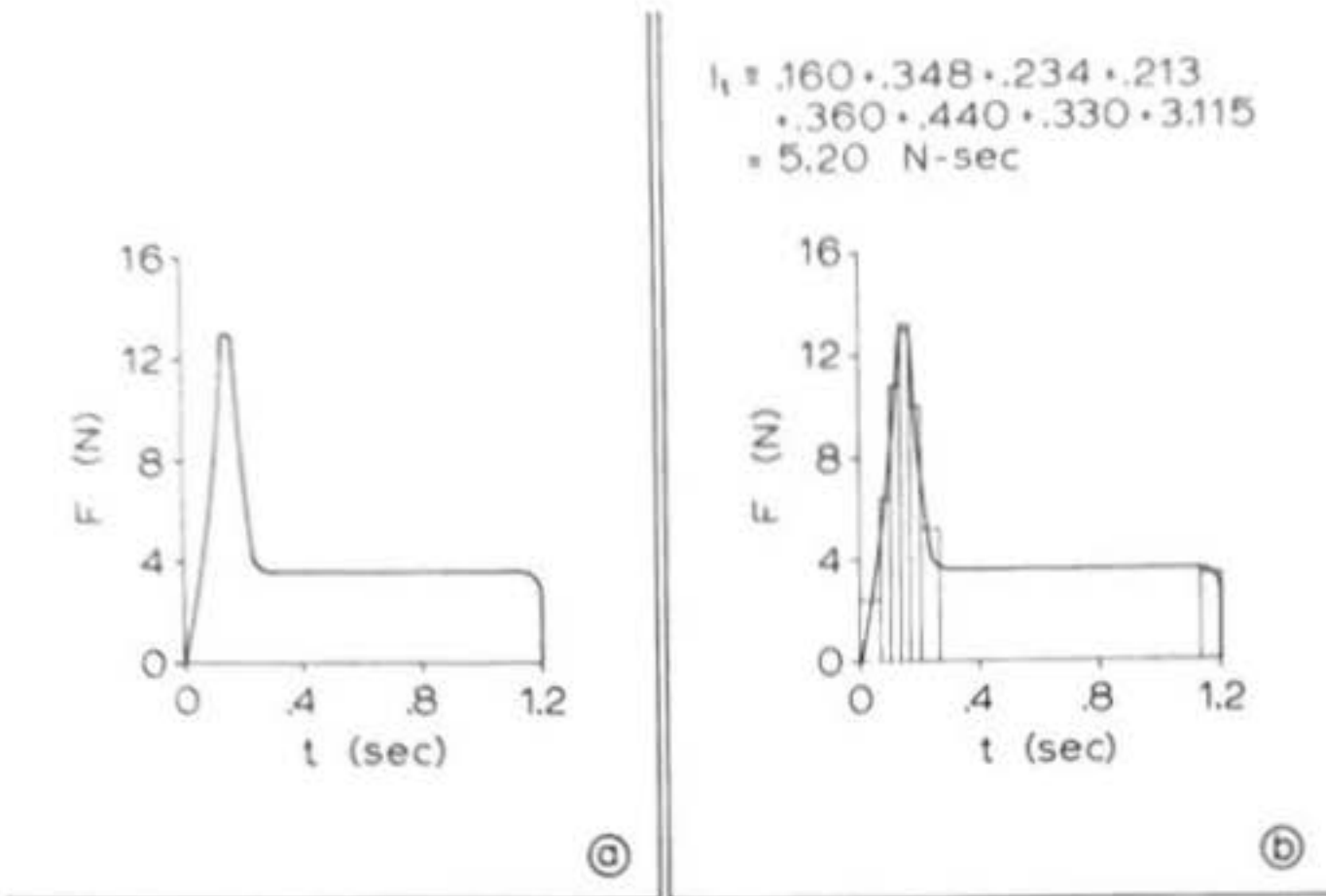
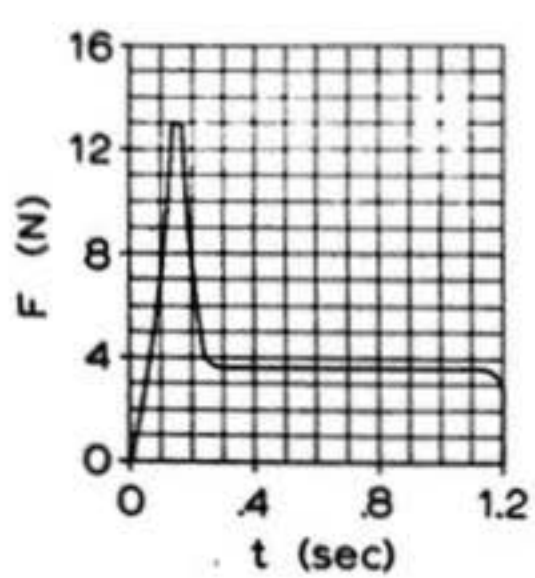


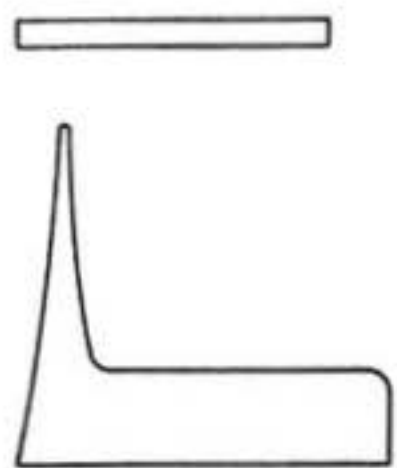
Figure 4: Total impulse and the concept of integration. Panel (a) shows the thrust-time curve of the NAR Type B4 engine. The total impulse I_t of the engine is equal to the integral of its thrust-time curve; that is, to the area (in N-sec) enclosed by it. The other three panels show some approximate methods of obtaining this integral. In (b) the curve has been approximated by a series of rectangles and I_t has been computed as the sum of the areas (in N-sec) of the rectangles. In (c) each square of the grid represents 0.1 N-sec and I_t is found by determining the approximate number of squares enclosed by the curve. In (d) the weight in gram-forces of a piece of cardboard 1 sec long and 1 N high has been determined and I_t has been found by comparing it with the weight of a cardboard cutout of the curve. Method (d) was most accurate in this case, as the actual I_t of the B4 engine is 5.0 N-sec.

$$I_t = 49.7 \times 0.1 \\ = 4.97 \text{ N-sec}$$



(c)

$$0.38 g = 1.0 \text{ N-sec}$$



(d)

the integral as used in calculus, for which the mathematical notation is

$$\lim_{n \rightarrow \infty} \sum_1^n F_i \Delta t_i = \int_0^t F(t) dt$$

A similar numerical method consists of "counting the squares on the graph paper" enclosed by the thrust-time curve and the axes. The number of newton-seconds represented by each square can be found from a knowledge of the vertical and horizontal graph scales. The impulse per square is then multiplied by the number of squares to give the total impulse, as shown in Figure 4c. An instrument called a planimeter is often used to compute total impulse in this manner. The instrument has a stylus which is used to trace the boundary of the thrust-time curve, resulting in a measurement of the area enclosed by the curve. The total impulse is directly proportional to this area, the constant of proportionality being equal to the amount of impulse represented by a unit area of the graph paper. Persons who do not have a planimeter can still make a good planimetric determination of total impulse using the method of Figure 4d. In this technique the thrust-time curve is traced onto cardboard, cut out, and weighed on a good laboratory gram balance. A rectangle of the same kind of cardboard cut to the size that represents a single newton-second of impulse in the scale to which the thrust-time curve is drawn is also weighed. The weight of the curve cutout divided by the weight of the one newton-second rectangle is then equal to the total impulse. You can see that all these numerical methods rely on the

essential relationship between the integral of a function and the area enclosed between the graph of that function and the coordinate axes with respect to which that graph is drawn. Appeals to the intuitive notion of an integral as "the area under the curve" of the integrand are in fact often used in teaching calculus at the senior high school and undergraduate college level.

The particular functional forms of $F(t)$ encountered in model rocketry fall into several well-defined classes. These categories are represented by the sample thrust-time curves of Figures 5a, 5b, and 5c. The curve of Figure 5a exemplifies the behavior of a typical end-burning motor. The vast majority of the NAR Class $\frac{1}{2}$ A through D engines, as well as some of the larger engines, have thrust-time curves of this type. Such engines are produced with a solid propellant grain having a slight indentation at the rear, immediately inside the nozzle. The indentation serves a dual purpose: it provides a convenient cavity into which the electrical igniter may be packed and it is also responsible for increasing the burning surface area of the propellant grain in the fraction of a second immediately following ignition, thereby producing the "spike" in the thrust-time curve shown in Figure 5a. This short period of higher thrust is useful in accelerating the model rapidly to velocities at which the stabilizing fins become effective. Thereafter the thrust decreases to the virtually constant level characteristic of a true end-burning, or "cigarette-burning", grain until burnout occurs.

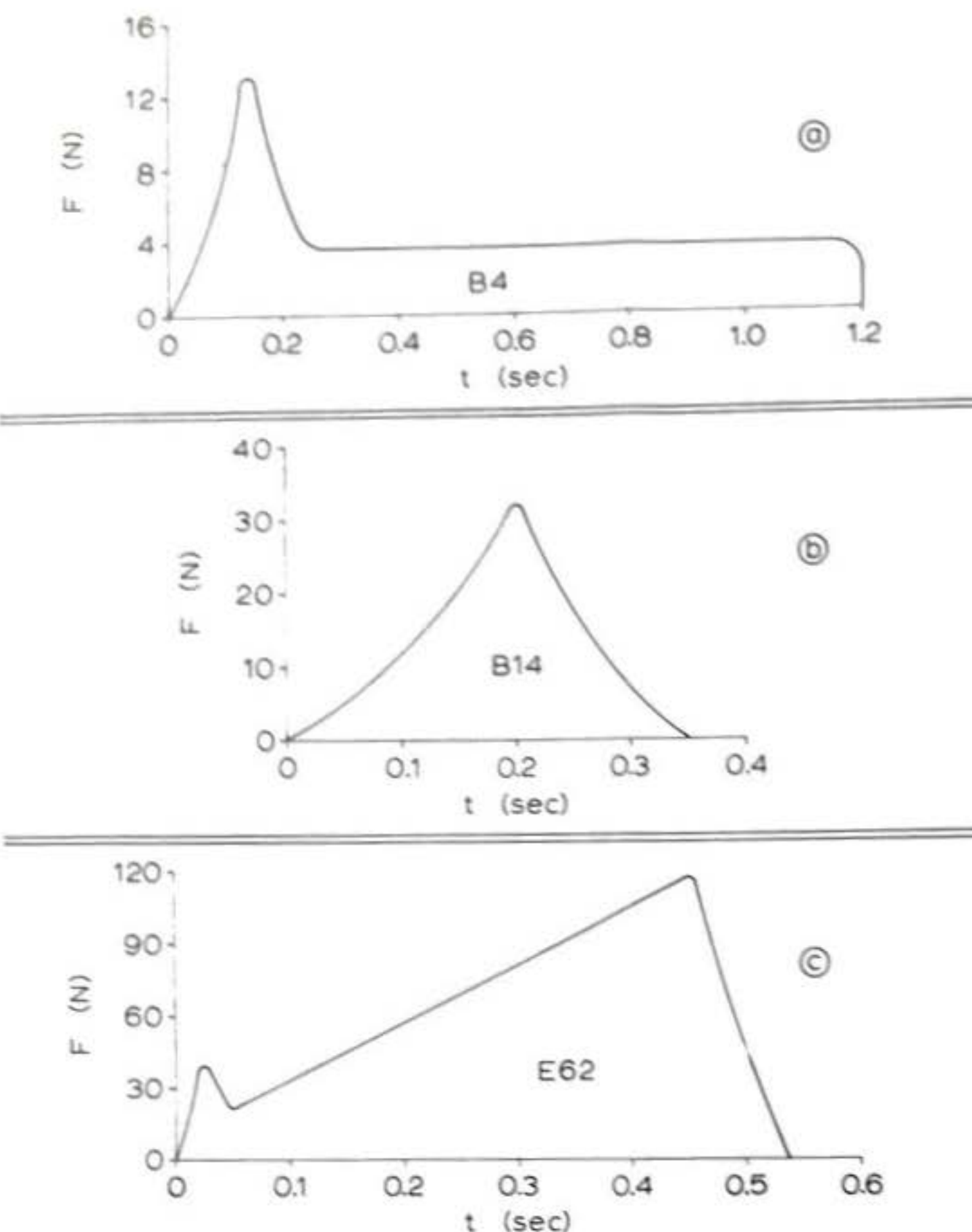


Figure 5: Major classes of model rocket thrust-time curves.

(a): Curve of Type B4 engine, representative of end-burning engines with initial peak. (b): Curve of Type B14 engine, a core-burning engine with a constant-diameter port. (c): Curve of Type E62 engine, an ammonium perchlorate/polyurethane engine also having a constant-diameter port. Its high-energy propellant is slow-burning, enabling it to produce thrust-time characteristics that would require a tapered port in a blackpowder engine.

Figure 5b represents the thrust-time curve of the NAR type Bl4 motor, a high-thrust, short-time engine used to accelerate heavy rockets and multistaged models. These engines have a hollow core, or port, along the central axis of the grain, causing burning to progress radially outward toward the wall of the casing rather than forward as in the end-burning motors. The burning surface area of the core-burning motor is thus much greater than that of the end-burner and its thrust-time curve consists of a single, high-thrust spike. The rapidity with which these engines can accelerate a model has been described by stating that they deliver a "sledge-hammer blow" or "kick in the tail" to the rocket in which they are installed.

Many of the largest model rocket engines -- those in NAR Classes E and F -- have thrust-time curves like that of Figure 5c. These engines are also port-burners but, unlike the Bl4, they have tapered ports; their grain configurations are said to be "three-dimensional". Although they also exhibit a characteristic peak in their thrust-time behavior, this peak is attained more gradually than is the case with the Bl4 engines and occurs near the end of the burning period.

Since the invention of the rocket in China during the Middle Ages a great many varieties of solid propellant have been developed. The first rockets used black gunpowder, an improved form of which is still the major constituent of most model rocket propellants. Smokeless powder was introduced at the beginning of the twentieth century, followed by "double-base" propellants -- essentially variations of nitroglycerin- and nitrocellulose-type compounds -- and "composite" propellants

like the polyurethane/ammonium perchlorate mixtures used in the Polaris and Minuteman guided missiles and many sounding rockets currently in use. When selecting a propellant from among the many available types, one of the first questions the rocket engineer asks is, "How powerful is it?" The answer to this question lies in a quantity called the specific impulse of the propellant; that is, the total impulse obtainable from the combustion of a unit mass of propellant. Specific impulse is thus a measure of a propellant's efficiency. Strictly speaking, the mathematical definition of specific impulse is

$$(5) \quad I_{sp} = I_t/m_f$$

where m_f is the mass of propellant consumed in providing the total impulse I_t . The strictly consistent physical units for I_{sp} in the MKS system used in model rocketry are therefore newton-seconds per kilogram. Rocket engineers, however, use weight measure when computing specific impulse, using the definition

$$(6) \quad I_{sp} = I_t/w_f$$

where w_f is the weight of propellant required to produce the total impulse I_t . According to this definition I_{sp} has units of newton-seconds per newton -- or simply seconds. The engineering definition is especially convenient in that it relates I_{sp} to the exhaust velocity through the simple relation

$$(7) \quad c = gI_{sp}$$

where g is the acceleration of the Earth's gravity field (9.8 meters/sec.²).

Model rocket engines using pressed blackpowder propellant grains exhibit values of specific impulse in the range of 48 to 103 seconds. More recently, several types of engines using high-performance, ammonium perchlorate/polyurethane propellants have been introduced in model rocketry. These motors deliver specific impulses in the neighborhood of 175 seconds. There exist solid propellants which deliver specific impulses in excess of 240 seconds when burned at high chamber pressures, but problems of temperature, pressure, ignition technology, and cost have so far prevented their use in model rocketry.

The specific impulse delivered by any given model rocket motor is a quantity that is measured and published, either by the manufacturer of that motor himself or by the NAR Standards and Testing Committee. It is therefore a simple matter to compute the average exhaust velocity of any given motor using equation (7), and to use the value of exhaust velocity thus obtained in computing the mass flow rate from equation (2) and a knowledge of the engine's thrust-time curve.

2.2 Weight

The weight of a model rocket is the force exerted on it by the Earth's gravitational field. A rocket of mass m will have a weight given by

$$(8) \quad \vec{w} = m\vec{g}$$

where, as before, \vec{g} is the (vector) acceleration of the Earth's

gravity field. The weight force always points in the direction of the gravity field, which in this case is the center of the Earth -- or "straight down" along the local vertical. Strictly speaking, the value of \vec{g} decreases with increasing altitude above the Earth's surface according to the relation

$$(9) \quad g = \left[\frac{R_0}{R} \right]^2$$

where R_0 is the radius of the Earth, g_0 is the magnitude of \vec{g} at the Earth's surface, R is any radius greater than R_0 and g is the magnitude of \vec{g} at that radius. Even a 20,000-foot model rocket flight (about 6,000 meters -- much higher than any ever officially confirmed), however, would result in an apogee value of R only one tenth of one percent greater than R_0 . The effect of altitude on the weight of a model rocket is, therefore, wholly negligible. In all the calculations in this book \vec{g} will be taken to have the magnitude g_0 .

The weight of a model rocket does vary during its flight, though. This in-flight weight variation is due to the expulsion of mass from the rocket motor as it produces thrust. In Section 2.1 the relationship between thrust and the rate of mass expulsion was established as equation (2). Equation (2) can now be used to determine the model's mass as a function of time in the form

$$(10) \quad m = m_0 - \int_0^t \frac{F(t)}{c} dt$$

When the engine ceases burning at time t_b , the mass of the rocket is

$$(11) \quad m_b = m_0 - \int_0^{t_b} \frac{F(t)}{c} dt \quad \text{or, since}$$

$$(12) \quad m_f = \int_0^{t_b} \frac{F(t)}{c} dt$$

where m_f is the total mass of propellant in the engine before ignition,

$$(13) \quad m_b = m_0 - m_f$$

Accordingly, the weight of the rocket decreases continuously during the engine burn and the model is lighter after burnout than at ignition. In large guided missiles and space boosters the propellant constitutes most of the liftoff mass of the vehicle, so that such a rocket at burnout has only a small fraction of the mass it had at ignition. In model rockets, however, the mass change due to the expenditure of the propellant is relatively slight. This fact, as will be shown in Chapter 4, considerably simplifies the calculation of model rocket altitude performance.

Unlike the thrust, the direction of the weight vector remains invariant when the rocket rotates or "tips" away from the vertical. The weight of a model rocket, or for that matter any object, appears to originate from a point called the center of mass, which for all practical purposes within the scope of this book may be taken as identical to the center of gravity, or balance point: the point by which the object may be suspended without showing any tendency to rotate in any direction. All rotations of a model in flight occur about the C.G., and the weight vector always acts through the C.G. downward along the local vertical.

2.3 Drag and Side Force

Probably the most interesting, and certainly the most complex and difficult to calculate, force acting on a body moving through the atmosphere is the aerodynamic resistance to its passage, which physicists and engineers call drag. The drag of a body is a function of the density and viscosity of the medium through which it moves, its size and shape, the velocity with which it moves, the quality of its finish, its detailed surface characteristics, and its angle of attack.

Detailed discussions of the physical mechanisms by which all these factors influence the drag of a model rocket will be presented in Chapter 3. For the present it will be enough to write down just a few of the most fundamental facts about drag as it pertains to model rockets. First of all, the total drag on a model rocket moving through air of density ρ at a velocity of magnitude v is given by

$$(14) \quad D = \frac{1}{2} \rho C_D A_r v^2$$

where A_r is a reference area which is usually taken to be the cross-sectional area of the largest diameter body tube used in the rocket and C_D is the drag coefficient, a dimensionless parameter which depends on the shape of the model and its angle of attack, and also (more generally) on the Reynolds number at which it is operating.

The angle of attack, usually denoted by the symbol α , is the angle between the instantaneous velocity vector of the model's C.G. with respect to the air and the orientation of the rocket's

longitudinal axis. The concept of angle of attack is illustrated in Figure 6. As the angle of attack of a model rocket increases from zero its drag coefficient also increases, since the effective area normal -- that is, perpendicular -- to the airflow which it presents becomes larger than the reference area A_r used in calculating the drag, and the effective shape of the rocket becomes more difficult for the airflow to negotiate.

The Reynolds number, named for the English physicist Osborne Reynolds (1842-1912), is usually denoted by R_e and is a dimensionless aerodynamic scaling factor given by the relation

$$(15) \quad R_e = \frac{\rho v L}{\mu}$$

where (again) ρ is the density of the air, μ is the viscosity of the air, v is the magnitude of the velocity vector and L is the length of the rocket or other object of interest. There is also a kinematic viscosity, defined as

$$(16) \quad \nu = \frac{\mu}{\rho}$$

so that the Reynolds number is sometimes written as

$$(17) \quad R_e = \frac{vL}{\nu}$$

The concept of viscosity will be more fully discussed and explained in Chapter 3. For the present, the importance of equations (15) and (17) can be summed up in two statements:

- (a) The flow about two geometrically similar objects is dynamically similar if the Reynolds numbers for

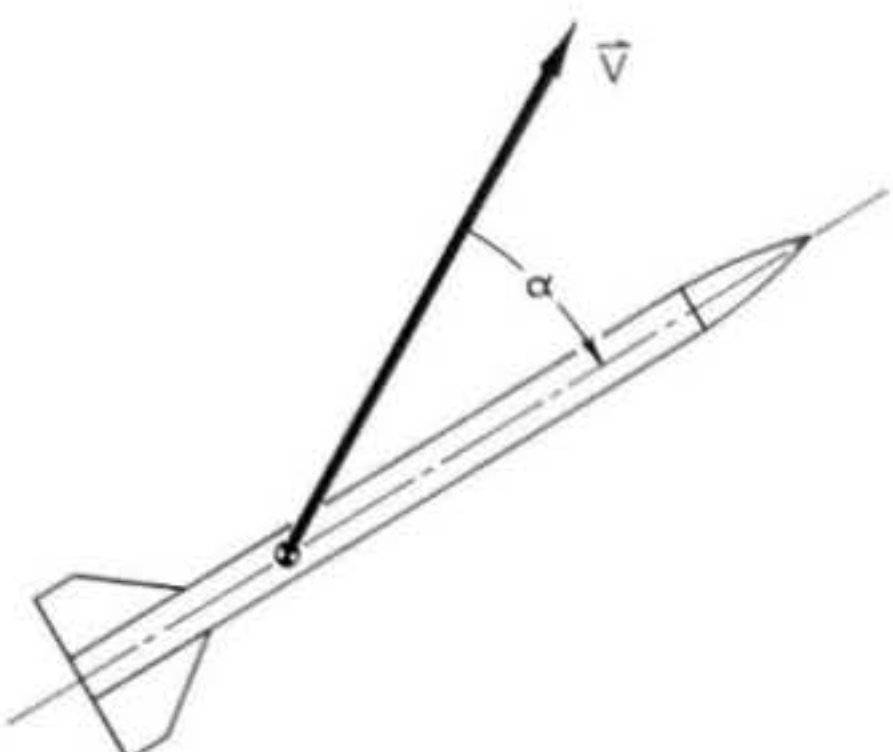


Figure 6: Angle of attack. The direction of the rocket's longitudinal axis is deflected through the angle α from the instantaneous velocity vector \vec{V} . α is referred to as the "angle of attack". This diagram assumes that there is no horizontal wind, so that the rocket's velocity with respect to the air is the same as its velocity with respect to the ground.

the two cases are identical; and

(b) The Reynolds number expresses the ratio of inertial force to viscous

force in any given fluid-flow situation. The effects of viscosity predominate at Reynolds numbers less than 1.0, while inertial effects predominate at Reynolds numbers greater than 1.0.

Statement (a) is important to the field of aerodynamic testing in which models are used, such as wind-tunnel testing. It means, for instance, that a quarter-scale model of an airplane placed in a wind tunnel will yield accurate information about the full-scale prototype if the tunnel airspeed is maintained at four times the flight speed of the prototype, so that the product vL is the same for the two cases (or if the tunnel is pressurized or some other fluid than air is used, so that the kinematic viscosity is decreased and a lower speed may be used). Conversely, data taken on a model rocket placed in a wind tunnel which can only generate an airspeed of 5 meters per second may not apply to that same model when it is flying 150 meters per second.

Statement (b) is important when considering the effect of varying Reynolds number on the drag coefficient. The density of sea-level air is 1.225×10^{-3} gram/cm.³, while its viscosity at room temperature (18° C) is 1.827×10^{-4} gram/(cm.-sec.). The unit combination gram/(cm.-sec.) is also known as the poise. In any case, this makes the value of ρ/μ in CGS units equal to

6.69 sec./cm.². With the length of a typical model rocket being about 30 centimeters, a flight velocity of 150 meters/sec. (15,000 cm./sec.) produces a Reynolds number of about 3×10^6 . An airspeed of 5 meters/second, on the other hand, gives an R_e of only 1×10^5 . Both numbers are considerably greater than one, of course, so that inertial forces are much greater than viscous forces in all cases involving model rockets. Still, the two cases differ by more than an order of magnitude, so that viscous effects are thirty times more important in the wind-tunnel test than in flight. Consequently, the flow behavior observed in the wind-tunnel test may be different from that actually encountered in flight. The drag coefficient, in particular, may be somewhat different.

Each component of a model rocket -- nosecone, body tube, fins, and so on -- contributes in some measure to the overall drag on the model, and hence to its drag coefficient. Each contributes both pressure drag due to the effect of its shape in displacing the airflow pattern about the rocket and friction drag due to the viscous shearing stress, or "friction", of the air directly adjacent to its lateral surfaces. The effect of the components in modifying the flow about each other also produces a small amount of additional drag, called the interference drag. Changes in Reynolds number over a great enough range can change the value of the overall drag coefficient through the phenomenon of transition, which alters the characteristics of the airflow about the rocket. At lower Reynolds numbers (less than 5×10^5), where viscous forces are more

important, the flow in the boundary layer directly adjacent to the model is likely to be arranged in neat, smooth, microscopically-thin layers and is thus said to be laminar. At higher Reynolds numbers (greater than 5×10^6) the importance of viscosity diminishes and the boundary layer is likely to undergo transition and become turbulent; the once-smooth layers mixing and swirling down the side of the model in a rough, chaotic manner. The friction drag of an object with a turbulent boundary layer is much higher than that of one with a laminar boundary layer, but a turbulent boundary layer follows the contour of an object's surface better than a laminar one and is less likely to separate from the surface, so it may lower the pressure drag. Detailed discussions of precisely how much Reynolds number changes, with their associated transition phenomena, alter a model rocket's drag coefficient will be presented in Chapter 3. The present brief discussion should be sufficient to give you a general idea of why the Reynolds number is important and how it can change the drag coefficient. Over the range of R_e usually encountered in practice, values of C_D for most model rockets range from 0.35 to about 1.0, averaging 0.7 to 0.75 for sport rockets of average design and finish quality.

Chapter 3 will also present a thorough treatment of methods for calculating how a model rocket's drag coefficient increases with angle of attack. A slightly different approach, but one which gives very nearly the same numerical results, will be used in Chapter 4 for determining the effect of dynamic oscillations

("wobbling" of the rocket on the way up) on a model's maximum altitude. According to this treatment, the coefficient of drag at zero angle of attack is written C_{D0} . A constant k can then be defined such that

$$(18) \quad k \equiv \frac{1}{2} \rho A_r C_{D0}$$

Then one can represent the drag as a function of angle of attack by

$$(19) \quad D = \{k + \epsilon f(\alpha)\} v^2$$

where ϵ is a constant and $f(\alpha)$ is some function of the angle of attack that decreases to zero as the angle of attack itself goes to zero. According to the method of analysis developed by James Barrowman, which is discussed in detail in Chapter 2, a rocket flying at a nonzero angle of attack experiences a normal force (i.e., one perpendicular to the model's centerline) whose magnitude is given by

$$(20) \quad N = \frac{1}{2} \rho C_{n\alpha} A_r v^2$$

where $C_{n\alpha}$ is the normal force coefficient, whose computation by the Barrowman method is described in Chapter 2. The component of force $N \sin \alpha$ is an additional contribution to the drag, while the component $N \cos \alpha$ is a side force tending to deflect the rocket's path by causing an acceleration component normal to the current direction of flight. The resolution of the normal force is shown in Figure 7.

Now at small angles of attack (less than about 15°) $\sin \alpha$

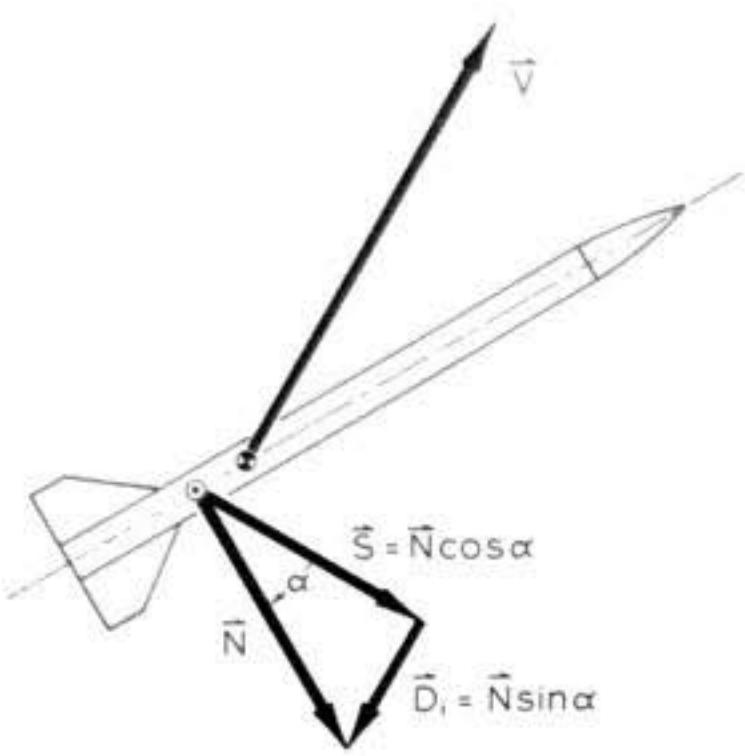


Figure 7: Resolution of normal force into side force and "drag due to lift". The normal force and its components are considered to act through the center of pressure. \vec{N} is perpendicular to the longitudinal axis of the rocket, \vec{S} is perpendicular to the velocity vector, and \vec{D}_1 is parallel to the velocity vector. A case of no wind has again been assumed.

is very nearly equal to the value of α itself in radians (one radian equals 57.3°), while $\cos\alpha$ is very nearly equal to 1.0. Accordingly, one can make the small-angle approximations

$$(21) \quad N \sin \alpha \approx N\alpha$$

$$(22) \quad S \approx N \cos \alpha$$

$$\approx N$$

where S denotes the magnitude of the side force. Now by inspection of equations (19), (20), and (21), one might be tempted to deduce that

$$\epsilon = \frac{1}{2} C_{n\alpha} A_r \quad \text{and}$$

$$f(\alpha) = \alpha^2$$

Unfortunately, things are not quite that simple. The drag increase due to the normal force is only one of several contributions to the increase in drag produced by a nonzero angle of attack. As explained in Chapter 3, viscous cross-flow and increased interference effects cause the increase in drag due to angle of attack to be somewhat greater than one would predict from Barrowman analysis alone. It will, however, be found quite accurate to represent $f(\alpha)$ by α^2 , and this property will be used in Chapter 4 to estimate the effects of the oscillatory responses to various in-flight perturbations on altitude capability.

In Figure 8 a complete vector diagram of all the forces influencing the center-of-mass motion of a model rocket in flight is presented. The making of such a drawing, called a free-body diagram, is one of the fundamental steps in the solution of any problem in statics or dynamics since it enables one to readily visualize all the components of the forces required to write down the equations of motion. You may find it helpful to consult Figure 8 of this chapter again when reading Chapter 4.

3. Description of the Perturbing Forces

This section will consider those forces encountered by a model rocket in flight that produce moments which rotate the

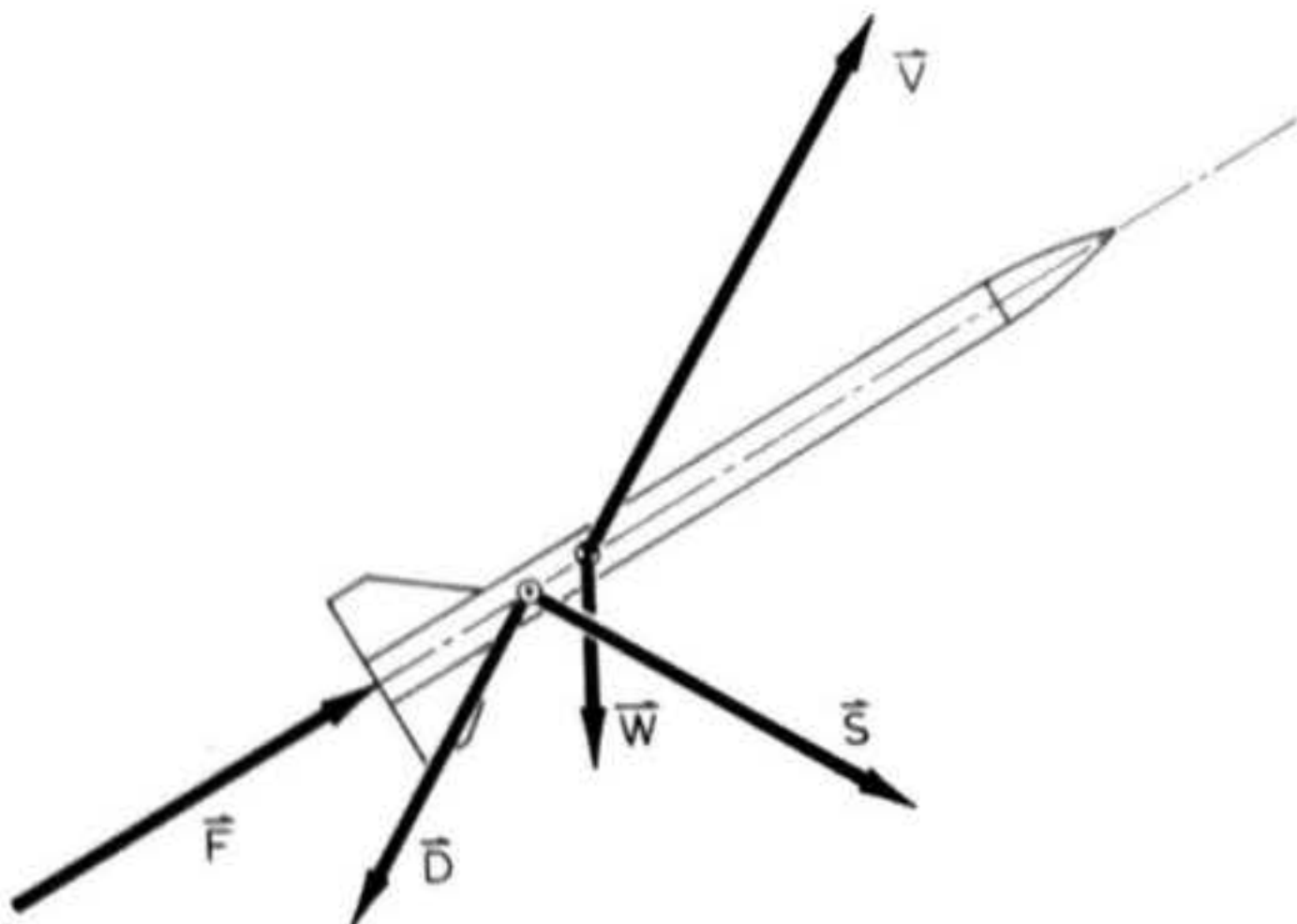


Figure 8: Forces on a model rocket in flight. Thrust, drag, weight, and side force, as well as the velocity vector, have been shown for a rocket in general flight attitude (that is, the rocket is neither flying vertically nor at zero angle of attack). Wind-free conditions have been assumed.

model about its center of gravity. The changes in angle of attack produced by such rotations result, as we saw in Section 2.3, in increased aerodynamic drag and also give rise to side forces which, if they persist for a long enough time, can seriously disturb the rocket's flight path. The perturbing forces generally arise from irregularities in the construction of the model, launching and staging effects, and local wind phenomena -- all of which must be allowed for in some degree when designing a model. Model rockets must be designed to respond as little as possible to the perturbing forces, and to return to straight and true flight as soon as possible after the disturbance has passed. Accordingly, the analyses of Chapters 2 and 4 will present in detail information useful in designing disturbance-resistant rockets.

3.1 Aerodynamic Disturbances

Aerodynamic effects that tend to rotate a rocket vehicle about its C.G. can arise from winds, misaligned fins or other components, "fluttering" of the fins, or protrusions such as launch lugs which cause asymmetries in the vehicle's shape. Winds may either blow continuously or arise in momentary gusts. In Chapter 2 it will be shown that a constant wind that persists for a long period of time can produce weathercocking, a phenomenon in which the model tends to tip toward the direction from which the wind is coming and fly off at an angle determined by the vector sum of the wind velocity and the vertical velocity of the rocket at the time it began to experience the wind. Weathercocking is illustrated in Figure 9. A gust of wind, on the other

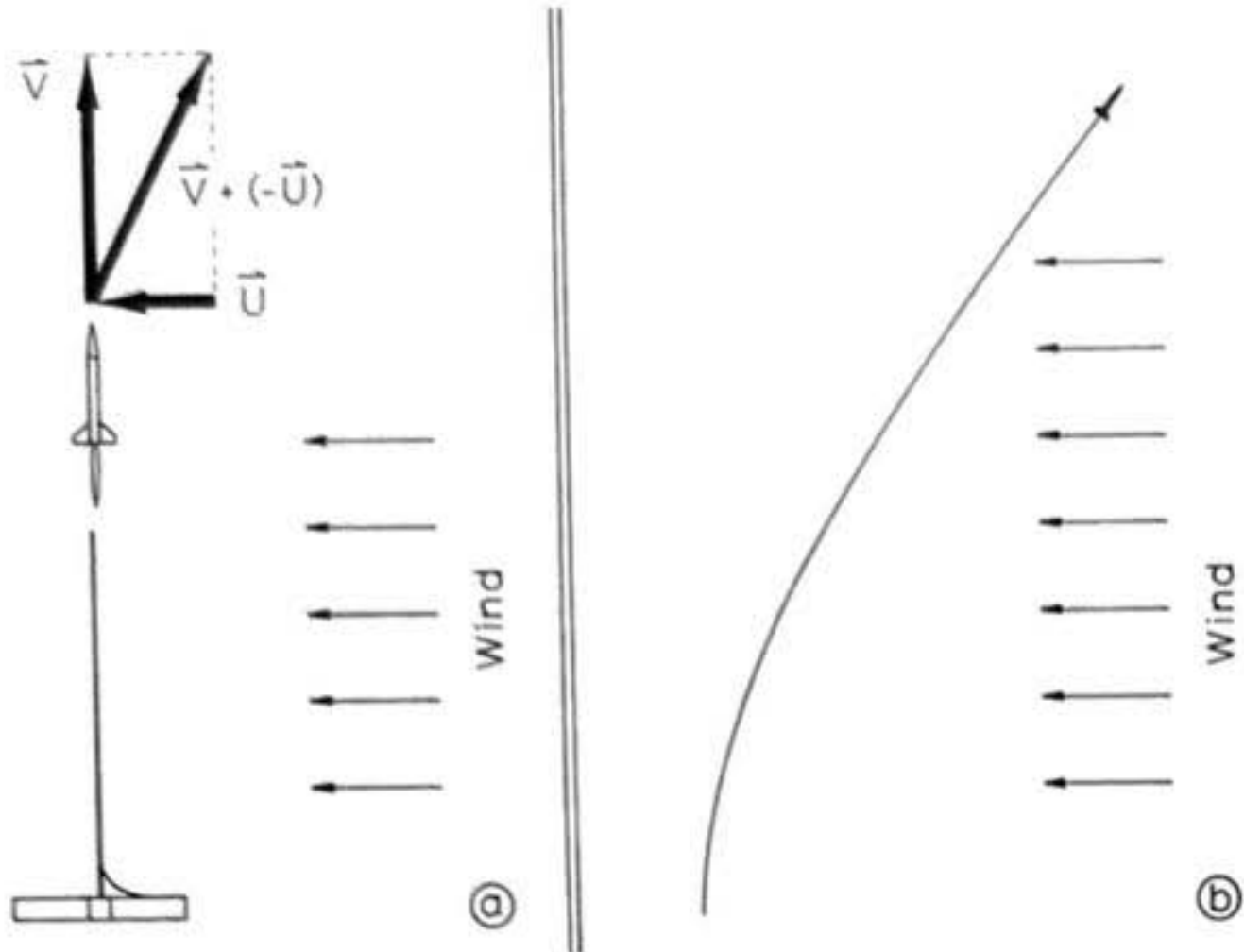


Figure 9: Weathercocking. The rocket leaves the launcher (a) at vertical velocity \vec{V} and encounters a horizontal wind of velocity \vec{U} . It then tends to fly off in the direction of the vector $\vec{V} + (-\vec{U})$ and "weathercocks" (b), or flies into the wind. This is because the wind acts through the center of pressure which, for any stable rocket, is behind the center of gravity.

hand, will succeed in temporarily deflecting the vehicle and will generally cause it to oscillate in rotation about its C.G., with its angle of attack passing back and forth through zero.

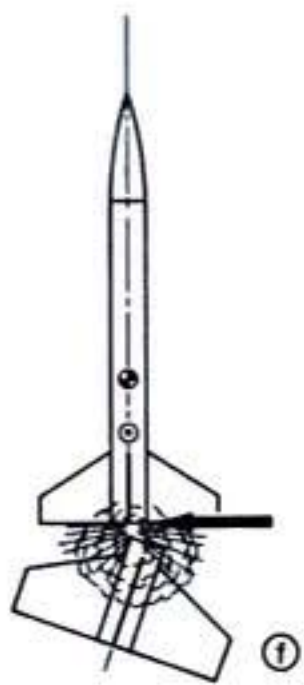
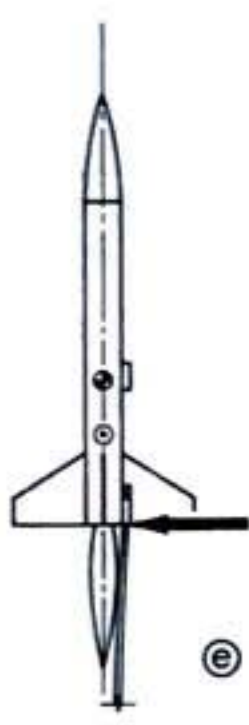
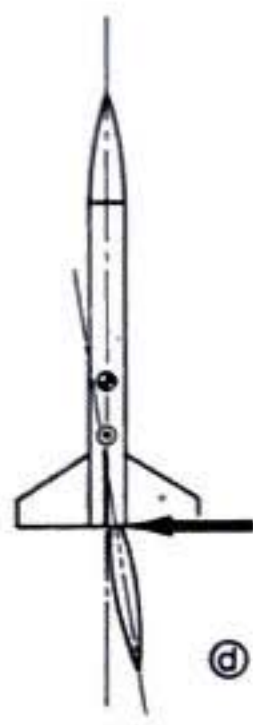
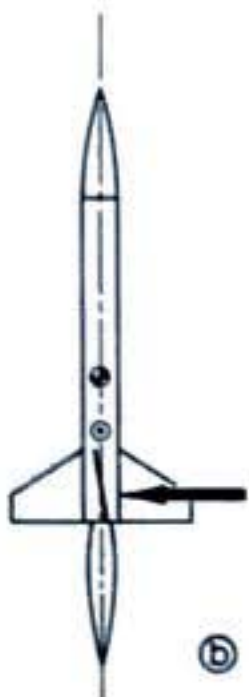
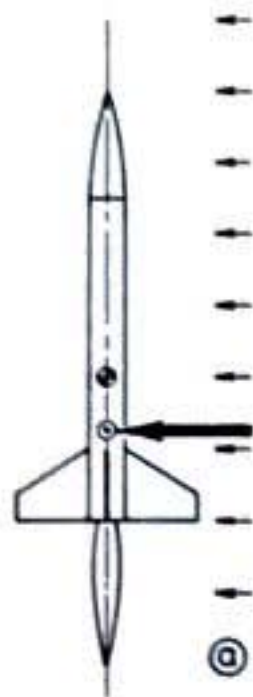
Fin flutter is a periodic force. That is, the fins are undergoing rapid vibrations from side to side (sometimes these vibrations are audible as a whirr, or buzz) which induce forces and moments on the model that are sinusoidal (i.e., if their magnitudes were graphed versus time the resulting graphs would look like sine waves). Flutter will be present in fins which are too thin to possess sufficient rigidity; it is evidence of poor design since it is perfectly possible (indeed, easy) to design fins which do not flutter at all. If you do encounter a case of fin flutter, though, you will want your rocket to survive it so you will have a chance to replace the model's fins. Consequently, the rocket as a whole should be designed for minimal response to any possible flutter.

Misaligned fins or other components and unsymmetrical surface protrusions will cause forces and moments which are constant in direction in a rocket that is not spinning (or "rolling") about its centerline, and which are sinusoidal in nature in one that is spinning. The angular frequency of the sine functions in the latter case is equal to the roll rate of the vehicle in radians per second.

3.2 Mechanical Disturbances

Mechanical perturbing forces and moments are distinguished from aerodynamic disturbances in that they in no way depend upon the aerodynamic coupling of the point-mass motion to

Figure 10: Examples of aerodynamic and mechanical disturbances. A horizontal wind (a) produces step forcing of constant intensity, while mismounted fins (b) cause a step disturbance of intensity proportional to the square of the airspeed. If only one fin is canted the rocket will spin, producing roll-coupled sinusoidal forcing. Torsionally vibrating fins (c) produce sinusoidal forcing of intensity proportional to the square of the airspeed. A mismounted or malfunctioning engine (d) produces step forcing proportional to the thrust level. Launch rod whip at departure (e) causes an impulse disturbance, as does staging (f). Since the lower stage has been blown to the right by the blow-through/ignition sequence, the base of the upper stage is pushed to the left. Cases (a), (b), and (c) are aerodynamic disturbances, while (d), (e), and (f) are mechanical disturbances.



the model's rigid-body rotations, and that they do not originate from any aerodynamic sources at all. Mechanical perturbations would arise even if one attempted to fly a model rocket in the hard vacuum of outer space. Examples of mechanical disturbances are those caused by thrust misalignment due to imperfect engine mounting or nozzle abnormalities, propulsive instabilities resulting in an oscillating thrust vector, force transients arising as the vehicle leaves the launch rod or tower, and forces due to a staging ignition sequence.

Mechanical disturbances arising from launch departure effects or staging are unidirectional in nature and are of extremely short duration, while those arising from thrust misalignment or thrust vector oscillation are of relatively long duration. Thrust oscillation effects are sinusoidal with an angular frequency determined by the rapidity of the oscillation itself. In the case of a spinning rocket the frequency of the thrust oscillation will be superimposed upon the model's roll rate. A constant thrust misalignment will be unidirectional in nature if the vehicle is not spinning, and sinusoidal with an angular frequency equal to the roll rate if it is.

All the perturbing effects mentioned here and in Section 3.1 will be discussed in detail, modeled mathematically, and treated as input moments ("inputs" or "forcing functions") causing the model to undergo various rigid-body rotations in Chapter 2. While reading Chapter 2 you may wish to consult Figure 10, in which a number of situations which will produce aerodynamic or mechanical disturbances have been illustrated.

REFERENCES

1. Halfman, Robert L., Dynamics: Particles, Rigid Bodies, and Systems, Volume 1, Addison-Wesley Publishing Company, Inc., Reading, Massachusetts, 1962.
2. Hill, Philip G., and Peterson, Carl R., Mechanics and Thermodynamics of Propulsion, Addison-Wesley Publishing Company, Inc., Reading, Massachusetts, 1965.
3. Thomas, George B. Jr., Calculus and Analytic Geometry, Third Edition, Addison-Wesley Publishing Company, Inc., Reading, Massachusetts, 1960.

CHAPTER 2

A UNIFIED APPROACH TO AERODYNAMIC STABILITY

Gordon K. Mandell

SYMBOLS

<u>Symbol</u>	<u>Meaning</u>
A	initial amplitude
A, B, C	space axes
A, B, C, D	roots of quartic equation used to determine angular frequencies of pitch and yaw in cases of rolling rockets
A', B', C'	roots of cubic equation used to determine angular pitch and yaw frequencies of a rolling rocket undergoing force-free precession
A _f	amplitude of sinusoidal forcing
A _r	amplitude of response to sinusoidal forcing
A ₁	initial amplitude of first mode of critically damped or overdamped motion; also initial amplitude of first mode of roll-coupled motion
A ₂	initial amplitude of second mode of critically damped or overdamped motion; also initial amplitude of second mode of roll-coupled motion
AR	amplitude ratio
AR _c	amplitude ratio of roll-coupled motion
AR _{cres}	resonant amplitude ratio of roll-coupled motion
AR _{res}	resonant amplitude ratio
R	aspect ratio
C _{Nα}	normal force coefficient
(C _{Nα}) _B	normal force coefficient of boattail
(C _{Nα}) _n	normal force coefficient of nose
(C _{Nα}) _S	normal force coefficient of shoulder
(C _{Nα}) _T	normal force coefficient of tailfin assembly
(C _{Nα}) _{T(B)}	normal force coefficient of tailfin assembly in the presence of the body

<u>Symbol</u>	<u>Meaning</u>
$(C_{N\alpha})_1$	normal force coefficient of one fin
C_1	corrective moment coefficient
C_2	damping moment coefficient
C_{2A}	aerodynamic damping moment coefficient
C_{2R}	propulsive damping moment coefficient
D	inverse time constant
D, E, F	body axes
D_1	inverse time constant of first mode in roll-coupled motion
D_2	inverse time constant of second mode in roll-coupled motion
F	thrust
\vec{F}	force
$F(\alpha_x)$	function of pitch angle
\mathcal{F}	abbreviated notation for a function of the dynamic parameters used in writing the angular frequencies of roll-coupled motion
$G(\omega_x)$	function of pitch angular velocity
H	strength of impulse
I	moment of inertia
I_D	moment of inertia about D axis
I_E	moment of inertia about E axis
I_F	moment of inertia about F axis
I_L	longitudinal moment of inertia
I_{Lch}	longitudinal moment of inertia of a hollow cylindrical component
I_{Lcs}	longitudinal moment of inertia of a solid cylindrical object
I_{Lo}	longitudinal moment of inertia of any object
I_{Lo}'	longitudinal moment of inertia of any object about its own center of gravity

<u>Symbol</u>	<u>Meaning</u>
I_R	radial moment of inertia
I_{Rch}	radial moment of inertia of a hollow cylinder
I_{Rcs}	radial moment of inertia of a solid cylinder
I_{Rf}	radial moment of inertia of a single fin
I_{Rn}	radial moment of inertia of the nose
I_{Rt}	radial moment of inertia of a complete set of fins
I_s	moment of inertia of reference standard
K	particular response to step forcing
$K_T(B)$	tail-body interference coefficient
L	length
L_{ne}	distance of nozzle exit from tip of nose
M	moment, torque; <u>also</u> mass of any component
M_D	moment about D axis
M_E	moment about E axis
M_F	moment about F axis
M_b	mass of boattail
M_c	corrective moment; <u>also</u> mass of cylinder
M_d	damping moment
M_e	mass of engine
M_f	mass of the fins as used in computing C.G. location; <u>also</u> mass of one fin as used in computing I_{Rf}
M_n	mass of nose
M_o	mass of any object
M_p	mass of payload section including contents
M_r	mass of rigged and packed recovery system
M_s	step moment; <u>also</u> mass of shoulder

<u>Symbol</u>	<u>Meaning</u>
M_t	mass of body tube
M_x	moment about x axis
M_y	moment about y axis
M_z	moment about z axis
N	normal force; <u>also</u> number of fins
R	radius
R_i	inner radius
R_o	outer radius
T_L	period of torsional oscillation of a rocket suspended on a torsion wire with its longitudinal axis horizontal
T_R	period of torsional oscillation of a rocket suspended on a torsion wire with its longitudinal axis vertical
T_s	period of torsional oscillation of reference standard
V	airspeed
V_e	exhaust velocity
\bar{w}	longitudinal position of complete vehicle C.G.
\bar{w}_b	longitudinal position of boattail C.G.
\bar{w}_c	longitudinal position of C.G. of a cylindrical component
\bar{w}_e	longitudinal position of engine C.G.
\bar{w}_f	longitudinal position of fin C.G.
\bar{w}_n	longitudinal position of nose C.G.
\bar{w}_o	longitudinal position of the C.G. of any object
\bar{w}_p	longitudinal position of payload section C.G.
\bar{w}_r	longitudinal position of recovery system C.G.
\bar{w}_s	longitudinal position of shoulder C.G.
\bar{w}_t	longitudinal position of body tube C.G.

<u>Symbol</u>	<u>Meaning</u>
X, Y, Z	intermediate axes; <u>also</u> abbreviations for functions of the dynamic parameters used in analysis of roll-coupled motion
\bar{Y}_T	radial position of C.P. of a single fin
\bar{Z}	longitudinal position of complete vehicle C.P.
\bar{z}_{CB}	longitudinal position of conical boattail C.P.
\bar{z}_{CS}	longitudinal position of conical shoulder C.P.
\bar{z}_n	longitudinal position of nose C.P.
\bar{z}_T	longitudinal position of tailfin C.P.
a	dummy variable used in analysis of roll-coupled motion
\dot{a}	linear acceleration
b	y-intercept of a straight line; <u>also</u> dummy variable used in analysis of roll-coupled motion
c_r	fin chord at root
c_t	fin chord at tip
$d(\)/dt$	derivative of () with respect to time
$d^2(\)/dt^2$	second derivative of () with respect to time
e	base of the Napierian logarithm system, numerically equal to approximately 2.718
$f_x(t)$	pitch forcing function
$f_y(t)$	yaw forcing function
k_d	roll damping interference coefficient
k_r	roll forcing interference coefficient
m	mass; <u>also</u> constant of proportionality in the equation of a straight line
\dot{m}	mass expulsion rate
m_p	mass of propellant
n	peak number
r_r	reference radius

<u>Symbol</u>	<u>Meaning</u>
r_t	radius of body section to which the fins are joined
s	span of one fin, root to tip
t	time
t_b	burning time of rocket engine
t_m	time at which maximum angle of attack occurs
t_{max}	time of occurrence of maximum overshoot angle
x	independent variable
x_t	longitudinal distance from leading edge of fin root to leading edge of fin tip
y	dependent variable
Γ_c	mid-chord sweep angle
$\Sigma()$	sum of all ()
Ω_x	angular velocity component about X axis
Ω_{x0}	yaw angular velocity at $t = 0$
Ω_y	angular velocity component about Y axis
Ω_{y0}	pitch angular velocity at $t = 0$
Ω_z	angular velocity component about Z axis
α	angular displacement, angle of attack
α_D	angular displacement (Euler's angle) about D axis
α_E	angular displacement (Euler's angle) about E axis
α_F	angular displacement (Euler's angle) about F axis
α_X	yaw angle
α_{xm}	maximum yaw angle
α_{x0}	yaw angle at $t = 0$
α_Y	pitch angle

<u>Symbol</u>	<u>Meaning</u>
α_{v0}	pitch angle at $t = 0$
α_0	initial angle of attack
α_1	maximum overshoot angle
β	frequency ratio
β_c	coupled frequency ratio
β_{cres}	resonant coupled frequency ratio
β_{res}	resonant frequency ratio
γ	angular acceleration
ζ	damping ratio
ζ_c	coupled damping ratio
θ	angle of fin cant
λ	c_t/c_r ratio
ρ	mass density of the atmosphere
τ	ratio $(s + r_t)/r_t$
τ_1	time constant of first mode of overdamped motion
τ_2	time constant of second mode of overdamped motion
φ	phase angle
φ_1	phase angle of first mode of roll-coupled motion
φ_2	phase angle of second mode of roll-coupled motion
ω	angular velocity; <u>also</u> angular frequency of oscillatory response
ω_D	component of angular velocity about D axis
ω_E	component of angular velocity about E axis
ω_F	component of angular velocity about F axis
ω_c	critical angular frequency
ω_{cres}	resonant coupled angular frequency

<u>Symbol</u>	<u>Meaning</u>
ω_f	angular frequency of sinusoidal forcing
ω_n	natural frequency
ω_{nc}	coupled natural frequency
ω_{res}	resonant frequency
ω_z	roll rate
ω_1	angular frequency of first mode of roll-coupled motion
ω_2	angular frequency of second mode of roll-coupled motion
$ (\) $	absolute value of ()

A UNIFIED APPROACH TO AERODYNAMIC STABILITY

Introduction

Model rocketeers have been familiar with the concept of aerodynamic stability for quite some time. As early as 1958 G. Harry Stine had published simplified treatments of aerodynamic stability as it pertains to model rocket design, in which the hobbyist was first made aware of the existence of a center of pressure (C.P.) and of the all-important relationship between it and the model's center of gravity (C.G.). In these early treatments the center of pressure was approximated by the center of lateral area, and for the next eight years the "cardboard cutout" method remained the standard model builder's technique for estimating the location of the C.P.

The next major advance in the field came in 1966 at the Eighth National Association of Rocketry Annual Meet, where James Barrowman of the National Aeronautics and Space Administration's Sounding Rocket Branch unveiled an algebraic method based on the theory of potential flow capable of determining the center of pressure of a model rocket flying subsonically and at small angles of attack to a high order of accuracy. Barrowman showed that the actual C.P. of a model rocket lies some distance aft of the location predicted by the cutout method, and that therefore model rocketeers had been designing their vehicles too conservatively.

All consideration of model rocket stability had thus far been confined exclusively to its static manifestations, with the nature of the C.P.-C.G. relationship being used to determine whether a rocket, once deflected from facing directly into the relative airstream, would experience a moment tending to return it to the undeflected state (in which case it would be considered stable) or one tending to further deflect it (in which case it would be considered unstable). Little attention had been paid to the details of the process by which a stable rocket, once disturbed in its flight, restores itself to alignment with its intended flight path, or to the process by which an unstable rocket goes head over heels (unless, strangely enough, it is spinning rapidly enough about its centerline). The statics of stability had been treated in admirable detail, but its dynamics remained virtually ignored.

This is not to say that our hobby had had no exposure to stability considered in a dynamic context. Luther W. Gurkin of the National Aeronautics and Space Administration's Wallops Station had presented an excellent short treatment of rocket dynamics to the contestants at the Sixth National Association of Rocketry Annual Meet in 1964. Although copies of Gurkin's "Basic Missile Aerodynamic Stability" were distributed to a number of interested persons at the meet, however, little was done to apply his results specifically to model rockets for nearly four years. Our vehicles continued to be subject to puzzling anomalies of behavior that could not be satisfactorily explained by considerations of static stability alone. Sometimes they "weathercocked" -- flew directly into the prevailing wind

at launch. In other cases they would mysteriously tip to some random orientation at launch and subsequently fly straight and true. Some models would oscillate excessively on the way up; others hardly at all, and still others would experience a sort of "semi-instability" in which the nose circled violently about the intended axis of flight.

This writer began to investigate the problem of dynamic stability early in 1968, working from a general consideration of the dynamical equations governing the rotational motions of a streamlined projectile about its center of gravity during free flight. Although the mathematical details of such an approach are sometimes formidable, I felt that the greatest amount of information could only be obtained from the most general analysis. In this section I am going to endeavor to present the results of this analysis and to apply them to model rockets by the use of the Barrowman equations, concluding with some suggestions which should help the model rocketeer formulate designs which will both fly stably and exhibit favorable dynamic behavior.

The dynamical equations describing the behavior we are interested in are necessarily of a type called differential equations, and as such require the techniques of calculus for their solution. I want to emphasize as strongly as I can, however, that it is not necessary that the reader understand calculus in order to follow the presentation. To the engineer, calculus is fundamentally a tool that enables him to obtain algebraic equations describing the behavior of the system he is investigating. Care has therefore been taken to emphasize the

algebraic results of calculus-dependent derivations, with the calculus operations being considered as formulae for altering differential equations to algebraic equations. No reader who has had his second year of high school algebra, and perhaps some exposure to analytic geometry, should have any difficulty in understanding the text.

As the exact forms of the equations governing the rotational motions of projectiles subject to aerodynamic moments are quite complex and introduce fundamental mathematical barriers to our obtaining physical solutions, I have made a number of approximations in order to cast the equations into a more readily soluble form. Approximations of the kind made here are quite common in the solution of the differential equations encountered in all branches of mathematical physics. Called linearizations, they involve physical and/or geometrical reasoning by which the investigator can neglect or modify certain of the characteristics of his mathematics in ways not immediately determinable or obvious from the mathematics itself. I have taken care to identify each such approximation and to give its physical justification in order to keep the treatment as basic as possible.

Certain portions of this analysis parallel Luther Gurkin's "Basic Missile Aerodynamic Stability", while others use information contained in James Barrowman's "Calculating the Center of Pressure of a Rocket", a National Aeronautics and Space Administration Educational Services Office pamphlet embodying the algebraic results of his analysis. In order to facilitate correlation of this treatment with theirs, appropriate references have been included.

1. The Dynamical Equations

1.1 Euler's Angles

Suppose we have a rocket which has been rotated about some set of mutually perpendicular axes fixed in space: A, B, and C. We can speak of this rotational displacement in a quantitative way if we consider a second set of axes, D, E, and F, to have been fixed in the rocket, with origin at the rocket's C.G., and with directions coincident with A, B, and C before the rotation began, and to have remained fixed in the rocket as it rotated. We can always uniquely determine the final orientation of the rocket if we agree to abide by the following rule: that, in undergoing any given rotation, the rocket first yaws through an angle α_D about axis D; then pitches through an angle α_E about axis E; and finally rolls through an angle α_F about axis F. This process is illustrated in Figure 1.

The body axes D, E, and F first rotate about D through angle α_D . Throughout this first rotation D coincides with axis A of the space axes and E and F remain in the plane defined by B and C. At its completion axis F coincides with the dashed line Of and axis E with Oe. Next the body axes rotate about the new position of E (that is, about Oe) through an angle α_E . This rotation occurs in the plane of A and Of, and at its conclusion axis F is in its final position as shown and axis D lies along line Od. E, of course, is still along Oe. Finally the body axes execute the roll through angle α_F about F, in the plane defined by Oe and Od, bringing all the axes into their final positions.

It is important that this order of rotations be observed;

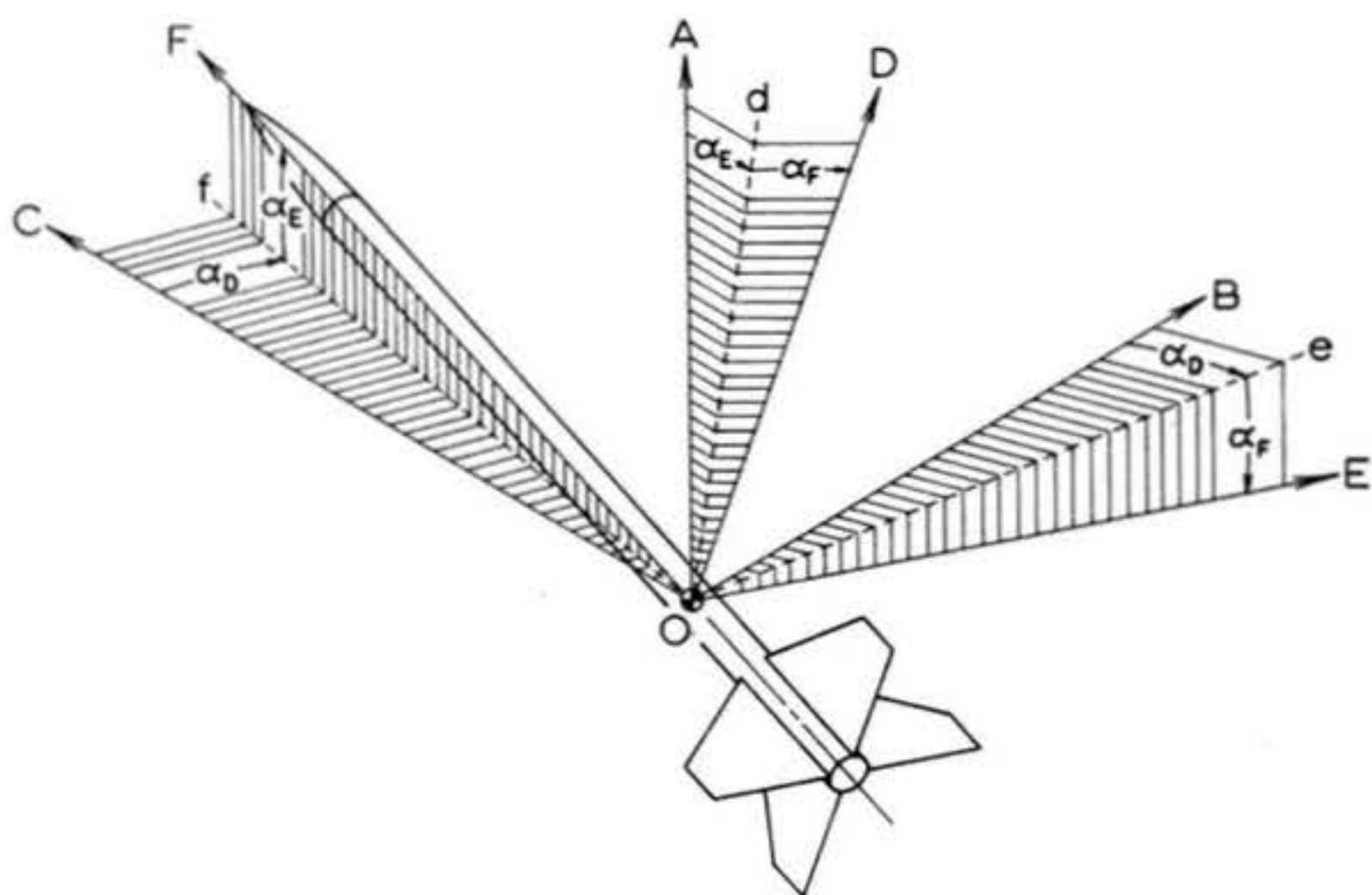


Figure 1: A set of Euler's angles for specifying the rotational position of a model rocket. α_D is the angle of yaw, α_E is the angle of pitch, and α_F is the angle of roll. The origin of the coordinate system is taken as the center of gravity of the rocket.

if the order in which the yaw, pitch, and roll occur is changed the final position of the rocket will be different. A mathematician would say that angular displacements, or rotations, are not vector quantities because, although they specify both a magnitude and a direction, they do not commute in addition. The three "locating angles" α_D , α_E , and α_F for specifying the rotational displacement of a solid body are called a set of Euler's angles after their discoverer, the Swiss mathematician and physicist Leonhard Euler (1707-1783). You can see that if for any reason we wish to postulate an intermediate set of axes which will perform some, but not all, of the movements of the rocket, we can find the rocket's final position by determining first the position of the intermediate axes with respect to the space axes, and then the position of the body axes with respect to the intermediate axes. At this point such a procedure seems a meaningless complication, but it will be very useful later on.

1.2 Angular Velocity

If you imagine the Euler's angles of a certain rotation becoming very small, so that the rocket is barely turned from its original position, you may notice a curious and very useful fact: the order of the angular displacements is no longer of such great importance. If, when the angles were large, the rocket was considered to first pitch, then yaw, and finally roll or to perform the rotations in any order other than the prescribed one of yaw, pitch, roll, we obtained a different final orientation in each case. Now, however, the effect of such alterations in the order of rotations is very slight;

nearly the same result is obtained no matter what the order in which the rotations occur. If the rotations are allowed to become infinitesimally small, so that they are, in the terminology of calculus, differential quantities, the equality becomes exact. Thus, differential rotations are vector quantities; they possess both a magnitude (though slight, to be sure) and a direction, and they do commute in addition. Differentials are denoted by a lower-case letter d in front of the quantity in question; differential angular displacements are thus $d\alpha_D$, $d\alpha_E$, and $d\alpha_F$.

Now suppose the rocket is turning continuously, so that its Euler's angles keep changing as time goes on. This can be represented mathematically by stating that, in every differential element of time dt , the rocket experiences differential angular displacements $d\alpha_D$, $d\alpha_E$, and $d\alpha_F$. We then form the fractions

$$(1) \quad \begin{aligned} \omega_D &= \frac{d\alpha_D}{dt} \\ \omega_E &= \frac{d\alpha_E}{dt} \\ \omega_F &= \frac{d\alpha_F}{dt} \end{aligned}$$

and define $\omega_D \equiv$ angular velocity about D, or D-component of angular velocity

$\omega_E \equiv$ angular velocity about E, or E-component of angular velocity

$\omega_F \equiv$ angular velocity about F, or F-component of angular velocity

Angular velocity is called the derivative with respect to time of angular displacement, or the time rate of change of angular displacement. Angular velocities are vector quantities: they

have both magnitude and sign, they do commute in addition, and all vector operations such as cross product, dot product, and coordinate transformation apply to them. Specifically, we represent them in a so-called right-handed coordinate system as positive about a given axis when they cause a rotation such that a screw with right-handed threads would advance along that axis in the positive direction, negative when such a progression would be in the negative direction. A right-handed system itself, such as our A,B,C axis set, is established by the requirement that the right-handed screw turned about its axis from A toward B advance positively along C. This convention is illustrated in Figure 2, while Figure 3 shows a rocket undergoing a rotation in which all components of angular velocity are positive. An angular velocity is conveniently represented by an arrow along the axis about which it occurs, of direction determined by the sign of the component, and of length proportional to its magnitude. This allows all the common vector operations to be performed. Figure 4 shows this convention in operation.

It is now necessary to go back and pick up a few loose ends in order to introduce some concepts which will be useful later on. First, there is the matter of defining positive and negative rotations; this must be done to obtain physically meaningful results from any investigation of rocket motion even though angular displacements do not have all the properties required of vectors. This is accomplished directly by the analogy of the right-handed screw through replacing the "turning direction" of the screw with the angular displacement. Secondly, the derivative relationship of angular velocity to angular displacement needs

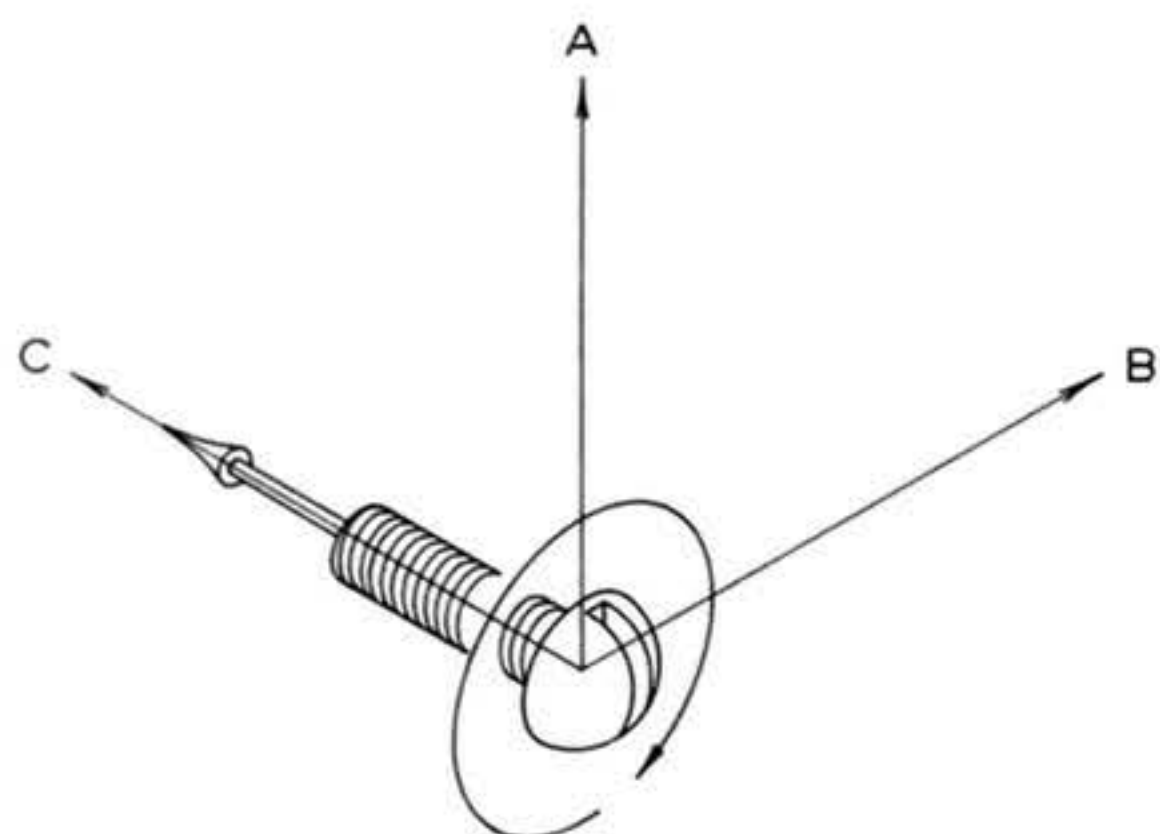


Figure 2: Definition of a right-handed coordinate system. Turning a screw with right-hand threads as if axis A were being turned toward axis B causes the screw to advance positively along axis C.

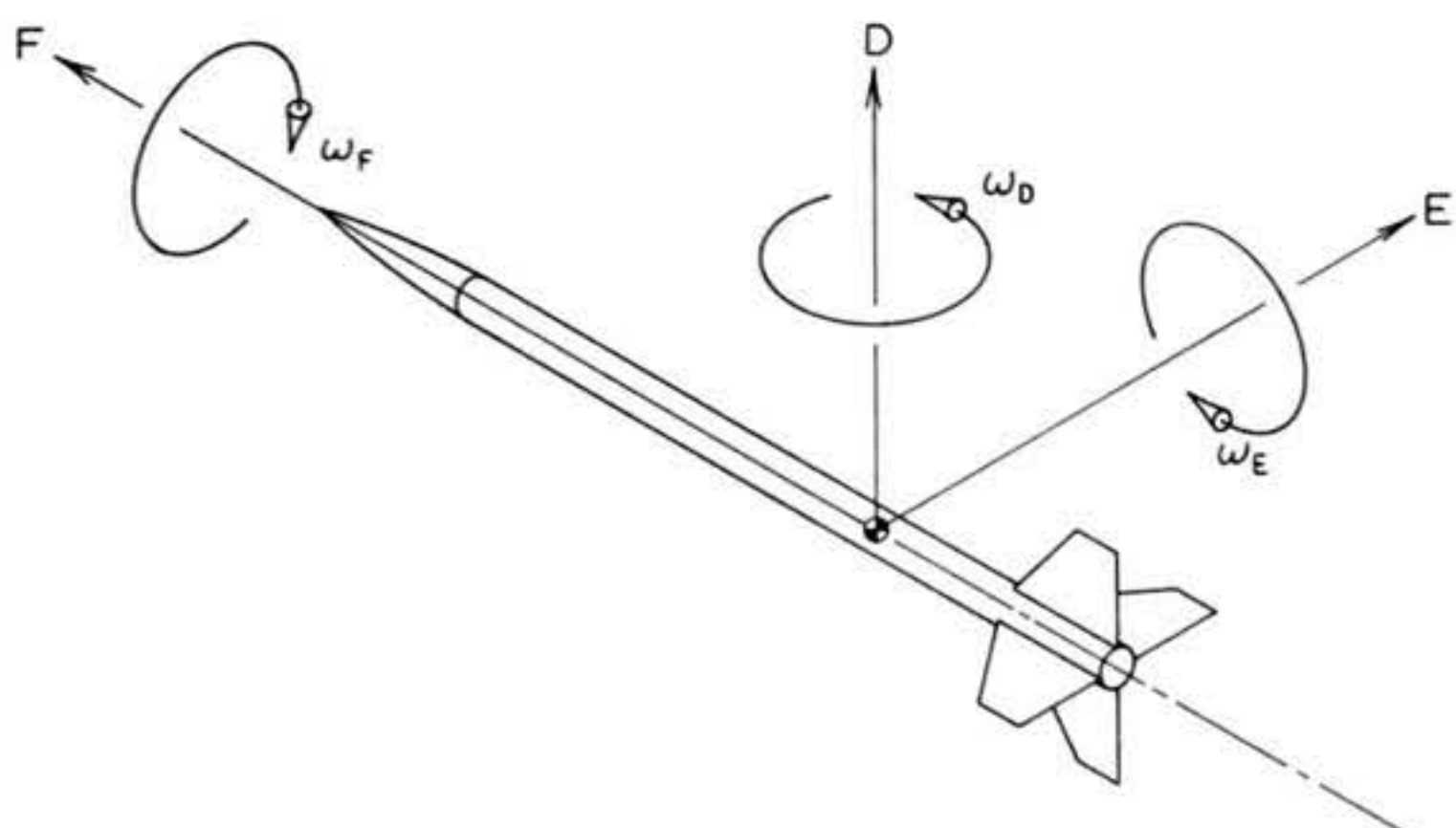


Figure 3: Positive components of angular velocity. ω_D is a positive yaw rate, ω_E is a positive pitch rate, and ω_F is a positive roll rate.

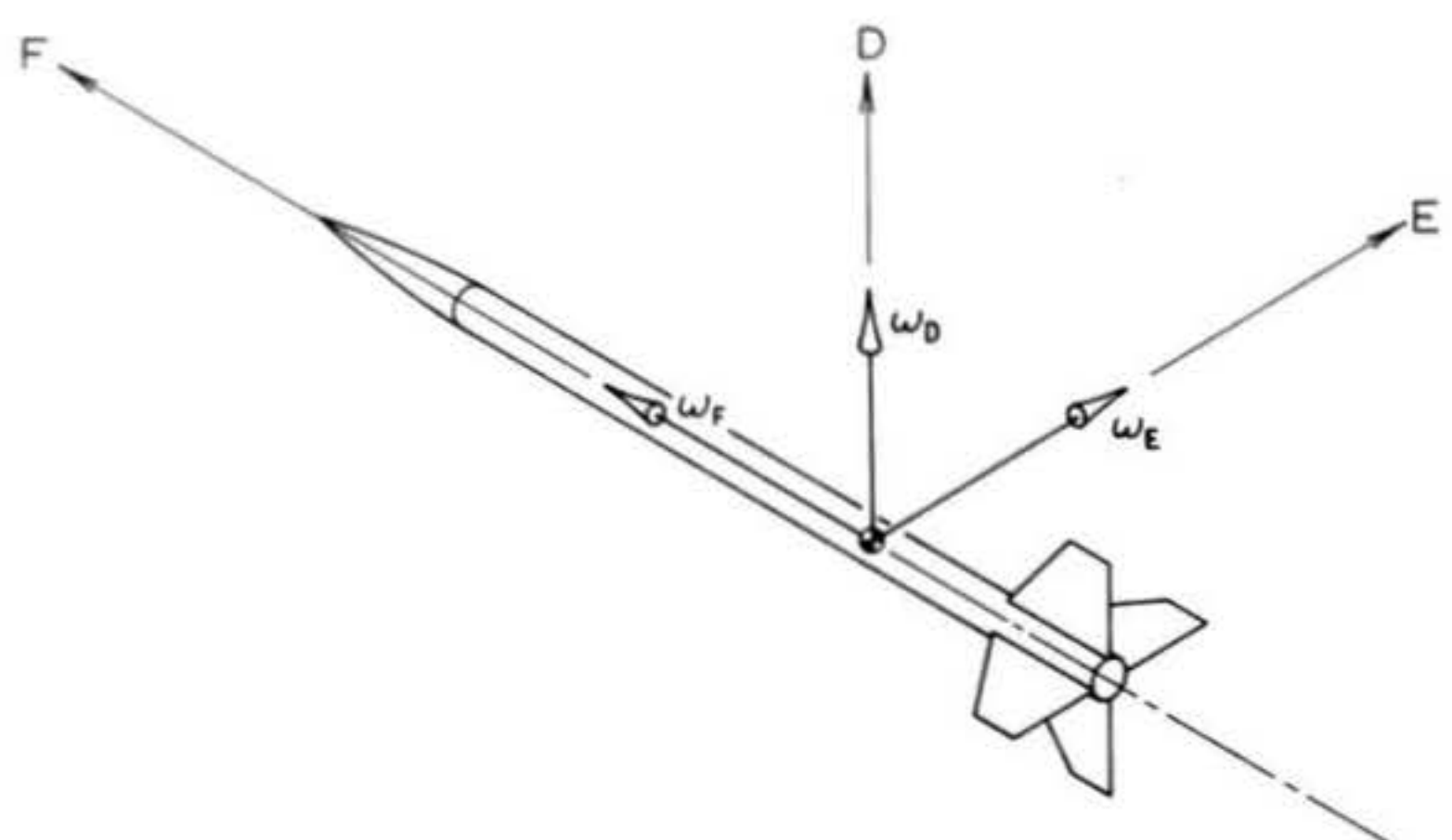


Figure 4: Vector representation of positive angular velocity components. Compare with Figures 2 and 3 to see how this representation is suggested by the direction of advance of a right-handed screw.

a little more explanation. While physical reasoning using differential quantities leads directly to the general form of equations (1), this technique is not very useful when the question is: "given the angular displacement as a function of time (that is, in an analytical formula), compute the angular velocity". In this case the relation

$$\omega = \frac{d\alpha}{dt}$$

is taken to mean: "given $\alpha(t)$ (the meaning of this notation is " α as a function of time" and it is read " α of t "), apply a known rule, or formula, for differentiating it with respect to time and obtain $\omega(t)$ ". The expression, or formula, for $\alpha(t)$ is subject to certain restrictions for this method to work properly, but these need not concern you in anything discussed here. I am going to list the formulae for the derivatives needed in this treatment wherever they appear, so that it will not be necessary to know them in order to follow the discussion.

1.3 Applied Moments, Angular Accelerations, and Moment of Inertia

Moment, or torque, is to rotational motion as force is to linear motion. It is the cause of all changes in the state of the rotational motion of a physical body. The simplest kind of relation between an applied moment and the resulting angular motion is identical in form to Newton's second law of motion for translational displacement: $\vec{F} = m\vec{a}$. To see this consider a flywheel, initially at rest, mounted in an axle held in frictionless bearings. At some time arbitrarily designated as $t = 0$ we begin to apply a constant moment about the shaft.

An angular velocity will then arise which starts from zero and increases linearly (i.e., at a constant rate) with time. The rate is directly proportional to the applied moment and inversely proportional to a property of the mass distribution in the wheel called its moment of inertia about its axis of radial symmetry. The relationship between an applied moment and the resulting angular acceleration is written

$$(2) \quad M = I \gamma$$

where M = applied moment
 I = moment of inertia
 γ = angular acceleration

Note that the angular acceleration γ is the time rate of change of the angular velocity ω , just as ω is the time rate of change of the angular displacement α . This sequence of derivative relationships is written

$$(3) \quad \begin{aligned} \gamma &= \frac{d\omega}{dt} \\ &= \frac{d}{dt} \left(\frac{d\alpha}{dt} \right) \\ &= \frac{d^2\alpha}{dt^2} \end{aligned}$$

where the expression $d^2\alpha/dt^2$ is read, "the second derivative of α with respect to t ". From a practical standpoint it means that the rule for differentiating $\alpha(t)$ has been applied twice in succession in order to obtain $\gamma(t)$. Thus γ , ω , and α are all related by derivatives with respect to time, a property of great value to analysis. In the case of a constant applied moment, for instance, the angular acceleration is given by

$$\gamma = \frac{M}{I}$$

while any mathematician could tell you that the angular velocity is

$$\omega = \frac{M}{I} \alpha$$

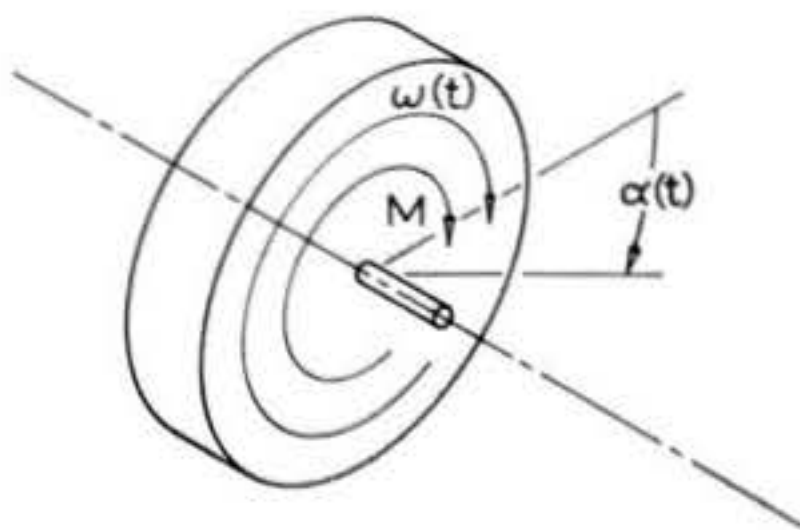
and the angular displacement after a time t is

$$\alpha = \frac{M}{2I} t^2$$

These relations are illustrated in Figure 5. Note also that both moment and angular acceleration are vectors, while moment of inertia, like mass, is a scalar. Moment of inertia gets its name not from the fact that an object exerts an equal and opposite moment on the cause of its angular acceleration (although it does), but from the fact that it is, mathematically speaking, the "second moment" of mass about a given axis, a term arising from the calculus formula for I . This analysis will not present the integral form that must be used to calculate I for the most general case, but the results for a few particular objects will appear later in the treatment.

1.4 Euler's Dynamical Equations

The general three-dimensional angular motion of rigid bodies in response to general applied moments is far more complicated than the simple flywheel example given above. Their derivation is of no interest to model rocketeers, and I have therefore omitted it entirely from this presentation. The results of interest to us are the dynamical equations for a body which has sufficient symmetry for the directions of the so-called principal axes to be geometrically obvious, and which is free to rotate about its center of mass in any direction. These equations, for a body with principal body axes D,E,F, rotating with respect to axes A,B,C fixed in space, are



$$\omega = \gamma t$$

$$= \frac{M}{I} t$$

$$\alpha = \frac{\gamma}{2} t^2$$

$$= \frac{M}{2I} t^2$$

Figure 5: Angular acceleration of a flywheel. At time $t = 0$ a constant moment M is applied to a flywheel whose moment of inertia about the axis is I , producing an angular acceleration $\gamma = M/I$.

$$M_D = I_D \frac{d\omega_D}{dt} - (I_E - I_F) \omega_E \omega_F$$

$$(4) \quad M_E = I_E \frac{d\omega_E}{dt} - (I_F - I_D) \omega_F \omega_D$$

$$M_F = I_F \frac{d\omega_F}{dt} - (I_D - I_E) \omega_D \omega_E$$

where M_D , M_E , and M_F are moments about D, E, and F impressed by external agencies and I_D , I_E , and I_F are the moments of inertia taken about axes D, E, and F respectively. These equations, also due to Euler, were a landmark in the history of classical dynamics and are named Euler's dynamical equations in his honor. For bodies having trigonal or greater mass symmetry about the longitudinal axis (this category includes most rockets) we have

$$I_D = I_E \equiv I_L$$

$$I_F \equiv I_R$$

and the equations reduce to

$$M_D = I_L \frac{d\omega_D}{dt} - (I_L - I_R) \omega_E \omega_F$$

$$(5) \quad M_E = I_L \frac{d\omega_E}{dt} - (I_R - I_L) \omega_F \omega_D$$

$$M_F = I_R \frac{d\omega_F}{dt}$$

It will become clear in a little while that these forms of the Euler equations are a bit inconvenient to use. It will be preferable to construct an intermediate system of axes X, Y, and Z which follow the rocket in yaw and pitch, but do not roll. Thus, Z always coincides with F but X and Y do not coincide with D and E

unless $\alpha_F = 0$. Therefore,

$$\begin{aligned}\alpha_x &= \alpha_D \\ \alpha_Y &= \alpha_E \\ \alpha_z &= 0 \neq \alpha_F\end{aligned}$$

This set of axes is shown in Figure 6. Since the rocket is symmetrical about Z, the intermediate axes remain principal regardless of the roll angle α_F . Let the angular velocity components of the intermediate axes be denoted by Ω_X , Ω_Y , and Ω_Z . Then we have

$$\begin{aligned}\Omega_x &= \omega_D \\ \Omega_Y &= \omega_E \\ \Omega_z &= 0 \neq \omega_F\end{aligned}$$

Since the Z axis always coincides with the F axis, the notation can be simplified to include only three coordinate variables by writing

$$\omega_z \equiv \omega_F$$

but we must be careful not to confuse ω_z (the roll rate of the rocket) with Ω_z (the roll rate of the intermediate coordinates, which is kept zero). The dynamical equations now become, for a body with trigonal or greater mass symmetry about Z,

$$(6) \quad \begin{aligned}M_x &= I_L \frac{d\Omega_x}{dt} + I_R \Omega_Y \omega_z \\ M_Y &= I_L \frac{d\Omega_Y}{dt} - I_R \Omega_x \omega_z \\ M_z &= I_R \frac{d\omega_z}{dt}\end{aligned}$$

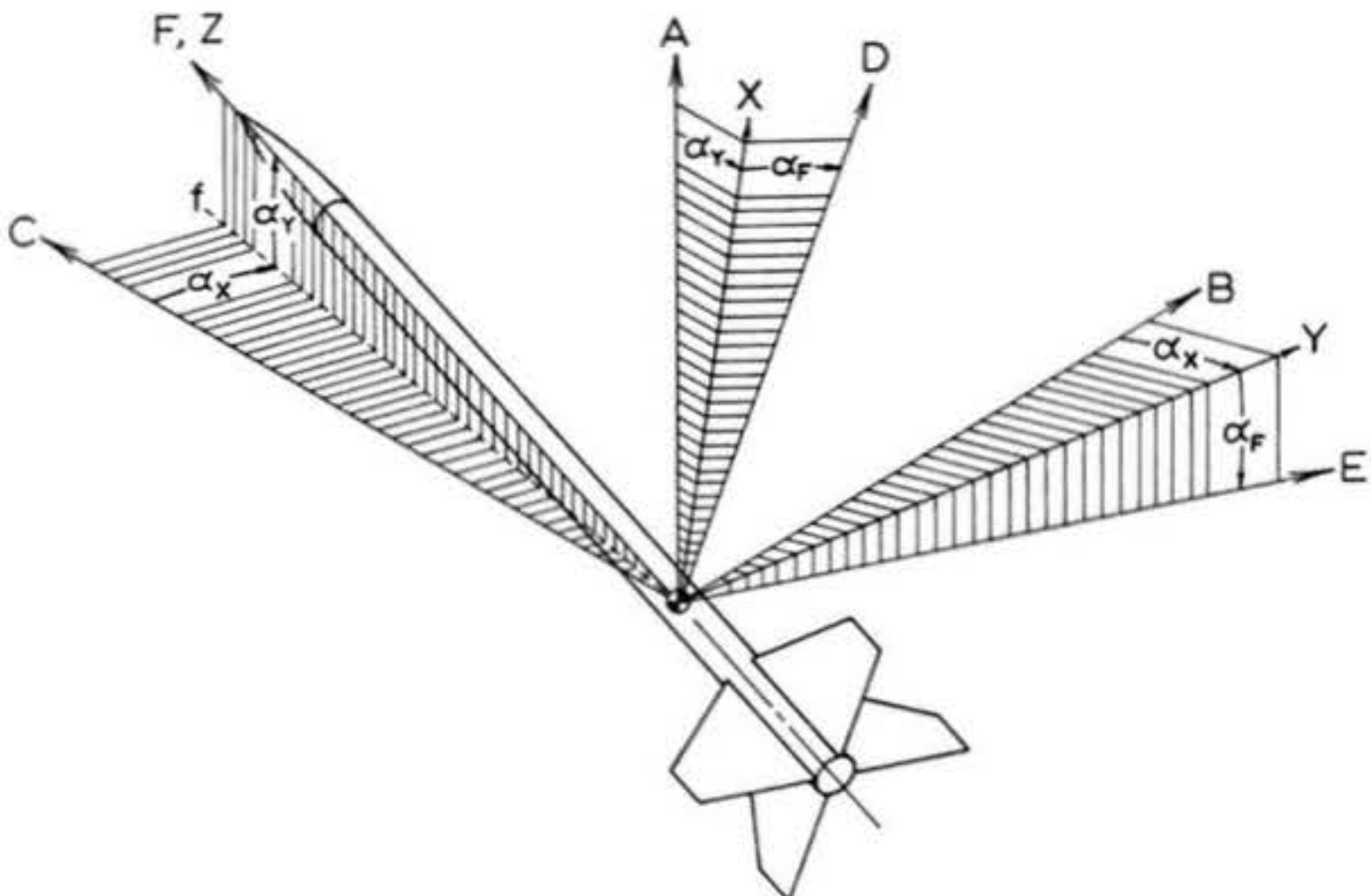


Figure 6: Space axes, intermediate axes, and body axes. The space axes (A,B,C) are rotationally fixed with respect to inertial space. The body axes (D,E,F) are fixed in the airframe of the rocket and follow it in yaw, pitch, and roll, while the intermediate axes (X,Y,Z) follow the rocket in yaw and pitch but maintain a zero roll angle.

2. The Linearized Theory

2.1 Corrective and Damping Moment

In considering the dynamics of a free-flying, fin-stabilized ballistic missile we are dealing principally with applied moments due to aerodynamic forces. Suppose that you have a model rocket which you have launched vertically, for instance. The model has begun its flight straight and true, but has subsequently been disturbed in some unknown manner such that it is rotated about its X axis. What happens next?

Ω_y and ω_z are both zero, and there is no M_y or M_z involved. The dynamical equations thus reduce to

$$M_x = I_L \frac{d\Omega_x}{dt}$$

Now if the rocket is statically stable a corrective moment M_c will be generated, of sign opposite to the displacement. Due to center of pressure travel, separation, and interference effects the precise dependence of corrective moment on angular displacement is quite complicated analytically. It is observed that the functional form of this relation is similar in appearance to Figure 7. As the rocket develops an angular velocity in response to the corrective moment, a damping moment M_d will also arise due to the consequent additional component of the relative velocity of the airstream normal (that is, perpendicular) to the longitudinal axis of the rocket. This moment will be opposite in sign to the angular velocity and has a functional form roughly as shown in Figure 8.

Suppose we denote M_c as an unspecified function of angular

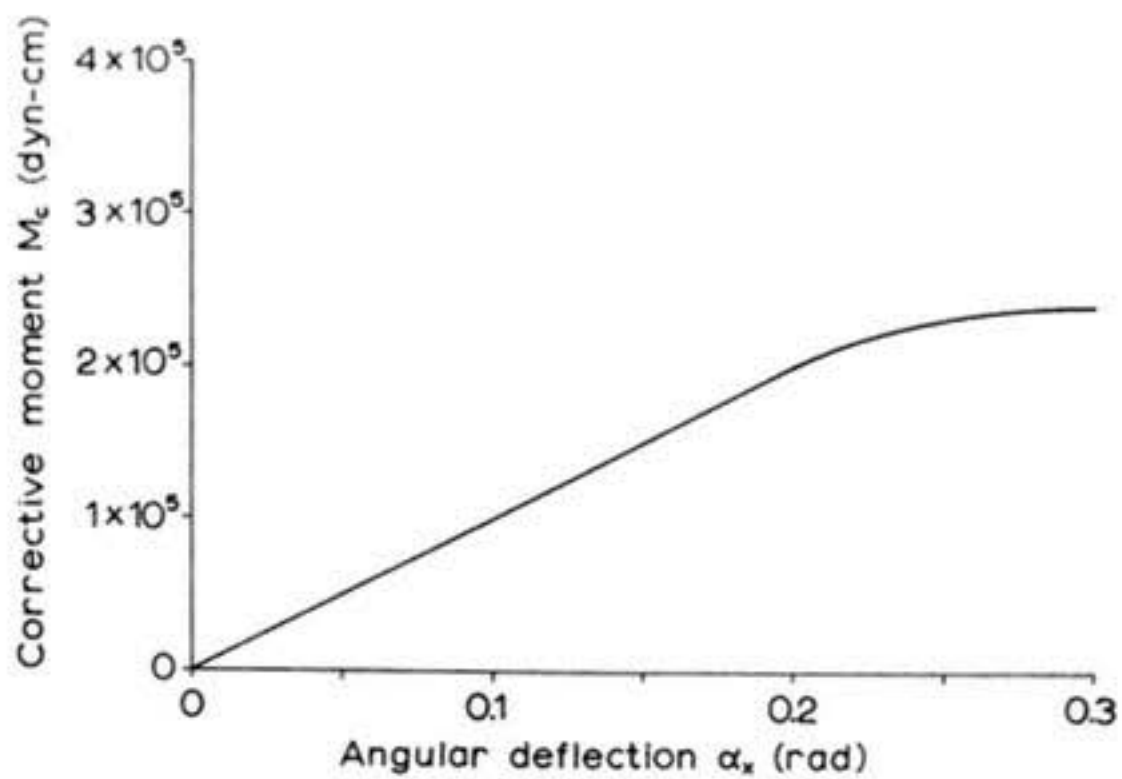


Figure 7: Variation of corrective moment with angular deflection for a typical model rocket at constant airspeed.

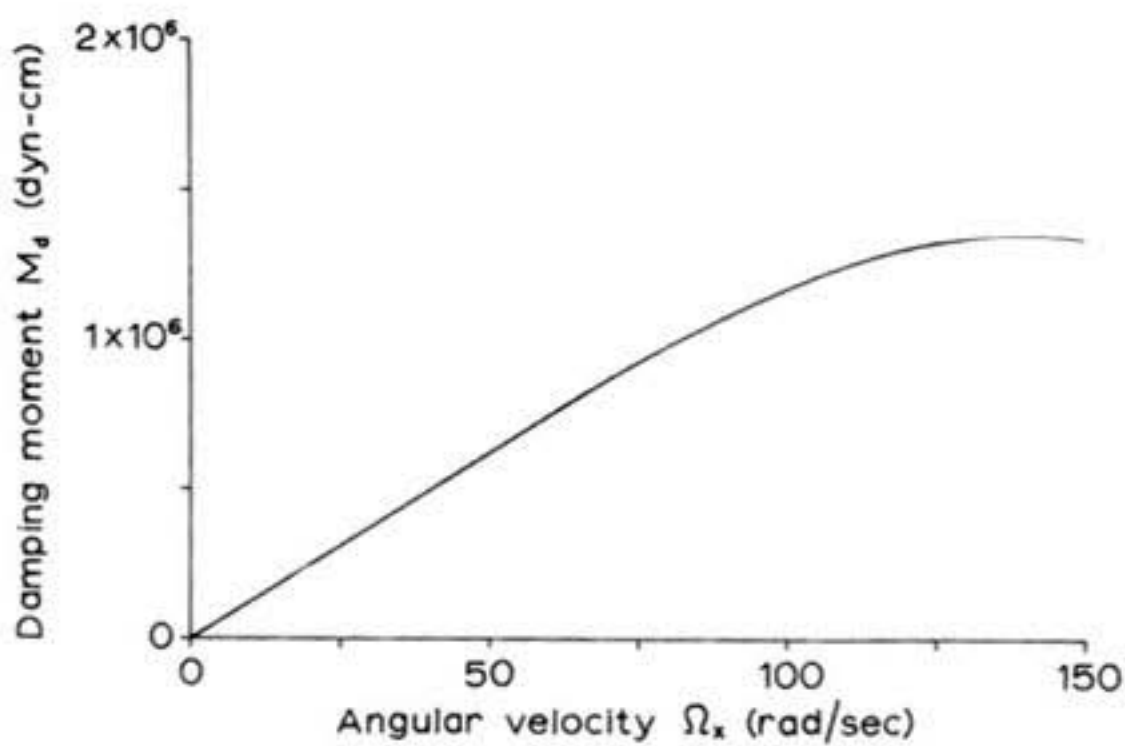


Figure 8: Variation of damping moment with angular velocity for a typical model rocket at constant airspeed.

displacement by writing $M_c = F(\alpha_x)$ and M_d as an unspecified function of angular velocity by writing $M_d = G(\Omega_x)$. Then we can write

$$\begin{aligned} M_x &= M_x \text{ due to } \alpha_x + M_x \text{ due to } \frac{d\alpha_x}{dt} \\ &= -M_c - M_d \\ &= -F(\alpha_x) - G(\Omega_x) \end{aligned}$$

Substituting these expressions in the dynamical equations, we have

$$I_L \frac{d\Omega_x}{dt} = -F(\alpha_x) - G(\Omega_x)$$

or

$$(7) \quad I_L \frac{d^2\alpha_x}{dt^2} + F(\alpha_x) + G\left(\frac{d\alpha_x}{dt}\right) = 0$$

An equation of this kind is called a homogeneous, nonlinear, differential equation -- "differential" because derivatives of α_x are involved; "homogeneous" because, when every term depending on α_x or its derivatives is moved to the left side of the equal sign, the right side of the equation is zero; and "nonlinear" because functions which may not be of the form " $y = mx + b$ " (the equation of a straight line) may be involved in relating corrective moment to angular displacement and damping moment to angular velocity. The "nonlinear" part is of particular importance: it means that, in general, the equation cannot be solved by any known means; it means that we have no assurance that a solution even exists, and, if it does, that there may not be more than one. It even means that the assumption that M_c and

M_d could simply be added to obtain M_x was incorrect.

2.2 The Linearization Approximations

In order to obtain a closed-form mathematical solution to the dynamical equations it is necessary to adopt a number of linearization approximations. The reasoning behind these proceeds as follows: although the functions representing M_c and M_d are not of the form " $y = mx + b$ ", they may be approximated by such forms over limited ranges of the values of their independent variables. An approximation of this kind is the tangent line to the exact function at some point of interest. Since the motions of a statically-stable rocket will all occur about $\alpha = 0$, $d\alpha/dt = 0$, and $d^2\alpha/dt^2 = 0$, zero is our tangent-point for these approximations. The linearization approximation for corrective moment states that

$$(8) \quad M_c \cong \left[\frac{dM_c}{d\alpha_x} \Big|_{\alpha_x=0} \right] \alpha_x = C_1 \alpha_x$$

which is read: " M_c is approximately equal to α_x times its derivative with respect to α_x at $\alpha_x = 0$ ". Similarly, the linearized damping moment is written

$$(9) \quad M_d \cong \left[\frac{dM_d}{d\Omega_x} \Big|_{\Omega_x=0} \right] \Omega_x = C_2 \Omega_x$$

The linearization procedure is illustrated in Figure 9. You can see that the approximations are just the slopes of the moment curves at α_x and $\Omega_x = 0$, respectively, multiplied by α_x and Ω_x , respectively. Another physical interpretation of the concept of the derivative is thus to view it as the local

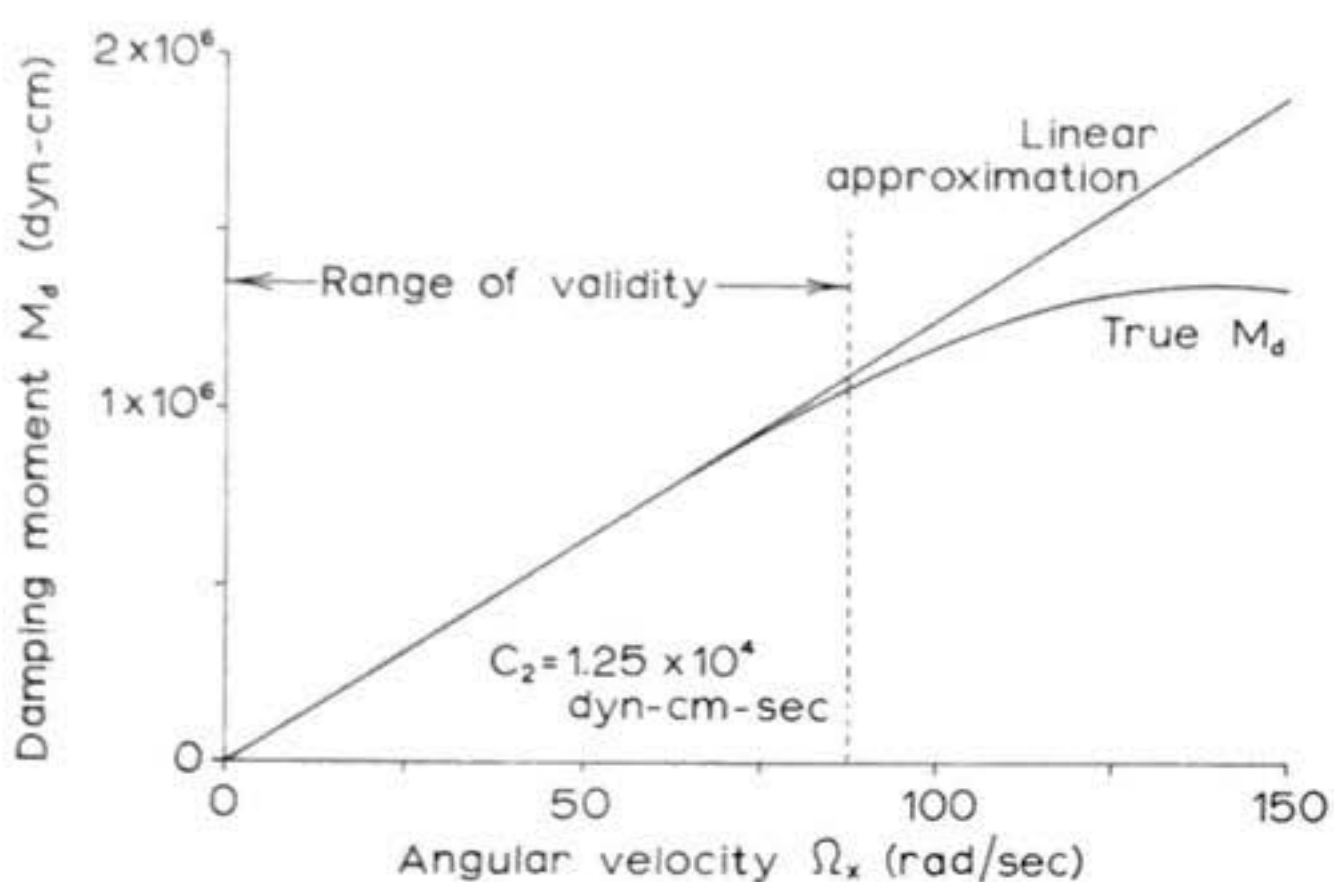
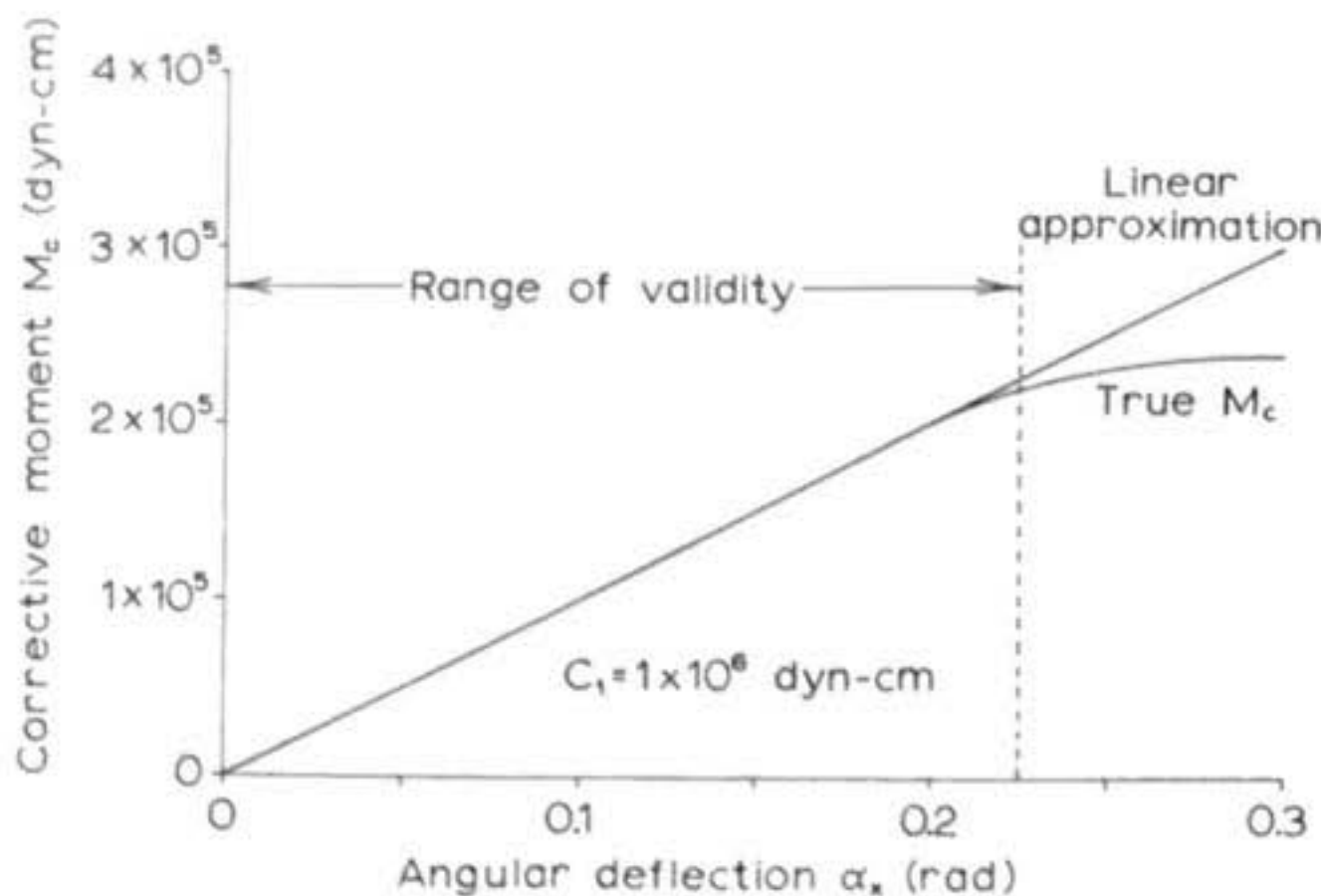


Figure 9: Linearization approximations used to determine corrective moment coefficient and damping moment coefficient for the model rocket of Figures 7 and 8. The corrective moment can be considered linearly proportional to the yaw deflection α_x for yaw angles less than 0.225 radian, while the damping moment can be considered linearly proportional to the yaw rate for yaw rates below 87 rad/sec.

slope of the graphical representation of the function whose derivative is being taken.

The linearized moment coefficients of this treatment are identical to those given in the Gurkin report. The correspondence between the two is as follows:

Present Treatment

$$\left. \frac{dM_c}{d\alpha_x} \right|_{\alpha_x=0} \equiv C_1$$

$$\left. \frac{dM_d}{d\Omega_x} \right|_{\Omega_x=0} \equiv C_2$$

Gurkin Report

$$\left. \frac{dM_c}{d\alpha_x} \right|_{\alpha_x=0} \equiv M_\alpha$$

$$\left. \frac{dM_d}{d\Omega_x} \right|_{\Omega_x=0} \equiv M_\phi$$

Within the ranges of validity of the linearization approximations it is permissible to express the total applied moment about the X axis as

$$M_x = -C_1 \alpha_x - C_2 \frac{d\alpha_x}{dt}$$

These approximations are valid for α_x and $d\alpha_x/dt$ sufficiently small: this means that the theory is restricted to cases of relatively small angular displacements and angular velocities; it is a so-called small-perturbation theory. This restriction is acceptable in statically stable rockets for two reasons: in the vast majority of cases, the yaw and pitch disturbances encountered during flight will be sufficiently small for a valid linear description and the angular velocities involved will not be out of the linear range of M_d . Secondly, should nonlinear behavior be encountered the description of the linear theory will still be qualitatively correct and, in any case, the motion will eventually damp down to within the linear displacement dependence range. Furthermore, should you ever obtain from this

theory a solution indicating continued large and violent motions (for which the theory itself is invalid), you will have, in a sense, obtained all the information you need: you will know that the rocket in question ought to be redesigned.

The limiting numerical values of yaw and pitch that can be treated within this theory are about 12 degrees (about 0.2 radian) either side of zero. The maximum permissible angular velocity will vary with the length of the rocket in question, the placement of its fins, and the speed at which it is travelling. As a practical matter, the inertial and aerodynamic characteristics of a well-designed rocket will invariably satisfy the angular velocity limit for that rocket.

The great advantage of using the intermediate axis system now becomes clear: the angular displacements of the rocket about the X and Y axes will generally be small perturbations, but since there is no restoring moment about the roll axis of a ballistic rocket the angular displacements about the Z axis will often not be small. The intermediate axes remove the necessity of keeping track of the third Euler's angle α_F and result in considerable analytical simplification. They allow us to view the motions in yaw and pitch from a position fixed in roll, without having to rotate with the rocket whenever it spins about its longitudinal axis. We can thus observe the yawing and pitching motions from a perspective relative to the space axes that is constant within the linear theory and can compute them directly as deviations of the longitudinal axis from the direction of flight.

Returning to the dynamical equation for our case of yaw displacement and substituting the linearized form of the applied moment M_x , we find that

$$(10) \quad I_L \frac{d^2\alpha_x}{dt^2} + C_2 \frac{d\alpha_x}{dt} + C_1 \alpha_x = 0$$

This is now a homogeneous linear differential equation with constant coefficients. It is known that such equations always have a solution and that the solution is unique (i.e., that there is only one). Furthermore, the functional form of the solution to this particular equation is well known and the solution itself is readily obtainable by a substitution technique called the method of undetermined coefficients. If the rocket under consideration has four identical fins, the equation describing the pitching motion will be precisely analogous to that describing the yawing motion, the two having the same linear moment coefficients:

$$I_L \frac{d^2\alpha_y}{dt^2} + C_2 \frac{d\alpha_y}{dt} + C_1 \alpha_y = 0$$

The pitch and yaw linear moment coefficients of a three-finned rocket may be expected to be slightly different and there will be some slight aerodynamic rolling moments arising from pitch and yaw angular displacements and angular velocities. Reasoning from the observed flight behavior of such rockets, though, it appears that these effects are slight and we shall restrict ourselves here to considering pitching behavior with the same constants as yawing behavior, both being aerodynamically decoupled from roll.

2.3 Coupled and Decoupled Systems of Equations

Once the linearization approximations have been made the dynamical equations of a rocket which is not rolling about its centerline become

$$(11) \quad I_L \frac{d^2\alpha_x}{dt^2} + C_2 \frac{d\alpha_x}{dt} + C_1 \alpha_x = 0$$
$$I_L \frac{d^2\alpha_y}{dt^2} + C_2 \frac{d\alpha_y}{dt} + C_1 \alpha_y = 0$$

For cases in which the rocket is spinning with some roll rate ω_z we have

$$(12) \quad I_L \frac{d^2\alpha_x}{dt^2} + C_2 \frac{d\alpha_x}{dt} + C_1 \alpha_x + I_R \omega_z \frac{d\alpha_y}{dt} = 0$$
$$I_L \frac{d^2\alpha_y}{dt^2} + C_2 \frac{d\alpha_y}{dt} + C_1 \alpha_y - I_R \omega_z \frac{d\alpha_x}{dt} = 0$$

Equations (11) are said to be decoupled because α_x and its time derivatives do not appear in the same equation with α_y and its time derivatives. Equations (12), however, have been coupled together by the presence of the terms due to ω_z . Each equation of a decoupled system of equations can be solved independently of any others, but coupled systems must be solved simultaneously (i.e., by using various mathematical techniques to combine them so that they can both be considered at once). In both systems, if the roll rate ω_z is constant, the third dynamical equation is identically zero and I have not written it down. It is important to notice that, in a radially symmetrical body like a rocket, pitch can be coupled to yaw by the presence of roll but roll itself is never inertially coupled either to pitch or to yaw.

2.4 Homogeneous, Particular, and Steady-State Solutions

Recall that we began our discussion of the linearization approximations with an example in which we considered a rocket which had been initially displaced and concerned ourselves with its subsequent return to alignment. The only moments applied to the rocket were those due to the angular deflection itself and its time derivatives. Motions of this kind are called homogeneous, force-free, or characteristic responses. The state of the rocket at the time the observation of its behavior begins is known as the set of initial conditions; these must be known in order to obtain a complete solution to the motion. Both the initial angular deflection and the initial angular velocity must be specified to complete the set.

Now suppose that there are additional moments acting on the rocket, and that these moments are functions of time due to causes other than angular displacement and its time derivatives. They might, for instance, be due to aerodynamic imbalances such as drag on the launch lug, misaligned fins, or the movement of control surfaces on the fins. They might also be due to off-center engine mounting, angled thrust, or the momentary expulsion of solid residue from the rocket nozzle. Such moments are called inputs, or forcing functions, and they appear on the right-hand side of the dynamical equations, which are therefore no longer homogeneous. For the case of zero roll rate with forcing in yaw and pitch we have

$$(13) \quad I_L \frac{d^2\alpha_x}{dt^2} + C_2 \frac{d\alpha_x}{dt} + C_1 \alpha_x = f_x(t)$$
$$I_L \frac{d^2\alpha_y}{dt^2} + C_2 \frac{d\alpha_y}{dt} + C_1 \alpha_y = f_y(t)$$

where $f_x(t)$ is read, "function of time, about the X-axis" and $f_y(t)$ is read, "function of time, about the Y-axis". With the presence of a constant roll rate the equations become

$$(14) \quad \begin{aligned} I_L \frac{d^2\alpha_x}{dt^2} + C_2 \frac{d\alpha_x}{dt} + C_1 \alpha_x + I_R \omega_z \frac{d\alpha_y}{dt} &= f_x(t) \\ I_L \frac{d^2\alpha_y}{dt^2} + C_2 \frac{d\alpha_y}{dt} + C_1 \alpha_y - I_R \omega_z \frac{d\alpha_x}{dt} &= f_y(t) \end{aligned}$$

The response of the rocket to these moments is the sum of the characteristic motion and a motion called the particular response which is directly attributable to the effect of the forcing. The initial angular positions and velocities in yaw and pitch must be specified, as before, to obtain the complete motion; in this case, however, it is the sum of the characteristic and particular responses which must satisfy the initial conditions. For a rocket flying straight and evenly upward before encountering a disturbance, these conditions are zero. From this you can see how the initial conditions of the characteristic motion arise: the rocket, initially undisturbed, is subjected to a forcing function which arises, persists for some interval of time, and then dies away to zero again. After the forcing has passed the rocket possesses some angular displacement and velocity -- the initial conditions of the characteristic response, which then ensues. As will be shown later, the characteristic response of a statically stable rocket decreases with time and finally becomes effectively zero. Thus after some time the condition of straight and true flight is restored.

Both the linearity of the dynamical equations and the decaying behavior of the characteristic response are extremely

valuable features of the motion from the standpoint of analysis. Linear differential equations possess the property of superposition, meaning that the response to any number of inputs applied simultaneously is just the sum of the particular responses due to each one separately, plus the homogeneous response. The effect of each disturbance can be computed separately and the total effect found by summing the individual effects. This is certainly far easier than solving an equation with one huge right-hand side! And since the characteristic response approaches zero with time, any forcing function which continues for a long enough time will cause the complete solution to approach the particular solution alone: after enough time has passed, the particular response is all that remains. You will thus see references in the literature of dynamics to the steady-state, or forced, response to this type of input, the term being most often applied when the input is specifically a smooth, periodic function of time such as a sine wave.

3. Solutions to the Dynamical Equations for Particular Cases of Interest

Having given the reader some background from which to proceed, I am going to compute the properties of some solutions to the dynamical equations which are of particular interest to the model rocketeer. The presentation will be divided into two parts: one which will treat rockets having a zero roll rate and a second which will consider the behavior of models spinning about their centerlines. Each section will consider the four basic dynamic responses: homogeneous, step, impulse, and steady-state sinusoidal. It can be shown mathematically that there is

no response that cannot be synthesized by adding together various combinations of these, so that by investigating the "basic four" a designer can obtain all the information he will ever need about the dynamic characteristics of his rocket.

I wish to emphasize here that you should not become concerned if you find it difficult to follow the detailed course of each calculation. You will not have to know how to solve the differential equations in order to design model rockets properly, and the mathematical derivations have been presented solely for the interest of those readers desiring a rigorous treatment. What you should try to concentrate on are the algebraic solutions obtained in each case, for it is from these that the response to any disturbance can be directly computed and it is on them that the dynamical characteristics of any given model rocket depend.

3.1 Dynamical Behavior at Zero Roll Rate

3.1.1 Generalized Homogeneous Response

The homogeneous response for generalized initial conditions describes the motion executed by a rocket in response to some transient disturbance which has since died away. Since there is no roll coupling only one of the equations (11) need be solved. The other, which is similar, will have an analogous solution for its own initial conditions. Suppose that, throughout this section, we adopt the convention that the rocket is considered to have been disturbed in yaw alone. In each of the four decoupled problems the pitching behavior is precisely analogous to the yawing behavior; an analysis of pitching motion can add nothing to the information already obtained from an analysis of yawing motion

and I have therefore omitted it. All you need remember on this score is that everything I say about yaw applies also to pitch.

The equation to be solved for the characteristic yaw response is

$$I_L \frac{d^2 \alpha_x}{dt^2} + C_2 \frac{d \alpha_x}{dt} + C_1 \alpha_x = 0$$

Over a certain range of relative values of I_L , C_1 and C_2 the solution is known to be of the form

$$(15) \quad \alpha_x = A e^{-Dt} \sin(\omega t + \varphi)$$

where e is the base of the Naperian, or natural logarithm system and is numerically equal to about 2.718. t denotes time and A , D , ω and φ are constants to be determined. By "time" I mean the time elapsed since the observation of the dynamic response has begun, not the time elapsed since the rocket was launched. To reference equation (15) to liftoff, call the time elapsed since launch t' and the time interval between launch and the beginning of the observation t'_0 . Then replace t in formula (15) by the quantity $(t' - t'_0)$. A is called the initial amplitude, D is defined as the inverse time constant, ω (not literally an angular velocity of the rocket's motion) is the angular frequency in radians/second (for time reckoned in seconds), and φ is the phase angle, or simply "phase", in radians. A radian, the fundamental natural unit of angle measure, is approximately equal to 57.3 degrees. The formulae for the time derivatives of the function described by equation (15) are:

$$\frac{d\alpha_x}{dt} = -ADe^{-Dt} \sin(\omega t + \varphi) + A\omega D e^{-Dt} \cos(\omega t + \varphi)$$

$$\frac{d^2\alpha_x}{dt^2} = A(D^2 - \omega^2)e^{-Dt} \sin(\omega t + \varphi) - 2A\omega D e^{-Dt} \cos(\omega t + \varphi)$$

Substituting these relations in the yaw equation gives

$$I_L A(D^2 - \omega^2)e^{-Dt} \sin(\omega t + \varphi) - 2I_L A\omega D e^{-Dt} \cos(\omega t + \varphi) - C_2 A D e^{-Dt} \sin(\omega t + \varphi) + C_2 A \omega e^{-Dt} \cos(\omega t + \varphi) + C_1 A e^{-Dt} \sin(\omega t + \varphi) = 0$$

Since Ae^{-Dt} is nonzero and appears in every term, we can divide by it and obtain

$$I_L (D^2 - \omega^2) \sin(\omega t + \varphi) - 2I_L \omega D \cos(\omega t + \varphi) - C_2 D \sin(\omega t + \varphi) + C_2 \omega \cos(\omega t + \varphi) + C_1 \sin(\omega t + \varphi) = 0$$

Since sine and cosine vary differently with time the only way in which a function involving both can be zero for all time is for the sine and cosine terms to sum independently to zero:

$$I_L (D^2 - \omega^2) \sin(\omega t + \varphi) - C_2 D \sin(\omega t + \varphi) + C_1 \sin(\omega t + \varphi) = 0$$

$$-2I_L \omega D \cos(\omega t + \varphi) + C_2 \omega \cos(\omega t + \varphi) = 0$$

Dividing the first of these by $\sin(\omega t + \varphi)$, the second by $\omega \cos(\omega t + \varphi)$, we obtain

$$I_L (D^2 - \omega^2) - C_2 D + C_1 = 0$$

$$-2I_L D + C_2 = 0$$

Solving these two algebraic equations for D and ω gives

$$(16) \quad D = \frac{C_2}{2 I_L}$$

$$(17) \quad \omega = \sqrt{\frac{C_1}{I_L} - \frac{C_2^2}{4 I_L^2}}$$

A and φ are now determined from the two initial conditions.

Let α_{x0} be the value of α_x at $t = 0$ and let Ω_{x0} be the value of $d\alpha_x/dt$ at $t = 0$. Setting t to zero in the formulae for α_x and $d\alpha_x/dt$ results in the following two expressions:

$$\alpha_{x0} = A \sin \varphi$$

$$\begin{aligned}\Omega_{x0} &= -AD \sin \varphi + A\omega \cos \varphi \\ &= -D\alpha_{x0} + A\omega \cos \varphi\end{aligned}$$

from which

$$\sin \varphi = \frac{\alpha_{x0}}{A}$$

$$\cos \varphi = \frac{D\alpha_{x0} + \Omega_{x0}}{A\omega}$$

We now make use of the following trigonometric identity to evaluate A and φ :

$$\frac{\sin \varphi}{\cos \varphi} = \tan \varphi$$

From this we have

$$(18) \quad \tan \varphi = \frac{\alpha_{x0} \omega}{D\alpha_{x0} + \Omega_{x0}} \quad \text{or} \quad \varphi = \arctan \left(\frac{\alpha_{x0} \omega}{D\alpha_{x0} + \Omega_{x0}} \right)$$

where the notation "arctan" has the interpretation, "that angle

whose tangent is..." From the expression for $\sin\varphi$ it is also evident that

$$(19) \quad A = \frac{\alpha_{x_0}}{\sin\varphi}$$

and thus we have all the information we require to completely describe the rocket's angular motion. Motion of this kind is called an exponentially-damped sinusoid and its behavior is determined by the relative values of I_L , C_1 , and C_2 .

For $C_2 = 0$, the case of zero damping, the expression for yaw becomes

$$\alpha_x = A \sin (\omega_m t + \varphi)$$

where $\omega_m = \sqrt{\frac{C_1}{I_L}}$. ω_m is known as the natural frequency of the rocket at the given airspeed. The yaw response is simple harmonic motion: sinusoidal oscillations of angular frequency ω_m at constant amplitude A , as shown in Figure 10. This motion never really occurs, as there always exists some degree of aerodynamic damping; it is a so-called limiting case, meaning that it is closely approximated for very small values of $C_2/2I_L$. Such vanishingly small damping is not desirable, for it means that the oscillations of the rocket will persist for many cycles without dying away. Under such conditions the rocket will present a greater average frontal area to the airstream; consequently the drag will be increased. Since there is also a side force on a yawed or pitched rocket, some altitude will be lost due to the resulting "ripple" in the flight path as the side force causes a side-to-side movement of the rocket considered as a

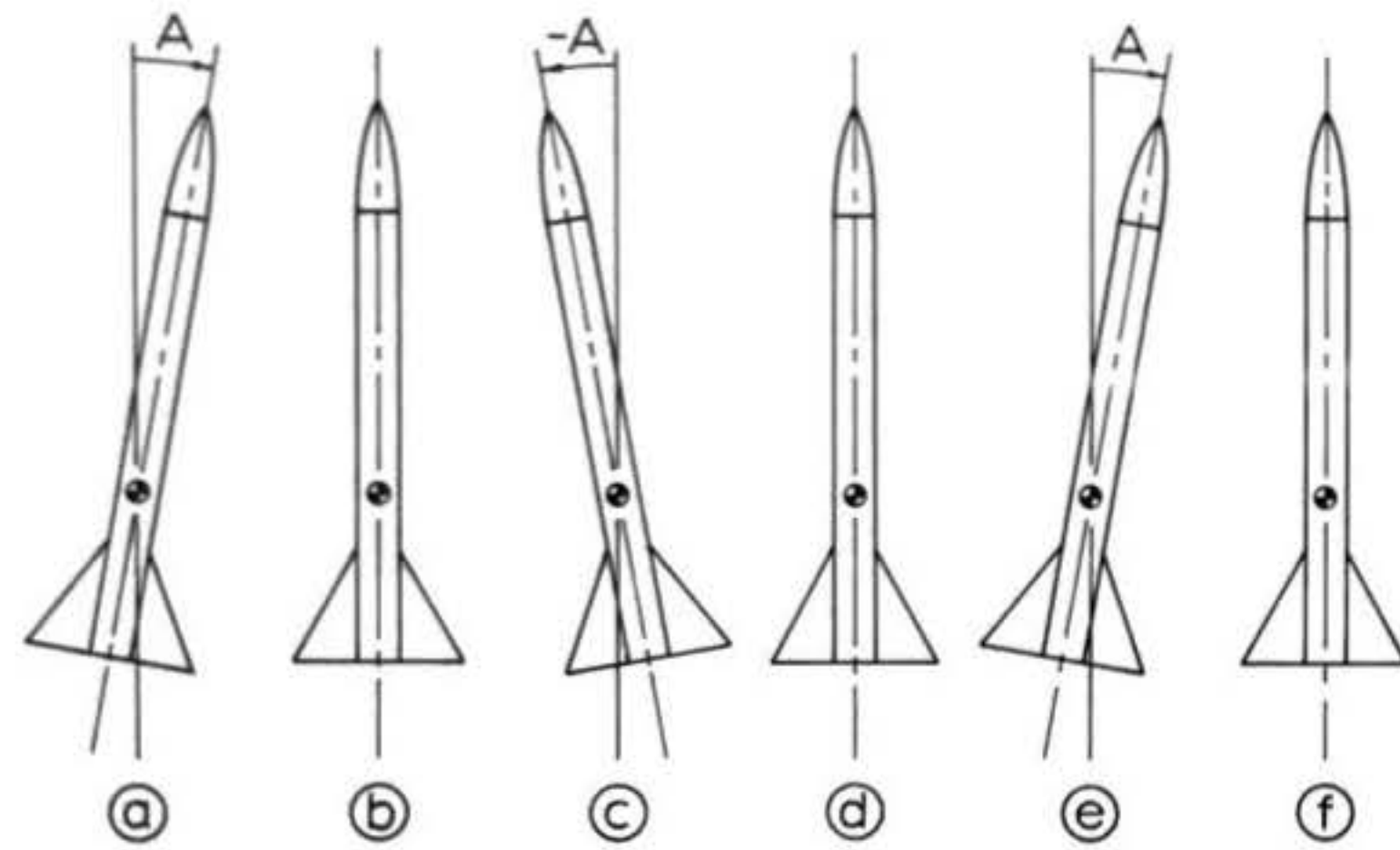
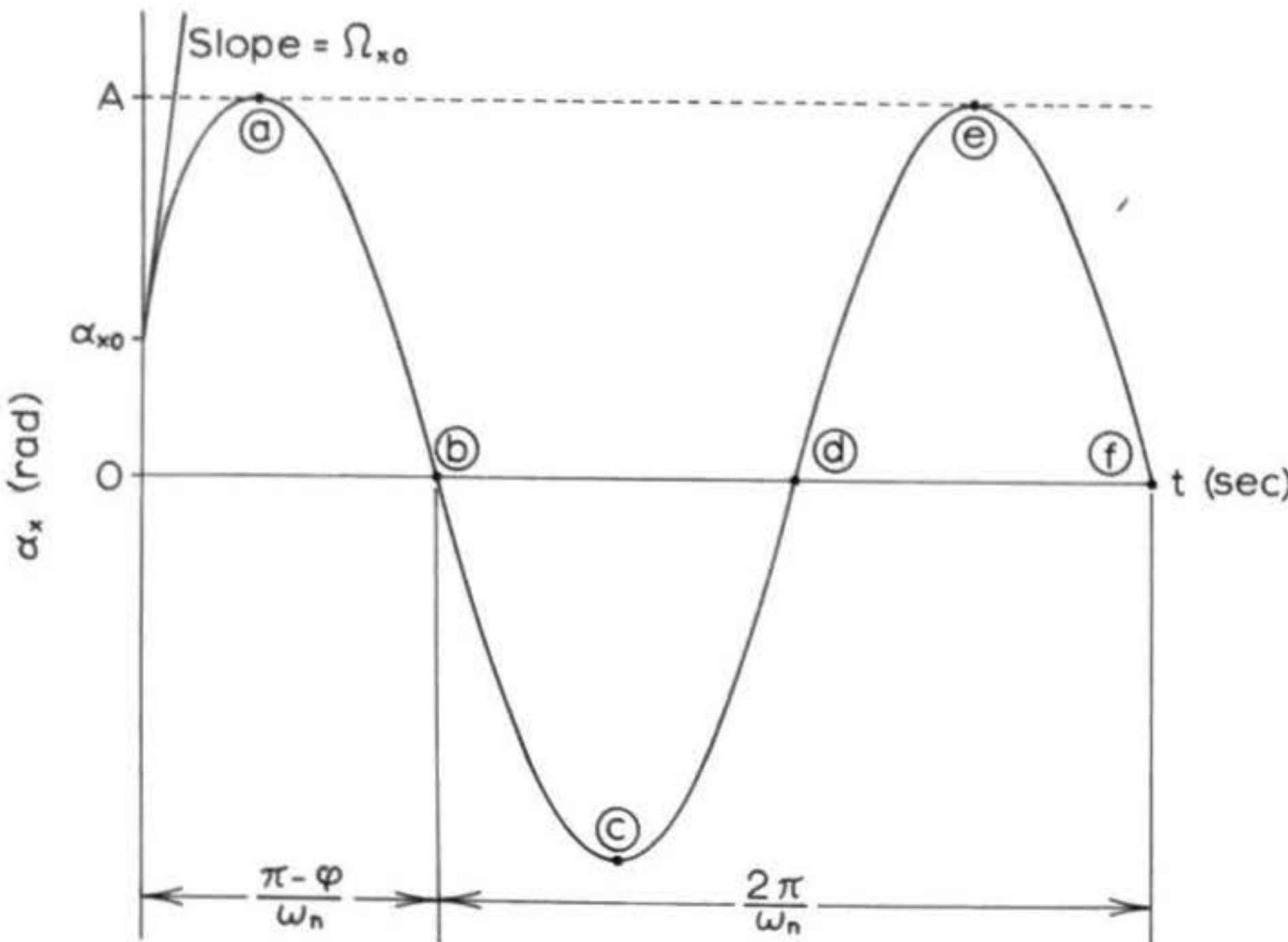


Figure 10: Model rocket with zero damping undergoing simple harmonic motion in homogeneous response to general initial conditions in yaw. The time to reach the first zero, the period of the oscillation, and the relation of the initial conditions to the properties of the response are shown. A guide to interpreting the graph is presented below it, showing the rocket as it would appear at various times if viewed from the negative y axis. This and all subsequent calculations of dynamic response presented in this chapter are based on the assumption of constant airspeed, so that C_1 and C_2 do not change during the response.

whole. For zero damping true alignment would never be regained.

I might remark at this point that Gurkin's "Basic Missile Aerodynamic Stability" contains references to quantities which are analogous to the natural frequency and the inverse time constant as defined in the present treatment. The correspondence between my forms and those of Gurkin is as follows:

	<u>Present Treatment</u>	<u>Gurkin Report</u>
Natural Frequency	$\omega_n = \sqrt{\frac{C_1}{I_L}}$	$\omega_n = \sqrt{\frac{M_\alpha}{I}}$
Inverse Time Constant	$D = \frac{C_2}{2I_L}$	$d = \frac{M_\alpha}{2I}$

For values of C_1 , C_2 , and I_L such that $0 < \frac{C_2^2}{4I_L} < \frac{C_1}{I_L}$ we have the case of underdamped motion. The oscillations have the appearance of a sine curve confined within a decaying exponential curve, as shown in Figure 11. The angular frequency ω is smaller than the natural frequency and the amplitude of the oscillations decreases toward zero with increasing time. The characteristics of almost all model rockets are such that the homogeneous response will be of this nature at any reasonable airspeed. This is a desirable type of behavior, for it is in this range of values of $C_2/2I_L$ that the quickest restoration of the rocket to the intended direction of flight occurs. If we define a damping ratio ζ by

$$(20) \quad \zeta = \frac{C_2}{2\sqrt{C_1 I_L}}$$

and agree to consider straight flight to have been restored when the magnitude of α_x drops below and never again exceeds 5% of A , we find that the most rapid restoration occurs when $\zeta = \frac{\sqrt{2}}{2}$,

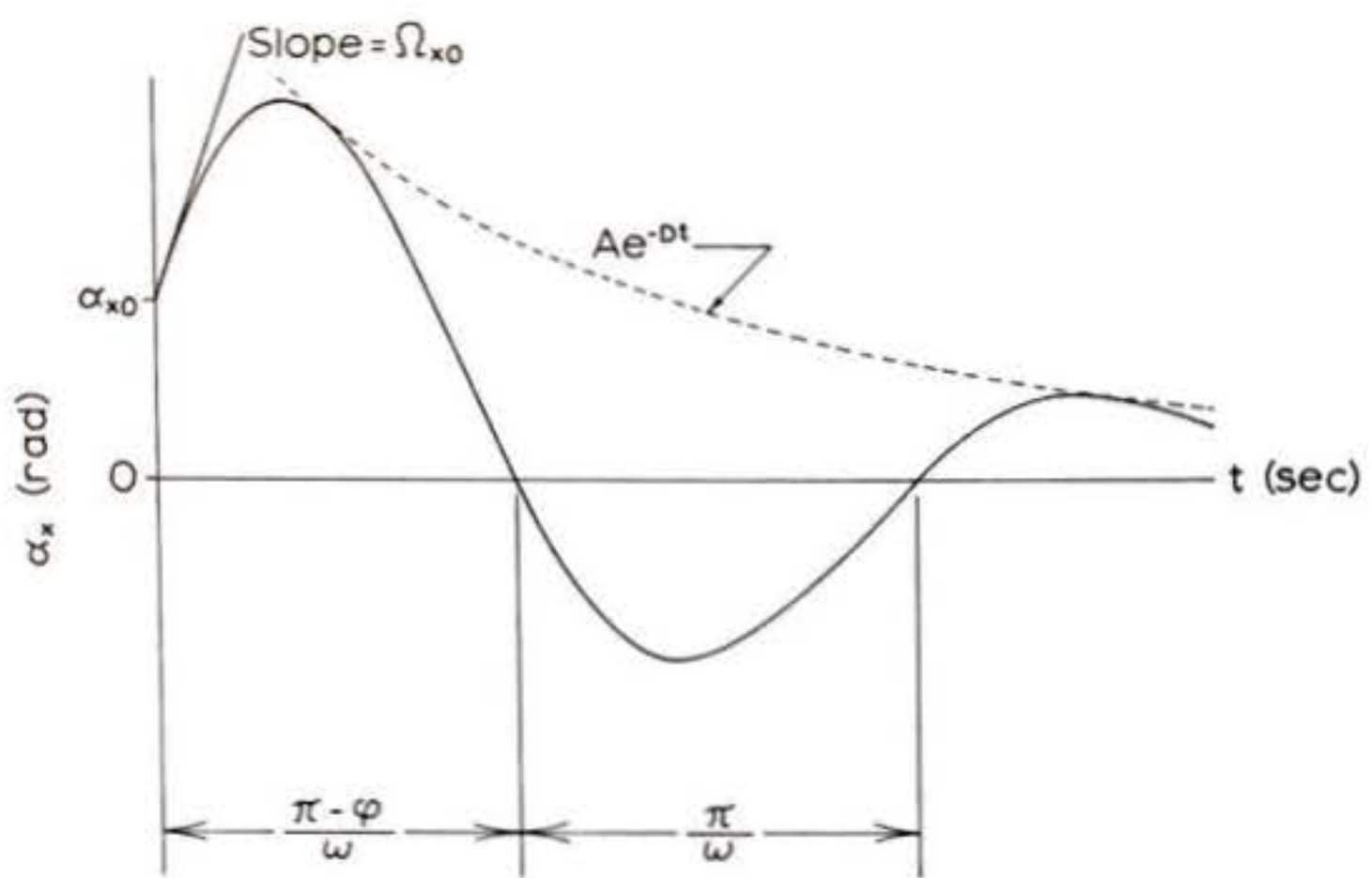


Figure 11: Underdamped characteristic response to general initial conditions in yaw. The amplitude of the sinusoidal oscillation is confined within an exponentially-decaying "envelope" as shown by the dotted line. Also illustrated are the relation between the initial conditions and the characteristics of the response, the time to reach the first zero, and one-half the period required for one full oscillation.

or about .7071. We therefore have the result

$$(21) \quad \text{optimum damping } \equiv \zeta = \frac{\sqrt{2}}{2}$$

Surprisingly, $\zeta > \frac{\sqrt{2}}{2}$ results in a slower restoration. This is because the decrease in angular frequency becomes more important than the decrease in the number of cycles required. This decrease in angular frequency has another, more serious effect: it invalidates one of the assumptions on which this analysis is based.

The reader will recall my references to "side forces" and the side-to-side lateral motion of the rocket which they produce when angular oscillation is occurring. This lateral motion necessarily involves the presence of velocity components normal (that is, at right angles) to the intended direction of flight. Such velocity components, in turn, have the effect of reducing the apparent yaw angle "sensed" by the deflected rocket with the result that the effective corrective moment is reduced and the frequency of the oscillations is decreased below that predicted by the linearized theory which considers the CG of the rocket to undergo no lateral displacement. Luckily, the frequencies at which most model rockets oscillate are such that the effect of lateral motion is far too small to be noticeable; however, should a given rocket have a very low frequency of oscillation for its mass (as it would if its damping ratio were high) the lateral displacements would become very large, so large, in fact, that the rocket might be very seriously deflected from its intended vertical trajectory. Too high a damping ratio is thus a dangerous condition and should be avoided at all costs.

To obtain a clearer picture of the effects of excessive damping, we can examine the predicted behavior of the rocket as ζ increases past $\frac{\sqrt{2}}{2}$. Now we can express ω in terms of the damping ratio as

$$\omega = \omega_m \sqrt{1 - \zeta^2}$$

For optimum damping at any airspeed, ω is just $.7071\omega_m$. As ζ approaches 1.0, ω approaches zero, and when a unity damping ratio is reached, the case of critical damping, the motion ceases to be oscillatory. The form of solution given by equation (15) is no longer valid.

For the case $\zeta = 1$, corresponding to $C_2^2/4I_L^2 = C_1/I_L$, the solution to the dynamical equation has the form

$$(22) \quad \alpha_x = (A_1 + A_2 t) e^{-Dt}$$

The formulae for the time derivatives of α_x are

$$\frac{d\alpha_x}{dt} = A_2 e^{-Dt} - D(A_1 + A_2 t) e^{-Dt}$$

$$\frac{d^2\alpha_x}{dt^2} = D^2(A_1 + A_2 t) e^{-Dt} - 2A_2 D e^{-Dt}$$

Substituting these in the dynamical equation and removing the common factor e^{-Dt} gives

$$I_L D^2(A_1 + A_2 t) - 2I_L A_2 D + C_2 A_2 - C_2 D(A_1 + A_2 t) + C_1(A_1 + A_2 t) = 0$$

The terms involving t must sum to zero independently of those not involving t . Imposing this condition, we obtain

$$I_L D^2 A_1 - 2 I_L A_2 D + C_2 A_2 - C_2 D A_1 + C_1 A_1 = 0$$

$$I_L D^2 A_2 - C_2 D A_2 + C_1 A_2 = 0$$

Removing A_2 from the second equation and solving for D , we have

$$D = \frac{C_2}{2I_L} \pm \sqrt{\frac{C_2^2}{4I_L^2} - \frac{C_1}{I_L}}$$

But in this case we already know that $C_2^2/4I_L^2 = C_1/I_L$. The expression under the radical sign is zero and

$$D = \frac{C_2}{2I_L} \quad \text{as before.}$$

If you substitute C_2/I_L for D in the first equation, you will find that the terms involving A_2 sum to zero. It is then possible to remove the now-common factor of A_1 and obtain

$$C_1 - \frac{C_2^2}{4I_L} = 0$$

But if we divide this by I_L we see that it is equivalent to

$$\frac{C_1}{I_L} - \frac{C_2^2}{4I_L^2} = 0$$

which we already know is true, since this is the case for which we are solving. The differential equation therefore imposes no constraint on A_1 and A_2 ; these are determined by the initial conditions. Setting $t = 0$ in the expressions for α_x and $d\alpha_x/dt$, we have

$$\alpha_{x_0} = A_1$$

$$\Omega_{x_0} = A_2 - DA_1$$

Then

$$(23) \quad \begin{aligned} A_1 &= \alpha_{x_0} \\ A_2 &= \Omega_{x_0} + D\alpha_{x_0} \end{aligned}$$

The motion for this case is illustrated in Figure 12. Note that in this case α_x never crosses to the opposite side of the t axis from that on which it originates. This behavior is said to exhibit no overshoot. If α_{x_0} and Ω_{x_0} are both positive (as shown) or both negative there will be a single "peak" in the curve of yaw angle versus time before the angular displacement dies away; otherwise it dies away directly to zero. Despite the fact that $A_2 t$ increases as time goes on, the decay of e^{-Dt} will eventually force the function as a whole to zero. Critically damped motion is a good deal less desirable than motion of the oscillatory, underdamped variety. The time to restore alignment is longer and the rocket will be shifted appreciably to one side by the action of the side force in one direction only for a substantial period of time. The velocity involved in this lateral displacement will cause the rocket's flight path to take a noticeable "set", acquiring an inclination away from the intended vertical trajectory.

For the class of cases in which $\frac{c_2^2}{4I_L^2} > \frac{c_1}{I_L}$, or $\zeta > 1$, the homogeneous response is of the form

$$(24) \quad \alpha_x = A_1 e^{-\frac{t}{\tau_1}} + A_2 e^{-\frac{t}{\tau_2}}$$

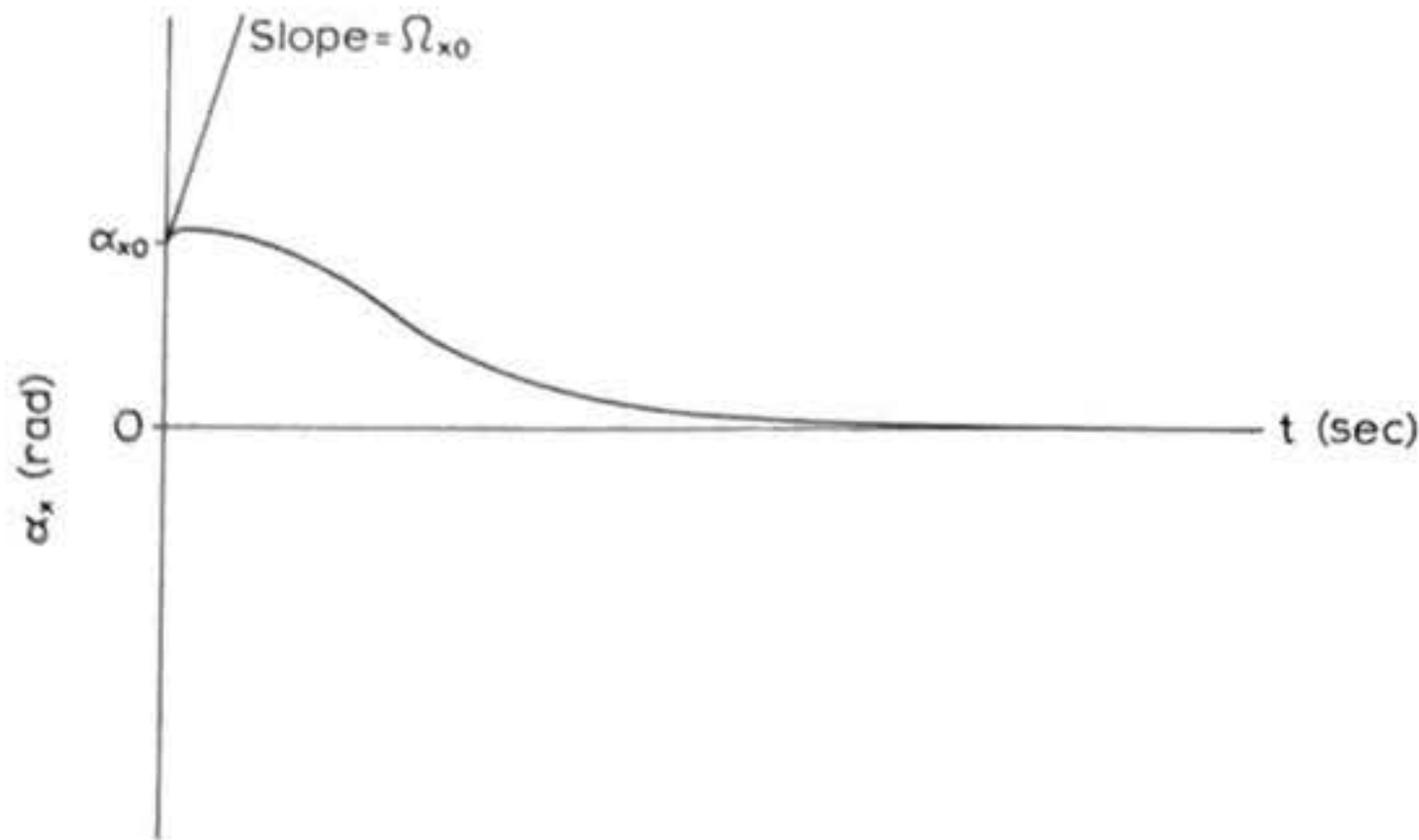


Figure 12: Critically damped characteristic response to general initial conditions in yaw. The yaw angle does not oscillate about zero, but approaches it asymptotically from above. The relation of the initial conditions to the properties of the response has been shown.

where τ_1 and τ_2 are called the time constants of the response. The derivative formulae are

$$\frac{dx}{dt} = -\frac{A_1}{\tau_1} e^{-\frac{t}{\tau_1}} - \frac{A_2}{\tau_2} e^{-\frac{t}{\tau_2}}$$

$$\frac{d^2x}{dt^2} = \frac{A_1}{\tau_1^2} e^{-\frac{t}{\tau_1}} + \frac{A_2}{\tau_2^2} e^{-\frac{t}{\tau_2}}$$

Substituting these expressions in the dynamical equation gives

$$I_L \frac{A_1}{\tau_1^2} e^{-\frac{t}{\tau_1}} + I_L \frac{A_2}{\tau_2^2} e^{-\frac{t}{\tau_2}} - C_2 \frac{A_1}{\tau_1} e^{-\frac{t}{\tau_1}} - C_2 \frac{A_2}{\tau_2} e^{-\frac{t}{\tau_2}} + C_1 A_1 e^{-\frac{t}{\tau_1}} + C_1 A_2 e^{-\frac{t}{\tau_2}} = 0$$

Those terms involving $A_1 e^{-\frac{t}{\tau_1}}$ and those involving $A_2 e^{-\frac{t}{\tau_2}}$ must sum to zero independently. The two algebraic equations thus obtained, with common factors removed, are identical. The form is

$$\frac{I_L}{\tau^2} - \frac{C_2}{\tau} + C_1 = 0$$

Solving for $1/\tau$, we obtain

$$\frac{1}{\tau} = \frac{C_2}{2I_L} \pm \sqrt{\frac{C_2^2}{4I_L^2} - \frac{C_1}{I_L}}$$

or
$$\tau = \frac{1}{\frac{C_2}{2I_L} \pm \sqrt{\frac{C_2^2}{4I_L^2} - \frac{C_1}{I_L}}}$$

We choose τ_1 , called the large time constant, as corresponding to the negative root. τ_2 , the small time constant, corresponds to the positive root:

$$(25) \quad \begin{aligned} \tau_1 &= \frac{1}{\frac{C_2}{2I_L} - \sqrt{\frac{C_2^2}{4I_L^2} - \frac{C_1}{I_L}}} \\ \tau_2 &= \frac{1}{\frac{C_2}{2I_L} + \sqrt{\frac{C_2^2}{4I_L^2} - \frac{C_1}{I_L}}} \end{aligned}$$

The condition $\frac{C_2^2}{4I_L^2} > \frac{C_1}{I_L}$ for the validity of this solution is seen to be the requirement that the square root of a negative number not occur, and that there be two different time constants.

In the same way, the condition $\frac{C_1}{I_L} > \frac{C_2^2}{4I_L^2}$ for the validity of the sinusoidal solutions was that the square root of a negative number not occur, and that there be both a nonzero ω and a value of D. The constants A_1 and A_2 in equation (25) are set by the initial conditions. Writing α_{x_0} and Ω_{x_0} by setting $t = 0$ in the expressions for α_x and $d\alpha_x/dt$, we obtain

$$\alpha_{x_0} = A_1 + A_2$$

$$\Omega_{x_0} = -\frac{A_1}{\tau_1} - \frac{A_2}{\tau_2}$$

Solving for A_1 and A_2 gives

$$(26) \quad \begin{aligned} A_1 &= \frac{\tau_1 \alpha_{x_0} + \tau_1 \tau_2 \Omega_{x_0}}{\tau_1 - \tau_2} \\ A_2 &= \frac{\tau_2 \alpha_{x_0} + \tau_1 \tau_2 \Omega_{x_0}}{\tau_2 - \tau_1} \end{aligned}$$

A response of this kind is called overdamped; its behavior is shown in Figure 13. Like the critically-damped motion, the overdamped response has no overshoot; it also decays more slowly than a critically-damped response. These features make overdamping an extremely hazardous condition. With overdamping large changes in the flight path almost as severe as those resulting from neutral

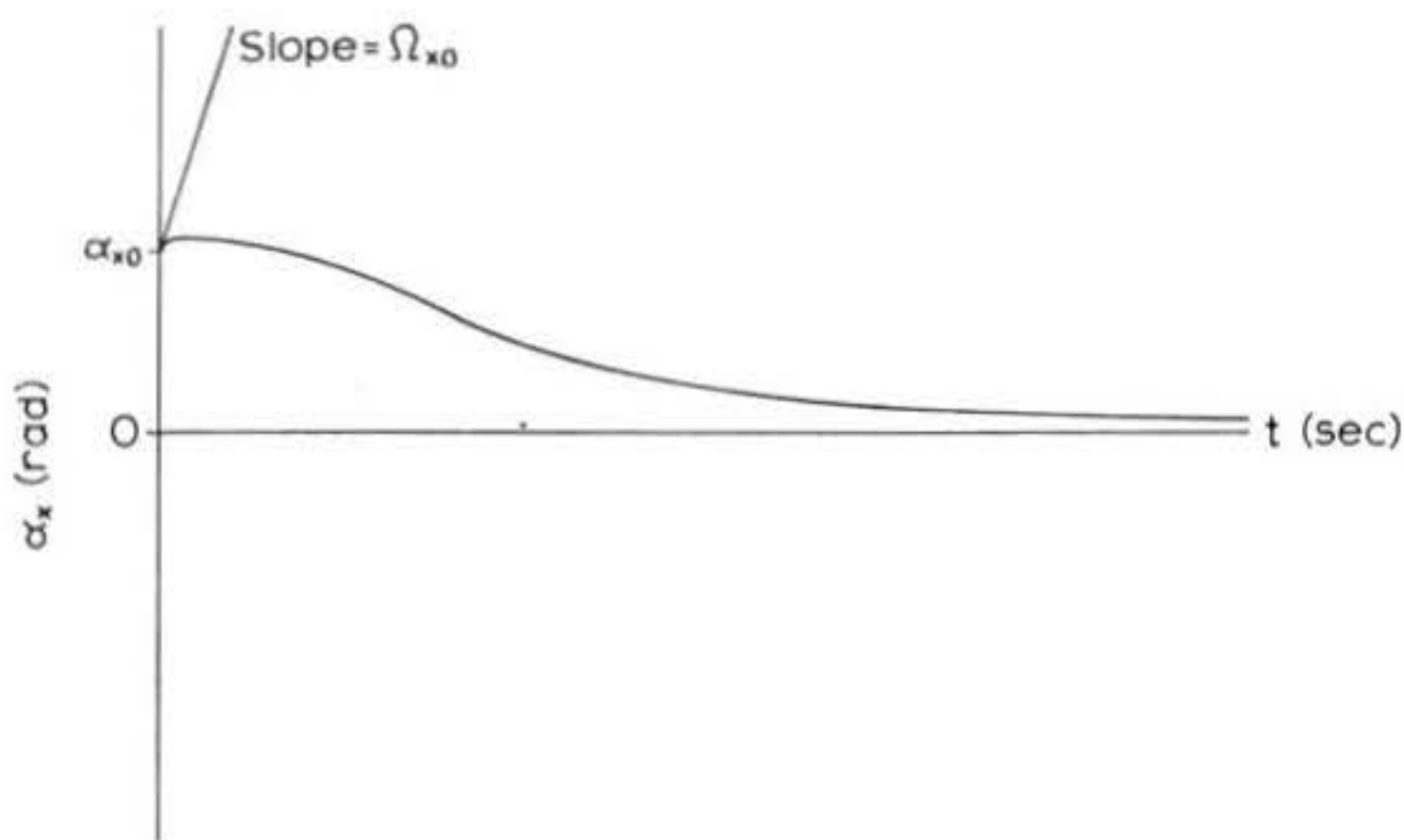


Figure 13: Overdamped characteristic response to general initial conditions in yaw, showing the relation of the initial conditions to the properties of the response. The yaw angle returns to zero more slowly than in the critically damped case, and in the limit of infinite damping ratio the rocket would instantly lose its initial yaw rate and remain "stuck" at the initial yaw angle x_0 as if encased in very thick glue or tar.

static stability can occur if the rocket is disturbed; in fact, neutral static stability ($C_1 = 0$) is a limiting case of overdamped motion.

A statically unstable rocket (one whose corrective moment coefficient is negative) also responds to a disturbance in a manner described by equation (24). Although the damping ratio is undefined for negative C_1 , both time constants and both initial amplitudes are computable from equations (25) and (26). If you carry out these computations you will find that τ_1 becomes negative when C_1 is less than zero, so that $e^{-\frac{t}{\tau_1}}$ becomes e raised to a positive power. The "exponential mode" associated with τ_1 thus increases with time, meaning that the yaw angle of the rocket grows larger and larger as time goes on. This is the dynamic description of a statically unstable rocket "going ape". Such an unstable, or divergent, response is illustrated in Figure 14. The statement " C_1 must be greater than zero" for a rocket to be stable is the dynamic equivalent of the statement "the center of pressure must lie aft of the center of gravity". No matter what the phraseology employed to say it, positive static stability is the prime requirement of a successful rocket design.

3.1.2 Complete Response to Step Input

Suppose that a rocket which has been flying straight and true in calm air suddenly breaks into a region of the sky in which a wind of constant velocity is blowing parallel to the ground (such a phenomenon is called a discontinuous wind shear). Or suppose such a rocket having four fins, each with a control tab, experiences a condition whereby the tabs on two opposing

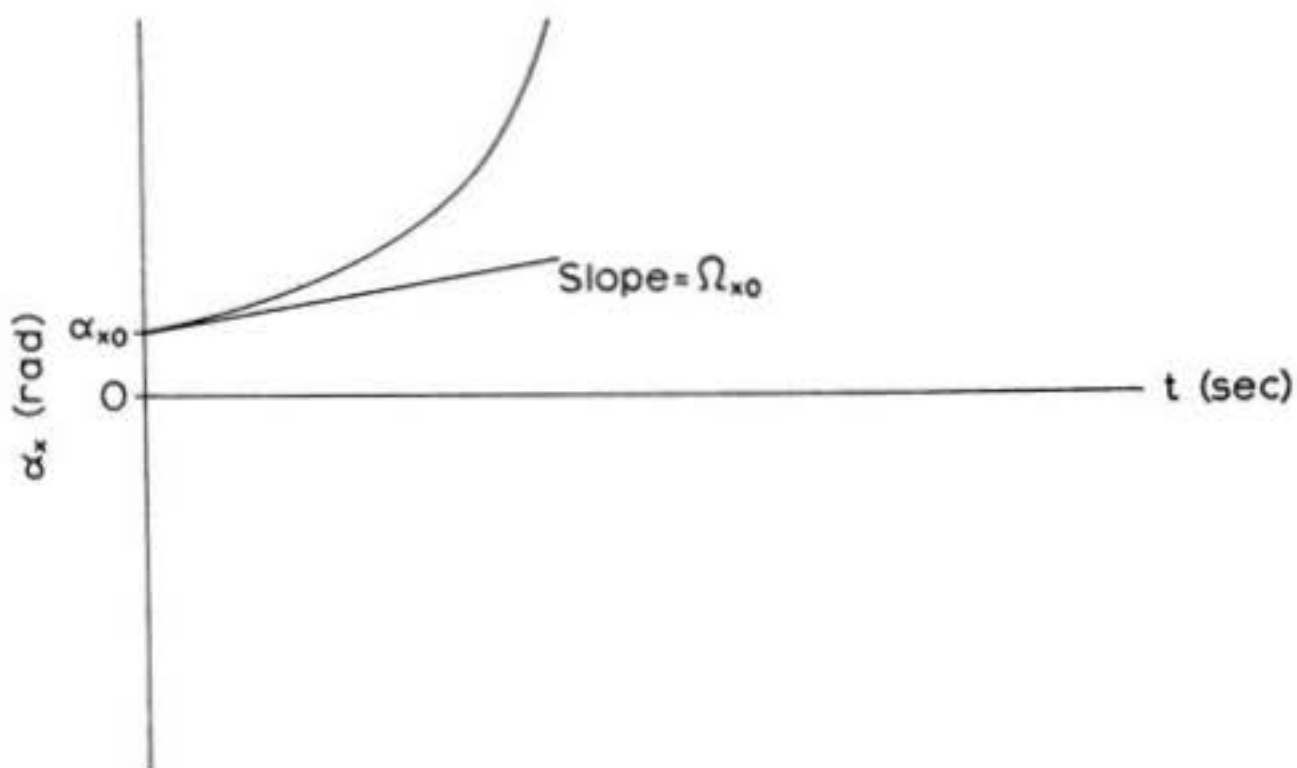


Figure 14: Characteristic response of a statically unstable rocket to general initial conditions in yaw, showing the relation of the initial conditions to the properties of the response. The yaw angle does not return to zero, but rather increases with time, so that the rocket will eventually flip end over end and execute completely unpredictable maneuvers. Negative static stability is thus a dangerous condition and should always be avoided when designing model rockets.

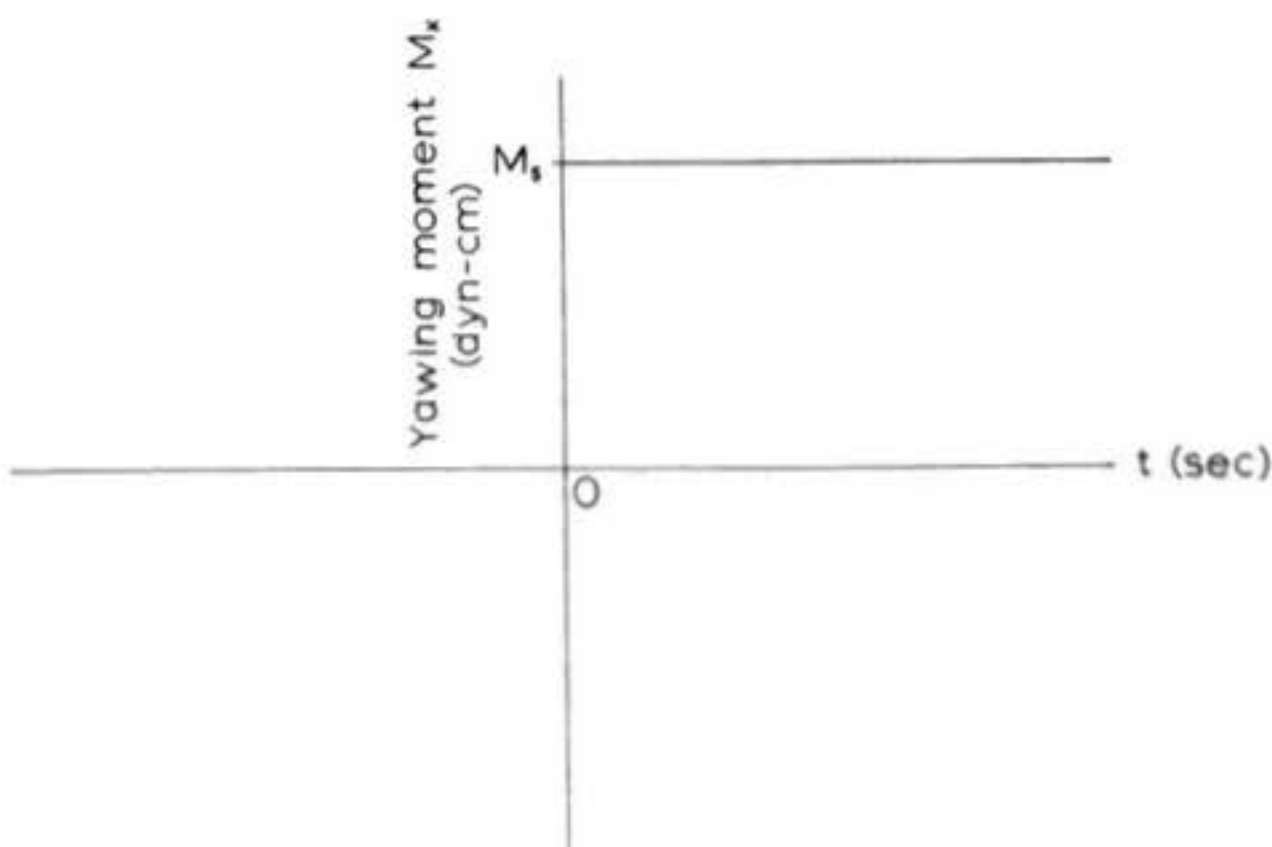


Figure 15: A step disturbance of intensity M_s . Before $t = 0$ the yawing moment is zero; after $t = 0$ it is M_s dyn-cm.

fins suddenly deflect an equal amount in the same direction. Finally, consider what would happen if such a rocket experiences an engine or engine mounting malfunction in which the thrust line suddenly assumes an angle relative to the rocket's centerline. Occurrences such as these fall into the category of step inputs, a name derived from the graphical appearance of their variation with respect to time. The moment-versus-time graph of a representative step function appears in Figure 15.

A step input, for the purposes of this analysis, takes the form of an applied moment whose value is zero before a given time and whose value is a constant after that time. The time at which the "step" occurs is considered to be $t = 0$. With this convention we can define a step input in yaw mathematically as follows:

$$f_x(t) = 0 \quad (t < 0)$$

$$f_x(t) = M_s \quad (t \geq 0)$$

A function of this form is, of course, an idealization. You couldn't expect to observe a perfectly sharp step in any real physical quantity; nevertheless an analysis of the response of a rocket to a step input (hereafter abbreviated "step response") provides the designer with information of considerable value, for step-response analysis is one of the two standard methods of defining the relative ease with which a given rocket can be displaced from true alignment with its intended flight path.

We recall that the differential equation describing the response of a non-rolling rocket to forcing in yaw is

$$I_L \frac{d^2\alpha_x}{dt^2} + C_2 \frac{d\alpha_x}{dt} + C_1 \alpha_x = f_x(t)$$

Substituting our definition of the step input, we have

$$(27a) \quad I_L \frac{d^2\alpha_x}{dt^2} + C_2 \frac{d\alpha_x}{dt} + C_1 \alpha_x = 0 \quad (t < 0)$$

$$(27b) \quad I_L \frac{d^2\alpha_x}{dt^2} + C_2 \frac{d\alpha_x}{dt} + C_1 \alpha_x = M_s \quad (t \geq 0)$$

Now I stipulated that the rocket under consideration be flying straight and evenly at the time the step is applied. This is equivalent to stating that the yaw angle and all its time derivatives are zero for all time preceding the application of the step. The rocket is said to be in a rotationally quiescent state for $t < 0$ and you can see that such a condition identically satisfies equation (27a).

Equation (27b) is solved by the sum of the characteristic and particular responses (cf. Section 2.4). The characteristic response, obtained in Section 3.1.1, is given by equation (15), equation (22), or equation (24), depending on the value of the quantity $\frac{C_1}{I_L} - \frac{C_2^2}{4I_L^2}$. The particular response in this case is

$$(28) \quad \alpha_x = K$$

where K is a constant. Since a constant cannot (by its very definition) vary with time, all of its time derivatives are zero. Upon substitution of K for α_x , equation (27b) thus becomes

$$C_1 K = M_s$$

from which

$$(29) \quad K = M_s/C_1$$

The complete step-response for the cases in which $\frac{c_1}{I_L} > \frac{C_2^2}{4I_L^2}$ is therefore

$$(30) \quad \alpha_x = Ae^{-Dt} \sin(\omega t + \varphi)$$

where D is given by equation (16) and ω by equation (17). As in Section 3.1.1, the values of A and φ are determined by the initial conditions. It can be shown that, for a rocket quiescent before the application of the step input, both the angular displacement α_x and the angular velocity $d\alpha_x/dt$ are zero at $t = 0$. Now setting time equal to zero in the expressions for α_x and $d\alpha_x/dt$ results in

$$\alpha_{x0} = A \sin \varphi + \frac{M_s}{c_1} \quad \text{and}$$

$$\Omega_{x0} = A (\omega \cos \varphi - D \sin \varphi)$$

which, when α_{x0} and Ω_{x0} are set equal to zero, give us

$$A \sin \varphi = -\frac{M_s}{c_1} \quad \text{and}$$

$$D \sin \varphi = \omega \cos \varphi$$

From the second of these we can obtain

$$(31a) \quad \varphi = \arctan\left(\frac{\omega}{D}\right) \quad \text{from which we have}$$

$$(31b) \quad A = -\frac{M_s}{c_1 \sin \varphi}$$

The motion described by equation (30) is an exponentially-damped sinusoid which oscillates about the offset horizontal line $\alpha_x = M_s/c_1$. For the case of zero damping it is simple harmonic

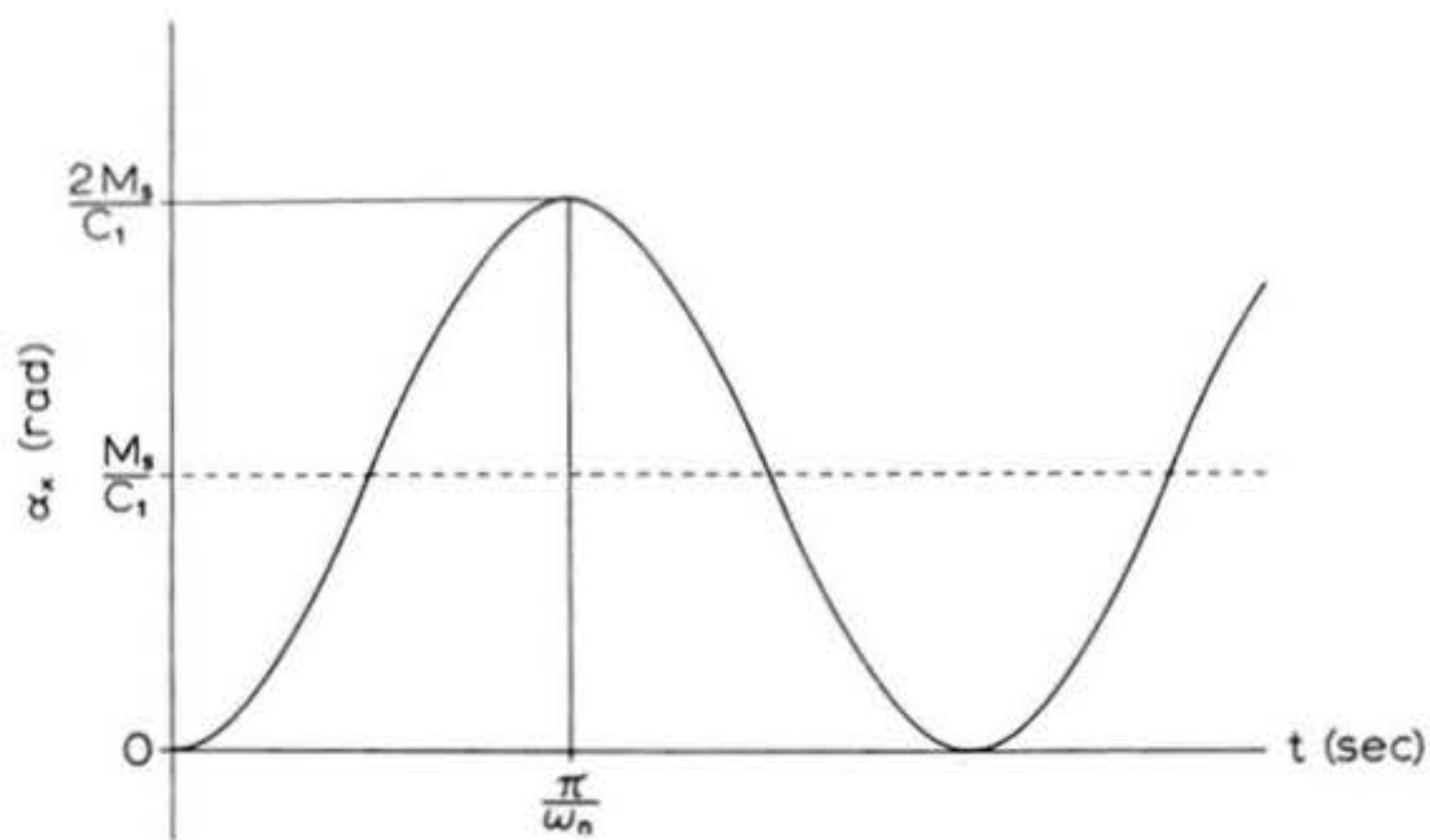


Figure 16: Undamped response to a step disturbance in yaw. The rocket oscillates indefinitely about the yaw angle M_s/C_1 . Also shown are the maximum yaw angle and the time at which it is first attained.

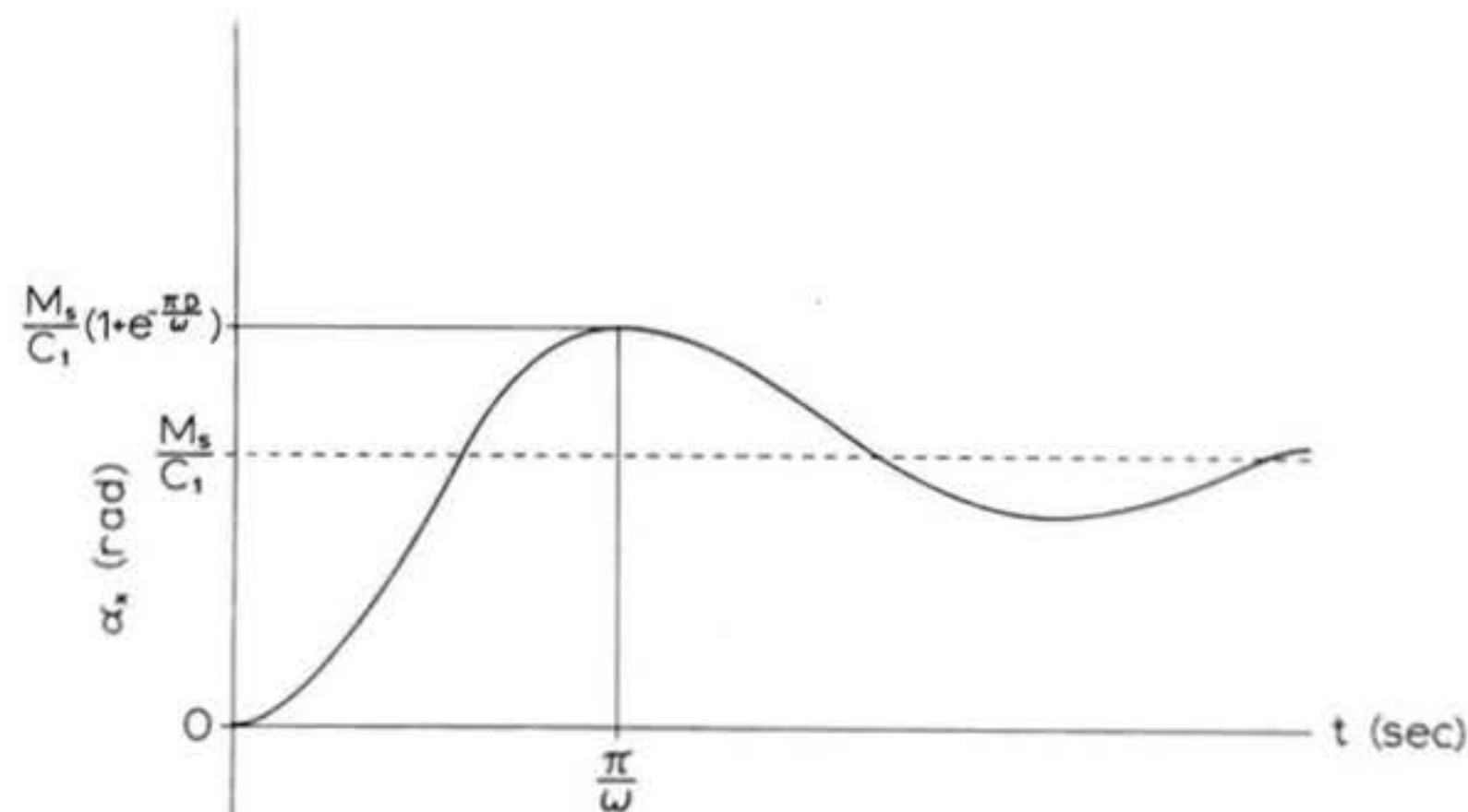


Figure 17: Underdamped response to a step disturbance in yaw. After a sufficiently long time the model will come to rest at the yaw angle M_s/C_1 . Also shown are the maximum yaw angle and the time at which it occurs.

motion about $\alpha_x = M_s/C_1$ as shown in Figure 16. The undamped oscillation varies in magnitude from zero to $2M_s/C_1$, starting from zero with a zero angular velocity at time $t = 0$. The underdamped case, which is again the desirable one for rocket behavior, is given in Figure 17. The angular displacement, again starting with zero magnitude and slope, "homes in" in an oscillatory manner on the displaced axis at M_s/C_1 . It is of interest to compute the value of the first "peak" of such an oscillation and the time at which it occurs, since this information is useful in evaluating the merits of a given rocket design with respect to dynamic behavior.

The first peak will occur at the smallest nonzero value of time for which the angular velocity is zero, i.e., for which $d\alpha_x/dt = 0$. Performing the operation of differentiation and setting the resulting expression equal to zero gives us

$$-ADe^{-Dt} \sin(\omega t + \varphi) + A\omega e^{-Dt} \cos(\omega t + \varphi) = 0$$

from which, dividing by Ae^{-Dt} , we obtain

$$-\frac{D}{\omega} \sin(\omega t + \varphi) + \cos(\omega t + \varphi) = 0$$

This requires that

$$\tan(\omega t + \varphi) = \frac{\omega}{D}$$

Now if you take the inverse trigonometric function of both sides of this equation, you will wind up with

$$\omega t + \varphi = \arctan\left(\frac{\omega}{D}\right) \quad \text{or}$$

$$t = \frac{\arctan(\frac{\omega}{D}) - \varphi}{\omega}$$

But since $\varphi = \arctan(\omega/D)$, the only solution obtainable from this equation is $t = 0$. While this is indeed a solution (our initial condition, $\alpha_x = 0$, is based on it), it does not identify the time of occurrence of the first peak. The general solution for the time at which the nth peak occurs is obtained by introducing the trigonometric identity

$$\tan(\omega t + \varphi + n\pi) = \tan(\omega t + \varphi) \quad (n \text{ an integer})$$

Now if we take the inverse trigonometric functions we obtain

$$\omega t + \varphi + n\pi = \arctan\left(\frac{\omega}{D}\right)$$

from which $t = \frac{n\pi}{\omega}$

The first peak occurs at the time associated with the value $n = 1$:

$$(32a) \quad t = \frac{\pi}{\omega}$$

The value of α_x at the first peak is computed by substituting this value of t into equation (30):

$$\alpha_x \Big|_{t=\frac{\pi}{\omega}} = A e^{-\frac{\pi D}{\omega}} \sin(\pi + \varphi) + \frac{M_s}{c_1}$$

By the use of the trigonometric identity

$$\sin(\pi + \varphi) = -\sin \varphi$$

and equation (31b) this may be simplified to read

$$(32b) \quad \alpha_x \Big|_{t=\frac{\pi}{\omega}} = \frac{M_s}{C_1} \left[1 + e^{-\frac{\pi D}{\omega}} \right]$$

A look at Figure 17 will reveal that this value of α_x represents the greatest magnitude the angular displacement attains during the step-response. Since the magnitude of the displacement decreases as C_1 increases, we conclude that a large value of C_1 will reduce the severity of a rocket's step response.

In the case where the values of C_1 , C_2 , and I_L are such that a condition of critical damping exists the complete step-response is given by

$$(33) \quad \alpha_x = (A_1 + A_2 t) e^{-Dt} + \frac{M_s}{C_1}$$

where D is again given by equation (16). Applying the initial conditions, we have

$$\begin{aligned} \alpha_{x0} &= A_1 + \frac{M_s}{C_1} \\ &= 0 \end{aligned} \quad \text{and}$$

$$\begin{aligned} \Omega_{x0} &= A_2 - DA_1 \\ &= 0 \end{aligned}$$

from which we obtain

$$(34a) \quad A_1 = -\frac{M_s}{C_1}$$

$$(34b) \quad A_2 = -D \frac{M_s}{C_1}$$

A critically-damped step-response is shown in Figure 18.

The complete expression for an overdamped step response is

$$(35) \quad \alpha_x = A_1 e^{-\frac{t}{\tau_1}} + A_2 e^{-\frac{t}{\tau_2}} + \frac{M_s}{C_1}$$

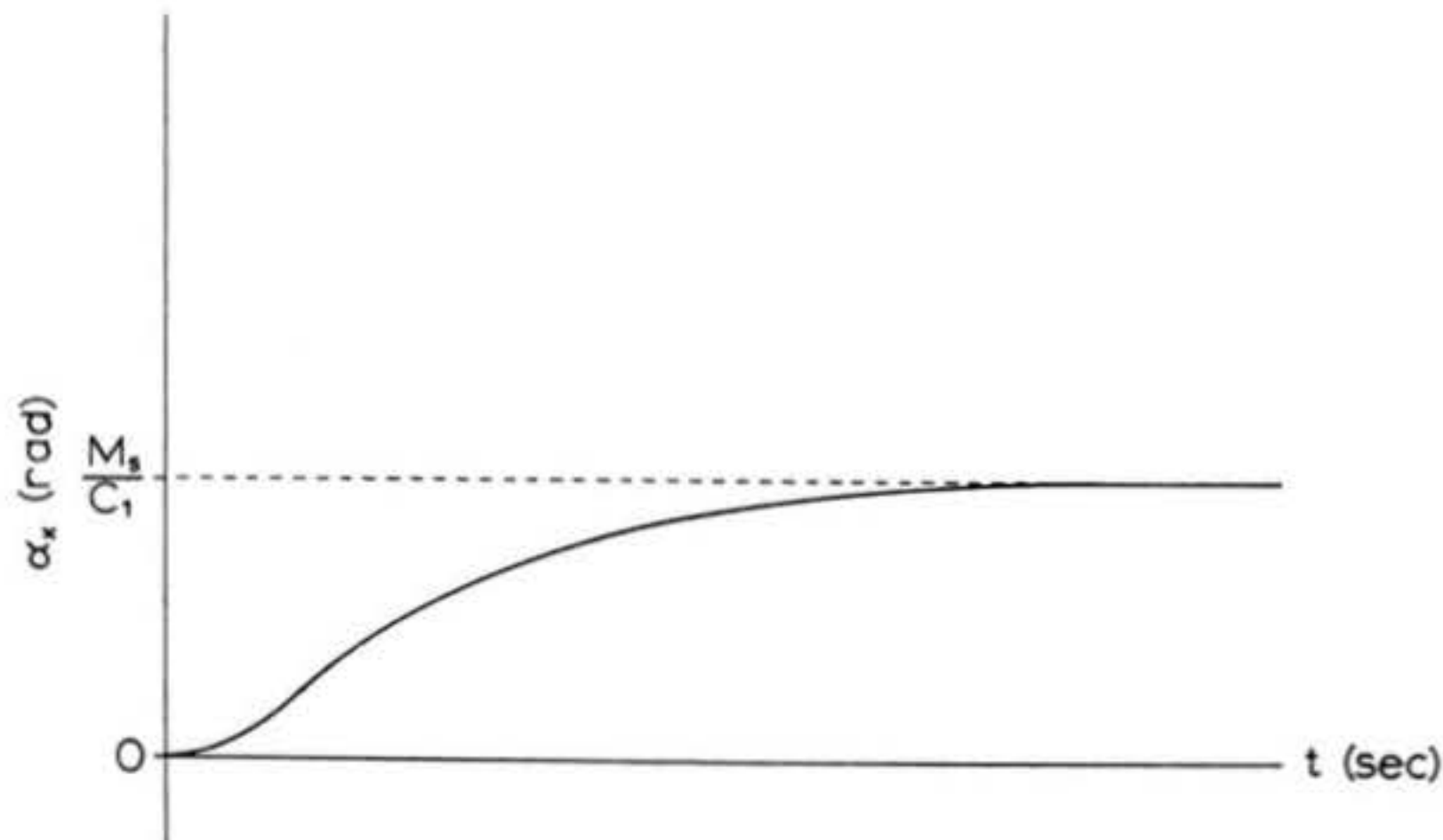


Figure 18: Critically damped response to a step disturbance in yaw.
The yaw angle approaches a value of M_s/C_1 asymptotically from below.

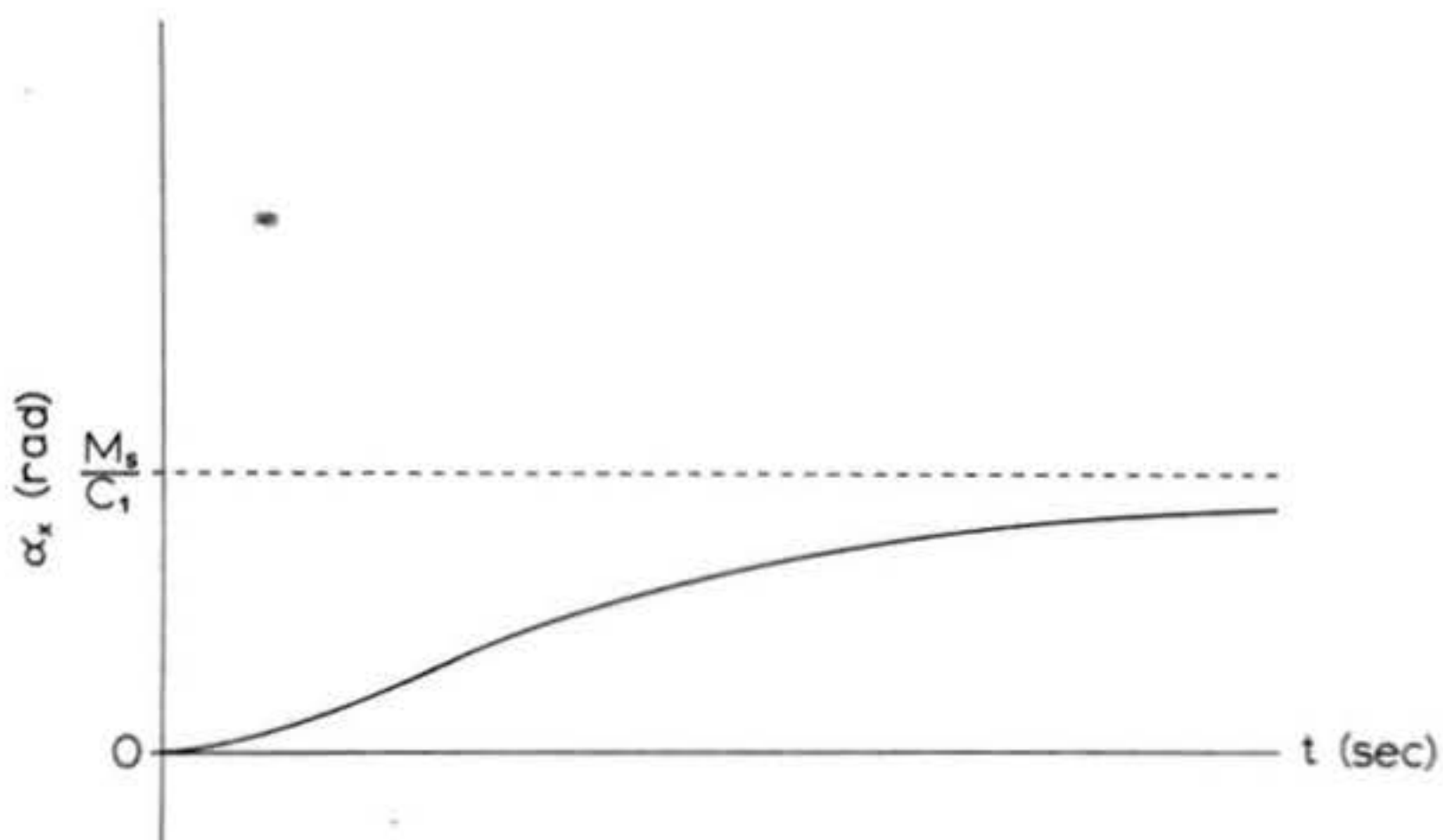


Figure 19: Overdamped response to a step disturbance in yaw.
The yaw angle M_s/C_1 is again approached asymptotically from below,
but more slowly than is the case for the critically damped response.

where τ_1 and τ_2 are given by equations (25). In this case the imposition of initial conditions results in the expressions

$$\alpha_{x0} = A_1 + A_2 + \frac{M_s}{C_1} \\ = 0$$

$$\Omega_{x0} = -\frac{A_1}{\tau_1} - \frac{A_2}{\tau_2} \\ = 0 \quad \text{and}$$

from which we have

$$(36a) \quad A_1 = -\frac{M_s \tau_1}{C_1(\tau_1 - \tau_2)} \quad \text{and}$$

$$(36b) \quad A_2 = \frac{M_s \tau_2}{C_1(\tau_1 - \tau_2)}$$

Figure 19 illustrates an overdamped step-response.

The critically-damped and overdamped step responses are both slower than the underdamped response, and in this sense the former are somewhat less sensitive to step inputs than the latter. Consider what would happen, though, if the step were to arise, persist for a considerable length of time, and then drop to zero again. An overdamped rocket would also be slow in returning to true alignment from a yaw angle of nearly M_s/C_1 radians. Moreover, since overdamped responses exhibit no overshoot, the deflection of the flight path from the vertical would be substantially greater than in the case of underdamped motion. It is therefore best to decrease a rocket's sensitivity to step inputs by the use of a large corrective moment coefficient rather than high damping.

3.1.3 Complete Response to Impulse Input

Imagine, if you will, that the rocket considered in Section 3.1.2 encounters a step input that does not persist for all time

$t \geq 0$, but rather "steps down" to zero again after some interval of time t_1 . The graphical representation of this forcing function, as shown in Figure 20, forms a rectangle whose area is $M_s t_1$. Now imagine the interval of time during which the step persists becoming shorter and shorter as the magnitude of the applied step input becomes greater and greater in such a way that the product $M_s t_1$, the area of the rectangle, remains constant. If we carry this process to its logical conclusion, we will ultimately arrive at a configuration such that t_1 is zero and M_s is infinity. In this case, however, M_s must be considered a rather special "type" of infinity, since the product of "this" infinity with zero has a definite value: $M_s t_1$, which I shall hereafter denote by H . A forcing function of this kind is called an impulse of strength H , and the response of a given rocket to such an input offers a second criterion by which the resistance of the rocket to transient disturbances may be evaluated. An impulsive input in yaw may be defined as follows:

$$\begin{aligned} f_x(t) &= 0 & (t \neq 0) \\ f_x(t) &= \infty & (t = 0) \\ 0 \cdot f_x(t) &= H & (t = 0) \end{aligned}$$

While there are more rigorous definitions of impulse inputs obtainable from the so-called limiting arguments of the theory of singularity functions (which includes, among other things, the study of steps and impulses), such formal precision is not necessary to an understanding of the effects of impulsive disturbances on physical systems. Like the step, the impulse is an idealization of physical reality. You know very well that a rocket can never encounter disturbing moments of infinite

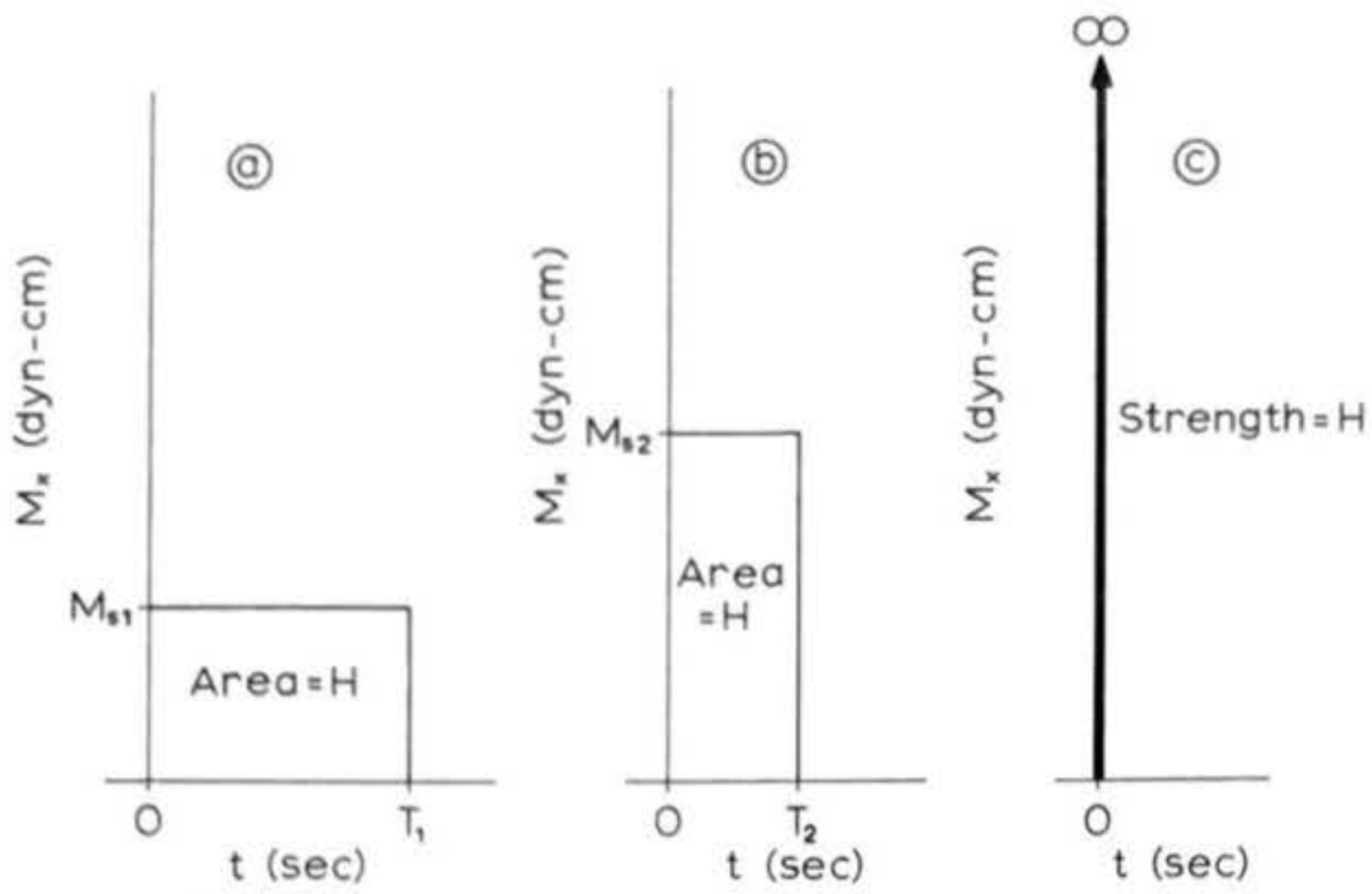


Figure 20: Development of the concept of an impulse from a series of steps of finite duration. The step in (a) has an intensity M_{s1} and persists for a time T_1 ; the product $M_{s1}T_1$ is equal to H dyn-cm-sec. The step in (b) has an intensity M_{s2} greater than M_{s1} , but a duration T_2 less than T_1 such that the product $M_{s2}T_2$ is still H dyn-cm-sec. The limiting case of this behavior is the impulse (c), a step of infinite intensity but infinitesimal duration such that the product of the intensity and the duration -- called the "strength" of the impulse -- is still H dyn-cm-sec.

intensity and zero duration; any strong disturbance of short duration, however, can be treated as an impulse to a high order of accuracy. Momentary fluctuations in the direction of the thrust line, oblique ejection of solid residue from the rocket nozzle, moments arising due to launcher contact during liftoff, and disturbances encountered during staging are examples of **forcing functions** which are virtually impulsive.

The response to an impulsive input is conceptually somewhat more difficult to grasp than the responses to other types of **inputs**. In order to facilitate a consideration of the impulse response let me return to our discussion of the angular acceleration of the flywheel as illustrated in Figure 5. Recall that, for a frictionless flywheel of inertial moment I to which a constant moment M is applied for a time t , the resulting angular velocity of the wheel is

$$\omega = \frac{Mt}{I}$$

and the resulting angular displacement from the original rotative position is

$$\alpha = \frac{1}{2} \frac{M}{I} t^2$$

Suppose, now, that the moment M approaches infinity and the time t approaches zero in such a way that the product Mt remains constant at the value H . The angular velocity imparted to the wheel by the moment during the interval t will, under these conditions remain constant at the value

$$\omega = \frac{H}{I}$$

The angular displacement α , however, will decrease, since it is given by

$$\alpha = \frac{H}{2I} t$$

When the limiting case is reached, the angular displacement will be zero. The sole effect of an impulsive input to the flywheel is thus to cause a finite angular velocity to appear instantaneously at the time of application of the impulse.

The problem of the yawing rocket is precisely analogous, provided the damping and corrective moments are both zero: an impulse of strength H will cause an angular velocity

$$\Omega_x = \frac{H}{I_L}$$

to arise instantaneously, while the angular displacement at time equal to zero will be zero. Does the presence of nonzero corrective and damping moments in any way alter the state of the rocket at $t = 0$?

Well, it is clear that there cannot be any effect due to static stability, as no angular displacement of the rocket has yet occurred; hence the corrective moment at $t = 0$ is itself zero. And, although there does arise a damping moment simultaneously with the angular velocity increment due to the impulse, this moment is finite and therefore can produce no change in either the angular displacement or the angular velocity in a zero amount of time. It thus turns out that the presence of aerodynamic moments does not modify the initial effect upon the rocket of an impulsive input. This effect produces the following set

of initial conditions:

$$(37a) \quad \alpha_{x_0} = 0$$

$$(37b) \quad \Omega_{x_0} = \frac{H}{I_L}$$

Unlike the step, the impulse input has associated with it no particular response for $t > 0$. More properly speaking, the particular response is zero, for as you can see from its definition the impulse itself is zero for all positive values of time. A complete impulse response is actually a homogeneous response with a special set of initial conditions: those given by equations (37).

The impulse-response of an underdamped rocket is given by equations (15) through (19). Applying the initial conditions given in equations (37) results in the following values for the phase angle and the initial amplitude:

$$\begin{aligned}\varphi &= \arctan(0) \\ &= 0\end{aligned}$$

$$A = \frac{H}{I_L \omega}$$

The characteristic response to an impulsive disturbance is then given by

$$(38) \quad \alpha_x = \frac{H}{I_L \omega} e^{-Dt} \sin \omega t$$

where ω and D are determined by equations (16) and (17). This motion is shown in Figure 21.

The critically-damped impulse response is described by equations (22) and (23). In this case we have

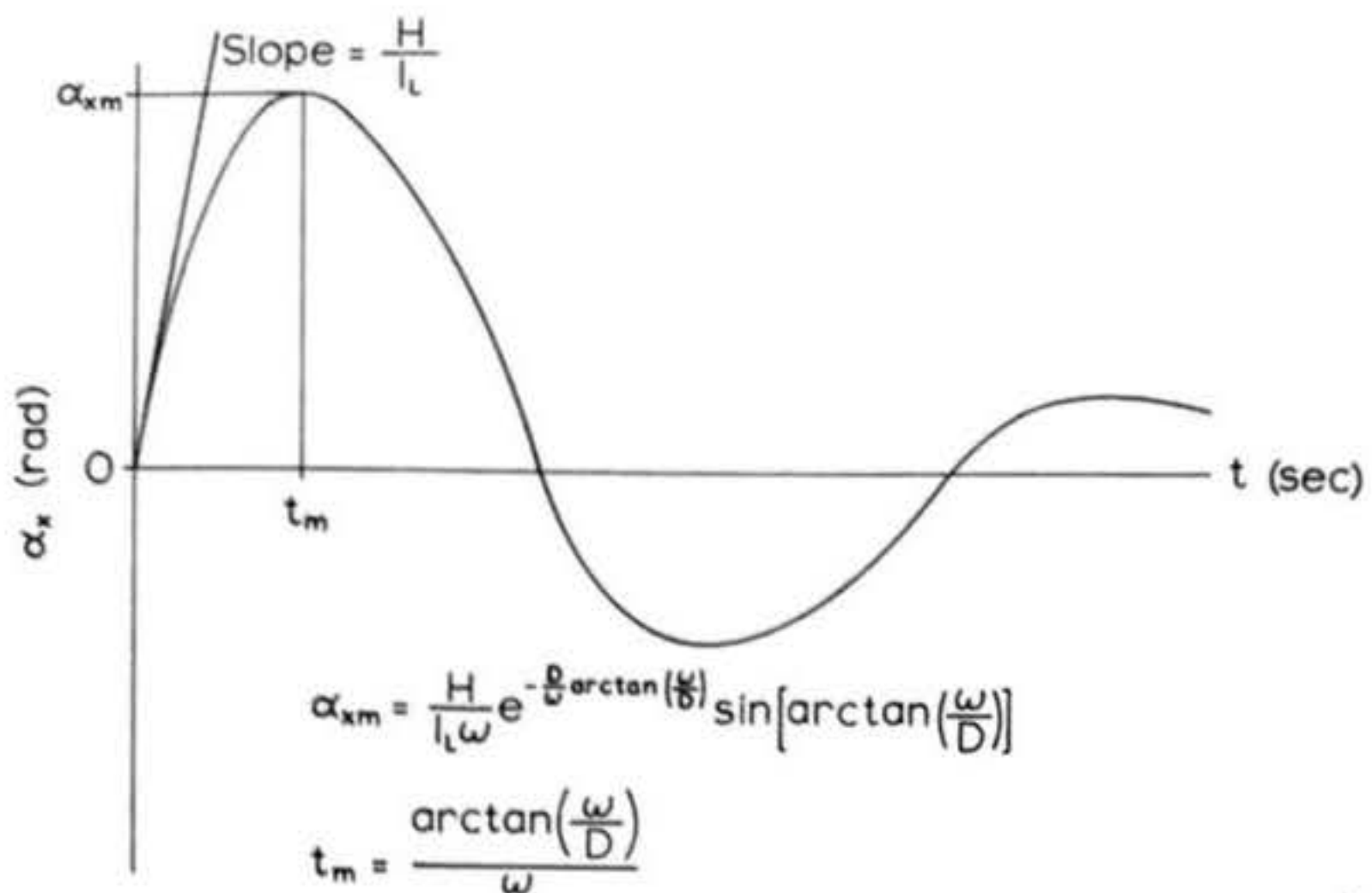


Figure 21: Underdamped response to an impulse of strength H in yaw. The initial angular velocity imparted by the impulse, the maximum yaw angle attained, and the time at which it occurs are shown.

$$A_1 = 0$$

$$A_2 = \frac{H}{I_L}$$

and the characteristic motion assumes the form

$$(39) \quad \alpha_x = \frac{H}{I_L} \tau e^{-Dt}$$

where D is again given by equation (16). The impulse response of a critically-damped rocket is illustrated by Figure 22.

Overdamped motion resulting from impulsive forcing obeys equations (24) through (26). Applying the initial conditions to these equations gives the results

$$A_1 = \frac{H \tau_1 \tau_2}{I_L (\tau_1 - \tau_2)}$$

$$A_2 = -\frac{H \tau_1 \tau_2}{I_L (\tau_1 - \tau_2)}$$

where τ_1 and τ_2 are determined by equation (25). An overdamped rocket will thus exhibit an impulse-response described by

$$(40) \quad \alpha_x = \frac{H \tau_1 \tau_2}{I_L (\tau_1 - \tau_2)} \left[e^{-\frac{t}{\tau_1}} - e^{-\frac{t}{\tau_2}} \right]$$

as illustrated in Figure 23.

Equation (37b) shows that the initial angular velocity resulting from an impulsive disturbance is inversely proportional to the longitudinal moment of inertia of the rocket which is being disturbed, and equations (38) through (40) reveal an inverse dependence of the initial amplitude factors on the value of I_L . It would thus seem that a large I_L is desirable to reduce the severity of a rocket's impulse response. We can

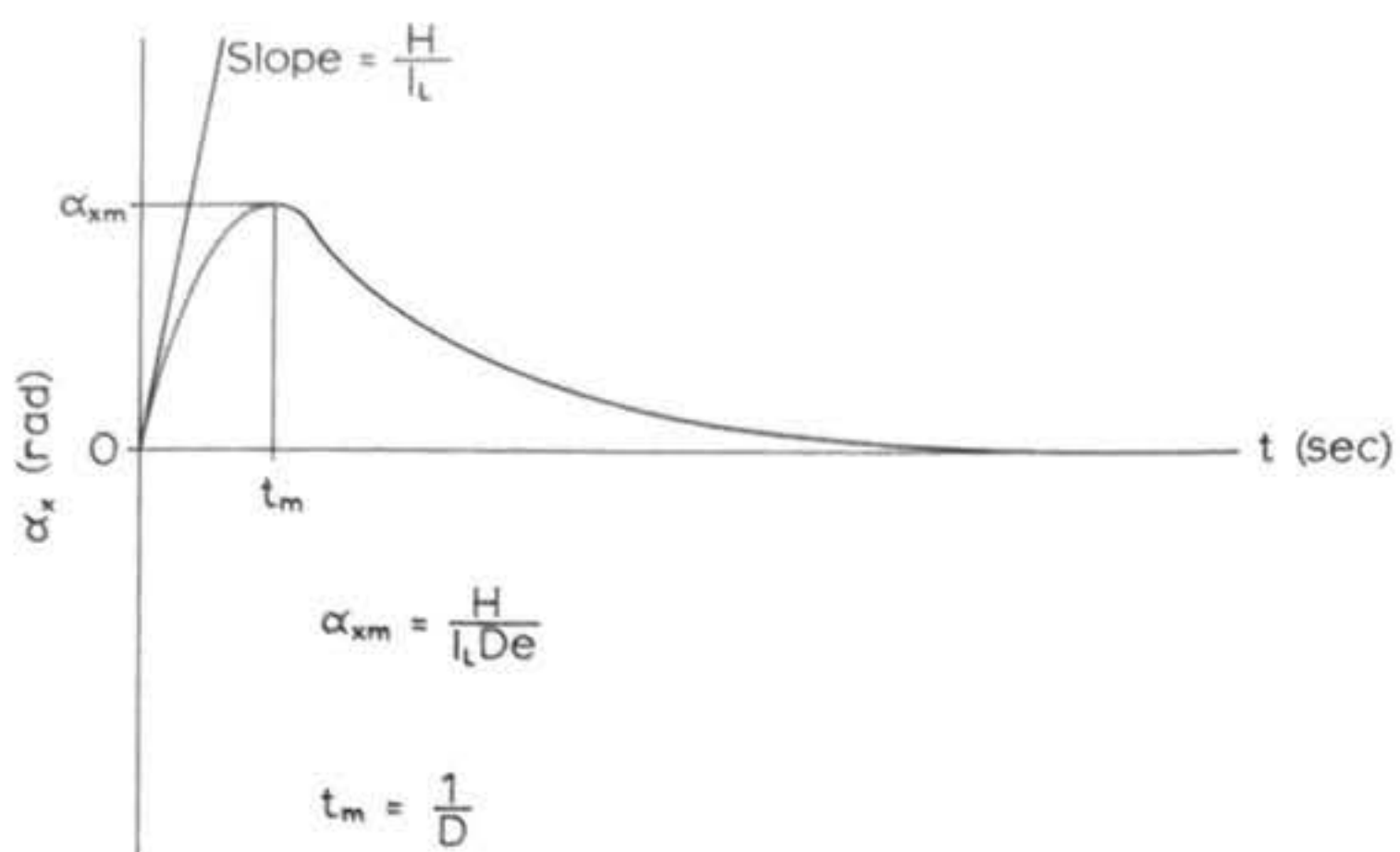


Figure 22: Critically damped response to an impulse of strength H in yaw, showing the initial yaw rate, the maximum yaw angle, and the time at which the maximum yaw angle occurs.

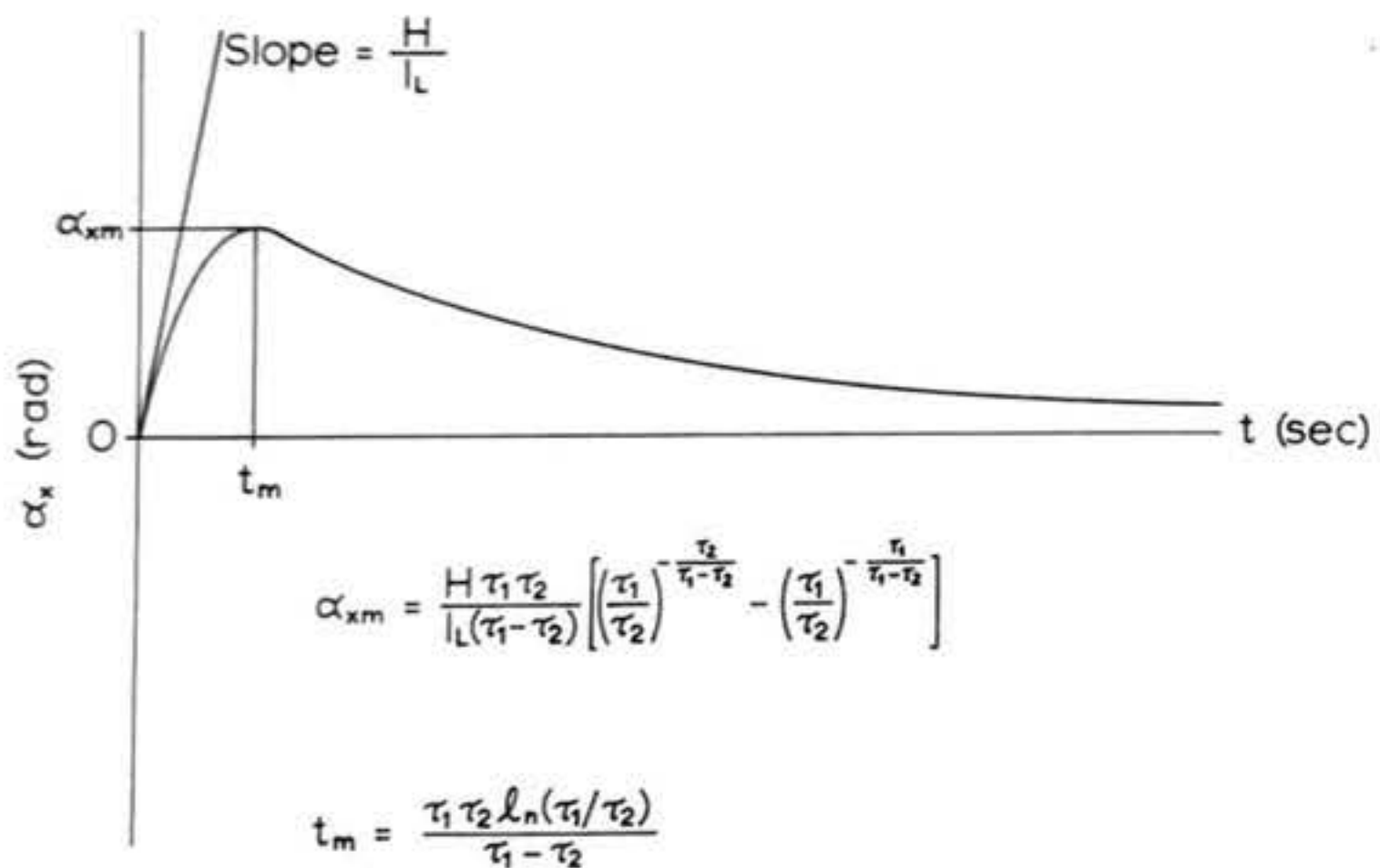


Figure 23: Overdamped response to an impulse of strength H in yaw, showing the initial yaw rate, the maximum yaw angle, and the time at which the maximum yaw angle is attained. The maximum deflection occurs sooner and its value is smaller than is the case for the critically damped response, and the return to zero yaw angle is also more gradual.

investigate the quantities governing the severity of the response more thoroughly by deriving the maximum angular displacement associated with each case of impulse-response. These maxima, and the values of t at which they occur, can be computed by setting $d\alpha_x/dt$ to zero and determining the smallest value of t that will satisfy the resulting equation.

The equation resulting from imposing the condition of zero angular velocity on the underdamped case is

$$-\frac{DH}{I_L \omega} e^{-Dt} \sin \omega t + \frac{\omega H}{I_L \omega} e^{-Dt} \cos \omega t = 0$$

from which we obtain

$$(41a) \quad t_m = \frac{\arctan(\frac{\omega}{D})}{\omega} \quad \text{so that}$$

$$(41b) \quad \alpha_{xm} = \frac{H}{I_L \omega} e^{-\frac{D}{\omega} \arctan(\frac{\omega}{D})} \sin [\arctan(\frac{\omega}{D})]$$

For the critically-damped motion we have

$$\frac{H}{I_L} e^{-Dt} - \frac{DH}{I_L} t e^{-Dt} = 0 \quad \text{from which}$$

$$(42a) \quad t_m = \frac{1}{D} \quad \text{and}$$

$$(42b) \quad \alpha_{xm} = \frac{H}{I_L D e^{-D t_m}}$$

Finally, in the case of overdamped motion the applicable equation is

$$-\frac{\tau_1 H \tau_2}{I_L (\tau_1 - \tau_2)} e^{-\frac{t}{\tau_1}} + \frac{\tau_1 H \tau_2}{I_L (\tau_1 - \tau_2)} e^{-\frac{t}{\tau_2}} = 0$$

which gives us

$$(43a) \quad t_m = \frac{\tau_1 \tau_2 \ln(\frac{\tau_1}{\tau_2})}{\tau_1 - \tau_2}$$

where the notation "ln" stands for the "natural logarithm of" the quantity in parentheses. Natural logarithms, also called Naperian logarithms, are the mathematical inverse of exponential functions and may be found in tables arranged in much the same way as are tables of trigonometric functions. From equations (43a) and (40) we can obtain, after some algebraic manipulation,

$$(43b) \quad \alpha_{xm} = \frac{H \tau_1 \tau_2}{I_L (\tau_1 - \tau_2)} \left[\left(\frac{\tau_1}{\tau_2} \right)^{-\frac{\tau_2}{\tau_1 - \tau_2}} - \left(\frac{\tau_1}{\tau_2} \right)^{-\frac{\tau_1}{\tau_1 - \tau_2}} \right]$$

Now if you substitute the expressions derived in Section 3.1.1 for ω , D, τ_1 and τ_2 into equations (41b), (42b), and (43b) you will make the following discoveries:

For underdamped motion, an increase in I_L decreases α_{xm} .

For critically-damped motion, changes in I_L have no effect on α_{xm} .

For overdamped motion, an increase in I_L increases α_{xm} .

These results might seem at first to indicate that large values of I_L are desirable only in the case of underdamped motion.

This is not the whole story, however, for if we examine equation (20), in which the damping ratio ζ is given as

$$\zeta = \frac{c_2}{2\sqrt{c_1 I_L}}$$

we see that an increase in I_L invariably reduces the damping ratio. In particular, increasing I_L can cause overdamped or critically-damped responses (which have already been shown to be undesirable

in themselves) to become underdamped, after which further increases in I_L will lessen the severity of the impulse response.

We can conclude from our analysis, then, that a large value of I_L is a desirable design characteristic in a model rocket, as a large longitudinal moment of inertia helps both to guard against overdamping and to reduce the rocket's sensitivity to impulsive forcing.

3.1.4 Steady State Response to Sinusoidal Forcing

In the previous sections we were concerned with responses to forcing functions of a transient or discontinuous nature. The behavior of a model rocket in these cases was such that both the homogeneous response and the particular response were of significant importance in determining the character of the resulting motion. In cases where the disturbing moments are of a prolonged and periodic nature, however, the behavior of the characteristic response (which, for positive static stability and finite damping, dies away with time) soon creates a situation in which the particular response alone is of significant interest. In the remainder of this section I am going to be talking about the properties of the particular response of a rocket having a zero roll rate to an input of the form

$$f_x(t) = A_f \sin \omega_f t$$

The analysis will be based on the assumption that this "sinusoidal" input has been going on for a time sufficiently long that all transient phenomena have died away, so that the complete response is identical to the particular response alone. The result obtained from an analysis based on such an assumption is

often referred to as the steady-state response to sinusoidal forcing, or simply the sinusoidal steady state. Such physical phenomena as periodic instability in the thrust line of the rocket motor and the aerodynamic "flutter" of fins or control tab surfaces are inputs which can be closely approximated by the sinusoidal representation.

Substituting the expression given above for $f_x(t)$ into equation (13) gives us the differential equation for the yawing oscillation in the form

$$I_L \frac{d^2\alpha_x}{dt^2} + C_2 \frac{d\alpha_x}{dt} + C_1 \alpha_x = A_f \sin \omega_f t$$

The particular solution to this equation is known to be of the form

$$(44) \quad \alpha_x = A_r \sin (\omega_f t + \varphi)$$

The rocket responds to the sinusoidal forcing with a sinusoidal motion of its own whose frequency is identical to the frequency of the disturbance. The amplitude is different, however, and the response "leads" the forcing function by a phase angle of φ radians. The time derivatives of the response thus described are

$$\frac{d\alpha_x}{dt} = \omega_f A_r \cos (\omega_f t + \varphi)$$

$$\frac{d^2\alpha_x}{dt^2} = -\omega_f^2 A_r \sin (\omega_f t + \varphi)$$

The values of A_r and φ are determined by substituting the expressions for α_x and its time derivatives into the differential

equation. When this is done we obtain

$$-I_L \omega_f^2 A_r \sin(\omega_f t + \varphi) + C_2 \omega_f A_r \cos(\omega_f t + \varphi) + C_1 A_r \sin(\omega_f t + \varphi) = A_f \sin \omega_f t$$

It is necessary to make use of the following trigonometric identities in order to solve this equation:

$$\sin(\omega_f t + \varphi) = \sin \omega_f t \cos \varphi + \cos \omega_f t \sin \varphi$$

$$\cos(\omega_f t + \varphi) = \cos \omega_f t \cos \varphi - \sin \omega_f t \sin \varphi$$

Substitution of the quantities on the right sides of these identities for those on the left sides in the differential equation casts it into the form

$$\begin{aligned} & -I_L \omega_f^2 A_r [\sin \omega_f t \cos \varphi + \cos \omega_f t \sin \varphi] \\ & + C_2 \omega_f A_r [\cos \omega_f t \cos \varphi - \sin \omega_f t \sin \varphi] \\ & + C_1 A_r [\sin \omega_f t \cos \varphi + \cos \omega_f t \sin \varphi] = A_f \sin \omega_f t \end{aligned}$$

Now the terms containing $\sin \omega_f t$ and those containing $\cos \omega_f t$ must be independent. This gives us two algebraic equations for A_r and φ :

$$\begin{aligned} & -I_L \omega_f^2 A_r \sin \omega_f t \cos \varphi - C_2 \omega_f A_r \sin \omega_f t \sin \varphi \\ & + C_1 A_r \sin \omega_f t \cos \varphi = A_f \sin \omega_f t \end{aligned}$$

$$\begin{aligned} & -I_L \omega_f^2 A_r \cos \omega_f t \sin \varphi + C_2 \omega_f A_r \cos \omega_f t \cos \varphi \\ & + C_1 A_r \cos \omega_f t \sin \varphi = 0 \end{aligned}$$

Dividing the first equation by $\sin \omega_f t$, the second by $A_r \cos \omega_f t$ simplifies these equations to

$$-I_L \omega_f^2 A_r \cos \varphi - C_2 \omega_f A_r \sin \varphi + C_1 A_r \cos \varphi = A_f$$

$$-I_L \omega_f^2 \sin \varphi + C_2 \omega_f \cos \varphi + C_1 \sin \varphi = 0$$

Now the second equation can be divided by $\cos \varphi$, producing a formulation containing the single trigonometric function $\tan \varphi$:

$$[C_1 - I_L \omega_f^2] \tan \varphi + C_2 \omega_f = 0$$

The phase angle is then determined as

$$(45a) \quad \varphi = \arctan \left[\frac{C_2 \omega_f}{I_L \omega_f^2 - C_1} \right]$$

The first equation may be divided by $\cos \varphi$ to yield

$$A_r [(C_1 - I_L \omega_f^2) - C_2 \omega_f \tan \varphi] = \frac{A_f}{\cos \varphi}$$

The trigonometric identities

$$\sec \varphi = \frac{1}{\cos \varphi} \quad \text{and}$$

$$\sec \varphi = \sqrt{\tan^2 \varphi + 1}$$

then permit us to write

$$A_r \left[(C_1 - I_L \omega_f^2) - \frac{C_2^2 \omega_f^2}{I_L \omega_f^2 - C_1} \right] = A_f \sqrt{\frac{C_2^2 \omega_f^2}{(I_L \omega_f^2 - C_1)^2} + 1}$$

Some algebraic manipulation transforms this expression to

$$A_r \left[(I_L \omega_f^2 - C_1)^2 + C_2^2 \omega_f^2 \right] = A_f \sqrt{(I_L \omega_f^2 - C_1)^2 + C_2^2 \omega_f^2}$$

from which we conclude that

$$(45b) \quad A_r = \frac{A_f}{\sqrt{(I_L \omega_f^2 - C_1)^2 + C_2^2 \omega_f^2}}$$

Now although equations (45) are perfectly acceptable solutions for φ and A_r , there is a standard formulation of these results which greatly simplifies their interpretation. Recall from Section 3.1.1 that the natural frequency of the rocket is given by

$$\omega_n = \sqrt{\frac{C_1}{I_L}}$$

while the damping ratio ζ is given by equation (20):

$$\zeta = \frac{C_2}{2\sqrt{C_1 I_L}}$$

If we define a frequency ratio β as

$$(46) \quad \beta = \frac{\omega_f}{\omega_n}$$

and an amplitude ratio AR as

$$(47) \quad AR = \frac{A_r}{A_f}$$

we can, after some rearrangement, obtain the forms

$$(48a) \quad \varphi = \arctan \left[\frac{2\zeta\beta}{\beta^2 - 1} \right]$$

$$(48b) \quad AR = \frac{1}{C_1 \sqrt{(\beta^2 - 1)^2 + (2\zeta\beta)^2}}$$

Graphs of the variation of phase angle and amplitude ratio with frequency ratio for various values of ζ are given in Figures 24 and 25. In Figure 24 the definition of the arctangent function has been artificially extended to run from $\varphi = 0$ to $\varphi = -\pi$ radians so that the phase shift will appear as a continuous function of β . Notice that for all nonzero frequencies of disturbance the motion of the rocket lags behind the input (that is, φ is negative). As β varies from zero to infinity φ varies from zero to $-\pi$ radians, passing through the value $(-\pi/2)$ when $\beta = 1.0$.

The more lightly damped the rocket, the more abrupt the transition from $\varphi = 0$ to $\varphi = -\pi$; in the limiting case of zero damping the transition becomes discontinuous. An examination of Figure 25 will reveal that, for rockets whose damping ratios are less than $\sqrt{2}/2$, there exists a range of values of β distributed about $\beta = 1$ in which the amplitude ratio has a value greater than $1/C_1$, its value for $\beta = 0$. This behavior is referred to as resonance; the greatest value of AR attained is called the resonance peak and the value of ω_f at which it occurs is termed the resonant frequency. These quantities are computed by locating the resonance peak analytically, using the fact that the slope of the amplitude-ratio curve is zero there. The slope, or derivative of AR with respect to β , is given by the equation

$$\frac{d(AR)}{d\beta} = \frac{-[(\beta^2 - 1) + 2\zeta^2](2\beta)}{C_1 [(\beta^2 - 1)^2 + (2\zeta\beta)^2]^{3/2}}$$

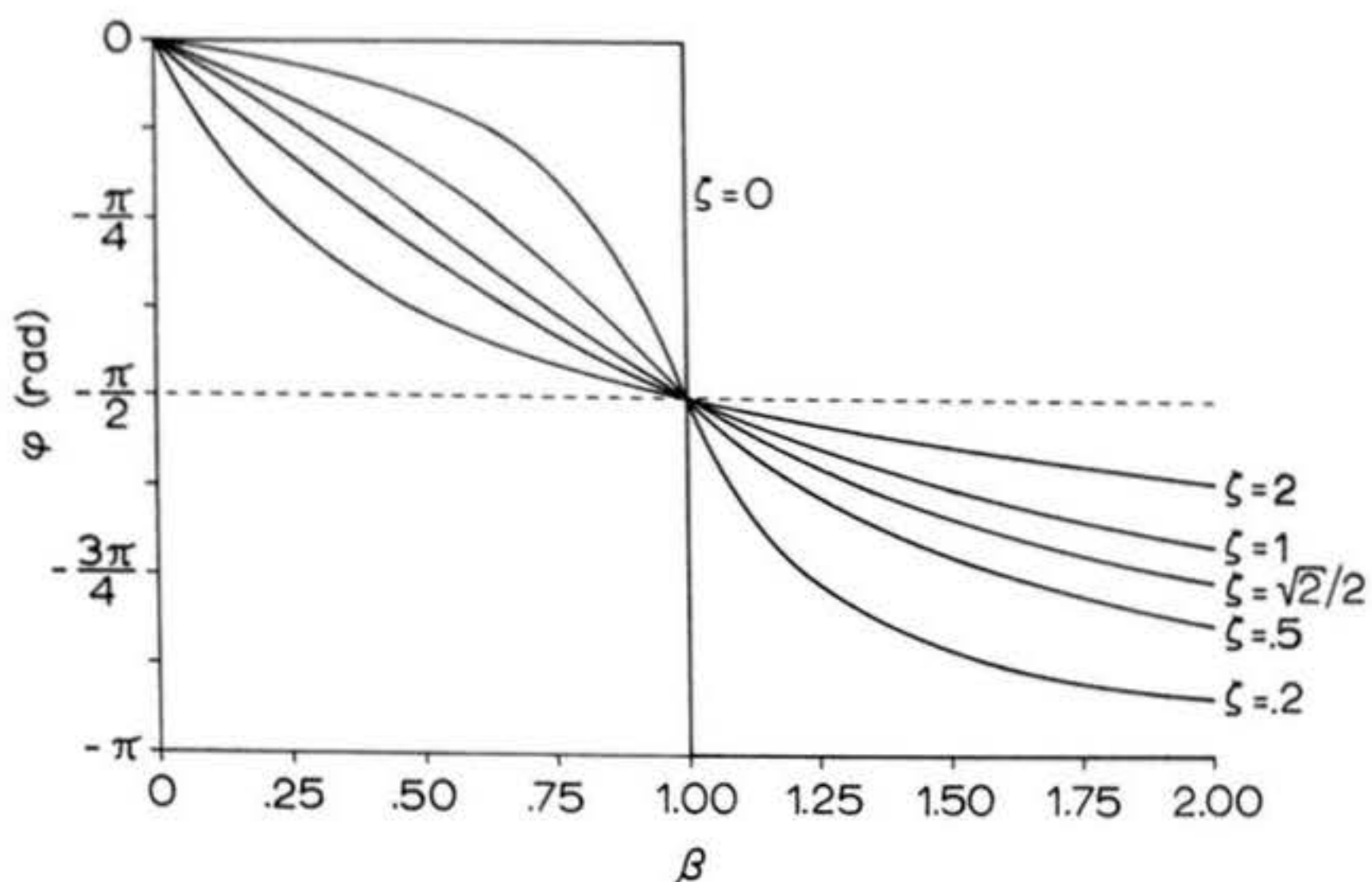


Figure 24: Variation of phase angle with frequency ratio for cases of steady-state response to sinusoidal forcing.

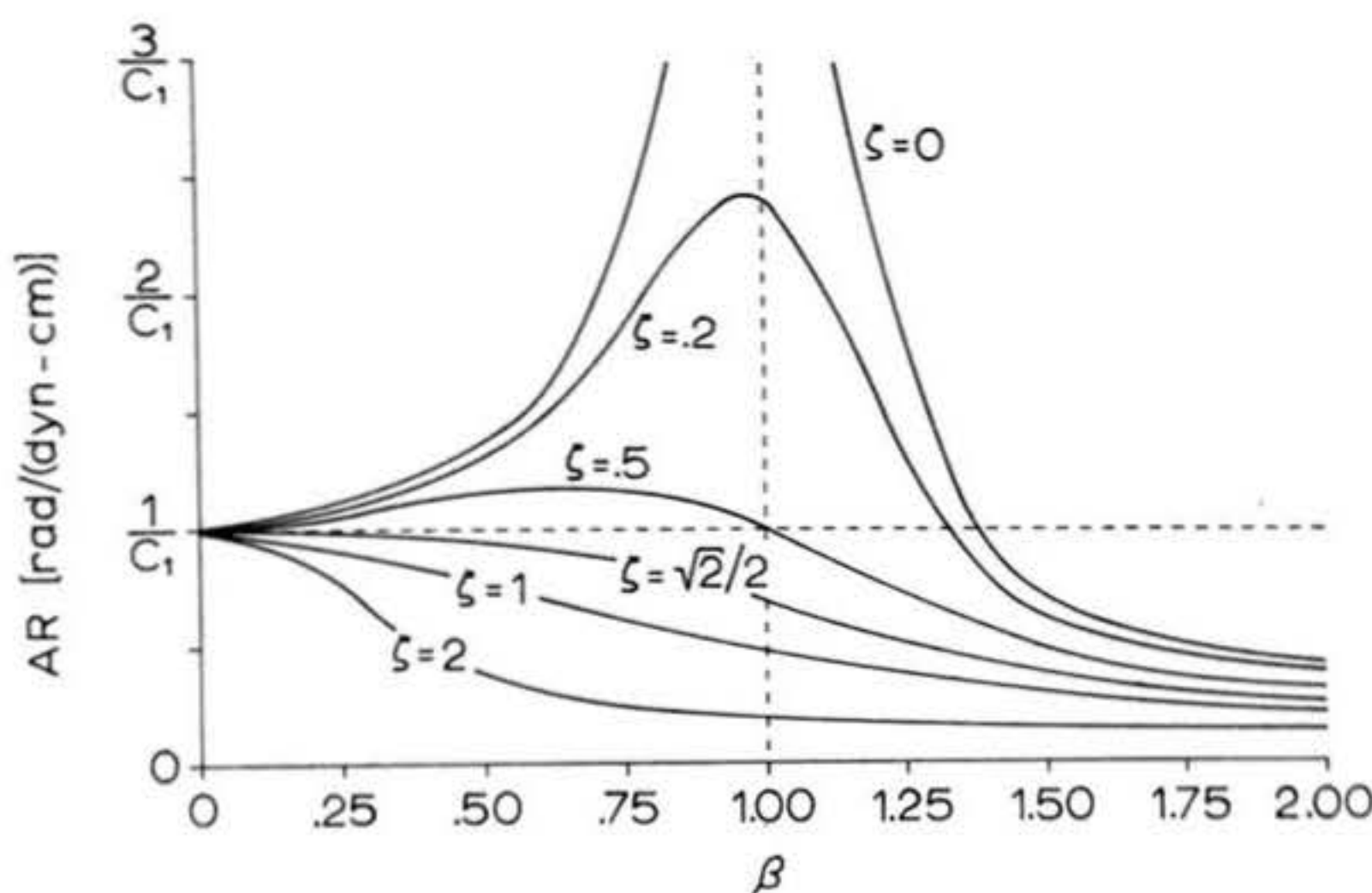


Figure 25: Variation of amplitude ratio with frequency ratio for cases of steady-state response to sinusoidal forcing. Resonant behavior can be seen for damping ratios less than $\sqrt{2}/2$, but does not occur at damping ratios greater than this value.

which is zero when its numerator is zero; that is when

$$\beta^2 - 1 + 2\zeta^2 = 0$$

The value of β at resonance is therefore

$$(49a) \quad \beta_{res} = \sqrt{1-2\zeta^2}$$

and the resonant frequency, ω_{res} , is given by

$$(49b) \quad \omega_{res} = \beta_{res} \omega_m$$

By substituting β_{res} for β in the equation for AR, we find that the resonance peak obeys the relation

$$(50) \quad AR_{res} = \frac{1}{2C_1\zeta\sqrt{1-\zeta^2}}$$

The value of AR_{res} can be quite large if the rocket is only lightly damped, meaning that the amplitude of the response can be much greater than that of the forcing function. In fact, equation (50) shows that the response amplitude increases without bound as the damping ratio decreases and becomes infinite at $\zeta = 0$. Resonance, therefore, can be an extremely dangerous state, resulting in violent oscillation of the rocket and consequent deflection of its trajectory. The designer of model rockets should spare no effort to minimize the effects of resonance. The use of an adequate corrective moment coefficient (large enough static stability margin and adequate airspeed), the maintenance of a sufficient amount of damping, and the use of a flight velocity profile whereby the rocket passes quickly

through the resonant state due to the resulting variation in ω_m are three techniques generally employed in various combinations for this purpose.

As you can see from equations (49), the resonant frequency decreases from ω_m toward zero as the damping ratio of the rocket increases from zero toward $\sqrt{2}/2$. This same variation in damping ratio causes the value of the resonance peak to decrease from infinity to $1/C_1$, and for $\zeta > \sqrt{2}/2$, there is no resonance peak at all; the value of AR is always less than $1/C_1$. Damping ratios greater than 0.7071 therefore result in the least severe response to disturbances of a steady sinusoidal nature.

3.2 Dynamical Behavior at a Constant, Nonzero Roll Rate

3.2.1 Generalized Homogeneous Response

The presence of a constant roll rate causes the pitching and yawing movements of the rocket to become coupled (cf. Section 2.3), so that the differential equations for pitch and yaw must be solved simultaneously. We recall that the homogeneous differential equations for this case are

$$I_L \frac{d^2\alpha_x}{dt^2} + C_2 \frac{d\alpha_x}{dt} + C_1 \alpha_x + I_R \omega_z \frac{d\alpha_y}{dt} = 0$$

$$I_L \frac{d^2\alpha_y}{dt^2} + C_2 \frac{d\alpha_y}{dt} + C_1 \alpha_y - I_R \omega_z \frac{d\alpha_x}{dt} = 0$$

Although the general form of the solutions to these equations is somewhat similar to the solutions of the decoupled case, the complete solutions themselves are a good deal more complicated. The most generally applicable ones are given by

$$\begin{aligned} \alpha_x &= A_1 e^{-D_1 t} \sin(\omega_1 t + \varphi_1) + A_2 e^{-D_2 t} \sin(\omega_2 t + \varphi_2) \\ (51) \quad \alpha_y &= A_1 e^{-D_1 t} \cos(\omega_1 t + \varphi_1) + A_2 e^{-D_2 t} \cos(\omega_2 t + \varphi_2) \end{aligned}$$

Now it is clear that the derivative formulae for those parts of equations (51) which carry the subscript "2" will be identical in form to those for the terms which are subscripted with a "1". I can therefore save a great deal of writing if, for now, I leave off the subscripts and just write down the derivatives of one term of each equation's right-hand member:

$$\frac{d\alpha_x}{dt} = -ADe^{-Dt} \sin(\omega t + \varphi) + A\omega e^{-Dt} \cos(\omega t + \varphi)$$

$$\frac{d^2\alpha_x}{dt^2} = A(D^2 - \omega^2)e^{-Dt} \sin(\omega t + \varphi) - 2A\omega D e^{-Dt} \cos(\omega t + \varphi)$$

$$\frac{d\alpha_y}{dt} = -ADe^{-Dt} \cos(\omega t + \varphi) - A\omega e^{-Dt} \sin(\omega t + \varphi)$$

$$\frac{d^2\alpha_y}{dt^2} = A(D^2 - \omega^2)e^{-Dt} \cos(\omega t + \varphi) + 2A\omega D e^{-Dt} \sin(\omega t + \varphi)$$

This amounts to pretending, for the present, that there is only one initial amplitude, only one inverse time constant, only one angular frequency and only one phase angle in the solution. Such an intentional error is perfectly permissible, just as it was in deriving equations (25), for the mathematics of the derivation will later point out that there are in fact two each of these quantities.

Upon substitution of the simplified derivative relations the first (yaw) differential equation becomes

$$\begin{aligned} & I_L A(D^2 - \omega^2)e^{-Dt} \sin(\omega t + \varphi) - 2I_L A\omega D e^{-Dt} \cos(\omega t + \varphi) \\ & - I_R \omega_z A D e^{-Dt} \cos(\omega t + \varphi) - I_R \omega_z A \omega e^{-Dt} \sin(\omega t + \varphi) \\ & - C_2 A D e^{-Dt} \sin(\omega t + \varphi) + C_2 A \omega e^{-Dt} \cos(\omega t + \varphi) + C_1 A e^{-Dt} \sin(\omega t + \varphi) = 0 \end{aligned}$$

Removing the common factor Ae^{-Dt} we have, from the requirement

that sine terms sum independently to zero,

$$I_L(D^2 - \omega^2) - I_R \omega_z \omega - C_2 D + C_1 = 0$$

and from the requirement that cosine terms sum independently to zero,

$$-2I_L \omega D - I_R \omega_z D + C_2 \omega = 0$$

Substituting the expressions for α , $d\alpha/dt$, and $d^2\alpha/dt^2$ into the second (pitch) equation gives

$$\begin{aligned} & I_L A (D^2 - \omega^2) e^{-Dt} \cos(\omega t + \varphi) + 2 I_L A \omega D e^{-Dt} \sin(\omega t + \varphi) \\ & + I_R \omega_z A D e^{-Dt} \sin(\omega t + \varphi) - I_R \omega_z A \omega e^{-Dt} \cos(\omega t + \varphi) \\ & - C_2 A D e^{-Dt} \cos(\omega t + \varphi) - C_2 A \omega e^{-Dt} \sin(\omega t + \varphi) + C_1 A e^{-Dt} \cos(\omega t + \varphi) = 0 \end{aligned}$$

from which the cosine terms give us

$$I_L (D^2 - \omega^2) - I_R \omega_z \omega - C_2 D + C_1 = 0$$

and the sine terms require that

$$2 I_L \omega D + I_R \omega_z D - C_2 \omega = 0$$

Now the sine equation from the first differential equation is identical to the cosine equation from the second, and the cosine equation from the first just equals the negative of the sine equation from the second and is therefore equivalent to it.

This confirms that a coupled solution of the form (51) does in fact exist and that we can proceed to solve for ω and D .

From the last equation above we can obtain D in terms of ω as

$$D = \frac{C_2 \omega}{2I_L \omega + I_R \omega_z}$$

Substituting this expression for D into the second to last equation above yields

$$\frac{I_L C_2^2 \omega^2}{4I_L^2 \omega^2 + 4I_L I_R \omega_z \omega + I_R^2 \omega_z^2} - I_L \omega^2 - I_R \omega_z \omega - \frac{C_2^2 \omega}{2I_L \omega + I_R \omega_z} + C_1 = 0$$

Multiplying the left and right sides of this equation by $(4I_L^2 \omega^2 + 4I_L I_R \omega_z \omega + I_R^2 \omega_z^2)$, collecting terms and dividing the resulting equation by a factor of $(-4I_L^3)$ to cast the equation into a form having a coefficient of 1 for the highest power of ω which appears (this is called normalizing), we obtain

$$\omega^4 + 2 \frac{I_R}{I_L} \omega_z \omega^3 + \left[-\frac{C_1}{I_L} + \frac{C_2^2}{4I_L^2} + \frac{5}{4} \frac{I_R^2}{I_L^2} \omega_z^2 \right] \omega^2 + \left[-\frac{C_1}{I_L} \frac{I_R}{I_L} \omega_z + \frac{C_2^2}{4I_L^2} \frac{I_R}{I_L} \omega_z + \frac{I_R^3}{4I_L^3} \omega_z^3 \right] \omega - \frac{C_1}{4I_L} \frac{I_R^2}{I_L^2} \omega_z^2 = 0$$

Now this is a quartic equation in ω , in which all powers of ω from the zeroth to the fourth are present. The solution of such equations is generally quite difficult, but we can reduce the complexity somewhat in this case by considering the physics of the situation and the limiting behavior of the solutions, rather than just plowing ahead with the formal mathematics. By "limiting behavior" I mean just this: should $I_R \omega_z$ become vanishingly small compared to I_L , the solution of the coupled motion will be very nearly identical to the solution of the decoupled case. A mathematician would say that the coupled solution approaches the decoupled solution in the limit as

$\frac{I_R \omega_z}{I_L}$ goes to zero, so that we recover the solution of the decoupled case from the more general solution of coupled motion. Similarly, for the case in which C_1 and C_2 become vanishingly small compared to I_L , we obtain the so-called force-free precession which is familiar to the designers of gyroscopic instruments; the coupled solution approaches a force-free precession in the limit as $\frac{C_1}{I_L}$ and $\frac{C_2}{I_L}$ go to zero. I am going to try to put these properties to use after making the following substitutions in order to simplify the algebra of the angular frequency equation:

$$X = \frac{I_R}{I_L}$$

$$Y = -\frac{C_1}{I_L}$$

$$Z = \frac{C_2^2}{4I_L^2}$$

The equation for ω then becomes

$$(52a) \quad \omega^4 + 2X\omega_z\omega^3 + [Y + Z + \frac{5}{4}X^2\omega_z^2]\omega^2 + [YX\omega_z + ZX\omega_z + \frac{X^3}{4}\omega_z^3]\omega + \frac{Y}{4}X^2\omega_z^2 = 0$$

Now since this is a fourth-degree polynomial equation, we know that there are four possible values of ω which will satisfy it (the roots of the equation). Let these values be A, B, C, and D. The equation can then be written as

$$(\omega - A)(\omega - B)(\omega - C)(\omega - D) = 0$$

which, when multiplied out, becomes

$$(52b) \quad \omega^4 - (A + B + C + D) \omega^3 + [AB + CD + (A+B)(C+D)] \omega^2 - [CD(A+B) + AB(C+D)] \omega + ABCD = 0$$

Now equations (52a) and (52b) are just different representations of the same equation. This being the case, the coefficient of a given power of ω in equation (52a) must be identical to the coefficient of that same power of ω in equation (52b). This allows us to write

$$(53a) \quad A + B + C + D = -2X\omega_z$$

$$(53b) \quad [AB + CD + (A+B)(C+D)] = [Y + Z + \frac{5}{4}X^2\omega_z^2]$$

$$(53c) \quad [CD(A+B) + AB(C+D)] = -[YX\omega_z + ZX\omega_z + \frac{X^3}{4}\omega_z^3]$$

$$(53d) \quad ABCD = \frac{Y}{4}X^2\omega_z^2$$

Equations (53) are sufficient to determine the roots A, B, C, and D in terms of the constants X, Y, and Z. This, however, would be an extremely difficult task if done by formal mathematics alone. Instead I am going to examine the limiting behavior of this particular dynamical system -- a model rocket -- to see if I cannot find some analytical "short cut" that will help me to guess the roots.

For $\frac{I_R\omega_z}{I_L} = 0$, equation (52a) becomes

$$\omega^4 + (Y + Z)\omega^2 = 0$$

Factoring this expression, we obtain

$$\omega^2 (\omega^2 + Y + Z) = 0$$

Two of the roots are thus $\omega = 0$. The remaining two are

$$\omega = \pm \sqrt{-(Y+Z)}$$

or $\omega = \pm \sqrt{\frac{C_1}{I_L} - \frac{C_2^2}{4I_L^2}}$

which are just cases of decoupled, underdamped oscillation.

For the limiting case $\frac{C_1}{I_L} = \frac{C_2}{I_L} = 0$, we have $Y = Z = 0$ and equation (52a) becomes

$$\omega^4 + 2X\omega_z\omega^3 + \frac{5}{4}X^2\omega_z^2\omega^2 + \frac{X^3}{4}\omega_z^3\omega = 0$$

Factoring gives us

$$\omega(\omega^3 + 2X\omega_z\omega^2 + \frac{5}{4}X^2\omega_z^2\omega + \frac{X^3}{4}\omega_z^3) = 0$$

One of the four roots is seen to be $\omega = 0$. The remaining factor is a cubic equation and will therefore have three roots. Let these be denoted by A' , B' , and C' . Then

$$(\omega - A')(\omega - B')(\omega - C') = 0$$

which, when expanded, becomes

$$\omega^3 - (A+B+C)\omega^2 + [(A+B)C + AB]\omega - ABC = 0$$

Then, equating coefficients of like powers, we have

$$-(A+B+C) = 2X\omega_z$$

$$(A+B)C + AB = \frac{5}{4} X^2 \omega_z^2$$

$$-ABC = \frac{X^3}{4} \omega_z^3$$

I can now exercise on a reduced scale the techniques which I shall have to apply to solve the general quartic equation (52a). The sum of the roots of the cubic equation must equal $-2X\omega_z$, while their product must equal $-\frac{X^3}{4} \omega_z^3$. From this I conclude that A' , B' , and C' each contain a factor of $X\omega_z$. If I attempt, reasoning from symmetry, to postulate three equal roots you can see that the coefficient equations will not be satisfied. If, however, I postulate two identical roots and a different third root, the sum and product conditions will allow me to write

$$A' = -\frac{X\omega_z}{2}$$

$$B' = -\frac{X\omega_z}{2}$$

$$C' = -X\omega_z$$

These roots also satisfy the center coefficient equation and are therefore the roots of the cubic equation. I am now faced with the problem of determining which of these roots are physical (i.e., which can really be observed in the physical universe) and which are "spurious" or "extraneous" roots not applicable to the physical problem being solved. In order to ascertain the physical roots I return to the equation obtained from the cosine

terms of the pitch differential equation and set $c_1 = c_2 = 0$. This sets D to zero and leaves me with

$$-I_L \omega^2 - I_R \omega_z \omega = 0$$

from which I obtain the two roots

$$\omega = 0$$

$$\omega = -\frac{I_R}{I_L} \omega_z$$

The first value represents a static displacement in pitch and yaw, and is the root already obtained by factoring the quartic. The second value represents the force-free precessional angular frequency of the rocket. Both values represent observable physical states of the rocket; in fact, for general initial conditions a combination of both states will occur. There will thus be two angular frequencies of oscillation associated with coupled motion, and we must be prepared to accept two of the four roots of the general quartic equation as physical possibilities.

In the reduced case of $Y = Z = 0$ these two roots are $\omega = 0$ and root C' of the cubic equation. Roots A' and B' are non-physical and must be discarded.

Having thus obtained complete information as to the limiting behavior of equation (52a), I am prepared to postulate solutions to the general quartic equation. Symmetry considerations and equation (53a) motivate me to guess that the roots are of the following form:

$$A = -\frac{X\omega_z^2}{2} + a$$

$$B = -\frac{X\omega_z^2}{2} - a$$

$$C = -\frac{X\omega_z^2}{2} + b$$

$$D = -\frac{X\omega_z^2}{2} - b$$

You can see that these values identically satisfy equation (53a).

Equation (53b) becomes

$$\frac{X^2\omega_z^2}{2} - (a^2 + b^2) + X^2\omega_z^2 = Y + Z + \frac{5}{4}X^2\omega_z^2$$

from which we obtain

$$b^2 = -(Y + Z) + \frac{X^2\omega_z^2}{4} - a^2$$

Equation (53c) now appears as

$$\left[\left(\frac{X^2\omega_z^2}{4} - b^2 \right) (-X\omega_z) + \left(\frac{X^2\omega_z^2}{4} - a^2 \right) (-X\omega_z) \right] = -X\omega_z \left[Y + Z + \frac{X^2\omega_z^2}{4} \right]$$

and, upon substitution of the expression for b^2 obtained in (53b), is seen to be identically satisfied. The final coefficient equation, (53d), becomes

$$\left(\frac{X^2\omega_z^2}{4} - a^2 \right) \left(\frac{X^2\omega_z^2}{4} - b^2 \right) = Y \frac{X^2\omega_z^2}{4}$$

Substituting for b^2 the expression obtained in (53b) we can obtain, after some rearrangement,

$$a^4 + \left[Y + Z - \frac{X^2\omega_z^2}{4} \right] a^2 - Z \frac{X^2\omega_z^2}{4} = 0$$

Now this is a special kind of quartic equation known as a

biquadratic equation. It can be solved as a quadratic equation for a^2 to give

$$a^2 = \frac{x^2 \omega_z^2}{8} - \frac{Y+Z}{2} \pm \frac{1}{2} \sqrt{\left(Y+Z - \frac{x^2 \omega_z^2}{4}\right)^2 + Z X^2 \omega_z^2}$$

Solving for b^2 as obtained in (53b), we have

$$b^2 = \frac{x^2 \omega_z^2}{8} - \frac{Y+Z}{2} \mp \sqrt{\left(Y+Z - \frac{x^2 \omega_z^2}{4}\right)^2 + Z X^2 \omega_z^2}$$

Now there is an option here in that we can choose the upper or lower sign for the square root terms. Having chosen a sign for the square root in a^2 , however, we are obliged to choose the corresponding sign for that in b^2 . Choosing the upper sign in each case, we have the following expressions for the complete roots of the quartic equation:

$$(54) \quad \begin{aligned} A &= -\frac{x \omega_z}{2} + \sqrt{\frac{x^2 \omega_z^2}{8} - \frac{Y+Z}{2} + \frac{1}{2} \sqrt{\left(Y+Z - \frac{x^2 \omega_z^2}{4}\right)^2 + Z X^2 \omega_z^2}} \\ B &= -\frac{x \omega_z}{2} - \sqrt{\frac{x^2 \omega_z^2}{8} - \frac{Y+Z}{2} + \frac{1}{2} \sqrt{\left(Y+Z - \frac{x^2 \omega_z^2}{4}\right)^2 + Z X^2 \omega_z^2}} \\ C &= -\frac{x \omega_z}{2} + \sqrt{\frac{x^2 \omega_z^2}{8} - \frac{Y+Z}{2} - \frac{1}{2} \sqrt{\left(Y+Z - \frac{x^2 \omega_z^2}{4}\right)^2 + Z X^2 \omega_z^2}} \\ D &= -\frac{x \omega_z}{2} - \sqrt{\frac{x^2 \omega_z^2}{8} - \frac{Y+Z}{2} - \frac{1}{2} \sqrt{\left(Y+Z - \frac{x^2 \omega_z^2}{4}\right)^2 + Z X^2 \omega_z^2}} \end{aligned}$$

We must determine which of these give us the correct limiting behavior. This is a rather tricky procedure in this case and must be carefully carried out step by step if inconsistencies are to be avoided. For the case $X \omega_z = 0$, the roots assume the form

$$A = \sqrt{-\frac{Y+Z}{2} + \frac{1}{2} \sqrt{(Y+Z)^2}}$$

$$B = -\sqrt{-\frac{Y+Z}{2} + \frac{1}{2}\sqrt{(Y+Z)^2}}$$

$$C = \sqrt{-\frac{Y+Z}{2} - \frac{1}{2}\sqrt{(Y+Z)^2}}$$

$$D = -\sqrt{-\frac{Y+Z}{2} - \frac{1}{2}\sqrt{(Y+Z)^2}}$$

In simplifying these results we must bear in mind always the following rule of algebra: when a quantity is squared, and the square root of the number thus obtained is taken, all knowledge of the algebraic sign of the original quantity is irrevocably lost. The final result of such a sequence of operations is the absolute value of the original quantity, which is by definition a positive number. In our example here,

$$\sqrt{(Y+Z)^2} = |Y+Z|$$

\equiv "the absolute value of $(Y+Z)$ "

Now $|Y+Z| = Y+Z$ if $(Y+Z) > 0$, but

$|Y+Z| = -(Y+Z)$ if $(Y+Z) < 0$

In discussing statically-stable rockets, we are referring always to the case in which Y is negative (that is, C_1 is positive). If we further stipulate that the motion be underdamped, we will always have $(Y+Z)$ negative. Then

$$\sqrt{(Y+Z)^2} = -(Y+Z)$$

and the roots become

$$A = \sqrt{-(Y+Z)}$$

$$B = -\sqrt{-(Y+Z)}$$

$$C = 0$$

$$D = 0$$

Thus A and B are the roots which correctly describe the motion of an underdamped, statically-stable rocket in the limit of roll coupling equal to zero. For the opposite limit, that of $Y = Z = 0$, we have

$$\begin{aligned} A &= -\frac{X\omega_z}{2} + \sqrt{\frac{X^2\omega_z^2}{8} + \frac{1}{2}\sqrt{(-\frac{X^2\omega_z^2}{4})^2}} \\ B &= -\frac{X\omega_z}{2} - \sqrt{\frac{X^2\omega_z^2}{8} + \frac{1}{2}\sqrt{(-\frac{X^2\omega_z^2}{4})^2}} \\ C &= -\frac{X\omega_z}{2} + \sqrt{\frac{X^2\omega_z^2}{8} - \frac{1}{2}\sqrt{(-\frac{X^2\omega_z^2}{4})^2}} \\ D &= -\frac{X\omega_z}{2} - \sqrt{\frac{X^2\omega_z^2}{8} - \frac{1}{2}\sqrt{(-\frac{X^2\omega_z^2}{4})^2}} \end{aligned}$$

Now in this case

$$\sqrt{(-\frac{X^2\omega_z^2}{4})^2} = \frac{X^2\omega_z^2}{4}$$

whereupon

$$\begin{aligned} A &= -\frac{X\omega_z}{2} + \sqrt{\frac{X^2\omega_z^2}{4}} \\ B &= -\frac{X\omega_z}{2} - \sqrt{\frac{X^2\omega_z^2}{4}} \\ C &= -\frac{X\omega_z}{2} \\ D &= -\frac{X\omega_z}{2} \end{aligned}$$

Also,

$$\begin{aligned} \sqrt{\frac{X^2\omega_z^2}{4}} &= \frac{X\omega_z}{2} \quad \text{if } \omega_z > 0, \text{ but} \\ \sqrt{\frac{X^2\omega_z^2}{4}} &= -\frac{X\omega_z}{2} \quad \text{if } \omega_z < 0 \end{aligned}$$

so that if $\omega_z > 0$,

$$A = 0$$

$$B = -X\omega_z$$

while if $\omega_z < 0$,

$$A = -X\omega_z$$

$$B = 0$$

Thus A and B are the physical roots in the limit of force-free precession as well as in the limit of decoupled motion. C and D are spurious roots and must be discarded. The two angular frequencies A and B describe the complete spectrum of dynamic behavior as we proceed continuously from motion dominated by roll coupling to motion dominated by aerodynamic moments (except in a few very special cases to be pointed out later).

From this point on I am going to refer to root A as angular frequency ω_1 and to root B as angular frequency ω_2 . The larger of the two will be called "the fast mode", the smaller "the slow mode". If ω_z is positive, ω_1 will be the slow mode and ω_2 the fast mode; if ω_z is negative, the reverse will be true (recall that a positive ω_z means that the rocket is spinning clockwise as viewed from astern).

I am also going to adopt the abbreviation

$$\tilde{F} = \frac{X^2\omega_z^2}{4} - (Y + Z)$$

which may be written in terms of the rocket's dynamic constants as

$$(55) \quad \tilde{\mathcal{F}} = \frac{I_R^2 \omega_z^2}{4 I_L^2} + \frac{c_1}{I_L} - \frac{c_2^2}{4 I_L^2}$$

Under this convention the two angular frequencies appear as

$$(56a) \quad \omega_1 = -\frac{I_R \omega_z}{2 I_L} + \sqrt{\frac{\tilde{\mathcal{F}}}{2} + \frac{1}{2} \sqrt{\tilde{\mathcal{F}}^2 + \frac{c_2^2 I_R^2 \omega_z^2}{4 I_L^2}}}$$

$$(56b) \quad \omega_2 = -\frac{I_R \omega_z}{2 I_L} - \sqrt{\frac{\tilde{\mathcal{F}}}{2} + \frac{1}{2} \sqrt{\tilde{\mathcal{F}}^2 + \frac{c_2^2 I_R^2 \omega_z^2}{4 I_L^2}}}$$

Since a complete description of the coupled motion of the rocket for general initial conditions must contain both modes, each with its own initial amplitude and its own phase angle, equations (51) must indeed be the solution to the problem. Substituting ω_1 and ω_2 , in turn, into the equation

$$D = \frac{c_2 \omega}{2 I_L \omega + I_R \omega_z}$$

obtained earlier, we obtain the values

$$(57a) \quad D_1 = \frac{c_2}{2 I_L} \left(\frac{\omega_1}{\omega_1 + \frac{I_R}{2 I_L} \omega_z} \right)$$

$$(57b) \quad D_2 = \frac{c_2}{2 I_L} \left(\frac{\omega_2}{\omega_2 + \frac{I_R}{2 I_L} \omega_z} \right)$$

for the two inverse time constants. Note that these both reduce to $c_2/(2 I_L)$ for the case where the roll rate is zero.

The values of A_1 , A_2 , φ_1 , and φ_2 are determined by the four initial conditions, which are:

α_{x0} = value of α_x at $t = 0$

α_{y0} = value of α_y at $t = 0$

Ω_{x0} = value of $d\alpha_x/dt$ at $t = 0$

Ω_{y0} = value of $d\alpha_y/dt$ at $t = 0$

From equations (51) and their time derivatives we have that

$$\alpha_{x_0} = A_1 \sin \varphi_1 + A_2 \sin \varphi_2$$

$$\alpha_{y_0} = A_1 \cos \varphi_1 + A_2 \cos \varphi_2$$

$$\Omega_{x_0} = -A_1 D_1 \sin \varphi_1 + A_1 \omega_1 \cos \varphi_1 - A_2 D_2 \sin \varphi_2 + A_2 \omega_2 \cos \varphi_2$$

$$\Omega_{y_0} = -A_1 D_1 \cos \varphi_1 - A_1 \omega_1 \sin \varphi_1 - A_2 D_2 \cos \varphi_2 - A_2 \omega_2 \sin \varphi_2$$

This system of four independent equations in four unknowns is reduced by eliminating terms between the equations one by one until explicit formulae for the initial amplitudes and phase angles are obtained. Beginning this process with the angular velocity equations, for instance, I can write

$$D_1 \Omega_{x_0} + \omega_1 \Omega_{y_0} = -A_1 \sin \varphi_1 (D_1^2 + \omega_1^2) - A_2 \sin \varphi_2 (D_1 D_2 + \omega_1 \omega_2) + A_2 \cos \varphi_2 (\omega_2 D_1 - \omega_1 D_2)$$

$$D_2 \Omega_{x_0} + \omega_2 \Omega_{y_0} = -A_1 \sin \varphi_1 (D_1 D_2 + \omega_1 \omega_2) - A_2 \sin \varphi_2 (D_2^2 + \omega_2^2) + A_1 \cos \varphi_1 (\omega_1 D_2 - \omega_2 D_1)$$

Now if you substitute $\alpha_{y_0} - A_2 \cos \varphi_2$ for $A_1 \cos \varphi_1$ in the second equation and subtract it from the first you will get

$$\begin{bmatrix} \Omega_{x_0} (D_1 - D_2) + \Omega_{y_0} (\omega_1 - \omega_2) \\ + \alpha_{y_0} (\omega_1 D_2 - \omega_2 D_1) \end{bmatrix} = \begin{bmatrix} A_1 \sin \varphi_1 (D_1 D_2 + \omega_1 \omega_2 - D_1^2 - \omega_1^2) \\ + A_2 \sin \varphi_2 (D_2^2 + \omega_2^2 - D_1 D_2 - \omega_1 \omega_2) \end{bmatrix}$$

Multiplying the equation for α_{x_0} by the factor $(D_2^2 + \omega_2^2 - D_1 D_2 - \omega_1 \omega_2)$ and subtracting the result from this equation results in the expression

$$A_1 \sin \varphi_1 \begin{bmatrix} 2(D_1 D_2 + \omega_1 \omega_2) - D_1^2 \\ - D_2^2 - \omega_1^2 - \omega_2^2 \end{bmatrix} = \begin{bmatrix} \Omega_{x_0} (D_1 - D_2) + \Omega_{y_0} (\omega_1 - \omega_2) + \alpha_{y_0} (\omega_1 D_2 - \omega_2 D_1) \\ + \alpha_{x_0} (D_1 D_2 + \omega_1 \omega_2 - D_2^2 - \omega_2^2) \end{bmatrix}$$

from which we can obtain

$$A_1 \sin \varphi_1 = \frac{\Omega_{x_0}(D_1 - D_2) + \Omega_{y_0}(\omega_1 - \omega_2) + \alpha_{x_0}(D_1 D_2 + \omega_1 \omega_2 - D_1^2 - \omega_1^2)}{2(D_1 D_2 + \omega_1 \omega_2) - D_1^2 - D_2^2 - \omega_1^2 - \omega_2^2}$$

By a similar sequence of algebraic operations we can obtain the value of $A_1 \cos \varphi_1$:

$$\omega_1 \Omega_{x_0} - D_1 \Omega_{y_0} = A_1 \cos \varphi_1 (\omega_1^2 + D_1^2) + A_2 \sin \varphi_2 (\omega_2 D_1 - \omega_1 D_2) + A_2 \cos \varphi_2 (\omega_1 \omega_2 + D_1 D_2)$$

$$\omega_2 \Omega_{x_0} - D_2 \Omega_{y_0} = A_1 \cos \varphi_1 (\omega_1 \omega_2 + D_1 D_2) + A_1 \sin \varphi_1 (\omega_1 D_2 - \omega_2 D_1) + A_2 \cos \varphi_2 (\omega_2^2 + D_2^2)$$

Substituting $\alpha_{x_0} - A_2 \sin \varphi_2$ for $A_1 \sin \varphi_1$ and subtracting,

$$\begin{bmatrix} \Omega_{x_0}(\omega_1 - \omega_2) + \Omega_{y_0}(D_2 - D_1) \\ + \alpha_{x_0}(\omega_1 D_2 - \omega_2 D_1) \end{bmatrix} = \begin{bmatrix} A_1 \cos \varphi_1 (\omega_1^2 + D_1^2 - \omega_1 \omega_2 - D_1 D_2) \\ + A_2 \cos \varphi_2 (\omega_1 \omega_2 + D_1 D_2 - \omega_2^2 - D_2^2) \end{bmatrix}$$

Multiplying α_{y_0} by $(\omega_1 \omega_2 + D_1 D_2 - \omega_2^2 - D_2^2)$ and subtracting the result from the above gives us

$$\begin{bmatrix} \Omega_{x_0}(\omega_1 - \omega_2) + \Omega_{y_0}(D_2 - D_1) \\ + \alpha_{x_0}(\omega_1 D_2 - \omega_2 D_1) + \alpha_{y_0}(\omega_2^2 + D_2^2 - \omega_1 \omega_2 - D_1 D_2) \end{bmatrix} = A_1 \cos \varphi_1 \begin{bmatrix} \omega_1^2 + D_1^2 + \omega_2^2 + D_2^2 \\ -2(\omega_1 \omega_2 + D_1 D_2) \end{bmatrix}$$

Multiplying both sides of this by (-1) and performing the appropriate division, we obtain

$$A_1 \cos \varphi_1 = \frac{\Omega_{x_0}(\omega_2 - \omega_1) + \Omega_{y_0}(D_1 - D_2) + \alpha_{x_0}(\omega_2 D_1 - \omega_1 D_2) + \alpha_{y_0}(\omega_1 \omega_2 + D_1 D_2 - \omega_2^2 - D_2^2)}{2(\omega_1 \omega_2 + D_1 D_2) - D_1^2 - D_2^2 - \omega_1^2 - \omega_2^2}$$

Dividing $A_1 \sin \varphi_1$ by $A_1 \cos \varphi_1$ and taking the inverse tangent function of both sides of the resulting equation will give us an explicit formula for φ_1 in terms of the initial conditions, angular frequencies, and inverse time constants:

$$(58a) \quad \varphi_1 = \arctan \left[\frac{\Omega_{x_0}(D_1 - D_2) + \Omega_{y_0}(\omega_1 - \omega_2) + \alpha_{x_0}(\omega_1 \omega_2 + D_1 D_2 - \omega_2^2 - D_2^2)}{\Omega_{x_0}(\omega_2 - \omega_1) + \Omega_{y_0}(D_1 - D_2) + \alpha_{x_0}(\omega_2 D_1 - \omega_1 D_2) + \alpha_{y_0}(\omega_1 \omega_2 + D_1 D_2 - \omega_2^2 - D_2^2)} \right]$$

φ_2 is now computed from the relations

$$A_2 \sin \varphi_2 = \alpha_{x_0} - A_1 \sin \varphi_1$$

$$A_2 \cos \varphi_2 = \alpha_{y_0} - A_1 \cos \varphi_1$$

This time, since $A_1 \sin \varphi_1$ and $A_1 \cos \varphi_1$ are both quantities which we have already computed for use in finding φ_1 , we can immediately write

$$(58b) \quad \varphi_2 = \arctan \left[\frac{\alpha_{x_0} - A_1 \sin \varphi_1}{\alpha_{y_0} - A_1 \cos \varphi_1} \right]$$

Both phase angles are now known and their sine and cosine functions can be determined from trigonometric tables. Since we also know the explicit formulae for $A_1 \sin \varphi_1$ and $A_2 \sin \varphi_2$, we can compute the initial amplitudes as follows:

$$(59a) \quad A_1 = \frac{A_1 \sin \varphi_1}{\sin \varphi_1}$$

$$(59b) \quad A_2 = \frac{A_2 \sin \varphi_2}{\sin \varphi_2}$$

Equations (51) and (55) through (59) contain all the information necessary to completely describe the angular oscillations of a rolling model rocket in pitch and yaw. For general initial conditions, both the pitching and yawing motions are sums of two different exponentially-damped sinusoids. The appearance of the motion is generally quite complicated. The slower mode sets the basic pattern: the nose of the rocket describes an inward spiral toward the position of zero deflection if the rocket is statically stable, an outward spiral if it is statically unstable, and a circle of constant radius if either (1) the corrective moment coefficient C_1 is zero, or (2) the corrective moment coefficient is positive but the damping moment coefficient C_2 is zero. The faster mode may impose intricate secondary motions called nutations upon the basic pattern if it is sufficiently high in frequency and its amplitude is small. As in the case of decoupled motion, however, the characteristics of the oscillations are dependent upon the relative values of the rocket's inertial and aerodynamic constants.

For the case of zero damping ($C_2 = 0$) the function \mathcal{F} becomes

$$\mathcal{F} = \frac{I_R^2 \omega_z^2}{4 I_L^2} + \frac{C_1}{I_L}$$

From which we have

$$\omega_1 = -\frac{I_R \omega_z}{2 I_L} + \sqrt{\frac{I_R^2 \omega_z^2}{4 I_L^2} + \frac{C_1}{I_L}}$$

$$\omega_2 = -\frac{I_R \omega_z}{2 I_L} - \sqrt{\frac{I_R^2 \omega_z^2}{4 I_L^2} + \frac{C_1}{I_L}}$$

as long as \mathcal{F} is positive, which it certainly will be for statically-stable rockets. Since C_2 is zero, D_1 and D_2 will

both be zero and the expressions describing the motion become

$$(60a) \quad \alpha_x = A_1 \sin(\omega_1 t + \varphi_1) + A_2 \sin(\omega_2 t + \varphi_2)$$

$$(60b) \quad \alpha_y = A_1 \cos(\omega_1 t + \varphi_1) + A_2 \cos(\omega_2 t + \varphi_2)$$

Both pitch and yaw are the sum of two simple harmonic motions. The oscillations do not decay; they persist indefinitely at undiminished amplitudes as shown in Figure 26. Needless to say, this condition is undesirable; as in the decoupled case, the restoration of the rocket to a position in which it is facing directly along the intended flight path never occurs. Since damping is always present in some degree, however slight, this case will not be literally observed for any real rocket. But, as in decoupled motion, too little damping can result in an oscillation that continues for an undesirably long time.

For nonzero damping such that

$$\frac{\tilde{F}}{2} + \frac{1}{2} \sqrt{\tilde{J}^2 + \frac{C_2^2 I_R^2 \omega_e^2}{4 I_L^4}} > \frac{I_R^2 \omega_z^2}{4 I_L^2}$$

coupled, positively-stable motion described by the complete forms of equations (51) and (55) through (59) will occur. The angular frequency of the fast mode will be opposite in sign to that of the slow mode: the fast mode will be of opposite sign to the roll rate, while the sign of the slow mode will be the same as that of the roll rate. The damping coefficients D_1 and D_2 will both be positive, meaning that the amplitudes of both modes will decay exponentially with time. The inverse time constant associated with the slow mode will be smaller in magnitude than that associated with the fast mode; the slow mode will

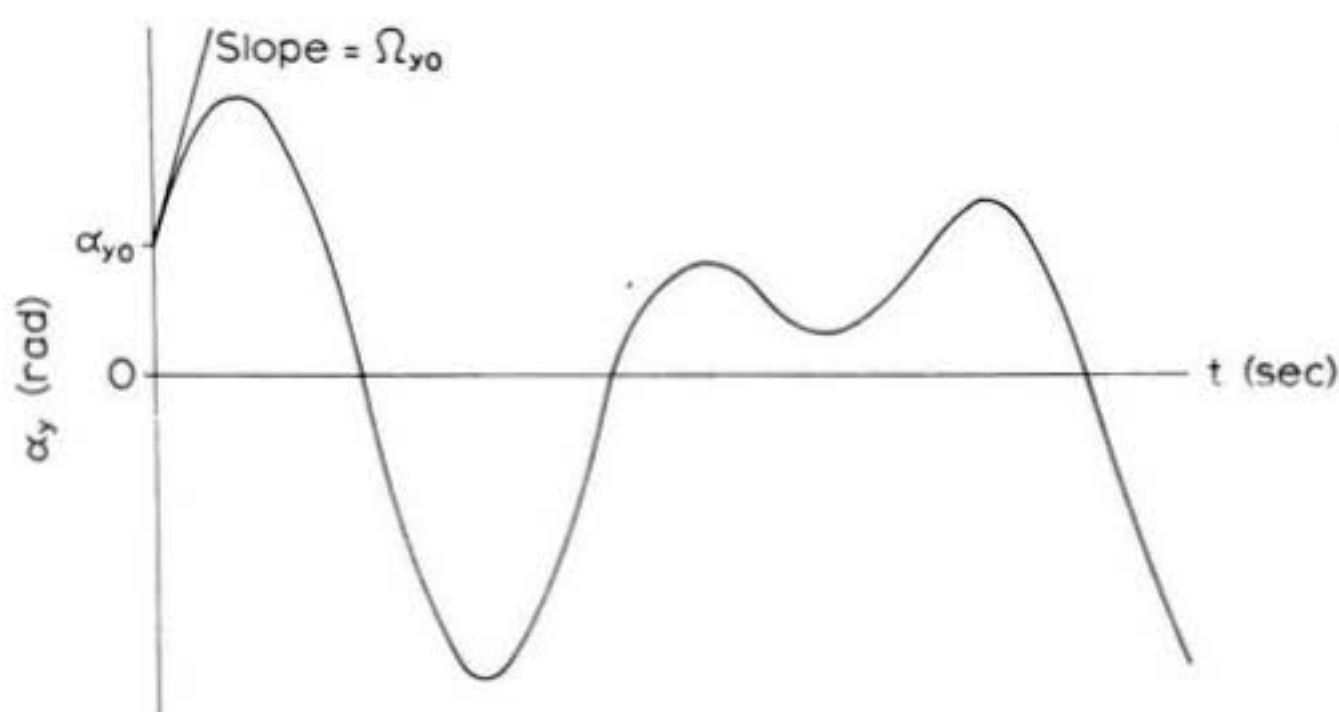
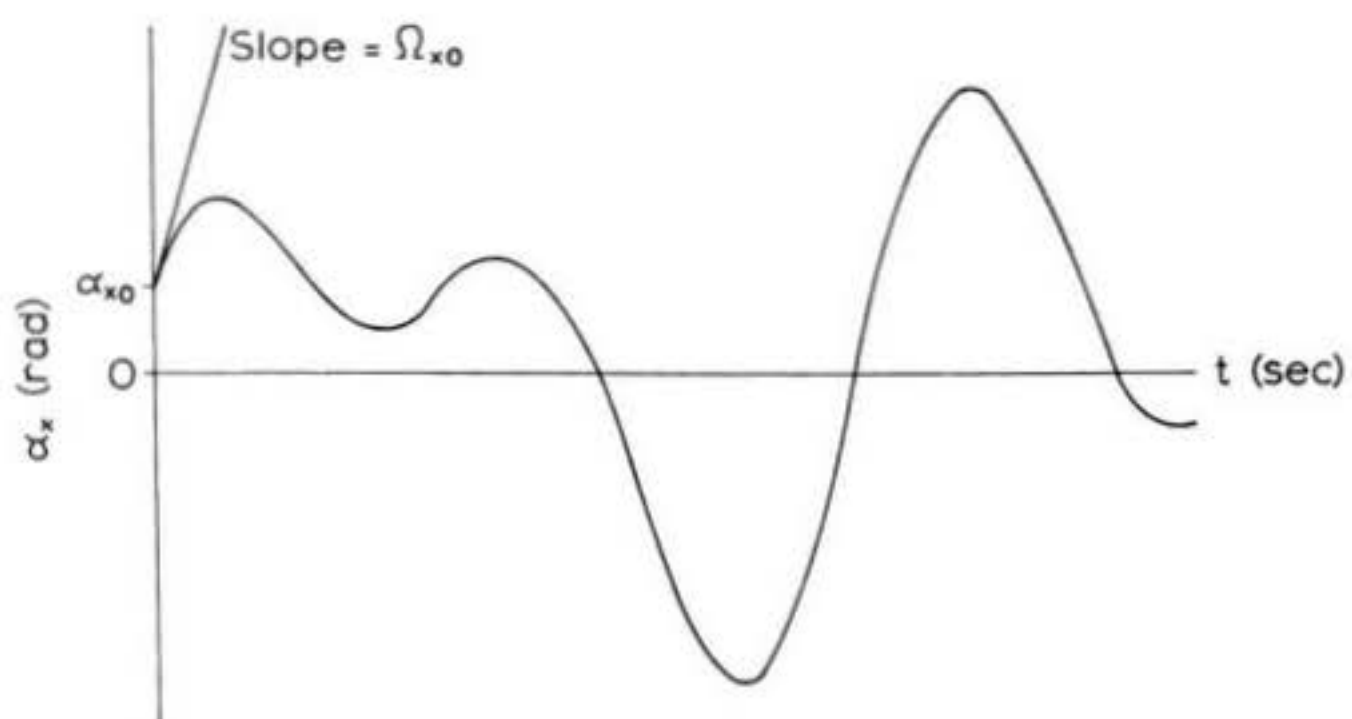


Figure 26: Undamped homogeneous response to general initial conditions in yaw and pitch of a model rocket spinning about its longitudinal axis at a nonzero roll rate ω_z . The relation of the initial conditions to the properties of the response has been illustrated. The pattern of pitching and yawing motions shown repeats itself periodically for all time, as there is no damping to dissipate the angular momentum of the oscillations.

therefore be a more slowly decaying mode than the fast mode. The fast mode decays more rapidly than a decoupled oscillation with the same values of C_1 , C_2 , and I_L , while the slow mode decays more slowly than such a decoupled oscillation. As a practical matter this means that the slow mode will be the most important part of the oscillation after a sufficient time has elapsed, so that roll coupling serves to reduce the effectiveness of damping. A representative case of coupled, positively-stable motion is shown in Figure 27. It is in this range of relative values of C_1 , C_2 , and I_L that the designer wants his model rocket to lie; under no other conditions do the oscillations subside, whether the rocket is rolling or not.

The condition which must be satisfied for roll-coupled characteristic motion to be positively stable can be made more explicit by solving the inequality

$$\frac{\gamma}{2} + \frac{1}{2} \sqrt{\gamma^2 + \frac{C_2^2 I_R^2 \omega_z^2}{4 I_L^4}} > \frac{I_R^2 \omega_z^2}{4 I_L^2}$$

for γ . We can express this relation as

$$\sqrt{\gamma^2 + \frac{C_2^2 I_R^2 \omega_z^2}{4 I_L^4}} > \frac{I_R^2 \omega_z^2}{2 I_L^2} - \gamma$$

Squaring both sides and collecting terms, we have

$$\frac{C_2^2 I_R^2 \omega_z^2}{4 I_L^4} > \frac{I_R^4 \omega_z^4}{4 I_L^4} - \gamma \cdot \frac{I_R^2 \omega_z^2}{I_L^2}$$

from which it can be seen that

$$\gamma > \frac{I_R^2 \omega_z^2}{4 I_L^2} - \frac{C_2^2}{4 I_L^2}$$

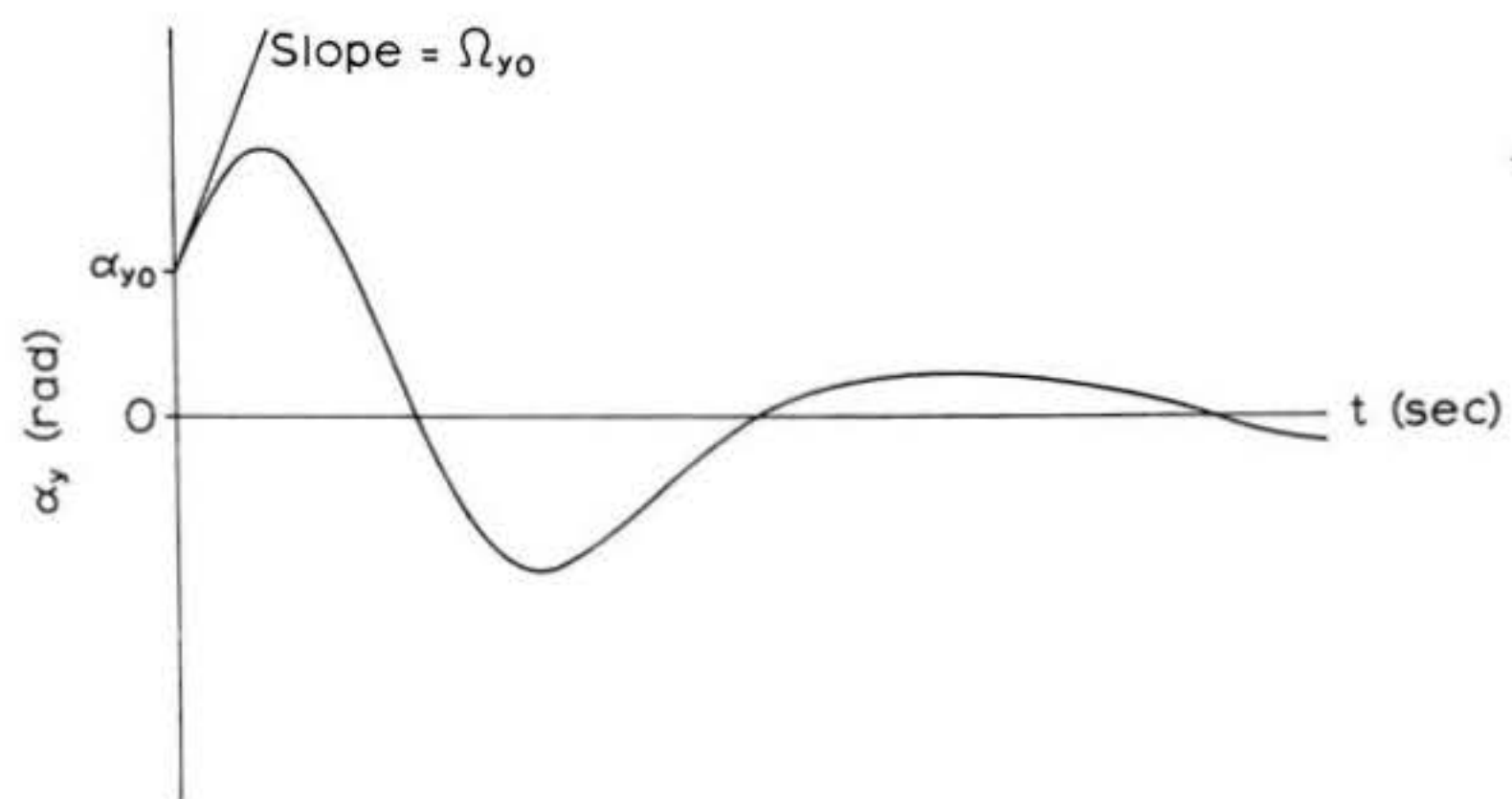
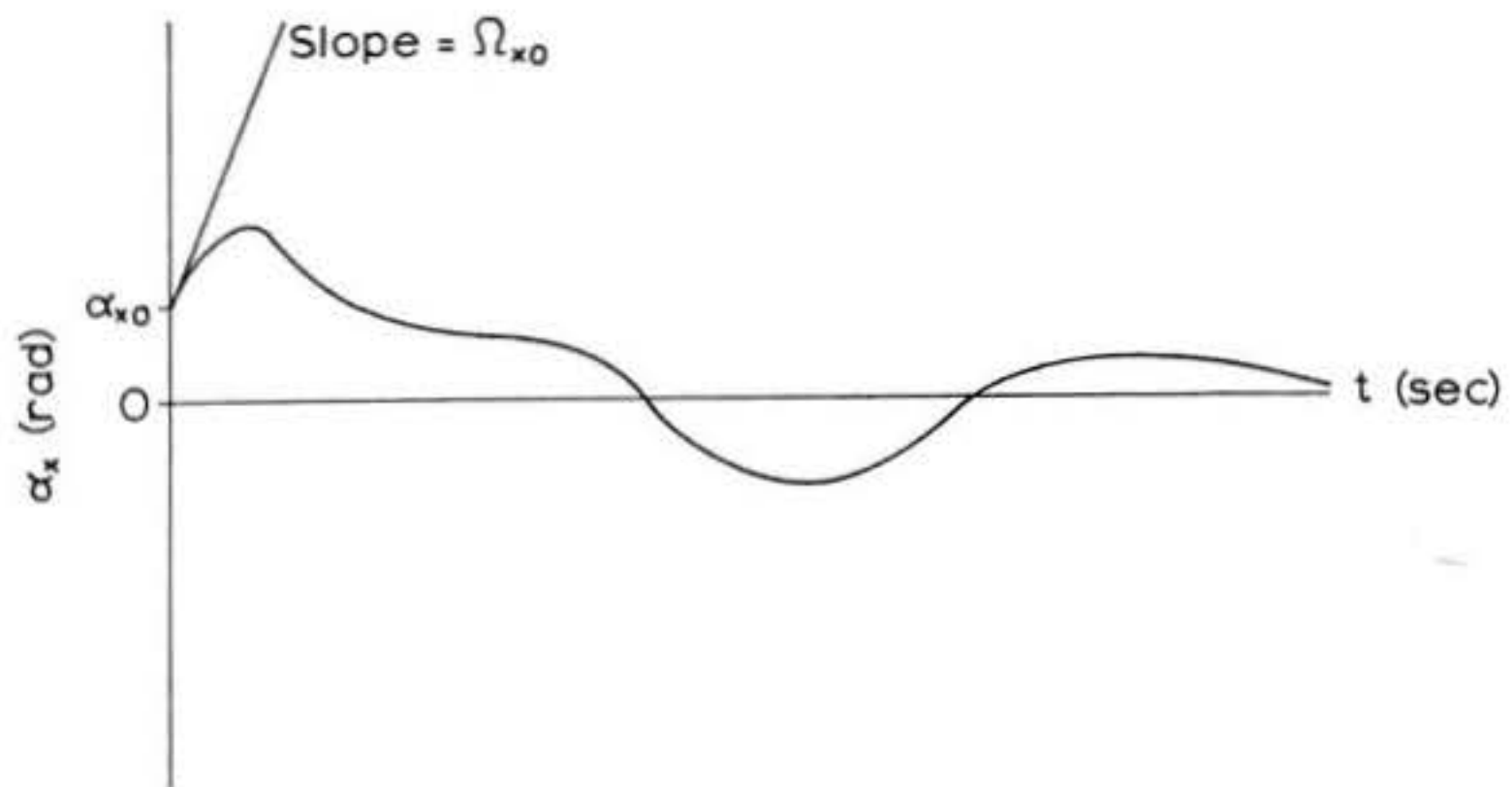


Figure 27: Characteristic response of a model rocket with finite damping and nonzero roll rate to general initial conditions in yaw and pitch, showing the relation of the initial conditions to the properties of the response. Both the yawing and pitching oscillations eventually decay to zero and the model regains straight and true flight.

Upon examining the original expression for $\tilde{\mathcal{F}}$ given in equation (55), we see that this is just the requirement that

$$C_1 > 0$$

Positive static stability is thus required for positively stable characteristic motion, whether or not the rocket is spinning about its centerline. As the value of

$$\frac{\tilde{\mathcal{F}}}{2} + \frac{1}{2} \sqrt{\tilde{\mathcal{F}}^2 + \frac{C_2^2 I_R^2 \omega_z^2}{4 I_L^4}}$$

decreases toward $\frac{I_R^2 \omega_z^2}{4 I_L^2}$ (that is, as the corrective moment coefficient decreases toward zero), the angular frequency of the fast mode approaches a value of $-\frac{I_R \omega_z}{I_L}$ while that of the slow mode approaches zero from above if ω_z is positive, from below if ω_z is negative. The inverse time constant of the fast mode approaches C_2/I_L , or twice the damping of the decoupled oscillation, but that of the slow mode approaches zero. At $C_1 = 0$ the rocket remains deflected indefinitely; it is neutrally stable, just as if it were not rolling. As C_1 becomes negative, so that

$$\frac{\tilde{\mathcal{F}}}{2} + \frac{1}{2} \sqrt{\tilde{\mathcal{F}}^2 + \frac{C_2^2 I_R^2 \omega_z^2}{4 I_L^4}} < \frac{I_R^2 \omega_z^2}{4 I_L^2}$$

the inverse time constant of the slow mode also becomes negative: the angular deflection of the rocket from its intended direction of flight increases with time. A rocket with a negative corrective moment coefficient is unstable, as emphasized above, whether it is rolling or not.

There is no fundamental change in the character of the rocket's

motion as damping gains ascendancy over corrective moment, as there is in the case of decoupled motion, but the effect of too much damping is every bit as serious in the case of roll-coupled oscillation as it is for decoupled response. The condition of critical damping for rockets whose roll rate is zero, you may remember, is

$$\frac{C_1}{I_L} = \frac{C_2^2}{4I_L^2}$$

Under this condition $\tilde{\mathcal{F}}$ becomes simply $\frac{I_R^2 \omega_z^2}{4I_L^2}$, and

$$\frac{\tilde{\mathcal{F}}}{2} + \frac{1}{2} \sqrt{\tilde{\mathcal{F}}^2 + \frac{C_2^2 I_R^2 \omega_z^2}{4I_L^4}} = \frac{I_R^2 \omega_z^2}{8I_L^2} + \frac{1}{2} \sqrt{\frac{I_R^2 \omega_z^2}{4I_L^2} \left(\frac{I_R^2 \omega_z^2}{4I_L^2} + \frac{C_2^2}{I_L^2} \right)}$$

Now $\frac{I_R^2 \omega_z^2}{4I_L^2} + \frac{C_2^2}{I_L^2} > \frac{I_R^2 \omega_z^2}{4I_L^2}$ and therefore

$$\frac{1}{2} \sqrt{\frac{I_R^2 \omega_z^2}{4I_L^2} \left(\frac{I_R^2 \omega_z^2}{4I_L^2} + \frac{C_2^2}{I_L^2} \right)} > \frac{I_R^2 \omega_z^2}{8I_L^2}$$

It follows that

$$\frac{\tilde{\mathcal{F}}}{2} + \frac{1}{2} \sqrt{\tilde{\mathcal{F}}^2 + \frac{C_2^2 I_R^2 \omega_z^2}{4I_L^4}} > \frac{I_R^2 \omega_z^2}{8I_L^2}$$

so that the motion is stable, no matter how great the value of C_2 . This, of course, is consistent with our result that the value of C_1 alone determines the stability of the oscillation. But the slow mode, you will recall, will have an inverse time constant whose value is less than that of the inverse time constant of an identical rocket which is not rolling; therefore the same condition which produces critical damping in a non-rolling rocket will, in an identical rocket which is rolling, produce an oscillation that decays more slowly than a critically-damped response. The

condition

$$\frac{C_2^2}{4I_L^2} > \frac{C_1}{I_L}$$

which produces overdamping in rockets which are not rolling, will aggravate this undesirable state of affairs, making the rate at which the deflections subside even less. Deflection amplitudes which are large and which persist for long periods of time can thus result from the same conditions which produce critically-damped or overdamped behavior in non-rolling rockets, so it remains good design practice to keep

$$\frac{C_1}{I_L} > \frac{C_2^2}{4I_L^2}$$

for any model rocket, rolling or not.

3.2.2 Complete Response to Step Input

In this section I am going to derive the equations describing the angular oscillations of a rolling model rocket subjected to a step input in yaw alone, of the same form as that considered in Section 3.1.2. This can be done without loss of generality because the principle of superposition (Section 2.4) permits us to obtain the solution of the effect of each component of a step input having both pitch and yaw components separately, and then to add the solutions thus obtained to form the complete solution. It is also true that the response to a step in pitch is analogous to the response to a step in yaw, so that everything a designer needs to know can be learned by doing the yaw problem alone. For this same reason the impulse response of Section 3.1.3 will be done assuming the only disturbing moment to act about the yaw axis.

Before time equal to zero, when the value of the step disturbance is zero, the coupled dynamical equations appear as

$$I_L \frac{d^2\alpha_x}{dt^2} + C_2 \frac{d\alpha_x}{dt} + C_1 \alpha_x + I_R \omega_z \frac{d\alpha_y}{dt} = 0$$

$$I_L \frac{d^2\alpha_y}{dt^2} + C_2 \frac{d\alpha_y}{dt} + C_1 \alpha_y - I_R \omega_z \frac{d\alpha_x}{dt} = 0$$

As in Section 3.1.2, we are considering a rocket whose pitch and yaw states are quiescent before the application of the step. The solution to the above equations is therefore

$$\alpha_x = \alpha_y = 0$$

which, as you can see, identically satisfies them both. After the step disturbance rises to the value M_s the equations become

$$I_L \frac{d^2\alpha_x}{dt^2} + C_2 \frac{d\alpha_x}{dt} + C_1 \alpha_x + I_R \omega_z \frac{d\alpha_y}{dt} = M_s$$

$$I_L \frac{d^2\alpha_y}{dt^2} + C_2 \frac{d\alpha_y}{dt} + C_1 \alpha_y - I_R \omega_z \frac{d\alpha_x}{dt} = 0$$

The particular solution to this set of equations is known to be

$$(61) \quad \alpha_x = \frac{M_s}{C_1}$$

$$\alpha_y = 0$$

The complete solution to the coupled step response for time greater than zero is then

$$(62a) \quad \alpha_x = A_1 e^{-D_1 t} \sin(\omega_1 t + \varphi_1) + A_2 e^{-D_2 t} \sin(\omega_2 t + \varphi_2) + \frac{M_s}{C_1}$$

$$(62b) \quad \alpha_y = A_1 e^{-D_1 t} \cos(\omega_1 t + \varphi_1) + A_2 e^{-D_2 t} \cos(\omega_2 t + \varphi_2)$$

where ω_1 and ω_2 are given by equations (56) and D_1 and D_2 are given by equations (57). A_1 , A_2 , φ_1 , and φ_2 are determined by the initial conditions of the motion, which, for a quiescent state prior to the disturbance, are all zero:

$$\alpha_{x0} = A_1 \sin \varphi_1 + A_2 \sin \varphi_2 + \frac{M_s}{C_1} \\ = 0$$

$$\alpha_{y0} = A_1 \cos \varphi_1 + A_2 \cos \varphi_2 \\ = 0$$

$$\Omega_{x0} = -A_1 D_1 \sin \varphi_1 + A_1 \omega_1 \cos \varphi_1 - A_2 D_2 \sin \varphi_2 + A_2 \omega_2 \cos \varphi_2 \\ = 0$$

$$\Omega_{y0} = -A_1 D_1 \cos \varphi_1 - A_1 \omega_1 \sin \varphi_1 - A_2 D_2 \cos \varphi_2 - A_2 \omega_2 \sin \varphi_2 \\ = 0$$

These equations can be cast into the form of the initial condition equations used in Section 3.2.1 for determining the values of the initial amplitudes and phase angles given in equations (58) and (59) by rewriting them in the following manner:

$$-\frac{M_s}{C_1} = A_1 \sin \varphi_1 + A_2 \sin \varphi_2$$

$$0 = A_1 \cos \varphi_1 + A_2 \cos \varphi_2$$

$$0 = -A_1 D_1 \sin \varphi_1 + A_1 \omega_1 \cos \varphi_1 - A_2 D_2 \sin \varphi_2 + A_2 \omega_2 \cos \varphi_2$$

$$0 = -A_1 D_1 \cos \varphi_1 - A_1 \omega_1 \sin \varphi_1 - A_2 D_2 \cos \varphi_2 - A_2 \omega_2 \sin \varphi_2$$

By analogy with the corresponding solutions to the equations of Section 3.2.1 we can then write

$$A_1 \sin \varphi_1 = \frac{M_s}{C_1} \left[\frac{(\omega_2^2 + D_2^2 - \omega_1 \omega_2 - D_1 D_2)}{2(D_1 D_2 + \omega_1 \omega_2) - D_1^2 - D_2^2 - \omega_1^2 - \omega_2^2} \right]$$

$$A_1 \cos \varphi_1 = \frac{M_s}{C_1} \left[\frac{(\omega_1 D_2 - \omega_2 D_1)}{2(\omega_1 \omega_2 + D_1 D_2) - \omega_1^2 - D_1^2 - \omega_2^2 - D_2^2} \right]$$

from which we obtain

$$(63a) \quad \varphi_1 = \arctan \left[\frac{\omega_2^2 + D_2^2 - \omega_1 \omega_2 - D_1 D_2}{\omega_1 D_2 - \omega_2 D_1} \right]$$

Then, using the relations

$$A_2 \sin \varphi_2 = -A_1 \sin \varphi_1 - \frac{M_s}{C_1}$$

$$A_2 \cos \varphi_2 = -A_1 \cos \varphi_1,$$

we have

$$A_2 \sin \varphi_2 = \frac{M_s}{C_1} \left[\frac{\omega_1^2 + D_1^2 - \omega_1 \omega_2 - D_1 D_2}{2(\omega_1 \omega_2 + D_1 D_2) - \omega_1^2 - D_1^2 - \omega_2^2 - D_2^2} \right]$$

$$A_2 \cos \varphi_2 = \frac{M_s}{C_1} \left[\frac{\omega_2 D_1 - \omega_1 D_2}{2(\omega_1 \omega_2 + D_1 D_2) - \omega_1^2 - D_1^2 - \omega_2^2 - D_2^2} \right]$$

and therefore, that

$$(63b) \quad \varphi_2 = \arctan \left[\frac{\omega_1^2 + D_1^2 - \omega_1 \omega_2 - D_1 D_2}{\omega_2 D_1 - \omega_1 D_2} \right]$$

The values of the initial amplitudes are then obtained from the identities

$$(64a) \quad A_1 = \frac{A_1 \sin \varphi_1}{\sin \varphi_1}$$

$$(64b) \quad A_2 = \frac{A_2 \sin \varphi_2}{\sin \varphi_2}$$

The special case of zero damping is obtained by setting $D_1 = D_2 = 0$. The characteristic appearance of this kind of motion should by now be familiar to you, so I won't bother to

illustrate it. The coupled step response of a stable rocket with nonzero damping is shown in Figure 28. As in Section 3.1.2, the severity of the step response is inversely proportional to the (positive) magnitude of the corrective moment coefficient. The desirability of a large corrective moment coefficient is therefore undiminished by the presence of a nonzero roll rate.

3.2.3 Complete Response to Impulse Input

Should a rocket which is spinning about its longitudinal axis encounter an impulsive disturbance acting about its yaw axis and of strength H , it may be verified by an argument similar to the one used in Section 3.1.3 that the initial effect of the impulse is identical to the effect of the same impulse upon the rocket when it is not rolling: an initial yaw rate of value H/I_L arises instantaneously. The subsequent motion is a roll-coupled characteristic response governed by equations (51) and (55) through (59) with initial conditions α_{x_0} , α_{y_0} , and Ω_{y_0} all equal to zero and initial condition Ω_{x_0} equal to H/I_L .

The impulse response is thus given by equations (51),

$$\alpha_x = A_1 e^{-D_1 t} \sin(\omega_1 t + \varphi_1) + A_2 e^{-D_2 t} \sin(\omega_2 t + \varphi_2)$$

$$\alpha_y = A_1 e^{-D_1 t} \cos(\omega_1 t + \varphi_1) + A_2 e^{-D_2 t} \cos(\omega_2 t + \varphi_2)$$

where ω_1 and ω_2 are given by equations (56) and D_1 and D_2 are computed according to equations (57). Substituting the values of the initial conditions into the equations used in deriving equation (58a), we have

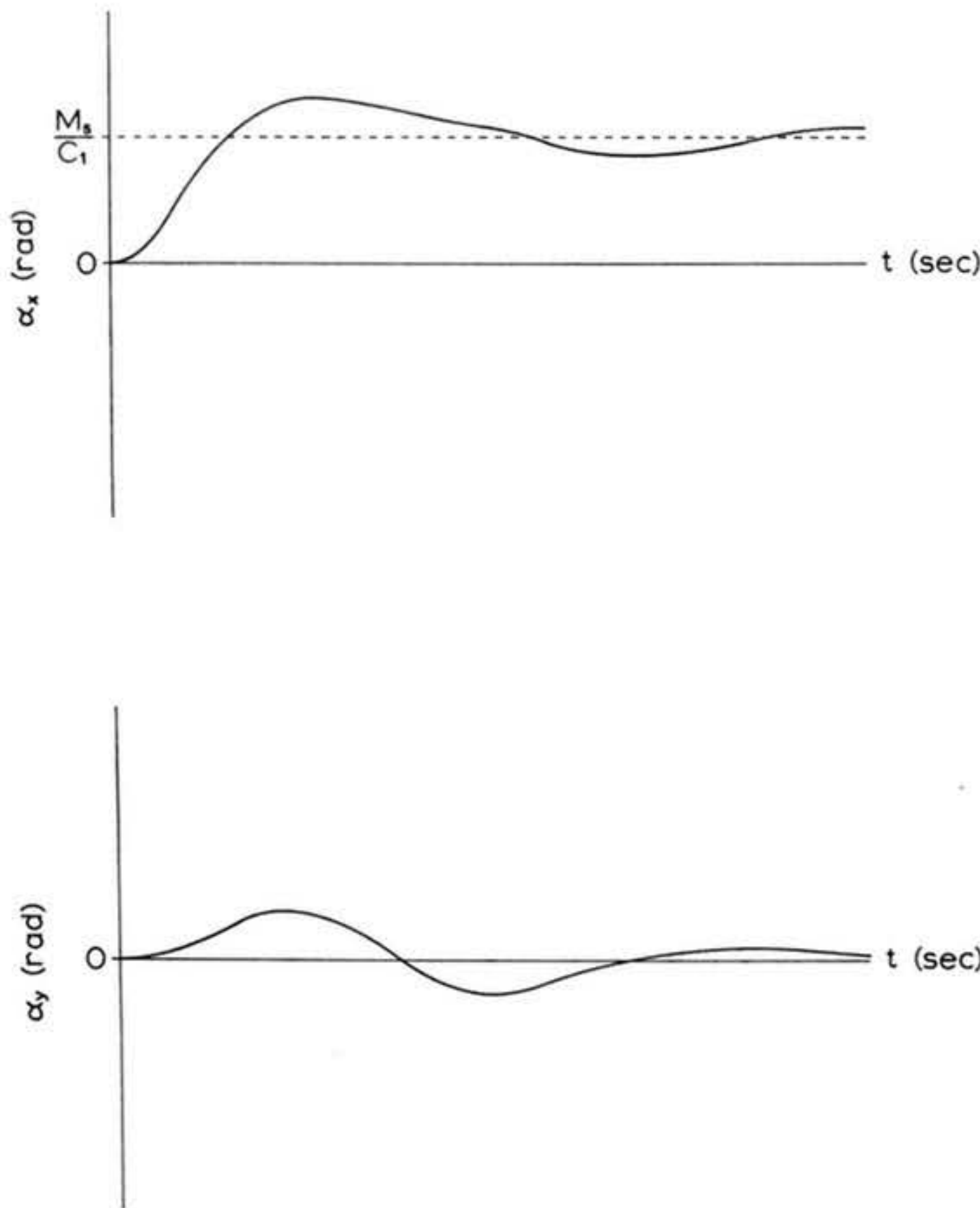


Figure 28: Roll-coupled response of a model rocket with finite damping to a step of intensity M_s in yaw. Both yawing and pitching oscillations occur; the pitching motion, however, decays to zero while the yaw angle eventually approaches the value M_s/C_1 .

$$A_1 \sin \varphi_1 = \frac{H}{I_L} \left[\frac{D_1 - D_2}{2(D_1 D_2 + \omega_1 \omega_2) - D_1^2 - D_2^2 - \omega_1^2 - \omega_2^2} \right]$$

$$A_1 \cos \varphi_1 = \frac{H}{I_L} \left[\frac{\omega_2 - \omega_1}{2(D_1 D_2 + \omega_1 \omega_2) - D_1^2 - D_2^2 - \omega_1^2 - \omega_2^2} \right]$$

from which we conclude that

$$(65a) \quad \varphi_1 = \arctan \left[\frac{D_1 - D_2}{\omega_2 - \omega_1} \right]$$

The equations used in deriving (58b) become

$$A_2 \sin \varphi_2 = -A_1 \sin \varphi_1$$

$$A_2 \cos \varphi_2 = -A_1 \cos \varphi_1$$

and thus yield the result

$$(65b) \quad \varphi_2 = \varphi_1$$

A simplification of notation is then possible, in that the single value $\varphi = \varphi_1 = \varphi_2$ may be applied to the phase angles of both modes. The equations for the initial amplitudes thus become

$$(66a) \quad A_1 = \frac{A_1 \sin \varphi}{\sin \varphi}$$

$$(66b) \quad A_2 = -A_1$$

so that the initial amplitude of the first mode may be denoted by A , that of the second mode by $(-A)$. The roll-coupled impulse response may then be written in the simplified form

$$(67) \quad \begin{aligned} \alpha_x &= A [e^{-D_1 t} \sin(\omega_1 t + \varphi) - e^{-D_2 t} \sin(\omega_2 t + \varphi)] \\ \alpha_y &= A [e^{-D_1 t} \cos(\omega_1 t + \varphi) - e^{-D_2 t} \cos(\omega_2 t + \varphi)] \end{aligned}$$

The coupled impulse response of a representative, statically-stable model rocket having a finite amount of damping is illustrated in Figure 29.

Although the analytically explicit forms of the equations governing the maximum angular displacement experienced in a roll-coupled impulse response are prohibitively complicated, it will be found that a large value of the longitudinal moment of inertia I_L is desirable, as it was in the decoupled case, in order to minimize the severity of the response. This characteristic of the behavior is (again as before) connected with the inverse dependence of the initial amplitude terms on I_L .

3.2.4 Steady State Response to Sinusoidal Forcing at the Roll Rate

While it is certainly possible for a rocket having a zero roll rate to experience sinusoidal forcing of the various types described in Section 3.1.4, it turns out that the vast majority of cases of sinusoidal motion encountered in practice are due to causes arising from the spinning of the rocket itself. Aerodynamic and inertial asymmetries and thrust misalignments, which appear as step disturbances to non-rolling rockets, become to a rolling rocket sinusoidal forcing functions whose angular frequency is identical to the rocket's roll rate. For this reason the roll-coupled pitch- and yaw-dynamics of cylindrical projectiles under sinusoidal forcing are usually analyzed only for the case $\omega_f = \omega_x$.

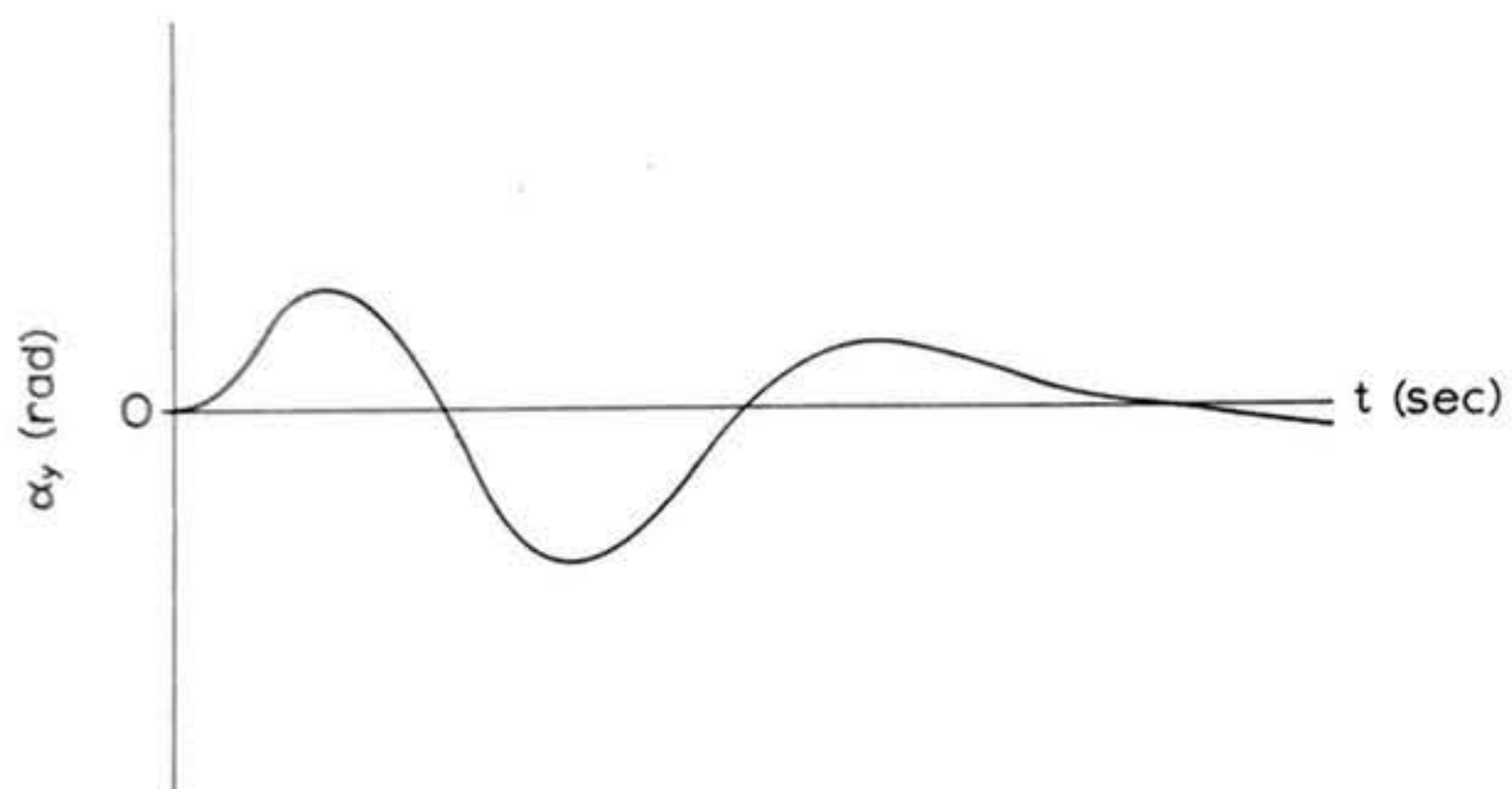
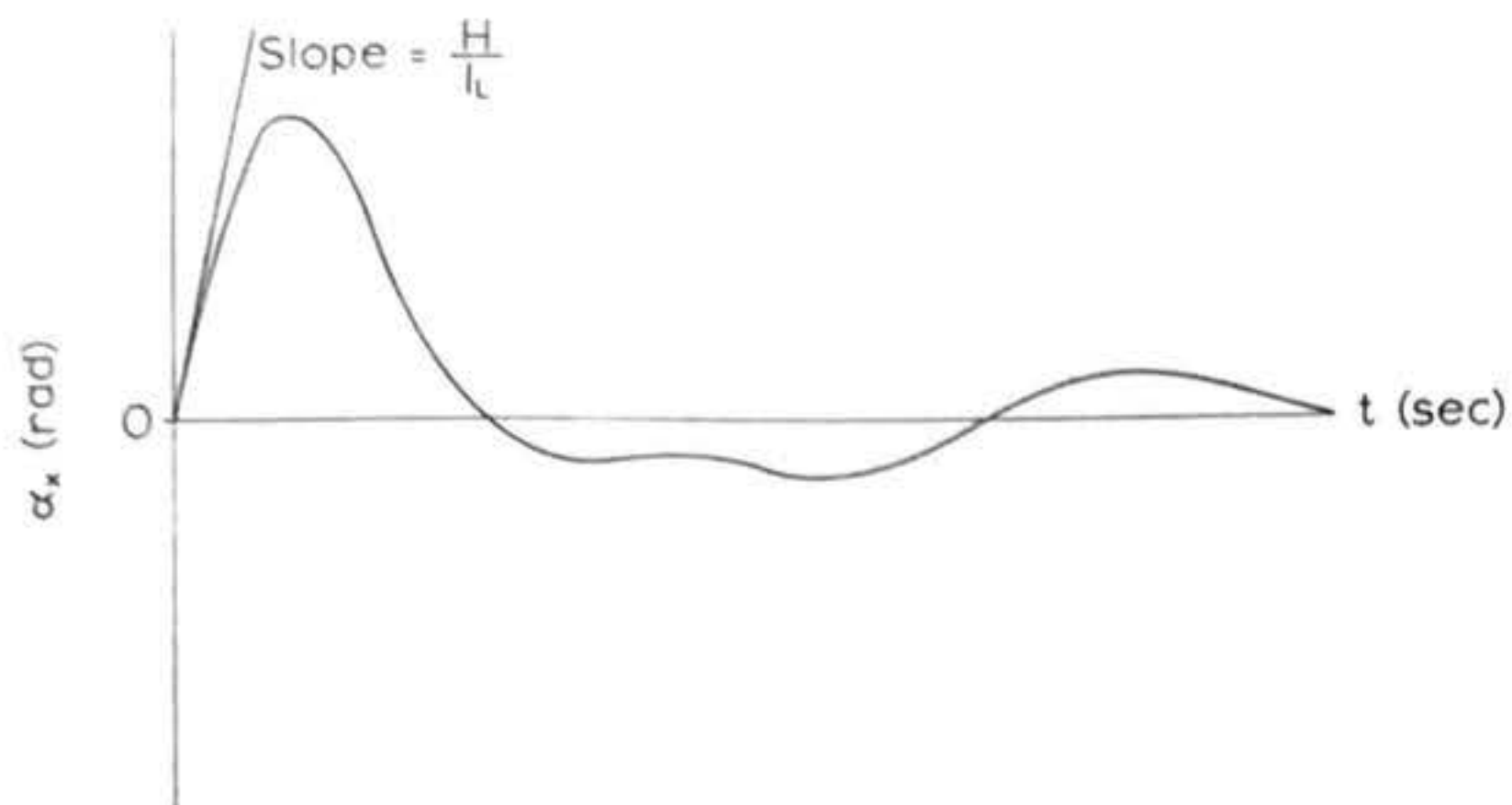


Figure 29: Roll-coupled response of a model rocket with finite damping to an impulse of strength H in yaw. Again, both pitching and yawing oscillations occur; the yawing motion, however, begins instantaneously with an angular velocity of H/I_L , while the initial pitch rate is zero.

I shall adhere to this convention and treat, in the remainder of this section, the particular response of a rolling rocket to forcing functions of the form

$$f_x(t) = A_f \sin \omega_z t$$

$$f_y(t) = A_f \cos \omega_z t$$

The dynamical equations that must be solved become, in this case,

$$I_L \frac{d^2 \alpha_x}{dt^2} + C_2 \frac{d \alpha_x}{dt} + C_1 \alpha_x + I_R \omega_z \frac{d \alpha_y}{dt} = A_f \sin \omega_z t$$

$$I_L \frac{d^2 \alpha_y}{dt^2} + C_2 \frac{d \alpha_y}{dt} + C_1 \alpha_y - I_R \omega_z \frac{d \alpha_x}{dt} = A_f \cos \omega_z t$$

The particular solution to these equations is known to be of the form

$$\alpha_x = A_r \sin (\omega_z t + \varphi)$$

$$\alpha_y = A_r \cos (\omega_z t + \varphi)$$

where A_r and φ are to be determined by substitution, as in Section 3.1.4. The time derivatives of these expressions are

$$\frac{d \alpha_x}{dt} = A_r \omega_z \cos (\omega_z t + \varphi)$$

$$\frac{d^2 \alpha_x}{dt^2} = -A_r \omega_z^2 \sin (\omega_z t + \varphi)$$

$$\frac{d \alpha_y}{dt} = -A_r \omega_z \sin (\omega_z t + \varphi)$$

$$\frac{d^2 \alpha_y}{dt^2} = -A_r \omega_z^2 \cos (\omega_z t + \varphi)$$

Substituting these into the dynamical equations yields the following set of algebraic equations:

$$\begin{aligned} -I_L A_r \omega_z^2 \sin(\omega_z t + \varphi) + C_2 A_r \omega_z \cos(\omega_z t + \varphi) + C_1 A_r \sin(\omega_z t + \varphi) \\ -I_R A_r \omega_z^2 \sin(\omega_z t + \varphi) = A_f \sin \omega_z t \\ -I_L A_r \omega_z^2 \cos(\omega_z t + \varphi) - C_2 A_r \omega_z \sin(\omega_z t + \varphi) + C_1 A_r \cos(\omega_z t + \varphi) \\ -I_R A_r \omega_z^2 \cos(\omega_z t + \varphi) = A_f \cos \omega_z t \end{aligned}$$

Making use of the trigonometric identities

$$\sin(\omega_z t + \varphi) = \sin \omega_z t \cos \varphi + \cos \omega_z t \sin \varphi$$

$$\cos(\omega_z t + \varphi) = \cos \omega_z t \cos \varphi - \sin \omega_z t \sin \varphi$$

we can obtain

$$A_r [C_1 - \omega_z^2 (I_L + I_R)] [\sin \omega_z t \cos \varphi + \cos \omega_z t \sin \varphi] \\ + C_2 A_r \omega_z [\cos \omega_z t \cos \varphi - \sin \omega_z t \sin \varphi] = A_f \sin \omega_z t$$

$$A_r [C_1 - \omega_z^2 (I_L + I_R)] [\cos \omega_z t \cos \varphi - \sin \omega_z t \sin \varphi] \\ - C_2 A_r \omega_z [\sin \omega_z t \cos \varphi + \cos \omega_z t \sin \varphi] = A_f \cos \omega_z t$$

The terms containing $\sin \omega_z t$ and those containing $\cos \omega_z t$ must be independent of each other. We then have, from the first relation above,

$$A_r \cos \varphi [C_1 - \omega_z^2 (I_L + I_R)] - A_r \sin \varphi C_2 \omega_z = A_f$$

$$A_r \sin \varphi [C_1 - \omega_z^2 (I_L + I_R)] + A_r \cos \varphi C_2 \omega_z = 0$$

From the second equation we see that

$$A_r \cos \varphi [C_1 - \omega_z^2 (I_L + I_R)] - A_r \sin \varphi C_2 \omega_z = A_f$$

$$-A_r \sin \varphi [C_1 - \omega_z^2 (I_L + I_R)] - A_r \cos \varphi C_2 \omega_z = 0$$

The two sets of equations are entirely equivalent; either pair can be chosen for determining A_r and φ . Suppose I choose the first pair. The second member of this pair gives us

$$(68a) \quad \varphi = \arctan \left[\frac{C_2 \omega_z}{\omega_z^2 (I_L + I_R) - C_1} \right]$$

The first member, when divided by $\cos \varphi$, becomes

$$A_r [C_1 - \omega_z^2 (I_L + I_R)] - A_r \left[\frac{C_2^2 \omega_z^2}{\omega_z^2 (I_L + I_R) - C_1} \right] = A_f \sec \varphi$$

which, upon substitution of the trigonometric identity

$$\sec \varphi = \sqrt{\tan^2 \varphi + 1}$$

may be written in the form

$$A_r \left[C_1 - \omega_z^2 (I_L + I_R) - \frac{C_2^2 \omega_z^2}{\omega_z^2 (I_L + I_R) - C_1} \right] = A_f \sqrt{\frac{C_2^2 \omega_z^2}{[\omega_z^2 (I_L + I_R) - C_1]^2} + 1}$$

This can readily be transformed into

$$A_r \left\{ [\omega_z^2 (I_L + I_R) - C_1]^2 + C_2^2 \omega_z^2 \right\} = A_f \sqrt{[\omega_z^2 (I_L + I_R) - C_1]^2 + C_2^2 \omega_z^2}$$

from which we obtain

$$(68b) \quad A_r = \frac{A_f}{\sqrt{[\omega_z^2 (I_L + I_R) - C_1]^2 + C_2^2 \omega_z^2}}$$

Equations (68) are precisely analogous to equations (45) (Section 3.1.4); the only difference between the two pairs of formulae is that the quantity I_L in equations (45) has been replaced by $(I_L + I_R)$ in equations (68). We can therefore conduct the remainder of the present analysis exactly as we did in the case of the non-rolling rocket, with the aid of a few definitions:

$$(69) \quad \omega_{nc} = \sqrt{\frac{c_1}{I_L + I_R}}$$

$$(70) \quad \zeta_c = \frac{c_2}{2\sqrt{c_1(I_L + I_R)}}$$

$$(71) \quad \beta_c = \frac{\omega_z}{\omega_{nc}}$$

$$(72) \quad AR_c = \frac{A_r}{A_f}$$

It is important to remember, however, that the quantities defined by equations (69) and (70) are highly artificial constructions created solely for the purpose of analytical convenience. The effective natural frequency ω_{nc} does not correspond to any real, physical angular frequency at which the rocket can be expected to oscillate if undamped; neither does the effective damping ratio ζ_c bear any relation to any damping parameter we can compute from the characteristics of the homogeneous response, as was the case for non-rolling rockets. Both ω_{nc} and ζ_c are excellent analytical tools, though, since they give us a maximum amount of information about the rocket with a minimum of writing, so you shouldn't let their somewhat tenuous physical bases bother you too much.

Using equations (69) through (72) we can write, by analogy

with equations (46) through (48)

$$(73a) \quad \varphi = \arctan \left[\frac{2\zeta_c \beta_c}{\beta_c^2 - 1} \right]$$

$$(73b) \quad AR_c = \frac{1}{C_1 \sqrt{(\beta_c^2 - 1)^2 + (2\zeta_c \beta_c)^2}}$$

and, for the roll coupled resonant frequency and resonance peak,

$$(74a) \quad \beta_{cres} = \sqrt{1 - 2\zeta_c^2}$$

$$(74b) \quad \omega_{cres} = \beta_{cres} \omega_m$$

$$(75) \quad AR_{cres} = \frac{1}{2C_1 \zeta_c \sqrt{1 - \zeta_c^2}}$$

Figures 30 and 31 illustrate the variation in φ and AR_c with β_c for a number of different values of ζ_c . These functions are, of course, identical to those illustrated in Figures 24 and 25.

All the dangers inherent in decoupled resonant responses are present also in the roll-coupled case, all the more so since the presence of a roll rate decreases the effective damping and makes the resonance peak of any given rocket more severe. In rockets that are not slender enough for I_R to be negligible compared to I_L the difference between the decoupled and coupled resonant responses can be significant. The effect of spinning upon a short, stubby rocket can be truly startling; it can even be serious enough to render unacceptable a design whose behavior might otherwise be within tolerable limits.

From our analysis of the roll-coupled sinusoidal steady state we thus conclude that a large slenderness ratio in the sense of a large ratio of I_L to I_R , as well as in the sense of

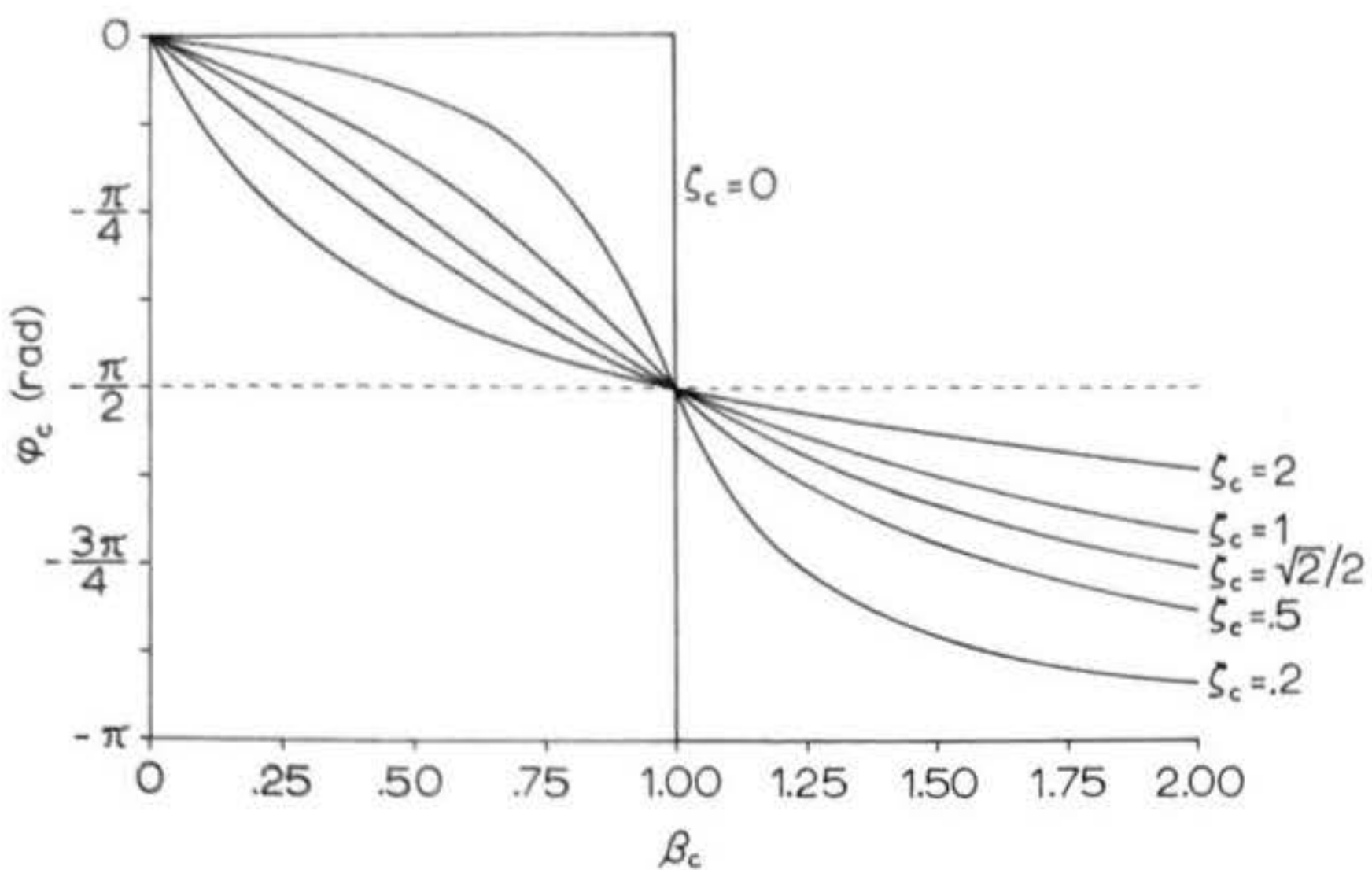


Figure 30: Variation of coupled phase angle with coupled frequency ratio in cases of roll-coupled response to sinusoidal forcing in pitch and yaw at the roll rate.

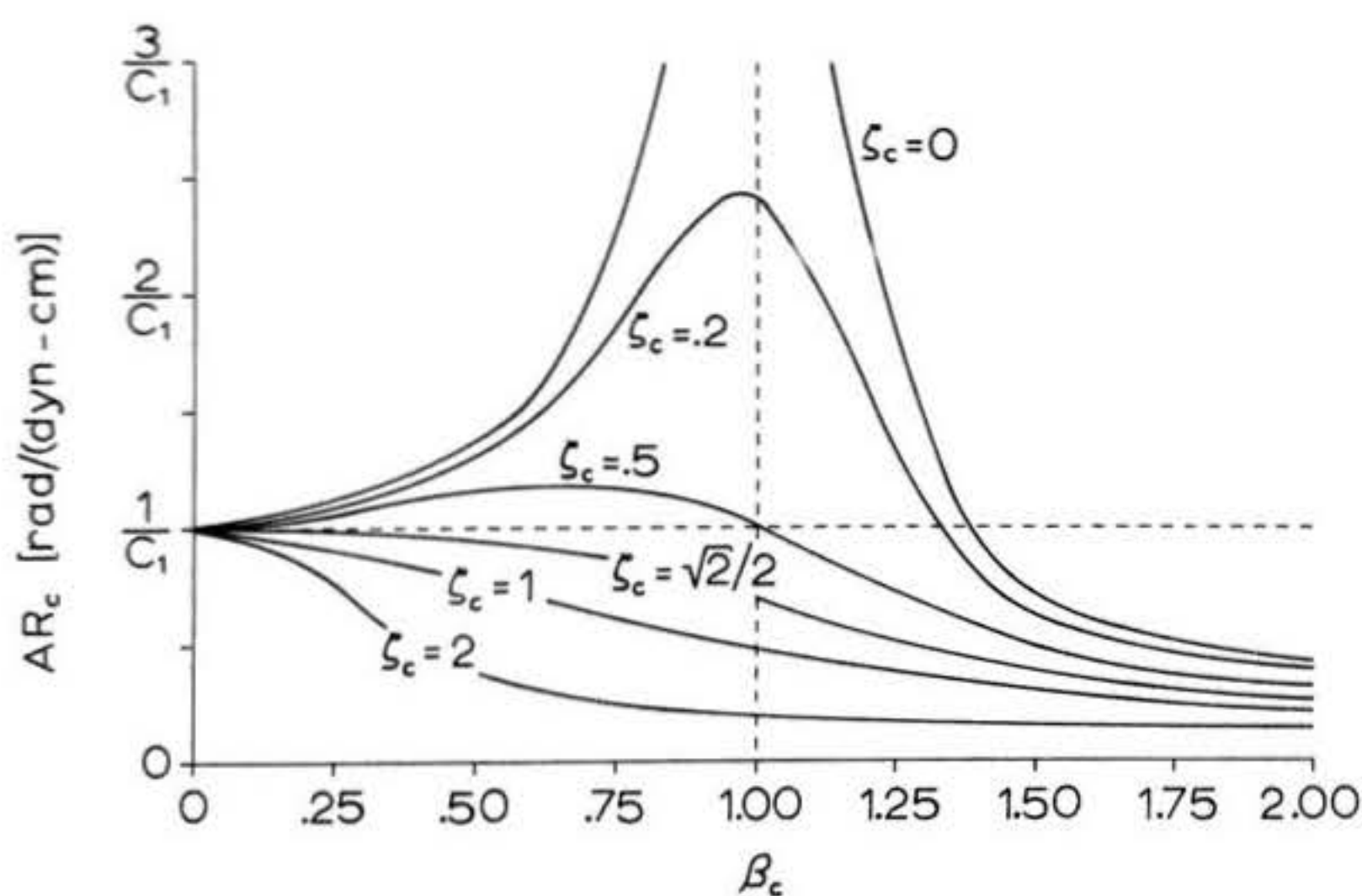


Figure 31: Variation of coupled amplitude ratio with coupled frequency ratio in cases of roll-coupled response to sinusoidal forcing in pitch and yaw at the roll rate.

a large value of I_L itself, is to be ranked along with a large corrective moment coefficient and an adequate damping coefficient as a design feature useful in minimizing the hazards of resonance.

3.2.5 Roll Stabilization

Since the early days of model rocketry it has been known that the flight path of a model which has an insufficient, or even slightly negative, static stability margin can be rendered reasonably straight and true by inducing a very rapid roll rate in the vehicle at launch. This technique generally goes by the name of spin stabilization or roll stabilization and it is widely believed that the presence of a rapid enough roll rate actually induces positive aerodynamic stability in an otherwise unstable rocket. As an examination of the relevant dynamical equations will reveal, it does nothing of the kind.

First of all, we have our results from Section 3.2.1 which indicate that the angle of deflection of a statically-unstable rocket from its intended direction of flight increases with time after the rocket is disturbed, just as it does for a statically-unstable rocket which is not rolling at all. The only case in which the presence of a finite roll rate prevents an unstable rocket from diverging is that of zero damping (equations (60)), in which negative values of C_l up to, but not including, $-\frac{I_R^2 \omega_z^2}{4 I_L}$ can be tolerated while an oscillation which neither grows nor decays with time is maintained. What happens when C_l reaches the critical value $-\frac{I_R^2 \omega_z^2}{4 I_L}$? Well, if C_l is precisely $-\frac{I_R^2 \omega_z^2}{4 I_L}$ the solution to the dynamical equations assumes the form

$$(76) \quad \begin{aligned} \alpha_x &= A_1 \sin(\omega_c t + \varphi_1) + A_2 t \sin(\omega_c t + \varphi_2) \\ \alpha_y &= A_1 \cos(\omega_c t + \varphi_1) + A_2 t \cos(\omega_c t + \varphi_2) \end{aligned}$$

where ω_c , the critical frequency, is given by

$$\omega_c = -\frac{I_R}{2I_L} \omega_z$$

Because equations (76) constitute a freak case which is of no interest whatsoever from the standpoint of design, I will not go into any detailed derivations of its properties. Suffice it to say that equations (76) describe a response which grows with time and is thus unstable.

Should C_1 have a larger negative value than $-\frac{I_R^2 \omega_z^2}{4I_L}$ a motion of the form

$$(77) \quad \begin{aligned} \alpha_x &= A_1 e^{-\frac{t}{\tau_1}} \sin(\omega_c t + \varphi_1) + A_2 e^{-\frac{t}{\tau_2}} \sin(\omega_c t + \varphi_2) \\ \alpha_y &= A_1 e^{-\frac{t}{\tau_1}} \cos(\omega_c t + \varphi_1) + A_2 e^{-\frac{t}{\tau_2}} \cos(\omega_c t + \varphi_2) \end{aligned}$$

will be observed where, again, $\omega_c = -\frac{I_R}{2I_L} \omega_z$. The values of the time constants are given by

$$(78a) \quad \tau_1 = \frac{1}{\sqrt{-\left(\frac{C_1}{I_L} + \frac{I_R^2 \omega_z^2}{4I_L^2}\right)}}$$

$$(78b) \quad \tau_2 = -\tau_1$$

Again, since this is a singular case never encountered in practice there is no useful purpose served in presenting its full derivation. Its only useful purpose is to confirm that a divergent dynamical response results from $C_1 < -\frac{I_R^2 \omega_z^2}{4I_L}$. We see that this is indeed

the case, as the time constant τ_2 is negative and will thus cause the amplitude of the sinusoidal mode with which it is associated to increase exponentially with time. I might mention here in passing that the behavior described by equations (76) and (77) through (78) is very like the "running down" of a toy top or gyroscope. Indeed, the equations involved are rather similar, so if you have such a device handy you might want to observe the decay of its motion a couple of times to get a "feel" for what the mathematics is saying.

At any rate, what we have established so far is that in the idealization of zero damping (which never occurs anyway) a rocket spinning at a rate ω_z is capable of tolerating negative stability up to, but not including, $C_l = -\frac{I_R^2 \omega_z^2}{4I_L}$ without diverging (albeit without the oscillations subsiding either, so that the motion is really only neutrally stable in the dynamic sense). Beyond this value the oscillations increase in violence until the rocket flips end for end entirely, destroying all semblance of a true and predictable flight path. In the real case of finite damping, moreover, any negative value of C_l , no matter how slight, results in unstable flight. What, then, does roll stabilization really do?

It suppresses the growth rate of the instability. A close look at equations (57) will help to clarify my meaning here. Both the inverse time constants D_1 and D_2 involve a fraction whose denominator contains the term $\frac{I_R \omega_z}{2I_L}$. This means that for a large enough radial moment of inertia, a fast enough roll rate, or both the magnitudes of the inverse time constants will be very small. Thus, even though one of them is negative

in cases where C_1 is less than zero, it is only slightly so, meaning that the amplitude of the oscillations, while it does indeed grow with time, does so at a much slower rate than would be the case if the rocket were spinning more slowly or not spinning at all. It is therefore entirely possible that, if the rocket is spinning with sufficient rapidity, the rate at which the deflection of the model from its intended flight path direction grows after it is once disturbed from equilibrium will be so slight that no appreciable instability will be evident during the entire upward flight. Once apex is reached and the recovery system is activated, of course, the stability question becomes irrelevant. If the spinning of the rocket is capable of holding it reasonably close to its proper attitude during the handful of seconds it takes to reach its maximum altitude it will have accomplished its purpose -- and this, as we know from experience, is in fact the case.

Secondly, the presence of a rapid spin rate causes the angular momentum of the rocket to be appreciable. Angular momentum, like linear momentum, is a vector quantity which can be resolved into components by the methods of trigonometry. If this is done we find that the Z-component of a rocket's angular momentum is just $I_R \omega_Z$; a rocket which is not rolling at all thus has no Z-component of angular momentum, and in fact if it is flying straight and true it has no angular momentum at all. Now the effect of any disturbing moment on the model is to change its angular momentum; if it is a yaw disturbance it will impart an X-component of angular momentum, while if it is a pitch disturbance it will give rise to a Y-component.

If the rocket is not spinning at all, the components of angular momentum imparted by disturbances will constitute all the angular momentum the rocket has after any given disturbance. If it is spinning, however, the disturbance-imparted components of angular momentum are only added vectorially to the Z-component which is already present. What this means is that a disturbance of a given strength will have less effect on a spinning rocket than on one which is not spinning because the change in angular momentum it imparts is of less importance to the spinning than to the non-spinning vehicle. The practical consequence of all this is that the initial amplitudes of the roll-coupled motion due to any given disturbance will be less than those of the decoupled response associated with that same disturbance (you can prove this to yourself by taking a representative disturbance and calculating its effect on both a rolling and a non-rolling rocket). Not only, therefore, does the angular displacement of a rapidly-spinning, unstable rocket increase very slowly after a disturbance is encountered, but the initial displacement produced by that disturbance is very slight.

In addition, the kind of physical phenomena that produce transient disturbances in model rockets generally tend to be evenly distributed about the rocket's longitudinal axis. That is, it is just as likely that a step or impulse will be encountered in one direction as it is that it will be encountered in any other direction. This being the case, it is rather likely that a rocket having encountered one disturbance will soon encounter another that cancels its effect -- if the rocket has not diverged too far from its intended flight direction by that time. If the

rocket is unstable and is not spinning at all, the first disturbance it encounters will send it head over heels in a tiny fraction of a second, so this "averaging" effect will be no help at all. If it is spinning rapidly enough, though, it will still be nearly enough "on course" when the second disturbance hits to take advantage of its ameliorating influence. A rapid roll rate makes a rocket "sluggish" in its rotational behavior, allowing it to respond more nearly to the time average of disturbances than to the individual disturbances themselves -- and since the time average is generally much less than any one individual disturbance, this is greatly to the rocket's advantage.

Finally, the presence of roll turns all disturbances due to imperfections in the rocket itself into sinusoidal forcing at the roll frequency, as mentioned in Section 3.2.4. You will soon see how important this is if you examine equation (68b) and imagine C_1 to be a negative number, for if C_1 is negative then $(-C_1)$ must be positive. This means that the quantity $[\omega_z^2(I_t + I_R) - C_1]$ will always be greater than $(-C_1)$ alone, which in turn means that the amplitude of the response will decrease uniformly as the roll rate increases from zero to infinity: an unstable rocket cannot experience resonance. To impart a rapid roll rate to an unstable rocket is thus to render the effect of a large class of disturbances upon it inconsequential.

So we see that the list of benefits available to statically unstable rockets through the mechanism of roll is impressive after all. The net effect of all of them taken together produces a condition that looks enough and works enough like stability that the use of the term "roll stabilization" is really not altogether unjustified.

4. Analytical Determination of the Dynamic Parameters

The results of Section 3 have shown that it is possible to calculate the response of any model rocket to any in-flight disturbance if the values of certain quantities which characterize the rocket and the nature of the motion at the beginning of the observation are known. Initial conditions, of course, vary from disturbance to disturbance; they are generally chosen to have any arbitrary values which insure that the response will remain within the range of validity of the linearized theory when doing actual calculations. The quantities of really fundamental importance to dynamic response

are those which characterize the rocket itself, the so-called dynamic parameters: C_1 , C_2 , I_L , I_R , and

ω_x . Since the formulae which describe the response of a rocket to a given disturbance depend on these quantities, you must know them in order to perform any actual numerical calculations. How, then, does one determine their values?

There are two broad classes of techniques for performing such determinations: the analytical method, in which basic considerations of mathematical physics are used to compute the dynamic parameters from a knowledge of the rocket's size, shape, and mass distribution, and the experimental method, in which the dynamic parameters are determined from observations of the dynamic responses of actual vehicles. The former of these two will be presented in this section, the latter in Section 5.

The analytical method has a distinct advantage in that, by its use, a rocket design can be completely evaluated (and altered if necessary) before construction is started. Of course, it also involves the use of a large number of calculations, some of them based on approximations which only a human being (not a computer) has the judgment to make. I would therefore recommend that the reader pay the most careful attention to the development which follows. If you failed to understand the derivations in Section 3 you can still have recourse to computer-generated solutions, but these will be of no use to you if you cannot tell the parameters of your rocket. A thorough comprehension of the following presentation is essential to a complete knowledge of the factors which influence the design of model rockets.

4.1 Normal Force Coefficients and Center of Pressure:

The Barrowman Method

In March, 1967, James S. Barrowman of the National Aeronautics and Space Administration completed a remarkable document entitled The Practical Calculation of the Aerodynamic Characteristics of Slender Finned Vehicles. Submitted as his Master's thesis to the School of Engineering and Architecture of the Catholic University of America, the report included, among other things, a method of calculating the aerodynamic forces on a streamlined, axially symmetrical body flying at velocities less than that of sound and subjected to small pitching and yawing deflections. Such calculations can be used to determine the location of the center of pressure of a model rocket, the value of its corrective moment coefficient, and the value of its damping moment coefficient. Additional applications of Barrowman's work enable the designer to determine the roll rate induced by canting the fins of his rocket a given amount at any given airspeed.

Barrowman's method is based on the concept of the normal force coefficient, $C_{N\alpha}$, a dimensionless number dependent upon the shape of the rocket which permits the calculation of the force acting in a direction perpendicular to the rocket's longitudinal axis whenever it is displaced from the direction of the relative airstream by some "angle of attack" (a pitching or yawing angle). The equation by which this is accomplished is

$$N = C_{N\alpha} \frac{\rho}{2} A_r V^2 \alpha$$

where N = normal force
 ρ = mass density of air
 V = airspeed of rocket

A_r = reference area, a scaling factor used to separate information regarding the rocket's size from the normal force coefficient. Barrowman uses the cross sectional area of the body tube at the base of the nosecone as his reference area, and I will follow his convention.

α = angle of attack in radians

Throughout the rest of this treatment I am going to be using the "centimeter-gram-second", or CGS system of physical units. This means that all lengths or coordinate values will be considered as given in centimeters, all areas will be considered to be expressed in square centimeters, all volumes will be considered to be given in cubic centimeters, all masses in grams, all forces in dynes, and all measurements of time in seconds. Those readers unfamiliar with CGS and other metric systems of units should consult a physics text or mathematical handbook for the appropriate conversion factors between English and metric units. The density of the Earth's atmosphere at sea level is, in CGS units,

$$\rho = 1.225 \times 10^{-3} \text{ grams/cm}^3$$

so that the value of the force acting on a deflected rocket is given numerically by

$$N = 0.6125 \times 10^{-3} C_{N\alpha} A_r V^2 \alpha \text{ dynes}$$

Now the normal force coefficient of the rocket considered as a whole is the sum of the normal force coefficients of the individual components of which it is composed: nosecone, body sections, adapters (if any), and fins. Each part of the rocket

is thus considered to provide a portion of the total normal force, and this portion is considered to act at a point on the component called its center of pressure (C.P.). The Barrowman method uses this technique of sectionalized analysis, together with the theory of moments, to derive the total normal force coefficient and center of pressure of the complete rocket.

Figure 32 illustrates the most general type of model rocket to which Barrowman analysis is applicable and the coordinate system used in performing the calculations. Those readers who have some familiarity with Newtonian mechanics will recognize that the moments due to the normal force components are being taken about the nose of the rocket by such an arrangement. The tip of the nose is considered to be $Z = 0$ and the value of the coordinate Z increases as we move from the nose toward the tail of the rocket. The rocket itself may have a nosecone, conical shoulder, conical boattail, body sections of constant diameter, and any number of fins (3 or greater) spaced symmetrically about the centerline. The particular equations presented here, however, will be such that the number of fins must be either three or four since there is no particular reason to use any other number. In addition to being axially symmetrical, the rocket must be relatively slender with a smoothly tapered nose, must be flying subsonically (in the low subsonic region below about 200 meters per second), must contain no abruptly-tapered sections, must not be deflected to an angle of attack greater than 0.2 radian, must have fins that are virtually flat plates, and must not be subject to excessive deflections (bending) of its structure under loading conditions encountered in flight.

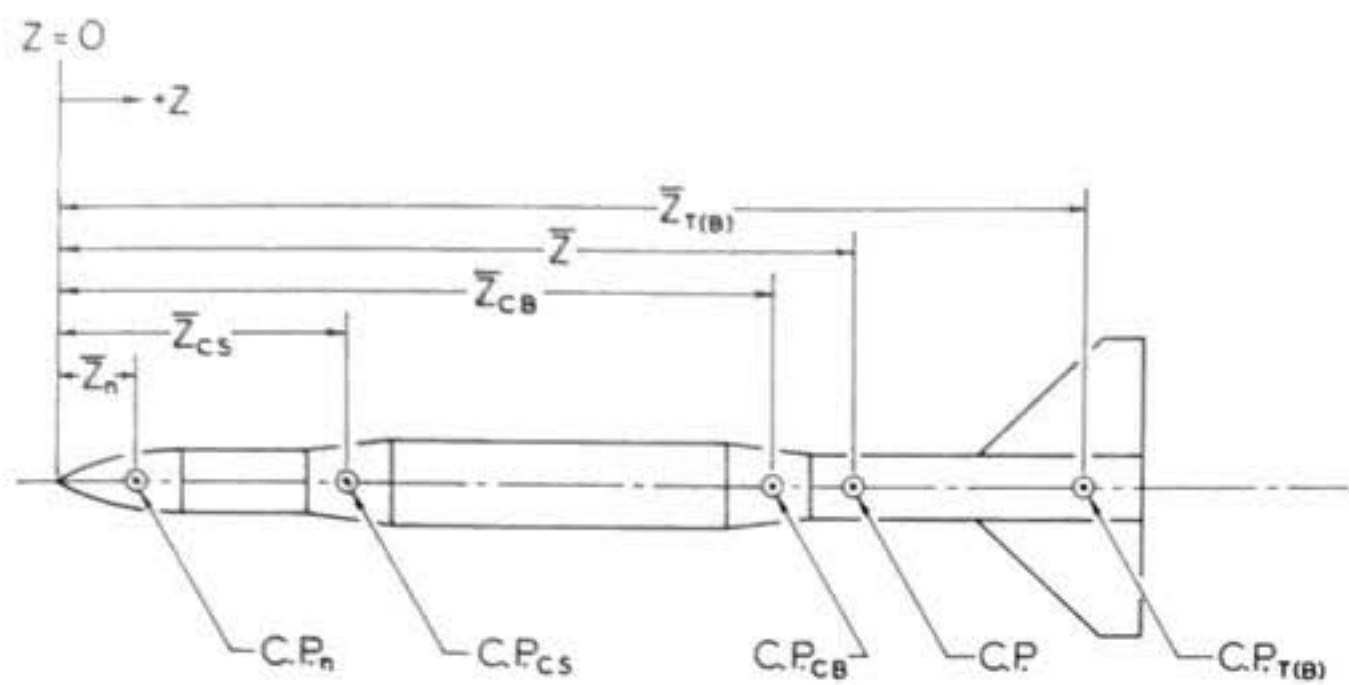


Figure 32: Notation and longitudinal coordinate system used in the Barrowman method of finding the center of pressure of a model rocket.

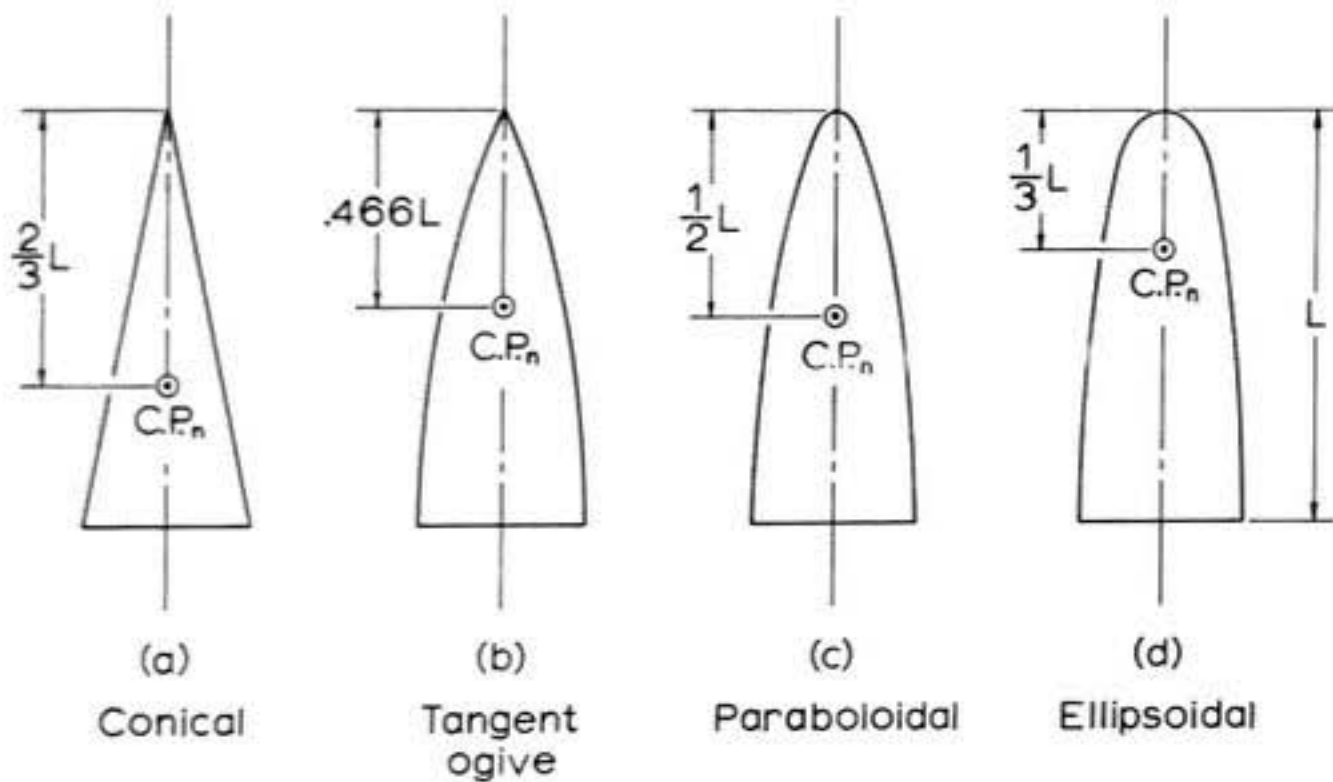


Figure 33: Center of pressure locations for some common nose shapes.

Under these conditions it can be shown that the normal force coefficient of the nose cone is independent of its shape, having the value 2.0 for all shapes which meet the assumptions of the analysis:

$$(79) \quad (C_{N\alpha})_m = 2.0$$

The location of the nose center of pressure is found by specialization of a more general relationship determined in Barrowman's paper: to determine the location of the C.P. of any axially symmetrical section of the rocket (nose, shoulder, or boattail) first compute the volume enclosed by its surface. Then divide this volume by the area of the base (i.e., the cross-sectional area of the component at its greatest diameter). The result of this division will have the units of length (centimeters, in CGS units). Starting from the position of the base, travel a distance equal to this length in the direction of the component's taper, and the point you will locate in this manner is the component's center of pressure. You can see that, in order to give an actual formula for the location of the C.P. of such a part, we must have a part whose volume is computable by some known geometrical equation. The volume of unusually-curved components for which closed-form volume equations do not exist must be computed by immersing the part in question in liquid contained in a graduated cylinder. Many nose cone shapes, however, closely approximate geometrical forms of known volume and Figure 33 lists the C.P. locations of four such shapes: conical, ogival, paraboloidal, and ellipsoidal. Note that center of pressure coordinates are identified by a superscript

bar, and also that a hemispherical nose is a special case of the ellipsoidal class, with its radius equal to its length. The listings of Figure 33 are repeated below for reference:

- (80a) $\bar{Z}_n = \frac{2}{3} L$ (conical nose)
(80b) $\bar{Z}_n = .466 L$ (tangent ogive nose)
(80c) $\bar{Z}_n = \frac{1}{2} L$ (paraboloidal nose)
(80d) $\bar{Z}_n = \frac{1}{3} L$ (ellipsoidal nose)

The notation used in determining the normal force coefficient and C.P. location of a conical shoulder is given in Figure 34. The normal force coefficient of any shoulder, whether or not it is conical, is given by

$$(81) \quad (C_{N\alpha})_s = 2 \left[\left(\frac{r_2}{r_r} \right)^2 - \left(\frac{r_1}{r_r} \right)^2 \right]$$

The conical form is, however, by far the most commonly used and the following equation for the C.P. location is valid only for the conical configuration:

$$(82) \quad \bar{Z}_{cs} = Z_1 + L \left[\frac{2}{3} - \frac{1}{3} \frac{r_1}{r_2} \left(\frac{r_1}{r_2} + 1 \right) \right]$$

Figure 35 illustrates the notation used in finding the normal force coefficient and C.P. of a conical boattail. The normal force coefficient equation is identical to that used in computing the normal force coefficient of a shoulder:

$$(83) \quad (C_{N\alpha})_B = 2 \left[\left(\frac{r_2}{r_r} \right)^2 - \left(\frac{r_1}{r_r} \right)^2 \right]$$

Note, however, that in this case r_2 is smaller than r_1 , meaning

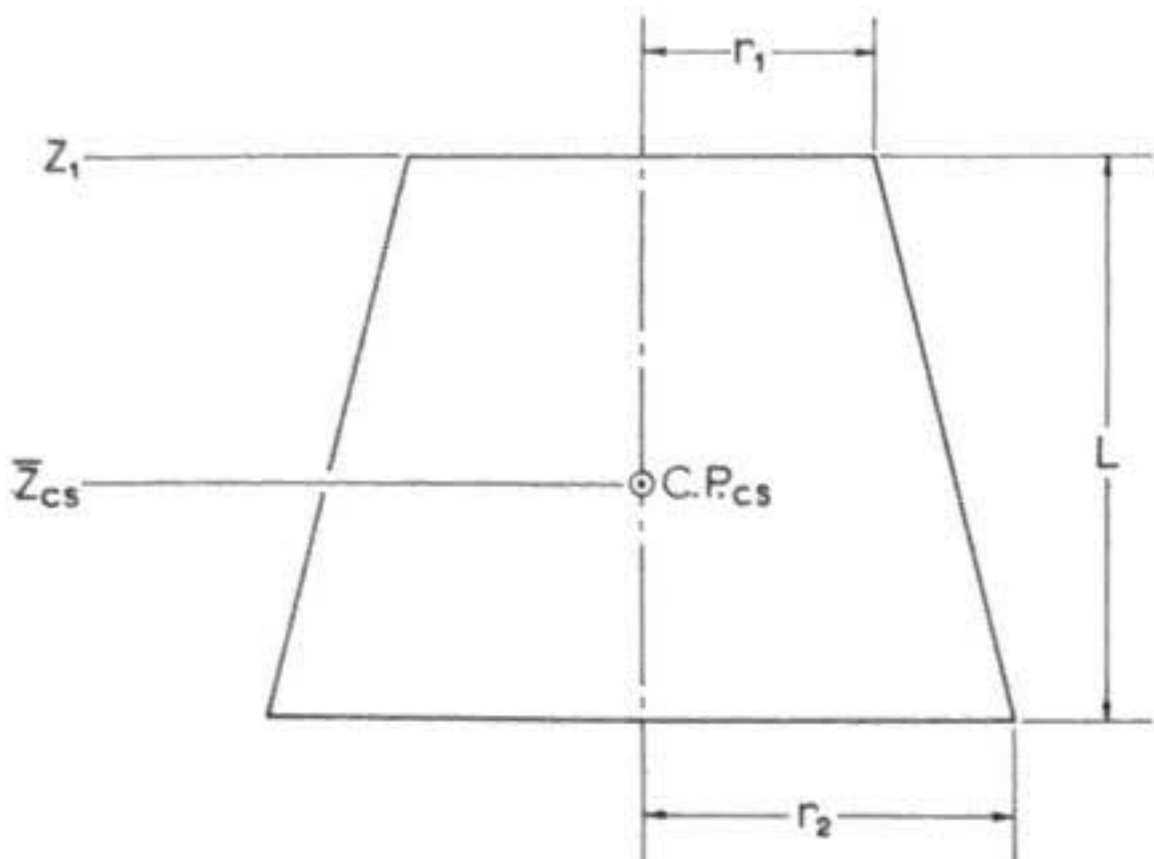


Figure 34: Notation used in determining the normal force coefficient and center of pressure location of a conical shoulder. Z_1 denotes the distance from the tip of the nose to the forward end of the shoulder, while \bar{Z}_{CS} is the distance from the tip of the nose to the center of pressure of the shoulder.

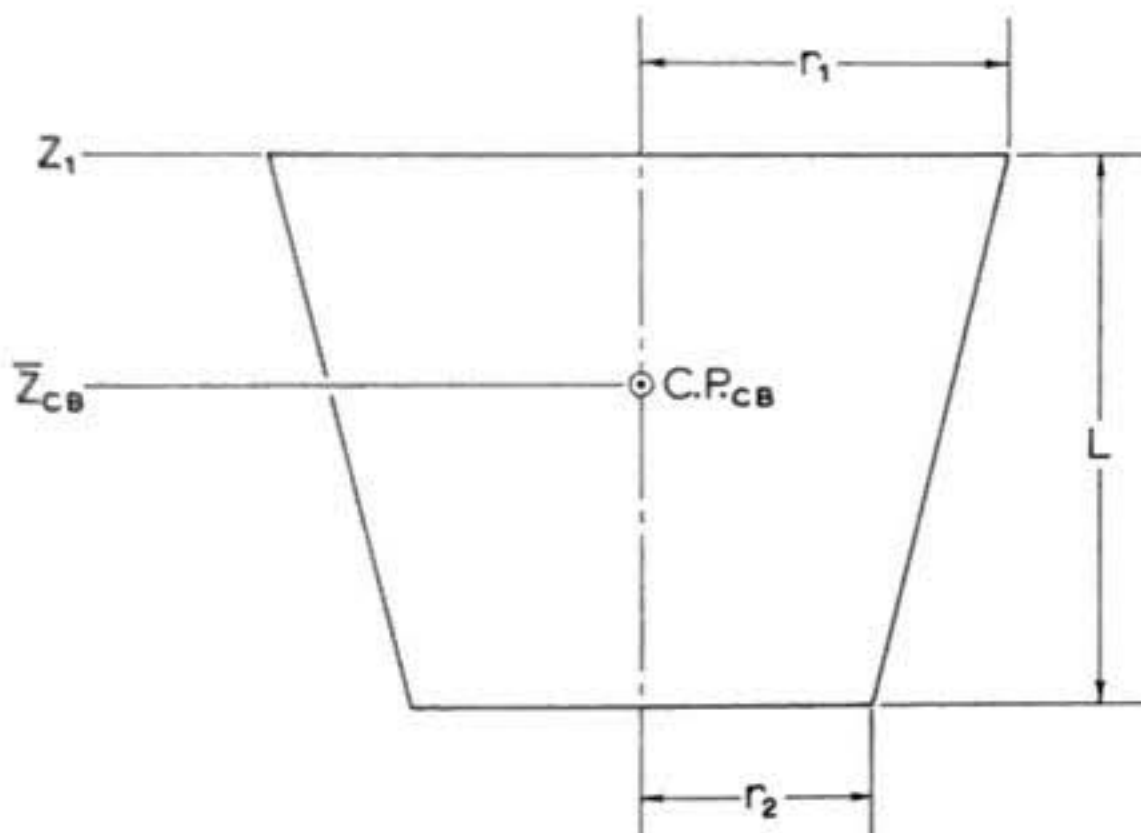


Figure 35: Notation used in determining the normal force coefficient and center of pressure location of a conical boattail. Again, Z_1 is the distance from the tip of the nose to the forward end of the boattail; \bar{Z}_{CB} is the distance from the nose tip to the boattail center of pressure.

that the value of $(C_{N\alpha})_B$ is negative: a conical boattail experiences a suction force when the rocket of which it is a part is yawed in a moving airstream. It follows that a boattail at the extreme after end of a rocket has a destabilizing effect, and any rocket incorporating such a device requires slightly larger fins than one which does not. The center of pressure location of a conical boattail is given by

$$(84) \quad \bar{Z}_{cB} = Z_1 + \frac{L}{3} \left[1 + \frac{r_2}{r_1} \left(\frac{r_2}{r_1} + 1 \right) \right]$$

Body tube sections of constant diameter exhibit no measurable normal force coefficient at zero angle of attack, and in fact produce no substantial normal force at all for angles of attack less than about 0.2 radian. For this reason body tube sections are omitted from the equations of Barrowman analysis.

Figure 36 shows the system of notation used in determining the normal force coefficient and center of pressure location of a fin or set of fins. Strictly speaking, the Barrowman method is applicable only to fins of the form shown in Figure 36, but in practical applications it is perfectly permissible to approximate a more complex fin shape by that shown in Figure 36. As long as the lateral area of the hypothetical approximation is identical to that of the actual fin, the numerical results obtained from the Barrowman analysis will be very nearly correct. If the approximate fin has less area than the true fin, the results will be conservative, while if it has more area than the true fin they will be overly optimistic. This latter condition is dangerous and should be avoided.

The normal force coefficient of a single fin is given by

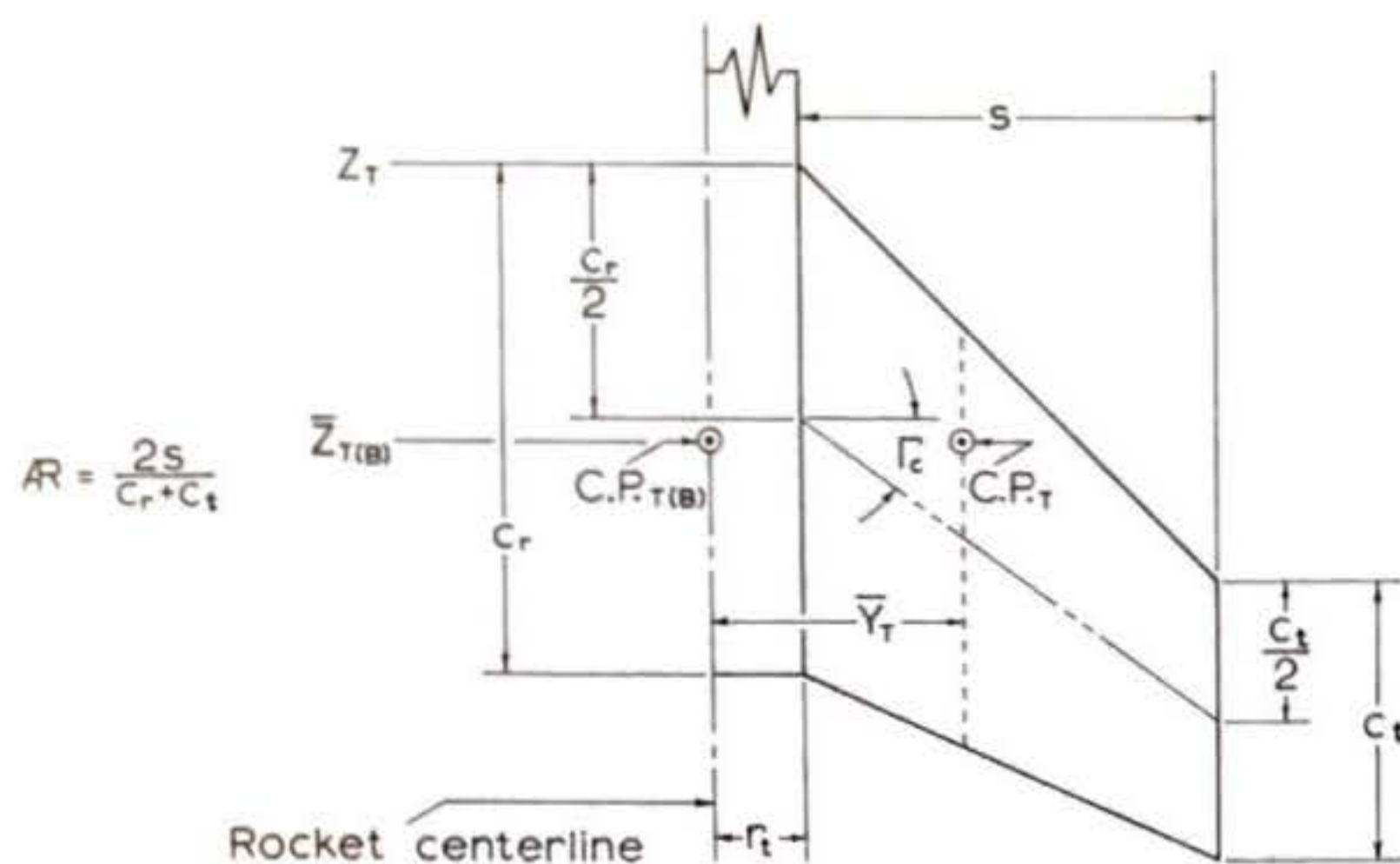


Figure 36: Notation used in determining the normal force coefficient and center of pressure location of single fins and symmetrical fin assemblies. Z_T is the distance from the tip of the nose to the intersection of the fin root and leading edge; $\bar{Z}_{T(B)}$ is the distance from the nose tip to the center of pressure of the fin assembly. The definition of $A.R.$, the aspect ratio of a single fin, is also given.

$$(85) \quad (C_{N\alpha})_1 = \frac{AR \left(\frac{c_r + c_t}{r_r} \right) \left(\frac{s}{r_r} \right)}{2 + \sqrt{4 + \left(\frac{AR}{\cos r_c} \right)^2}}$$

while that of a complete set of N fins, where N must be either three or four, is

$$(86) \quad (C_{N\alpha})_T = \frac{N AR \left(\frac{c_r + c_t}{2 r_r} \right) \left(\frac{s}{r_r} \right)}{2 + \sqrt{4 + \left(\frac{AR}{\cos r_c} \right)^2}}$$

The airflow about the fins, however, is disturbed by the presence of the body with the result that the effective normal force coefficient of a set of fins is not equal to the expression given in equation (86). The influence of the body is accounted for by postulating an "interference coefficient" $K_{T(B)}$ by which (86) is to be multiplied to obtain the effective value of the normal force coefficient. If we let

$$\gamma = \frac{s + r_t}{r_t}$$

then the value of the interference coefficient for three- and four-finned configurations is given by

$$(87) \quad K_{T(B)} = 1 + \frac{1}{\gamma}$$

so that the applicable value of the normal force coefficient is

$$(88) \quad (C_{N\alpha})_{T(B)} = K_{T(B)} (C_{N\alpha})_T$$

The longitudinal position of the C.P. of any one fin (which is also equal to the longitudinal position of the C.P. of the

entire fin assembly) is computed according to

$$(89) \quad \bar{Z}_T = Z_T + \frac{x_t}{3} \left[\frac{C_r + 2C_t}{C_r + C_t} \right] + \frac{1}{6} \left[C_r + C_t - \frac{C_r C_t}{C_r + C_t} \right]$$

while the radial position of the C.P. of an individual fin is

$$(90) \quad \bar{Y}_T = r_t + \frac{s}{3} \left[\frac{C_r + 2C_t}{C_r + C_t} \right]$$

The C.P. of any radially-symmetrical set of three or more fins, of course, lies on the centerline of the rocket and thus has a radial coordinate of zero.

Having thus determined the normal force coefficients and longitudinal center of pressure locations of all applicable components, we are now in a position to compute the normal force coefficient of the complete rocket and the C.P. location of the vehicle considered as a whole. For the total normal force coefficient we have

$$(91) \quad C_{N\alpha} = (C_{N\alpha})_m + (C_{N\alpha})_s + (C_{N\alpha})_B + (C_{N\alpha})_{T(B)}$$

while the C.P. location is given by

$$(92) \quad \bar{Z} = \frac{(C_{N\alpha})_m \bar{Z}_m + (C_{N\alpha})_s \bar{Z}_{cs} + (C_{N\alpha})_B \bar{Z}_{cb} + (C_{N\alpha})_{T(B)} \bar{Z}_T}{C_{N\alpha}}$$

These last two are the most general forms of the Barrowman equations in that they account for the presence of conical shoulders and boattails. Not all rockets have such components, but the equations are easily altered to apply to those that do not by omitting the terms due to the shoulder, the boattail, or both.

4.2 Locating the Center of Gravity

In order to compute the static stability margin, corrective and damping moment coefficients, and moments of inertia of a model rocket it is necessary to determine the location of its center of gravity. This is done by a method of moments very similar to that of the Barrowman equations, except that here we work with moments of mass rather than moments of pressure forces.

If you have a complete rocket which has already been built, of course, it is a simple matter to balance the flight-ready vehicle (with payload, engine, and recovery system in place) on a cord or knife-edged object in order to find the C.G. directly, for the C.G. is defined as the balance point. We are concerned here, though, with designing model rockets and must therefore have some means of predicting the C.G. location of a rocket before construction is begun. In order to do this precisely you must know the exact mass and the balance point of each component -- nosecone, body tube, shoulder and boattail (if any), engine(s), fin assembly, and recovery system -- of which the rocket is comprised. The payload, if any, must also be taken into account.

The notation used in computing the C.G. location is illustrated in Figure 37. Note that moments are again taken about the tip of the nose, and that the longitudinal coordinate increases as we move from the nose toward the tail, but the name of this coordinate has been changed from Z to W to avoid the use of elaborate subscript notation to distinguish between centers of gravity and centers of pressure. The masses of certain of the components -- lengths of body tubing, rocket engines, shoulders,

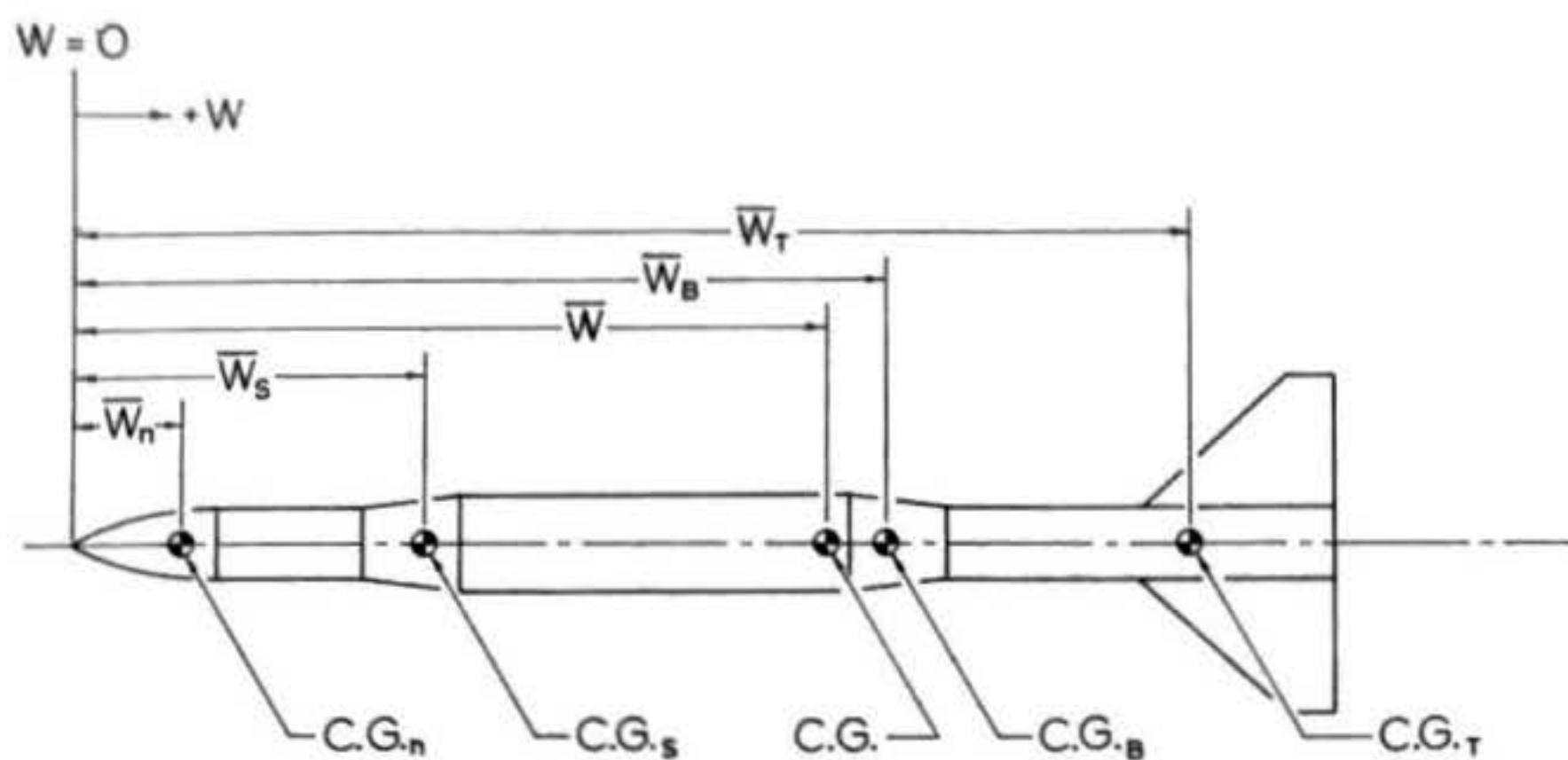


Figure 37: Notation and longitudinal coordinate system used in determining the center of gravity location of a model rocket. For the sake of clarity, not all components have been considered in this drawing; the two constant-diameter tube sections forward of the conical boattail, for instance, have been omitted and the tail section -- tube, engine, and fins -- has been considered as a unit.

boattails, nosecones, and the standard National Association of Rocketry payload, for instance -- can be determined from information given by the manufacturer, although you will have to take care to express weights given in ounces as masses given in grams by multiplying them by the factor 28.35. The masses of fins, fully-rigged recovery systems, and nonstandard payloads and components, however, must be determined by weighing on a laboratory gram balance. The C.G. of each individual component can be determined by string or knife-edge balancing, except for those parts of the rocket which have not yet been made or cut to length, such as the body tube and fins. The C.G. of a uniform body tube is, of course, its geometrical center. The C.G. of a proposed set of fins can be found by cutting a pair of the proposed design, joined root to root, out of cardboard and balancing the fin set thus obtained on a knife-edge held spanwise. The weight of a fin is found by multiplying its area by the weight per unit area of the balsa sheet or other material of which it is composed. The weight per unit area of fin material, in turn, can be determined by weighing a sample sheet of fin material whose area is known (such as a complete three-by-thirty-six inch sheet of balsa, which has an area of 698 square centimeters) on a laboratory gram balance and dividing the weight thus obtained by the area of the sheet. To obtain conservative estimates you should completely **fill and paint** such balsa sample sheets and also use the hardest sheet of balsa you can find. This is because painting adds significantly to the weight of the fins and the weight of balsa itself varies greatly from piece to piece, being the greatest for the hardest material. C.G. estimates

should also be made on the basis of the most powerful (that is, heaviest) engine(s) with which it is intended that the rocket be flown.

Once the mass and C.G. location of each individual component have been determined, the total mass at liftoff and C.G. of the complete rocket at liftoff can be calculated as follows:

$$(93) \quad M = M_n + M_s + M_p + M_b + M_r + M_t + M_e + M_f$$

where M_n = mass of nosecone

M_s = mass of shoulder

M_p = mass of payload and payload section of tube

M_b = mass of boattail

M_r = mass of fully rigged and packed recovery system

M_t = mass of body tube

M_e = mass of engine

M_f = mass of fins

$$(94) \quad \bar{W} = \frac{M_n \bar{W}_n + M_s \bar{W}_s + M_p \bar{W}_p + M_b \bar{W}_b + M_r \bar{W}_r + M_t \bar{W}_t + M_e \bar{W}_e + M_f \bar{W}_f}{M}$$

As in the Barrowman calculations, any component which a given rocket design does not contain can simply be omitted from the equations. Unlike the Barrowman equations, however, the C.G. equations always contain nonzero contributions from the lengths of body tubing employed in building the rocket.

Now it so happens that in the vast majority of actual model designs the location of the C.G. is very largely determined by the mass properties and locations of the nose, payload, body and engine alone. Because of this it is often possible to get

a very good estimate of the C.G. location of the finished rocket by performing a "preassembly balancing" -- cutting the body tube to length, inserting engine and payload, and fitting the nosecone; then simply balancing the partly-completed rocket thus obtained. If your design is relatively standard or intended only for sport flying you can save a lot of work by measuring the C.G. location in this way, but a knowledge of the analytical method of equations (93) and (94) is invaluable when working to high tolerances, doing competition work, or experimenting with unusual designs.

4.3 The Corrective Moment Coefficient

The results of Sections 4.1 and 4.2 enable the calculation of the dynamic parameter C_1 as follows:

$$(95) \quad C_1 = \frac{f}{2} V^2 A_r C_{N\alpha} [\bar{Z} - \bar{W}]$$

The numerical value of C_1 in CGS units is given by

$$(96) \quad C_1 = (0.6125 \times 10^{-3}) V^2 A_r C_{N\alpha} [\bar{Z} - \bar{W}] \quad \text{dyne-centimeters}$$

Note that \bar{W} must be smaller than \bar{Z} for C_1 to be a positive number; this is just the equation's way of telling us that the C.P. must lie behind the C.G. for the rocket to be stable. The distance $(\bar{Z} - \bar{W})$ is referred to as the static stability margin of the rocket. The static stability margin is often "nondimensionalized" by dividing it by the maximum body diameter of the rocket. The resulting quantity is some multiple of the rocket's maximum diameter, or "caliber", and it is thus standard practice to refer to the static stability margin of a given rocket in calibers. The notation associated with computing C_1 and the static stability

margin is explained in Figure 3B.

4.4 The Damping Moment Coefficient

The dynamic parameter C_2 is the sum of two components, one of which is aerodynamic in origin, the other propulsive. The aerodynamic contribution to damping has been obtained by Barrowman as

$$(97) \quad C_{2A} = \frac{\rho}{2} V A r \left\{ (C_{N\alpha})_{T(B)} [\bar{Z}_T - \bar{W}]^2 + (C_{N\alpha})_n [\bar{Z}_n - \bar{W}]^2 + (C_{N\alpha})_s [\bar{Z}_{cs} - \bar{W}]^2 + (C_{N\alpha})_B [\bar{Z}_{cb} - \bar{W}]^2 \right\}$$

for which the CGS numerical result is

$$(98) \quad C_{2A} = (0.6125 \times 10^{-3}) V A r \left\{ (C_{N\alpha})_{T(B)} [\bar{Z}_T - \bar{W}]^2 + (C_{N\alpha})_n [\bar{Z}_n - \bar{W}]^2 + (C_{N\alpha})_s [\bar{Z}_{cs} - \bar{W}]^2 + (C_{N\alpha})_B [\bar{Z}_{cb} - \bar{W}]^2 \right\} \text{ dyne-centimeter-seconds}$$

As in Section 4.1, any component which a given rocket does not possess is simply omitted from the calculation.

During the time in which the rocket motor is firing there is an additional contribution to the damping moment arising from the expulsion of mass from the nozzle. If the nozzle exit is considered to be located a distance L_{ne} from the tip of the nose this propulsive damping moment coefficient is given by

$$(99) \quad C_{2R} = \dot{m} [L_{ne} - \bar{W}]^2 \text{ dyne-centimeter-seconds}$$

where \dot{m} = rate of mass expulsion from the nozzle, grams/second. The phenomenon of damping due to rocket thrust is generally referred to as "jet damping". Readers desiring to explore the topic further should consult The Exterior Ballistics of Rockets,

by Davis, Follin, and Blitzer. This text, while highly mathematical in parts, contains an excellent development of the physics of propulsive damping.

You should notice that C_{2R} is not generally constant during the time of thrusting, since \dot{m} depends on the motor's thrust F and exhaust velocity V_e according to

$$\dot{m} = \frac{F}{V_e}$$

Both F and V_e vary with time during the burning of the motor, so that the determination of \dot{m} with precision can be quite difficult. Fortunately, though, most model rocket motors of the end-burning type have a thrust and exhaust velocity that are virtually constant over much of the burning time. A rough average of the mass expulsion rate may then be computed by dividing the mass of propellant (call it m_p) contained in the motor before ignition by the duration of burning, t_b :

$$\dot{m} = \frac{m_p}{t_b}$$

Whenever this approximation is valid the contribution of jet damping to the damping moment coefficient is

$$(100) \quad C_{2R} = \frac{m_p}{t_b} (L_{ne} - \bar{W})^2$$

The value of the damping moment coefficient during the time the rocket motor is thrusting is thus

$$(101a) \quad C_2 = C_{2A} + C_{2R}$$

$$A_r = \pi r_r^2$$

$$\text{Static stability margin in calibers} = \frac{\bar{Z} - \bar{W}}{d_{\max}}$$

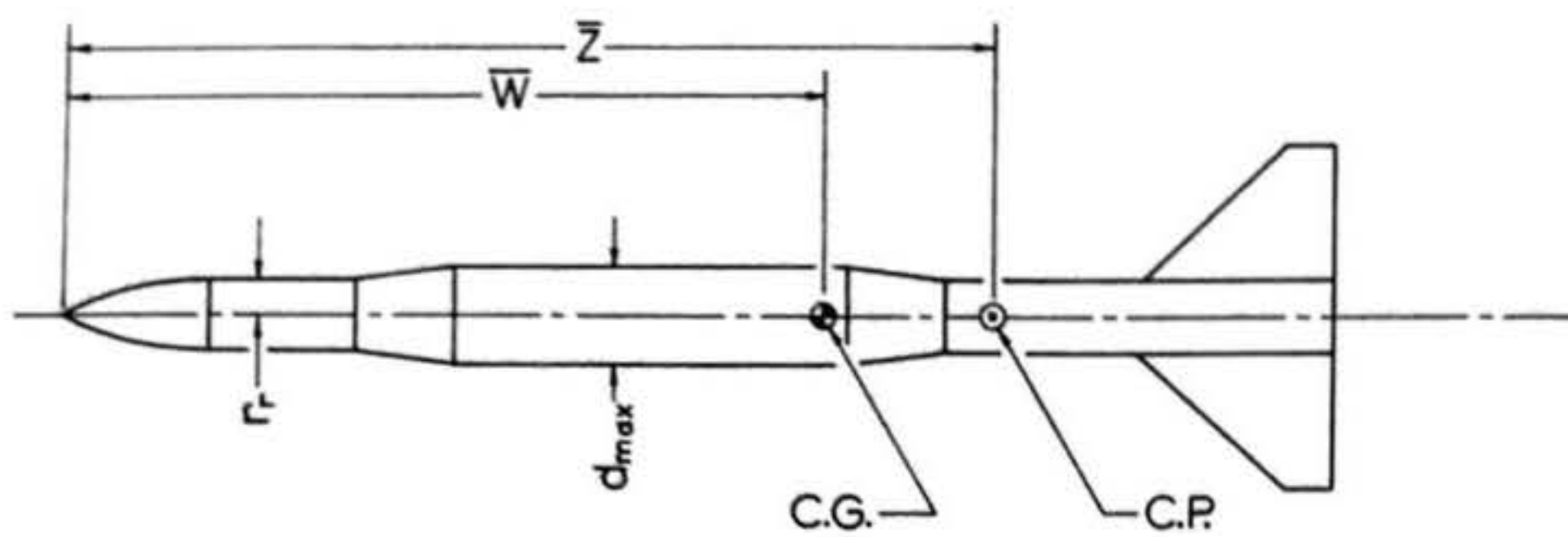


Figure 38: Notation used in computing corrective moment coefficient and static stability margin.

and the damping moment coefficient during the coasting phase of flight is given by

$$(101b) \quad C_2 = C_{2A}$$

Figures 39 and 40 illustrate the notation and procedure used in computing the aerodynamic and propulsive contributions to the damping moment coefficient.

4.5 The Longitudinal Moment of Inertia

A model rocket consists primarily of coaxial, circular cylindrical objects, of which some -- such as the propellant grain, solid bulkheads, and NAR standard payload (if any) -- are solid throughout and others -- the body tube and motor casing, for example -- are hollow. The nose cone, shoulders, and boattails can be of any radially symmetrical configuration, while there is less restriction on the geometry of fins and most models carry some small, dense, irregularly-shaped objects such as the bits of lead which are sometimes used as nose weights. Each component of the rocket contributes in some measure, depending on its mass, shape, and location, to the moments of inertia, and the inertial properties of the completed rocket are computed by determining each such contribution and adding all the contributions together.

The contribution of any extended body to the longitudinal moment of inertia is equal to its mass multiplied by the square of the longitudinal distance between its C.G. and the C.G. of the complete rocket, plus its moment of inertia measured about a transverse axis passing through its own C.G. The contribution to I_L of any extended body (call it o) may thus be written

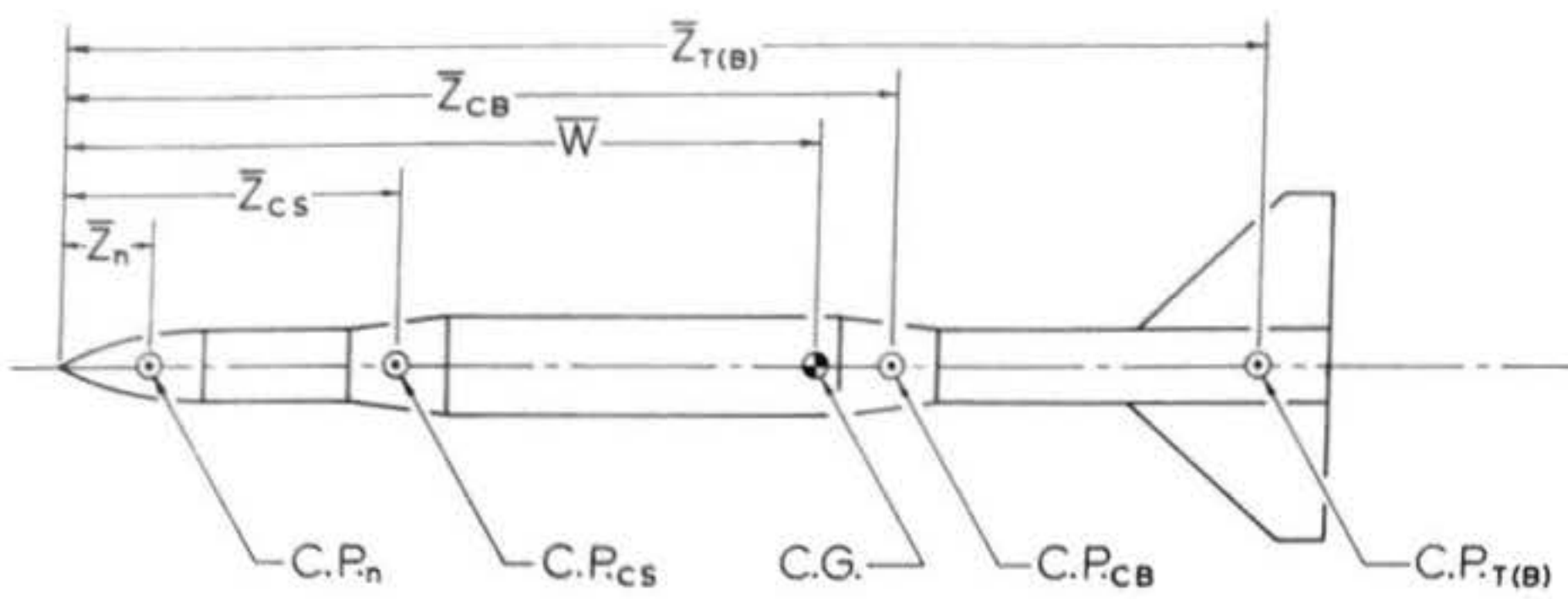


Figure 39: Notation used in computing aerodynamic damping moment coefficient.

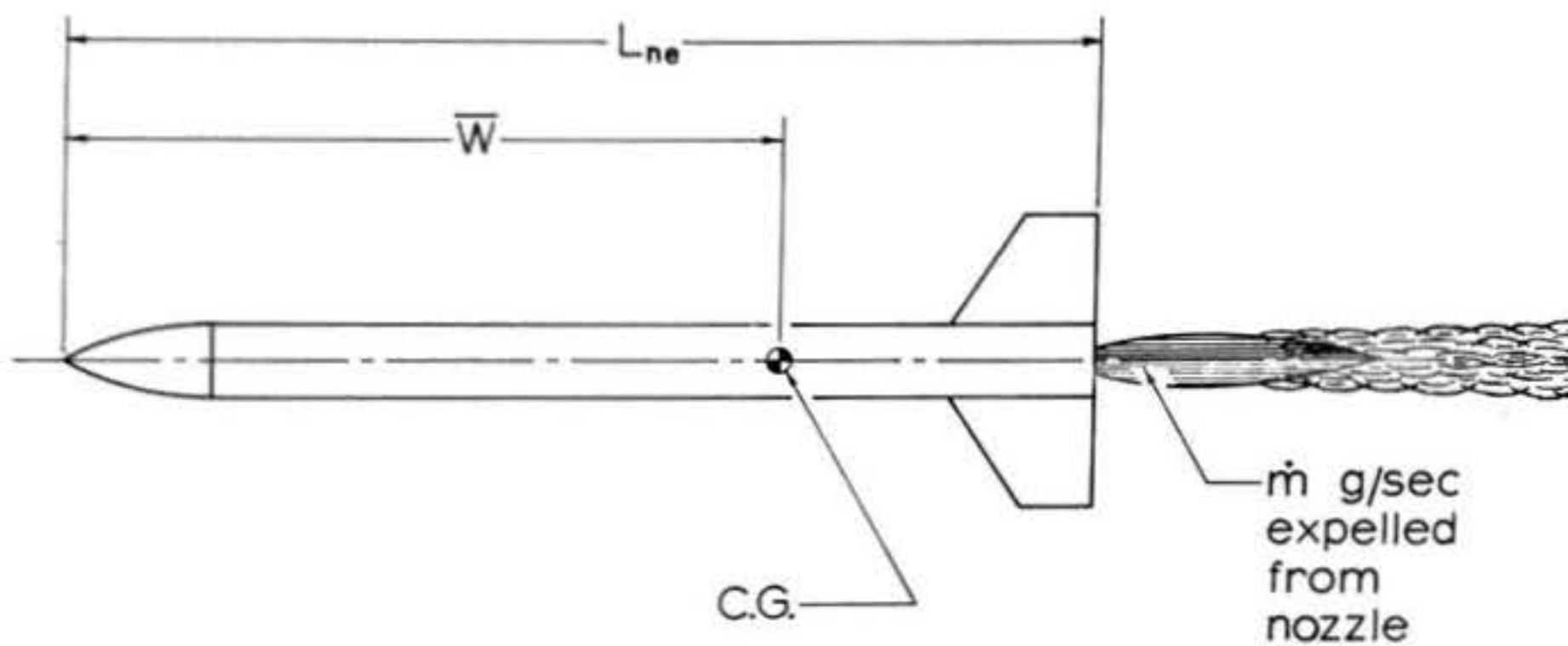


Figure 40: Notation used in computing propulsive damping moment coefficient.

$$(102) \quad I_{L_o} = M_o [\bar{W} - \bar{W}_o]^2 + I'_{L_o}$$

where I_{L_o} denotes the actual contribution of o to the longitudinal moment of inertia of the rocket and I'_{L_o} refers to the object's longitudinal moment of inertia with respect to its own C.G., which is located a distance \bar{W}_o from the tip of the nose.

In particular, the contribution of a solid, right, circular cylindrical object of uniform density to the longitudinal moment of inertia is given by

$$(103a) \quad I_{L_{cs}} = M_c \left\{ [\bar{W} - \bar{W}_c]^2 + \frac{R^2}{4} + \frac{L^2}{12} \right\}$$

where M_c = mass of cylinder

L = length of cylinder

R = radius of cylinder

\bar{W}_c = location of cylinder's C.G. (midpoint)
reckoned as distance back from tip of nose

while the contribution due to a hollow cylindrical object of outer radius R_o , inner radius R_i , is

$$(103b) \quad I_{L_{ch}} = M_c \left\{ [\bar{W} - \bar{W}_c]^2 + \frac{R_o^2 + R_i^2}{4} + \frac{L^2}{12} \right\}$$

There also exist analytical expressions for the contributions of various nose cone shapes, shoulders, and boattails, and (in principle, at least) the contribution of any object whatsoever, regardless of shape or density properties, is computable by the methods of integral calculus. Unfortunately, however, the majority of algebraic solutions obtainable by such techniques are so long and complex that they are utterly impractical to work with.

The best course for the designer in this situation is to resort to an approximate technique for taking these components into account. Such a procedure is the "point-mass approximation", in which all the mass of a given object is considered to be concentrated at its own C.G. This deprives the object in question of the property of extension and causes the term I_{Lo}' in equation (102) to become zero; the point-mass approximation thus always results in an underestimate of the component's inertial contribution, since it ignores the object's mass distribution. The point-mass assumption is most nearly valid when the component under consideration is far from the C.G. of the complete rocket in comparison with its own dimensions; one thus often hears the method referred to as computing the inertial contribution of a "remote object". As it turns out, nose cones, nose weights, and payloads usually obey the approximation rather well but the technique is not as good when applied to shoulders, boattails, and fins. Some designers prefer to replace the distance between the component C.G. and the rocket C.G. by the distance from the rocket C.G. to the most remote point of the component (the trailing edge of the fins, for example) in order to increase the magnitude of the point-mass estimate in cases where its accuracy is questionable. Figure 41 summarizes the various notations used to compute the contributions of some representative components to the longitudinal moment of inertia of a hypothetical rocket.

The longitudinal moment of inertia of any given component about a transverse axis through its own C.G. can also be measured experimentally by the use of the torsion-wire method, the same

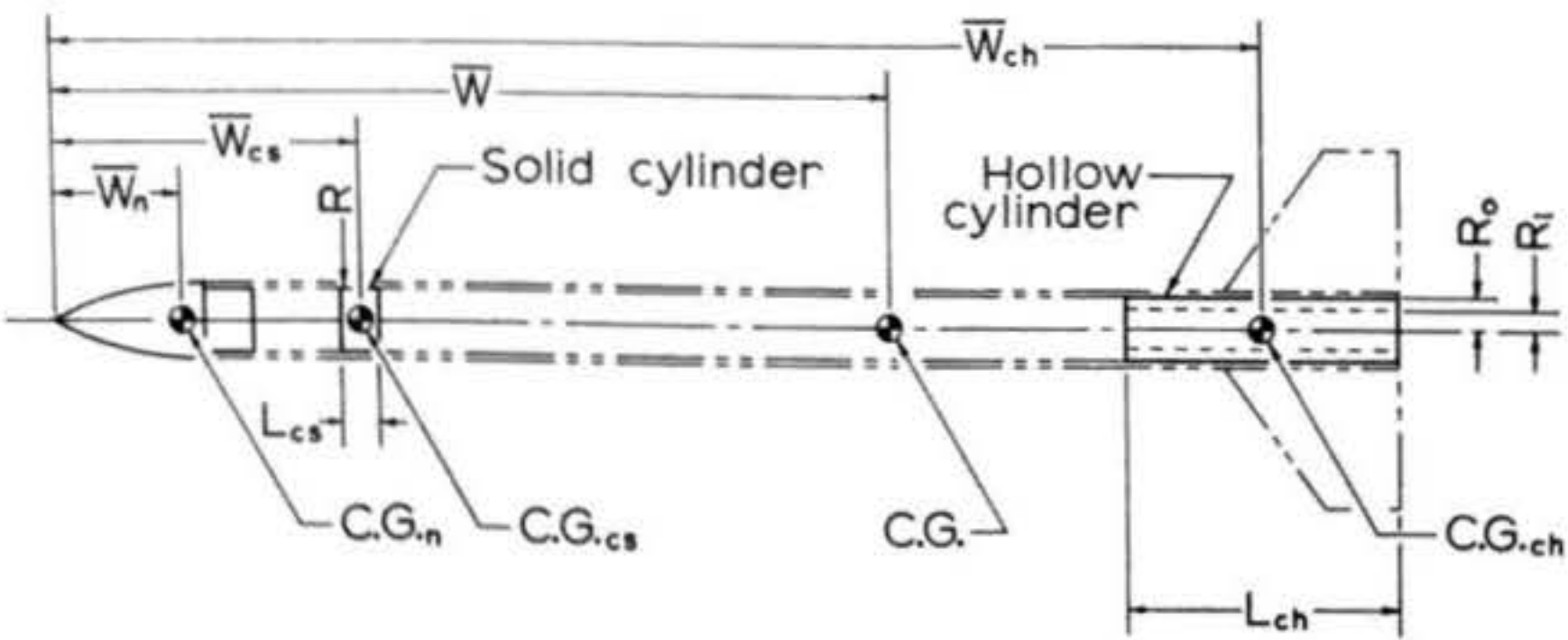


Figure 41: Examples of the notation used in computing contributions to the longitudinal moment of inertia. An object subject to the point-mass approximation (nosecone), a solid cylindrical component (NAR payload), and a hollow cylindrical component (engine casing) are illustrated.

technique used to determine the inertial properties of a completed, flight-ready rocket (to be discussed in detail in Section 5). The diameter of the wire used for the measurement of moments of inertia of some of the smaller components, however, will need to be smaller than that used for full-vehicle experiments. In some cases it may have to be as small as .005 or even .003 inch.

Once the contribution to I_L of each component of the rocket has been determined, the longitudinal moment of inertia of the assembled vehicle can be computed by taking the sum of all the contributions. The number of contributions will vary from rocket to rocket, and in addition most designers use their own judgment in selecting only those components large enough and/or far enough from the C.G. of the complete rocket to include in the computations. The minimum set of components necessary to take into consideration generally consists of body tube, engine, nose cone, payload (if any), and fins. Shoulders, boattails, and substantial bulkheads should also be included if the rocket has such components, but lesser items such as screw eyes, shock cords, streamers, and launch lugs are commonly omitted since their contributions are minuscule. Because the number and nature of inertial contributions varies so widely from rocket to rocket, a mathematical shorthand called "summation notation" is usually used to express the equation for the longitudinal moment of inertia as follows:

$$(104) \quad I_L = \sum_i I_{L,i}$$

This symbolism, literally translated into English, means simply "the longitudinal moment of inertia of the entire rocket is

equal to the sum of the contributions to the longitudinal moment of inertia from all the components of the rocket". As you can see, summation notation saves a great deal of writing. It could equally as well have been applied to a number of other equations in this section; this I did not do, however, since I feel that the presence of examples of the explicit form of writing out summations aids in understanding the nature and purpose of summation notation.

4.6 The Radial Moment of Inertia

The radial moment of inertia of an assembled rocket is also predicted by summing the contributions due to all its components. The contribution of a solid cylindrical component of mass M_c and radius R to this quantity is given by

$$(105a) \quad I_{R_{cs}} = \frac{1}{2} M_c R^2$$

while that of a hollow cylindrical component of inner radius R_i and outer radius R_o is

$$(105b) \quad I_{R_{ch}} = \frac{1}{2} M_c [R_o^2 + R_i^2]$$

The algebraic formulae for the radial moment of inertia contributions due to most nose cone shapes are, fortunately, much more tractable than in the case of longitudinal moment of inertia contributions. A few of the more elementary ones are those for a conical nose,

$$(106) \quad I_{R_n} = \frac{3}{10} M_n R^2$$

and for an ellipsoidal or hemispherical nose,

$$(107) \quad I_{R_n} = \frac{2}{5} M_n R^2$$

where, in each equation M_n denotes the mass of the nose cone and R its radius at the shoulder.

Fins are difficult to treat analytically in any great generality due to the great variety of planform shapes possible. They cannot be ignored in computing the radial moment of inertia, despite the fact that their mass is often small, because it is also true that they extend farther from the centerline of the rocket than any other component. Nor can the point-mass approximation be made, as the spanwise extent of a fin is of comparable magnitude to the distance between its C.G. and the model's centerline. If, as when performing Barrowman calculations, however, we idealize the fin planform to a trapezoid, we can obtain a good approximation to the radial moment of inertia due to a thin, flat fin of uniform density in the form

$$(108a) \quad I_{R_f} = \left\{ \left[(s+r_t)^3 - r_t^3 \right] \frac{c_r}{3} - \frac{(c_r - c_t)}{4(s+r_t)} \left[(s+r_t)^4 - r_t^4 \right] \right\} \frac{M_f}{A_f}$$

where M_f = mass of fin

A_f = lateral area of one side of fin

r_t = radius of fin root from rocket centerline

s = span of one fin

c_r = root chord of fin

c_t = tip chord of fin

It follows that the contribution of a tail assembly of N identical fins, symmetrically arranged, is

$$(108b) \quad I_{R_t} = N I_{R_f}$$

The notation used in computing radial moment of inertia contributions of some representative components is shown in Figure 42. Generally speaking, consideration of body tube, fins, engine, nosecone, and payload, shoulder, and boattail (if any) in the calculations will suffice to give an accurate prediction of the radial moment of inertia of the completed model. As in the case of the longitudinal moment of inertia, the contribution of any given component can be determined experimentally by torsion wire. Once all the contributions to I_R from the various components have been determined, the radial moment of inertia of the assembled rocket can be calculated according to

$$(109) \quad I_R = \sum_i I_{R_i}$$

You should notice that moments of inertia, both longitudinal and radial, have units of gram-centimeters².

4.7 General Properties of the Parameters

Having derived expressions by which the various dynamic parameters may be computed, we are now in a position to make some observations concerning their general nature and properties. We can, for instance, determine the physical dimensions of the various angular frequencies and time constants derived in the analyses of Section 3. From Sections 4.1 through 4.6 we have that the units of C_1 are dyne-centimeters, those of C_2 are dyne-centimeter-seconds, and those of I_L and I_R are gram-centimeters². The definitions of C_1 and C_2 from Section 2.2, however, indicate

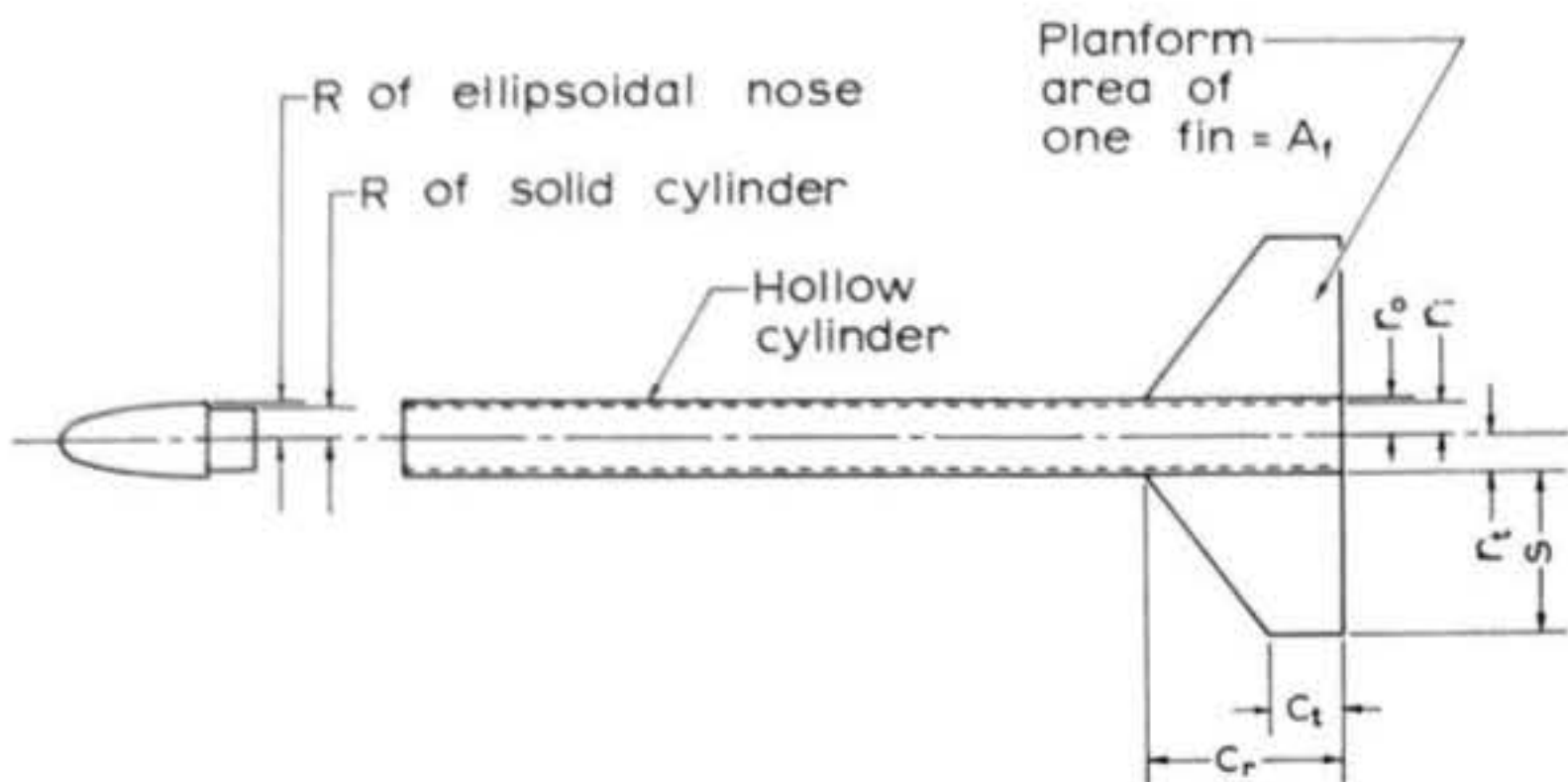


Figure 42: Examples of the notation used in computing contributions to the radial moment of inertia. An ellipsoidal nosecone, a solid cylindrical component (nosecone shoulder), a hollow cylindrical component (body tube), and a set of four fins are illustrated.

that the correct units of these parameters should be dyne-centimeters/radian for C_1 and dyne-centimeter-seconds/radian for C_2 . There is nothing inconsistent here, however, because radians are by definition dimensionless (that is, they have no physical units). Their presence or absence thus cannot be detected in a dimensional analysis and one must remember to supply them whenever necessary in determining angular frequencies.

Both angular frequencies and time constants should be computed using units for the dynamic parameters as obtained from Sections 4.1 through 4.6, which do not contain radians. If this is done we obtain for any angular frequency the units (1/seconds). To this we must supply radians, thereby obtaining the physically meaningful result that angular frequencies have units of radians/second. Radians per second are thus the physical dimensions of ω , ω_m , ω_1 , ω_2 , ω_f , and ω_z . Any inverse time constant (D , D_1 , or D_2) will be found to have units of (1/seconds). Radians should not be supplied to this result. Ordinary time constants (that is, τ_1 or τ_2) will turn out to have dimensions of seconds. Initial amplitudes and phase angles, of course, are in radians.

The coupled and decoupled damping ratios, ζ and ζ_c , will be found to be dimensionless; like normal force coefficients, they have no physical units at all. Moreover, since C_1 varies as the square of airspeed while C_2 varies linearly with airspeed, you can see from equations (20) and (70) that neither damping ratio varies at all with airspeed. Damping ratio is therefore velocity-independent -- an enormously valuable property from the standpoint of analysis, for it means that the damping ratio (aside from small variations due to jet damping) of any given rocket will remain

constant throughout its flight even though the velocity of the rocket may vary by an order of magnitude or more. It is then possible to define "acceptable" and "optimum" ranges of damping ratio which contribute to better flight characteristics, since the damping ratio can be designed into the model. ζ and S_c are relationships among geometrical and mass properties of the rocket and are independent (within the linearized theory) of its aerodynamic environment.

5. Experimental Determination of the Dynamic Parameters

Mathematical analysis is a powerful and elegant technique that enables the designer of model rockets to obtain all the necessary information concerning the properties of his model while it is still "on the drawing board". Such analytical methods, however, are always based on approximations to the phenomena under consideration, for there invariably exist factors for which it is either impossible or impractical to account with absolute precision. The value of an engineering approximation is based on the fact that the errors it introduces under normal conditions are small, while the analytical simplification it permits is considerable. Even the most valuable of such approximations, though, is likely at one time or another to encounter some set of circumstances under which it becomes invalid. The limitations of analysis, the questionable nature of certain of its approximations with respect to nonstandard designs, and the necessity to establish limits of operating conditions for the validity of the approximations make it essential that we have recourse to empirical measurement to supplement and check the results of analytical computation. The subject matter of this section concerns itself with the

experimental techniques by which such measurements may be obtained.

5.1 Moments of Inertia: The Torsion-Wire Experiment

The torsion-wire experiment is one of the standard techniques currently in use by professional industry for measuring the moments of inertia of such things as the rotative components of electric motors and turbomachinery and the indicating movements of various instruments. The experiment is ideally suited to model rocket work, providing rapid, precise, and independent determinations of the longitudinal and radial moments of inertia. The experimental apparatus can be put together in about twenty minutes at a cost that can be less than fifty cents, depending on the materials at hand, and the measurement can be made directly using the actual model in its ready-to-launch configuration without altering or damaging it in any way.

The basis of the measuring system is the torsion wire itself, a three-foot length of thin music wire. Wire diameters in the range .010 inch to .020 inch are acceptable for most model rocket work, with the lower end of the range best suited to smaller rockets or radial moments of inertia, the upper end to larger rockets or longitudinal moments of inertia. The last inch on each end of the torsion wire is bent over the center of a two-inch length of .045-inch music wire, then twisted to hold it tightly and soldered in place, forming a "T" fitting at each end of the wire. These "T" configurations are the means by which the torsion wire is secured to the test rocket at one end and the mounting structure at the other.

Figure 43 shows a complete torsion wire system set up for measuring the moments of inertia of a model rocket. Illustration

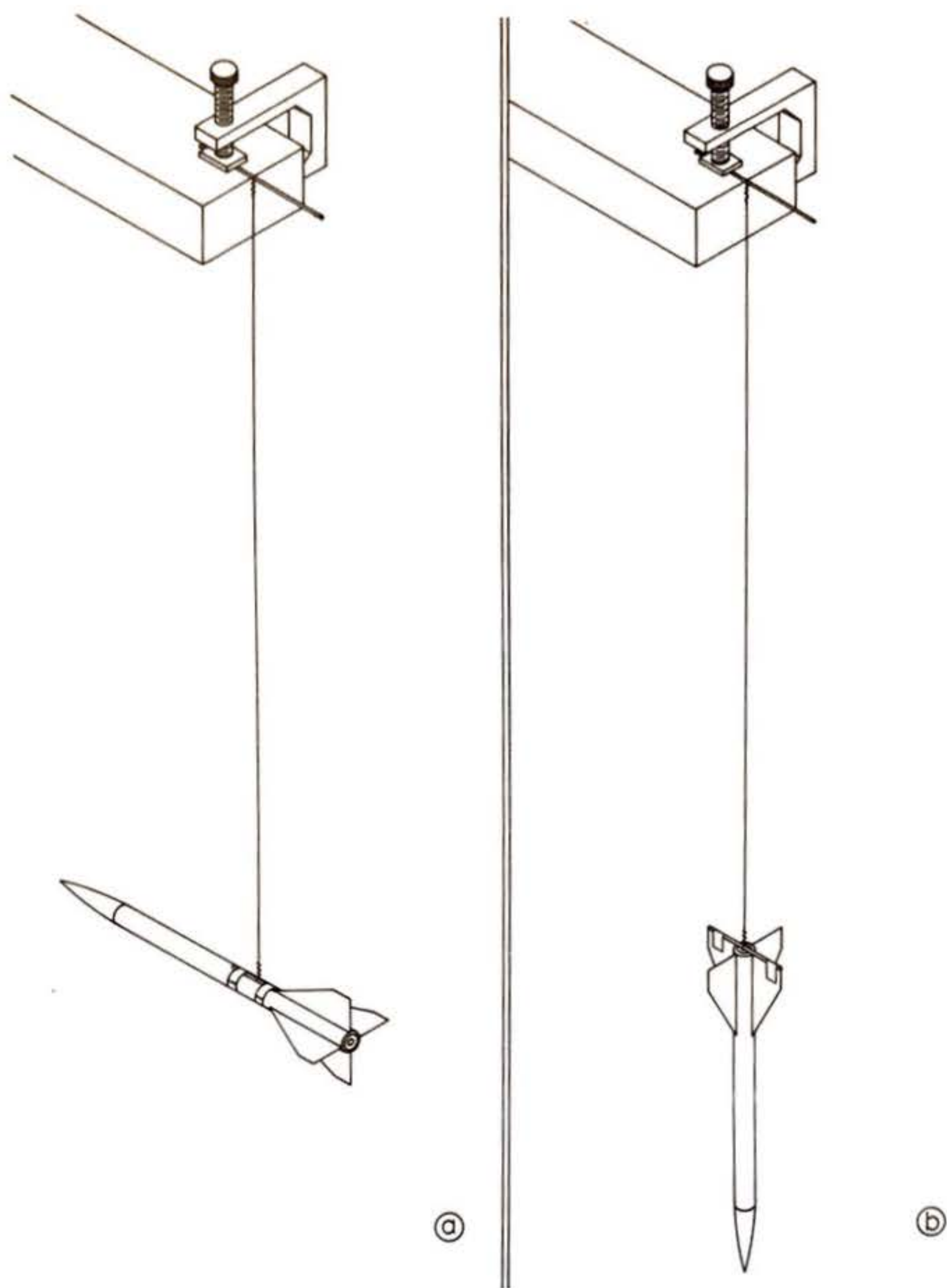


Figure 43: Measurement of moments of inertia using a torsion wire. Illustration (a) shows a model rocket suspended in the position used for determining its longitudinal moment of inertia; (b) shows the mounting position used for a determination of the radial moment of inertia.

A demonstrates the correct method of mounting the rocket to obtain a measurement of its longitudinal moment of inertia, while illustration B shows the mounting configuration for measuring the radial moment of inertia. The upper "T" fitting is clamped or otherwise fastened to an overhanging beam mount, which can be a simple two-by-four with its other end clamped to a shelf, a table, or any other structure that will allow the suspended rocket to clear the floor of the laboratory. Torsion wire experiments should always be done indoors in order to minimize disturbances of the apparatus caused by stray air currents.

The lower "T" is strapped to the rocket or component whose moment of inertia is to be measured by means of drafting or masking tape. The lighter the entire attachment assembly is, the better will be the accuracy of the measurement, and this may make some designers prefer to use a thinner crossbar and/or Scotch Magic Tape. The use of Magic Tape requires a great deal of care, however, to avoid damaging the finish of the model when removing the tape after a test is completed.

In order to calibrate a newly-built torsion wire system a reference standard is needed. The reference standard must be some object having a simple shape and a known density or mass, so that its moment of inertia is computable by means of a simple algebraic formula. One of the most convenient reference standards you can use is a half-inch aluminum rod about one foot long, suspended with its longitudinal axis parallel to the floor as in Figure 43A. The rod's moment of inertia, designated I_s , is given by

$$(110) \quad I_s = M \left[\frac{R^2}{4} + \frac{L^2}{12} \right] \quad \text{gram-centimeters}^2$$

where

M = mass of rod in grams

R = radius of rod in centimeters

L = length of rod in centimeters

A diameter of one-half inch corresponds to a radius of 0.635 centimeters; if such a rod is cut to a length of 29.7 centimeters and is of aluminum alloy 6061 it will have a mass of 101.8 grams and therefore a moment of inertia of precisely 7500 gram-centimeters². Reference standards of different values of I_s may be prepared by using rods of different lengths, diameters, and materials, but you should find that the one described above is convenient for the majority of the measurements you will be making.

A timing device completes the equipment needed to perform the experiment. An ordinary wristwatch with a sweep second hand will do for this purpose, but much better accuracy is obtainable from a stopwatch or an electric laboratory stopclock. If a timing device accurate to a hundredth of a second is used, the experiment will yield values of moments of inertia which are repeatable to better than 2%.

A torsion-wire determination is performed by measuring the period of torsional oscillation of the model and comparing it to that of the reference standard. This means that the wire must first be calibrated by performing the experiment with the reference standard affixed to the wire as in Figure 43A. The oscillations are started by twisting the wire between the fingers until the reference standard makes nearly one full revolution about the axis of the wire, then releasing it, taking care not to start the whole arrangement swinging like a pendulum in the process. Upon being released the reference standard will begin

to turn slowly about the wire axis, first in one direction, then the other, twisting the wire this way and that. This is what is meant by the term "torsional oscillation". The period of the oscillation is the time in seconds taken for the suspended object to execute one complete cycle; that is, to twist from one extreme of the oscillation to the other and back again.

To increase the accuracy of the determination, you should measure ten such periods in a single timing, starting the time when the reference standard is at one extreme of its oscillation and stopping it when the reference standard returns again to that position for the tenth time. If the time thus measured is divided by ten, a much more accurate determination of the period will result than could be obtained by measuring a single cycle.

Denote the period of the reference standard by T_s and keep a careful record of its value, for once you have obtained it you need never measure it again; the wire has been calibrated and the known values I_s and T_s may be used in reducing data from any further experiments done with that particular wire.

To determine the moments of inertia of the model, remove the reference standard from the wire and affix the model as in Figure 43A for determining I_L or as in Figure 43B for determining I_R . In each configuration, the oscillations are started and the torsional period is measured just as in the case of the reference standard. With most model rockets, torsion wires of diameters between .010 and .020 inch produce relatively slow oscillations which are easy to time with a high degree of accuracy and which are very lightly damped. It should thus not be difficult to observe the oscillations of the model for

a full ten cycles.

With the rocket mounted as in Figure 43A an oscillation period whose value I shall denote by T_L will have been measured. The longitudinal moment of inertia of the rocket can then be computed according to

$$(111) \quad I_L = I_s \left(\frac{T_L}{T_s} \right)^2$$

Similarly, when the model is mounted as in Figure 43B an oscillation period T_R will result, from which the radial moment of inertia of the rocket can be calculated as

$$(112) \quad I_R = I_s \left(\frac{T_R}{T_s} \right)^2$$

5.2 The Corrective Moment Coefficient

The value of the corrective moment coefficient is determined by measuring the static angular deflection of the rocket produced by a known pitching moment. This experiment, as well as those to be described in subsequent sections, requires a small wind tunnel -- one which has a test section whose transverse dimensions are at least twelve by twelve inches and which is capable of producing an airspeed of at least 15 meters per second. It would also be preferable if the airspeed were continuously variable, since this makes some of the experiments more convenient, but this feature is not essential. I am not going to try to explicitly describe the construction of a wind tunnel here; the variety of types is considerable and any such discussion would require a complete book of its own. Building such a device is a major project in itself, and most rocketeers would rather have recourse

to a facility that already exists, such as those owned by some universities, NAR sections, and model rocket manufacturers.

Those readers who would like to build their own tunnels can find information on the subject in Wind Tunnel Testing, by Alan Pope (Second Edition, John Wiley and Sons, Inc., New York, 1954).

A reading of this comprehensive work should give you a good idea of the variety of wind tunnel types available and the nature of the design process involved in their planning.

The experiment to determine the corrective moment coefficient is performed using a moment balance and test rocket as shown in Figure 44. The balance is basically a single-degree-of-freedom gimbal consisting of a pulley wheel attached to a steel shaft which runs through ball bearings to terminate in an aluminum plug fitting. The test rocket is constructed in two sections, such that the forward section can be snugly slid onto one end of the plug fitting, the after section onto the other. Because it is necessary to build the rocket in this way only a design can be tested, not an actual rocket which is to be flown, but the arrangement has the advantage that it produces a minimal disturbance in the airflow.

That portion of the shaft on which the plug is mounted extends through a hole in the wall of the wind tunnel test section and out into the airstream, such that the plug is located approximately in the center of the test section. The case is bolted to the side of the test section opposite the viewing area in order to hold the instrument in place.

The moment balance in Figure 44 is shown with a pointer-and-protractor device for indicating the angle of deflection.

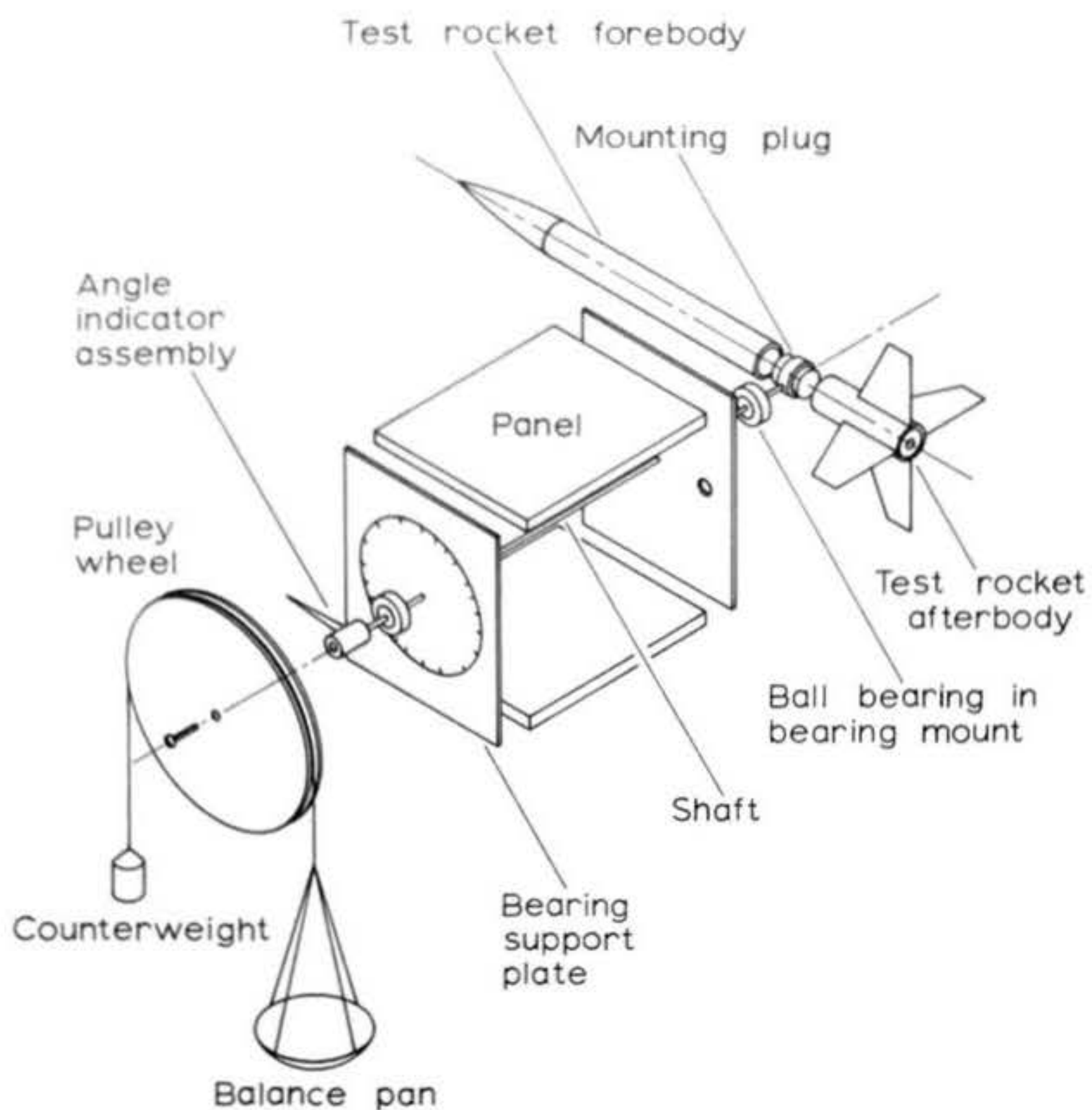


Figure 44: Experimental apparatus for determining the corrective moment coefficient. The same instrument, with the pulley wheel, counterweight, and balance pan assembly removed, can be used for determining the damping moment coefficient. Bolt holes are provided in the bearing support plate nearest the test rocket for mounting the apparatus on the wall of a wind tunnel test section.

This arrangement is perfectly adequate for static-deflection experiments; in the experiments described in later sections, though, where the rocket is set to oscillating, it will become desirable to record the value of the angular deflection at any given time. This can be done with motion pictures and in various other ways using the protractor system, but it is usually preferred to substitute some electrical device for measuring the angle and to feed its output into a chart recorder, which then automatically draws a graph of deflection versus time.

To generate the moment which will cause the rocket to assume an angle of pitch relative to the oncoming airstream it is necessary to apply a force tangential to the pulley wheel at its outer radius. This is done by suspending a balance pan from a thin cord which has been wrapped around the pulley and adding known weights to the pan. The balance pan itself must be suitably counterweighted so that there is no moment applied when there is no weight in the pan.

The experiment is prepared by adjusting the weights of the forward and after sections of the test rocket so that, when assembled on the plug with an engine installed, it balances when the airstream is off and there is no weight in the pan. Under these conditions the shaft centerline passes through the C.G. of the rocket, so that free-flight conditions are being accurately simulated.

The airstream is then turned on and adjusted to some fixed velocity value which is not to be altered during the course of the experiment. The model should come to rest facing directly into the oncoming wind, which in a good wind tunnel will coincide with the test

section centerline. If it fails to face into the wind, or turns tail-on to the wind, it is of course statically unstable and must be redesigned. Assuming the model is facing the airstream properly, the last remaining preliminary step is to check the angle indicator and adjust it if necessary so that it reads zero.

The addition of weights to the pan can now be started, beginning with a unit weight that produces a small deflection (between 1° and 2°), but which is an even quantity such as a single laboratory balance weight or simple combination thereof. Record the mass, in grams, of the weight used and the exact deflection in degrees which it produced. Then add another weight identical to the first and record the new deflection from the zero-degree line produced by the two acting together, making certain that all movement has subsided before you take a reading. Continue adding weights in this manner, recording the deflection angle associated with each value of total mass in the pan, until you reach a point at which the rocket will no longer come to equilibrium and the slightest additional weight in the pan will cause the rocket/balance assembly to become unstable. This will generally occur at some value of deflection angle between 12° and 18° and is due to the slope of the corrective moment curve becoming zero at that point (refer back to Figure 7 for an illustration of the corrective moment curve).

The experiment is now complete and data reduction can begin. The first step here is to transform the units in which the data are expressed, so that angular deflections are given as radians and pitching moments as dyne-centimeters. Deflections in

degrees are converted to radian measure by dividing by 57.3; a moment in dyne-centimeters is computed by multiplying the mass (in grams) placed in the pan by 980 and then multiplying the result thus obtained by the radius of the pulley wheel in centimeters. These procedures are illustrated in Figure 45. The completed data reduction should provide a table listing each deflection in radians next to the moment required to produce it in dyne-centimeters.

The data points are then plotted on a graph in cartesian coordinates whose horizontal axis represents pitching angle in radians and whose vertical axis represents pitching moment in dyne-centimeters. Such a plot is made by locating each point described by a coordinate pair in the table (a deflection and its associated moment) on the graph and marking it with a small "x" or dot, then drawing a smooth curve which, as nearly as possible, connects all the points. Since experimental data normally contains some "scatter", it is more likely that your curve will be accurate if it is smooth than if it connects each and every point with all its neighbors. The resulting graph is a representation of the first part of the curve in Figure 7: corrective moment as a function of angle of attack. In order to compute C_1 from this graph, place a straightedge on it such that its edge is tangent to the curve at the intersection of the coordinate axes (the origin) and draw a line using the straightedge as a guide. This is the graphical method of performing the "linearization about zero" discussed in Section 2.2 as applied to the corrective moment curve. The corrective moment coefficient C_1 is just the slope of this straight line

$$\text{Deflection angle (rad)} = \frac{\alpha^\circ}{57.3}$$

$$\text{Moment (dyn-cm)} = M \times 980 \times R$$

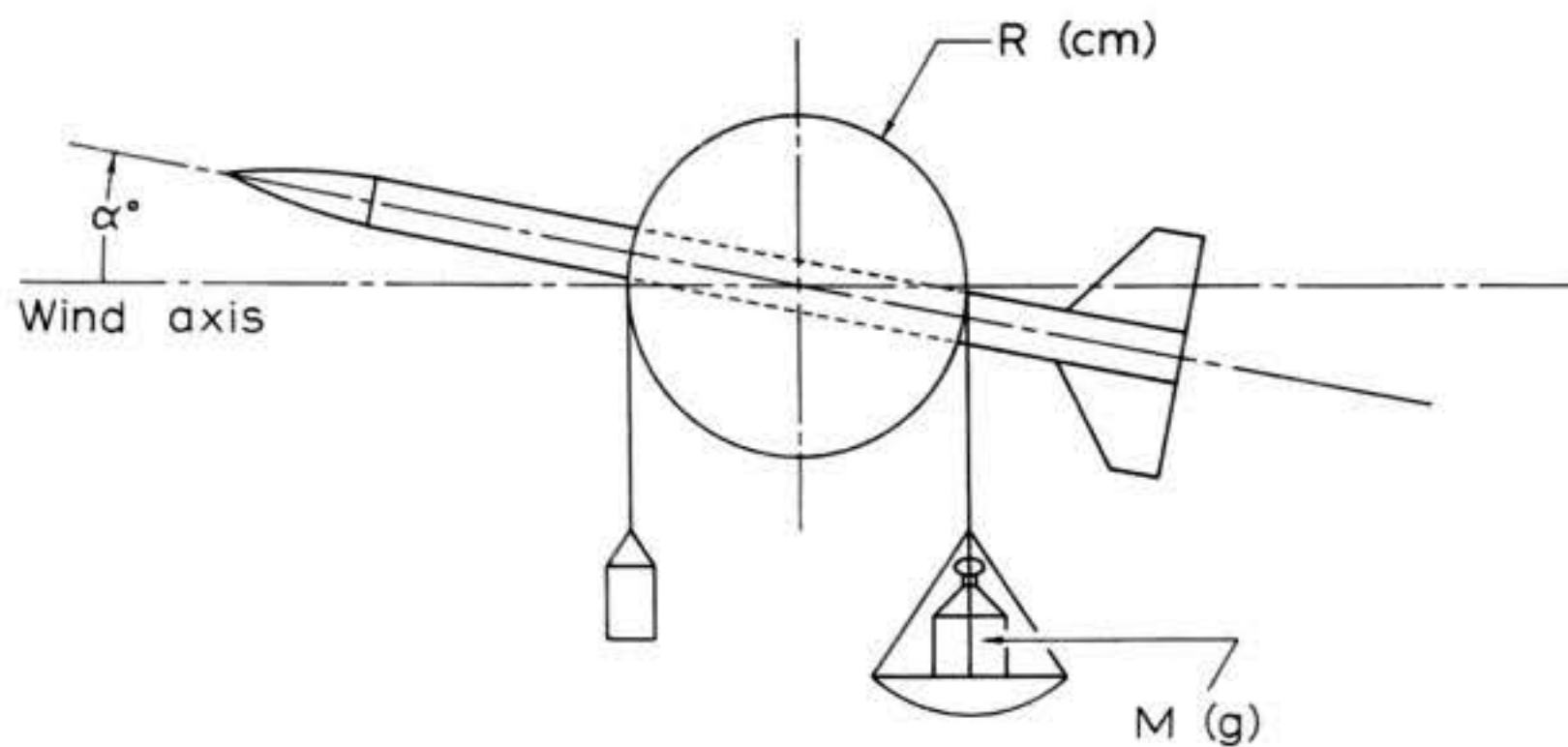


Figure 45: Computing angle of attack in radians and corrective moment in dyne-centimeters. The angle of attack in degrees is divided by 57.3 to convert to radians; the mass on the balance pan, in grams, is multiplied by 980 times the radius of the pulley wheel in centimeters to give the moment in dyn-cm.

and may be computed by locating any point on the straight line and dividing its moment coordinate by its deflection coordinate. The result is C_1 given in dyne-centimeters per radian, but this should be expressed as simply dyne-centimeters because radians (as stated in Section 4.7) are physically dimensionless. Figure 46 illustrates the graphical reduction of data for a hypothetical rocket.

You may wish to repeat the experiment at a number of different values of airspeed to determine the dependence of C_1 upon velocity. If you do this, you will find that C_1 is directly proportional to the square of the airspeed.

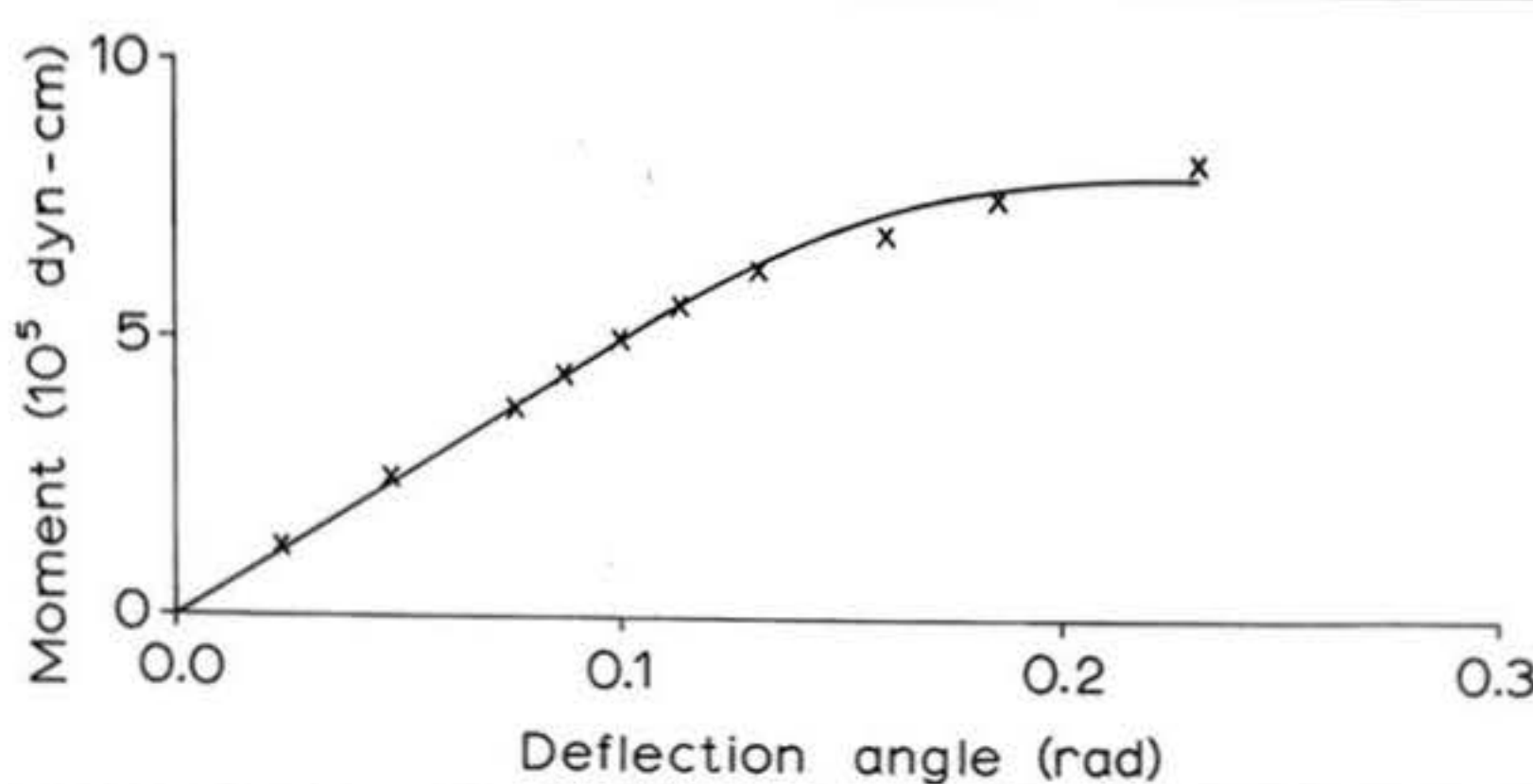
5.3 The Damping Moment Coefficient

The dynamic parameter C_2 is determined using the same gimbal arrangement as in the first experiment, with the exception that the pulley wheel and its associated pan and counterweight system must be removed. This must be done in order to reduce the moment of inertia contributed by the rotating parts of the balance system, and unless this modification is carried out the rocket will behave as if its longitudinal moment of inertia were much greater than it actually is.

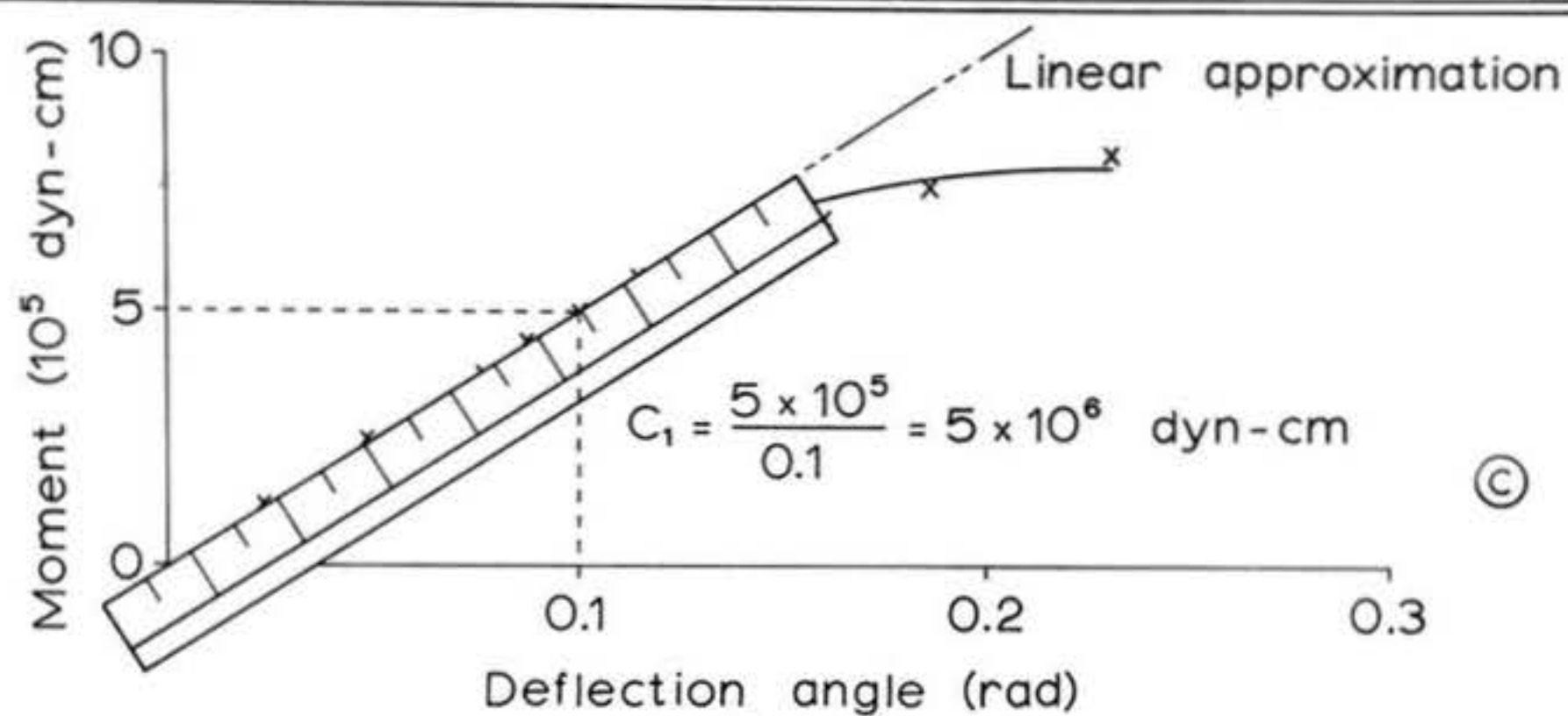
The experiment is prepared by balancing the test rocket so that the shaft passes through its center of mass as before, setting the airspeed to the desired value -- which must remain constant throughout the test -- and checking to make certain that the angle indicator is reading zero. Having completed these preliminary steps, deflect the rocket to some moderate angle of attack, say 10° , and hold it steady in this position. You may wish to have an assistant do this by turning the shaft

Moment (10^5 dyn-cm)	Deflection angle (rad)
0.0	.0000
1.250	.0240
2.500	.0490
3.750	.0770
4.375	.0875
5.000	.1000
5.625	.1135
6.250	.1340
6.875	.1610
7.500	.1852
8.125	.2315

(a)



(b)



(c)

Figure 46: Graphical reduction of wind tunnel test data to determine the corrective moment coefficient. (a): A table of corrective moment vs. deflection angle is compiled. (b): The data points on the table are transferred to a graph and a smooth curve is drawn (as nearly as possible) through the points. (c): A straightedge is placed along the lower portion of the curve, tangent to it at the origin, and a line is drawn using the straightedge as a guide. The slope of this line is the corrective moment coefficient.

with his hand in order to allow you to best observe the subsequent motion, or you may devise various automatic systems to do the job. One simple technique for obtaining the initial deflection would be to wrap a length of strong thread around the end of the shaft from which the pulley has been removed and tie a weight to the thread. In any case, record the value of the initial deflection thus produced, identifying it as α_0 .

Now release the rocket and allow it to rotate into the wind of its own accord. If you have used the thread-and-weight system for producing the initial deflection, you can do this by carefully snipping the thread with a pair of scissors. The rocket should swing toward alignment with the wind axis and overshoot it, reaching a maximum angle which I shall refer to as α_1 , on the opposite side of zero from that on which the model was released, and subsequently oscillating with smaller and smaller amplitude about zero until it is facing steadily into the oncoming wind. The convention for representing α_0 and α_1 , whose algebraic signs are both taken as positive, is shown in Figure 47. The maximum overshoot angle α_1 will be reached at a time defined as t_{max} after the rocket is released. You must accurately record both the maximum overshoot angle and the time at which it occurs. In the case of indicating systems consisting only of a simple pointer-and-protractor α_1 must be recorded by eye (or by photographic means) and t_{max} by a stopwatch. An electrical system for measuring and recording the deflections has a significant advantage here, in that it takes the guesswork out of the observations.

If, upon being released, the model does not oscillate at

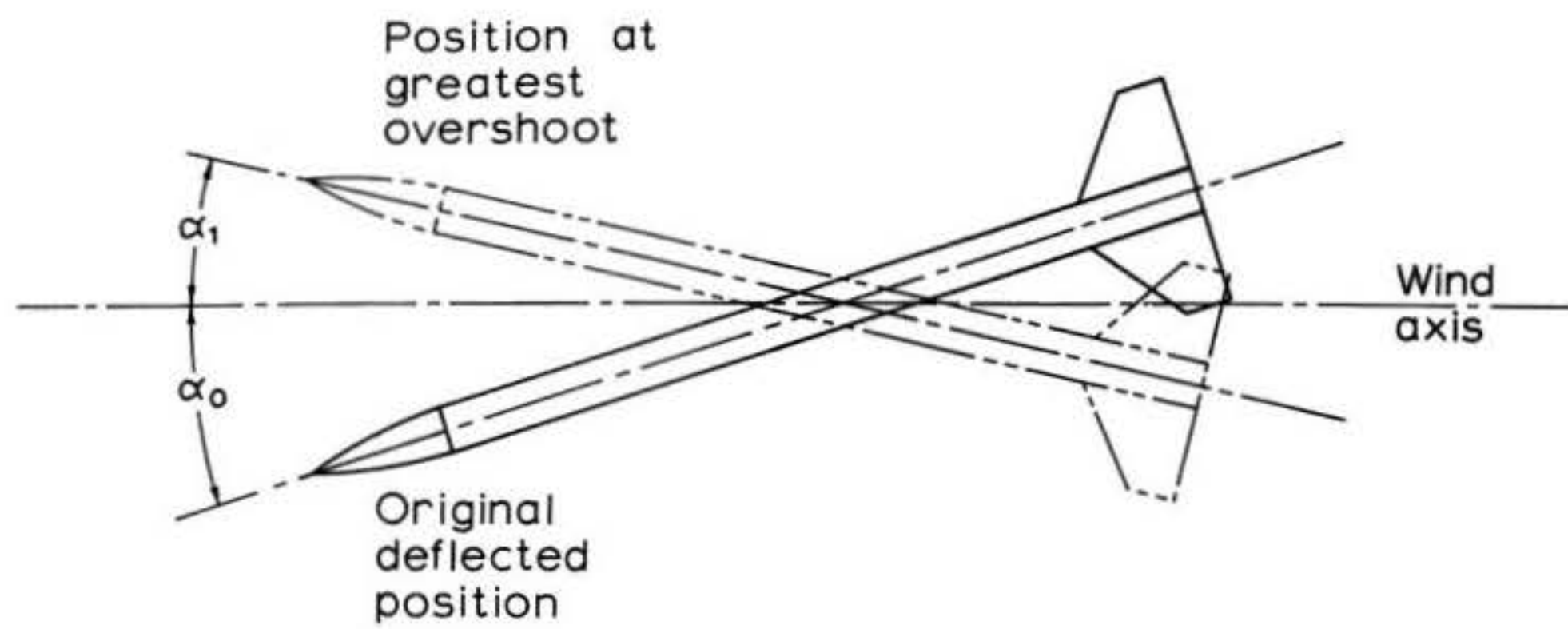


Figure 47: Convention for defining α_0 and α_1 in the experiment for determining the damping moment coefficient.

all but instead slowly faces into the relative wind from the position of initial deflection, it is overdamped. As shown by the results of Section 3.1.1, this is a hazardous condition which may result in an erratic flight path and the rocket must be redesigned to correct it. Additional nose weight will usually take care of this problem, but since this moves the center of mass forward it will require the building of a new test model which is divided in two further toward the nose. Alternatively, both the nose and the tail of the model can be weighted, keeping the C.G. in the same place but increasing the longitudinal moment of inertia.

Assuming that the rocket has behaved in a properly oscillatory fashion and that α_0 , α_1 , and t_{\max} have all been duly recorded, the value of the damping moment coefficient may now be computed. The first step is to determine the inverse time constant D according to the relation

$$(113) \quad D = \frac{\ln(\alpha_0/\alpha_1)}{t_{\max}}$$

where the reader is reminded that the notation " $\ln(\alpha_0/\alpha_1)$ " refers to the natural logarithm of (α_0/α_1) . Readers who are mathematically adept may recognize that equation (113) is derived from the peaking characteristics of decoupled, underdamped step-response presented in equations (32), Section 3.1.2.

With D known from equation (113) and I_L known from torsion-wire determinations, it is possible to calculate C_2 from equation (16), Section 3.1.1, as

$$(114) \quad C_2 = 2 I_L D$$

As when determining the corrective moment coefficient, you may wish to perform this test at various airspeeds. In doing this you will find that C_2 increases linearly with airspeed so that the values of the decoupled and coupled damping ratios, as predicted by the Barrowman equations, remain constant.

Equation (114) determines C_2 in units of dyne-centimeter-seconds.

6. Model Rocket Design

I have often remarked during the foregoing presentations that the true purpose and real value of all the mathematical analyses to which we have turned our attention in this volume lies in the fact that they enable the formulation of rational rules for the design of model rockets. We have now progressed sufficiently far in our analytical considerations of the dynamic behavior of model rockets that we are prepared to discuss the subject of model rocket design insofar as it is influenced by dynamical considerations. To "design" a rocket, from the standpoint of dynamics, is to adjust its shape and mass distribution so as to produce values of the dynamic parameters which give rise to favorable characteristics in its dynamic response. "Favorable characteristics," in turn, mean that:

- (a) The rocket is not easily disturbed, or deflected from its intended direction of flight. For a given disturbing influence, the angle through which it rotates is small.
- (b) The rocket soon returns to a straight and true flight path once the disturbance has passed, and does so in an oscillatory fashion so that the effect of the disturbance is evenly distributed about the intended flight axis.

6.1 Representative Parameters

The solutions to the dynamical equations given in Section 3 predict that favorable dynamic behavior in various particular situations will be associated with certain ranges of values of the dynamic parameters or combinations thereof. As it happens, however, the dynamic parameters of a model rocket cannot be varied independently of one another. Even if they could, it turns out that relations between the parameters best for one response are not necessarily best (or even acceptable) with respect to other types of disturbances. The designer of model rockets thus finds himself faced with the necessity to make certain compromises -- "tradeoffs", they are called by professional engineers -- in order to arrive at a configuration which, on the whole, has favorable performance. The situation is further complicated by the fact that characteristics which are best for dynamics may not always be best for other aspects of rocket performance -- altitude capability, for example. In order to guide himself to a rationale by which design compromises can be made the rocketeer needs two classes of information: first, what values of the parameters characterize a typical, or representative model; and second, what is the effect of varying the configuration of the model upon the values of its parameters?

In order to supply an answer to the first question the typical model rocket configuration DTV-1, illustrated in Figure 48, was constructed and tested according to the methods of Section 6 in the low-turbulence wind tunnel of the Massachusetts Institute of Technology's Aeronautical Projects Laboratory.

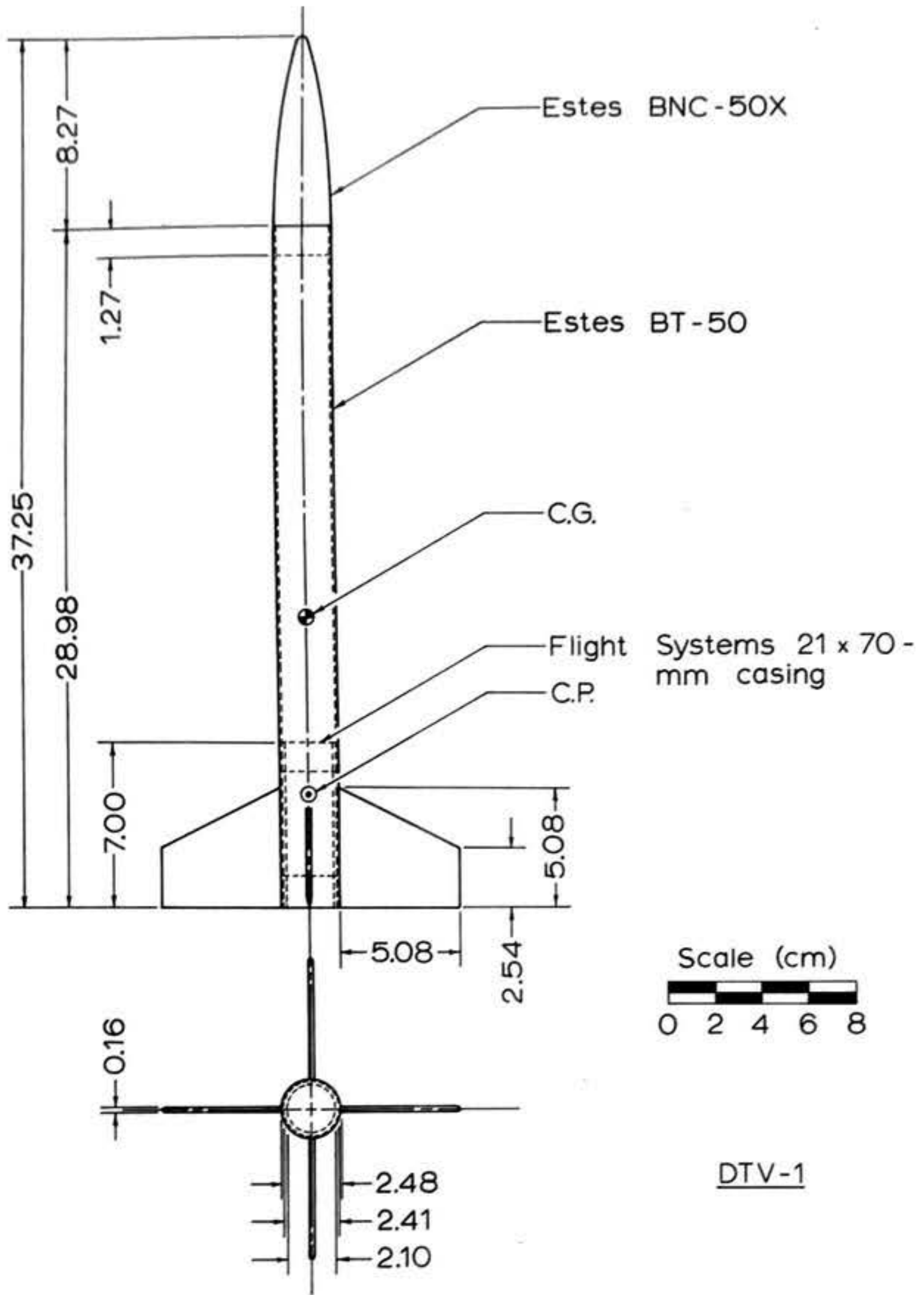
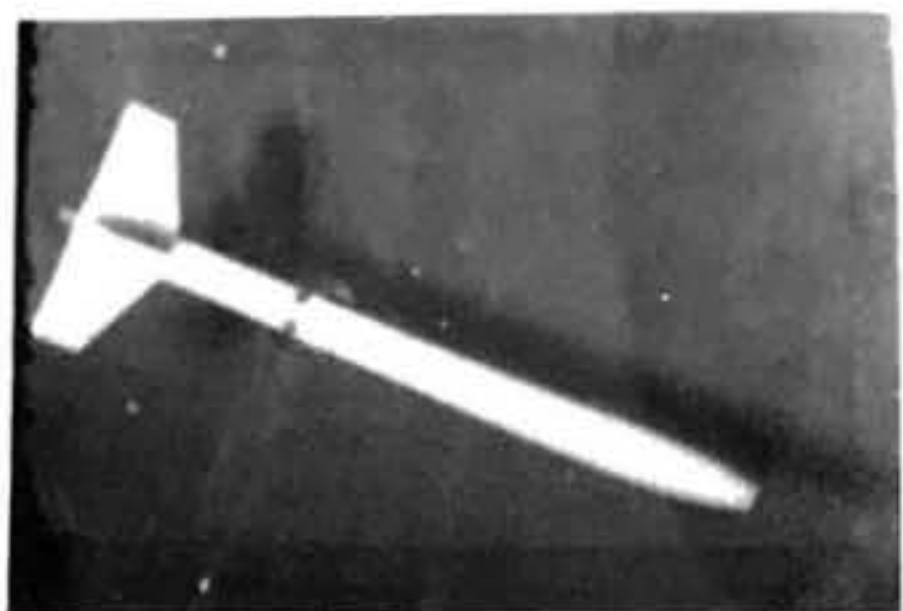
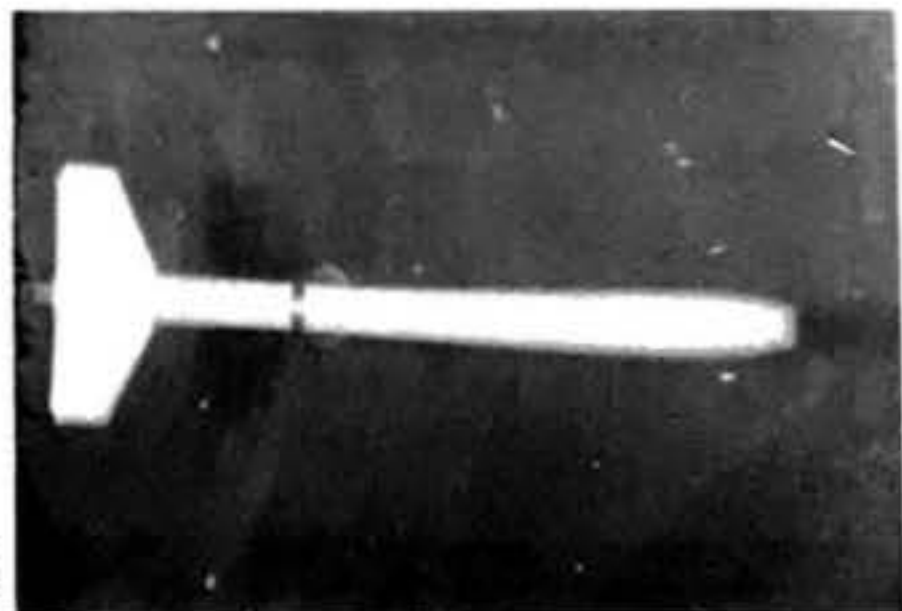


Figure 48: Dynamic test rocket DTV-1. All dimensions are given in centimeters, with the exception of the engine casing specifications. These are given in millimeters in accordance with international convention.

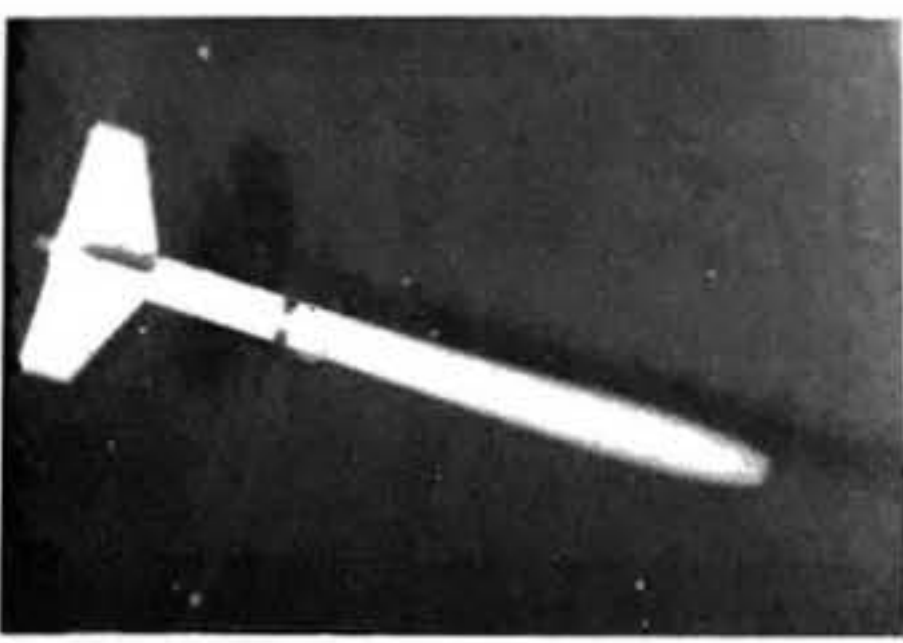
Plate 1: DTV-1 undergoing wind tunnel test to determine its damping moment coefficient. The model is mounted on a moment balance similar to the one pictured in Figure 44, but without the pulley wheel assembly and equipped with a photoelectric angle indicating device. In frame (a) the model has just been released from the angle α_0 . In (b) and (c) it is accelerating in pitch up. (d): The model passes through zero angle of attack at its maximum pitch rate, still pitching up but slowing in (e) and (f). (g): The rocket is at its maximum pitch-up deflection, α_1 . (h), (i): The model begins to pitch downward again. (j), (k), (l): The rocket passes through zero again on its way down to complete its first full cycle of oscillation.



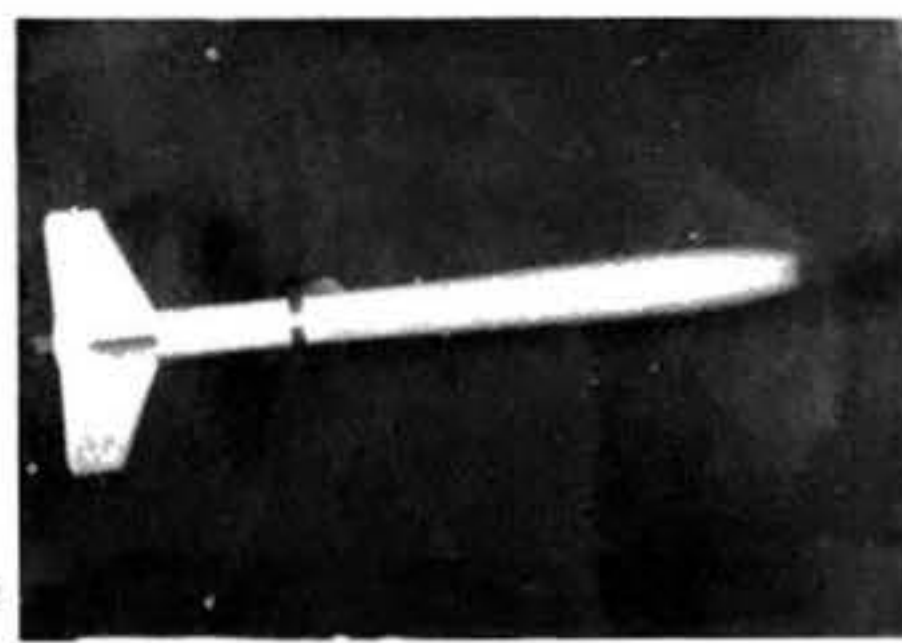
a



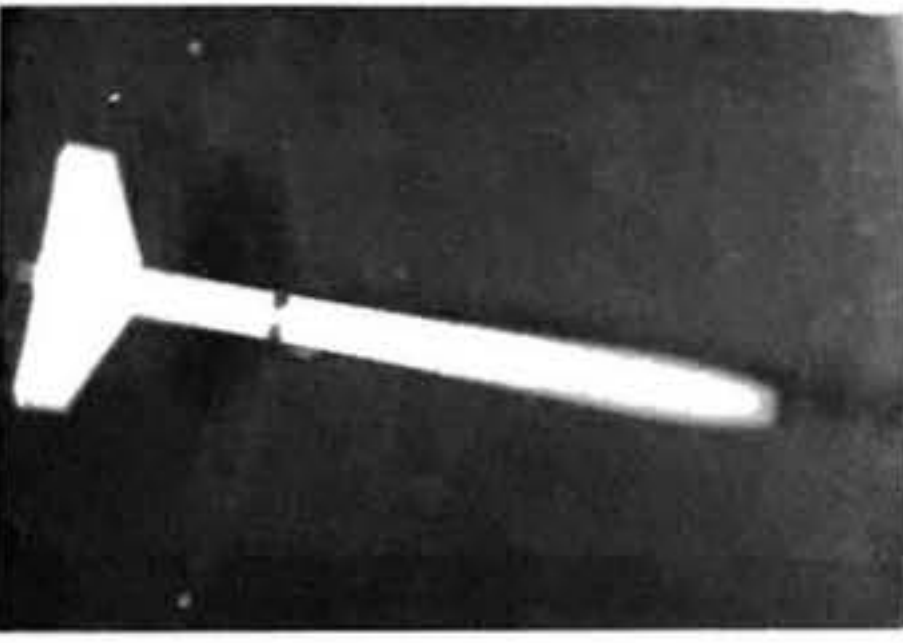
d



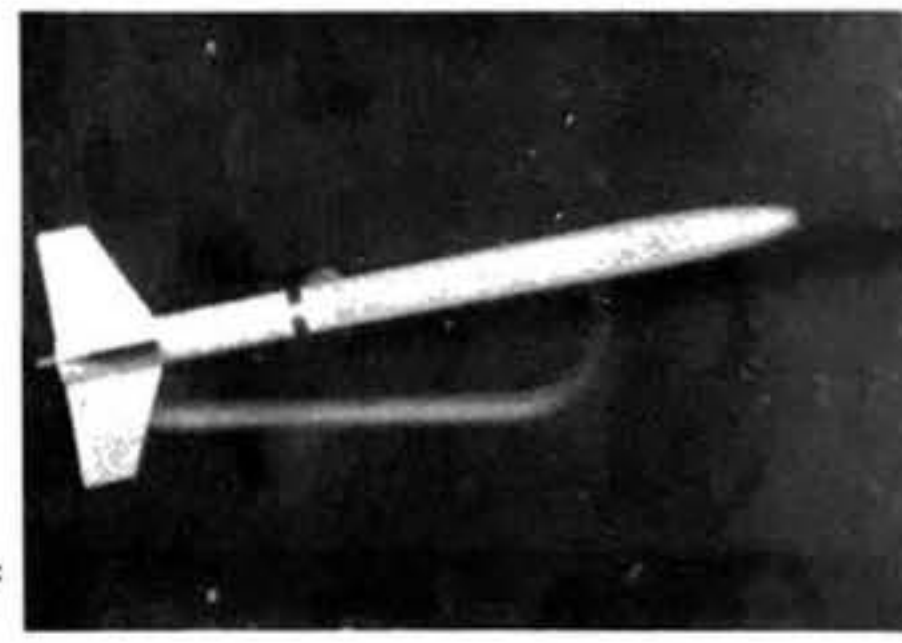
b



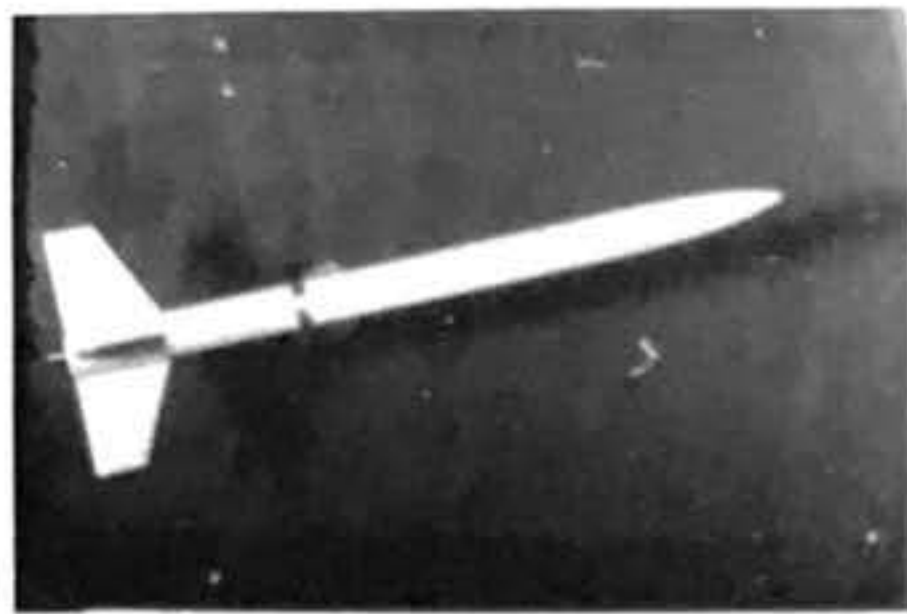
e



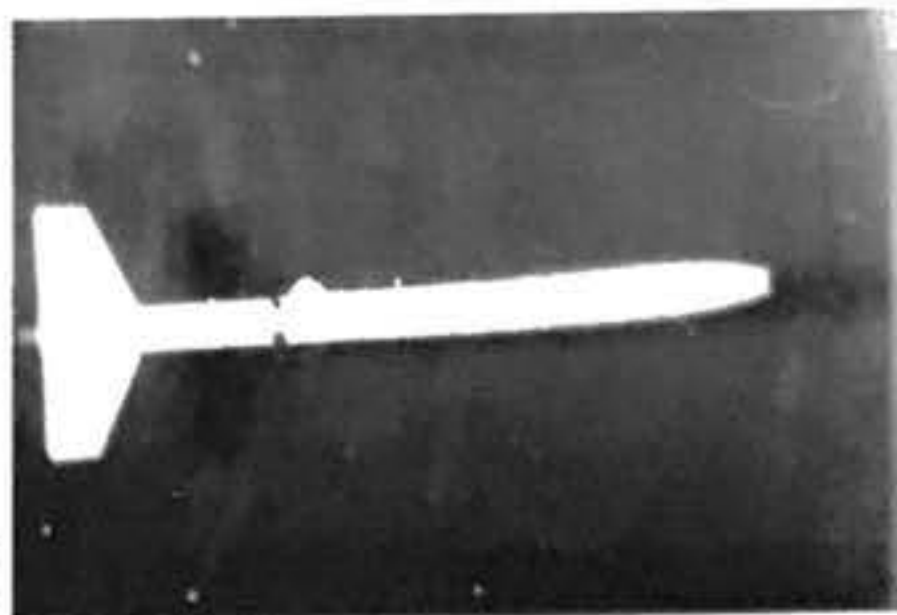
c



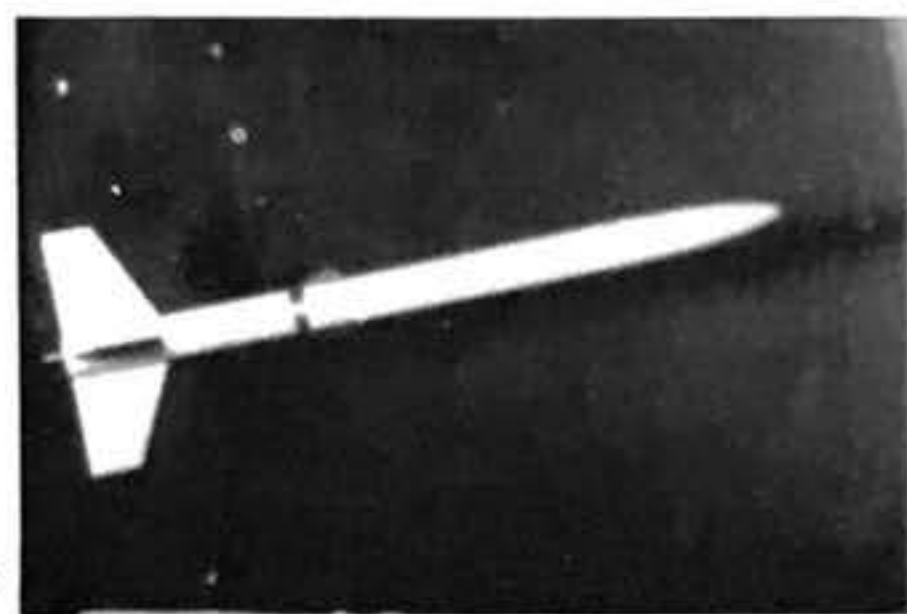
f



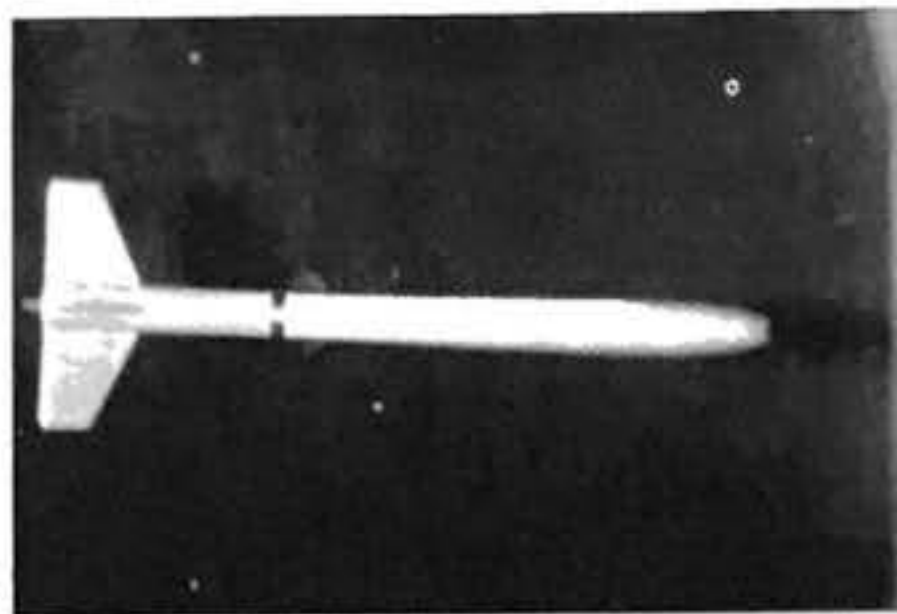
g



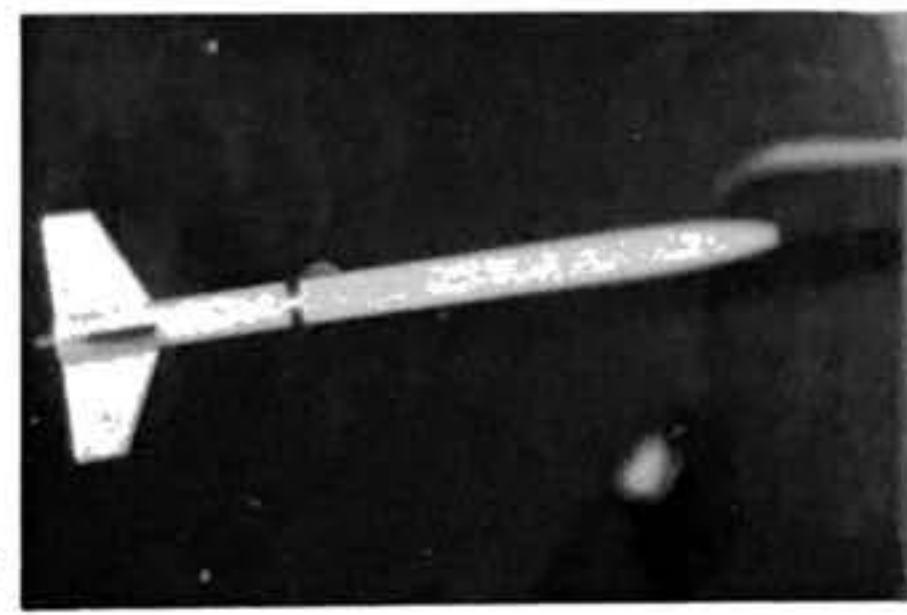
j



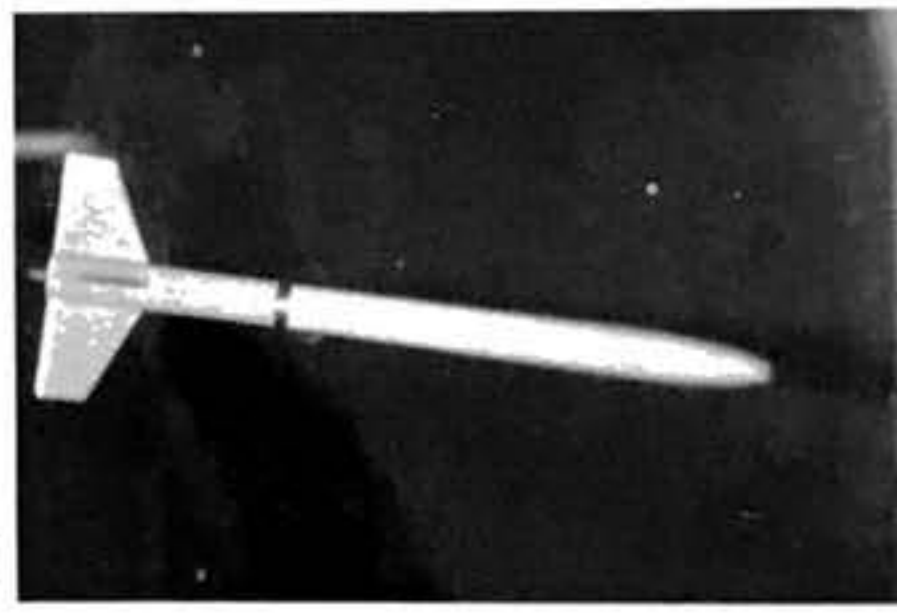
h



k



i



l

DTV-1 was found to have the following dynamic parameters:

$$c_1 = 0.65V^2 \text{ dyne-centimeters, where } V \text{ is given in centimeters per second}$$

$$c_2 = 10.5V \text{ dyne-centimeter-seconds}$$

$$I_L = 9100 \text{ gram-centimeters}^2$$

$$I_R = 173 \text{ gram-centimeters}^2$$

The rocket's roll rate during a number of additional experiments in which its behavior under roll-coupled resonance was investigated was an independent variable determined by the speed of an electric motor mounted on a balance system that was essentially a more refined form of that discussed in Section 5.3. It will be seen from the above figures that the following quantities are also characteristic of the rocket:

$$\omega_m = .00845V$$

$$\zeta = .0682$$

$$\frac{I_R \omega_z}{I_L} = .0195 \omega_z$$

$$\omega_{mc} = .00838V$$

$$\zeta_c = .0675$$

where V , the airspeed, is given in centimeters per second and ω_z in radians per second. Now it is probable that DTV-1 is not precisely in the center of the average range of model characteristics; it is rather on the heavy side and has a static stability margin of three calibers. Nevertheless, it is certainly representative enough to allow the following general statements to be made:

- (1) In a model rocket of average design, the damping ratio tends to be low -- on the order of one tenth. Resonance, when

it occurs, tends to be a problem and will usually be caused by the development of a roll rate whose value is close to the natural frequency. Overdamping, on the other hand, is much less common and not usually to be feared.

(2) The radial moment of inertia is very slight compared to the longitudinal moment of inertia -- on the order of a few percent. The roll rate must be very rapid to produce appreciable gyroscopic moments. Therefore, the angular frequencies and rate of decay of the response of an average model rocket subjected to transient disturbances while spinning about its longitudinal axis are very nearly equal to those that would describe the behavior of the same rocket if it were not spinning at all, unless the spin is very rapid. By "very rapid" I mean that the gyroscopic precessional frequency $\frac{I_R \omega_x}{I_L}$ is, say, 10% or more of the natural frequency. For DTV-1 during powered flight this would mean a spin rate on the order of 100 radians (about 16 revolutions) per second.

(3) As another consequence of the small radial moment of inertia, the resonance condition for a given rocket is nearly the same when it is rolling as when it is not; i.e., the natural frequency is nearly equal to the coupled natural frequency and the damping ratio is nearly equal to the coupled damping ratio. This is an advantage in that the presence of roll does not appreciably increase the severity of the resonance.

6.2 Effects of Varying the Parameters

Having roughly bracketed the "average" or "representative" dynamic parameters, we can start to investigate what happens when a rocket departs from the average range in various ways.

We must remember, when doing this, to take into account factors affecting other aspects of the rocket's performance (such as its overall weight and drag) as well as those affecting its rigid-body dynamics.

First, consider the effect of increasing the longitudinal moment of inertia of the rocket. This can be done by adding weight at points far fore and aft of the center of gravity, usually making the rocket longer as well as heavier. The damping ratio and natural frequency of oscillation will decrease, and the rocket will be more difficult to deflect from its intended path. If this is carried to extremes, however, the rocket will become so heavy that its altitude capabilities will be sharply reduced and it will experience catastrophic resonance at very low roll rates, resonance so severe that the model may behave as if it had insufficient static stability. The dramatic manner in which resonant amplitude ratio increases with decreasing damping ratio is shown in Figure 49. There is evidence that some model rockets have actually been caused to crash by excessive resonance at low roll rates early in the flight. Rocket A of Figure 50 is an example of how a model designed with too great a longitudinal moment of inertia might look.

Decreasing the longitudinal moment of inertia will increase both the damping ratio and the natural frequency; the actual angular frequency of oscillation will increase only up to a point, then begin to decrease towards zero as the damping ratio approaches 1.0. The resonance problem will disappear, but the rocket will be more easily deflected from alignment with the intended flight path. The slightest disturbance will be enough to start it

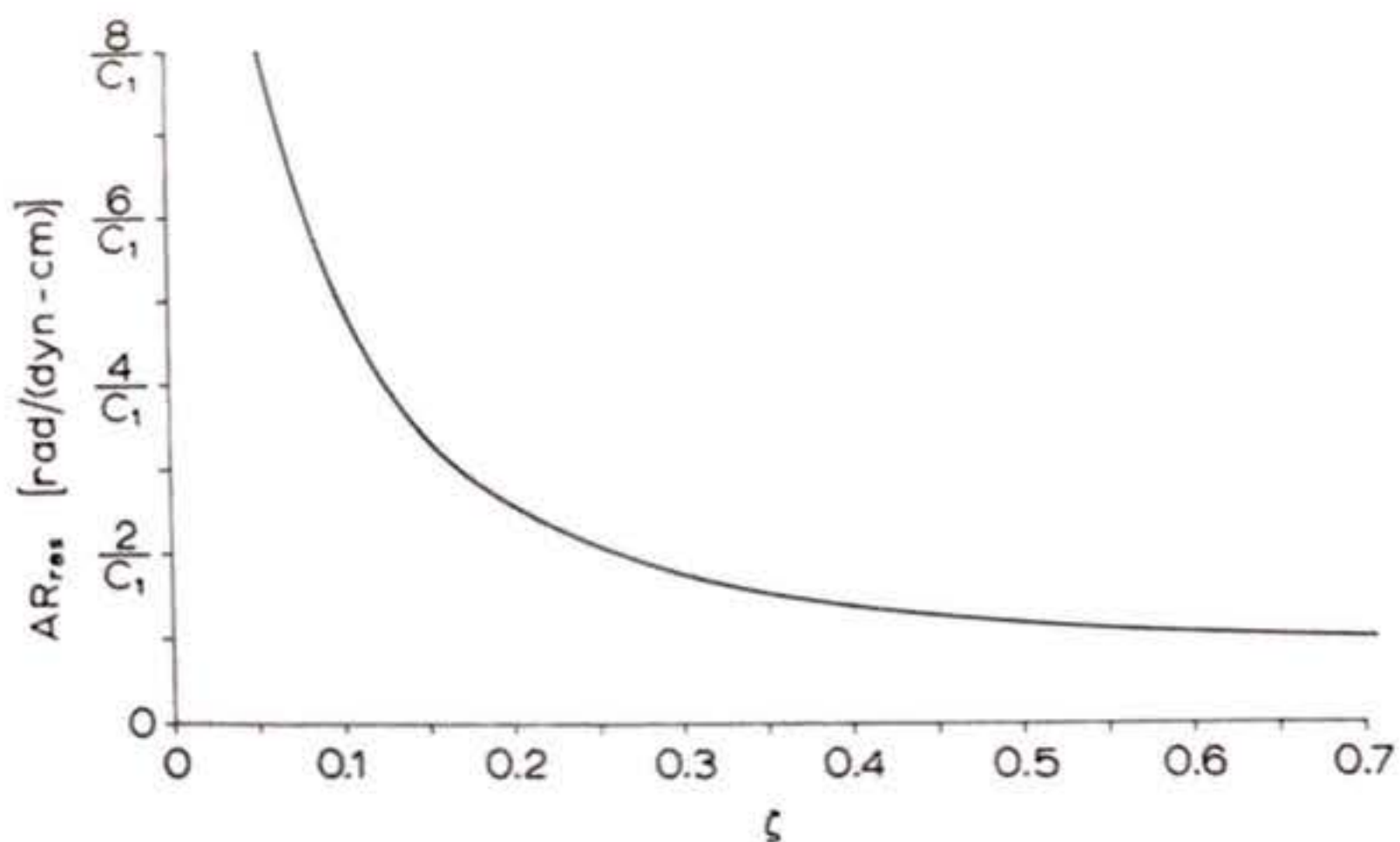


Figure 49: Variation of resonant amplitude ratio with damping ratio. A curve of precisely the same form describes the variation of coupled resonant amplitude ratio with coupled damping ratio.

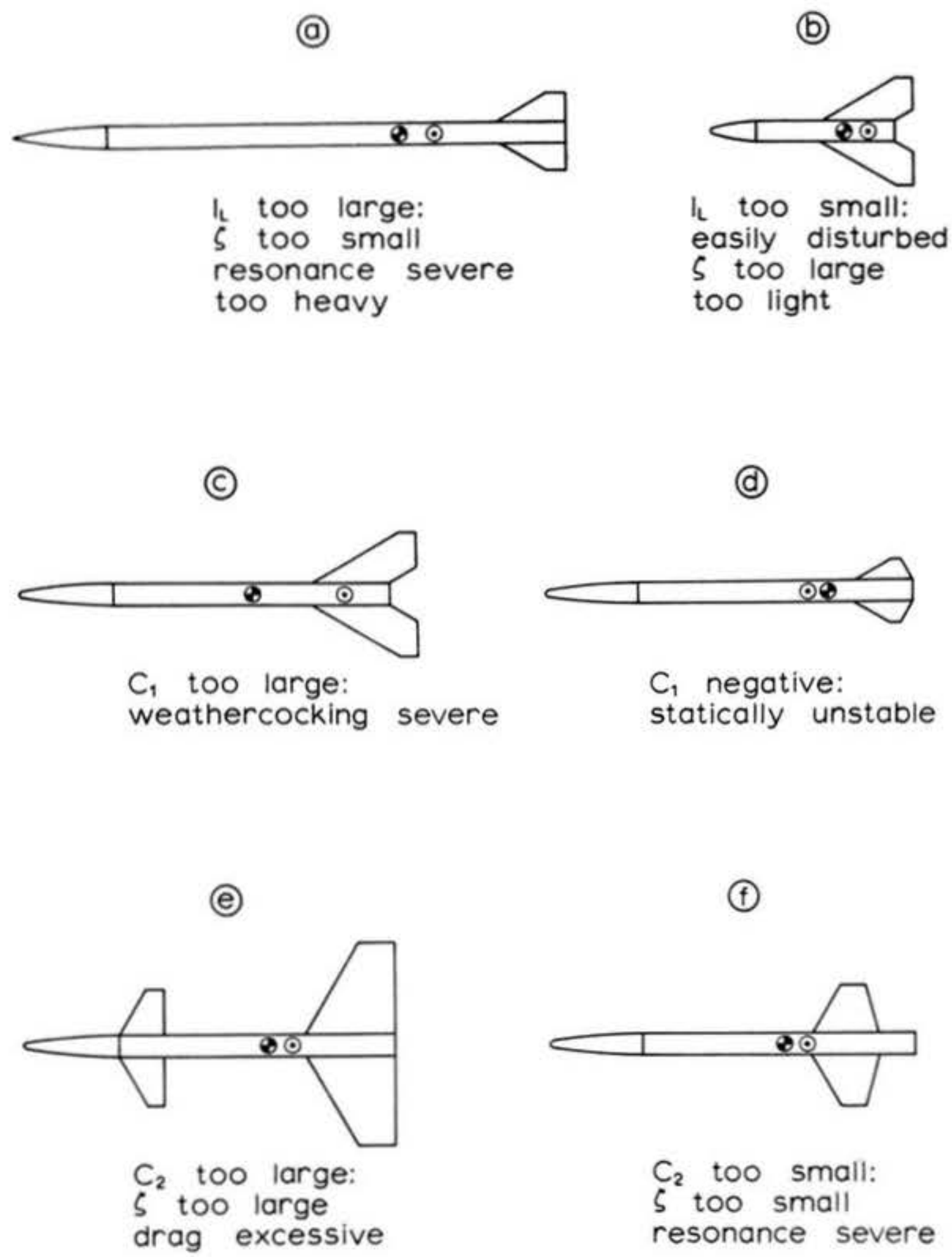


Figure 50: Improperly designed model rockets resulting from extreme variations in the relative values of the dynamic parameters.

wobbling, and although the oscillations will die away after only a few cycles the rocket will be disturbed so often that it will spend much of its upward flight at a considerable angle of attack. Its drag will thus be increased and its altitude lowered -- particularly since a low longitudinal moment of inertia usually means a low weight and the rocket may already be ballistically off-optimum*. Continued reduction of I_L causes overdamping, and the model behaves as if it had an insufficient static stability margin. An example of this extreme is rocket B of Figure 50. Between 1962 and 1967 there was a marked trend toward this kind of design in the United States. Modelers at that time believed that the lighter a rocket was, the higher it would go, and so constructed all their altitude competition designs to be very light and stubby, with huge fins. The result was often excessive damping, sometimes even overdamping, causing severe launcher tipoff, erratic flight paths, and many a pile of wreckage. Thanks to Malewicki and Caporaso -- who developed the equations of model rocket ballistics -- and to Barrowman -- who demonstrated analytically the fin areas actually needed by model rockets -- and to much sad experience and observation, this fetish is largely a thing of the past.

Suppose we now consider the effect of increasing the corrective moment coefficient. If this is done by increasing the static stability margin -- by increasing the area of the fins and/or moving them further toward the rear of the rocket -- the frequency at which the rocket oscillates when disturbed

*There is an optimum weight for any rocket, which gives the greatest altitude. See George Caporaso's chapter on trajectory analysis in this volume for an explanation.

will increase. Since altering the fin geometry in this way also increases the damping moment coefficient, the damping ratio will not necessarily decrease; it may even increase if the practice is carried to extremes. Thus, the time required for the disturbed rocket to return to proper alignment with the intended flight direction becomes shorter -- and, because the longitudinal moment of inertia has not been appreciably changed, the rocket is no easier to disturb than it was before. On the face of it, the modification appears to be a favorable one.

Unfortunately, though, there are also disturbances whose magnitude is directly proportional to the static stability margin and normal force coefficient of the model, notably the step disturbances due to horizontal winds. If the value of the static stability margin is made too great the rocket will therefore be subject to excessive "weathercocking", or turning into the wind during flight. This impairs altitude performance, makes recovery difficult, and can be dangerous. Most designers soon learn to steer clear of configurations like that of illustration C in Figure 50.

There is, of course, a better way to obtain a large corrective moment coefficient. The value of C_l , you will recall, increases as the square of the airspeed. This does not necessarily indicate that the "way to go" in model rocket design is to try for the highest possible velocities throughout the flight. While high burnout velocity generally means higher altitude, excessive accelerations achieved at the expense of burnout altitude cause excessive aerodynamic drag which can actually cause the

altitude achieved to be reduced. What it does mean is that you should observe a reasonable minimum in the velocity at which your rocket leaves its launcher. Model rocket engines with end-burning grains are designed with a small port at the after end of the grain, just inside the nozzle. The purpose of this, besides providing a place to pack the igniter, is to provide a high initial thrust to achieve a substantial airspeed -- and thus a substantial corrective moment -- before the guiding influence of the launcher is left behind. You can best take advantage of this initial thrust peak by providing a long enough launching device and avoiding excessive liftoff weight, thereby insuring that your rocket leaves its launcher at a sufficient velocity to be stable. 9 meters per second should be considered a minimum safe launch speed, and 12 meters per second, if possible, would be advisable. If you are using a core-burning engine, of course, velocities on this order should never be a problem.

Reducing the corrective moment coefficient by reducing the static stability margin will cause the natural frequency to decrease. As the center of pressure moves forward and approaches the center of gravity, the damping ratio will increase, lowering the actual frequency of oscillation until overdamping occurs. Moving the center of pressure still further forward will result in neutral, and finally negative, static stability. Only the novice designer is ever caught making an error of this kind, and when he does the result is spectacular. "Going ape" is the colorful and appropriate phrase applied by the model rocketeer to the behavior of a statically-unstable

rocket such as the one appearing in illustration D of Figure 50.

The damping moment coefficient may be increased by the addition of fin area or the movement of fins to a position farther from the rocket's C.G., in the same way that the static stability margin is increased. Adding large amounts of fin area both forward and aft of the center of gravity, however, and the use of excessive fin area in general, will tend to increase the damping moment coefficient without a commensurate increase in corrective moment coefficient. Dynamically, up to a point (the point at which the damping ratio becomes .7071) this is good. Ballistically, however, such large surfaces are almost always associated with a decrease in altitude because of excessive drag. Working at such high damping ratios is not a good idea in general anyway, because a slight change of design or modification to a rocket in service or under construction could well send it "over the line" into an overdamped configuration. Rocket E of Figure 50 is an example of what the designer may wind up with if he is too liberal with his sheet balsa.

The damping moment coefficient, insofar as it is dependent on fin geometry, may be reduced by making certain that all fin area is aft of the center of gravity but not greatly distant from it. Since placing the fins relatively near the center of gravity tends to reduce the corrective moment coefficient also, this procedure may not always reduce the damping ratio and may even increase it. Reducing the damping ratio to very small values is not a good idea in any case, since under these conditions the oscillations of a deflected rocket persist for a long time

and resonance becomes destructively severe. Making the damping moment coefficient too small thus has the same effect as making the longitudinal moment of inertia too large. The rocket of illustration F in Figure 50 has had its damping ratio made too small by placing the fins insufficiently far from the center of gravity. While the designer has apparently been able to keep the static stability margin adequate, his rocket will not be a good performer. Much of its trajectory will be spent oscillating in response to various disturbances even if it does not happen to develop a resonant roll rate -- in which case its useful operating life will be short indeed.

The limitations of reasonable design and the standardization of component proportions arising from mass-produced model rocket supplies do not really leave much leeway for regulating the radial moment of inertia independently of the longitudinal moment of inertia. Assuming that I_R could be substantially reduced, the effect of such a reduction would be negligible since I_R is so small to begin with. The radial moment of inertia could conceivably be greatly increased by placing weighted pods, or "bobs" at the tips of the fins, but there would be no point in doing so. No advantage would be gained if the rocket were properly designed to begin with; in fact there would be some unfavorable consequences attendant upon such a modification. The rate of decay of the rocket's oscillations would be suppressed by gyroscopic moments if it were rolling, and its roll-induced resonance would be much more severe than its non-rolling resonant behavior.

6.3 Rolling Rockets

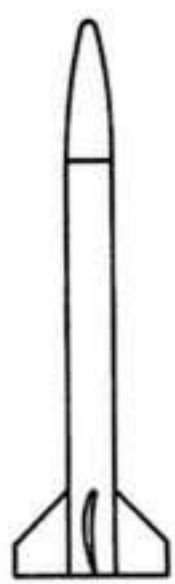
My last statements above were, of course, promulgated on the assumption of a statically-stable rocket. In cases of insufficient, neutral, or negative static stability it is necessary to induce a rapid spinning of the rocket about its centerline in order to generate the stability-like effect described in Section 3.2.5. The extent to which stability is effected by this artifice is dependent, it will be recalled, on the magnitude of the product of I_R and ω_z . It is thus desirable to have a rapid spin, a high radial moment of inertia, or both. Successful spin-stabilized rockets and projectiles tend to be short, squat, and heavy. It is this fundamental difference in the physical mechanism by which stable behavior is produced that accounts for the configurational differences between aerodynamic vehicles such as sounding rockets and objects such as artillery shells. Well-designed sounding rockets are long in relation to their diameters, while artillery shells are short. Why the difference? The reason, of course, is that the sounding rocket is aerodynamically stable while the artillery shell is not. It is an advantage to the shell to have a large diameter in relation to its length because this means a large radial moment of inertia, facilitating spin stabilization. The sounding rocket, on the other hand, performs best at a higher slenderness ratio since it relies on the corrective and damping characteristics due to its fins and on its high longitudinal moment of inertia for favorable dynamic response, not to mention the great advantage in altitude capability that goes with a more slender profile.

Stabilization is not, however, the only motive for inducing

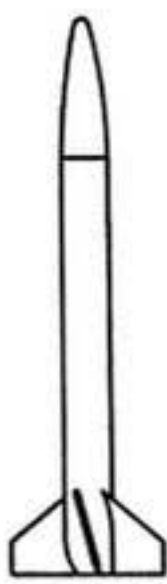
spin in model rockets. It has been found that rolling models are less subject to "dispersion" by horizontal winds and tipoff during launch and staging than those which are not, where by "dispersion" I mean the horizontal displacement of the rocket at the time of recovery system actuation. The roll rates used in dispersion-reduction are much lower than those used in roll stabilization, since the rockets to which they are applied are already statically stable; the inertial effect is generally slight and its only purpose is to induce just enough roll coupling to distribute the effects of disturbances in a radially symmetrical fashion about the intended axis of flight.

A roll rate may be induced in a model rocket in a variety of ways. The major aerodynamic techniques in current use include "spinnerons" (that is, fin tabs), canted fins, and airfoiled fins as illustrated in Figure 51. Canted main propulsion or outrigger engines have also been used to "spin up" model rockets, and from time to time flywheel-like devices have appeared whereby a product $I_R \omega_z$ other than that of the rocket airframe itself has been used to provide inertial coupling. The number and variety of roll-inducing techniques possible is so great, indeed, that it is impossible to write down any single analytical expression accounting for them all. In the particular case of spin produced by canting each fin of a rocket at some angle θ to the longitudinal axis, however, Barrowman analysis permits computation of the equilibrium roll rate in the form

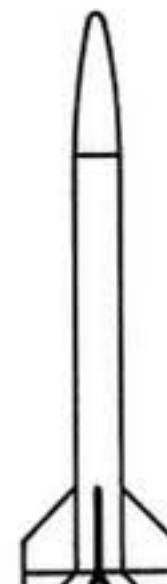
$$(115) \quad \omega_z = \frac{12 \theta V A_r \bar{T}_r k_r}{S C_r k_d [(1+3\lambda) S^2 + 4(1+2\lambda) S r_t + 6(1+\lambda) r_t^2]}$$



Airfoiled fins



Canted fins



Spinnerons

Figure 51: Aerodynamic techniques used for inducing roll in model rockets.

where k_r , the roll forcing interference coefficient, is given by

$$(116) \quad k_r = \frac{1}{\pi^2} \left[\frac{\pi^2}{4} \left(\frac{\tau+1}{\tau} \right)^2 + \frac{\pi}{\tau^2} \left(\frac{\tau+1}{\tau-1} \right)^2 \arcsin \left(\frac{\tau^2-1}{\tau^2+1} \right) - \frac{2\pi}{\tau} \left(\frac{\tau+1}{\tau-1} \right) + \frac{8}{(\tau-1)^2} \ln \left(\frac{\tau^2+1}{2\tau} \right) \right. \\ \left. + \left(\frac{\tau^2+1}{\tau(\tau-1)} \right)^2 \left(\arcsin \frac{\tau^2-1}{\tau^2+1} \right)^2 - \frac{4(\tau+1)}{\tau(\tau-1)} \arcsin \left(\frac{\tau^2-1}{\tau^2+1} \right) \right]$$

and k_d , the roll damping interference coefficient, is

$$(117) \quad k_d = 1 + \frac{\frac{\tau-\lambda}{\tau} - \frac{1-\lambda}{\tau-1} \ln \tau}{\frac{(\tau+1)(\tau-\lambda)}{2} - \frac{(1-\lambda)(\tau^3-1)}{3(\tau-1)}}$$

\bar{Y}_t is given by equation (90), λ is the ratio c_t/c_r , and τ is the ratio $(s+r_t)/r_t$. The reader should refer back to Section 4.1 for additional information concerning the notation used in equations (115) through (117).

Given the ability to regulate the roll rate of his rocket, the designer will next want to know what roll rates are favorable to good performance. This question is generally answered by eliminating those ranges of roll rate which are deleterious to good performance and stating that the ranges then remaining are acceptable. The roll rate that should be avoided at all costs is, of course, the roll-coupled resonant rate. In models where roll is produced by fin canting this is relatively easy to do, as both the resonant frequency and the roll rate are linear functions of airspeed. ω_z can thus be kept as nearly zero as possible (the most common course of action), uniformly much lower than ω_{rc} (the technique adopted when dispersion-reduction is desired), or uniformly much higher than ω_{rc} . This last technique is not recommended, as it results in large coupling moments, a high-drag configuration, and (often) tangling of the shrouds of parachute recovery systems. The selection of

available relations between ω_z and ω_{mc} in rockets whose roll rate is set by fin canting is illustrated in Figure 52. Perhaps you can now see the danger of resonance associated with too high a value of I_L : a very high longitudinal moment of inertia means a very low resonant frequency, and it is entirely possible that small fin cant angles arising from imperfections in construction will be just sufficient to produce the low spin rate needed for resonance.

In cases where it is desired to stabilize a statically-unstable design by inducing roll, there is of course no resonance problem. The fin cant angles and spin rates required for roll stabilization are very high, though, and this means very poor altitude performance and a high probability of tangling the recovery system shrouds at ejection. The relative ease with which positive aerodynamic stability can be achieved by proper design procedures and the relatively poor performance of unstable rockets which require high roll rates for spin stabilization make it really inexcusable to use roll stabilization as the primary means of achieving a predictable flight path. Spin stabilized rockets are to be regarded as curiosities, in the final analysis suitable only for demonstration purposes.

6.4 Design Procedures and Criteria

With the results of all our investigations now lying ready to hand, it is possible to formulate a rational procedure permitting the modeler to design, with a high degree of confidence, a model that will behave both ballistically and dynamically in a favorable manner. Such a method, suitable for all general-purpose design and competition work, may be summarized as follows:

6.4.1 Design Definition; Center of Gravity and Moments of Inertia

Define, as nearly as possible, the purpose of the proposed model. Is it to be, for instance, used in altitude or payload competition, for photographic or sounding work, or some other "mission"? Need it be staged? Should it be clustered? What must be the payload capacity, if any? What recovery system is to be used? The answers to questions such as these will roughly define the size and shape of the rocket's body and nose sections. A preliminary drawing can then be made showing the body and nose and all the components contained within them or of which they are comprised (engines, payload, bulkheads, etc.). A preliminary estimate of the C.G. location and moments of inertia of the design thus far evolved should then be computed.

6.4.2 Static Stability Margin

Add a fin design to the drawing and compute the various normal force coefficients and C.P. locations of the components and of the complete rocket by the Barrowman method. If the rocket is multistaged it will be necessary to perform the calculations for each configuration of stages in which the model is intended to fly. The C.P. should lie between one and two calibers behind the C.G.; if it is outside this range, try a new design. In contest or record work, where reduction of weathercocking is of paramount importance, many designers prefer to try for precisely one-caliber stability.

6.4.3 Damping Ratio

Using the information obtained thus far, compute the corrective moment coefficient and the damping moment coefficient

according to the methods outlined in Section 4. From these and the moments of inertia compute the damping ratio and the coupled damping ratio. Check to insure that the coupled damping ratio is not less than 0.05 and that the decoupled damping ratio is not greater than 0.30. A too-low damping ratio can be cured by lightening the rocket and increasing its fin area; an excessively high one by adding weight to the nose and decreasing the fin area. While damping ratios up to 1.0 would be theoretically permissible, I have established an upper limit of 0.30 because it is my considered opinion that more heavily damped rockets are likely to be too light for good ballistic performance. The resonant deflection of the rocket's centerline from its intended flight path at a damping ratio of 0.3 is only 1.746 times the deflection a static disturbance would produce (see Figure 49). It should thus not really be necessary to use damping ratios higher than this value. In accepting a lower limit of 0.05, on the other hand, you will really be pushing the builder's art; the roll-coupled resonant deflection will be ten times the static deflection due to a given disturbance. Assuming that a carefully-built model will incorporate unintentional asymmetries causing static deflections of no more than one-half of one degree, a damping ratio of 0.05 will permit such a model experiencing roll-coupled resonance to precess about its flight direction with a cone half-angle of five degrees. Clearly, this is about the most we can accept.

6.4.4 Roll Rate

Determine whether it is desirable to induce a roll rate in your vehicle for the reduction of dispersion and tipoff.

Such a determination will be almost entirely a matter of your opinion as a designer, since the tradeoff between control of roll rate and control of static stability margin as a means of reducing dispersion is extremely subtle. The decisions of most designers seem to run in favor of roll rate control only in the case of multistaged models. If you decide to induce a roll rate by means of canted fins, compute the fin angle required for the linear velocity-dependence you desire, being careful to keep away from the resonant frequency. The analytical prediction of roll rates due to other means must await further advances in the state of our technology.

6.4.5 Construction and Testing

When the above steps are completed and the dynamic parameters of the proposed design have been found to be **satisfactory**, construction can be started. It would be desirable to measure the C.G. location and moments of inertia at several stages during the construction, and to measure the dynamic parameters of the completed model before the first flight to check the accuracy of the estimates and calculations. Barring any major errors in these, the design determined by the above method will be sound.

In practice, of course, a wide variation in design procedures will be found to be acceptable. The designer of a sport model need only be concerned with the static stability margin, while competition and research modelers will want to make full use of all the available analytical techniques in adjusting their designs for the greatest possible fulfillment of the missions for which they are designed. As our technology advances it may

be expected that many designers will have recourse to parametric data generated by automatic computation as they apply ever more detailed design procedures to the challenging problems of model rocket optimization.

REFERENCES

1. Barrowman, James S., The Practical Calculation of the Aerodynamic Characteristics of Slender Finned Vehicles, a Dissertation Submitted to the Faculty of the School of Engineering and Architecture of the Catholic University of America in Partial Fulfillment of the Requirements for the Degree of Master of Science in Aerospace Engineering, Washington, D.C., March 1967.
2. Barrowman, James, Calculating the Center of Pressure of a Model Rocket, Centuri Engineering Company Technical Information Report TIR-33, 1968.
3. Clark, Robert N., Introduction to Automatic Control Systems, John Wiley and Sons, Inc., New York, 1962.
4. Davis, L. Jr., Follin, James W. Jr., and Blitzer, Leon, The Exterior Ballistics of Rockets, D. Van Nostrand Company, Inc., Princeton, New Jersey, 1958.
5. Gurkin, Luther W., "Basic Missile Aerodynamic Stability", paper presented at the Sixth Annual National Model Rocket Championship Meet, NASA Wallops Station, Virginia, 1964.
6. Halfman, Robert L., Dynamics: Particles, Rigid Bodies, and Systems, Volume 1, Addison-Wesley Publishing Company, Inc., Reading, Massachusetts, 1962.
7. Mandell, Gordon K., "Fundamentals of Dynamic Stability", series in Model Rocketry, October 1968-March 1969, Model Rocketry, Inc., Cambridge, Massachusetts, 1969.
8. Mandell, Gordon K., "Inertias by Torsion Wire", in Model Rocketry, April, 1969, Model Rocketry, Inc., Cambridge, Massachusetts, 1969.
9. Stine, G. Harry, "Model Missile Design", in American Modeler, July, 1958, The Conde-Nast Publications, Inc., New York, 1958.
10. Stine, G. Harry, "'Ogive' Me a Ring-Tailed Cylindrical Bird", in American Modeler, November, 1958, The Conde-Nast Publications, Inc., New York, 1958.
11. Stine, G. Harry, Handbook of Model Rocketry, First Edition, Follett Publishing Company, Chicago, 1965.

CHAPTER 3

THE AERODYNAMIC DRAG OF MODEL ROCKETS

William P. Bengen

SYMBOLS

<u>Symbol</u>	<u>Meaning</u>
A	area
A_c	face area of elastic cube
A_{lug}	frontal area of launch lug
A_r	reference area for determining drag coefficient
R	aspect ratio
ΔR	change in effective aspect ratio due to lateral displacement of tip vortices
B	function of critical Reynolds number used in analysis of boundary-layer transition
C_D	coefficient of drag
C_{Db}	base drag coefficient
$(C_{Db})_m$	base drag coefficient based on maximum frontal cross-sectional area
$C_{D_B}(\alpha)$	coefficient of body drag due to angle of attack
C_{Dc}	cross-flow drag coefficient of a circular cylinder of infinite length
C_{Df}	forebody drag coefficient; also fin friction drag coefficient based on area of one side of fin
ΔC_{Df}	increase in fin friction drag coefficient due to the effect of fin thickness
C_{Df}'	fin friction drag coefficient corrected for the effect of fin thickness
C_{DI}	coefficient of interference drag at zero angle of attack
$(C_{Df})_b$	forebody drag coefficient as used in Datcom equations
C_{Di}	induced drag coefficient of fins based on fin area in side view

<u>Symbol</u>	<u>Meaning</u>
C_{D1}'	induced drag coefficient of fins based on maximum frontal cross-sectional area
$(C_{D1}')_{\text{cant}}$	increase in drag coefficient due to canting of fins
$(C_D)_{\text{lug}}$	drag coefficient of launch lug based on lug frontal area
$(\Delta C_D)_{\text{lug}}$	increase in vehicle drag coefficient based on maximum frontal cross-sectional area, due to the presence of a launch lug
$(C_{D0})_B$	body drag coefficient at zero angle of attack
$(C_{D0})_F$	fin drag coefficient at zero angle of attack
$(C_{D0})_{FB}$	drag coefficient of fin/body assembly at zero angle of attack
C_{Ds}	subsonic drag coefficient
C_{Dv}	friction drag coefficient
$C_{D\alpha}$	coefficient of drag due to angle of attack
C_f	skin friction coefficient
C_{fb}	forebody friction drag coefficient based on cross-sectional area of base
$(C_f)_B$	skin friction coefficient of body
ΔC_f	change in skin friction coefficient
$(C_f)_F$	skin friction coefficient of fins
$(C_f)_{\text{lam}}$	laminar skin friction coefficient
$(C_f')_{\text{lam}}$	corrected laminar skin friction coefficient
$(\Delta C_f)_{\text{lam}}$	increase in laminar skin friction coefficient due to 3-dimensional effects
$(C_f)_{\text{turb}}$	turbulent skin friction coefficient
$(C_f')_{\text{turb}}$	corrected turbulent skin friction coefficient
$(\Delta C_f)_{\text{turb}}$	increase in turbulent skin friction coefficient due to 3-dimensional effects
C_L	coefficient of "lift" or side force

<u>Symbol</u>	<u>Meaning</u>
C_p	coefficient of pressure
D	drag
D_a	approximating function for drag based on the assumption of a constant drag coefficient
D_b	base drag
D_e	exact drag as determined by Datcom method
D_f	pressure foredrag
D_p	pressure drag
D_v	skin friction drag
D_{α}	drag due to angle of attack
E	modulus of elasticity
F	shearing force
G	torsional or shear modulus of elastic solid
$\left\{ \begin{matrix} G_1() \\ G_2() \\ G_3() \\ G_4() \\ G_5() \end{matrix} \right\}$	drag coefficients expressed as functions of Datcom parameters
$\left\{ \begin{matrix} H_1() \\ H_2() \\ H_3() \\ H_4() \\ H_5() \\ H_6() \end{matrix} \right\}$	drag coefficients expressed as functions of Datcom parameters for General Configuration Rocket
$K_B(F)$	body side force interference factor
$K_F(B)$	fin side force interference factor
L	characteristic length

<u>Symbol</u>	<u>Meaning</u>
M	Mach number
P	perimeter of body cross section
R	Reynolds number
R_c	Reynolds number based on fin chord
R_{crit}	critical Reynolds number
R_k	roughness Reynolds number
$(R_k)_t$	critical roughness Reynolds number
R_ℓ	Reynolds number based on length
R_x	local Reynolds number based on longitudinal coordinate
S	surface area
S_b	base cross sectional area
S_E	exposed planform area of all fins
S_e	exposed fin planform area in side view
S_F	planform area of fins in side view, including "hidden" area projected within body; <u>also</u> total planform area of all fins as used in Datcom equations
S_m	maximum frontal cross sectional area of body
S_0	frontal cross sectional area of body at x_0
S_s	forebody wetted area
S_x	frontal cross sectional area of body at x
T	temperature
$T_{std.}$	temperature of standard, sea-level atmosphere
U	free-stream longitudinal velocity, airspeed
U_∞	free-stream longitudinal velocity as used in boundary layer analysis
V	volume; <u>also</u> velocity
\vec{V}	vector velocity

<u>Symbol</u>	<u>Meaning</u>
ΔV	change in volume
V_0	initial volume
b	span; <u>also</u> width
c	speed of sound; <u>also</u> fin chord
$c_{std.}$	speed of sound in standard, sea-level atmosphere
$d(\)$	differential of ()
$d(\)/d(\)$	derivative
$d^2(\)/d(\)^2$	second derivative
d_b	base diameter
$d_{equiv.}$	equivalent diameter
d_{lug}	diameter of launch lug
d_m	maximum diameter of body, used as reference diameter in Datcom equations
d_r	reference diameter
$f(\)$	function of ()
g	acceleration of gravity
h	height or thickness of fluid layer; <u>also</u> height of control volume in momentum-integral boundary layer analysis
k	drag parameter as used in Chapter 4
k_{adm}	admissible roughness height
k_{crit}	critical height of transverse cylindrical roughness element
k_t	critical height of distributed roughness particles
(k_2-k_1)	apparent mass factor
l	length; <u>also</u> distance measured around body profile, starting at nose
l_b	body length
l_T	length of boattail

<u>Symbol</u>	<u>Meaning</u>
n	rotation rate, revolutions per second
n	unit normal vector
p	pressure
Δp	change in pressure
p_b	base pressure
p_o	ambient static pressure
p_s	static pressure
p_s (stag.)	static pressure at a stagnation point
p_{tot}	total pressure
p_∞	free-stream static pressure
q	dynamic pressure
Δq	change in dynamic pressure
r	radius
r_x	radius of body at station x
s	distance coordinate measured along surface
t	time; <u>also</u> fin thickness
t	unit tangent vector
u	longitudinal component of flow velocity; <u>also</u> circumferential velocity of the surface of a spinning rocket
u_k	longitudinal flow velocity at the top of a roughness element
v	transverse component of flow velocity
x	longitudinal coordinate; <u>also</u> distance fallen by rocket undergoing a drop test
x_{crit}	longitudinal location of transition point
x_0	longitudinal station on body where flow ceases to obey potential theory
x_1	station on body where dS_x/dx first reaches its minimum value

<u>Symbol</u>	<u>Meaning</u>
y	coordinate perpendicular to surface
$\Delta()$	change in ()
α	angle of attack; <u>also</u> $f''(0)$ in Blasius boundary-layer analysis
$\bar{\alpha}$	average effective angle of attack
γ	engineering shear strain
δ	boundary layer thickness
ϵ	boattail angle; <u>also</u> parameter of drag due to angle of attack as used in Chapter 4
η	dimensionless coordinate perpendicular to surface; <u>also</u> ratio of cross-flow drag on a cylinder of finite length to cross-flow drag on a cylinder of infinite length
η_B	η as defined in Blasius analysis, $2\eta_3$
η_k	nondimensional roughness height
η_3	η as used in reference 3
θ	deformation angle of elastic solid; <u>also</u> momentum thickness of boundary layer; <u>also</u> angle of fin cant
μ	absolute viscosity
ν	kinematic viscosity
ρ	mass density
$\Delta\rho$	change in mass density
ρ_0	initial mass density
$\rho_{std.}$	mass density of standard sea-level atmosphere
σ_E	exposed planform area of one fin
σ_F	planform area of one fin, including projected area "hidden" within body
τ	shearing stress
τ_0	shearing stress at surface

<u>Symbol</u>	<u>Meaning</u>
τ_{ok}	surface shear stress at station of roughness element
ϕ	angle of deviation between perpendicular to free stream and perpendicular to surface
φ	central angle of a point on the surface of a cylinder held transverse to the stream, measured from the stagnation point
ψ	streamfunction
ω_z	rotation rate, radians per second
$\partial()$	partial differential of ()
$\partial()/\partial()$	partial derivative
$\partial^2()/\partial()^2$	second partial derivative
	infinity

THE AERODYNAMIC DRAG OF MODEL ROCKETS

Introduction

Like stability, aerodynamic drag has been a topic of intense interest in the field of model rocketry since the hobby was in its infancy in the late 1950's. One does not have to look very far to find the reason for such interest: model rockets, owing to their lightweight construction and the fact that their operation is restricted to flight entirely within the lower reaches of the atmosphere, are more strongly affected by atmospheric resistance than any other type of ballistic, rocket-propelled vehicle. The influence of drag upon the altitude performance of a model rocket is not a slight correction, but a major controlling factor, and no modeler who is seriously interested in accurate predictions of altitude capability can afford to ignore it or dismiss its effect lightly.

The early recognition of this fact by members of the National Association of Rocketry during the first year of that organization's existence led in 1958 to the first wind-tunnel test of a model rocket to determine its coefficient of drag. The results of this test sequence, performed on a model of the Aerobee-Hi sounding rocket in the subsonic wind tunnel of the United States Air Force Academy, were published that same year by G. Harry Stine in the first NAR Technical Report, "Basic Model Rocket Flight Calculations". The same document contained

the observation that aerodynamic drag is responsible for lowering the maximum altitude of a typical model rocket by more than 50%, and an expanded discussion of the same material contained in Stine's Handbook of Model Rocketry (First Edition, 1965) reported altitude reductions due to drag of more than 90% in cases of exceptionally poor design.

The Aerobee-Hi tests remained nearly the sole source of experimental model rocket drag data for the next eight years. From time to time various modelers would construct home-built wind tunnels and balance systems in an effort to obtain more data; most of these test facilities, however, were too crude to provide a low enough air turbulence level for accurate measurements. Whatever valid data were obtained, moreover, appeared to receive only local attention, and virtually no modelers attempted to adapt theoretical or semiempirical analytical treatments of the drag problem to cases of model rocket flight. During the winter of 1965-1966, however, the NARHAMS Section of the National Association of Rocketry constructed a single-return-flow, low-speed wind tunnel with sufficiently low air turbulence to permit relatively accurate measurements of model rocket drag coefficients. Mark Mercer of that section subsequently conducted an extensive parametric investigation of various modified forms of the Javelin, a commercially-available kit produced by the Centuri Engineering Company of Phoenix, Arizona. The results of his tests, incorporated by Douglas J. Malewicki into Centuri's Technical Information Report TIR-100, Model Rocket Altitude Performance, represent the most complete

set of experimental data on model rocket drag available to date.

During the same period, serious analytical and semiempirical studies of the model rocket drag problem first began to appear. The Research and Development competition event at the Eighth Annual National Model Rocket Championships in 1966 saw the presentation of a paper by Dr. Gerald M. Gregorek of Ohio State University, entitled "A Critical Examination of Model Rocket Drag for Use with Maximum Altitude Performance Charts". Dr. Gregorek's paper, a milestone in the hobby comparable to the advent of Barrowman analysis in stability determination, and to Malewicki's publication of altitude graphs based on closed-form solutions to the equations of vertical motion for model rockets, presented a semiempirical method for calculating the drag coefficient of a model rocket based on the United States Air Force Stability and Control Datcom (Datcom being an acronym for Data Compendium). The Gregorek treatment deserves credit, not only for being the first in-depth, analytical discussion of the topic of model rocket drag, but also for motivating the growing body of literature on the subject that has appeared in the hobby since the original paper was presented and subsequently, widely circulated among interested local sections of the National Association of Rocketry. Since its first appearance in 1968, the periodical Model Rocketry has carried a number of articles concerned with the topic of drag coefficient determination by both experimental and analytical means. Contributors to the literature over the past three years have included George J. Caporaso, Douglas J. Malewicki, Forrest M.

Mims, Thomas T. Milkie, Gary Schwede, Dr. Gregorek himself, and several others. It is in this atmosphere of increased interest in the determination of model rocket drag properties to a high degree of precision that the present chapter has been written.

The treatment to be presented here is divided into eight major sections, of which the first is a basic survey of the properties and importance of model rocket drag. Section 2 presents discussions of the basic concepts -- drag coefficient, Reynolds number, and so on -- which will be employed repeatedly in the subsequent sections. Sections 3 and 4 contain analyses of the two major contributions to drag at a zero angle of attack: pressure forces and skin friction, while Section 5 examines drag due to the side force (or "lift") on a yawed rocket, drag due to nonzero roll rate, and drag due to surface roughness. Section 6 contains information of use in the practical calculation of drag coefficients for specific model rockets. I have, for this purpose, used a slight modification of the USAF Stability and Control Datcom method which is applicable to the regime of relatively low Reynolds numbers (usually under 3×10^6) typically encountered in model rocketry. In Section 7 a semiempirical method of accounting for the effects of compressible airflow on the drag coefficients of extremely high-performance model rockets is considered, and the chapter is concluded with a survey of experimental methods for the determination of model rocket drag.

The accurate determination of model rocket drag requires a rather precise knowledge of the airflow pattern which exists

around the vehicle in question. This, in turn, must be determined by applying the theories of fluid dynamics -- that branch of mathematical physics which concerns itself with the study of liquids and gases in motion. The general equations of fluid dynamics, named the Navier-Stokes equations in honor of those who first formulated them in the mid-Nineteenth Century, are among the most complex and difficult known to man. A strongly coupled set of nonlinear, partial differential equations with nonconstant coefficients, they have never been solved in their full generality. Even most of the highly-specialized approximations to these equations used in determining model rocket drag are therefore quite complicated and require the methods of calculus for their solution. Mathematical derivations employing calculus have been used freely throughout the chapter for the benefit of those advanced readers who have an interest in them and who require some analytical justification for the conclusions eventually reached through their application. Those who have no knowledge of (or interest in) advanced mathematics need not give up in despair, however, for the equations ultimately derived by all the calculus manipulation -- the equations actually used in the calculation of model rocket drag coefficients -- are all algebraic and capable of being solved by anyone who has had **the first year** of high school algebra.

A number of books and papers have been used as references in the compilation of this chapter. Rather than refer to each one by name as material based on it is presented, I have cited references by footnote numbers. The work identified by

a given number may be found by consulting the reference list at the end of the chapter.

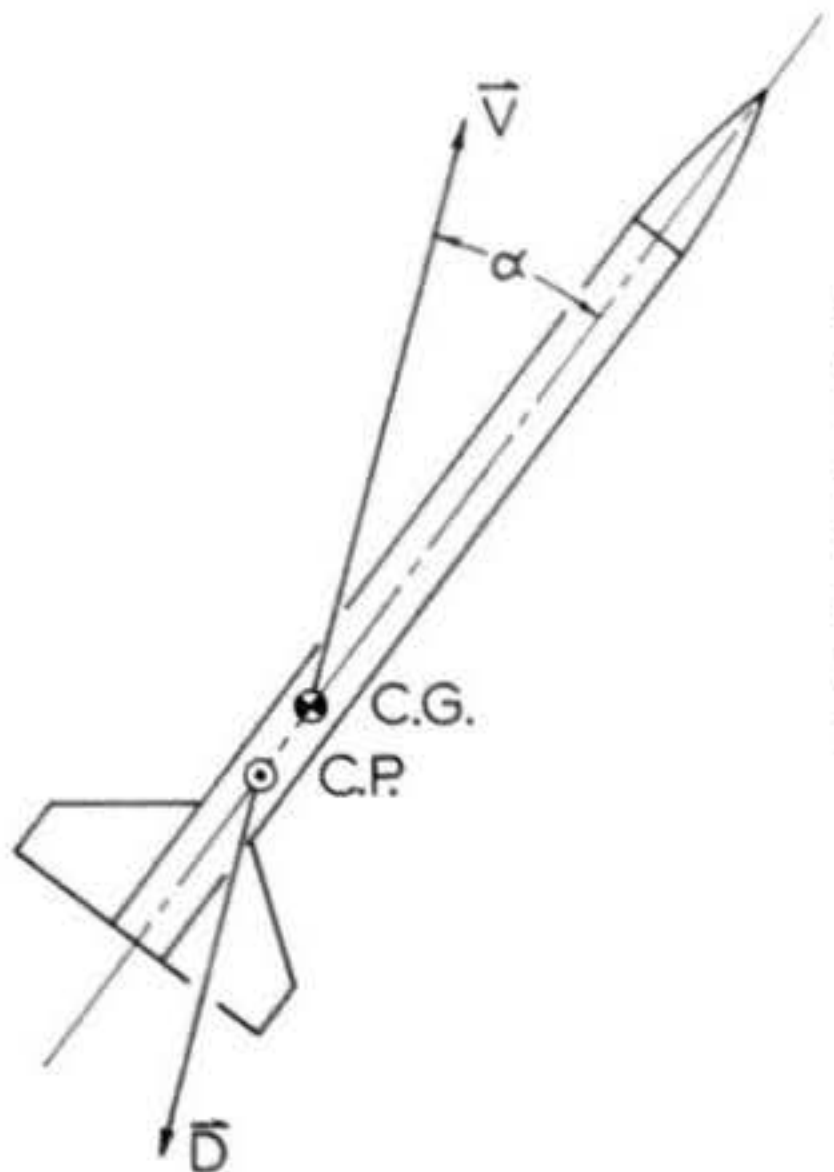
1. Basic Considerations

The study of drag forces on model rockets is one of the most difficult, exciting, and important problems facing the modeler today. The amount of experimental work of significant value which has been accomplished in this field is relatively limited; many questions remain unanswered, and many of the physical phenomena involved are imperfectly understood. My intention in writing this is not to close the question of model rocket drag, but to provide basic information and methods which, it is hoped, will be extended, refined, improved upon and added to by modelers engaged in future serious research. The reader is encouraged to view all applications of theory to model rockets presented in the following pages with a critical eye, for until a really sizeable body of experimental data is available, many conclusions must remain tentative and subject to revision.

By definition, drag is the sum of the components of all the aerodynamic forces acting on a body parallel to its instantaneous velocity vector with respect to the air. The algebraic sign of any component of drag is taken as positive when it acts in a direction opposite to the direction of the model's motion. Defined in this manner, the total drag of any body is, of course, positive. The drag of a model rocket is a complicated function of its size, shape, finish, velocity, and angle of attack, and of the thermodynamic state of the air.

Even for relatively simple rocket shapes, the relationship between drag and the variables upon which it depends is virtually impossible to predict with any precision on a purely theoretical basis. Resort must be had to semiempirical methods -- composites of theoretical predictions and experimental data -- like the one employed in Section 6; hence the need for extensive experimental research on model rocket shapes, to confirm (or if necessary, correct) any such method. In Figure 1 the definition of drag (which is considered to originate from the model's center of pressure, or C.P.), and the multiplicity of factors which determine its magnitude, have been illustrated.

Because of their lightweight, low-density construction, model rockets have lower ratios of weight to frontal and surface area than any other class of ballistic, rocket-propelled bodies. Hence, aerodynamic drag has a greater influence on the flight of model rockets than it does on the flight of other rocket-propelled vehicles. In a typical model rocket at burnout, the drag is of the same order of magnitude as the weight, and thus has a considerable effect on the coasting portion of the model's flight. During the powered portion of flight, when the engine is providing a thrust that is normally eight or ten times the model's weight, the influence of drag is of course lessened; its effect on the overall flight performance, however, is always considerable, and it is a rare occurrence for a model rocket to reach more than half the altitude it could have achieved, were aerodynamic drag altogether absent. In some high-performance models, moreover, the drag can become



Drag is determined by:

- rocket size
- rocket shape
- airspeed
- finish smoothness
- angle of attack (α)
- density of air
- viscosity of air
- speed of sound

Figure 1: Definition of drag and the variables that determine its magnitude. The size, shape, surface finish, and to some extent the airspeed and angle of attack of the rocket are under the designer's control. The atmospheric density and viscosity, and the speed of sound, are properties of the medium to which model rocket flight is confined. The sound speed influences drag through its relation to compressibility effects.

much greater than the weight, so that the drag and weight taken together are equal and opposite to the thrust of the engine.

This condition creates a terminal velocity which the rocket cannot exceed, even if the burning time of the engine is relatively long. The minimization of aerodynamic drag is, therefore, one of the prime considerations in the design of high-performance model rockets.

Analytical knowledge of the physical phenomena which underlie drag is, like most scientific knowledge, of interest for its own sake. More important to the model rocketeer, however (and the reason it is presented in this book), is that it has distinctly practical applications in the design of rockets. It helps to explain, for instance, why rounded nosecones, streamlined fins, and smooth surface finishes -- features which have been advocated for years -- are in fact effective means of reducing the drag. As another example, it is impossible to predict the drag of a rocket accurately without an understanding of the boundary-layer approximation, and of the transition phenomenon characteristic of boundary-layer flow in the Reynolds number regime in which model rockets operate. And so it is that rather extensive use of mathematical derivation, though admittedly burdensome to the average hobbyist, is unavoidable in any thorough discussion of model rocket drag. I reiterate, however, that one need not be a mathematician to make use of the information contained herein. Remember that we are taking a basically engineering approach: we are interested in the results of the mathematical derivations. And in each case

and each constituent of aerodynamic drag considered, it will be found that these results are no more difficult to work than, say, the equations of Barrowman analysis.

2. Basic Concepts Relating to the Study of Drag

This section will lay the foundation for a detailed analysis of drag forces by presenting a number of basic concepts and ideas. Section 2.1 will examine certain physical properties of the atmosphere, and the variation of these properties as they affect calculations of drag (and hence, altitude performance). The dimensionless quantities defined and discussed in Section 2.2 will be used extensively in succeeding sections, particularly the Reynolds number R and the drag coefficient C_D . Section 2.3 concludes the treatment of basic concepts with a discussion of the scheme by which the total drag force is separated into components and analyzed in later sections.

2.1 Atmospheric Properties for Model Rocket Flight

The physical properties of the atmosphere of greatest interest to model rocketry are its mass density ρ , its absolute coefficient of viscosity μ , and the ratio between these two quantities, the kinematic viscosity $\nu = (\mu/\rho)$. Hence we shall restrict our attention to phenomena associated with these variables.

The atmospheric data presented herein is based on the United States Standard Atmosphere, 1962 (19), whose figures have been converted to MKS (meter-kilogram-second) metric units for model rocketry work. This model of the atmosphere,

based partly on experimental data, is an "idealized, middle latitude (approximately 45°) year-round mean over the range of solar activity between sunspot minima and maxima" (19). The assumed sea-level temperature for the tabulations is 59° Fahrenheit (15° Celsius or 288° Kelvin), with a standard sea-level pressure of 101,325 newtons per square meter (the MKS equivalent of the familiar 14.7 pounds per square inch).

2.1.1 Density

A measure of the drag force exerted on a rocket is the total momentum the rocket imparts to the originally stationary fluid through which it travels. Momentum is directly proportional to the mass of the fluid displaced; and since the density of a fluid is simply its mass per unit volume, its connection with drag is established. As mentioned in Chapter 1 and shown later in this chapter, the overall drag on a model rocket is directly proportional to the mass density of the air through which it flies.

Atmospheric density generally decreases with altitude, as seen in Figure 2. At an altitude of 300 meters, ρ departs from its sea-level value by just under 3%. At 1000 meters, a respectable altitude for a model rocket, the deviation is just over 9%. By the time a height of 3000 meters, the practical altitude limit for a model rocket, is reached the density has decreased by 25.6%. Except in cases of extremely high performance models, the variation in atmospheric density during the course of a flight is rarely considered. It is, however, fairly common for modelers to account for the elevation of their launch

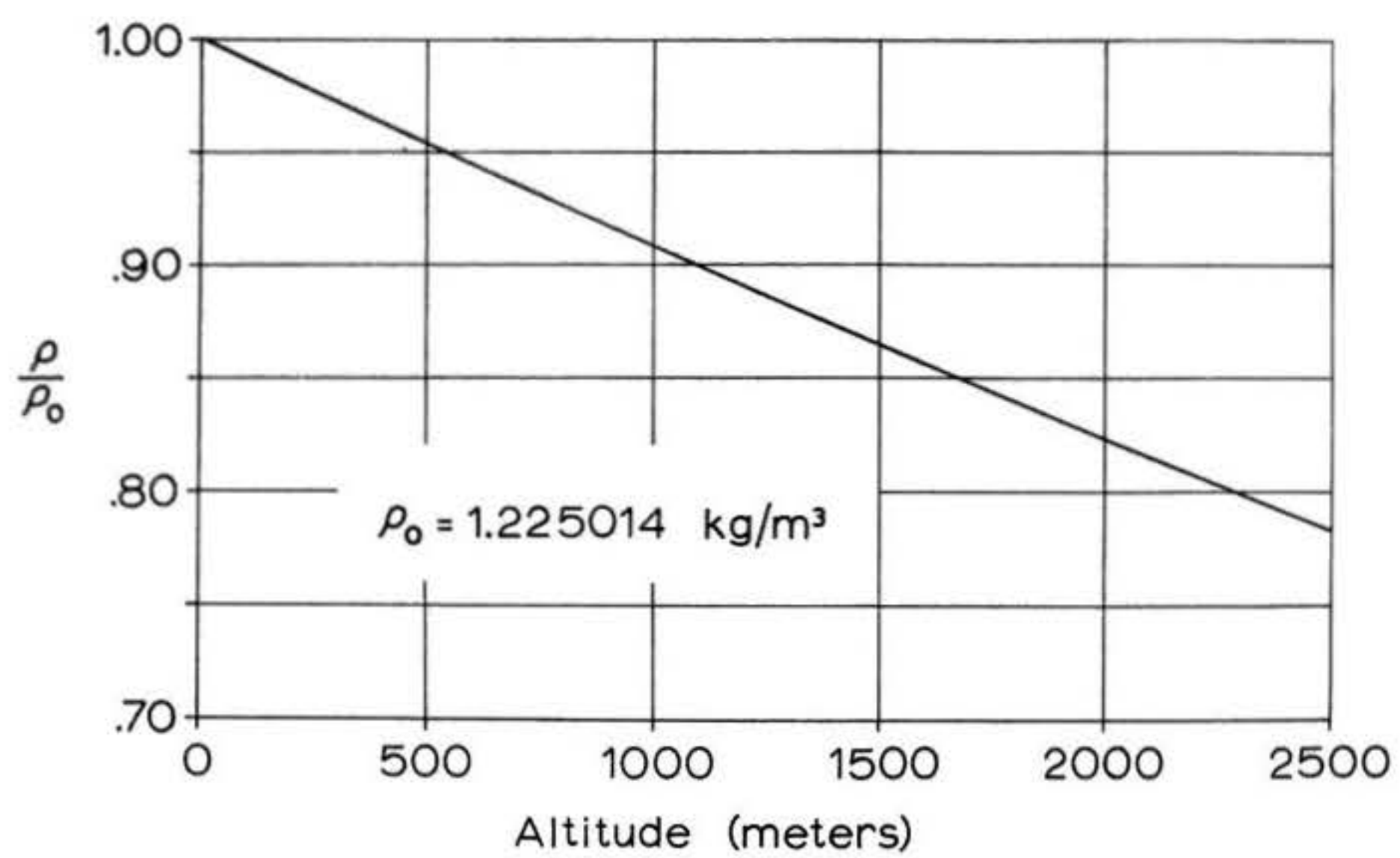


Figure 2: Variation of standard atmospheric density with altitude above sea level.

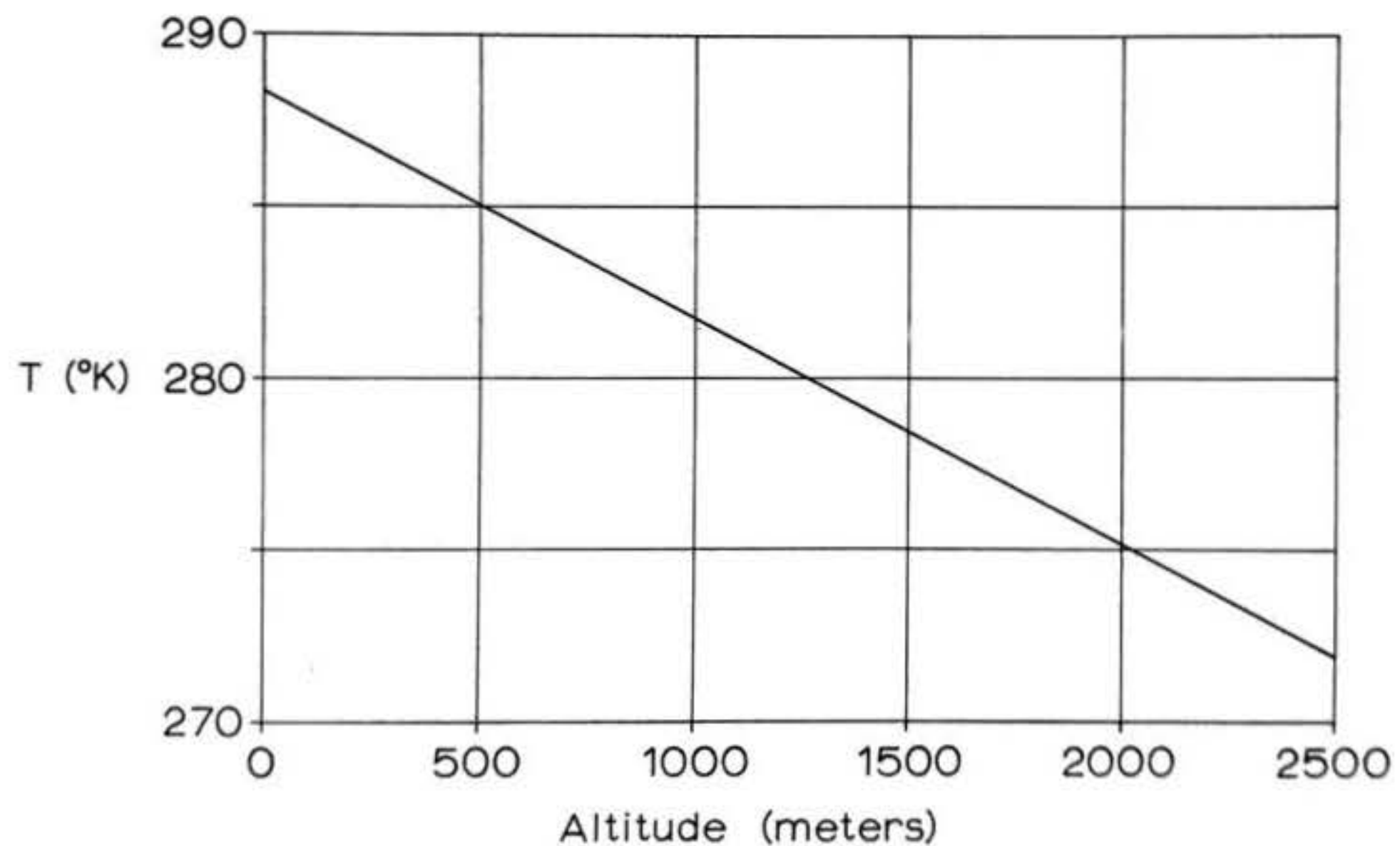


Figure 3: Variation of standard atmospheric temperature with altitude above sea level.

sites by using the atmospheric density at the launcher elevation in their calculations of drag.

Density is also affected by the temperature of the air; in fact, the Standard Atmosphere density graph of Figure 2 is based on the relationship of temperature to altitude shown in Figure 3. It can be seen from the graph that the Standard Atmosphere assumes a so-called "linear lapse rate" of about 1° C. for each 154 meters of altitude. As we all know from experience, however, the temperature at any given launch site may vary widely from day to day; for very precise performance calculations one might therefore wish to use the perfect gas law for correcting the density according to

$$\rho = \rho_{\text{std.}} \frac{T_{\text{std.}}}{T}$$

where the temperature T is measured on an absolute scale. If you have a Fahrenheit thermometer you can convert its reading to the absolute Rankine scale by adding 460° , while the reading of a Celsius ("Centigrade") thermometer is converted to the absolute Kelvin scale by adding 273° . Strictly speaking, variations in air pressure due to changes in the weather also change the atmospheric density, but in any weather good enough for flying high-performance model rockets safely such effects are relatively minute.

Finally, the movement of a body through the air produces local changes in density, since the increased pressures on the body's surface resulting from such motion tend to compress the surrounding air. If the motion is slow enough to keep these

effects small, results from incompressible flow theory can be used in our analysis of drag which permit considerable simplifications over theories which take compressibility into account. The magnitude of compression effects due to velocity can be estimated following the method of Schlichting (15).

The modulus of elasticity of air, denoted by E , is defined by

$$(1) \quad \Delta p = -E \frac{\Delta V}{V_0}$$

where $\Delta V/V_0$ denotes the change in each unit volume of air produced by the change in pressure Δp . For air at sea level, assuming isothermal (constant-temperature) pressure changes, E is just equal to the sea-level pressure of $101,325 \text{ nt/m}^2$. The total mass of air present in the volume V_0 must be equal to the total mass present after the pressure change has altered the volume to $V_0 + \Delta V$. Since mass is just the product of density and volume, this means

$$(2) \quad (V_0 + \Delta V)(\rho_0 + \Delta \rho) = V_0 \rho_0$$

Carrying out the multiplication and neglecting the products of differences in volume and density,

$$(3) \quad \frac{\Delta \rho}{\rho_0} = -\frac{\Delta V}{V_0}$$

so that

$$(4) \quad \Delta p = E \frac{\Delta \rho}{\rho_0} \quad \text{or, equivalently,} \quad \frac{\Delta \rho}{\rho_0} = \frac{\Delta p}{E}$$

Now the speed of sound, denoted by c , can be found by solving

a calculus problem known as Laplace's equation, given the density and elasticity of the air. The result of the calculation is

$$(5) \quad c^2 = \frac{E}{\rho_0}$$

Bernoulli's equation, one of the basic formulae of fluid dynamics, gives the relation between the pressure exerted by a moving fluid in the direction transverse to its motion (the static pressure) and the flow velocity u as

$$(6) \quad p + \frac{1}{2} \rho_0 u^2 = \text{constant}$$

The maximum change in pressure Δp caused by flow of velocity u about a body is therefore (assuming there is some so-called stagnation point on the body's surface at which the fluid is decelerated to rest) of the order $\frac{1}{2} \rho_0 u^2$. This last quantity is often denoted by the symbol q and referred to as the dynamic pressure. Substituting $E = c^2 \rho_0$ and

$$(7) \quad \Delta p \cong \frac{1}{2} \rho_0 u^2$$

into equation (4), we obtain

$$(8) \quad \frac{\Delta p}{\rho_0} \cong \frac{\rho_0 u^2}{2 c^2 \rho_0} = \frac{1}{2} \left(\frac{u}{c} \right)^2$$

The ratio u/c is known as the Mach number M of the flow (named for Ernst Mach (1838-1916)). Since, for approximate incompressibility to prevail, $\Delta p/\rho_0$ must be small compared to one, equation (8) gives

$$(9) \quad \frac{1}{2} M^2 \ll 1$$

If one assumes $\Delta P/P_0 = 0.05$ to be the largest tolerable relative compression for which compressibility need not be considered, one derives $\frac{1}{2}M^2 = .05$, or $M = 0.316$. Since the velocity of sound at sea level (see Figure 4) is about 340 meters/second, this value of Mach number corresponds to a rocket velocity of about 107 meters/second. High-performance model rockets certainly attain, and often exceed, this value in flight, but for the majority of model rockets it is a fairly high figure, attained only during the final instants of powered flight, if at all, and then persisting for only a short time after burnout. As we shall see in Section 7, moreover, slender, finned projectiles like model rockets possess the fortunate property that, throughout much of the higher subsonic flight regime, the influence of compressibility on the overall drag characteristics of the body as computed according to incompressible flow theory is relatively slight even though the relative compression itself is not. Hence, it will be assumed throughout this chapter's Sections 1 through 6 that effects due to the compressibility of air are negligible.

2.1.2 Viscosity and Kinematic Viscosity

Suppose we had a cube of some elastic solid material, such as hard rubber or some "springy" metal like steel or aluminum. Suppose, moreover, that we had somehow arranged to apply forces parallel to four faces of the cube in the manner shown in Figure 5a. The force on each face (which is equal in magnitude to that on each of the other faces), divided by the area of that face, is known as the shearing stress τ ,

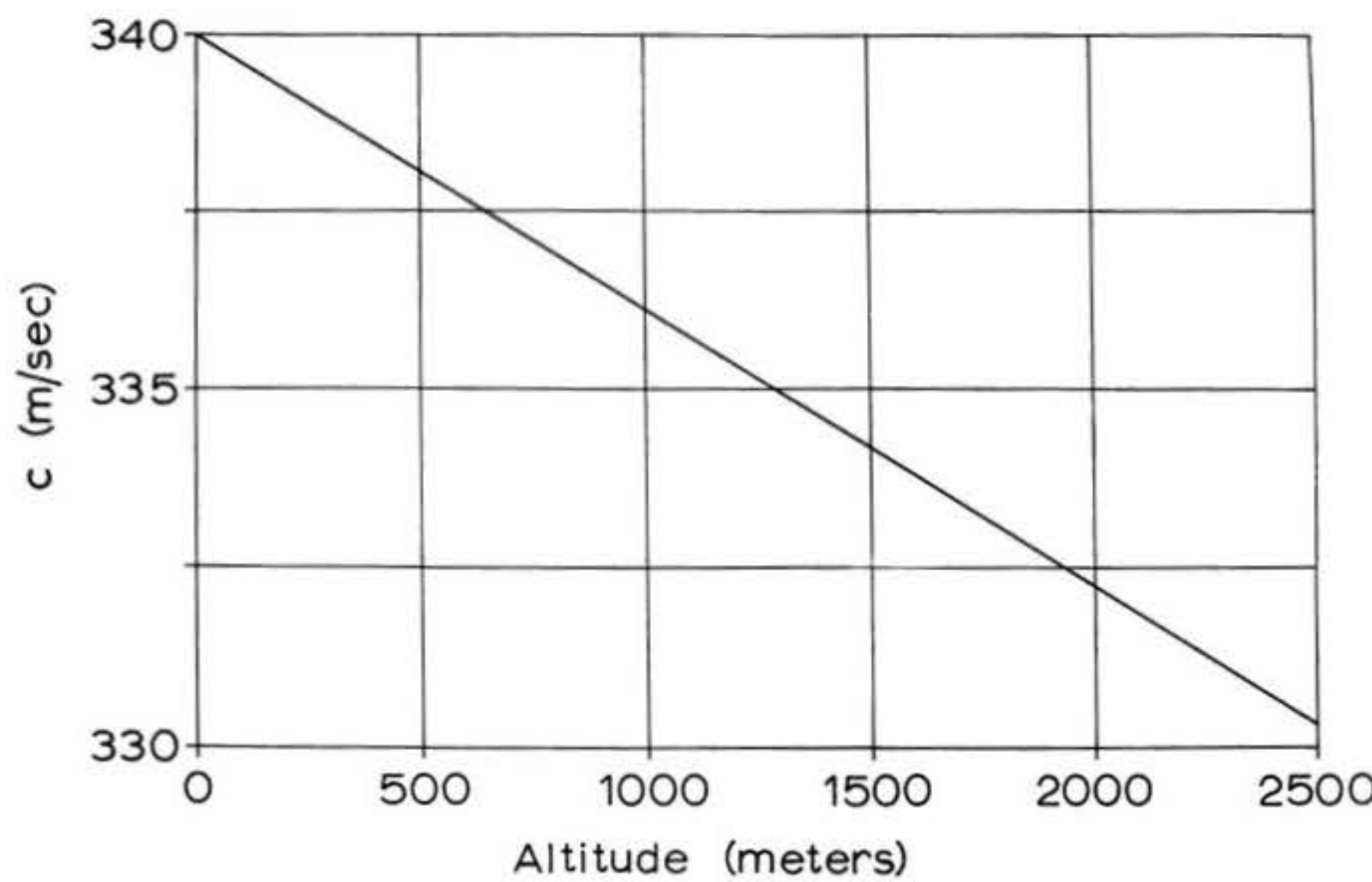
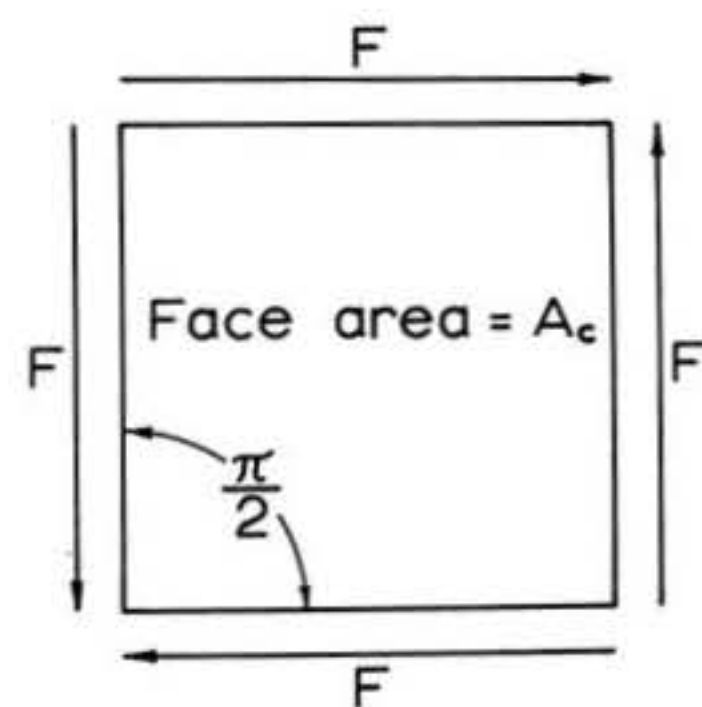


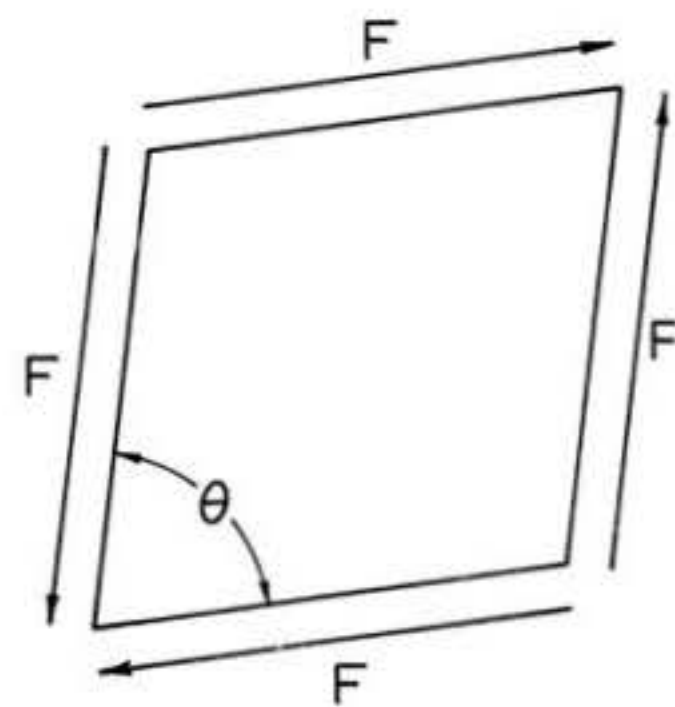
Figure 4: Variation of standard atmospheric sound speed with altitude above sea level.

$$\tau = \frac{F}{A_c}$$

$$\gamma = \frac{\pi}{2} - \theta$$



(a)



(b)

Figure 5: Shearing deformation of an elastic solid. A cube of elastic material is subjected to a shearing stress τ on its lateral faces (a), placing it in a state of uniform shearing strain γ as shown in (b). The cube is viewed directly from the front, so that only its forward face is visible.

given in MKS units as newtons/meter². Thus, if the face area is denoted by A_c and the force by F , $\tau = F/A_c$. Since the cube is placed in static equilibrium by the force system thus described, it will neither move away nor turn -- but it will deform into a rhomboidal parallelepiped as shown in Figure 5b, where the angle θ as illustrated is less than 90°. If the stress is reasonably small; i.e., within the so-called elastic limit for the material, the cube will not be permanently bent out of shape by it, but will return to its original form when the stress is removed. In most materials this results in the difference $(\pi/2 - \theta)$, where θ is given in radians (1 radian = 57.3°), being small. For such cases, the quantity $(\pi/2 - \theta)$ is defined as γ , the engineering shear strain which is effectively dimensionless although it is often written in units such as meters per meter. The stress required to produce a given shear strain is given by Hooke's law as

$$(10) \quad \tau = G\gamma$$

where G , given in newtons/meter², is called the torsion modulus or shear modulus. In elastic solids, then, the shearing stress is directly proportional to the amount of shearing strain. In fluids, however, the deformation law assumes a different dependence on strain, as the following experiment demonstrates.

Consider two very long parallel plates, containing a viscous fluid between them (the meaning of "viscous" will become clear as the experiment proceeds), as in Figure 6 (after 15). The lower plate is fixed in the observer's reference frame, while the upper plate, at a height h above the lower, moves to the

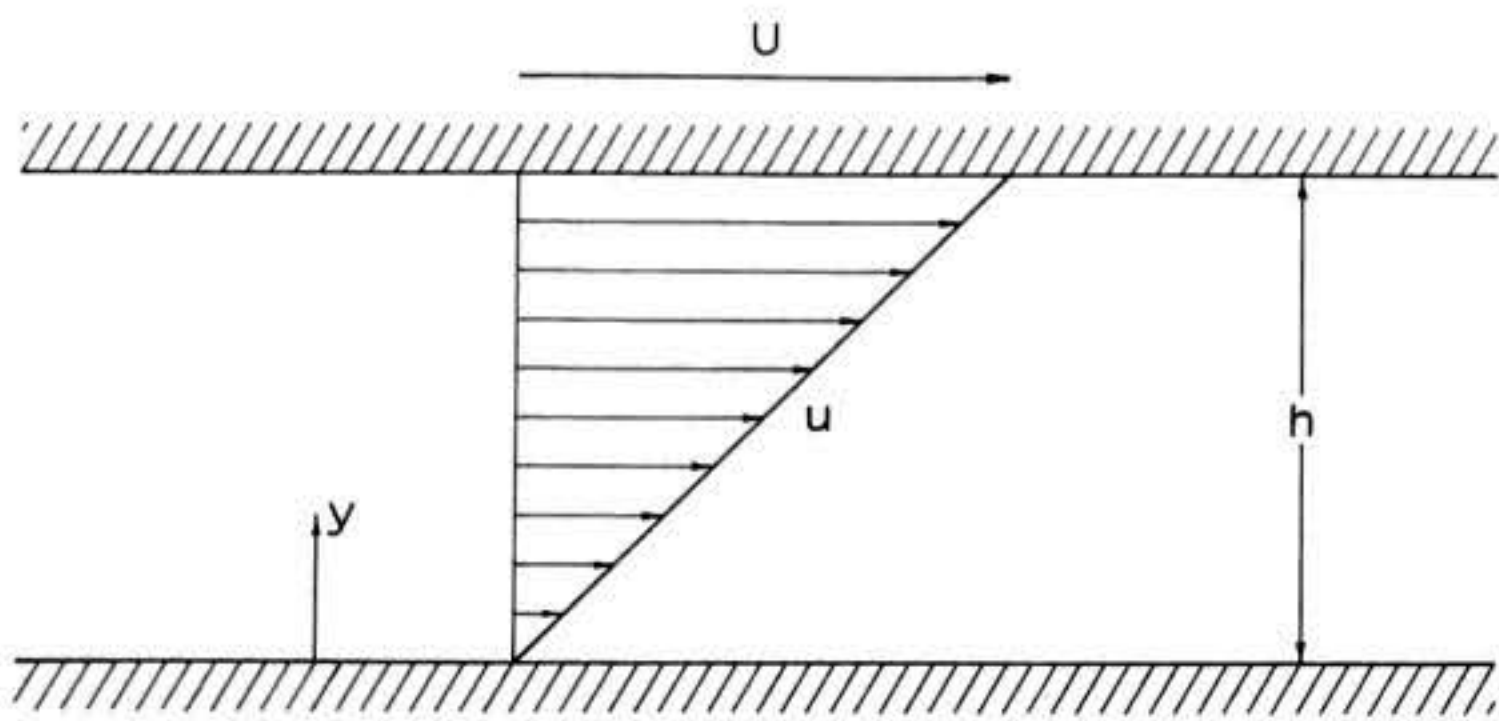


Figure 6: Shearing deformation of a viscous fluid. The lower plate is fixed, while the upper plate moves at horizontal velocity U . The horizontal velocity of the fluid confined between the plates is given by $u = Uy/h$.

right with a constant velocity U .

An extremely important experimental observation about viscous fluid flow is that the fluid behaves as if it were adhering to any surface with which it comes in contact -- that is, the fluid directly adjacent to any given surface undergoes no relative motion with respect to that surface; it "sticks" to it. This phenomenon, known as the no-slip condition at the wall, means that the material of which the plates are constructed is immaterial to the flow (assuming hydraulically smooth surfaces). The no-slip condition is a useful physical assumption in continuum fluid dynamics, although it is by no means an absolutely valid physical model of what actually happens near a surface in fluid flow. In fact, there are cases of the flow of extremely rarified gases in which a considerable amount of "slip" relative to the wall occurs and a finite-slip condition must be applied. In all cases of interest to model rocketeers, however, the validity of the no-slip condition can be assumed. The no-slip condition has a number of ramifications in application to model rockets which will be detailed in Section 3.

In our experiment, a consequence of the no-slip condition is that the velocity of the fluid increases linearly with height above the lower plate, from zero at the lower plate to U at the upper plate. Assuming the lower plate to be fastened to some fixture that prevents it from moving, there must be a force F applied tangentially to the upper plate to Maintain its velocity at U , and since there is no acceleration F must equal the frictional (or viscous) forces applied to the upper plate by the fluid. Furthermore, experiment reveals that

$$(11) \quad F \propto \frac{UA}{h}$$

where A is the area of the upper plate in contact with the fluid. The frictional shearing stress τ is then proportional to U/h . Since the fluid velocity varies linearly with y , the vertical coordinate, U/h is just equal to the rate at which the fluid velocity u increases with height above the lower plate; i.e., the derivative of u with respect to y , or du/dy . Thus,

$$(12a) \quad \tau \propto \frac{du}{dy}$$

where the symbol \propto reads in English, "is directly proportional to". Specifically, it has been found that

$$(12b) \quad \tau = \mu \frac{du}{dy}$$

where μ is the coefficient of viscosity, a physical property of the fluid. From (12b) it is seen that the shearing stress in a fluid is dependent on the rate, not the amount of deformation.

The constant μ is then a measure of a fluid's resistance to deformation. At room temperature, water is roughly 75 times as viscous as air. Substances like glycerine and molasses are more viscous still. Thus you can see that the word "thick", as applied to fluids colloquially, is roughly equivalent to the more technical term "viscous". For gases, to a first approximation, μ can be considered independent of pressure, depending only on temperature. In Figure 7, μ is seen to decrease steadily with increasing altitude.

The ratio of the coefficient of viscosity to the density of a fluid is called its kinematic viscosity $\nu = \mu/\rho$. It is

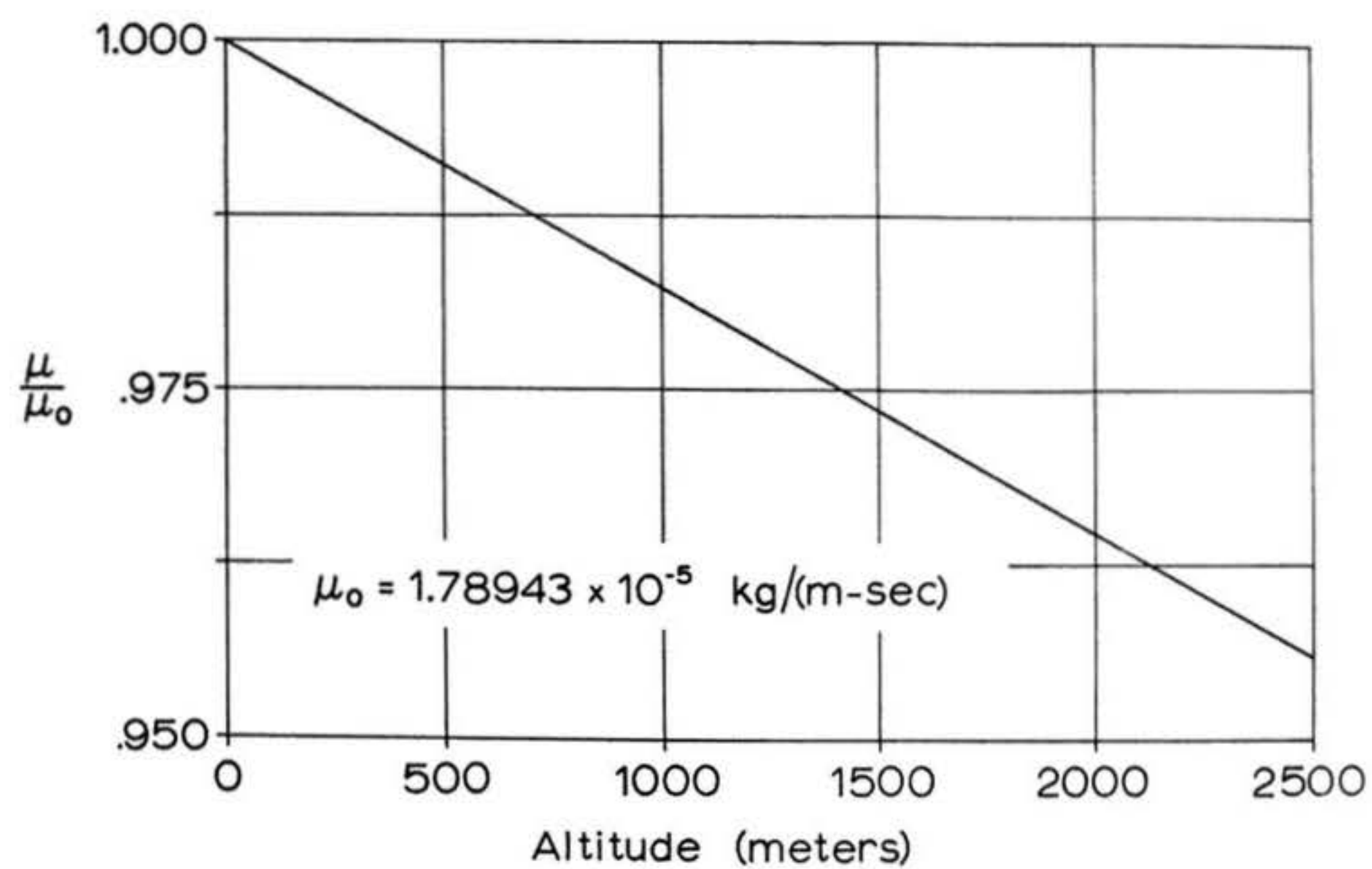


Figure 7: Variation of the absolute viscosity of standard atmosphere with altitude above sea level.

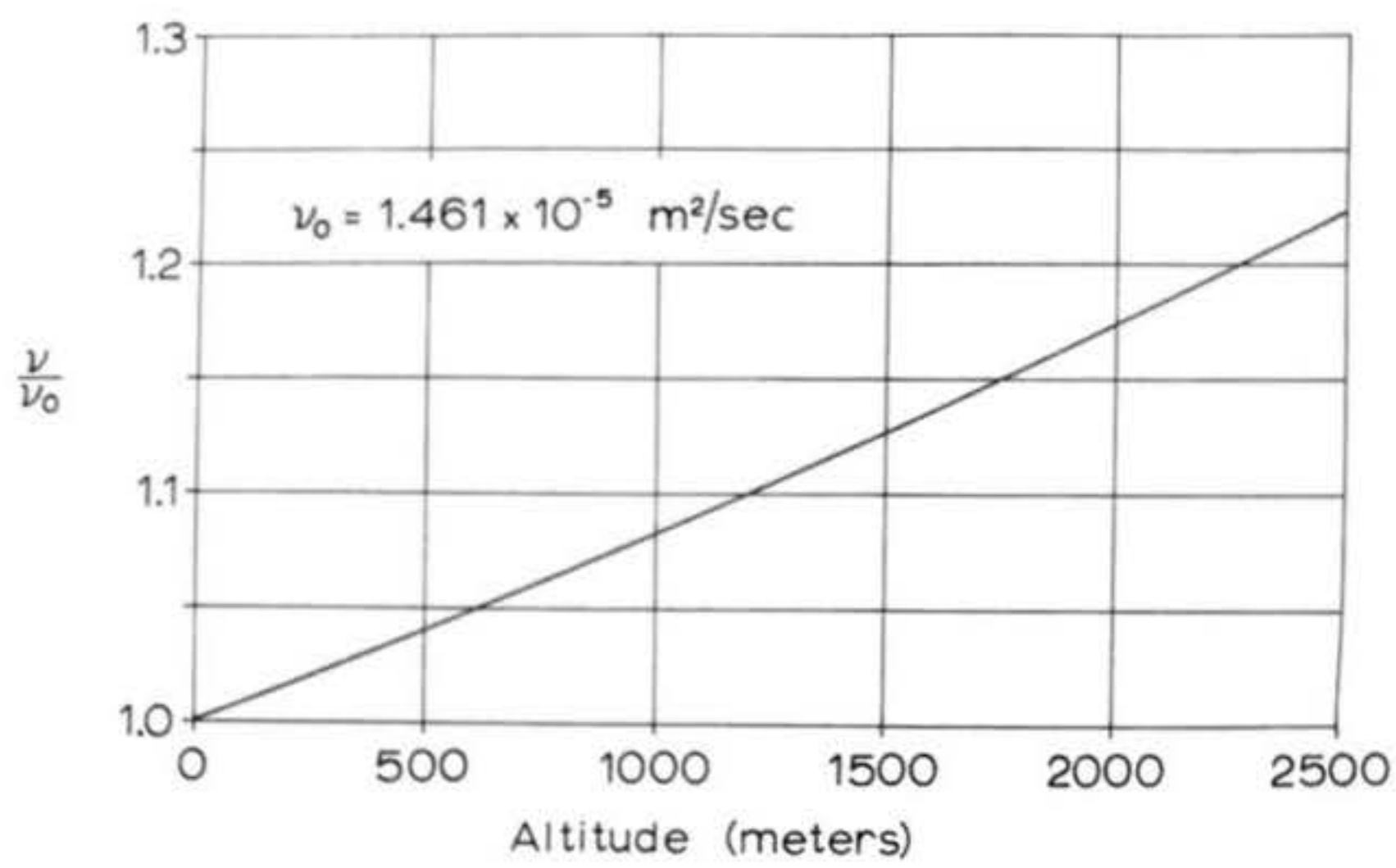


Figure 8: Variation of the kinematic viscosity of standard atmosphere with altitude above sea level.

this quantity, rather than μ independently, that will appear repeatedly in our analysis of drag; its significance is discussed in the treatment of Reynolds number. For the present, we observe from Figure 8 that ν increases relatively slowly with altitude. This is because at altitudes typical of model rocket flight, although ρ and μ are both decreasing, ρ is decreasing at a faster rate than μ with increasing altitude. At an altitude of 300 meters, ν is only about 2.4% greater than its sea-level value. In the calculations of this chapter ν will be assumed to have a constant value of 1.495×10^{-5} meter²/second, an average valid for the temperature and density variations normally encountered in flying model rockets.

2.2 Dimensionless Coefficients and Quantities

2.2.1 The Reynolds Number

In our study of model rocket drag, we will make frequent use of a dimensionless quantity called the Reynolds number, denoted by R . Named for the English physicist Osborne Reynolds (1842-1912), its value reflects the nature of the flow about a body. Under certain conditions the drag coefficient (see 2.2.2) may be expressed as a function of Reynolds number alone.

The theoretical derivation of the Reynolds number may be accomplished in a variety of ways: by dimensional analysis, by a consideration of the forces acting on a fluid element in incompressible flow, or by examination of the Navier-Stokes equations of fluid equilibrium. I shall use the second approach, since I feel it is of greatest interest to model rocketeers; those readers who desire to follow the other lines of argument

are referred to the excellent accounts in Shapiro (17) and Schlichting (15).

Suppose we consider the forces acting on a fluid element moving parallel to the x -axis of a Cartesian coordinate system at a velocity u , where u is a function of both the x and y coordinate values (Figure 9). The size of the fluid element is large compared with the dimensions of a molecule of fluid, and large compared with the average distance between the molecules, but small compared with the dimensions of the region in which fluid is flowing and small compared to the dimensions of any physical boundary or solid object nearby. The flow itself is composed of a very large number of fluid elements, such that variations in density, velocity, and all other physical properties between adjacent elements are small enough to permit the flow to appear continuous.

There are essentially two types of forces which act upon an individual fluid element: body forces, which act from a distance (such as gravity), and surface forces, which act through the physical contact of one fluid element with another. Surface forces may be further subdivided into normal stresses (pressure), which act perpendicular to the surface, and shear stresses (viscous friction), which act parallel to the surface of the element.

In this analysis, the body force due to gravity is assumed to be balanced by buoyancy forces in the fluid, and hence is neglected. Furthermore, the fluid is assumed incompressible, which means that the volume of each fluid element is constant;

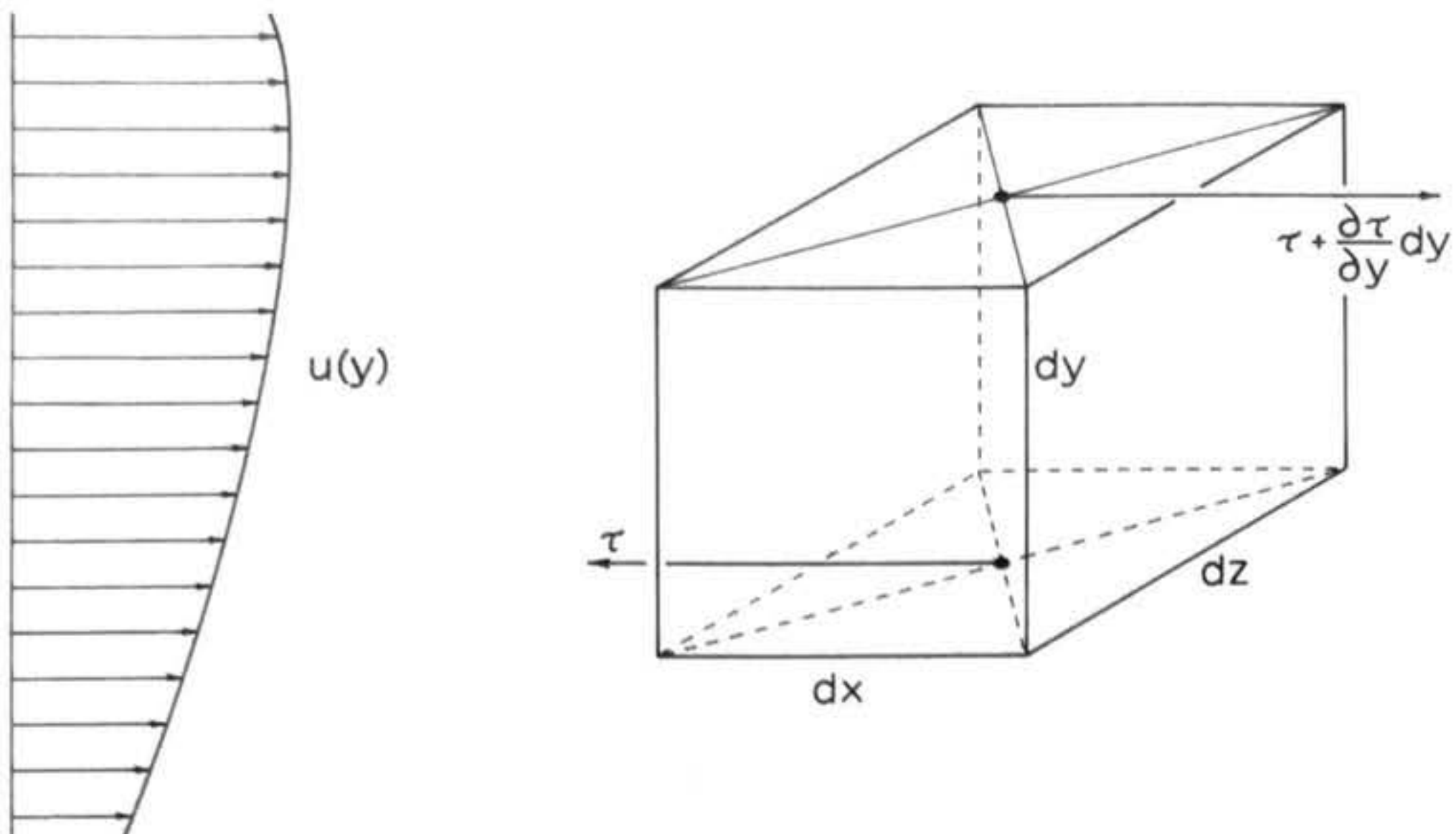


Figure 9: A fluid element in Cartesian coordinates, showing the variation of the x-component of velocity with the y coordinate and the shearing stress on the upper and lower y-faces of the element.

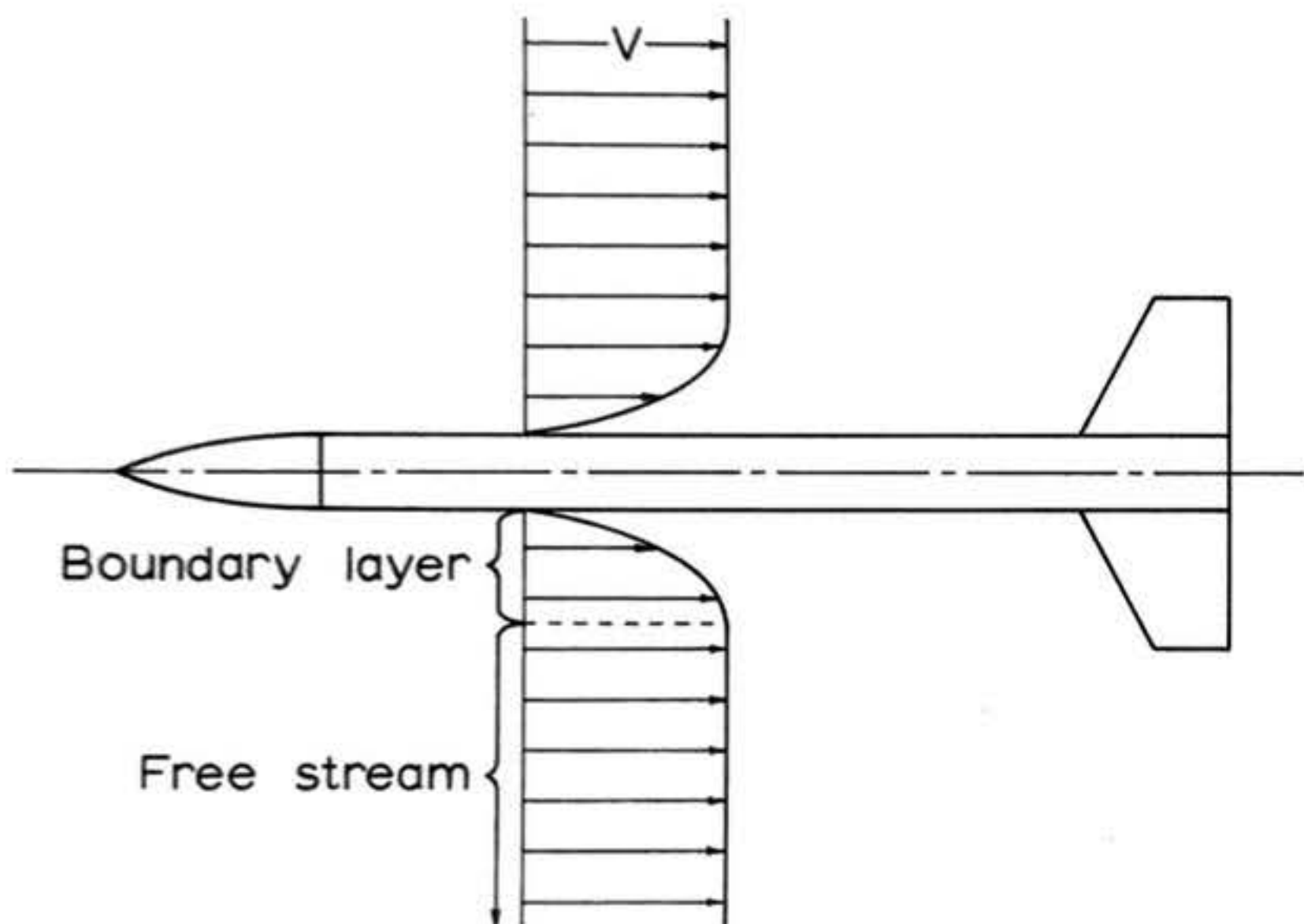


Figure 10: The concept of free-stream velocity. The air in the free stream moves past the rocket at velocity V , while the air in the "boundary layer" next to the rocket's surface is slowed down by viscous friction. The thickness of the boundary layer has been greatly exaggerated to make it visible; actual boundary layers have thicknesses on the order of 10^{-2} or 10^{-3} cm.

hence any elastic forces which might arise from a change in volume are neglected.

The only forces left to consider, then, are inertia forces and viscous friction forces. We shall attempt to express the ratio of these two forces in terms of the variables which determine the nature of the flow: the density ρ , the coefficient of viscosity μ , the free-stream velocity V , and a characteristic linear dimension of any given solid body in the flow, L .

The free-stream velocity V is the velocity of the undisturbed fluid relative to the solid body. For a model rocket, V is the velocity of the airstream as seen by an imaginary observer moving with the rocket, at points far enough from the rocket's surface to be undisturbed by its passage (Figure 10). It is important to distinguish V from the velocity of elements very near the body; for the elements at the surface itself this velocity is effectively zero. In most cases applicable to model rockets, L will refer to the total length of the rocket. When we consider friction drag in Section 3, however, we will find that the nature of the flow over the fins is determined by the fin chord c , so L will be taken as c in that instance.

From considering Figure 9, one can determine that the net resultant of all shearing forces on the element is

$$(13) \quad (\tau + \frac{\partial \tau}{\partial y} dy) dx dz - \tau dx dz = \frac{\partial \tau}{\partial y} dxdydz$$

Applying equation (12b) and dividing through by $dxdydz$, the volume of the element, we find the shear force per unit volume as

$$(14) \quad \frac{\partial \gamma}{\partial y} = \mu \frac{\partial^2 u}{\partial y^2}$$

Note that the symbol ∂ , rather than d , is used in writing the derivatives of a function of more than one independent variable. The derivative of such a function is called a partial derivative. The inertia force per unit volume, assuming steady (i.e., not oscillating) flow conditions, is equal to $\rho u \frac{\partial u}{\partial x}$. Consequently,

$$(15) \quad (\text{inertia force})/(\text{friction force}) = \frac{\rho u \frac{\partial u}{\partial x}}{\mu \frac{\partial^2 u}{\partial y^2}}$$

Now using order-of-magnitude approximations, we can say that the velocity u is of the same order of magnitude as the free stream velocity V , $\frac{\partial u}{\partial x}$ is of the order V/L , and $\frac{\partial^2 u}{\partial y^2}$ is of the order V/L^2 . Hence the ratio of inertia force to friction force is given approximately by

$$(16) \quad \frac{\text{inertia force}}{\text{friction force}} = \frac{\rho \frac{V^2}{L}}{\mu \frac{V}{L^2}} = \frac{\rho}{\mu} VL = \frac{VL}{\nu}$$

The quantity $\frac{VL}{\nu}$ is the Reynolds number. Part of the significance of this quantity (which is dimensionless when evaluated in a consistent set of units) stems from the answer to the following question: given two bodies, geometrically similar but of different sizes, what is the condition that must be satisfied for the flow over these two bodies to be similar; i.e., for the streamlines to be geometrically similar also? Some thought reveals that the forces acting on any two fluid elements at geometrically similar positions must bear the same ratio in both cases, at each and every instant of time.

If we consider now the type of flow from which we derived

the Reynolds number; i.e., an incompressible flow with no free surfaces (so that gravity and buoyancy forces cancel) it is apparent that the inertial and viscous forces bear a fixed ratio in any two cases of flow about geometrically similar bodies if the Reynolds numbers of the two flows are identical. Two such flows are referred to as dynamically similar.

To illustrate this principle by example, consider the airflow about the Saturn V moon rocket and that about an accurate 1/100 scale model of that vehicle. For the flow about the two bodies to be dynamically similar, the Reynolds numbers must be equal; hence

$$(17) \quad \left(\frac{V_L}{\nu}\right)_{\text{full-scale}} = \left(\frac{V_L}{\nu}\right)_{\text{model}}$$

Since the fluid is air in both cases, and we can restrict the problem to low-altitude flight with standard launch-site atmospheric conditions, the values of ν are identical. With $L_{\text{full-scale}} = L_{\text{model}} \times 100$, the requirement of equal Reynolds numbers becomes

$$V_{\text{model}} = 100V_{\text{full-scale}}$$

The airflow about the model Saturn flying at, say, 100 meters/second is then dynamically similar to that about the full-scale rocket when it is moving only one meter/second! Throughout almost all of its flight, the full-scale Saturn V is in a Reynolds number regime far above that which model rockets ever experience. This suggests that the types of flow problems encountered in model rocketry tend to be somewhat different from those of full-

scale astronautics -- a conclusion which, to a large degree, is correct.

The principle of dynamic similarity is the basis for the technique of model testing, whether by wind tunnel or any other means. To achieve the same flow characteristics about a scale model which are found at typical operating velocities about the full-scale version, it is possible to vary both the test velocity and the kinematic viscosity, as seen in equation (17). Practically speaking, the velocity of a wind tunnel cannot be made large enough to attain the desired Reynolds number if the disparity in size between model and prototype is too great. For instance, the subsonic aerodynamic characteristics of the Saturn V could not be determined by the wind-tunnel testing of a 1/100 scale model, since simulation of a prototype velocity of 100 meters/second would require a wind-tunnel test at 10,000 meters/second; and while the Reynolds numbers would then be equal the extreme compressibility effects on the model test would destroy its validity. By choosing another test fluid with a lower value of ν , however, it is possible to conduct dynamically similar model tests for moderate scaling ratios between model and prototype. Water, for instance, has a kinematic viscosity at room temperature less than 8% that of air; it would therefore be possible to test a 1/4 scale model of a light airplane which is to fly 45 meters/second, using a test velocity of 15 meters/second in water, and have flow about the model which is dynamically similar to that about the full-scale airplane. Increasing the model size has the same effect as reducing the kinematic viscosity:

it permits dynamically similar testing at lower velocities. For this reason, many wind tunnels are built today with very large test-section dimensions.

To get an idea of the Reynolds numbers commonly encountered in model rocketry, suppose we compute the value of R for a model 0.3 meter long travelling at 60 meters/second. Using $\rho = 1.495 \times 10^{-5}$ meter²/second, we obtain from equation (16) $R = 1.205 \times 10^6$. Because a consistent set of units was used, the Reynolds number is dimensionless; this must be the case, as the ratio of forces should not depend on the system of units used to evaluate it.

It appears that model rocket flight thus enters regimes in which inertia forces on the air in regions surrounding the model are about a million times greater than frictional forces. One might assume, for this reason, that it would be possible to ignore friction forces completely in our analysis. Despite the attractiveness of this proposition, it does not stand up to experiment; friction forces exert a great influence on the flow around a body, no matter how great the Reynolds number, but their action is confined essentially to a very thin layer at the body's surface known as the boundary layer. This concept will be discussed more thoroughly in Section 3.

2.2.2 The Drag Coefficient

The drag coefficient of a body, denoted by C_D , is defined as

$$(18) \quad C_D = \frac{D}{\frac{1}{2} \rho V^2 A_r}$$

where D is the drag force, A_r is a characteristic "reference area" of the body (in model rockets, usually the body tube cross-sectional area), and $\frac{1}{2} \rho V^2$ is known as the dynamic pressure. In this form, evaluated with a consistent set of units, the drag coefficient is dimensionless.

Under certain conditions the drag coefficient possesses a very useful and valuable property: given two geometrically similar bodies, the only difference in drag coefficient between them (if any) will be due to their being operated at different Reynolds numbers; the drag coefficient is a function of Reynolds number alone. Mathematically,

$$(19) \quad C_D = f(R)$$

Conditions required for the validity of (19), in addition to geometric similarity, are that the flow be incompressible and the angle of attack be zero, so that the only forces acting on a fluid element in the vicinity of the body are due to friction and inertia. The functional dependence of C_D on R must usually be determined experimentally, as present theory is generally inadequate to predict drag coefficients for any but the simplest geometric shapes. For the model rocketeer, this would imply the necessity for extensive wind tunnel tests on each of his models. Unfortunately, there are few individuals with access to the necessary equipment for such tests.

One solution to this problem is to resort to semi-empirical expressions for the drag coefficient which have been compiled from statistics derived by testing a great many subsonic rocket

vehicles. In Section 6, one such method is presented and analyzed in detail. Although these formulae are not applicable to bizarre model rocket shapes, and have not yet been extended to multistaged vehicles with any considerable degree of confidence in their accuracy, they do permit sizeable variations in nose cone shape, fin planform, number of fins, boattail characteristics, and general physical dimensions for single-stage rockets.

Since the empirical expression must necessarily be dependent on Reynolds number, it would appear that a laborious computational procedure is still required to determine graphically the relationship between C_D and R for any given model. Fortunately, as we shall see later, the drag force on a model rocket over a considerable range of Reynolds numbers of interest is very nearly proportional to the square of the velocity:

$$(20) \quad D = k V^2$$

where k is a constant. Comparison of equation (2.20) with equation (2.18) reveals that k is just equal to $\frac{1}{2} \rho C_D A_r$, so that the condition of constant k requires

$$(21) \quad C_D = \text{constant}$$

Hence, to obtain a drag coefficient of acceptable accuracy for almost all model rocketry purposes it is necessary to calculate only a single value of C_D from the semiempirical expression, using a Reynolds number roughly estimated as the average value to be encountered in flight. The "average" C_D thus determined may then be used in performance analyses.

2.2.3 The Coefficient of Pressure

Undisturbed air has an ambient, or "static", pressure (denoted p_0) which may be measured on a gauge or barometer. At sea level, the ambient pressure is equal to 101,325 newtons/meter². In flow past a body such as a model rocket, however, the static pressure as measured on a gauge by an imaginary observer moving with the airstream will be seen to undergo changes in value. At a stagnation point (where the flow has been brought to rest relative to the body, as happens at the tip of the nose), for example, the static pressure will increase. In incompressible flow the amount of this increase is just $q = \frac{1}{2}\rho V^2$, where V is the free-stream velocity. At other points on the body, the static pressure will vary between its value at the stagnation point -- $(p_s)_{\text{stag}} = p_0 + \frac{1}{2}\rho V^2$ -- and some minimum value which can be less than the ambient static pressure p_0 .

The fundamental relationship which relates changes in static pressure to changes in dynamic pressure q is Bernoulli's Principle, which states that the total pressure P_{tot} is a constant in frictionless, incompressible flow. The total pressure is simply the sum of the local static and dynamic pressures, at any location in the flow:

$$(22) \quad P_{\text{tot}} = p_{s1} + \frac{1}{2}\rho u_1^2 = p_{s2} + \frac{1}{2}\rho u_2^2 = \text{constant}$$

where p_{s1} , p_{s2} , and u_1 , u_2 are the static pressures and velocities at any two points which have been designated point 1 and point 2, respectively. If we choose point 1 to be a stagnation point, u_1 is zero and

$$(23) \quad p_{\text{tot}} = (p_s)_{\text{stag}} = p_s + \frac{1}{2} \rho u^2 = \text{constant}$$

The total pressure of the flow is thus seen to be equal to the static pressure at a stagnation point.

The increment in static pressure at stagnation, $q = \frac{1}{2} \rho V^2$, is an important quantity in aerodynamics, as in many applications the force experienced by an object resulting from the flow of fluid around it is proportional to q . This explains, for instance, why the drag coefficient is defined as

$$(24) \quad C_D \equiv \frac{D}{q A_r}$$

In an analogous manner we can define a pressure coefficient. It is apparent from the above discussion that differences in pressure, rather than absolute pressures, are important in determining fluid dynamic forces. Hence we define

$$(25) \quad C_p \equiv \frac{\Delta P}{q} \equiv \frac{p - p_\infty}{q}$$

where p is the local static pressure, p_∞ is the ambient atmospheric pressure (free-stream static pressure) -- 101,325 newtons/meter² at sea level -- and q is the free-stream dynamic pressure, $\frac{1}{2} \rho V^2$. At a stagnation point, equation (25) gives the result $C_p = +1.0$.

In Section 4, Bernoulli's Principle and the concept of the pressure coefficient will be used to explain the existence of pressure drag.

2.3 Constituents of the Total Drag Coefficient

It has been found in practice that a systematic analysis of drag requires some scheme for dividing the drag into components,

which can then be studied separately. In subsonic flow problems, the most common partitioning technique is to divide the total drag into skin-friction drag (due to forces tangential to the body surface) and pressure drag (resulting from forces perpendicular to the body surface). Integration of the components of the tangential and normal forces which are parallel to the direction of motion leads to the following general expressions for the drag (14):

$$(26) \quad \text{pressure drag: } D_p = - \iint_S p \cos(\vec{n}, \vec{V}) dS$$

$$(27) \quad \text{skin-friction drag: } D_v = \iint_S \tau \cos(\vec{t}, \vec{V}) dS$$

The notation associated with these so-called double integrals or surface integrals is illustrated in Figure 11. The effect of performing the calculus operation called "integration" is just to add up all the infinitesimal contributions to drag resulting from the pressure and viscous skin-friction stress on each infinitesimal bit of surface area dS . The pressure integration results in equation (26), while the friction integration results in equation (27). The area S includes the base area of the rocket.

The pressure drag may be further subdivided into the integral over the base area, called base drag, and the integral over the rest of the model's surface, called pressure foredrag:

$$(28) \quad D_p = - \iint_{S_b} p \cos(\vec{n}, \vec{V}) dS_b - \iint_{S_s} p \cos(\vec{n}, \vec{V}) dS_s$$

where S_b denotes the base area and S_s the total forebody surface, or "wetted", area. Equation (28) may also be written using

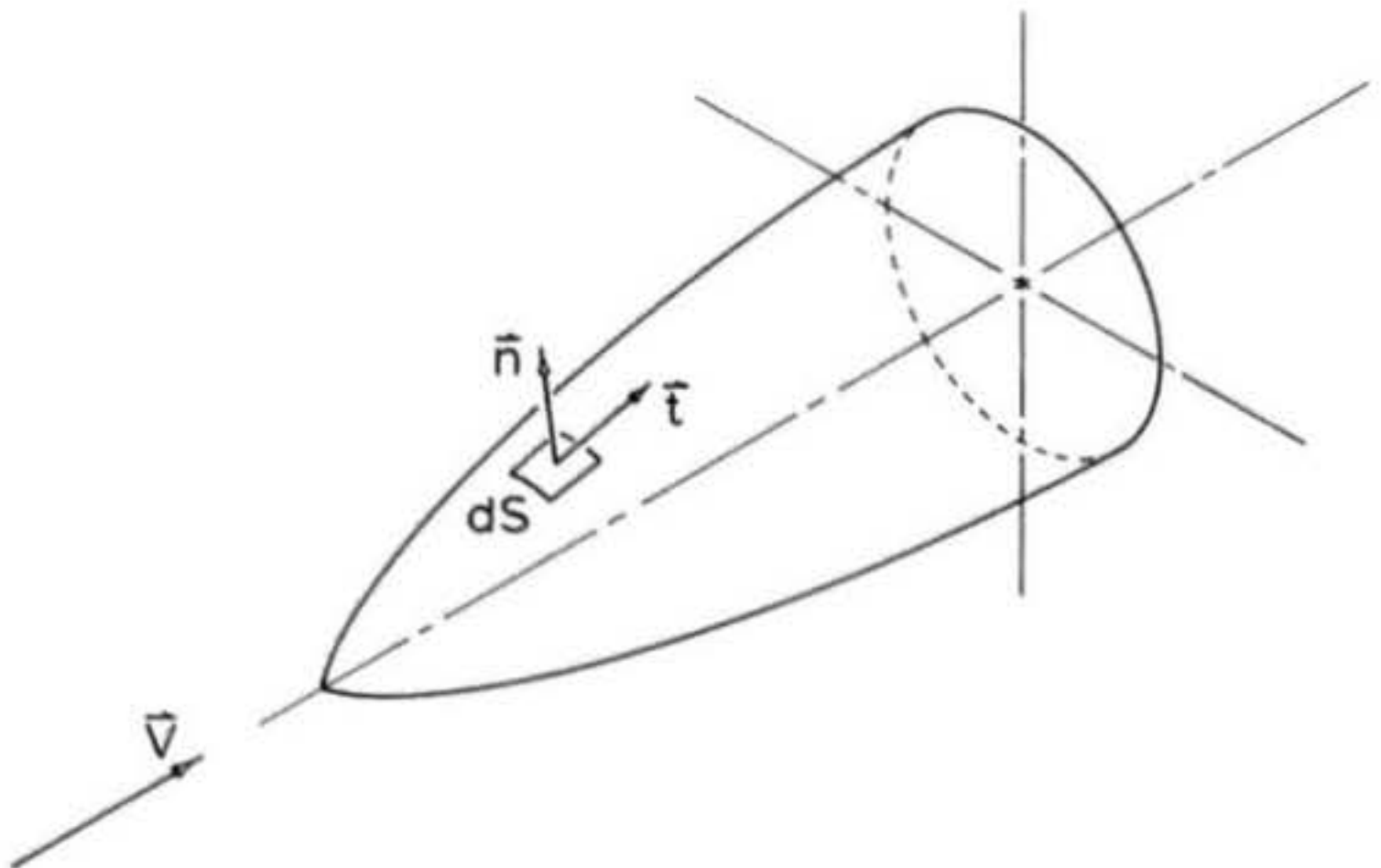


Figure 11: Notation used in the surface integrations for calculating friction drag and pressure drag. The unit vector \hat{n} , perpendicular to the surface, and the unit vector \hat{t} , tangent to the surface, originate from the center of the small element of area dS . The notation $\cos(\hat{n}, \vec{V})$ refers to the cosine of the angle between \hat{n} and \vec{V} , while $\cos(\hat{t}, \vec{V})$ is the cosine of the angle between \hat{t} and \vec{V} .

the abbreviated notation

$$(29) \quad D_p = D_b + D_f$$

where D_b denotes the base drag and D_f the pressure foredrag.

This arrangement is convenient because base drag is an important topic in itself, and special techniques are employed to reduce it. The total drag at zero angle of attack is then

$$(30) \quad D = D_b + D_f + D_v$$

Skin friction drag is discussed in Section 3, and base drag in Section 4. The analysis of these sections will be valid only for zero angle of attack; in Section 5, the additional drag D_α due to angular deflection of the rocket longitudinal axis from the direction of the relative airstream will be considered. The total drag at a general, nonzero angle of attack may then be written

$$(31) \quad D = D_b + D_f + D_v + D_\alpha$$

Dividing by $\frac{1}{2} \rho V^2 A_r$, where the A_r we will be using is the rocket's maximum frontal area, we can express the drag in nondimensional form as the sum of constituent drag coefficients:

$$(32) \quad \frac{D}{\frac{1}{2} \rho V^2 A_r} = C_D = C_{D_b} + C_{D_f} + C_{D_v} + C_{D_\alpha}$$

You should note the use of maximum cross-sectional area in this chapter for computing drag coefficients, as opposed to the use of the cross-sectional area at the base of the nose as the reference area for determining the normal force coefficients of Chapter 2's Barrowman analysis.

The above scheme of componentization will be used to study model rocket drag in succeeding sections. At this point something might be said about the relative importance of the various terms in equation (32). According to experimental evidence to date, the order of importance of the drag components of a typical streamlined, well-constructed model rocket might appear as follows:

- 1) Launch lug drag: In models having launch lugs, the lug produces a component of pressure drag that must be added to the pressure foredrag. This component accounts for about 35% of the total C_D .
- 2) Skin-friction drag of forebody: Accounts for 25% to 30% of the total C_D in models having launch lugs, 35% to 45% in lugless models.
- 3) Skin-friction drag of fins: Accounts for 25%-30% of the total C_D in models with lugs, 35%-45% in lugless models.
- 4) Base drag: Accounts for about 10% of the total C_D in models having lugs, about 15% in lugless models.
- 5) Pressure foredrag: Forebody pressure drag from sources other than launch lugs accounts for less than 1% of the total C_D .

The order of this list, and the relative magnitudes of the contributions, can be altered drastically by improper construction techniques. Failing to provide the fins with the

proper airfoil shape gives rise to a pressure drag several times greater than the total drag would be with properly-shaped fins. Rough surface finishes and blunt nosecones also lead to considerable increases in drag, though not so great as do unshaped fins, and the increase in drag due to nonzero angle of attack can be quite large even for a well-streamlined vehicle. It is not uncommon for a model rocket to have twice the drag at a 10° angle of attack than it exhibits at 0° .

Typical values of the total drag coefficient for model rockets with launch lugs range from 0.5 to 0.8, depending on the quality of the design and construction of the model. By comparison, a circular disc held perpendicular to the flow has a C_D of 1.1; the disc thus experiences a drag force 50% to 100% greater than that on a model rocket of the same diameter in an airstream of the same velocity. This result foreshadows our later discussion on the undesirability of blunt shapes and abrupt protrusions in model rocket work. To quote an example, removing the launch lug from a certain model rocket may reduce its drag coefficient from 0.7 to about 0.45.

Figure 12 summarizes diagrammatically the important topics in model rocket drag to be considered in detail in the following pages.

3. Viscous (Skin-Friction) Drag

3.1 The Importance of Viscosity in Real Fluid Flow

In Section 2 the skin-friction drag was defined as

$$(33) \quad D_v = \iint_s \tau_o \cos(\vec{t}, \vec{v}) dS$$

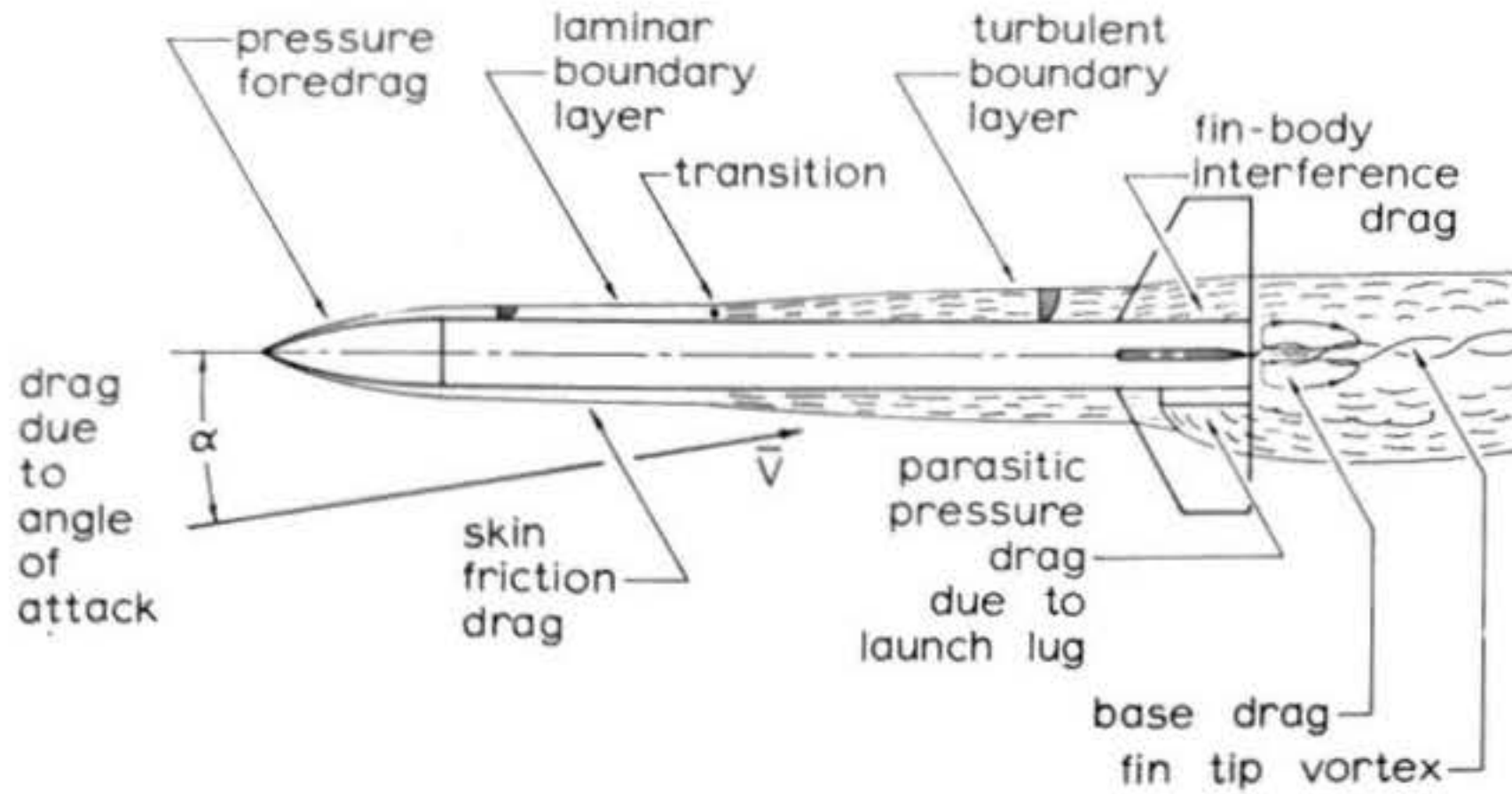


Figure 12: Causes and constituents of model rocket drag. The various drag constituents and flow phenomena shown here are discussed in detail in later sections of this chapter. The thickness of the boundary layer in this drawing has been greatly exaggerated to make it visible to the eye.

where τ_0 is the skin-friction force per unit area at the surface of the model (equal to the viscous shearing stress in the air directly adjacent to the model surface). Recalling equation (12b), we can write τ_0 as

$$(34) \quad \tau_0 = \mu \left(\frac{\partial u}{\partial y} \right)_{y=0}$$

where we have adopted a "local" coordinate system in which the y-axis extends perpendicularly upwards from the point on the rocket's surface at which τ_0 is being evaluated. Earlier we saw, via an estimate of typical model rocket Reynolds numbers, that inertial forces are about a million times greater than viscous forces at average model rocket flight speeds. Why, then, not ignore the viscous forces completely in our analysis?

The mathematical model which corresponds to this assumption is the so-called "perfect fluid" of classical hydrodynamics. The theory of the perfect fluid model, which assumes a fluid that is incompressible and has a coefficient of viscosity of zero, was well developed before the beginning of the 20th Century since the mathematical simplifications permitted by the perfect fluid assumption are considerable. The results one obtains from calculations based on classical hydrodynamics, however, assert that the drag on a closed body of any shape moving at constant velocity through a perfect fluid is exactly zero. This prediction was so contradictory to all experimental evidence -- even that available in the mid-19th Century -- that it came to be called d'Alembert's Paradox. It was apparent that one of the fundamental assumptions of the ideal fluid

theory was physically inaccurate.

In 1904 the great German scientist Ludwig Prandtl (1875-1953) resolved this dilemma by introducing the concept of the boundary layer. According to this theory, the influence of viscosity in fluids whose viscosity is small (or in situations where the Reynolds number is large) is confined to a thin region near the surface of any solid body immersed in the flow. The fluid obeys the rule of no slip at the wall -- contrary to the behavior of the perfect fluid, which was allowed to flow past a body freely -- and hence the fluid velocity must increase from zero at the body wall to the full free-stream value in a very short distance, perhaps a few hundredths or thousandths of a centimeter (note that the terms "wall" and "surface" are being used interchangeably in this discussion). This condition requires that the fluid velocity increase very rapidly with distance from the body surface; i.e., that the velocity gradient $\frac{\partial u}{\partial y}$ be very large in the boundary layer, and hence τ_0 in equation (34) may not be negligible even if μ is small.

This theory essentially divides the flow about a body at high Reynolds numbers into two regions. Within the thin boundary layer viscous forces are of about the same magnitude as inertial forces, and hence cannot be ignored. Outside the boundary layer, the flow conforms very closely to the behavior of a perfect fluid: frictional forces are negligible in this region. This partitioning of the flow permits a mathematical solution to the problem of flow about a body at high Reynolds numbers to be obtained. This is generally done by first

determining the flow about the body by the methods of classical hydrodynamics -- the so-called "potential flow" theory. The solution thus obtained for the flow outside the boundary layer provides what mathematicians call "boundary conditions" which allow the solution of the boundary-layer equations to be carried out. The two solutions are then "grafted together" where the boundary layer ends and the outer flow begins, to provide a picture of the total flow pattern.

The mathematical difficulties involved in the solution of a three-dimensional boundary layer, as on a model rocket, are nevertheless of momentous proportion. Several basic problems, such as the location of the "transition point" where the character of the boundary-layer flow changes from "laminar" to "turbulent" (these terms will be discussed in detail later on), as yet lack a firm theoretical foundation for their solution. Furthermore, it is doubtful whether a complete mathematical description of the flow pattern about his model would be of great benefit to the hobbyist, as such a description can only be obtained by laborious numerical techniques requiring the use of an electronic computer for each and every case to be solved.

This section will therefore confine itself to a discussion of the basic concepts of boundary-layer theory likely to be of greatest interest and utility to the model rocketeer. The ultimate aim, of course, is to develop expressions for the viscous stresses in the boundary layer which can be related directly to the skin-friction drag. Fortunately, with the aid of certain assumptions which will be enumerated as we go on,

one can derive results which are applicable to the calculation of skin-friction drag on model rockets.

3.2 The Distinction Between Laminar and Turbulent Flow

The fluid flow within a boundary layer may be characterized as either laminar or turbulent. The distinction between these two states may be observed in the stream of smoke rising from a burning cigarette in very still air (Plate 1). For a short vertical distance the column is narrow and straight, but above this region the flow disintegrates into a disorderly, eddying stream. The smooth, unmixed phase of the flow is termed laminar; the rough, eddying part is called turbulent.

Whether the flow in the boundary layer along an object will be laminar or turbulent depends to a large extent on the Reynolds number, although physical conditions such as air turbulence and surface roughness can assume important roles. Experimentally, the value of R at which the transition from laminar to turbulent flow in the boundary layer over a flat plate will occur has been found to lie in the range between 3×10^5 and 3×10^6 (15). Since this interval includes the previously calculated typical value of R for a small model rocket, we may expect both laminar and turbulent boundary-layer flows to exist on model rockets during flight, depending on the velocity.

Consequently, we shall examine both types of boundary-layer flow. Because the analysis for a three-dimensional body can be extremely complicated, our discussion will be



Plate 1: Smoke rising from a cigarette in a still room. The path of the smoke is at first smooth and straight (laminar flow), but after it has risen for a certain distance it becomes rough and mixed (turbulent flow).

restricted to the steady, two-dimensional flow past a thin, flat plate held parallel to the airstream. Although this is geometrically a quite simple case, the skin-friction coefficients derived from the analysis of the flat plate in laminar and turbulent flow form the basis for the calculation of skin-friction drag on all three-dimensional shapes (assuming that boundary-layer separation, discussed in Section 4.2, is not present). The results of Sections 3.3 and 3.4 for laminar and turbulent flow, respectively, will be used extensively later on in this chapter for the determination of model rocket drag coefficients.

Next, in Section 3.5, a discussion of the mechanism of boundary-layer transition is presented. Since laminar and turbulent boundary layers produce markedly different skin-friction coefficients, even at identical Reynolds numbers, it is important to know the location of the transition zone in order to calculate viscous drag accurately. This problem, unfortunately, has not as yet been well-researched for model rockets, and it is necessary to assume a location for the transition. Section 3.5 analyzes the important factors affecting the location of the transition point and discusses the calculation of the total skin-friction coefficient for boundary layers exhibiting both laminar and turbulent regions.

Section 3 will conclude with some estimates of the correction factors required to apply the flat-plate results to three-dimensional configurations. This will be seen to be small, usually 5% or less, for the fins and body of a model rocket.

3.3 The Laminar Boundary Layer on a Smooth, Flat Plate

In laminar flow, the fluid elements move parallel to the surface of the body and there is little or no mixing of the fluid -- i.e., transfer of momentum -- between adjacent streamlines. Historically, the first application of Prandtl's boundary-layer theory was accomplished by H. Blasius, who in 1908 computed the laminar boundary layer in uniform potential flow past a flat plate. Since this example illustrates many of the important features of boundary-layer analysis, we shall examine it in detail.

Steady fluid motion about such a plate is depicted in Plate 2 (12). The streamlines of the flow were made visible by sprinkling aluminum particles on the water; the length of the streaks left by the particles is proportional to their velocity. Very near the surface of the plate, the traces are much shorter than in the exterior flow; this region of reduced velocity is the boundary layer. Note also that the apparent thickness of the boundary layer, which we shall shortly define in mathematical terms, increases with distance downstream along the plate. This is because the boundary-layer shearing stresses are retarding a greater volume of fluid as distance from the leading edge increases.

Note that there is no indication of the absolute size of the plate in the photograph. Hence we expect the velocity profiles (see Figure 13) at all x-stations on the plate to be mathematically similar; i.e., the dimensionless ratio u/U_∞ may be expressed as some function of the dimensionless coordinate

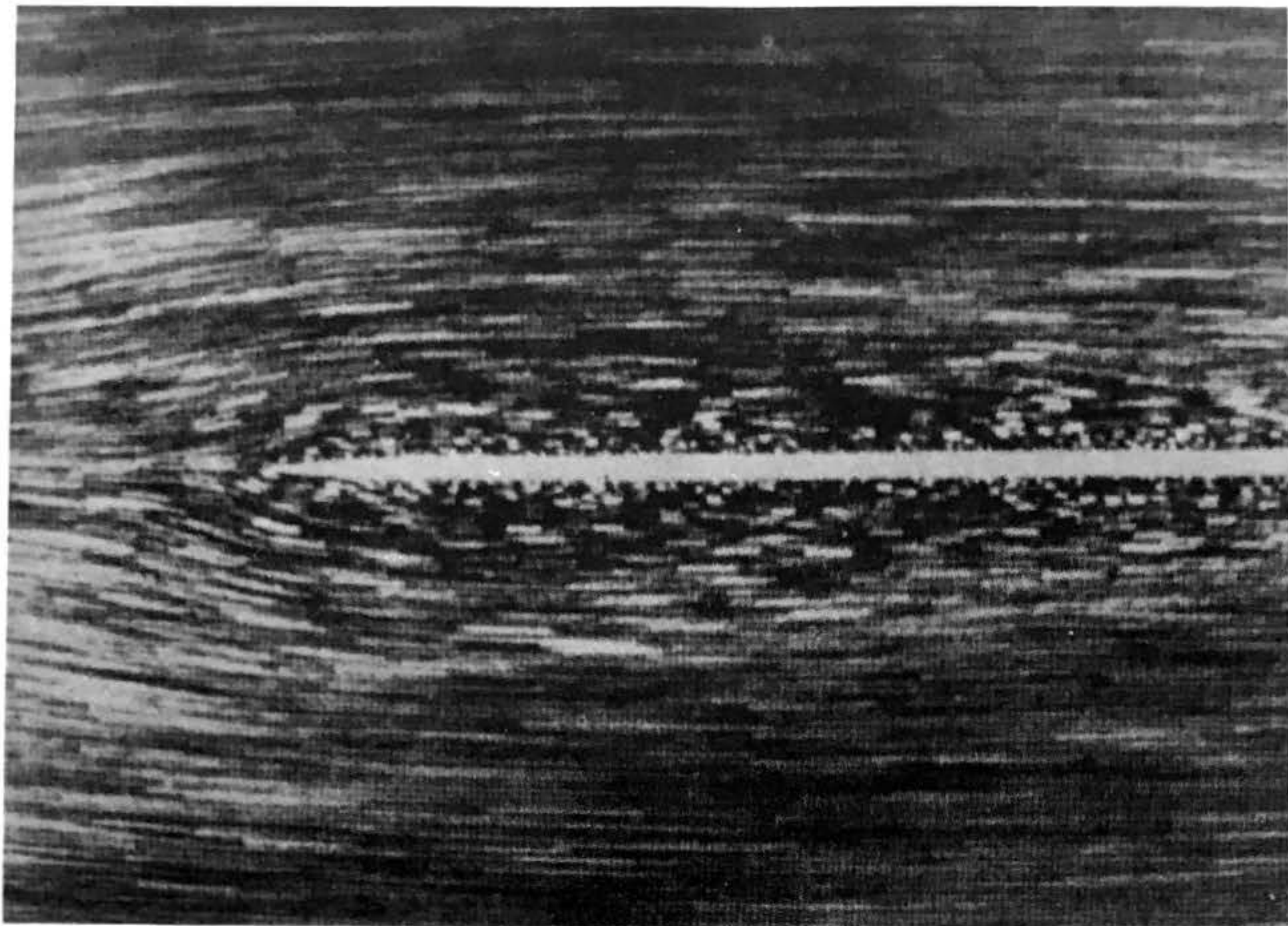


Plate 2: Flow about a thin plate of length ℓ at a Reynolds number R_ℓ of 3.

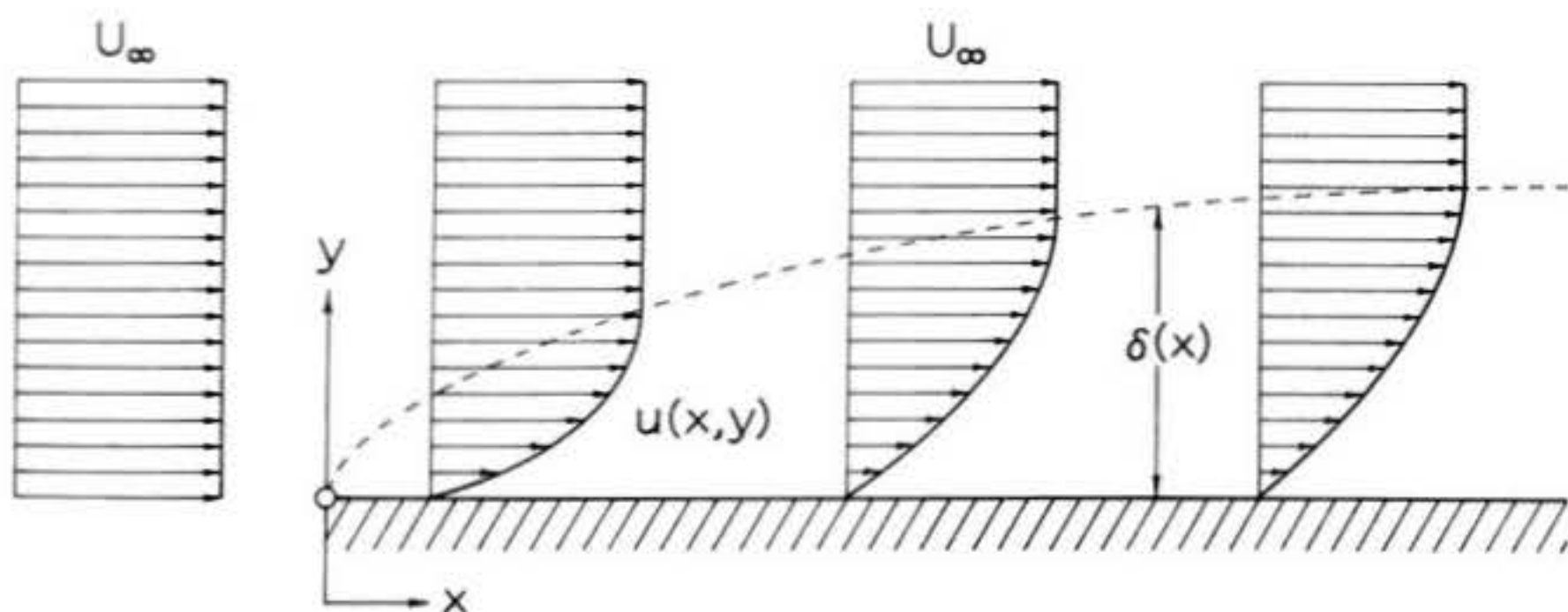


Figure 13: Profiles of longitudinal velocity in a laminar boundary layer over one side of a flat plate at zero angle of attack.

ratio y/δ , where U_∞ is the velocity of the exterior flow immediately outside the boundary layer (calculated by potential-flow theory) and δ is the boundary-layer thickness at any given location on the plate. This function must be the same at all distances x from the leading edge of the plate, although δ itself becomes greater as x increases.

We can make an estimate of the boundary-layer thickness δ by equating the viscous and inertial forces within the boundary layer and solving for the value of δ at which this condition occurs. As seen in Section 2.2, the inertial forces in the fluid flowing near an object of characteristic dimension L are of the order $\rho U_\infty^2/L$. The friction forces per unit volume in a boundary layer of thickness δ are of the order $\mu U_\infty / \delta^2$, as the velocity gradient $\frac{\partial u}{\partial y}$ exists only within the thickness of the boundary layer itself. We then obtain

$$(35) \quad \frac{\mu U_\infty}{\delta^2} \sim \frac{\rho U_\infty^2}{L}$$

Solving for the boundary-layer thickness δ ,

$$(36) \quad \delta \sim \sqrt{\frac{\mu L}{\rho U_\infty}} = \sqrt{\frac{\nu L}{U_\infty}}$$

In the case of the flat plate the characteristic length of interest is the distance from the leading edge x . Substituting x for L , we obtain the boundary-layer thickness as

$$(37) \quad \delta \sim \sqrt{\frac{\nu x}{U_\infty}}$$

The thickness of the boundary layer is thus seen to vary with the square root of the distance from the leading edge.

The object of a mathematical solution to this problem is to obtain the constant of proportionality in the expression for δ , and to determine functions for the boundary-layer velocity profile and the skin-friction drag.

The equations of fluid flow for a general, two-dimensional boundary layer are

$$(38) \quad \frac{\partial u}{\partial t} + u \frac{\partial u}{\partial x} + v \frac{\partial u}{\partial y} = - \frac{1}{\rho} \frac{dp}{dx} + \nu \frac{\partial^2 u}{\partial y^2}$$

$$(39) \quad \frac{\partial u}{\partial x} + \frac{\partial v}{\partial y} = 0$$

where u and v are the local components of velocity in the x - and y -directions, respectively. The boundary conditions required to completely define the solution to this set of equations are

$y = 0: u = v = 0$ (both the tangential and the normal velocity components must vanish at the wall)

$y = \infty: u = U_{\infty}(x, t)$ (the tangential velocity component must be identical to that computed from potential-flow theory at large distances from the wall)

Those readers who are interested in the derivation of these equations from the complete Navier-Stokes equations for general fluid flow may consult Schlichting (15).

The Blasius problem assumes a steady flow, so all derivatives with respect to time will vanish. Furthermore, the potential flow cannot detect the existence of a thin, flat plate held parallel to it; U_{∞} just remains constant at the free-stream value far from the plate, and hence dp/dx is zero (there is no pressure gradient along the plate), as may be determined from Bernoulli's equation. The boundary-layer equations are

then seen to reduce to

$$(40) \quad u \frac{\partial u}{\partial x} + v \frac{\partial u}{\partial y} = \nu \frac{\partial^2 u}{\partial y^2}$$

$$(41) \quad \frac{\partial u}{\partial x} + \frac{\partial v}{\partial y} = 0$$

and the boundary conditions become

$$y = 0: \quad u = v = 0$$

$$y = \infty: \quad u = U_\infty \quad (\text{note that } U_\infty \text{ is now independent of } x \text{ and } t)$$

To solve these equations Blasius introduced a new dimensionless variable $\eta = \frac{y}{\delta}$, or, using the expression for the approximate boundary-layer thickness from equation (37),

$$(42) \quad \eta = y \sqrt{\frac{U_\infty}{\nu x}}$$

A dimensionless streamfunction $f(\eta)$ was also introduced, such that

$$(43) \quad f(\eta) = \frac{\psi}{\sqrt{\nu x U_\infty}}$$

where $\psi(x, y)$ is the streamfunction that had been well known to potential-flow theorists of the 19th Century; it is related to the flow velocities u and v in such a manner that it identically satisfies equation (39):

$$(44a) \quad u = \frac{\partial \psi}{\partial y}$$

$$(44b) \quad v = -\frac{\partial \psi}{\partial x}$$

from which we see that

$$\frac{\partial u}{\partial x} = \frac{\partial^2 \psi}{\partial y \partial x}$$

$$\frac{\partial v}{\partial y} = - \frac{\partial^2 \psi}{\partial x \partial y} = - \frac{\partial^2 \psi}{\partial y \partial x}$$

$$\frac{\partial u}{\partial x} + \frac{\partial v}{\partial y} = \frac{\partial^2 \psi}{\partial y \partial x} - \frac{\partial^2 \psi}{\partial y \partial x} \equiv 0$$

Using equations (42) and (43) to substitute into the expressions for the velocity components, Blasius obtained

$$(45) \quad u = \frac{\partial \psi}{\partial y} = \frac{\partial \psi}{\partial \eta} \frac{\partial \eta}{\partial y} = U_\infty \frac{df(\eta)}{d\eta} = U_\infty f'(\eta)$$

$$(46) \quad v = - \frac{\partial \psi}{\partial x} = \frac{1}{2} \sqrt{\frac{\nu U_\infty}{x}} (\eta f' - f)$$

The prime symbol (') is often used in calculus to denote a derivative; hence $\frac{df(\eta)}{d\eta}$ is also written $f'(\eta)$, or simply f' .

Higher-order derivatives are denoted by multiple primes; hence $\frac{d^2 f(\eta)}{d\eta^2}$ is equivalent to f'' , etc.

From equations (45) and (46) it is possible to obtain expressions for the velocity derivatives of equation (40) in terms of the nondimensional vertical coordinate η and the nondimensional streamfunction f :

$$(47) \quad \frac{\partial u}{\partial x} = \frac{\partial u}{\partial \eta} \frac{\partial \eta}{\partial x} = [U_\infty f''] \left[-\frac{\eta}{2x} \right]$$

$$(48) \quad \frac{\partial u}{\partial y} = \frac{\partial u}{\partial \eta} \frac{\partial \eta}{\partial y} = [U_\infty f''] \sqrt{\frac{U_\infty}{\nu x}}$$

$$(49) \quad \frac{\partial^2 u}{\partial y^2} = U_\infty \sqrt{\frac{U_\infty}{\nu x}} \frac{\partial f''}{\partial \eta} \frac{\partial \eta}{\partial y} = \frac{U_\infty^2}{\nu x} f'''$$

Substituting (45) through (49) into (40), we have

$$(50) \quad -\frac{U_\infty^2}{2x} \eta f' f'' + \frac{U_\infty^2}{2x} (\eta f' - f) f'' = \nu \frac{U_\infty^2}{x \nu} f'''$$

which can be algebraically simplified to

$$(51) \quad ff'' + 2f''' = 0$$

with the boundary conditions

$$(52) \quad \eta = 0 : \quad f = 0 ; \quad f' = 0$$

$$(53) \quad \eta = \infty : \quad f' = 1$$

Now the advantage Blasius obtained by introducing the dimensionless vertical coordinate and dimensionless stream-function was that he was able to reduce equations (40) and (41), a nonlinear system of two partial differential equations, to equation (51), which is known as an ordinary, homogeneous, nonlinear differential equation: "ordinary" because f is a function of the single variable η , "homogeneous" because the right side is zero, and "nonlinear" because the product of f with f'' appears in the equation. Such an equation is easier to solve than the original system of equations; "easier", however, does not mean "easy", and a solution to equation (51) has never been obtained in closed form. Power series methods have been used to obtain accurate solutions by numerical means, but the procedure is rather complex and its mechanics are of little interest to model rocketeers (readers desiring a presentation of the method are urged to consult Reference 15). Table 1 presents the numerical tabulation obtained by L. Howarth from his highly accurate solution of equation (51).

These data can be used to obtain a picture of the velocity distribution in the boundary layer; the results for the horizontal velocity component are plotted in Figure 14. Near the wall

TABLE 1

$\eta = \gamma \sqrt{\frac{U_\infty}{2x}}$	f	$f' = u/U_\infty$	f''
0.0	0.00000	0.00000	0.33206
0.2	0.00664	0.06641	0.33199
0.4	0.02656	0.13277	0.33147
0.6	0.05974	0.19894	0.33008
0.8	0.10611	0.26471	0.32739
1.0	0.16557	0.32979	0.32301
1.2	0.23795	0.39378	0.31659
1.4	0.32298	0.45627	0.30787
1.6	0.42032	0.51676	0.29667
1.8	0.52952	0.57477	0.28293
2.0	0.65003	0.62977	0.26675
2.2	0.78120	0.68132	0.24835
2.4	0.92230	0.72899	0.22809
2.6	1.07252	0.77246	0.20646
2.8	1.23099	0.81152	0.18401
3.0	1.39682	0.84605	0.16136
3.2	1.56911	0.87609	0.13913
3.4	1.74696	0.90177	0.11788
3.6	1.92954	0.92333	0.09809
3.8	2.11605	0.94112	0.08013
4.0	2.30576	0.95552	0.06424
4.2	2.49806	0.96696	0.05052
4.4	2.69238	0.97587	0.03897
4.6	2.88826	0.98269	0.02948
4.8	3.08534	0.98779	0.02187
5.0	3.28329	0.99155	0.01591
5.2	3.48189	0.99425	0.01134
5.4	3.68094	0.99616	0.00793
5.6	3.88031	0.99748	0.00543
5.8	4.07990	0.99838	0.00365
6.0	4.27964	0.99898	0.00240
6.2	4.47948	0.99937	0.00155
6.4	4.67938	0.99961	0.00098
6.6	4.87931	0.99977	0.00061
6.8	5.07928	0.99987	0.00037
7.0	5.27926	0.99992	0.00022
7.2	5.47925	0.99996	0.00013
7.4	5.67924	0.99998	0.00007
7.6	5.87924	0.99999	0.00004
7.8	6.07923	1.00000	0.00002
8.0	6.27923	1.00000	0.00001

Table 1: Numerical solution of the laminar boundary layer over a flat plate at zero angle of attack, obtained after the method of H. Blasius by L. Howarth.

TABLE 1 (continued)

$\eta = \gamma \sqrt{\frac{U_\infty}{\nu x}}$	f	$f' = u/U_\infty$	f''
8.2	6.47923	1.00000	0.00001
8.4	6.67923	1.00000	0.00000
8.6	6.87923	1.00000	0.00000
8.8	7.07923	1.00000	0.00000

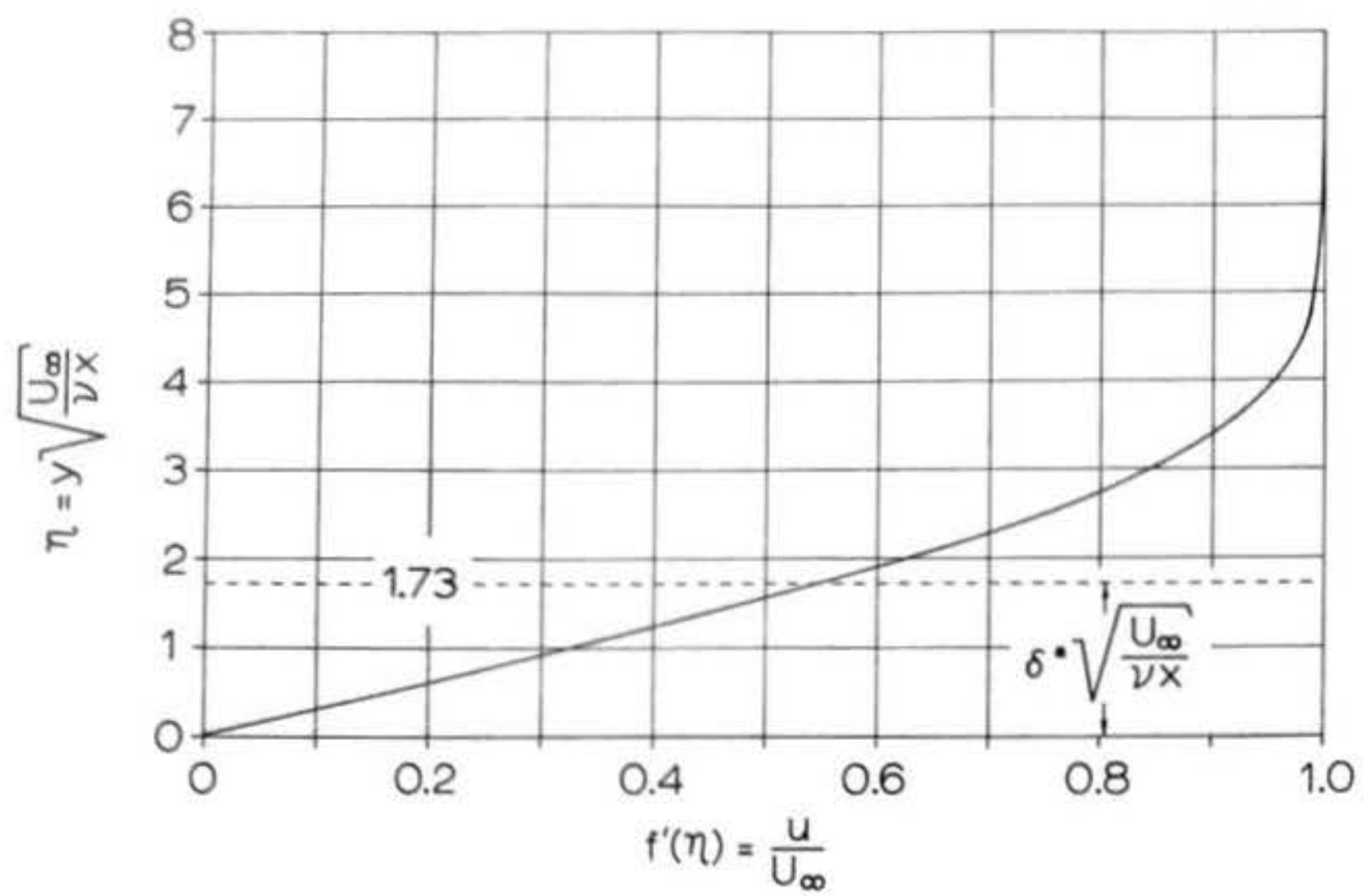


Figure 14: Horizontal velocity component vs. η in a laminar boundary layer over a flat plate at zero angle of attack. η has been taken as the vertical axis because it is the dimensionless coordinate perpendicular to the plate's surface. The quantity δ^* is called the displacement thickness and is equal to approximately $1/3 \delta$.

the horizontal velocity component is nearly a linear function of the y coordinate, but as y increases the slope of the curve rapidly steepens as u approaches the potential-flow velocity U_∞ .

Notice that the free-stream velocity is attained asymptotically; i.e., that the boundary layer shades gradually into the exterior flow, so that the concept of "boundary-layer thickness" is ambiguous. The generally-accepted definition is based on the distance from the wall where the velocity differs by 1% from U_∞ ; i.e., where $u = 0.99U_\infty$. From Table 1 we see that this corresponds to $\eta \approx 5.0$; hence

$$(54) \quad \delta = 5 \sqrt{\frac{v x}{U_\infty}}$$

Evaluating this expression for $U_\infty = 60$ meters/second (6000 centimeters/second) and $v = 1.495 \times 10^{-5}$ meter 2 /second (0.1495 cm 2 /second), we obtain

$$(55a) \quad \delta = 3.10 \times 10^{-3} \sqrt{x}$$

for x and δ in meters, and

$$(55b) \quad \delta = 3.10 \times 10^{-2} \sqrt{x}$$

for x and δ in centimeters. At $x = 1$ cm., then, the boundary-layer thickness δ is .031 cm.; at $x = 10$ cm. δ is .098 cm., while at $x = 100$ cm. (1 meter) δ is .310 cm. The corresponding Reynolds numbers based on x are 4.02×10^4 , 4.02×10^5 , and 4.02×10^6 , respectively.

The transverse component of velocity, v , can also be

determined from the Blasius solution by substituting values for f and f' at each value of η desired into equation (46). The variation of the nondimensional quantity $\frac{v}{U_\infty} \sqrt{\frac{U_\infty x}{\nu}}$ with η is plotted in Figure 15. As η approaches infinity v does not vanish, but instead attains the asymptotic value

$$(56) \quad v_\infty = 0.865 U_\infty \sqrt{\frac{\nu}{x U_\infty}}$$

Examining again the case of $U_\infty = 60$ meters/second, we obtain

$$(57) \quad v_\infty = \frac{3.22 \times 10^{-2}}{\sqrt{x}} \text{ meters/second}$$

where x must be given in meters. Thus, at a point 1 cm. from the plate leading edge (that is, 0.01 meter), the value of v_∞ is 0.322 meter/second -- insignificant, of course, compared with U_∞ but still nonzero. The nonzero value of the transverse velocity at the upper edge of the boundary layer is explained by the fact that the increasing boundary-layer thickness causes the airstream to be displaced from the wall as it flows along it, creating a slight outward velocity component. This is not the same as the flow separating entirely from the wall, a phenomenon that occurs only in an "adverse pressure gradient"; i.e., when the pressure in the boundary layer is increasing in the direction of flow. The flat plate at zero angle of attack, it will be recalled, exhibits a zero pressure gradient.

The Blasius solution enables us to determine the skin-friction drag on the flat plate with a laminar boundary layer by specializing the equation for the viscous drag on a surface in general, two-dimensional flow:

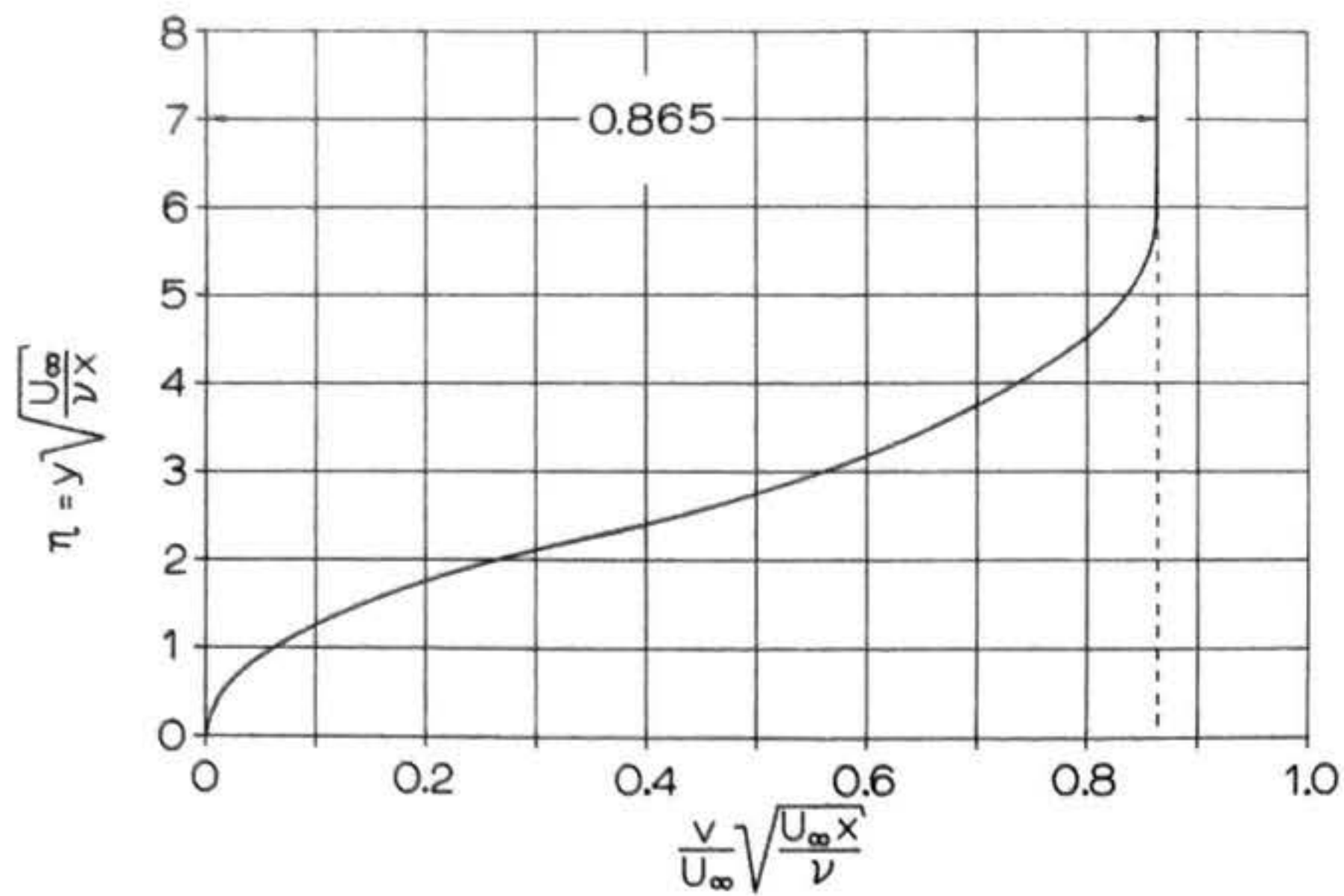


Figure 15: Nondimensionalized transverse velocity component $\frac{v}{U_\infty} \sqrt{\frac{U_\infty x}{\nu}} \eta$ vs. η in a laminar boundary layer over a flat plate at zero angle of attack. Again, η has been taken as the vertical axis.

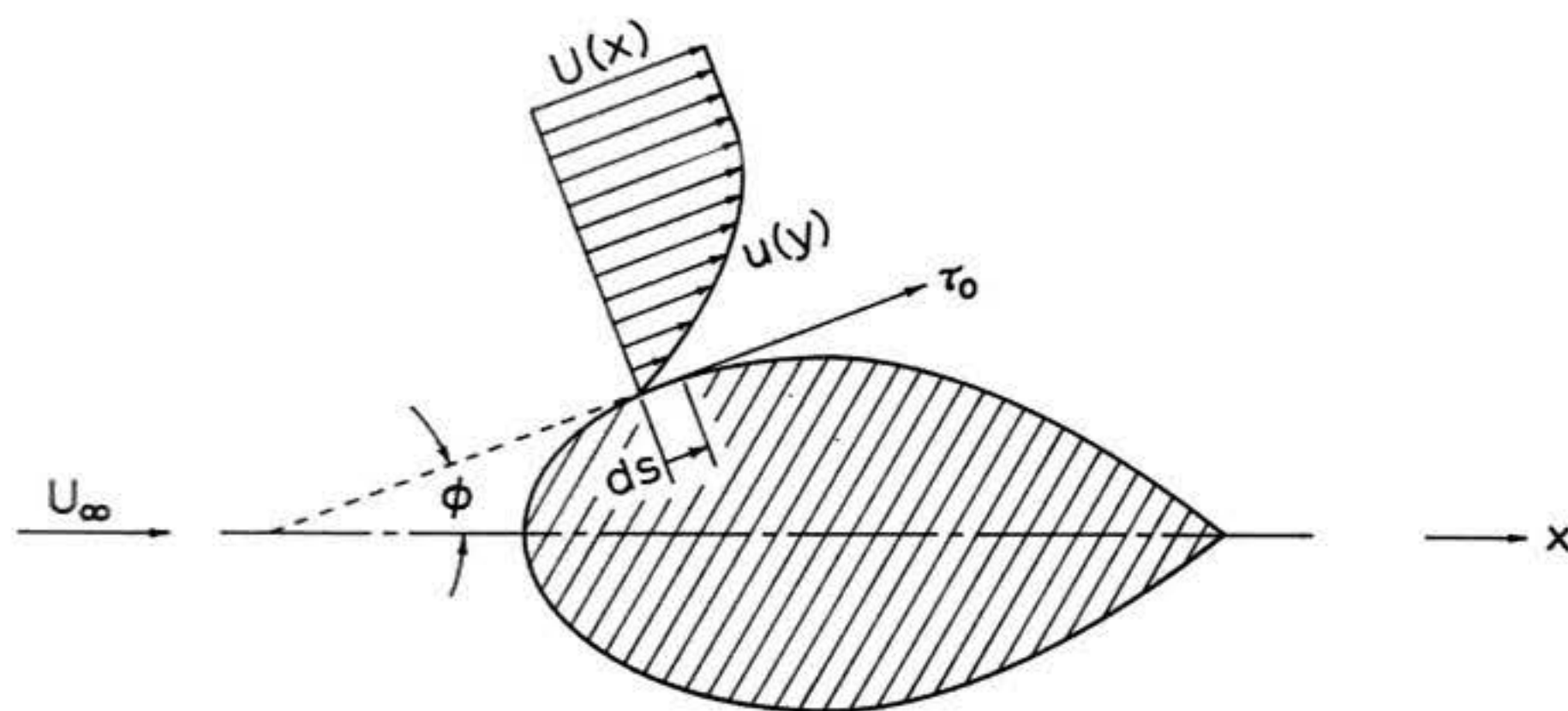


Figure 16: Notation used in determining the friction drag of an object of finite thickness in laminar flow.

$$(58) \quad D_v = b \int_{s=0}^l \tau_o \cos \phi ds$$

where τ_o is the shearing stress at the wall, b is the span of the object (dimension transverse to the flow), and l is distance measured around the object's profile from front to rear. The notation of equation (58) is explained pictorially in Figure 16. For a flat plate of negligible thickness the angle ϕ is zero everywhere, so $\cos \phi = 1.0$. In such a case the differential path length ds is also equal to dx , so

$$(59) \quad D_v = b \int_{x=0}^l \tau_o dx$$

From equations (34) and (48)

$$(60) \quad \tau_o(x) = \mu \left(\frac{\partial u}{\partial y} \right)_{y=0} = \mu U_\infty \sqrt{\frac{U_\infty}{\nu x}} \cdot f''(0) = \alpha U_\infty \sqrt{\frac{U_\infty}{\nu x}}$$

where the quantity $f''(0)$ has been represented by the symbol α (not to be confused with angle of attack in this application). From Table 1, α is found to be 0.332. Hence, the skin-friction drag on one side of the plate is

$$(61) \quad D_v = .332 \mu b U_\infty \sqrt{\frac{U_\infty}{\nu}} \int_{x=0}^l \frac{dx}{\sqrt{x}} = .664 b U_\infty \sqrt{\mu \rho l U_\infty}$$

For both sides (the total friction drag), we have

$$(62) \quad 2D_v = 1.328 b \sqrt{U_\infty^3 \mu \rho l}$$

The friction drag coefficient for laminar flow over a flat plate wetted on both sides is thus

$$(63) \quad C_f = \frac{2D_v}{\frac{1}{2} \rho U_\infty^2 A} = \frac{1.328}{\sqrt{Rl}}$$

where A , the lateral area of both sides of the plate, is $2bl$

and R_f is the Reynolds number based on the length of the plate if the plate is too short for transition to turbulent flow to occur anywhere on its surface. If the plate is sufficiently long for transition to occur, R_f is the Reynolds number based on the distance from the leading edge to the transition zone and the coefficient computed according to equation (63) is valid only for that portion of the plate forward of the transition region. Recalling our numerical example of $U_\infty = 60$ meters/second, suppose we compute the friction drag coefficient of a typical model rocket fin with an average chord of 3 cm. (.03 meter). For such a case we obtain

$$(64) \quad C_f = \frac{1.328}{\sqrt{12.06 \times 10^4}} = .00382$$

We must remember, however, that friction drag coefficients as originally computed are based on wetted area -- that is, total lateral surface area. To use them in calculating the overall drag coefficient of a model rocket, one must convert them to coefficients based on maximum body frontal area. This procedure will be described later on.

3.4 The Turbulent Boundary Layer on a Smooth, Flat Plate

At a certain value of the Reynolds number, the fluid flow in the boundary layer above a given surface will change from laminar to turbulent -- a phenomenon known as transition. Plate 3 illustrates a case of transition occurring in a channel of water. As the Reynolds number increases from subcritical (fully laminar flow) to supercritical (fully turbulent flow) values, a thread of dye injected into the fluid is subjected

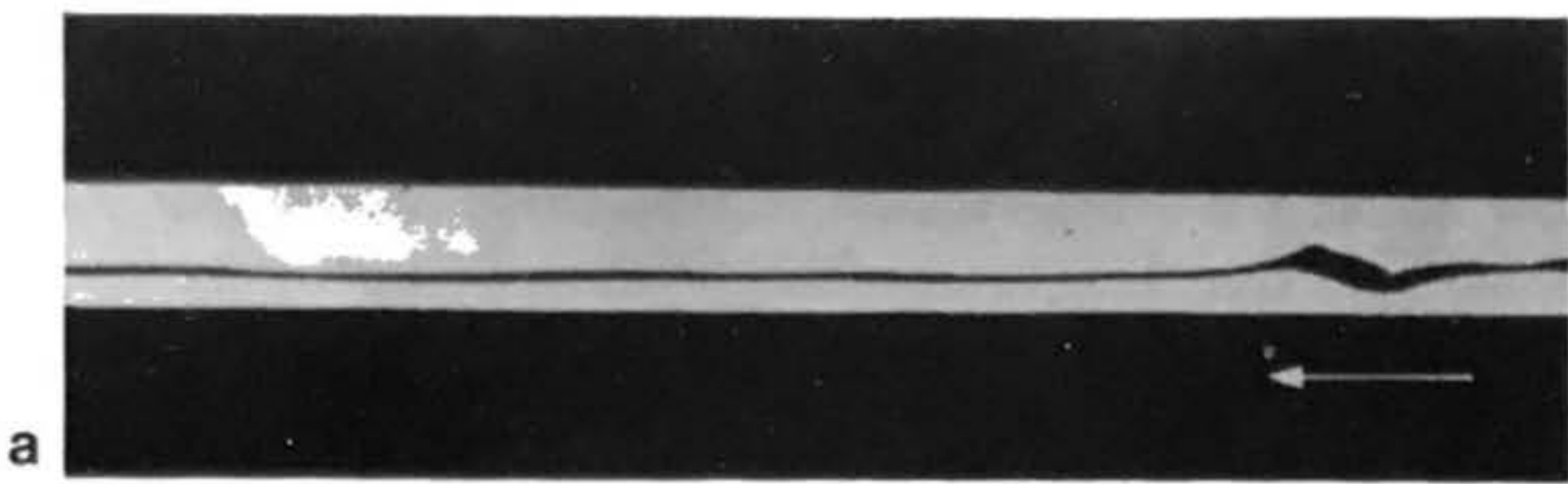


Plate 3: The Reynolds dye experiment, illustrating the transition from laminar to turbulent flow in a channel of liquid. A thread of dye injected into the flowing fluid at first remains smooth and straight (a), but farther down the channel the critical Reynolds number of the flow has been exceeded and the stream is turbulent (b), causing the dye to be mixed.

to increasing mixing action until finally the entire channel is colored. In this section we will consider the structure of the fully-turbulent boundary layer in the flow over a smooth, flat plate, noting how the velocity profiles, boundary-layer thickness, and skin-friction drag differ from the laminar case.

In laminar flow, streamlines move more or less parallel to each other with negligible mixing, and if the flow is steady the velocity at any point in the flow remains constant as time goes on. When turbulent flow is observed closely, however, subsidiary motions of the fluid transverse to the main motion downstream are detected (15). The velocity at a point is no longer constant, but is subject to excursions, or variations, about some average value. This behavior amounts to mixing between the streamlines and causes an exchange of momentum in the transverse direction, because each fluid element essentially retains its forward momentum while mixing is occurring. Hence, the velocity profile in the turbulent boundary layer is such that the x-component of velocity increases far more slowly with height over most of the boundary-layer thickness than is the case for the laminar boundary layer.

The distinctive feature of turbulent flow is the irregular, high-frequency oscillations exhibited by the velocity and pressure at a point. These quantities can be considered constants only as an average over an extended period of time. Turbulent flow must still observe the no-slip condition at the wall, however, and there is thus a region very close to the wall where viscous stresses are of larger magnitude than the stresses due to

turbulence which dominate the rest of the boundary layer. Since the conditions of flow in this very thin region -- perhaps 1% or so of the total turbulent boundary layer thickness -- are essentially laminar, it is known as the laminar sublayer. Despite its small thickness, the sublayer plays a vital role in determining the magnitude of the viscous shearing stress at the wall and hence the turbulent skin-friction drag. We shall encounter it again in Section 5.4 when we examine drag due to surface roughness.

Because of its extensive applicability, we would like to determine the turbulent skin-friction drag on a smooth, flat plate as we did in the laminar-flow case. The same general methods of derivation cannot, however, be used again owing to two major difficulties: (a) very little is known about the nature of the transition that occurs as one passes upward from the laminar sublayer to the turbulent region; and (b) the laws of friction which are effective in the sublayer are also unknown. We proceed, then, on a different tack, by assuming that the boundary-layer velocity distribution over a plate is similar to that within a circular pipe. This allows us to avail ourselves of the extensive data available for pipe flow, which has been studied in experiments preferentially to the plate case since it is much more difficult to carry out measurements in the boundary layer of a plate than in that within a pipe (15).

The validity of this assumption has been established, at least for moderate Reynolds numbers, by experimental investigations. Since the boundary layer in a pipe is formed under

the influence of a pressure gradient (the pressure at the downstream end of the pipe must be less than that at the upstream end, or no fluid would flow through it), while for the flat plate dp/dx was assumed equal to zero, the velocity distributions for the two configurations certainly cannot be exactly identical. Because the friction drag is calculated from a spatial integral of the fluid momentum in cases of turbulent flow, however, small differences in the velocity distribution are not critical (15).

In order to compute skin-friction drag for a turbulent boundary layer, it is first necessary to introduce the concept of the momentum thickness, θ , of the boundary layer. The rate at which x -momentum per unit span of the plate (or per unit circumferential distance of the pipe) is being lost due to the presence of the boundary layer instead of potential flow is given by $\int_0^\infty u(U_\infty - u) dy$. We may therefore define a quantity θ such that

$$(65) \quad \rho U_\infty^2 \theta = \int_{y=0}^\infty u (U_\infty - u) dy$$

or

$$(66) \quad \theta = \int_{y=0}^\infty \frac{u}{U_\infty} \left(1 - \frac{u}{U_\infty} \right) dy$$

Then in the case of laminar flow, since $(u/U_\infty) = f'$,

$$(67) \quad \theta = \sqrt{\frac{\nu x}{U_\infty}} \int_{\eta=0}^\infty f' (1-f') d\eta$$

or

$$(68) \quad \theta = 0.664 \sqrt{\frac{\nu x}{U_\infty}}$$

This is approximately 1/8 of the boundary-layer thickness defined by equation (54).

Now we may relate θ to the skin-friction drag in the following manner: consider a flat plate surrounded by a rectangular control surface (an imaginary surface in space -- a concept often used in the analysis of fluid-flow problems) identified by its corner points, A_1B_1B , as in Figure 17. Segment A_1B_1 , parallel to the plate, is sufficiently far from the wall that it lies in the region of undisturbed velocity U_∞ . Pressure forces in such a case are constant over the whole control surface, so one need not consider their contribution to the fluid momentum. Due to symmetry, moreover, segment AB contributes nothing to the momentum in the x -direction. Assigning positive value to mass flowing in and negative value to mass flowing out of the region enclosed by the control surface, the momentum balance may be expressed as in Table 2.

Momentum conservation requires that the drag force D be exactly equal to the total momentum flux through the control surface, or

$$(69) \quad D = \rho b \int_0^h (U_\infty^2 - u^2 - U_\infty^2 - uU_\infty) dy$$

The upper limit of integration may be changed to infinity, as the integrand is zero for $y > h$; hence

$$(70) \quad D = \rho b \int_0^\infty u(U_\infty - u) dy$$

This expression applies to a plate wetted on only one side; to obtain the drag for a plate wetted on both sides, we evaluate

TABLE 2

Cross-Section	Rate of Flow	Momentum Flux in x-Direction
AB	0	0
AA ₁	$b \int_0^h U_\infty dy$	$\rho b \int_0^h U_\infty^2 dy$
BB ₁	$-b \int_0^h u dy$	$-\rho b \int_0^h u^2 dy$
A ₁ B ₁	$-b \int_0^h (U_\infty - u) dy$	$-\rho b \int_0^h U_\infty (U_\infty - u) dy$
sum = control surface	total net rate of flow = 0	total momentum flux = drag

Table 2: Volume flow and momentum flux accounting associated with the control surface pictured in Figure 17, for use in calculating turbulent skin-friction drag.

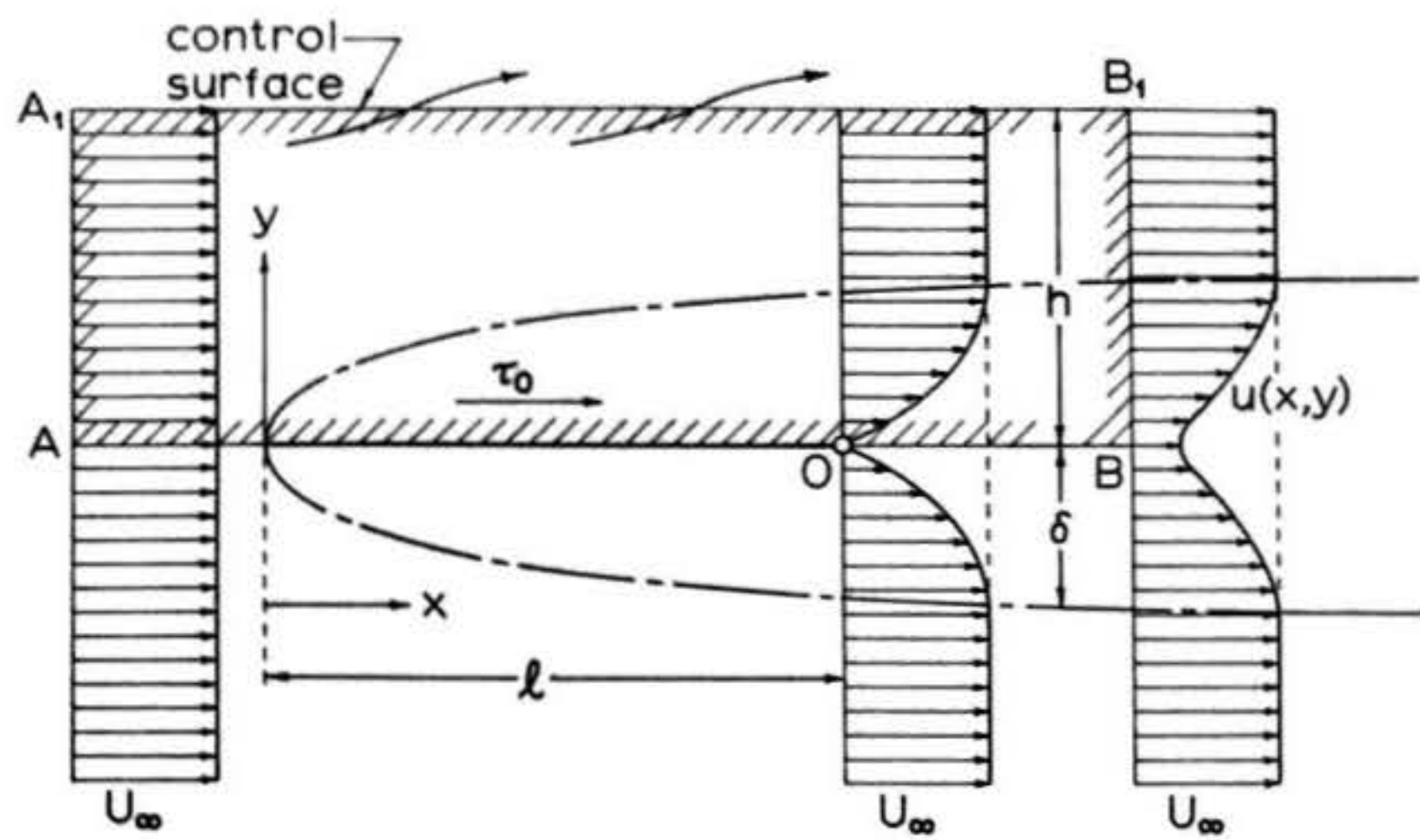


Figure 17: Control surface for calculating the friction drag due to a turbulent boundary layer over a flat plate at zero angle of attack.

$$(71) \quad 2D = \int_{-\infty}^{\infty} u(U_{\infty} - u) dy$$

Two remarks concerning these integrals should be made here. First, equation (70) is applicable to any symmetrical cylindrical body, not only a flat plate; in the case of a cylindrical body b is merely replaced by the circumference of the cylinder. Second, the integral may be evaluated at any station x on the body, in which case it will give the drag due to skin friction on the region extending from the leading edge to that particular station.

Now from equation (65) it will be recalled that

$$(72) \quad U_{\infty}^2 \theta = \int_{y=0}^{\infty} u(U_{\infty} - u) dy$$

This expression is identical to the integral appearing in equations (70) and (71); hence we have

$$(73) \quad D = b \int_{y=0}^{\infty} U_{\infty}^2 \theta dy$$

We return now to an explicit consideration of the turbulent boundary layer on a flat plate. From the empirical results for turbulent boundary layers in pipe flow we adopt the "1/7th-power velocity distribution law" in the form

$$(74) \quad \frac{u}{U_{\infty}} = \left(\frac{y}{\delta} \right)^{1/7}$$

As in the laminar case, this relationship requires that all the velocity profiles along a flat plate in turbulent flow be of the same form, and thus one curve plotted in dimensionless coordinates can represent them all.

The results of experiments with turbulent boundary layers

in circular pipes have also shown that the shearing stress at the wall obeys the relation

$$(75) \quad \frac{\tau_o}{\rho U_{\infty}^2} = 0.0225 \left(\frac{y}{U_{\infty} \delta} \right)^{1/4}$$

The momentum thickness can now be obtained in terms of the boundary-layer thickness δ by direct integration from equations (66) and (74):

$$\begin{aligned} \Theta &= \int_{y=0}^{\delta} \frac{u}{U_{\infty}} \left(1 - \frac{u}{U_{\infty}} \right) dy \\ &= \int_{y=0}^{\delta} \left(\frac{y}{\delta} \right)^{1/2} \left[1 - \left(\frac{y}{\delta} \right)^{1/2} \right] dy \\ &= \int_0^{\delta} \left(\frac{y}{\delta} \right)^{1/2} dy - \int_0^{\delta} \left(\frac{y}{\delta} \right)^{2/2} dy = \frac{7}{8} \delta - \frac{7}{9} \delta \end{aligned}$$

Then

$$(76) \quad \Theta = \frac{7}{72} \delta$$

Now if we differentiate equation (73) with respect to x we obtain

$$(77) \quad \frac{1}{b} \frac{dD}{dx} = \tau_o(x) = \rho U_{\infty}^2 \frac{d\theta}{dx}$$

Combining equations (76) and (77) then yields

$$(78) \quad \frac{\tau_o}{\rho U_{\infty}^2} = \frac{d\theta}{dx} = \frac{7}{72} \frac{d\delta}{dx}$$

Substituting (78) into (75), we have

$$(79) \quad \frac{7}{72} \frac{d\delta}{dx} = 0.0225 \left(\frac{y}{U_{\infty} \delta} \right)^{1/4}$$

An explicit expression for δ as a function of x can now be obtained by integrating this ordinary differential equation in δ , assuming that $\delta = 0$ at $x = 0$. The result is

$$(80) \quad \delta = 0.37 X \left(\frac{U_\infty X}{\nu} \right)^{-\frac{1}{5}}$$

and

$$(81) \quad \theta = 0.036 X \left(\frac{U_\infty X}{\nu} \right)^{-\frac{1}{5}}$$

The boundary-layer thickness in turbulent flow is thus seen to increase more rapidly with distance than in the laminar case: $\delta(x)$ is proportional to $x^{\frac{4}{5}}$ for a turbulent boundary layer, while $\delta(x)$ for a laminar boundary layer varies as $x^{\frac{1}{2}}$. The difference is due to the mixing action present in turbulent flow, which causes greater momentum and energy losses per unit time than is the case for laminar boundary layers.

From equations (73) and (81), the turbulent skin-friction drag on one side of a flat plate may now be written as

$$(82) \quad D = b \delta U_\infty^2 \theta = 0.036 \rho U_\infty^2 b l \left(\frac{U_\infty l}{\nu} \right)^{-\frac{1}{5}}$$

The drag varies as $U_\infty^{\frac{9}{5}}$ and $l^{\frac{4}{5}}$, as compared to $U_\infty^{\frac{3}{2}}$ and $l^{\frac{1}{2}}$ for the laminar boundary layer. The skin-friction coefficient C_f can then be determined from its definition and equation (82):

$$(83) \quad C_f = \frac{D}{\frac{1}{2} \rho U_\infty^2 b l}$$

$$(84) \quad C_f = \frac{2 \theta(l)}{l}$$

and finally, we arrive at the result

$$(85) \quad C_f = 0.072 \left(\frac{U_\infty l}{\nu} \right)^{-\frac{1}{5}}$$

This expression has been found to represent experimental results very well, provided the value of the numerical coefficient is altered slightly to 0.074 (15):

$$(86) \quad C_f = 0.074 \left(\frac{U_\infty l}{\nu} \right)^{-\frac{1}{5}} = 0.074 (R_l)^{-\frac{1}{5}}$$

This relationship, valid for a flat plate with a completely turbulent boundary layer from the leading edge downstream, is limited to the range of Reynolds numbers between 5×10^5 and 1×10^7 -- a range which, fortunately, includes the upper limit of R to be expected in the vast majority of model rocket flights.

Table 3 summarizes the results of our analyses of purely laminar and purely turbulent boundary layers:

TABLE 3

characteristic	laminar value	turbulent value
C_f	$\frac{1.328}{(R_l)^{1/2}}$	$\frac{0.074}{(R_l)^{1/5}}$
δ	$5 \sqrt{\frac{\nu x}{U_\infty}}$	$0.37x \left(\frac{U_\infty x}{\nu} \right)^{-\frac{1}{5}}$
u/U_∞	as given in Table 1	$\left(\frac{y}{\delta} \right)^{1/7}$

To give a representative example of a turbulent skin-friction coefficient, suppose we consider again the free-stream velocity $U_\infty = 60$ meters/second and a plate with a length of 0.3 meter, giving a Reynolds number of 1.206×10^6 . Assuming that some condition of free-stream turbulence or some device like a trip-wire has caused the boundary layer to be turbulent all along the length of the plate, we derive the result

$$C_f = .0045$$

3.5 Boundary Layer Transition

3.5.1 Effect of Pressure Gradient and Reynolds Number

The two preceding sections dealt with boundary layers that are entirely laminar or entirely turbulent in character. In reality, the flow over a flat plate may exhibit both forms of behavior. Laminar conditions will generally exist from the leading edge downstream to a point at which the local Reynolds number $R_x = U_\infty x/\nu$ attains a value somewhere between 3×10^5 and 3×10^6 . At higher local Reynolds numbers the flow is almost certain to be turbulent.

The exact value of the Reynolds number at which this phenomenon of transition from laminar to turbulent flow occurs depends on a number of factors: the turbulence level of the free stream, the roughness of the surface, centrifugal body forces due to rotation of the body, and whether or not heat is being transferred to the boundary layer from the body or from external sources. The pressure gradient in the external flow (which is uniformly zero for a flat plate) also exerts a considerable influence on transition, as will be seen shortly.

The hypothesis which underlies theoretical studies of transition was first enunciated by Osborne Reynolds: that the process of transition from laminar to turbulent flow comes about as the consequence of an instability in the laminar flow (15). Small disturbances, which may arise from any of the sources listed above, are assumed to act upon the laminar flow. The theory of stability attempts to determine whether these disturbances magnify or die away with time. If they decay, the flow is considered stable; if, instead, they grow in magnitude, the

flow is regarded as unstable and transition to a turbulent pattern may result. The ultimate object of the stability theory is a prediction of the critical Reynolds number, R_{crit} , for which transition may be expected.

The results of the stability analysis for a flat plate will not be presented here (readers interested in this analysis may consult Reference 15), as they are not directly applicable to the three-dimensional boundary layer on a model rocket. Instead, we shall investigate briefly the effects of the pressure gradient in the external flow on boundary-layer stability, and then present the hypothetical model of transition on model rockets which will be used for the calculation of drag coefficients in Section 6.

The great English scientist, Lord Rayleigh (1842-1919) was the first to propose that velocity profiles with a point of inflection (point at which the curvature reverses) are unstable. Figure 18 compares such a profile with one found in a region of stable flow. Rayleigh's observation is of great practical significance, because there is a direct relationship between the existence of an inflection point and the nature of the local pressure gradient. The pressure distribution on a surface in fluid flow (for cases in which there is no separation of the boundary layer) is determined by the theory of potential flow, which, it will be remembered, applies to the inviscid, "perfect" fluid. In real cases it is found that this theoretical pressure distribution agrees very closely with measured pressure distributions, as if the boundary layer were not present. In a sense, then, the external flow impresses its pressure distribution

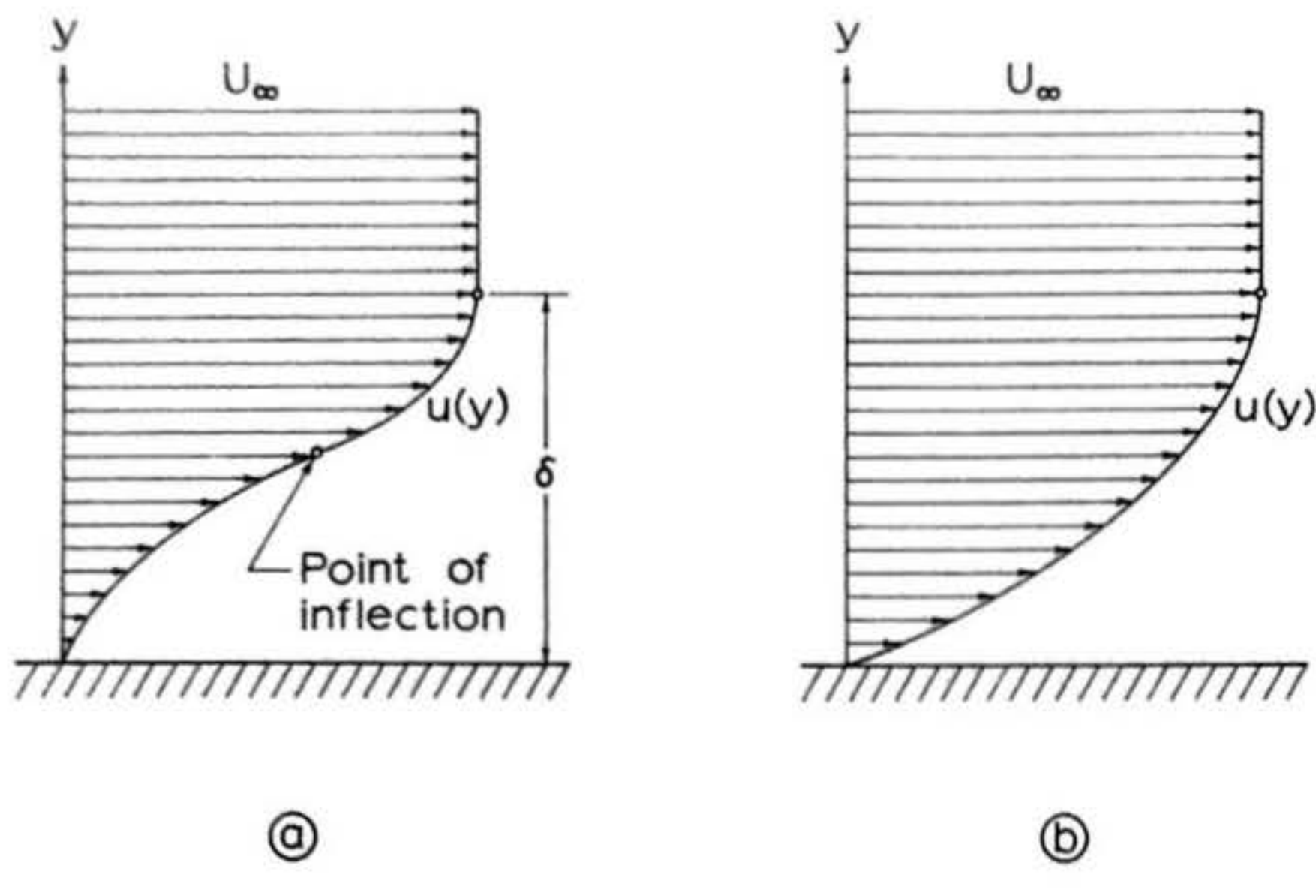


Figure 18: Stable and unstable boundary layer velocity profiles. Profile (a) has a point of inflection; that is, a point at which the curvature of the velocity profile reverses. Profile (b) is fully convex in the direction of flow. The flow of profile (a) is unstable, while that of (b) is stable.

on the boundary layer. Along a surface with a favorable pressure gradient; that is, with the pressure decreasing in the downstream direction, the boundary-layer velocity profiles will be full and without inflection points, as in Figure 18b. In the presence of an adverse pressure gradient; i.e., where the pressure increases downstream, the velocity profiles will generally develop inflection points, as in Figure 18a. In summary, then, a favorable pressure gradient tends to stabilize the flow in the boundary layer, while an adverse pressure gradient tends to destabilize it. The point of minimum pressure on a body is therefore of considerable importance; it determines the point of transition, and the two are generally in close proximity.

For an object such as a circular cylinder held with its axis perpendicular to the stream, the region of minimum pressure occurs near the shoulder as seen in Figure 24 (the angles φ = 0° and 180° correspond to the front and rear stagnation points, respectively). This experimental fact could also be deduced from equation (23): since the flow must be accelerated initially to pass over the upstream half of the cylinder, there is a corresponding decrease in static pressure in this region. Along the downstream side (in the ideal case) the flow is decelerated to its original undisturbed velocity and static pressure.

Something analogous to this process occurs on the nose of a model rocket: the flow is accelerated slightly and a point of minimum pressure is attained somewhere in the vicinity of the body-to-nosecone joint. If the rocket possesses a circular

cylindrical body, no further deflection of the flow will occur until the vicinity of the base is reached. Along the body, then, it is expected that the pressure gradient is either zero or very small; hence no adverse pressure gradient is expected anywhere along the airframe of such a rocket and it is assumed that the location of the transition point on a typical model rocket is independent of the external pressure distribution. If the model has a boattail, however, an adverse pressure gradient will exist on it and transition -- or even separation -- can be expected in the flow about such a component.

No data are available to indicate either where transition first occurs on a model rocket or the corresponding critical Reynolds number. The following hypothetical description, based on the flow behavior observed about streamlined bodies similar to model rockets, is advanced with some reservations as a model for boundary-layer transition on model rockets: at low velocities, corresponding to Reynolds numbers based on body length below about 3×10^5 , the boundary layer on a model rocket will be completely laminar. As the velocity increases, the local Reynolds number $R_x = U_\infty x / \nu$ (based on axial distance from the nosecone tip) will exceed at some station x the experimentally-determined (or assumed) value of R_{crit} for the rocket. This event will first occur near the model's tail, where the local Reynolds numbers are greatest; hence a small region of turbulent flow will first appear on the body near the base. As the velocity continues to increase, all values of R_x also increase and the transition point, determined by $R_x = R_{crit}$, will move progressively toward the nose.

A similar progression of events will occur on the fins, but at much higher body Reynolds numbers R_f , because the nature of the flow over the fins is determined by the Reynolds number based on fin chord length $R_c = U_\infty c/\nu$. For typical model rockets, R_f is an order of magnitude greater than R_c ; a turbulent boundary layer will therefore not generally be found on model rocket fins except in cases of exceptionally large rockets and/or exceptionally high velocities. The reasoning of this and the last paragraph is based on the assumption of perfectly smooth surfaces. Roughness, as will be shown in the following section, can induce premature transition.

3.5.2 Effects of Surface Roughness

The presence of roughness elements, whether isolated or distributed in groups, in a laminar flow is known to be generally conducive to transition. Under otherwise identical conditions, transition occurs at a lower Reynolds number on a rough wall than on a smooth one. This behavior follows from the theory of stability, as the roughness elements create disturbances in the flow which add to those already present in the boundary layer and the external flow. Transition will occur at a lower value of R than would otherwise be the case if the disturbances created by the roughness exceed those due to the turbulence already present in the flow. If, however, the roughness elements are very small, turbulent disturbances from the free stream will dominate and the roughness should have no effect on transition.

We examine first the effect of a cylindrical wire which is attached to a wall at right angles to the stream direction.

S. Goldstein has determined the critical height k_{crit} of such a wire; i.e., the wire diameter just small enough so as not to influence transition, to be (15)

$$(87) \quad k_{crit} = \frac{7\nu}{\sqrt{\frac{\tau_{ok}}{f'}}$$

where τ_{ok} is the shearing stress at the wall in the laminar boundary layer at the location of the wire. Now for a flat plate, equation (60) gives

$$(88) \quad \tau_o(x) = \mu U_\infty \sqrt{\frac{U_\infty}{\nu x}} f''(0)$$

and from Table 1, $f''(0) = 0.332$. Recognizing that $\mu = \nu f'$,

$$(89) \quad \tau_o(x) = \frac{0.332}{\sqrt{R_x}} f' U_\infty^2 = \tau_{ok}$$

Then for a flat plate,

$$(90) \quad k_{crit} = \frac{12.2 \nu (R_x)^{1/4}}{U_\infty} = 12.2 \left(\frac{\nu}{U_\infty} \right)^{3/4} x^{1/4}$$

where the quantities involved must all be members of the same consistent set of units. For example, if $U_\infty = 60$ meters/second and $x = 3$ cm. (0.03 meter), the critical height will be

$$k_{crit} = 5.67 \times 10^{-5} \text{ meter} = 5.67 \times 10^{-3} \text{ cm.}$$

The cylindrical wire of the foregoing analysis could represent a paintbrush hair, the body-to-nosecone joint, or any similar small, cylindrical protuberance on the model's surface. If such protuberances have heights greater than the value of k_{crit} computed according to equation (90), there is some danger of premature transition. For the nosecone joint or surface, considering the stabilizing effect of the favorable pressure

gradient, the value of k_{crit} given by equation (90) is probably somewhat too small. Assuming it does give the correct order of magnitude, however, it is apparent that a model rocket requires a rather smooth surface to minimize the possibility of transition occurring prematurely, with its consequent marked increase in skin-friction drag.

In reality, the transition point will occur somewhat downstream of a roughness element which just exceeds k_{crit} as determined by equation (90). This is due to the fact that a finite "amplification time" is required for the disturbances due to the protrusion to generate turbulent flow. In order to induce effectively instantaneous transition, the height of the protrusion must be two or three times that predicted by equation (90).

Distributed roughness elements; i.e., particles typified by dust or sandpaper grit, can also induce premature transition. We present here a simplified method (Ref. 3) for determining the minimum height k_t of distributed particles which will be just sufficient to cause the development of premature transition to turbulent boundary-layer flow.

We first define a parameter η_k , which may be used as a nondimensional representation of a given roughness particle of height k :

$$(91) \quad \eta_k = \frac{k}{2x} \sqrt{R_x}$$

where $R_x = U_\infty x / \nu$, and x is the distance from the leading edge (or nose). A roughness Reynolds number R_k , based on particle

height and flow velocity at the point in the boundary layer corresponding to the top of the particle, is also defined as

$$(92) \quad R_k = \frac{k u_k}{\gamma}$$

It is possible to express η_k as a function of $R_k/\sqrt{R_x}$, assuming the velocity and temperature distribution throughout the boundary layer is known. In Reference 3, these calculations have been carried out for the cases of two-dimensional flow past a flat plate and three-dimensional flow past a conical body held with its axis parallel to the stream. The relationships thus obtained are presented graphically in Figures 19 and 20. To use these charts, it is necessary to choose a value of the critical roughness Reynolds number $(R_k)_t$. Attempts to measure $(R_k)_t$ experimentally have yielded values anywhere from 250 to 600, but Reference 3 suggests that the higher value is the most accurate. Once $(R_k)_t$ is selected, the value of k required to induce transition at a given distance x from the nose or leading edge can then be determined by calculating the ratio $(R_k)_t/\sqrt{R_x}$ and reading the corresponding value of η_k from Figure 19 or 20; this value of η_k is used in equation (91) to give

$$(93) \quad k_t = \frac{2x \eta_k}{\sqrt{R_x}}$$

By way of example, if we take $(R_k)_t$ as 600 and base R_x on $U_\infty = 60$ meters/second, we have

$$\frac{(R_k)_t}{\sqrt{R_x}} = \frac{0.299}{\sqrt{x}} \quad (\text{for } x \text{ given in meters})$$

Suppose, now, we want to know the particle size needed to induce

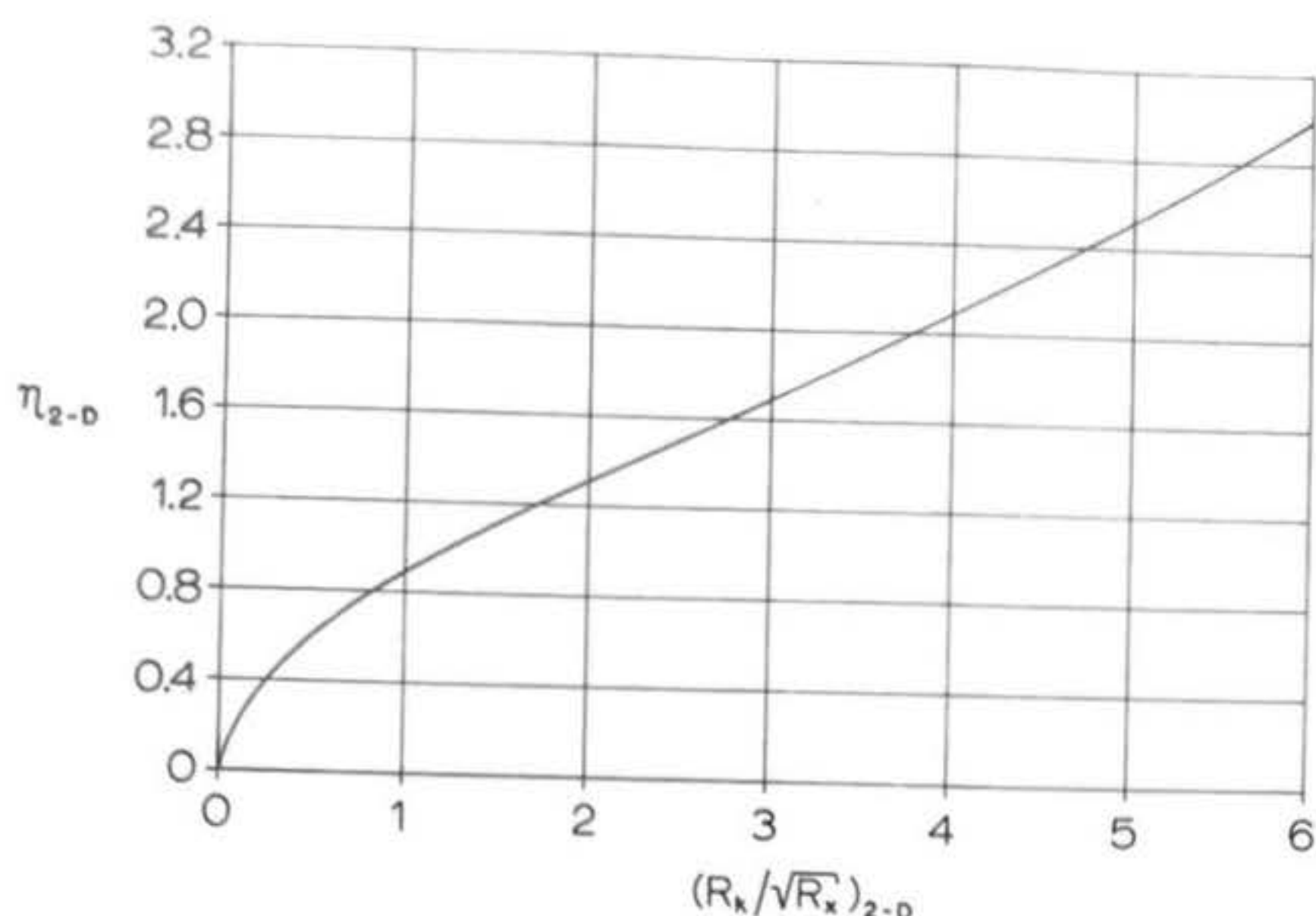


Figure 19: η_k , the nondimensionalized roughness particle height required to cause transition from laminar to turbulent flow, plotted as a function of $\frac{R_k}{\sqrt{R_x}}$, the ratio of the "roughness Reynolds number" to the square root of the "station Reynolds number" for a flat plate at zero angle of attack.

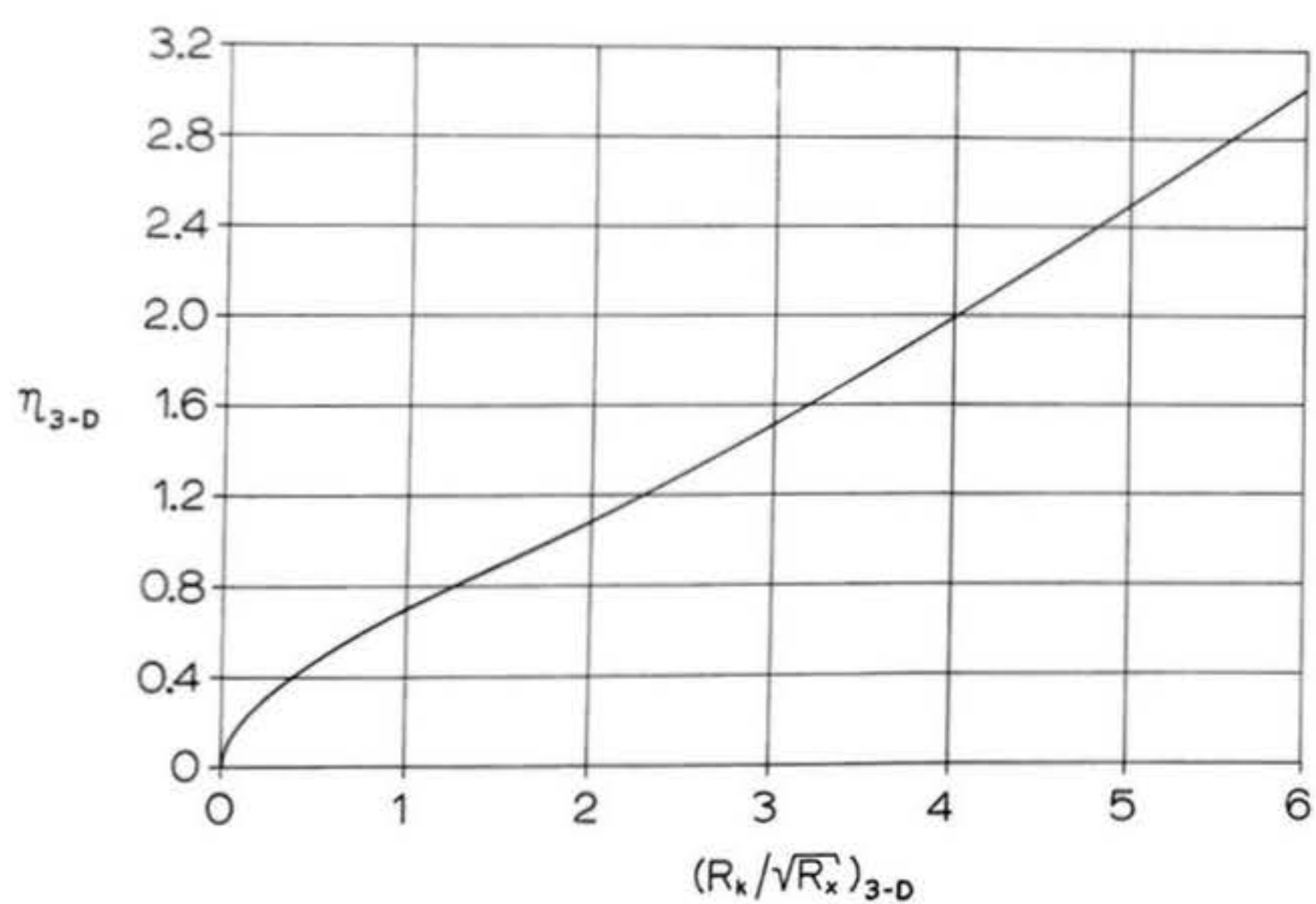


Figure 20: η_k , the nondimensionalized roughness particle height required to cause transition from laminar to turbulent flow, plotted as a function of $\frac{R_k}{\sqrt{R_x}}$, the ratio of the "roughness Reynolds number" to the square root of the "station Reynolds number" for a cone whose axis is at zero angle of attack.

transition at a distance of 3 cm. (.03 meter) from the nose or leading edge of the surface in question. The quantity $(R_k)_t/\sqrt{R_x}$ is then 1.73; from the graphs we find the associated two-dimensional value of η_k is 1.20, while the three-dimensional value is 0.96. Substituting in equation (93), we then calculate critical particle sizes k_t of 2.08×10^{-4} meter for the two-dimensional case and 1.66×10^{-4} meter for the three-dimensional case. The two-dimensional results may be applied with good accuracy to fins, body tubes of constant diameter, and other surfaces of zero pressure gradient; the three-dimensional results are applicable to nosecones, shoulders, and similar components whose boundary-layer pressure gradients are favorable. In either case, the critical size of distributed roughness particles is found to be on the order of 1/100 of a centimeter -- further demonstration of the necessity for a smooth surface finish on model rockets to minimize the skin-friction drag. It should also be noted that the case of our example has an R_x of 1.206×10^5 , which is well above the lower limit of 6×10^4 given in Reference 15 as the Reynolds number below which a laminar flow cannot be disturbed into a turbulent pattern. Hence, transition can occur under the conditions given in the example.

There are certain limitations to this method. First, a zero pressure gradient has been assumed in its derivation; it seems likely, however, that the pressure gradient on most reasonably well-designed model rockets is small enough to keep the method accurate enough for practical use. Second, the critical roughness Reynolds number $(R_k)_t$ can be assumed to have the constant value of 600 only if the roughness elements are

completely submerged in the laminar boundary layer. The height of the roughness particles compared with the boundary-layer thickness can be determined from the value of η_k found for a particular case and the boundary-layer velocity profiles of Figures 21a and 21b (3). The values of η_k found for the example above are seen to lie well within the boundary layer.

The reader should note at this point that the variable η as used in Reference 3, from which Figures 19 through 21 are taken, is not the same as the variable η used in the presentation of the Blasius solution of Section 3.3. If we identify the η of Ref. 3 as η_3 and the η of Blasius by η_B , we have

$$(94) \quad \eta_3 = \frac{y}{2x} \sqrt{R_x} = \frac{y}{2x} \sqrt{\frac{U_{\infty} x}{\nu}} = \frac{y}{2} \sqrt{\frac{U_{\infty}}{\nu x}}$$

$$(95) \quad \eta_B = y \sqrt{\frac{U_{\infty}}{\nu x}}$$

so that

$$(96) \quad \eta_B = 2\eta_3$$

The two-dimensional boundary-layer profile of Figure 21a is thus identical to that of Figure 14, except for a scale factor of two in the vertical coordinate.

The station $x = 3$ cm. generally corresponds to a position on the nosecone or fins of a model rocket. As x is increased, the boundary layer becomes thicker (varying as \sqrt{x} for a laminar boundary layer in zero pressure gradient) and the particle size required to induce transition at that value of x is also increased. Eventually, the increase in downstream distance from the nose or leading edge will result in a value of R_x sufficiently great

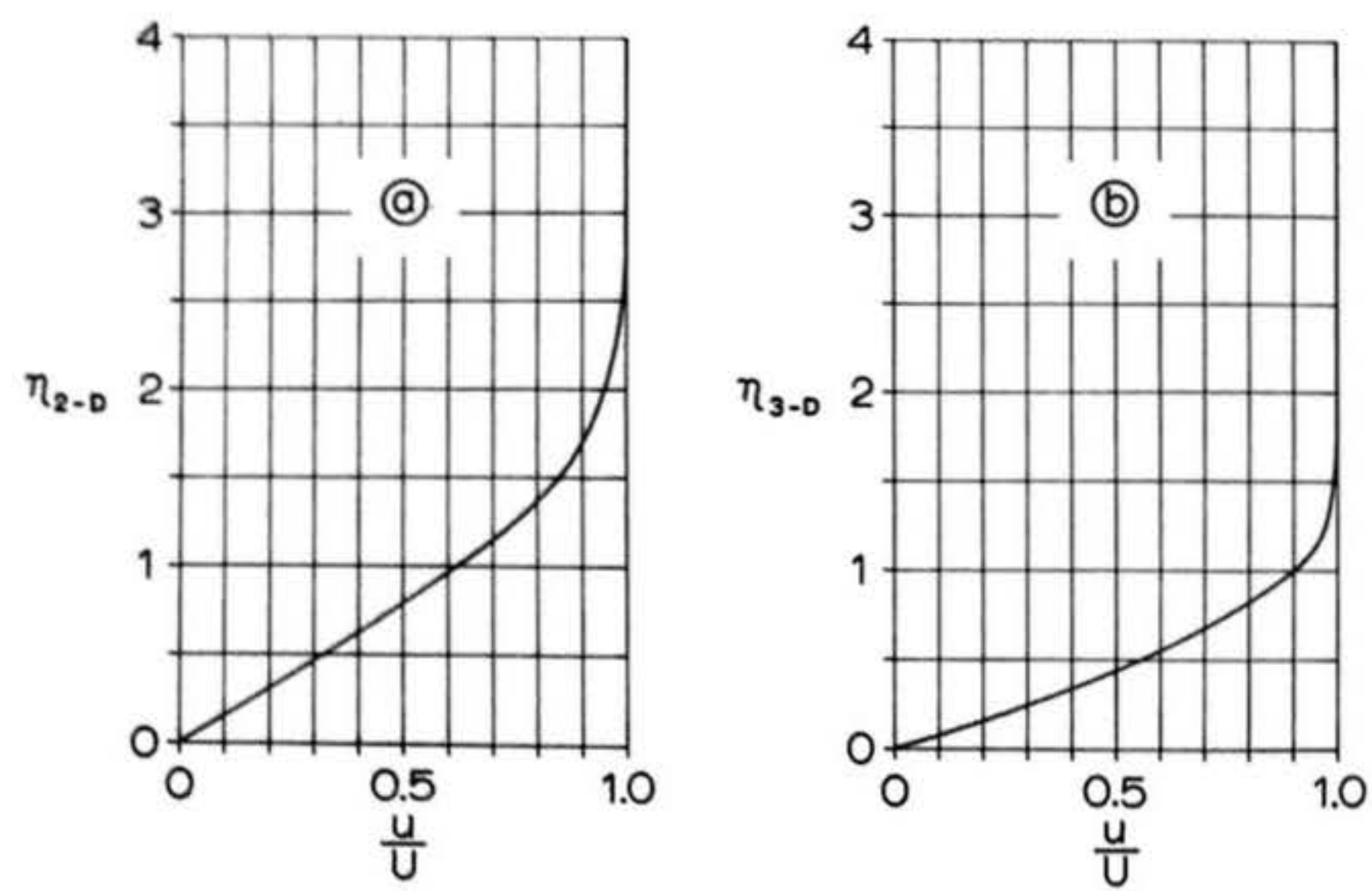


Figure 21: Boundary layer velocity profiles for laminar flow over flat plates (a) and cones (b).

to cause natural transition without the presence of any surface roughness. Calculations of induced transition due to surface roughness are, of course, applicable only for values of R_x less than the critical Reynolds number R_{crit} .

An increase in the free-stream velocity will decrease the boundary-layer thickness at a given station x , so the particle size required to cause premature transition will also decrease. High-performance model rockets, which are expected to travel at extreme velocities, therefore require exceptionally smooth surface finishes to minimize their friction drag.

Finally, we should note a third limitation on the general applicability of the calculation method presented in this section: the "distributed" roughness particles are actually assumed to lie in a thin band transverse to the stream direction so that the given value of R_x can apply to them all, and the transition induced by particles of diameter k_t is presumed to occur instantaneously as the air flows over this band. In actuality, of course, the roughness in a model rocket's finish is usually distributed fairly evenly over the entire surface of the rocket and the transition induced by the particles occurs at some finite distance downstream of them. The calculation method presented does, however, provide the kind of order-of-magnitude information useful to the model rocketeer in ascertaining the permissible roughness of surface finishes that will avoid premature transition and keep friction drag as low as possible.

3.5.3 Skin-Friction Drag of Boundary Layers with Transition

One can estimate the skin-friction drag on a flat plate on which boundary-layer transition occurs if it is assumed that, behind the transition point, the turbulent boundary layer behaves as if it had been turbulent all the way from the leading edge. Since the laminar region introduces a reduction in drag from what the drag would be if the entire boundary layer were turbulent, we can just substitute the laminar drag up to the transition point for the turbulent drag over the same distance (15). The incremental decrease in drag force is then

$$(97) \quad \Delta D = -\frac{\rho}{2} U_{\infty}^2 b x_{\text{crit}} [(C_f)_{\text{turb}} - (C_f)_{\text{laminar}}]$$

where $(C_f)_{\text{turb}}$ and $(C_f)_{\text{laminar}}$ are the respective coefficients of turbulent and laminar skin friction.

The change in overall skin-friction coefficient becomes

$$(98) \quad \Delta C_f = -\frac{x_{\text{crit}}}{\ell} [(C_f)_{\text{turb}} - (C_f)_{\text{laminar}}]$$

or

$$(99) \quad \Delta C_f = -\frac{R_{\text{crit}}}{R_{\ell}} [(C_f)_{\text{turb}} - (C_f)_{\text{laminar}}]$$

Letting

$$(100) \quad B = R_{\text{crit}} [(C_f)_{\text{turb}} - (C_f)_{\text{laminar}}]$$

we derive the overall skin-friction coefficient as (15):

$$(101) \quad C_f = \frac{0.074}{R_{\ell}^{1/5}} - \frac{B}{R_{\ell}}$$

where the laminar and turbulent skin-friction coefficients are evaluated from the previously derived expressions, equations (86) and (63):

$$(102a) \quad (C_f)_{turb} = \frac{0.074}{(R_l)^{1/5}}$$

$$(102b) \quad (C_f)_{lam} = \frac{1.328}{(R_l)^{1/2}}$$

Approximate values of B for several possible values of R_{crit} are listed below (15):

R_{crit}	3×10^5	5×10^5	1×10^6	3×10^6
B	1050	1700	3300	8700

In order to apply equation (101) in a particular case, the value of R_{crit} must be known. Since no value of this quantity has been determined for a model rocket, we shall assume an average value for calculation purposes of $R_{crit} = 5 \times 10^5$, corresponding to a B of about 1700. Since this value is near the lower end of the R_{crit} range for flat plates (3×10^5 to 3×10^6), the results obtained should be somewhat conservative, making it unlikely that the drag will be underestimated. Section 6 discusses the matter of critical Reynolds number for model rockets further in the light of data gathered by Mark Mercer. The transition curve described by equation (101) for $B = 1700$ is plotted as function C in Figure 22, along with the pure laminar and pure turbulent functions from equations (63) (function A) and (86) (function B). Figure 22 can be used directly to find skin-friction coefficients for use in the method described in Section 6.

3.6 Three-Dimensional Corrections to the Flat-Plate Skin-Friction Coefficients

Approximate methods have been developed for estimating

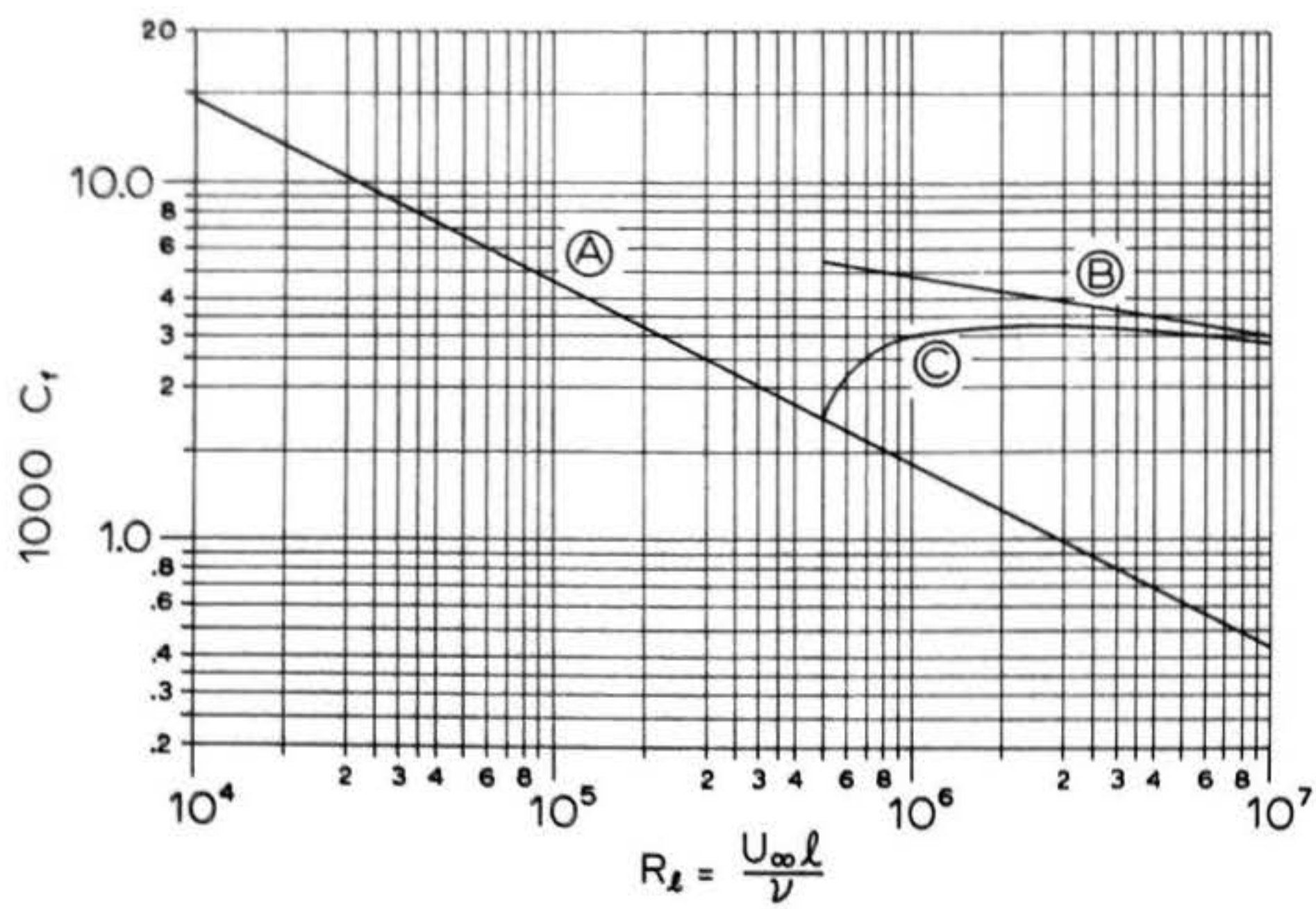


Figure 22: Skin friction coefficient for flow over a flat plate with boundary layer transition, based on the assumption of $R_{crit} = 5 \times 10^5$ (corresponding to $B = 1740$ in equation (101)).

the effects of three-dimensionality on the values of the skin-friction coefficients derived for the flat plate. The results of an approximate method described in Reference 9, which can be used to correct two-dimensional skin-friction coefficients for application to three-dimensional surfaces, are presented below.

3.6.1 Body Corrections

For laminar boundary-layer flow over a circular cylinder held with its axis parallel to the stream, the increase in skin-friction coefficient over that of a two-dimensional plate having the same length ℓ is given approximately by (9)

$$(103) \quad (\Delta C_f)_{lam} = \frac{2\ell/d}{R_\ell}$$

In a previous example, we determined a skin-friction coefficient of 0.00382 for laminar flow over a flat plate at a Reynolds number of 1.206×10^5 . For a model rocket body with a length-to-diameter ratio of 10 at the same Reynolds number, we obtain

$$(\Delta C_f)_{lam} = 1.66 \times 10^{-4}$$

The adjusted skin-friction coefficient is thus

$$(C_f')_{lam} = (C_f)_{lam} + (\Delta C_f)_{lam} = \frac{1.328}{R_\ell^{1/2}} + \frac{2\ell/d}{R_\ell} = .003986$$

with equation (103) accounting for a 4.4% increase in the value of C_f .

In the case of turbulent flow, the increase in skin-friction coefficient is found from (9)

$$(104) \quad (\Delta C_f)_{turb} = \frac{.022(l/d)}{(R_\ell)^{1/5}} (C_f)_{turb}$$

or, since $(C_f)_{turb} = .074/R_\ell^{1/5}$ for a flat plate,

$$(105) \quad (\Delta C_f)_{turb} = \frac{1.6 \times 10^{-3}(l/d)}{(R_\ell)^{2/5}}$$

In our turbulent-flow example, it will be recalled that the skin-friction coefficient for a completely turbulent boundary layer over a flat plate at a Reynolds number of 1.206×10^6 was found to be 0.0045. Assuming a length-to-diameter ratio of 10 and the same Reynolds number, we have for the cylinder

$$(\Delta C_f)_{turb} = 5.93 \times 10^{-5}$$

Then the adjusted skin-friction coefficient is

$$(C'_f)_{turb} = \frac{.074}{(R_\ell)^{1/5}} + \frac{1.6 \times 10^{-3}(l/d)}{(R_\ell)^{2/5}} = .0045593$$

with equation (105) accounting for a 1.3% increase from the flat-plate value -- a bit less than 1/3 the percentage increase for the laminar case. In Section 6, corrections of these magnitudes will be used to determine the skin-friction drag on the constant-diameter body tube sections of a model rocket.

3.6.2 Fin Corrections

A model rocket fin is generally not quite thin enough to be represented as a flat plate. The average tangential velocity of the airstream about a fin with a symmetrical airfoil section is higher than that of the undisturbed flow, even at zero angle of attack when the fin produces no side force (or "lift", as the side force is sometimes colloquially called) (9). The

friction drag coefficient of a flat plate wetted on both sides, with the planform area (area of one side only) used as the reference area, is

$$(106) \quad C_{Df} = 2C_f$$

Now the increase in friction drag with thickness is proportional to the increment in dynamic pressure caused by the increase in flow velocity required for the air to negotiate a fin of finite thickness. This increment, in turn, is proportional to the thickness ratio t/c , where t denotes fin maximum thickness and c denotes fin chord:

$$(107) \quad \frac{\Delta C_{Df}}{2C_f} = \frac{\Delta q}{q} = 2 \frac{t}{c}$$

Then for the fin drag coefficient, based on fin planform area, corrected for thickness effects, we obtain

$$(108) \quad C'_{Df} = 2C_f \left(1 + 2 \frac{t}{c}\right)$$

For a typical model rocket fin having a thickness ratio of 0.05 the correction introduced by the use of equation (108) is seen to be 10%.

Again, we shall have occasion to return to these formulae in Section 6. In that section also, procedures for converting skin-friction drag coefficients based on body tube lateral area and fin planform area to coefficients based on maximum frontal area will be presented.

4. Pressure Drag

4.1 Introduction

Pressure drag was defined previously in Section 2 as the integral over the body surface of the components of pressure forces acting directly opposite the direction of the rocket's motion; that is,

$$(109) \quad D_p = \iint_S p \cos(\vec{n}, \vec{v}) ds$$

where the unit vector n is everywhere normal to the surface (you may wish to refresh your memory in regard to the notation by consulting Figure 11 again). For purposes of analysis, it is useful to divide this integral into two parts: first, the integral over the base area of the rocket, called base drag, which will be discussed in Section 4.4; and second, the integral over the remainder of the rocket body and fins (pressure foredrag), to be discussed in Section 4.3.

The existence of pressure drag is intimately associated with the phenomenon of boundary-layer separation. In general, for a rocket with a streamlined nose, streamlined fin profile, and no launch lug, the base drag will be considerably larger than the pressure foredrag. This is because separation of the boundary layer from the rear of the rocket, unavoidable due to the presence of the opening into which the engine casing must be inserted, creates a relatively large component of pressure drag. In the event that extensive flow separation occurs on the forebody, however -- as the result of blunt surfaces directed against the airflow -- the pressure drag of the forebody can

be quite large, perhaps several times the base drag.

Since an understanding of the mechanism and prevention of boundary-layer separation is essential to the study of pressure drag, we begin with a discussion of this phenomenon in Section 4.2. Unfortunately, there is very little quantitative information available concerning the two most important sources of pressure drag on well-constructed model rockets: the launch lug (if the model has one) and the base. Section 4.3 discusses Mark Mercer's data concerning the first question, and in Section 4.4 the empirically-derived expression which is used to evaluate base drag is presented, although it is noted that this formula does not take into account either the effects of stabilizing fins or the influence of the engine exhaust on the base drag.

4.2 Boundary-Layer Separation

The skin-friction coefficients which were derived in Section 3 for laminar and turbulent flow presuppose that the boundary layer remains attached to the solid surface on which it is formed. This assumption is generally valid for a flat plate, as the pressure gradient along the plate's surface dp/dx is zero; but in regions of increasing pressure (dp/dx positive, a so-called adverse pressure gradient) the boundary layer may be unable to follow the contour of the body surface beyond a certain point and it will break away from the surface. When this happens, the skin-friction coefficients of Section 3 are not applicable beyond the point of separation.

To illustrate this phenomenon, we examine the flow past a blunt body, such as the circular cylinder shown in Figure

23. In the inviscid flow of a "perfect" fluid, the fluid elements are accelerated from point A to point B, and are decelerated from point B to point C. In accordance with Bernoulli's equation, there is an increase in static pressure between A and B and a corresponding decrease along the downstream surface from B to C. This theoretical pressure distribution (which appears in Figure 24 as the curve $C_p = 1 - 4\sin^2\varphi$) is impressed upon the boundary layer in real fluid flow; that is, at any station in the boundary layer the pressure over the thickness of the layer is virtually constant and is taken as equal to the pressure in the exterior flow at the same station.

An element in the exterior flow, because of the pressure distribution, undergoes a continual change in kinetic energy as it moves from the front to the rear of the cylinder, first increasing, then decreasing. Because there is no dissipation of energy in inviscid flow, the theory of perfect fluids predicts that a fluid element will arrive at C with the same velocity it had at A. Within the boundary layer, however, fluid elements are subjected to large frictional forces which consume much of the kinetic energy gained in travelling from A to B. Hence an element near the wall will not have sufficient kinetic energy to overcome the positive pressure gradient on the downstream side of the cylinder, and at some point its motion will be arrested. Acting under the influence of the pressure gradient, it will then reverse the direction of its motion so that it is actually moving against the exterior airstream.

This process and its consequences are depicted in Figure 25, which shows how the velocity profiles in the boundary layer

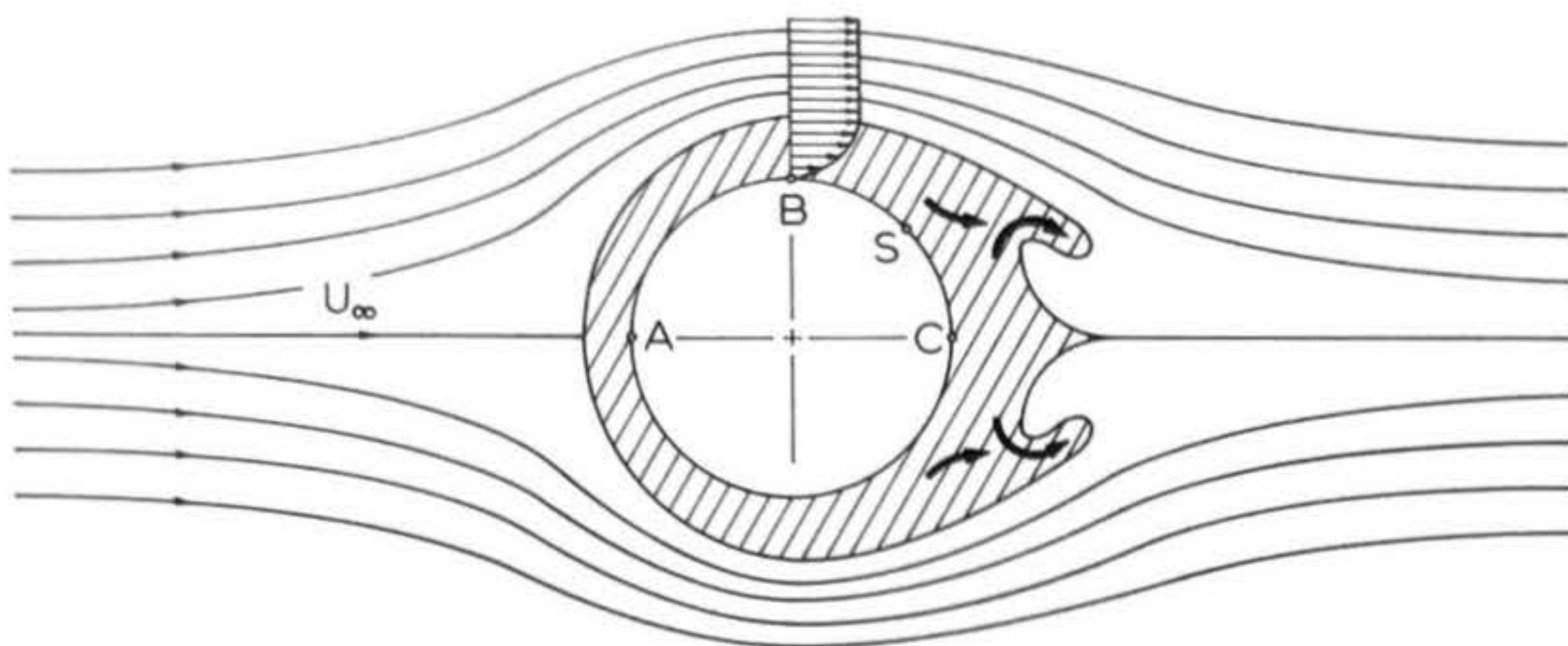


Figure 23: Flow about a circular cylinder held transverse to the airstream. Inviscid ("potential") theory predicts that the flow near the surface of the cylinder will be accelerated from point A to point B and decelerated again from B to C. In actuality, the boundary layer develops an inflection point due to the adverse pressure gradient between B and C, and separation occurs at S.

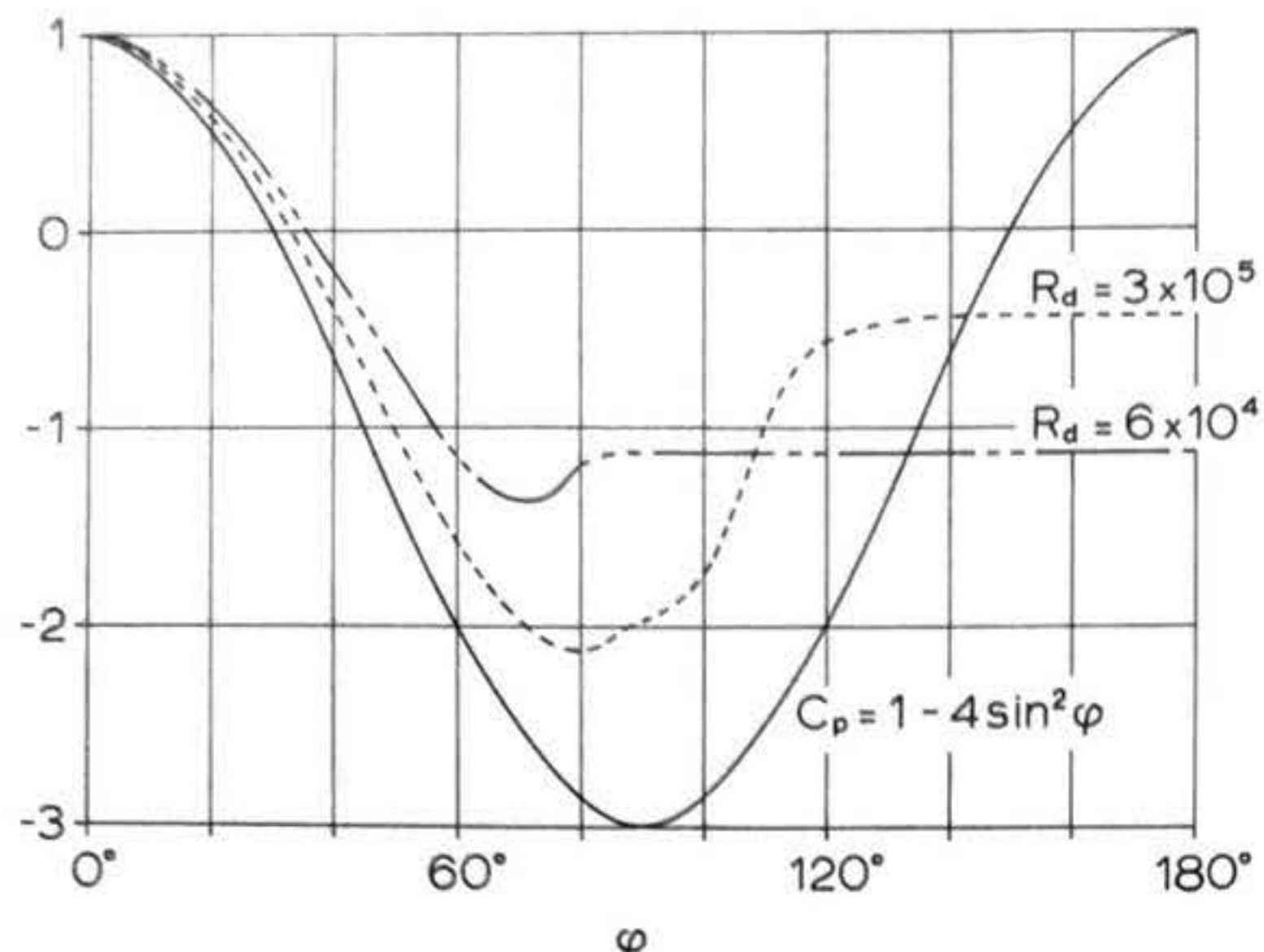


Figure 24: Theoretical and experimental variation of pressure coefficient in flow about a circular cylinder. The theoretical curve obtained from potential flow theory is displayed and compared with average curves of experimental data taken at the subcritical Reynolds number 6×10^4 and the supercritical Reynolds number 3×10^5 (based on cylinder diameter). The angle φ is the angle between a line drawn from the cylinder axis to point A in Figure 23 and a line drawn from the axis to any other point on the cylinder periphery. Point B in Figure 23 thus corresponds to $\varphi = 90^\circ$ and point C to $\varphi = 180^\circ$.

are altered near a point of separation. The boundary layer has a full, stable velocity profile at point a, well upstream of the separation point c. As the flow moves into the region of increasing pressure, however, the particles at the wall begin to be retarded until, at c, the velocity profile develops an inflection point and has a zero velocity gradient at the wall. The layer of fluid nearest the wall has consequently lost all its forward momentum. The condition of zero normal velocity gradient at the wall is expressed mathematically as

$$(110) \quad \left(\frac{\partial u}{\partial y} \right)_{y=0} = 0$$

Downstream of c, the separation point, the layers of fluid nearest the wall reverse their motion, a vortex is formed, and the general accumulation of fluid in the boundary layer leads to a rapid increase of boundary-layer thickness (points d and e). The layer becomes so thick, in fact, that the original assumptions which were made in the derivation of the boundary-layer equations (equations 38 and 39) are no longer valid and a "boundary layer" as such can no longer be said to exist. Hence, the boundary-layer approximations apply only up to the point of separation, and resort must be had to experiment to determine the conditions on the rear of the body from which the flow has separated.

The remarkable series of photographs in Plates 4a through 4j, made by Prandl and Tietjens (Reference 12), illustrates the actual development of separation at the rear of a circular cylinder. In Plate 4a, the flow has just begun; the boundary layer is very thin, and conditions conform very closely to ideal,

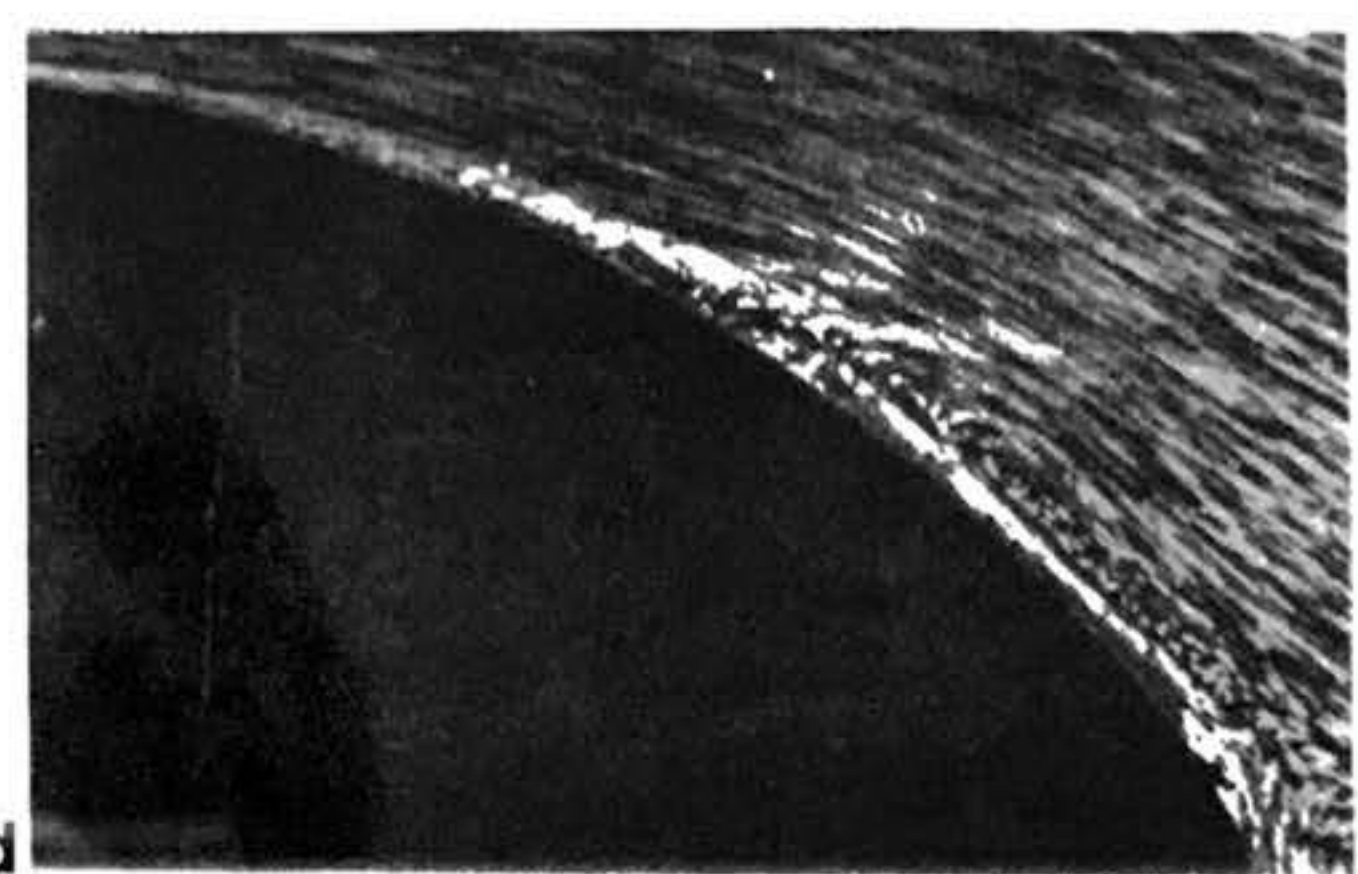
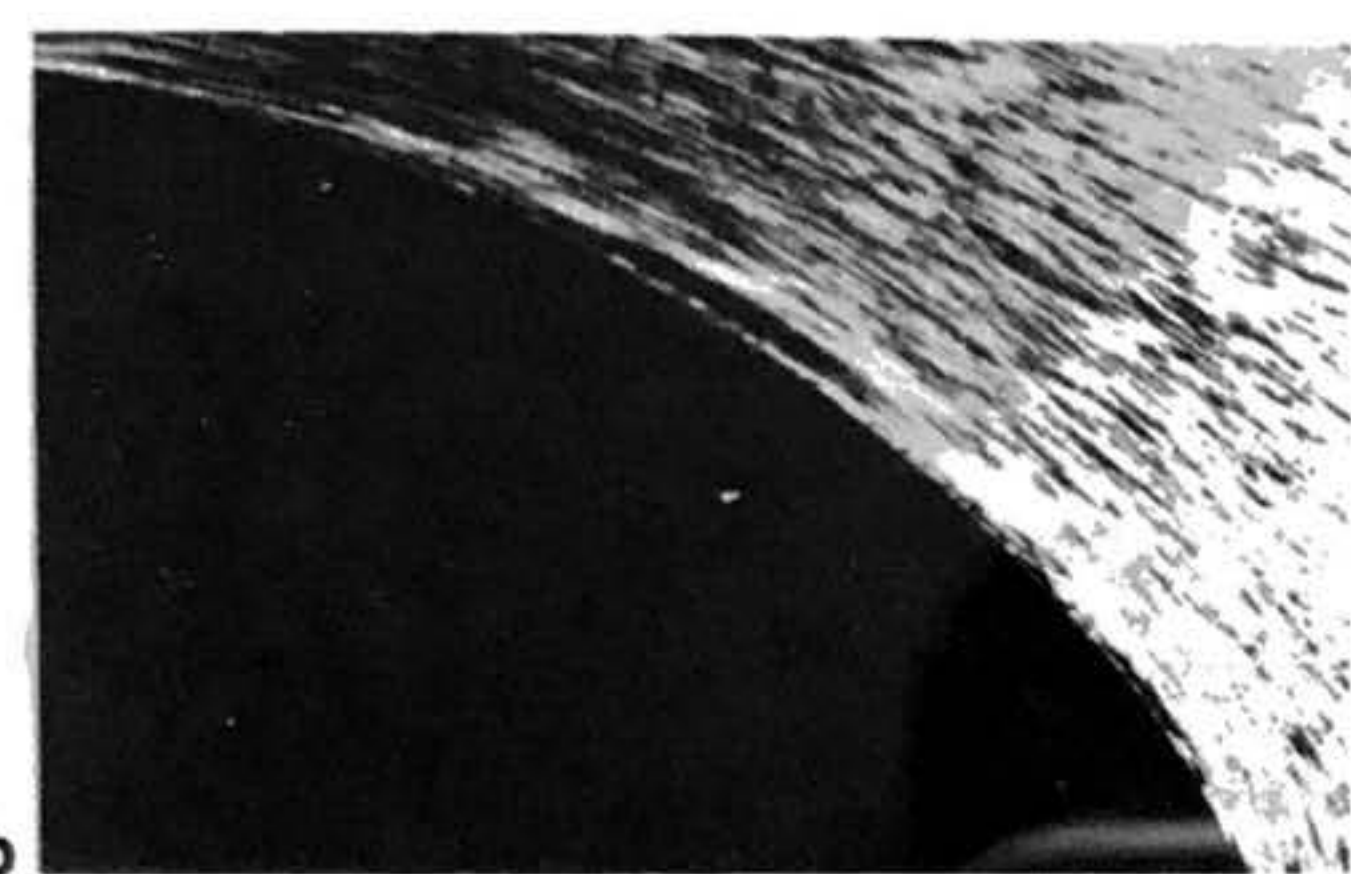
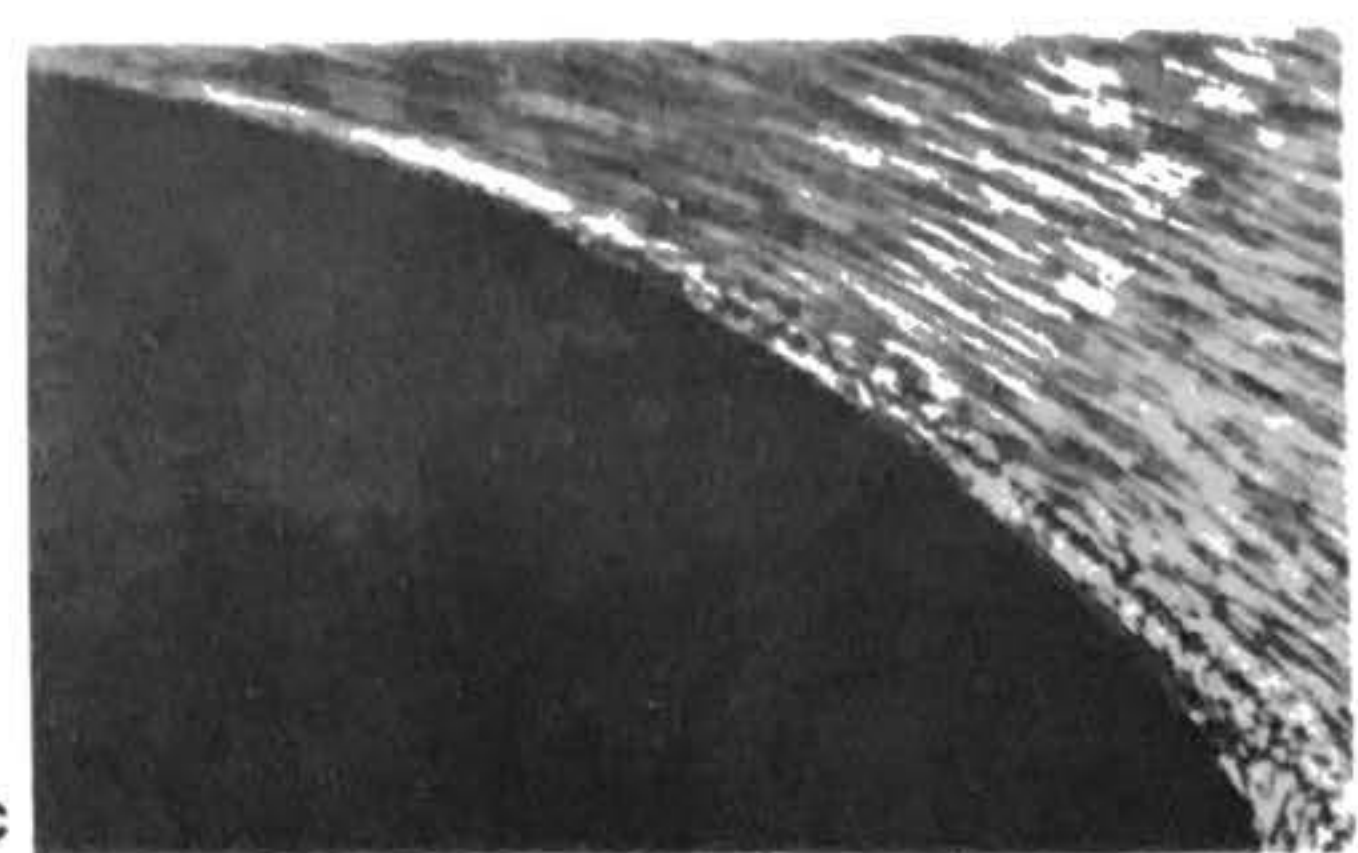
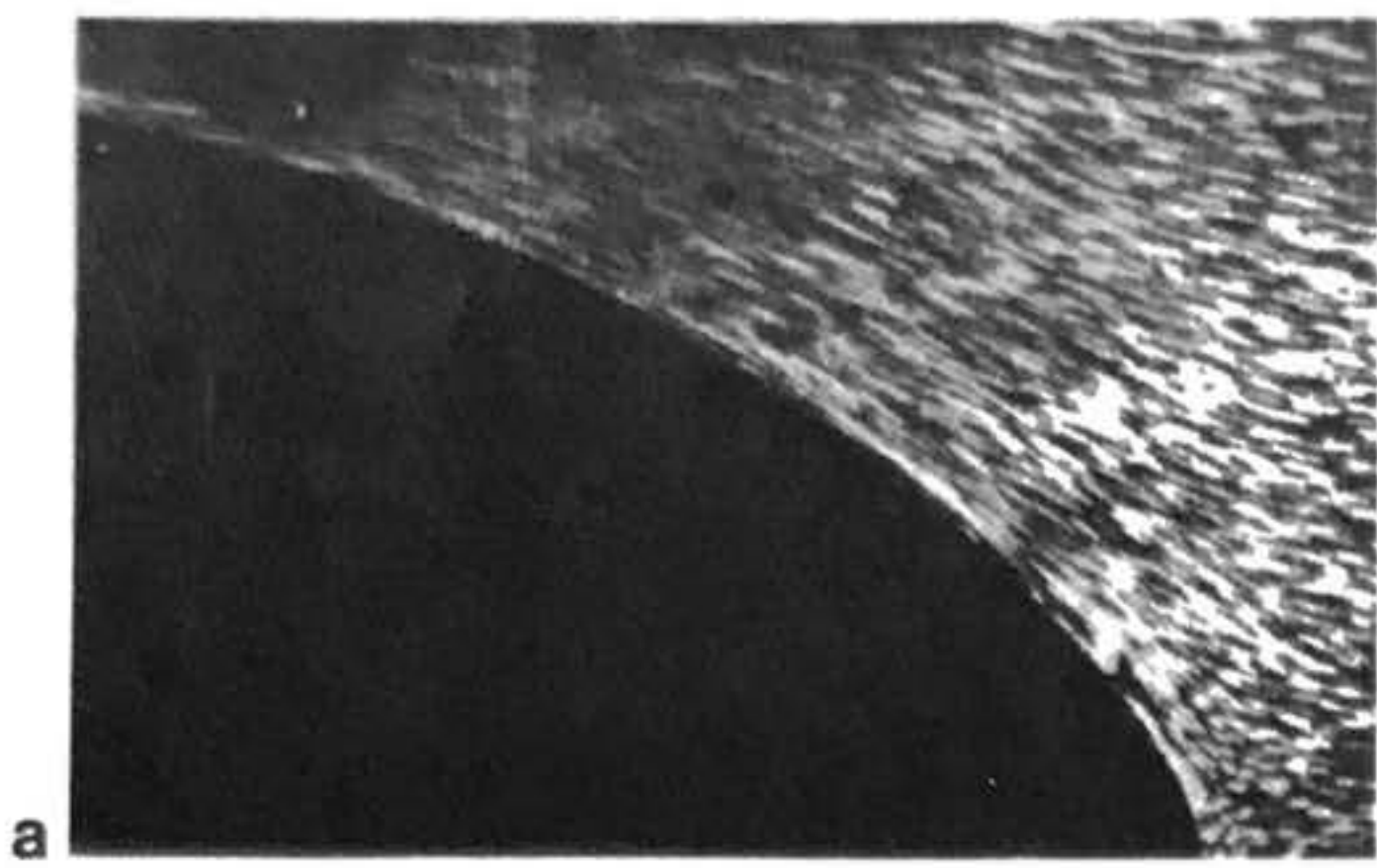
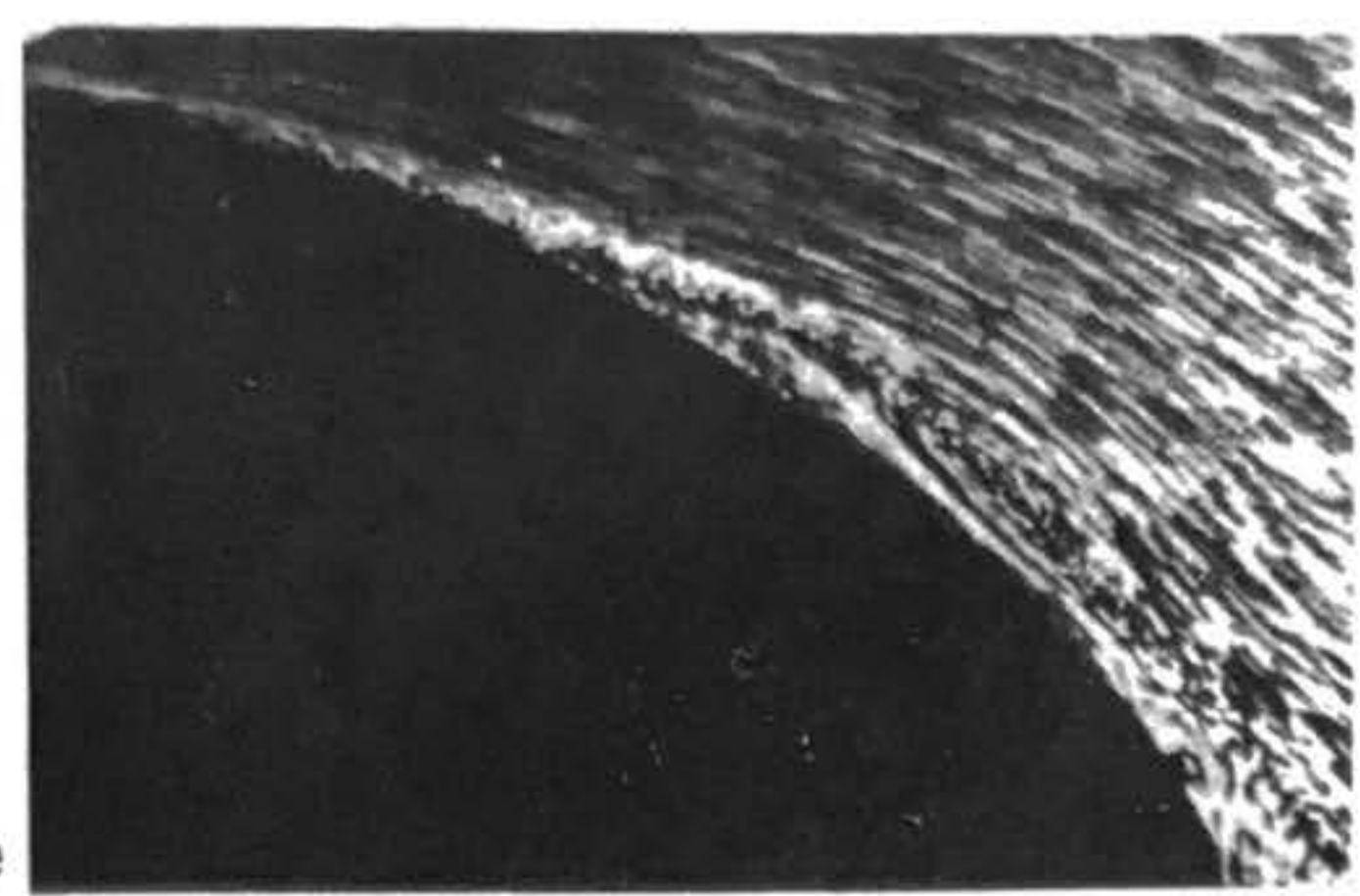
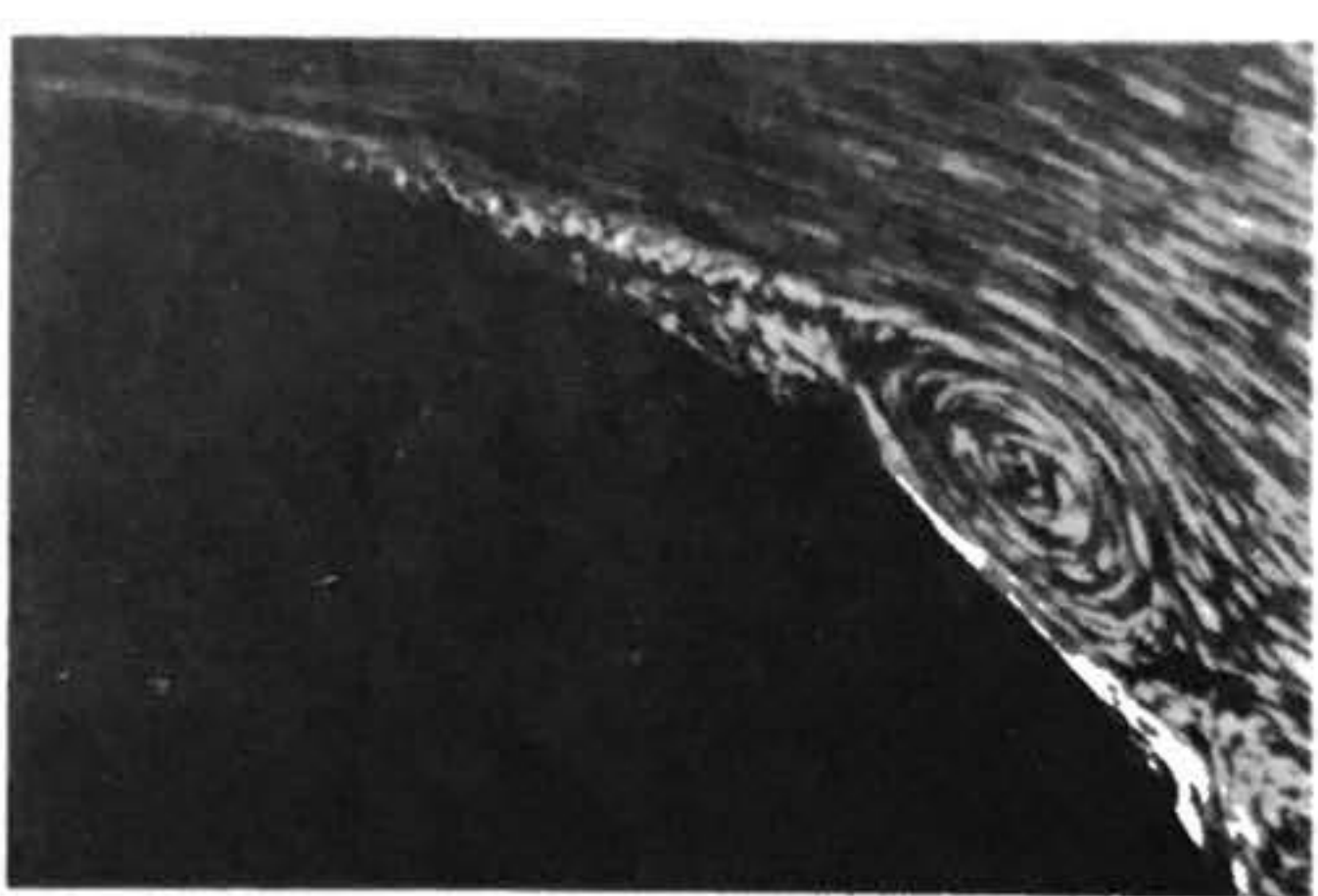


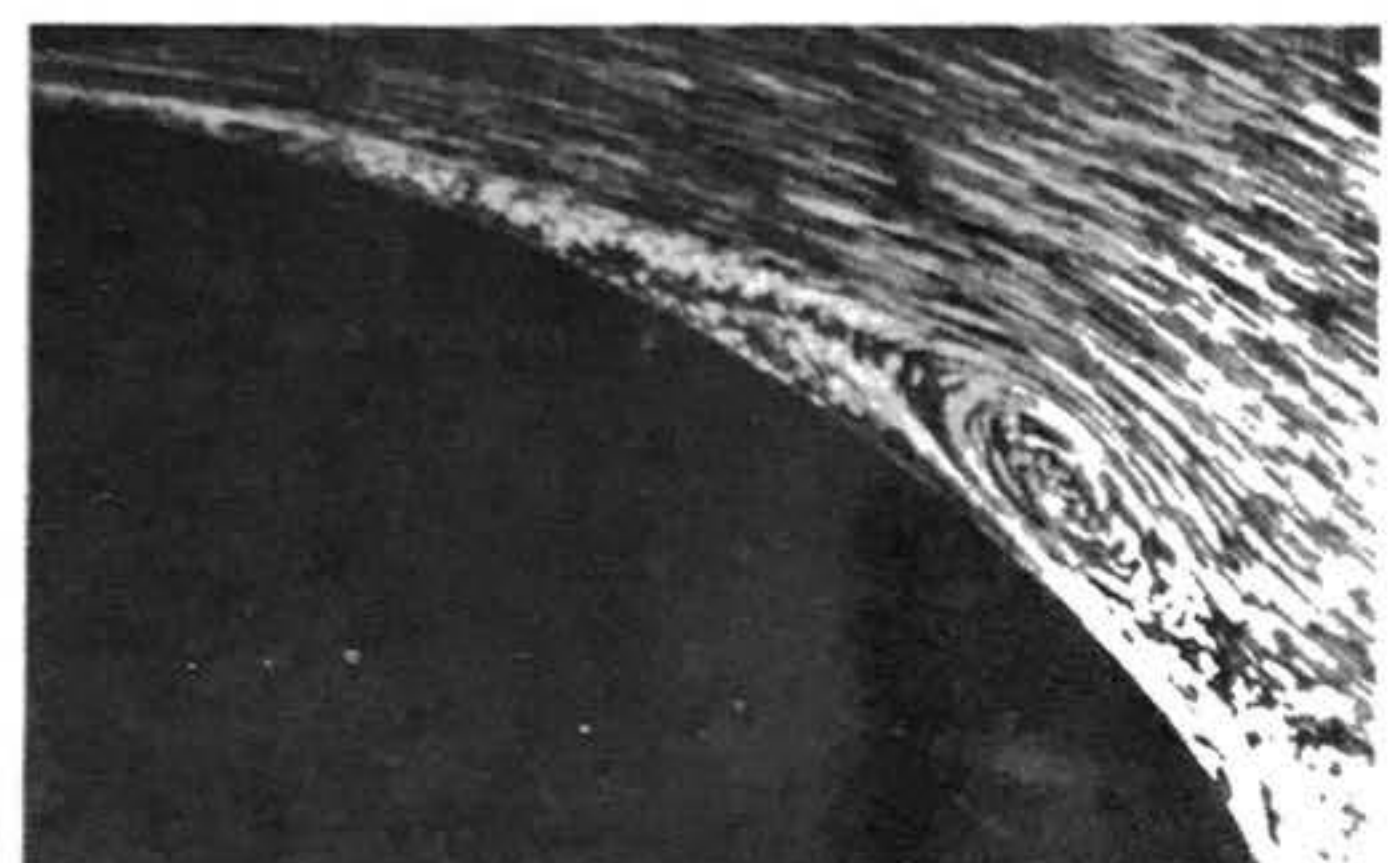
Plate 4: Flow around the rear end of a blunt body, illustrating the onset of boundary layer separation due to an adverse pressure gradient.



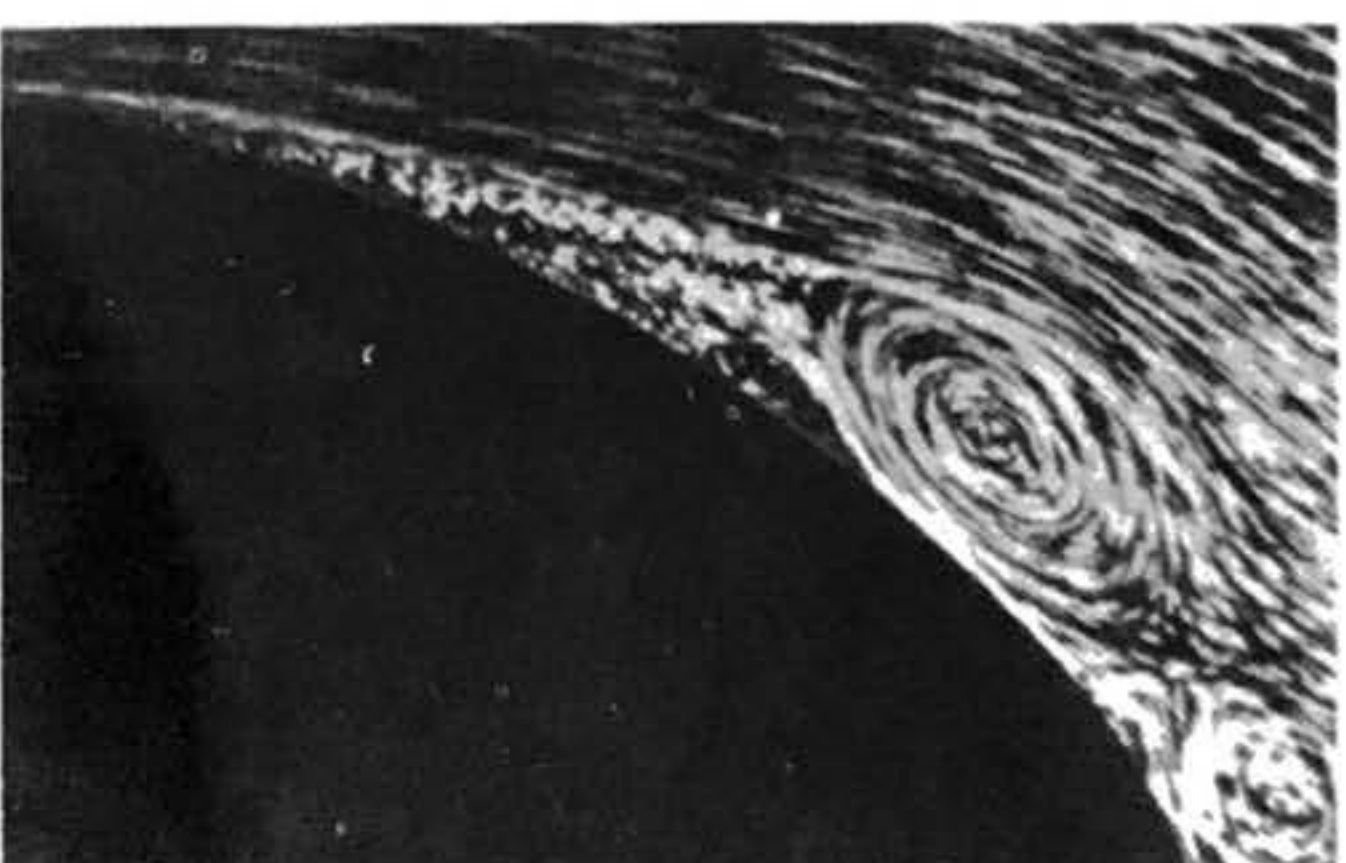
e



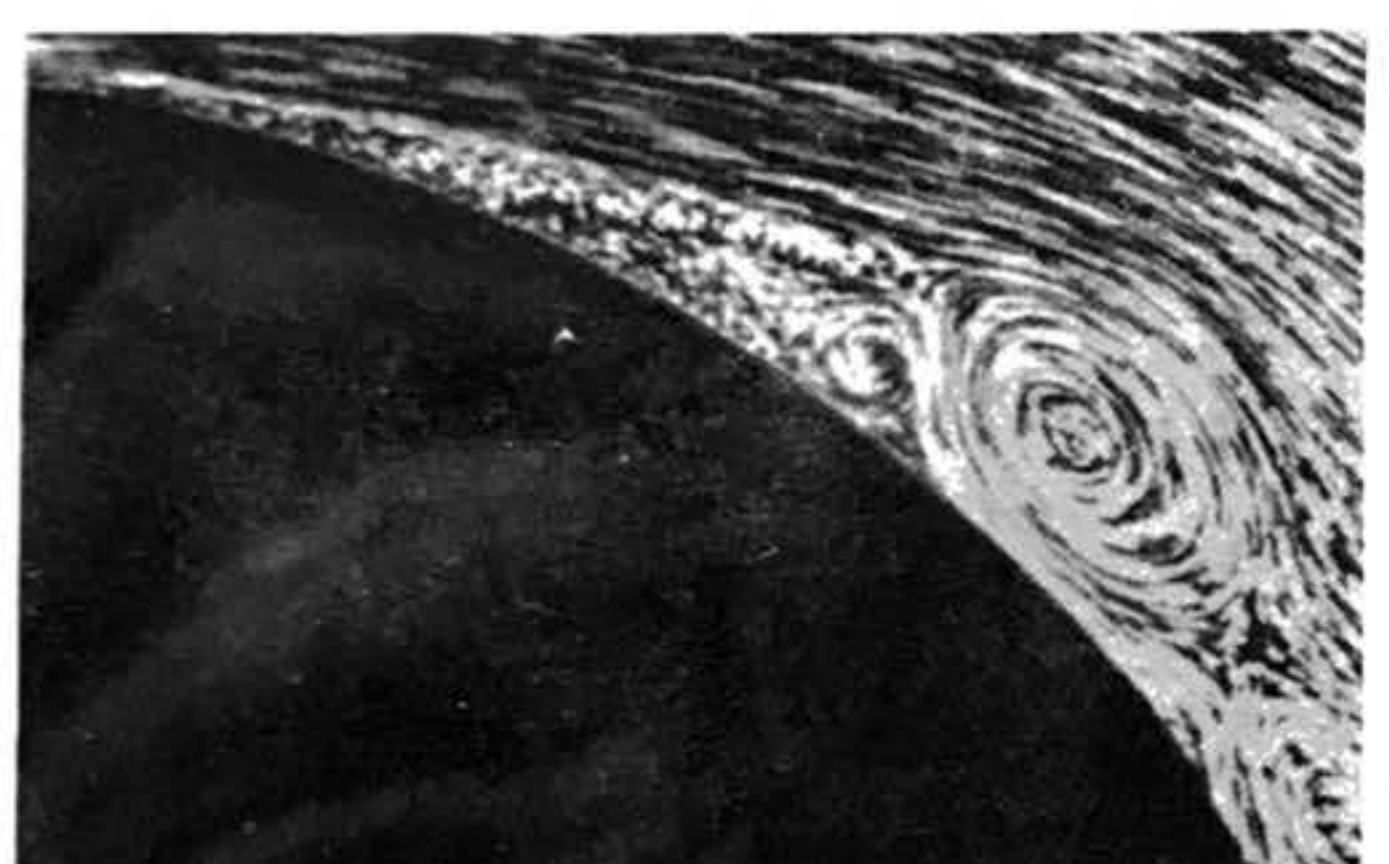
g



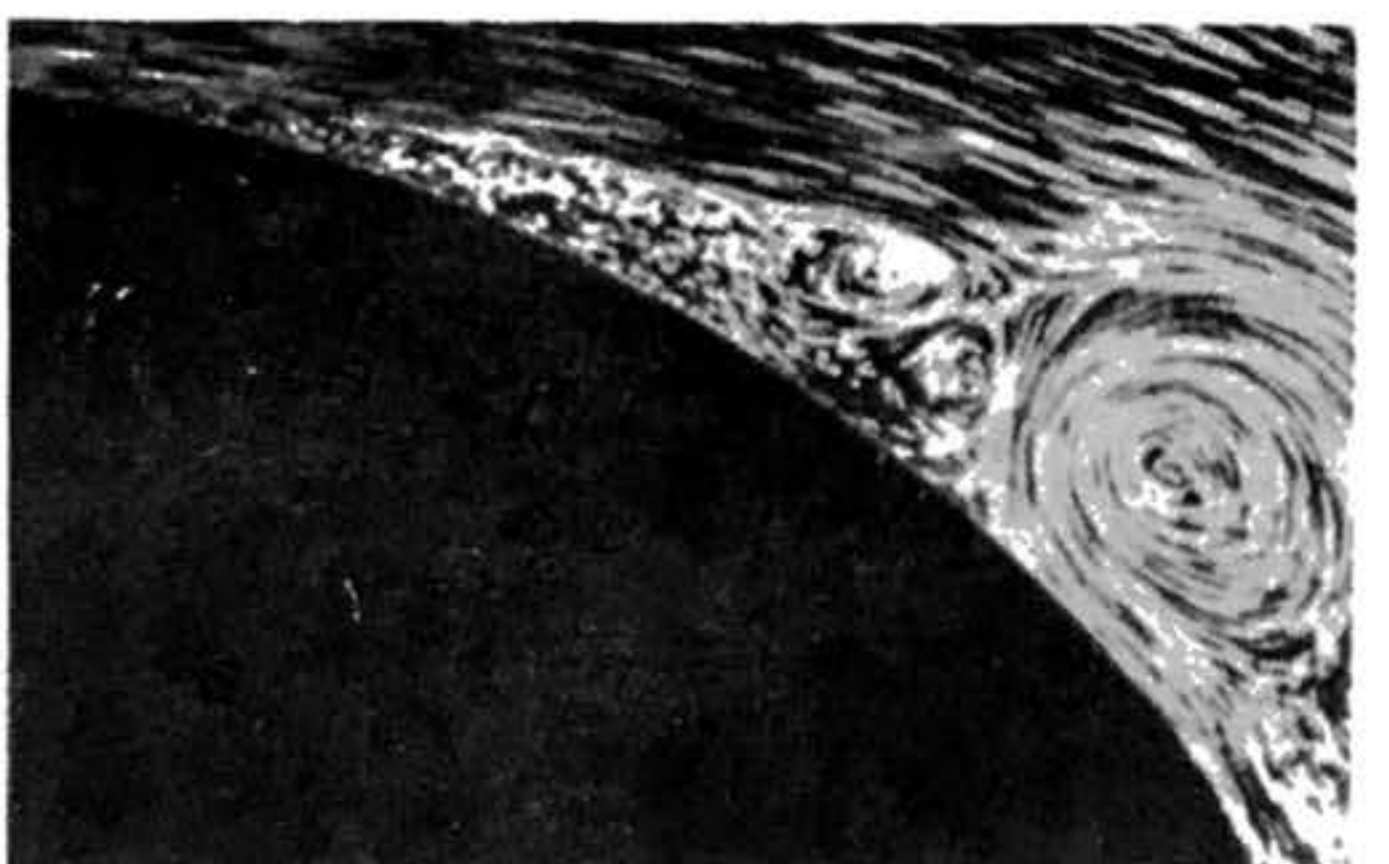
f



h



i



j

inviscid potential flow. In the next picture, some particles nearest the wall have been retarded by the adverse pressure gradient; they appear as bright, white dots. This corresponds to the velocity profile of point c in Figure 25. These particles have acquired a backwards velocity in Plate 4c, and a line of stationary fluid now exists at some distance from the wall, as at points d and e in Figure 25. The external flow persists in forward (left-to-right) motion outside this line. The instability of the dividing line is demonstrated in the concluding plates of the sequence as it breaks up into separate vortices, grossly altering the pressure distribution beyond the separation point.

Figure 24 compares the theoretical pressure distribution ($C_p = 1 - 4\sin^2\phi$) on a circular cylinder with experimental results obtained at various Reynolds numbers. Because of the symmetry of the theoretical curve, integration of the pressure forces over the surface of the cylinder will yield a pressure drag of zero -- the same result obtained for an object of any shape using potential-flow theory alone. In the experimental cases, however, the pressure over the rear of the cylinder never attains its original value at $\phi = 0^\circ$. Pressure recovery is thus said to be incomplete. The suction forces due to the negative pressure coefficient at the rear will predominate over the suction forces acting on the upstream side, and a net positive pressure drag (force in the direction of the stream) will result.

The existence of a point of inflection in the velocity distribution is a necessary condition for separation (15).

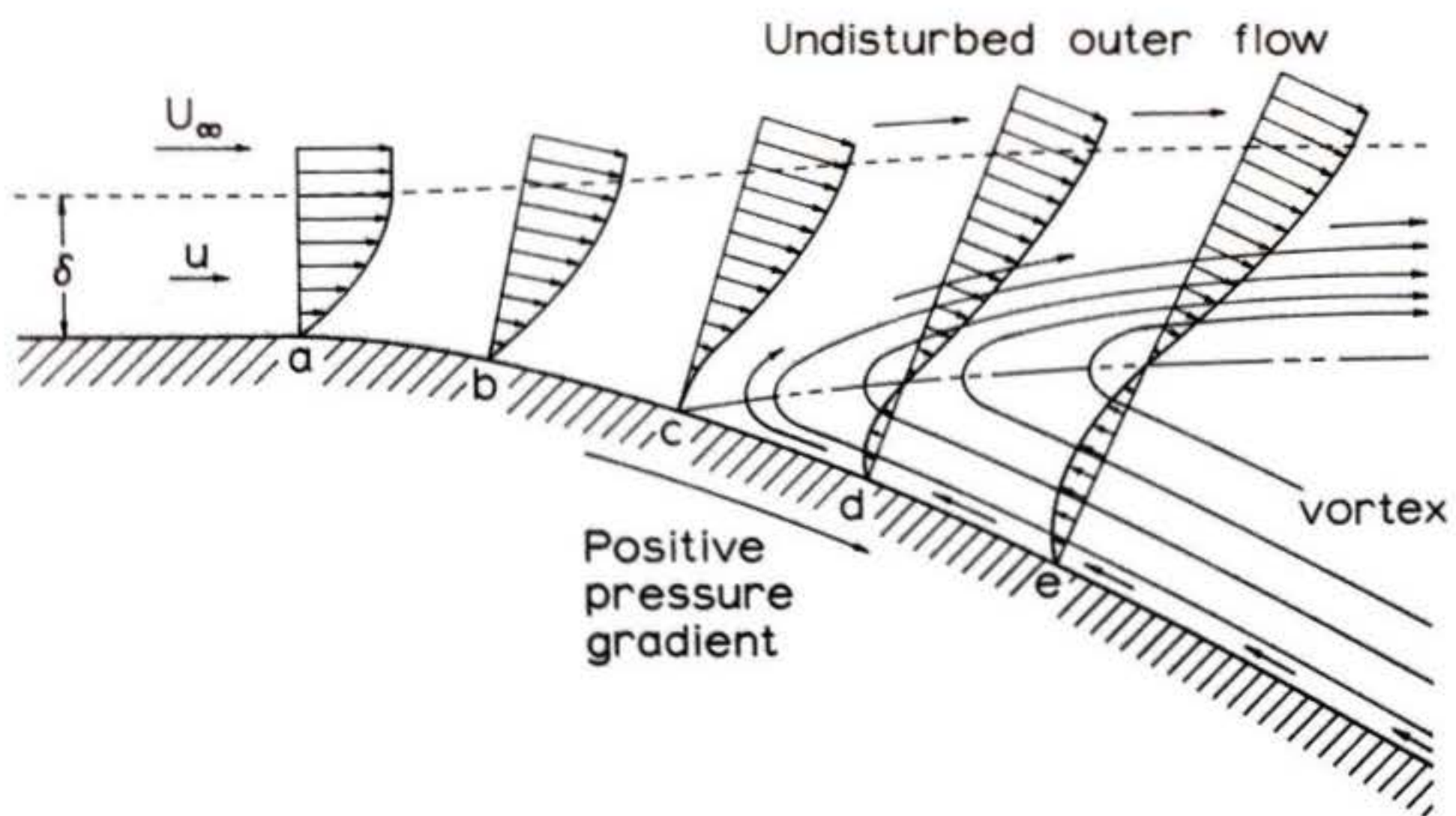
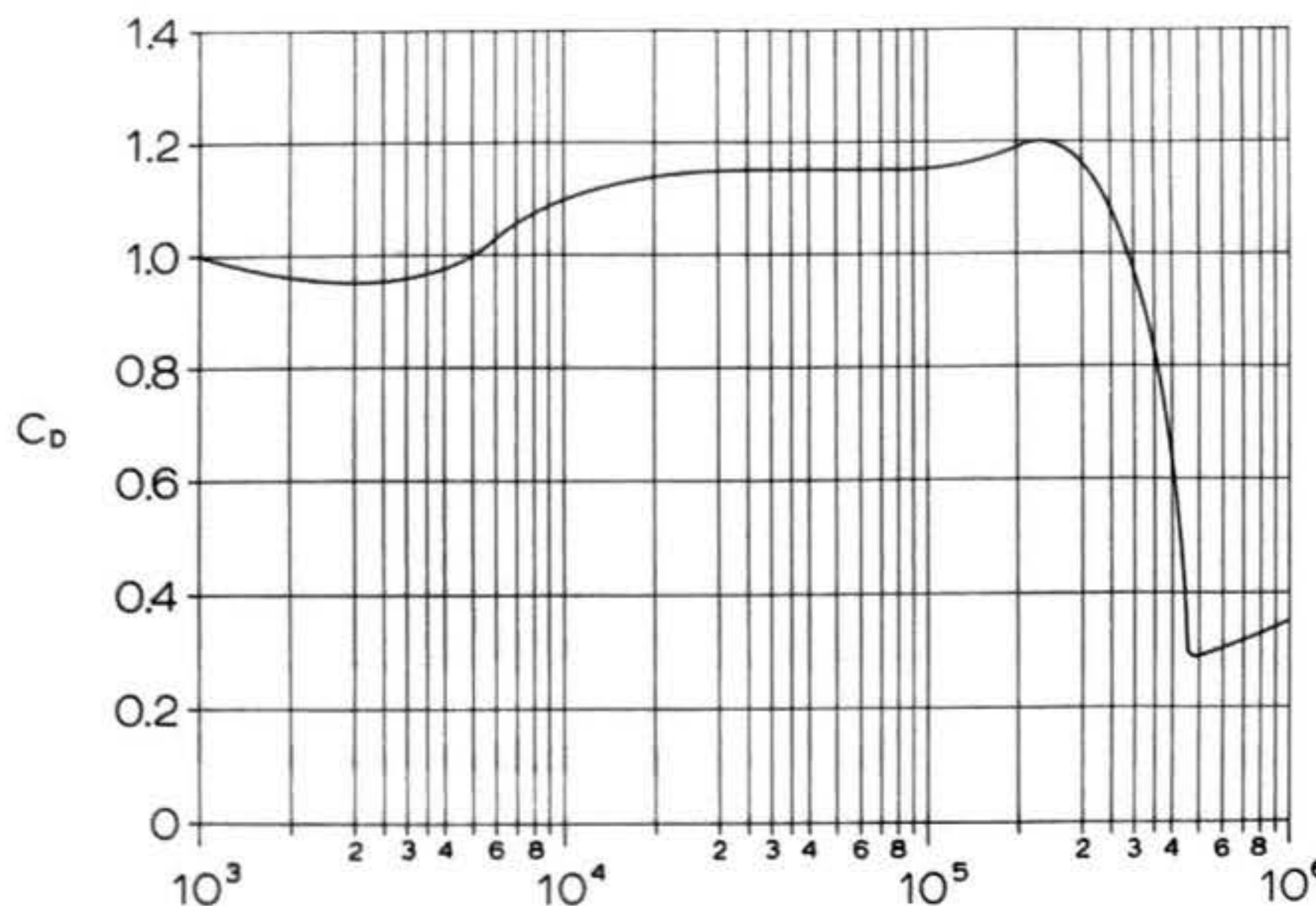


Figure 25: The development of boundary layer separation from a surface due to the influence of a positive (adverse) pressure gradient.

In Section 3 we saw that the stability of a laminar flow is also related to this characteristic of the velocity profile: the existence of a point of inflection is a necessary and sufficient condition for the amplification of turbulent disturbances. The significance of this correlation is revealed when one considers the variation of the drag coefficient of a sphere or circular cylinder with Reynolds number, as shown in Figure 26.

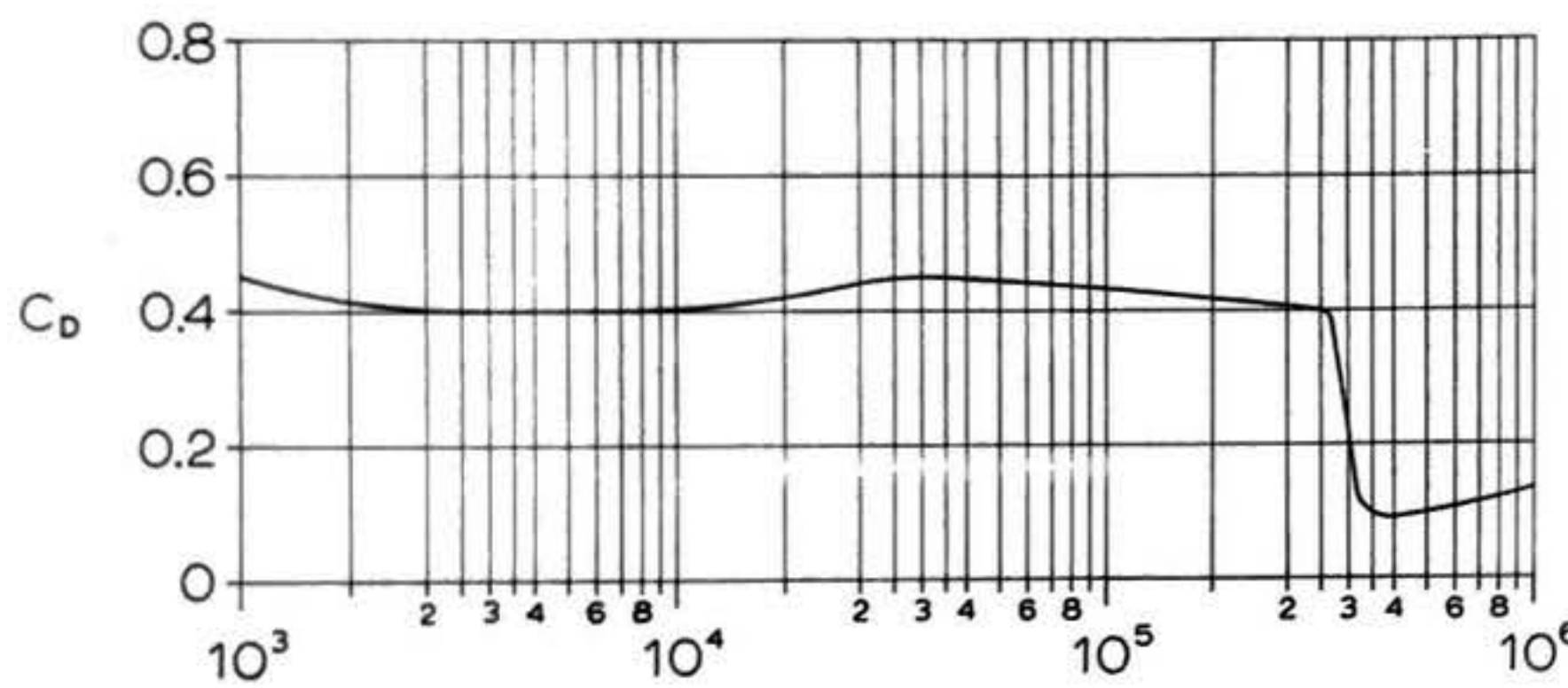
At a Reynolds number of about 3×10^5 for a sphere, and about 5×10^5 for a circular cylinder held transverse to the flow, the drag coefficient exhibits a sudden and considerable decrease. This phenomenon is due to the transition of the boundary layer from laminar to turbulent flow, causing the separation point to move downstream -- and, therefore, causing the total width of the "stagnant" or "dead-air" region created by the separation to decrease. This effect is also demonstrated in the experimental pressure distributions of Figure 24, as for supercritical (post-transition) Reynolds numbers, the pressure recovery is more complete than at subcritical (pre-transition) Reynolds numbers. Hence the fluid flow resembles frictionless flow more closely, and the pressure drag is correspondingly reduced. The magnitude of the decrease in pressure drag is considerably greater than the increase in the friction drag due to the attached turbulent boundary layer. This accounts for the sharpness of the drag coefficient curve's slope at the critical Reynolds number.

A striking flow-visualization experiment, originally performed by Prandtl (12), demonstrates the validity of these assertions.



(a)

$$R_D = \frac{U_\infty D}{\nu}$$



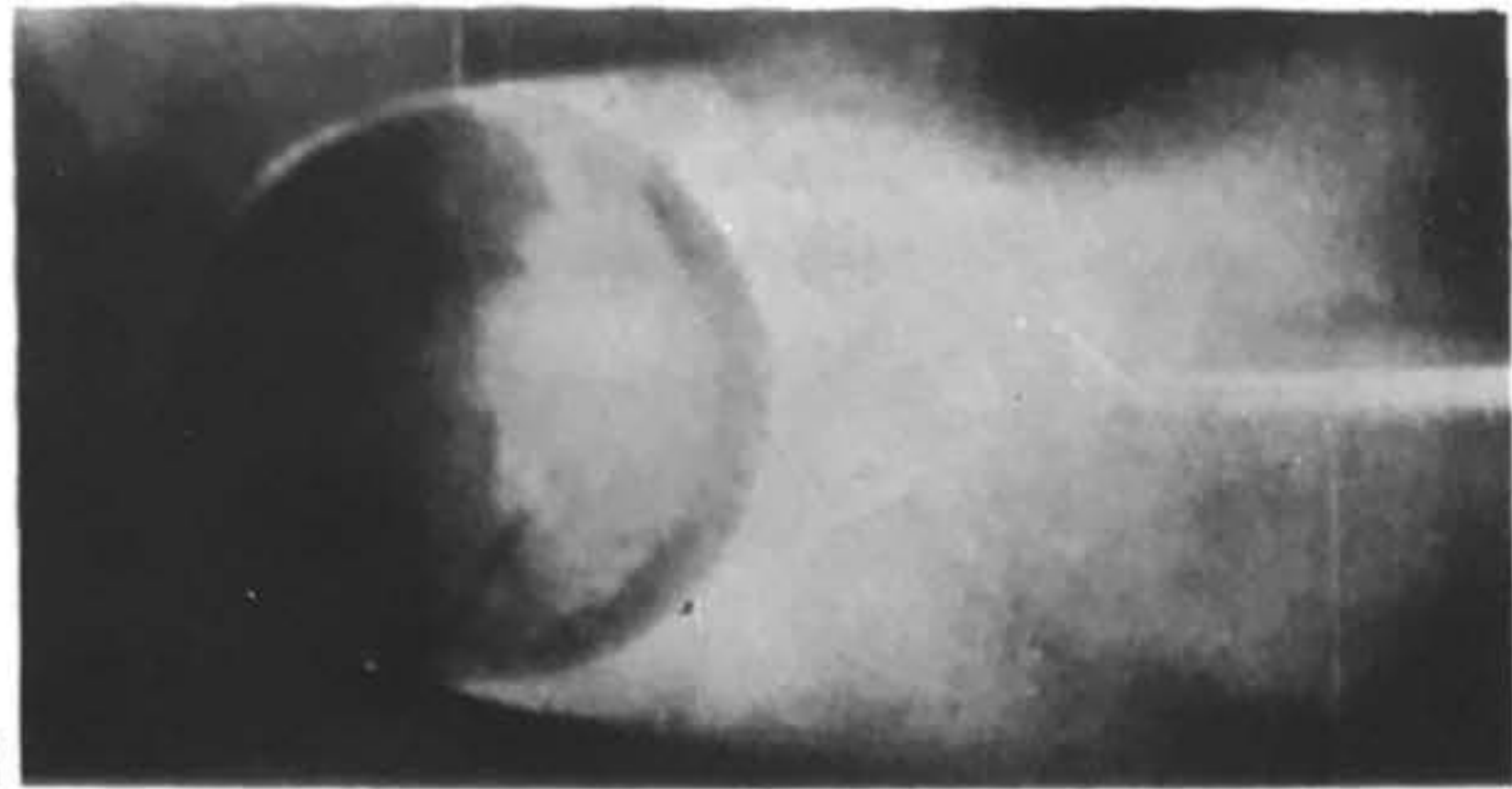
(b)

$$R_D = \frac{U_\infty D}{\nu}$$

Figure 26: Variation of drag coefficient with Reynolds number based on diameter for circular cylinders (a) and spheres (b). The curves shown are average values obtained from a large number of experiments.

He placed a sphere in subcritical flow and observed the resulting flow pattern, made visible by smoke (Plate 5a). As expected, the laminar flow separated just before the shoulder, and there was a very wide wake trailing the body. When a thin wire ring was mounted upstream of the sphere's equator, artificially inducing turbulence as a subcritical Reynolds number (see Section 3.5), the separation point moved well downstream as shown in Plate 5b. This movement was accompanied by a decrease in the measured drag coefficient, similar to that achieved at supercritical Reynolds numbers. The experiment is thus a convincing demonstration that the sharp decline in the drag coefficient of spheres and cylinders observed at the critical Reynolds number can only be interpreted as a boundary-layer phenomenon (15).

It remains to be explained why transition affects the position of the separation point. The physical phenomenon determining this behavior is that a turbulent boundary layer can withstand a stronger adverse pressure gradient than can a laminar boundary layer. This results from the mixing action present in the turbulent layer, which transfers momentum from the outer layers of the flow to the strata of fluid near the wall, permitting them to continue their forward motion for greater distances against adverse pressure gradients than would otherwise be the case. This same mechanism accounts for the low drag of many bodies with streamlined aftersections, such as airplane fuselages: the transition of the boundary layer to turbulent flow prevents the flow from separating in the relatively mild adverse pressure gradient at the rear of such a body, and



a



b

Plate 5: Flow about a sphere at a subcritical Reynolds number. In (a) the laminar boundary layer separates slightly upstream of the shoulder. In (b) the presence of a wire ring "trips" the boundary layer, artificially inducing transition to turbulent flow and delaying separation until the flow is far downstream of the shoulder.

thus the pressure drag is very small. Since the skin friction of such a body in fluids such as air is also small, the overall drag coefficient is close to zero.

4.3 Pressure Drag of the Forebody and Fins

From our discussion of separation, we derive a cardinal rule for low-drag model rocket design: never present a blunt surface to the flow. In general, there are four areas on a typical model rocket which are capable of violating this rule: the body base, the launching lug or other protuberances (if present), the leading and trailing edges of the fins, and the nosecone. Although at least a portion of the base of any model rocket must necessarily be cut off abruptly to permit insertion or removal of the rocket engine, boattailing offers a considerable reduction in base drag and will be discussed separately later on. In the present section, we shall examine the effects of separation on the rest of the rocket body and fins and describe techniques for minimizing them.

4.3.1 Nosecone (Forebody) Pressure Drag

For the purposes of analysis, it is possible to consider the nosecone of a model rocket as being attached to a body tube of effectively infinite length oriented with its axis parallel to the flow. Such a configuration is known as a half-body. An expression for the drag on such a body is a good approximation to the pressure drag on the forebody (nosecone and body tube) of an actual model rocket, provided that the rocket is long enough so conditions near the base do not have a sizeable influence on the flow near the nose. The data of Mark Mercer's

investigation suggest that this approximation is a good one for a typical model rocket, since Mercer found changes in nosecone shape to cause the same absolute increment in drag coefficient for both the blunt-finned and the streamline-finned version of the model he tested.

We first examine the flow about a half-body for an incompressible, inviscid -- that is, perfect -- fluid (12). The mathematics of this problem are such that it cannot be solved unless some specifications are made regarding the pressure at the rear of the body. To circumvent this difficulty, aerodynamicists assume that, at a sufficient distance from the nose, there exists a slot into which the surrounding pressure penetrates (Figure 27). The pressure drag on such a half-body is then the resultant integral of pressure over the surface of the "amputated" forebody.

The techniques of potential-flow theory, involving the mathematical concepts of sources and sinks, could be used to obtain the pressure drag, but a simpler model is presented here (12). As in Figure 27, we enclose the half-body in a wide, hollow cylinder and integrate over a right, cylindrical control surface as indicated by the dotted line. Denoting the cross-sectional area of the cylinder as A_1 , and the frontal area of the half-body as A_2 , the requirement of mass conservation yields

$$(111) \quad A_1 u_1 = (A_1 - A_2) u_2$$

or, letting $R_a = A_2/A_1$.

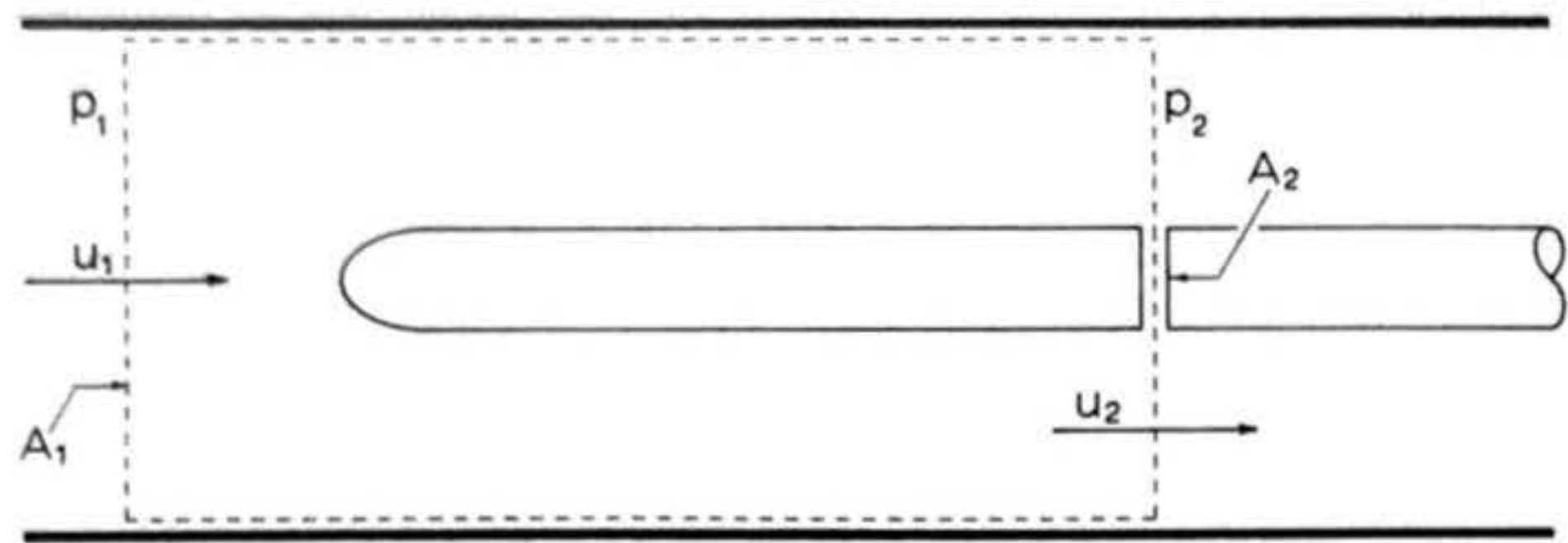


Figure 27: Scheme for computing the pressure drag of a half-body.
 A_1 is the frontal cross-section area of the control surface; A_2 is the frontal cross-section area of the half-body.

$$(112) \quad u_1 = (1 - R_a) u_2$$

Bernoulli's equation for steady, incompressible flow requires that

$$(113) \quad p_1 + \frac{1}{2} \rho u_1^2 = p_2 + \frac{1}{2} \rho u_2^2$$

so one can write

$$(114) \quad p_1 - p_2 = \frac{\rho}{2} u_2^2 [1 - (1 - R_a)^2]$$

Drag, it will be recalled, represents the momentum flux through the control surface (as in the friction-drag calculations of Section 3). Hence,

$$(115) \quad D = A_1 (p_1 - p_2) + A_1 \rho u_1^2 - (A_1 - A_2) \rho u_2^2$$

Applying the condition of mass conservation,

$$(116) \quad D = A_1 (p_1 - p_2) + A_1 \rho u_1 (u_1 - u_2)$$

From equation (113), then,

$$(117) \quad D = A_1 \frac{\rho}{2} u_2^2 \left\{ 1 - (1 - R_a)^2 + 2 [(1 - R_a)^2 - 1 + R_a] \right\}$$

Finally, simplifying the algebra, one obtains

$$(118) \quad D = A_1 \frac{\rho}{2} u_2^2 R_a^2 = A_2 \frac{\rho}{2} u_2^2 R_a$$

or $C_D = R_a$. If we let the cross-sectional area A_1 of the enclosing cylinder become infinitely large, R_a goes to zero -- resulting in the prediction that the drag of a half-body in a fluid flow of infinite extent is zero.

A better understanding of this result can be had by examining

the pressure distribution over the nose of the half-body under the assumption that the flow remains attached to the surface. The streamlines (Figure 28a) near the stagnation point are convex toward the body; this causes an excess pressure in that region. As the flow proceeds downstream along the nose, however, the streamlines turn their concave sides to the body, indicating the existence of a diminished pressure. The net effect, as can be seen in Figure 28b, is an equilibrium between positive pressures and suction (negative pressure increments), yielding zero pressure drag.

Although this result was derived for inviscid flow, it has important applications to real fluid flow. Consider, for instance, a nose shape with a smooth, gently-sloping profile, such as a paraboloid or tangent ogive. We do not expect the flow over such shapes to differ much from that predicted by potential theory, as separation does not occur. The streamlines will be displaced outward some small distance by the boundary layer, but they will retain essentially the same contours. Hence, it seems reasonable to assume that the pressure drag of a streamlined nosecone should be very close to zero in real fluid flow.

There is a considerable body of experimental data supporting this contention. Figure 29, due to Hoerner (9), presents a variety of possible nose shapes with their tested values of pressure foredrag coefficient (based on frontal cross-sectional area). As we surmised, the first two shapes, having no sharp edges or blunt surfaces, have pressure drag coefficients near zero. Furthermore, as the "degree of bluntness" increases

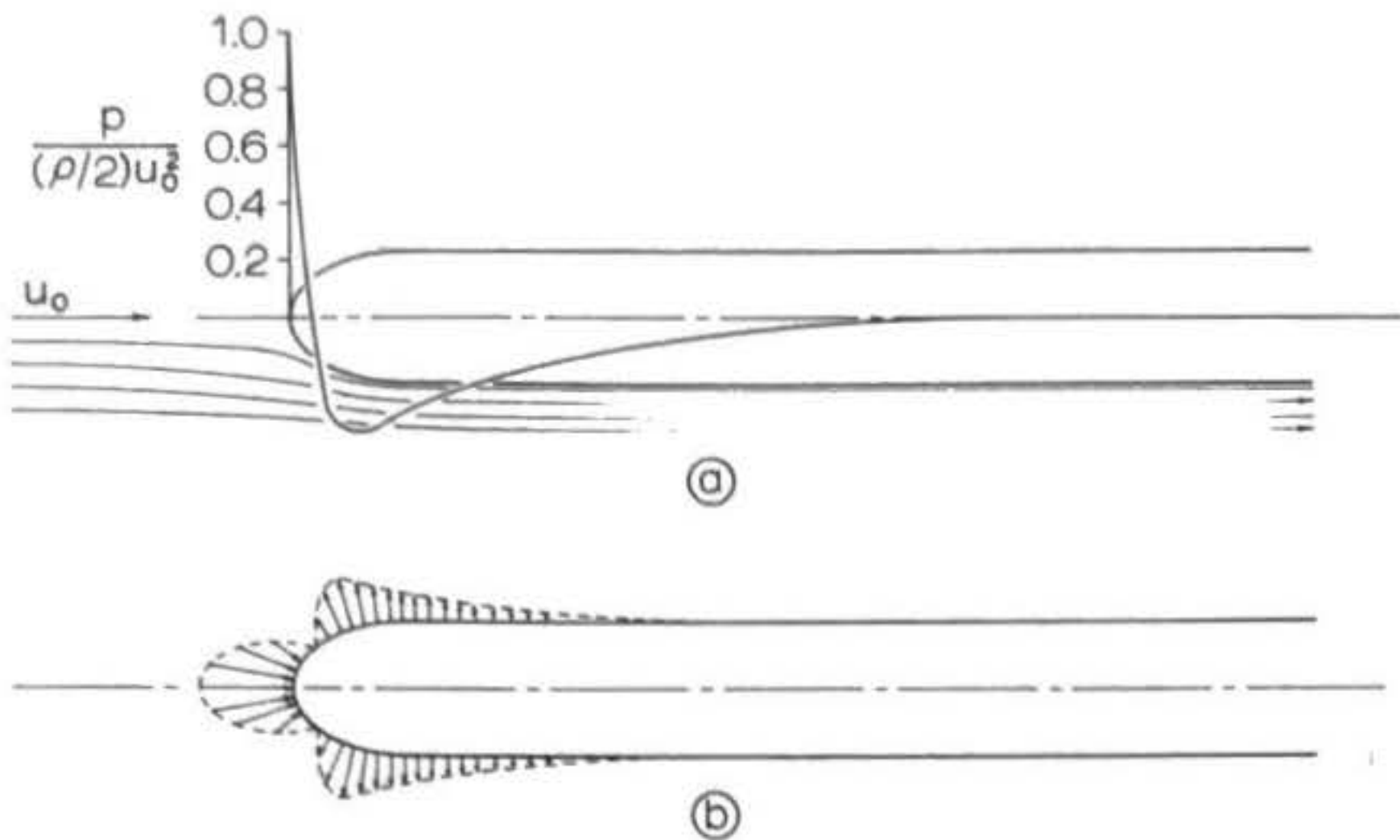


Figure 28: Streamlines and pressure distribution in flow about a half-body. Drawing (a) shows the streamline pattern and the ratio of local static pressure to free-stream dynamic pressure, while drawing (b) shows the distribution of pressure over the surface. Note that there is positive pressure on the forward part of the nose region and suction on the after portion of the nose. According to potential theory the two effects counteract each other and the drag of a half-body is zero.

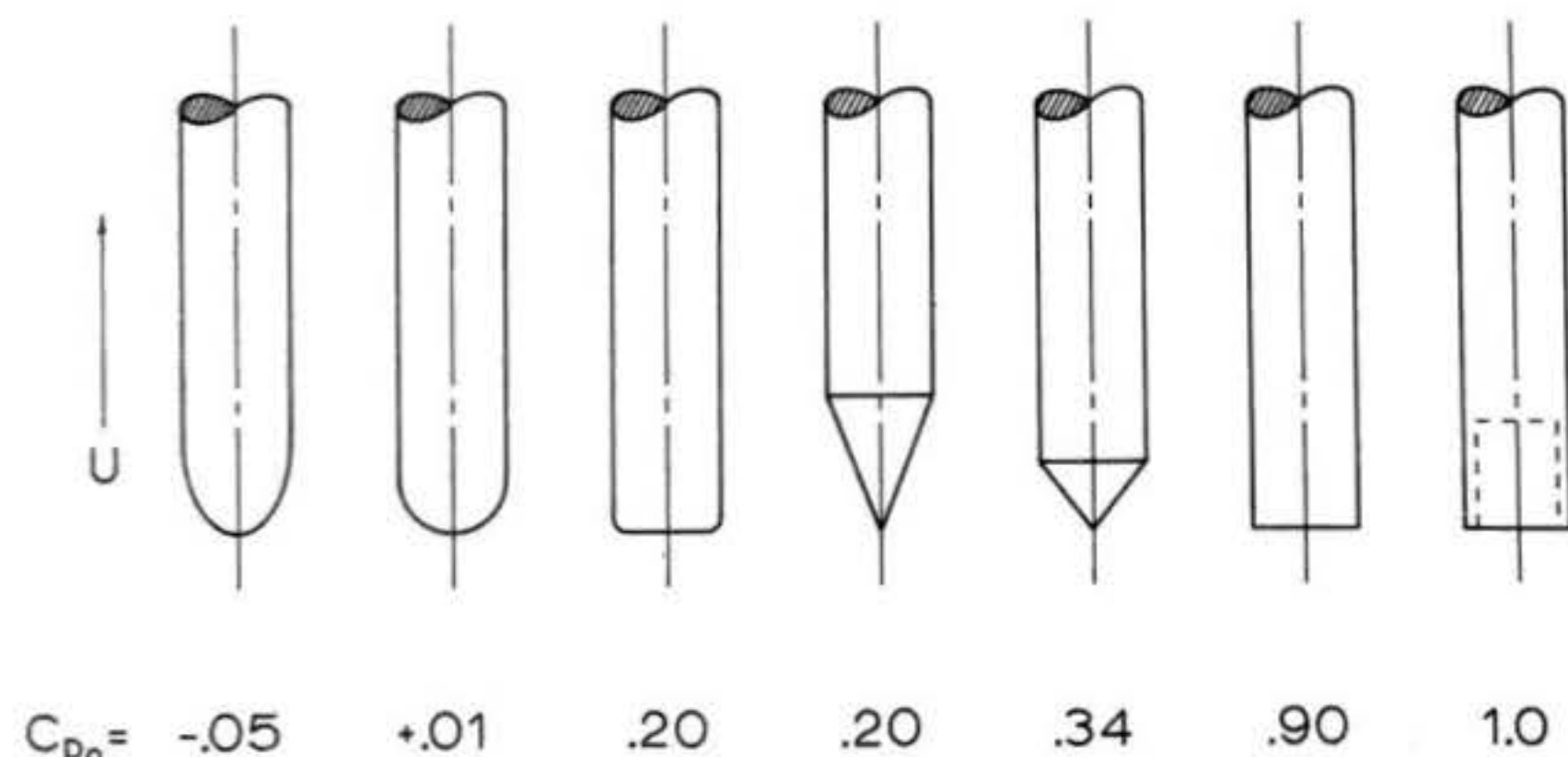


Figure 29: Pressure foredrag coefficients of various nose shapes. The rounded shapes exhibit very low drag coefficients, in good agreement with the potential-flow prediction for a half-body.

(from top to bottom in the diagram) the drag coefficient shows a corresponding increase.

Evidently the first shape, which might represent a conic section (ellipsoid, paraboloid, or hyperboloid of revolution), is superior for model rocketry applications; in fact, an ellipsoid of revolution whose length is about twice its base diameter is considered near-optimum by many designers. Its negative pressure drag coefficient is due to the predominance of suction forces over positive pressure increments on its surface. This result can be understood by reexamining the experimental pressure distributions determined for a circular cylinder held transverse to the flow. The flow over the forward half of the cylinder is the two-dimensional analog of the three-dimensional flow about a nosecone of rounded profile, and it can be seen that integration of the coefficient of pressure over the cylinder's forward half ($\varphi \leq 90^\circ$) will result in a negative pressure drag coefficient.

A comparison of shapes #3 and #6 reveals what even a small amount of rounding of sharp edges can accomplish. The quantitative variation of drag coefficient with "rounding radius" for a variety of two-dimensional and three-dimensional shapes is illustrated in Figure 30. At a value of $r/h \approx 0.1$ for three-dimensional shapes, C_D declines sharply in a manner analogous to its behavior at the critical Reynolds number (Figure 26). The physical cause of this behavior is not transition, however, but a progressive decrease in separation from the forward edges. The "critical radius ratio" $r/h = 0.1$ is then the minimum value above which the effects of separation on the pressure drag are

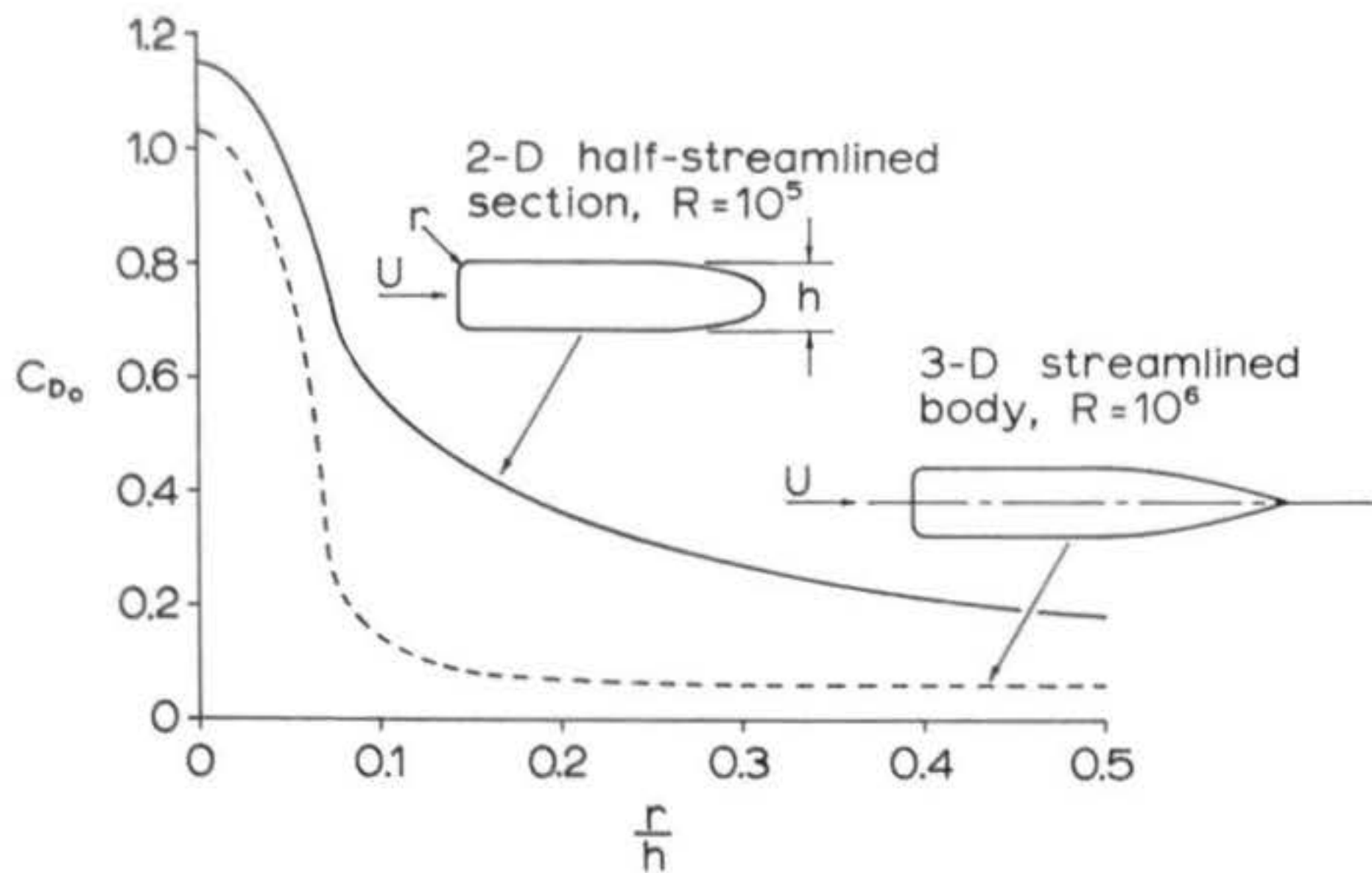


Figure 30: Variation of drag coefficient with rounding radius for two-dimensional and three-dimensional bodies. The two-dimensional result can be applied to fin design, while the three-dimensional curve is applicable to nosecones. Both curves are averages of experimental data.

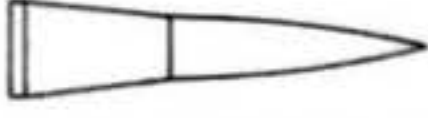
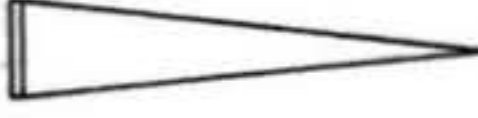
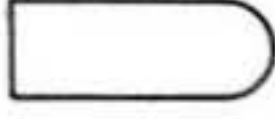
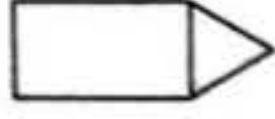
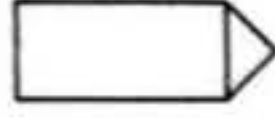
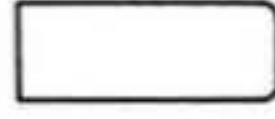
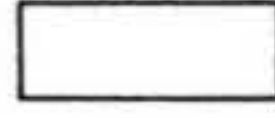
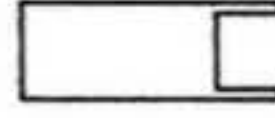
Nosecone shape	Nosecone designation	C_D of Javelin with airfoiled fins	C_D of Javelin with square edged fins
	BC-70	0.41	2.10
	BC-78	0.41	2.13
	BC-72	0.42	2.12
	BC-76	0.42	2.14
	BC-74	0.43 (0.70)	2.15 (2.35) [2.76]
	BC-79	0.51	2.14
	Hemisphere	0.51	2.16
	60° cone	0.59	2.24
	45° cone	0.61	2.24
	Slightly rounded	0.87	2.51
	Flat	1.32	2.77
	Plug	1.75	3.26

Figure 31: Drag coefficient of the Javelin rocket with various nosecone shapes and fin profiles. The first column displays diagrams of the nose shapes tested. The second lists designations for the shapes (designations beginning with BC- are catalog numbers used by the Centuri Engineering Company, producers of the cones and of the Javelin rocket). The third column lists drag coefficients obtained for the Javelin rocket sanded, painted, and with airfoiled fins using each nose shape. The fourth column lists drag coefficients obtained for a sanded and painted Javelin with no airfoiling on the fins. Figures in parentheses were obtained after adding a launch lug; the figure in brackets is for an unsanded, unpainted Javelin with a launch lug and without fin airfoiling.

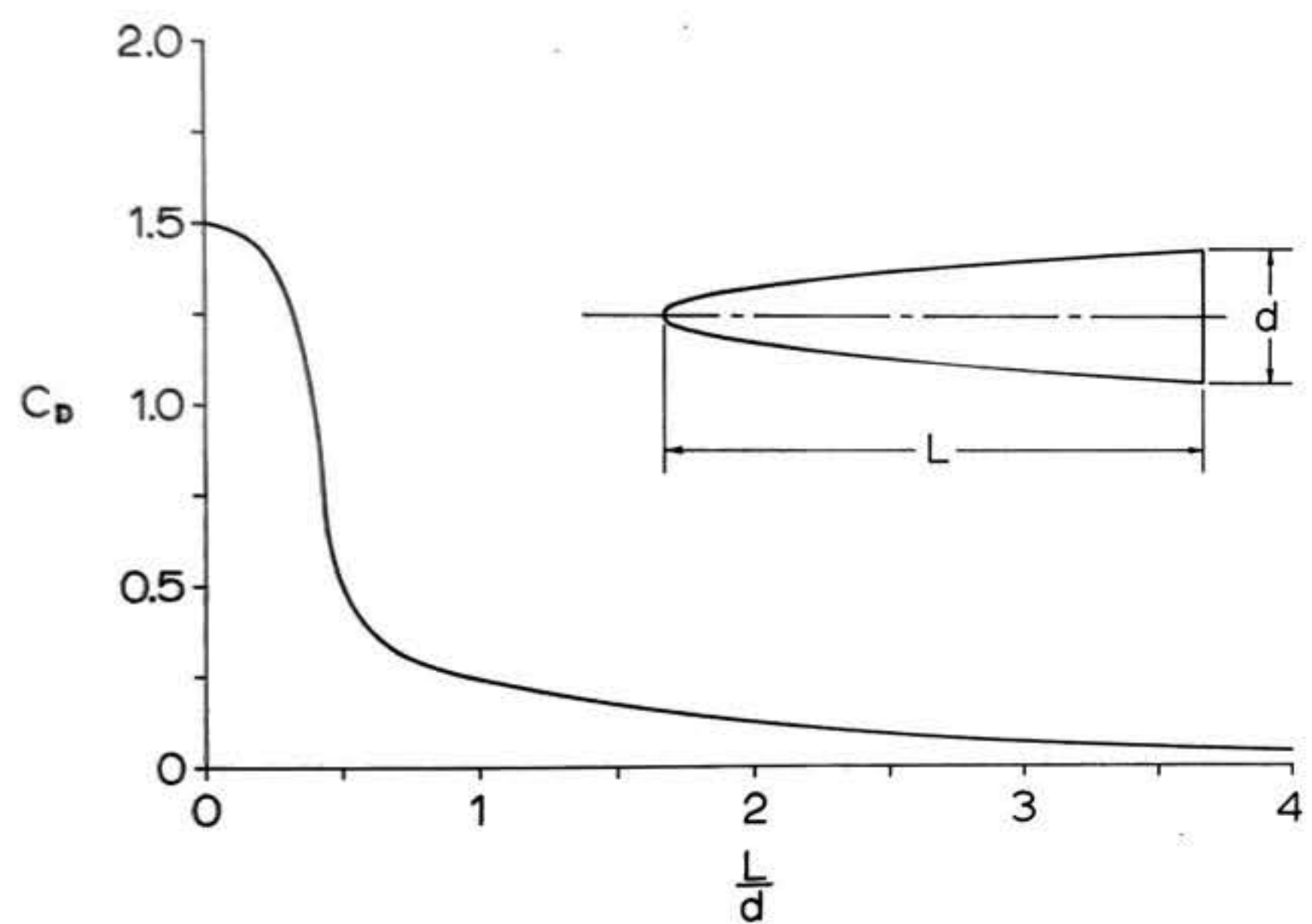


Figure 32: Variation in the drag coefficient of a paraboloidal nose shape with fineness ratio L/d .

negligible. It appears from tests that $(r/h)_{crit}$ is a slowly-varying function of Reynolds number, decreasing as R is increased.

Mark Mercer (10) has wind-tunnel tested all seven of the shapes in Figure 29, plus some additional ones of interest, on an actual model rocket -- the Javelin, a commercially-available kit produced by the Centuri Engineering Company, which he modified to various configurations for test purposes. The trend toward greater drag with increasing nosecone bluntness is clearly demonstrated in his measurements (Figure 31). Note particularly that the five shapes exhibiting the lowest drag (Centuri stock nosecones, catalog numbers BC-70, BC-78, BC-72, BC-76 and BC-74) are roughly similar to the first shape in Figure 29; furthermore they are representative of what might be considered "typical" model rocket nosecones. The essential features which distinguish these shapes from the others tested are (a) a length-to-diameter ratio of at least 2; (b) a smooth transition between nosecone and body, the nosecone being generally tangent to the tube at its base; (c) a smooth boundary curve with its convex side toward the flow; and (d) no blunt surfaces facing the flow. Mercer's data may thus be considered an empirical guide to model rocket nosecone streamlining.

The importance of the length-to-diameter ratio in nosecone streamlining is demonstrated quantitatively in Figure 32, taken from Stine (18). The pressure drag coefficient is reduced significantly as the ratio L/d of the paraboloidal shape is increased up to about 2.0; further extension of the nose reduces the drag only slightly. This behavior accounts for the relatively slight differences in drag among the five streamlined nosecones

in Mercer's tests.

4.3.2 Fin Pressure Drag

Since the fin surfaces are generally parallel to the flow direction, any pressure drag due to the fins must result from separation of the flow from the leading and/or trailing edges. Mercer's data indicate that the effect of blunt fin edges, as opposed to streamlined edges, is considerable in this respect (Figure 31). The Javelin rocket used in his tests experienced an increase in C_D from 0.70 to 2.35 when all the fin edges were left squared off, rather than rounded at the leading edges and tapered at the trailing edges -- a 236% increase in drag over that of the streamlined-fin configuration.

At the thickness-to-chord ratios commonly encountered in model rocketry (usually 0.02 or greater), the separated flow from a blunt leading edge will reattach itself to the fin at some point downstream. If the trailing edge is also squared off, separation will occur there also, resulting in a "base drag" analogous to that of the rocket's main body.

To prevent -- or rather, to minimize -- fin separation, streamlining of the fin section (or "profile") is required. Adequate streamlining can usually be accomplished simply by providing a rounded leading edge (the two-dimensional analogy to the streamlined nose shape) and a gently-sloping aftersurface culminating in a sharp trailing edge (the so-called "knife-edge"). One must compromise with structural durability requirements here, since a paper-thin trailing edge is very easily damaged. The profile of a well-streamlined model rocket fin is illustrated

in Figure 38. The character of the lateral edges of the profile -- whether they are flat or "airfoiled" -- does not substantially affect pressure drag, but it does play an important role in determining drag due to lift as discussed in Section 5.

4.3.3 Launch Lug Drag

A remarkable aspect of aerodynamic drag is that small changes in the shape of a body can produce large variations in its drag coefficient. Mercer's research showed that the addition of a launch lug (presumed location: near the rear of the body tube) increased the C_D of the streamlined-fin version of his Javelin test rocket by about 0.28, or 67% of the value for a lugless rocket. This finding agrees rather well with estimates of 50% or more reported for much larger rockets (7).

The culprit, once again, is boundary-layer separation -- in this case, from the blunt face of the lug. Pressure drag due to lugs and similar objects which protrude from the boundary layer is often referred to as parasitic drag. The only available data on this important effect as it relates to model rockets is that of Mercer, so the influence of a launch lug on the C_D values of rockets of different body diameters and fin configurations, as well as the effects of launch lug placement, cannot now be accurately assessed. We note, however, that the addition of a lug to the blunt-fin version of Mercer's Javelin increased the drag coefficient by about 0.21, an increment roughly equal to that for the streamline-fin version. On this basis it is possible to suggest an average drag coefficient increment

of $\Delta C_D = 0.25$ due to the presence of a launch lug on model rockets whose configurations are such that the ratio of body diameter to lug diameter is identical to that of Mercer's Javelin, and such that the lug placement is similar.

We can develop a tentative formula for extending Mercer's results to models in which the launch lug diameter stands in a different ratio to the body tube diameter than was the case in the Javelin experiments, by computing the drag coefficient of the launch lug when in place based on its own included frontal area. To do this we note that the standard launch lug used on a model of the Javelin's size has a diameter of about 0.40 centimeter, while the body tube of the Javelin has an outer diameter of 1.93 centimeters. The ratio of the tube diameter to the lug diameter is then 4.8, and the ratio of A_r , the reference area for computing the drag of the entire rocket (which, it will be recalled, is equal to the cross-sectional area of the body tube), to the area included within the circular cross-section of the lug -- which we shall denote by A_{lug} -- is the square of the diameter ratio, or $A_r/A_{lug} = 23.0$. The drag coefficient of the lug based on its own frontal area is therefore 23 times greater than that based on the body tube cross-sectional area. Denoting it by $(C_D)_{lug}$, we have $(C_D)_{lug} = 5.75$ -- quite a large value, and one that indicates that the lug must cause flow separation, not only from itself, but from a substantial area of the body tube in its vicinity. The general expression for the drag coefficient increment due to a body-mounted launch lug may then be written

$$(119) \quad (\Delta C_D)_{\text{lug}} = 5.75 \frac{A_{\text{lug}}}{A_r} = 5.75 \left(\frac{d_{\text{lug}}}{d_r} \right)^2$$

Data taken by Douglas J. Malewicki (20) indicate that placing the launch lug in one of the joints between the model's fins and its body can substantially decrease the launch lug drag increment. Malewicki determined an overall C_D of about 0.50 for his Skychute XI rocket tested with a launch lug at Reynolds numbers ($R\ell = 2.5 \times 10^5$) about the same as those of Mercer's tests. Since, according to the methods of Section 6, the C_D of the Skychute XI without a launch lug is probably not less than 0.35, the increment in C_D due to the presence of the lug located at the fin-body joint cannot be much more than 0.15 -- only 60% of the increase determined by Mercer for a body-mounted lug on a configuration of the same ratio A_{lug}/A_r . The wind tunnel used by Malewicki (the low-speed tunnel at Wichita State University near Wichita, Kansas) may have had a significantly lower air turbulence level than that used by Mercer, so it is not necessarily accurate to compare their results directly. Given the extremely limited nature of the data concerning this important problem presently available to model rocketeers, however, the best we can do is to present the following tentative formula for the drag coefficient increment due to a launch lug mounted at the fin-body joint:

$$(120) \quad (\Delta C_D)_{\text{lug}} = 3.45 \frac{A_{\text{lug}}}{A_r} = 3.45 \left(\frac{d_{\text{lug}}}{d_r} \right)^2$$

The development of accurate, empirical expressions for $(\Delta C_D)_{\text{lug}}$ covering variations in lug configuration, size, and placement is a problem requiring considerable further research.

The most effective means of reducing launch lug drag is to eliminate the lug completely and launch from a tower or closed-breech launching device. Mechanisms by which the lug can be retracted soon after launch or left behind on the launch rod have also been experimented with, resulting in varying degrees of success. One firm, Competition Model Rockets of Alexandria, Virginia, has developed a particularly successful form of pop-off launch lug and has incorporated the design in several commercially-available kits.

In conclusion, however, I must reiterate that the prediction of drag due to launch lugs remains at the time of writing almost wholly a matter of empirical art -- of "guesstimating", to adopt a colloquialism from professional rocketry. It is hoped that in the near future this area of model rocket drag will be more thoroughly investigated, and that formulae for predicting launch lug drag will be established on a firmer analytical foundation.

4.4 Base Drag

The only section of the rocket now remaining to be considered in our analysis of pressure drag is the base. Since the plane of the base is generally perpendicular to the flow direction (at zero angle of attack), base pressures act along the drag axis and the second term in equation (28) may be written simply as

$$(121) \quad D_b = - \iint_{S_b} p_b dS_b$$

so

$$(122) \quad C_{D_b} = \frac{D_b}{\frac{1}{2} \rho U_\infty^2 S_b}$$

Theoretical analysis of the base drag is extremely difficult; in fact, there is at this time no theory which can accurately predict the base drag of a model rocket during all phases of flight. Complications arise from the following sources:

- (a) The boundary layer separates from the blunt base and, as mentioned previously, the boundary-layer equations are not valid beyond the separation point;
- (b) The presence of the fins disturbs the flow, generally resulting in a decrease in base drag from that observed for finless bodies; and
- (c) A jet exhausting into the base region is believed to cause a further decrease in base drag.

The last two problems, peculiar to rocketry, have not been well researched on either the hobby or the professional level for subsonic flow. The empirical expression for base drag presented here is consequently unable to take either of the last two phenomena into account.

Base drag is essentially a separation phenomenon. Figure 33 depicts the flow to be expected about the base of a model rocket when the engine is not firing. The boundary layer separates and then converges downstream, enclosing a volume known as the "dead-air" region. This term is actually a misnomer, as there is considerable motion of the air in this region

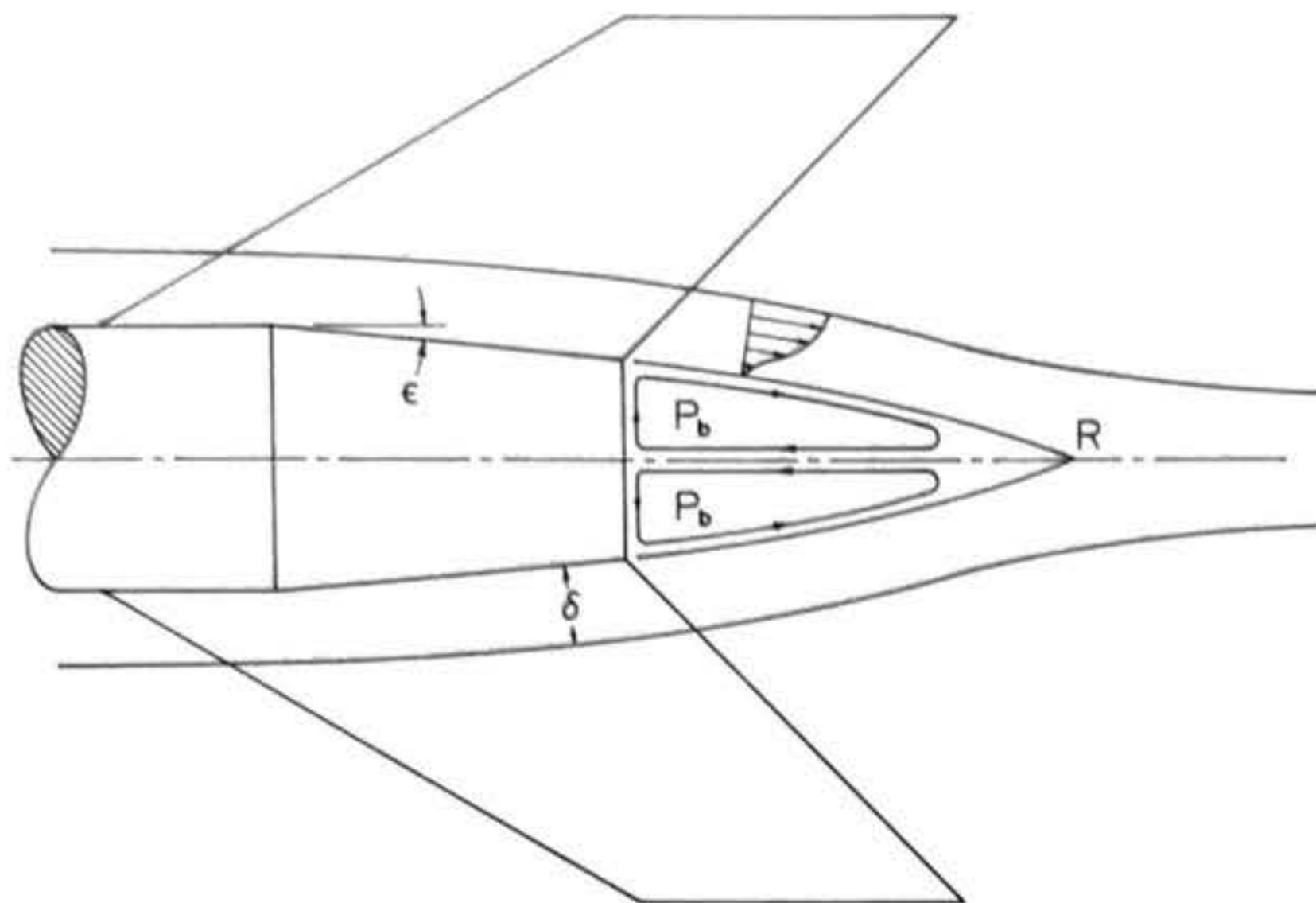


Figure 33: Flow about the base of a model rocket with a conical boattail. ϵ is the boattail angle and δ is the boundary-layer thickness. The boundary layer thickens as the flow passes over the boattail and then separates when the flat base is reached, forming a region of low pressure -- the "base pressure" P_b -- and then reattaching at point R downstream of the rocket. Viscous effects cause the circulation pattern shown in the base pressure region.

resulting from mixing along the free shear layer -- the boundary region between the dead-air volume and the free stream -- and from flow reversal at the convergence point (16).

The character of the flow as a whole, as Hoerner (9) suggests, is somewhat like a jet pump: the external flow, acting as a "jet", mixes with the "dead air" and tries to "pump" it away. The static pressure at the base is consequently reduced, and base drag results (see equation 121). The boundary layer (which becomes the free shear layer after separation), however, acts as an insulating sheet between the jet pump effect of the outer flow and the dead-air region, and the effective dynamic pressure of the pump is reduced. An increase in boundary-layer thickness therefore results in a smaller reduction of base pressure, which in turn implies a smaller base drag.

We have seen that the boundary-layer thickness is proportional to the skin-friction drag (for example, compare equations (54), (59), and (60)). If we now define a forebody friction drag coefficient C_{fb} such that

$$(123) \quad C_{fb} = \frac{D_{\text{forebody, friction}}}{q S_b} = C_f' \frac{S_s}{S_b}$$

where S_s is the wetted area of the body exclusive of the base, S_b is the area of the base, and C_f' is the forebody skin-friction coefficient as determined by the methods of Section 3, we expect (on the basis of the above discussion) that

$$(124) \quad C_{D_b} = f(C_{fb})$$

The nature of this relationship -- that is, the form of the

function f -- can be determined from a plot of experimental data, as in Figure 34. The empirical function that has been determined for equation (124) is

$$(125) \quad C_{D_b} = \frac{0.029}{\sqrt{C_{f_b}}} \equiv \frac{D_b}{q S_b}$$

As we expected, an increase in the body viscous drag (which includes the effects of roughness) produces a decrease in base drag. Equation (125), however, as previously stated, does not take into account the effects of fins or rocket exhaust.

Although there has been some experimentation with trading increased friction drag for reduced base drag by varying the roughness of a model's surface finish, model rocketeers are generally limited to variations in rocket geometry to effect reductions in base drag. The most widely-used technique, employed on models which require a main body tube section greater in diameter than that which would be a "glove fit" to the engine, is referred to as boattailing. A gradually-tapered section (see Figure 33) is added to the rear of the rocket body, to guide the flow downstream to a reduced base area. If the boattail angle ϵ is small enough (about 5 or 10 degrees) the flow will not separate from the boattail lateral surface, and the increase in base pressure due to pressure recovery along the boattail reduces the base drag. The technique is limited in usefulness to those models which, for some reason, must use a main body section significantly greater in diameter than the engine casing; there is, of course, no sense in enlarging the diameter of a rocket just to enable it to be built with a boattail!

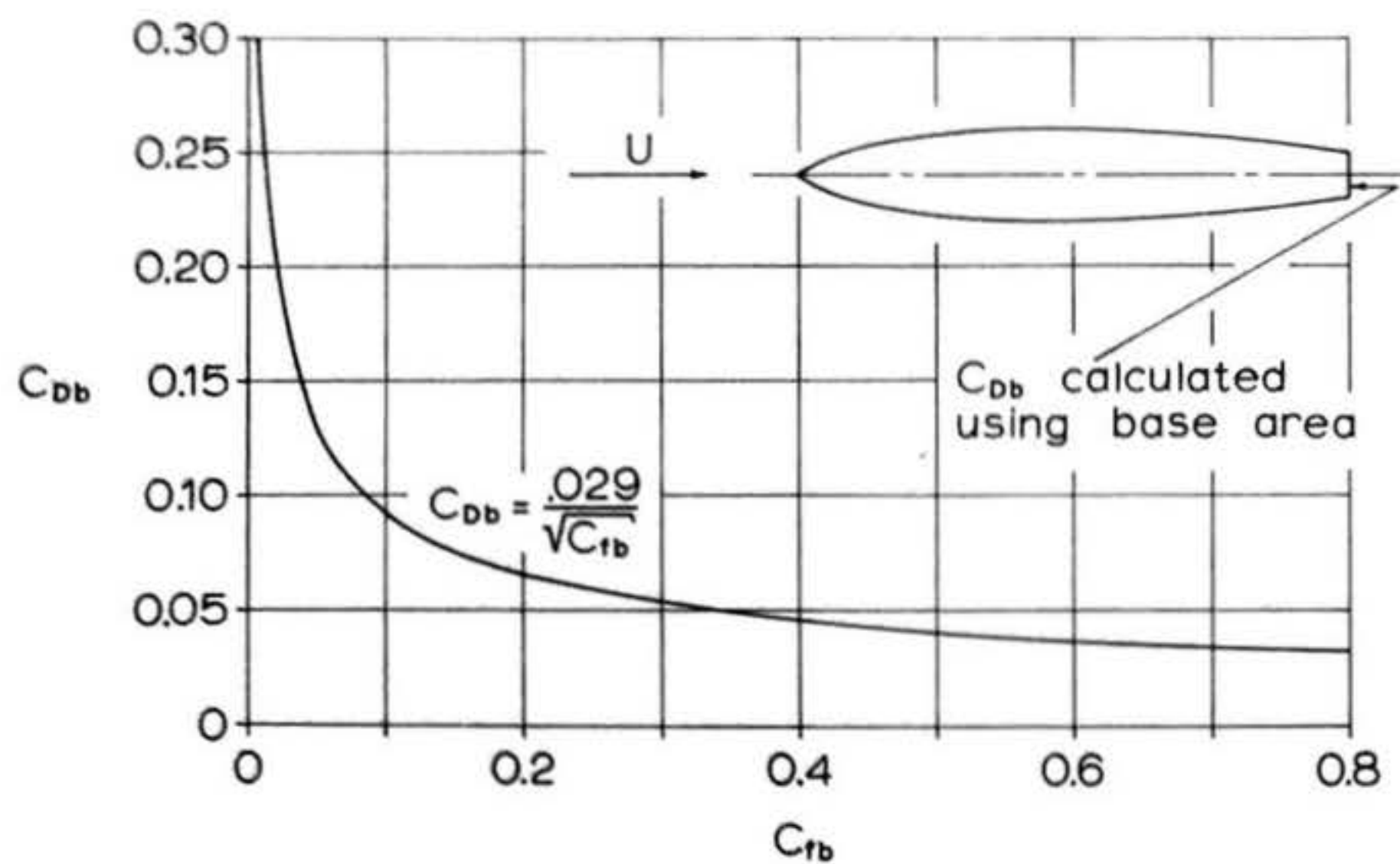


Figure 34: Variation of the base drag coefficient of a body of revolution with forebody friction drag coefficient. The curve and semiempirical function shown represent a "best fit" to a large collection of experimental data.

An expression for the base drag of a boattailed configuration can be developed from equation (125). If the body maximum frontal area is denoted S_m , and its associated body diameter d_m , then

$$(126) \quad S_b = S_m \left(\frac{d_b}{d_m} \right)^2$$

The friction drag coefficient of the forebody based on maximum body frontal area is

$$(127) \quad C_{Df} = \frac{D_{\text{forebody}}}{q S_m}$$

Now

$$(128) \quad C_{fb} = \frac{D_{\text{forebody}}}{q S_b} = \left(\frac{D_{\text{forebody}}}{q S_m} \right) \left(\frac{d_m}{d_b} \right)^2 = C_{Df} \left(\frac{d_m}{d_b} \right)^2$$

Furthermore,

$$(129) \quad (C_{Db})_m = \frac{D_b}{q S_m} = \frac{D_b}{q S_b} \left(\frac{d_b}{d_m} \right)^2 = C_{Df} \left(\frac{d_b}{d_m} \right)^2$$

where $(C_{Db})_m$ is the base drag coefficient based on maximum body frontal area. Then

$$(130) \quad (C_{Db})_m = \left(\frac{d_b}{d_m} \right)^2 \frac{0.029}{\sqrt{C_{Df} (d_m/d_b)^2}}$$

or, simplifying algebraically,

$$(131) \quad (C_{Db})_m = \left(\frac{d_b}{d_m} \right)^3 \frac{0.029}{\sqrt{C_{Df}}}$$

It is apparent that $(C_{Db})_m$ can be reduced, either by decreasing the ratio d_b/d_m or by increasing the skin-friction drag of the body. The first technique is limited by the diameter of the engine itself. The danger of separation from the boat-tail as the boattail angle ϵ (as defined in Figure 33) is

increased also imposes a lower limit on d_b/d_m for a given boattail length. The maximum permissible value of ϵ generally lies somewhere between 5° and 10° ; if ϵ is greater than this value separation will occur on the boattail and equation (131) will not apply.

Increasing the skin-friction drag of the body can be accomplished by lengthening the boattail, but it can be demonstrated from equation (131) that the boattail should not be longer than the section of cylindrical body tube it replaces; or more precisely, that the rocket with boattail should not be any longer than it would have been if designed without a boattail. Differentiation of (131) with respect to C_{Df} gives

$$(132) \quad \frac{d(C_{Db})_m}{dC_{Df}} = -\left(\frac{d_b}{d_m}\right)^3 \frac{0.029}{2(C_{Df})^{3/2}}$$

where care must be taken to distinguish the letter d as used to denote differentiation on the left-hand side from d as used to denote diameter on the right, and the assumption has been made that d_b/d_m is unrelated to C_{Df} . Since, for the increase in skin-friction drag to be less than the decrease in base drag, we require $\Delta(C_{Db})_m < -\Delta(C_{Df})$,

$$(133) \quad -\left(\frac{d_b}{d_m}\right)^3 \frac{0.029}{2(C_{Df})^{3/2}} < -1$$

giving

$$(134) \quad (C_{Df})^{3/2} < .0145 \left(\frac{d_b}{d_m}\right)^3$$

and finally,

$$(135) \quad C_{Df} < .059 \left(\frac{d_b}{d_m}\right)^2$$

The largest value of C_{Df} for which an increase in C_{Df} will result in a decrease in overall drag occurs for the limiting case $d_b/d_m = 1.0$, and even then C_{Df} must be less than 0.059. Model rockets do not have body skin-friction drag coefficients this small. A typical value of C_{Df} for a well-designed model rocket is three or more times this value (see Section 6). This is because well-designed model rockets have a fineness (length-to-diameter) ratio sufficiently great so that the ratio of wetted area to frontal area is relatively large, and so, therefore, is C_{Df} . Hence, insofar as equation (131) is valid, the contention that an increase in C_{Df} cannot result in a decrease in base drag sufficient to lower the overall drag of the rocket is proved. Note that the means by which C_{Df} is to be increased has not been specified in the derivation, and that equation (135) consequently refers to variations in C_{Df} effected by any means whatsoever; i.e., whether by altering the length of the body to change S_s or by altering the surface finish of the body to change C_f' . Equation (135) therefore indicates, not only that a rocket should not be lengthened to incorporate a boattail, but that it should not be roughened in the hope that increasing C_{Df} will decrease C_{Db} enough to lower the overall drag coefficient of the model. Having determined to design a model with a boattail no longer than it would have been without one, the modeler may follow Stine (18) who suggests a boattail length of two or three body diameters for best results at moderate ratios d_b/d_m .

A recent experimental investigation (5) indicates that recessing the base of a boattailed configuration may be an effective means of reducing base drag. Since the nozzle of a

model rocket engine provides a natural concavity at the base, this technique, although not regarded as such, has been in use for some time. By recessing the engine slightly into the tube, thereby creating a deeper concavity, it may be possible to reduce base drag still further. Care must be taken not to recess the engine further than about half a body diameter, or the conditions of nozzle overexpansion responsible for the notorious Krushnic effect (named for Richard Krushnic, who discovered it in 1958) will be created, destroying most of the effective thrust (and probably the aft section of the model). Those readers desiring a further explanation of this interesting phenomenon may consult the article by Gordon Mandell in Model Rocketry magazine for November, 1969.

5. Other Contributions to Model Rocket Drag

5.1 Introduction

The two preceding sections examined the contributions to drag of the tangential (viscous) and normal (pressure) forces acting on a model rocket body. Several important assumptions were inherent in these presentations; namely that (a) the body was inclined at zero incidence (zero angle of attack) to the flow; (b) the body was not rotating about its longitudinal axis; and (c) surface roughness affected the drag only through inducement of premature transition. We are now interested in determining the effects on the drag of relaxing these assumptions.

The determination of tail-body drag at angle of attack is extremely difficult, because little is known about tail-body interference effects at different flow inclinations. We will

restrict our attention to small angles of attack (less than about 10°), since at larger values of α the relationship between drag and angle of attack is far more complex and, in any case, flight at large angles of attack generally indicates a dynamic stability problem necessitating a redesign of the rocket. Furthermore, only very simple single-stage model rocket configurations will be examined. Article 5.2 presents a practical method (from Reference 6) for calculating the drag coefficient at angles of attack, although (as with many methods discussed in this chapter) it still requires experimental data to confirm its applicability to model rockets.

In Section 5.3 we examine the effects of rotation about the roll axis, which generally produces a drag increase. It will be found that the increase in drag coefficient due to spin is usually small compared to that due to the mechanism which induces the rotation (usually canted fins).

Previously, in Section 3.5.2, it was seen that surface roughness due to single or distributed particles can lead to premature transition, and hence to an increase in the skin friction. In a purely turbulent region surface imperfections, since they represent obstacles to the flow, have a viscous drag of their own. This component of model rocket drag will be examined in Section 5.4.

5.2 Drag at Small Angles of Attack

Due to forces which may arise from causes such as wind gusts, off-center thrust, misaligned fins, or staging transients, a model rocket may assume an angle of attack α to the instantaneous

velocity vector, as seen in Figure 37. If the vehicle is aerodynamically stable the angle is usually quite small and quickly reduced by the restoring moment and damping moment characteristic of a stable model. During the time in which the response to the disturbance produces discernable angles of attack, however, the drag may be increased considerably. A knowledge of the extent to which the drag coefficient of a given rocket increases with angle of attack is therefore of considerable value. In Sections 5.2.1 and 5.2.2 expressions will be presented for estimating the increase in drag coefficient of the body and tailfin assembly alone, respectively, with angle of attack. The magnitude of the corrections required due to fin-body interference will be discussed in 5.2.3, and the overall variation of C_D with angle of attack, as found by experiment and through semiempirical formulae, is analyzed in 5.2.4.

5.2.1 Body Drag at Angle of Attack

The drag of a slender body (such as that of a model rocket) at an angle of attack is closely related to its side force (if any) and drag at zero angle of attack. The total drag^{coefficient} of a model rocket body (nosecone plus cylindrical body tube, but excluding fins, launch lugs, and any other protuberances) at a nonzero angle of attack can be expressed as

$$(136) \quad C_{D_B} = (C_{D_0})_B + C_{D_B}(\alpha)$$

where

$(C_{D_0})_B$ is the body drag^{coefficient} at zero angle of attack.

A detailed method of estimating this quantity is presented in Section 6. A typical value for a slender model rocket is $(C_{D_0})_B = 0.27$ at a Reynolds number of 1×10^6 . This coefficient includes base drag.

$C_{D_B}(\alpha)$ is the drag coefficient of the body due to angle of attack (the notation is read "C_{D_B} as a function of α ", or simply "C_{D_B} of α "), which will be discussed herein.

When a model rocket assumes a very small angle of attack (about 2 degrees or less), the external flow is not significantly disturbed from its behavior at zero incidence. Since it was shown in Section 4 that (for a streamlined nose) this external flow resembles closely that predicted for an inviscid fluid, it is reasonable to attempt the use of potential flow theory for the determination of aerodynamic forces at very small angles of attack -- and, indeed, such analyses have been carried out. The forces produced are a side force, perpendicular to the free-stream flow direction, and a much smaller drag force, parallel to U_∞ .

Potential theory predicts a side force (also referred to as "lift") coefficient which varies linearly with angle of attack. According to Van Dyke (6), the body lift-curve slope at zero incidence is given by

$$(137) \quad \frac{dC_L}{d\alpha} = \frac{2(k_2 - k_1)}{S_m} S_0$$

so that the lift coefficient C_L is given by

$$(138) \quad C_L = \frac{2(k_2 - k_1) S_o}{S_m} \alpha$$

Applying the approximation $\sin(\alpha) \approx \alpha$, valid for small angles, we then have

$$(139) \quad C_{D_B}(\alpha) = \alpha C_L = \frac{2(k_2 - k_1) S_o}{S_m} \alpha$$

where

$(k_2 - k_1)$ is the "apparent mass factor" as determined by Munk, given in Figure 35 as a function of body fineness ratio.

x is the distance from the nosecone tip measured along the longitudinal body axis.

x_0 is the body station where the flow ceases to obey the predictions of potential theory. This location can be found from the expression

$$(140) \quad x_0 = 0.55 x_1 + 0.36 \ell_B$$

x_1 is the body station where the rate of change of cross-sectional area with x (dS_x/dx) first reaches its minimum value.

S_x is the body cross-sectional area at station x .

S_0 is the body cross-sectional area at x_0 .

S_m is the maximum body cross-sectional area.

These terms will be clarified when a numerical example is computed shortly. It should be noted that equation (140)

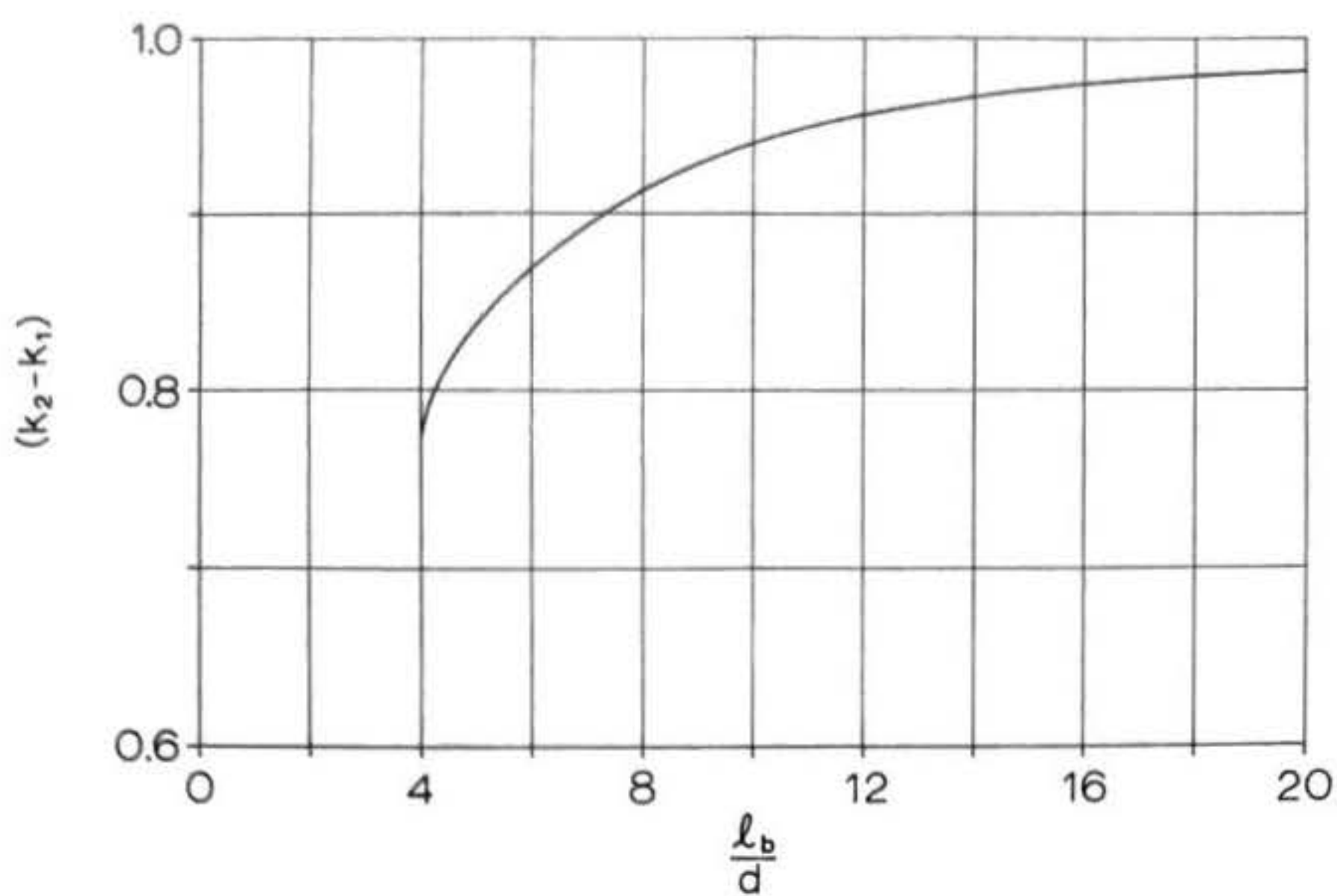


Figure 35: Apparent mass factor ($k_2 - k_1$) as a function of body fineness ratio ($\frac{l_b}{d}$).

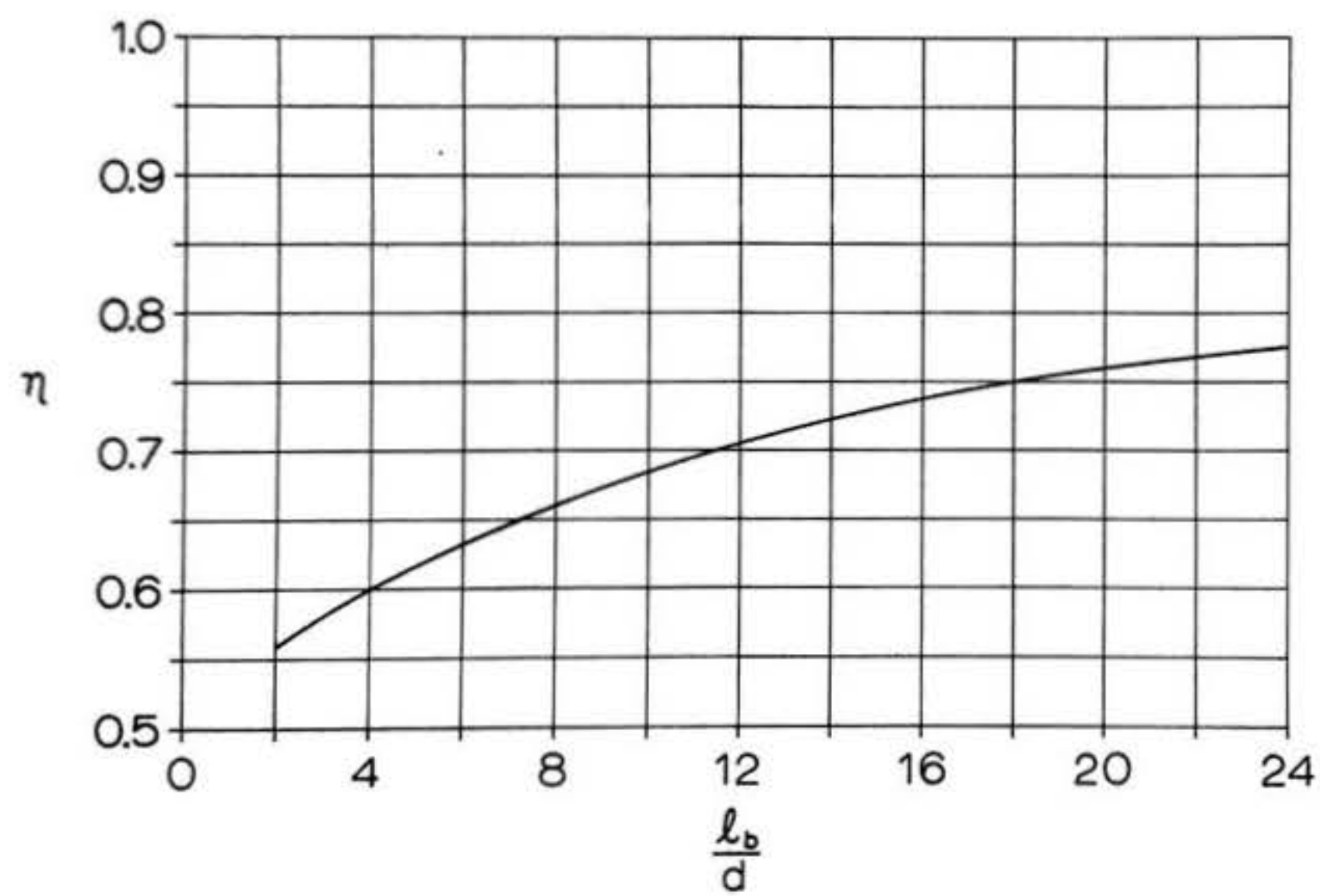


Figure 36: Ratio of the drag coefficient of a circular cylinder of finite length to the drag coefficient of a circular cylinder of infinite length, η , as a function of cylinder fineness ratio ($\frac{l_b}{d}$).

has been constructed by slope and intercept extrapolation from a graph contained in Reference 6, and that the validity of this extrapolation has not as yet been demonstrated.

As the angle of attack increases beyond about two degrees, separation of the boundary layer from the leeward side of the body occurs and potential theory no longer yields an accurate result; the normal (i.e., perpendicular) forces, and hence the lift, increase nonlinearly with angle of attack. The flow in the boundary layer exhibits a component in the circumferential direction due to the increasing magnitude of viscous cross-flow forces. Theories have been developed which take account of these effects by adding to the potential-flow solution of equations (138) and (139) another, viscous term. The method we will present here assumes, as before, that the flow is potential over the forward part of the body and that there is no viscous contribution to drag due solely to the angle of attack. On the aft part of the body, where the flow is assumed entirely viscous, lift and drag arise solely from cross-flow forces. Then, according to Hopkins (6),

$$(141) \quad C_L = \frac{2(k_2 - k_1)S_o}{S_m} \alpha + \frac{2\alpha^2}{S_m} \int_{x_o}^{l_b} \eta r_x C_{Dc} dx$$

$$(142) \quad C_{Dg}(\alpha) = \frac{2(k_2 - k_1)S_o}{S_m} \alpha^2 + \frac{2\alpha^3}{S_m} \int_{x_o}^{l_b} \eta r_x C_{Dc} dx$$

where

η is the ratio of the cross-flow drag on a cylinder of finite length to the cross-flow drag on a cylinder of infinite length, given in Figure 36;

C_{Dc} is the experimental steady-state cross-flow drag coefficient of a circular cylinder of infinite length. C_{Dc} is equal to 1.2 for all practical model rocket problems; and

r_x is the body radius at any station x .

The reader is reminded here that equations (138), (139), (141), and (142) must be applied using α given in radians rather than degrees. In most cases, equation (142) is quite simple to apply to model rockets, as x_0 (the station where the external flow ceases to be potential) usually occurs downstream of the nosecone-body joint. The quantity S_0/S_m thus usually equals 1.0, and the integral, since γ , r_x , and C_{Dc} are all constant along the aft section of a rocket having no shoulder or boattail, involves only an exact differential dx . In such a case,

$$(143) \quad \int_{x_0}^{l_b} \gamma r_x C_{Dc} dx = (l_b - x_0) \gamma r_x C_{Dc}$$

In order to acquire some "feel" for the kind of numerical results one obtains from equation (142), we shall employ the simple, single-stage model rocket configuration shown in Figure 37. Its length, 13 inches (33 cm.) and body diameter, 0.813 inch (2.06 cm.), are identical to the corresponding dimensions of the Aerobee-Hi for which Stine (18) has reported the experimentally-determined variation of the total C_D with α . We do not seek or expect good agreement with Stine's data, as the methods of this and the following sections are approximate, and as the trial rocket is somewhat different from the Aerobee-Hi. Specifically, the trial rocket has 4 fins as opposed to 3 for the Aerobee-Hi,

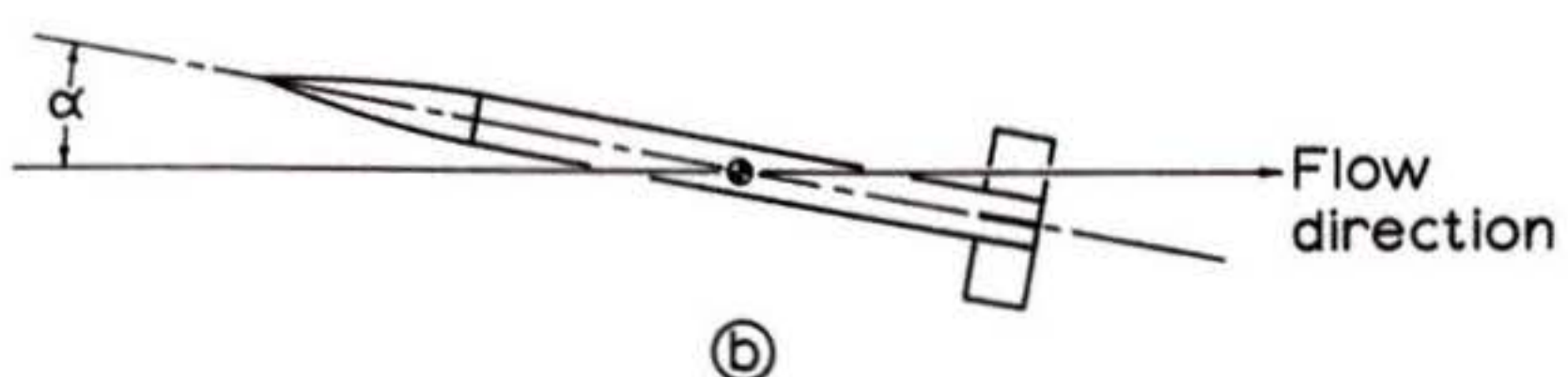
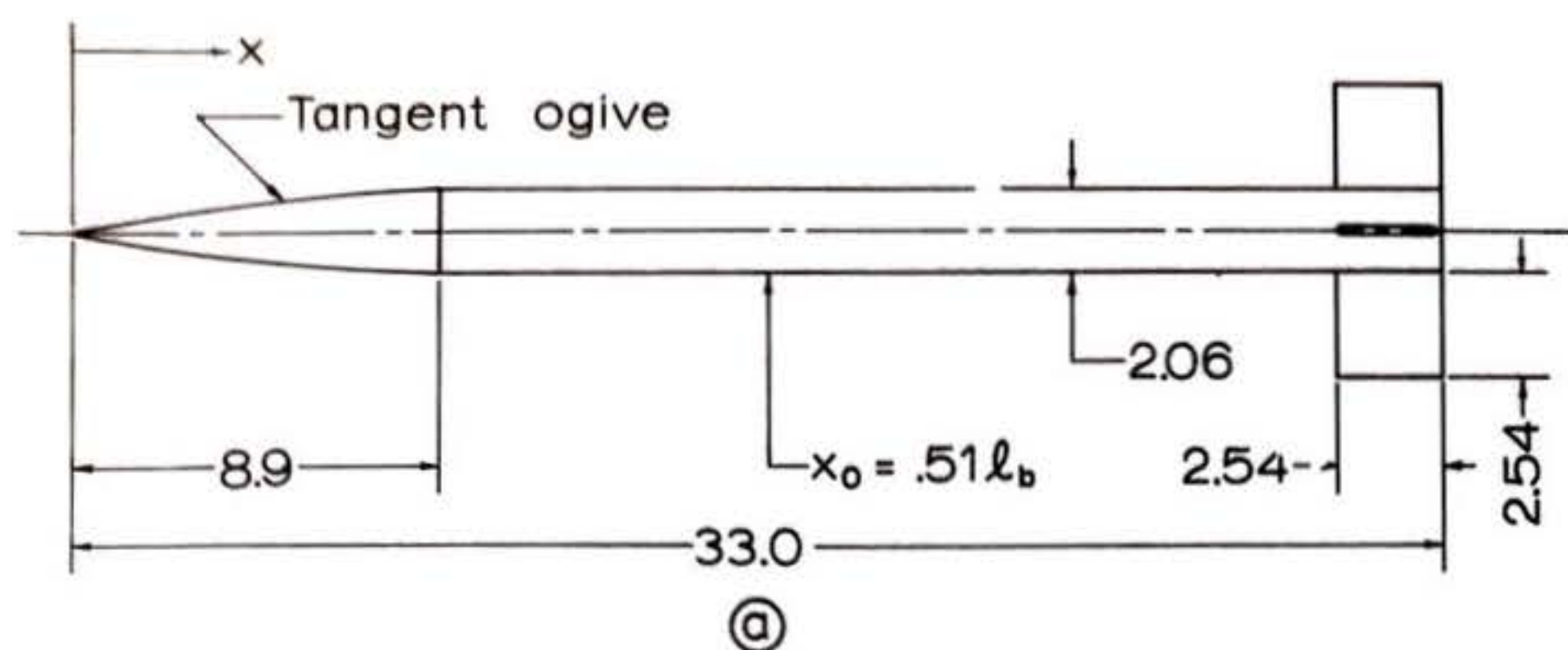


Figure 37: Trial rocket used to compute drag increase due to nonzero angle of attack. All dimensions are given in centimeters.

a different fin shape, no launch lug, and is without the Aerobee's longitudinal fairings. Comparing the experimental results with analytical predictions for a rocket of roughly similar configuration, however, will give us a "feel" for whether our results are, in the colloquialism of engineering, "in the right ball park".

From Figure 37, $l_b/d = 16$, for which Figure 35 yields $(k_2 - k_1) = 0.97$. The quantity dS_x/dx attains its minimum value, zero, at the body-nosecone junction, so $x_1 = 8.9$ cm. We determine x_0 from equation (140) as follows:

$$x_0 = .55(8.9) + .36(33) = 16.8 \text{ cm.}$$

Since x_0 is located on the cylindrical body, $S_0/S_m = 1.0$; the first term in equation (142) then becomes

$$2(k_2 - k_1) \frac{S_0}{S_m} \alpha^2 = 1.94 \alpha^2$$

From Figure 36, $\eta = 0.74$. The body radius r_x is a constant, 1.03 cm., between x_0 and l_b . Hence,

$$\begin{aligned} \frac{2\alpha^3}{S_m} \eta r_x C_{Dc}(l_b - x_0) &= \alpha^3 \left[\frac{2 \times 0.74 \times 1.03 \times 1.2 \times 16.2}{\pi \times (1.03)^2} \right] \\ &= 8.86 \alpha^3 \end{aligned}$$

Finally, we obtain

$$(144) \quad C_{D_B}(\alpha) = 1.94 \alpha^2 + 8.86 \alpha^3$$

This coefficient is based on maximum body frontal area S_m . For $\alpha \leq 0.022$ radian (about 1.25°), the α^2 term is at least ten times greater than the α^3 term. This essentially defines the range of validity for the potential-flow solution. The

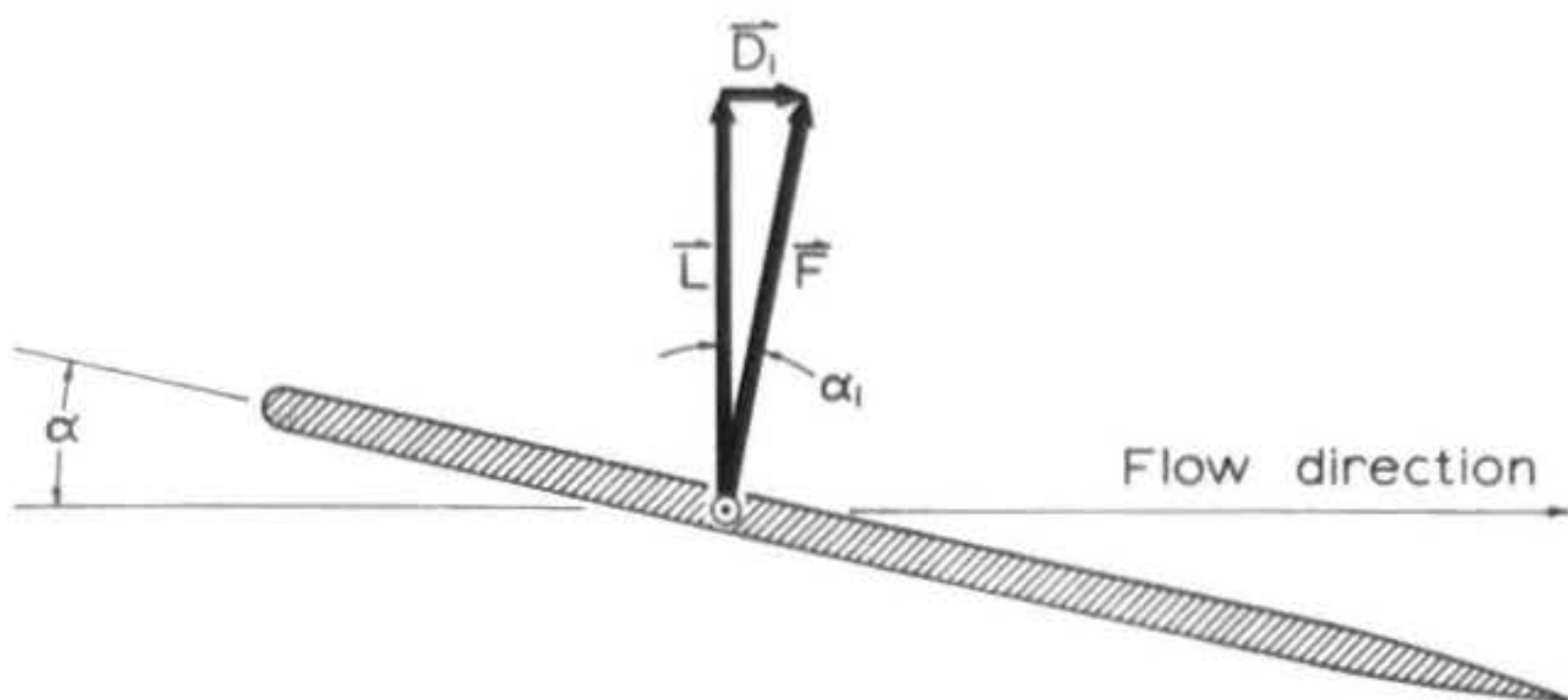
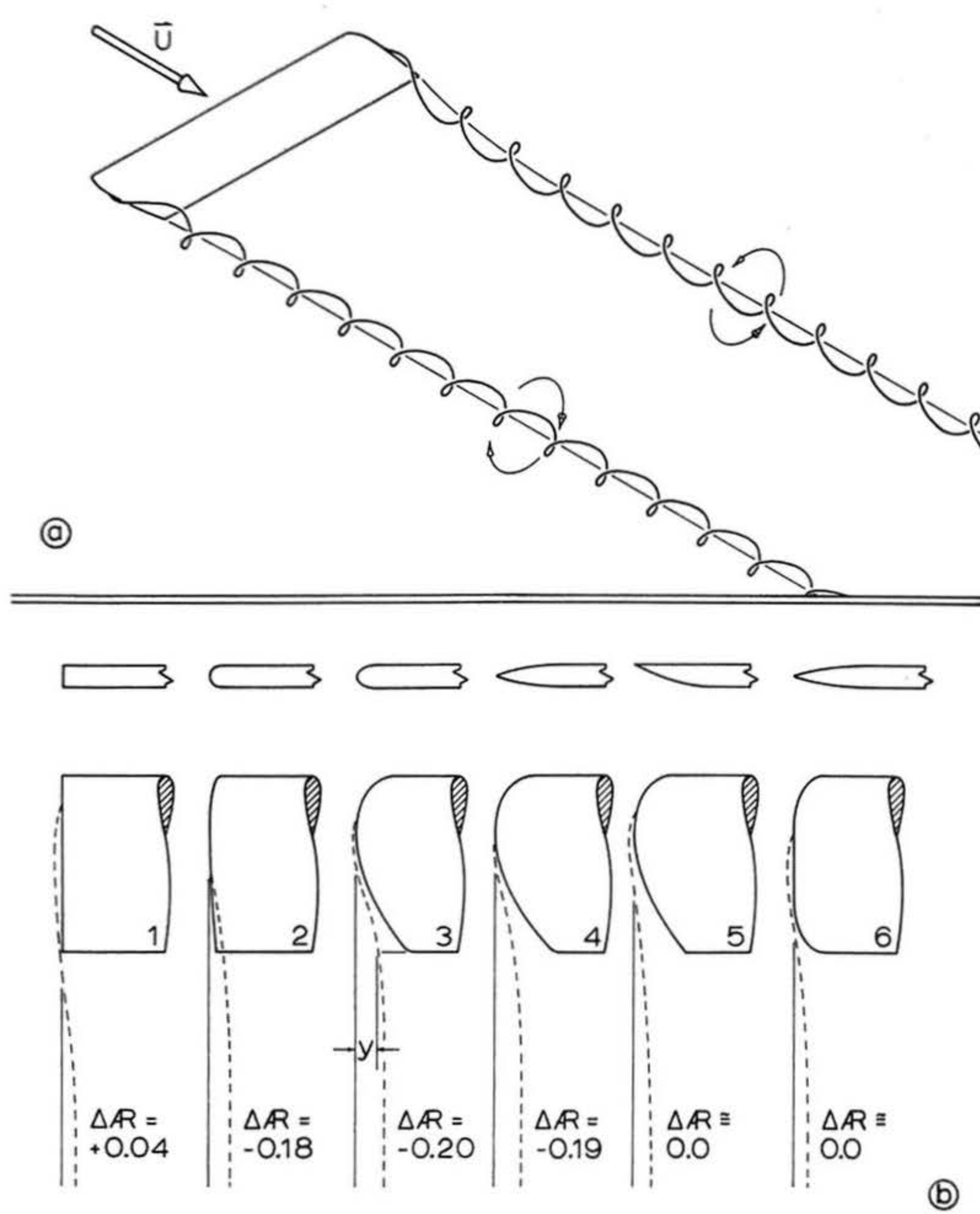


Figure 38: The origin of induced drag. The fin is held at an angle of attack α , causing the force \vec{F} to act through the center of pressure. \vec{F} is tilted back at the angle α_1 ; and is resolved into lift \vec{L} and induced drag \vec{D}_I .

Figure 39: Trailing vortices and effective aspect ratio. An airplane wing or a pair of diametrically opposed rocket fins sheds trailing vortices from its tips (a). As viewed from behind the wing the left vortex rotates clockwise; the right one counterclockwise as shown. The vortices descend after leaving the wing and also "tuck in" slightly, reducing the effective span of the wing and therefore reducing the effective aspect ratio, since the aspect ratio $A\!R$ is defined as the span divided by the average chord. Panel (b) shows the change in effective aspect ratio and vortex core position (dotted line) measured for a number of different tip shapes on wings of $A\!R = 3.0$. Since wings of higher $A\!R$ can generate a given lift at lower angle of attack and lower induced drag than wings of lower $A\!R$, zero or positive values of $\Delta A\!R$ are desirable.



two terms are of equal magnitude at $\alpha = 12.5^\circ$. It should be noted here that $C_{DB}(\alpha)$ is independent of velocity, a result which agrees with the predictions of slender-body theory for incompressible flow.

5.2.2 Fin Drag at Angle of Attack

A model rocket fin, which is here assumed to have a symmetrical, streamlined section profile, will behave like an aircraft wing when it is inclined at an angle to the flow. It will naturally produce a side force, or "lift", as shown in Figure 38 -- which, after all, is why rockets have fins in the first place. Due to the deflection of the flow in the vicinity of the fin, however, the total aerodynamic normal force N will not be perpendicular to the free-stream flow. Instead, it is turned backwards to some angle α_i to the line perpendicular to the free stream, so that it exhibits a drag component. This drag component is known as the induced drag of the fin, and its associated drag coefficient is denoted C_{Df} .

As in the case of the body, the induced drag of a fin is related to the lift force it produces. One cannot, however, obtain an expression for C_{Df} unless he has specific knowledge of the distribution of lift on the fin. We shall assume for the purposes of our numerical example that the following values given by Hoerner (9) for a rectangular wing of aspect ratio $R = \text{span/chord} = 3$ with sharp chordwise edges are valid for the trial rocket:

$$\frac{d\alpha^o}{dC_L} = 18.6$$

$$\frac{dC_D}{dC_L^2} = .123$$

Then for α given in radians,

$$\frac{d\alpha}{dC_L} = 0.32$$

so that

$$C_{D_i} = .123 C_L^2 = .123 \left(\frac{\alpha}{.32}\right)^2 = 1.2 \alpha^2$$

This coefficient, based on fin planform area, can be converted to a coefficient based on maximum body frontal area by multiplying by the factor S_F/S_m . We shall assume the angle of attack to exist entirely about the x-axis (yaw) or y-axis (pitch) of the rocket, so that only two fins are producing lift. Then

$$\frac{S_F}{S_m} = \frac{7.14 \times 2.54}{\pi (1.03)^2} = 5.42$$

$$(145) \quad C_{D_i}' = 5.42 \times 1.2 \alpha^2 = 6.51 \alpha^2$$

You should note here that the fin planform area used includes the imaginary extension of the fins within the body tube, and that "planform" refers to the fact that only the area of one side of the fins is used.

The assumption of square chordwise edges (squared tips) in the above calculations is of some significance, as the shape of the fin tip can affect the value of the induced drag considerably. When a fin is producing lift, it has a lower pressure on its upper, or "suction" side, than on its lower side. This phenomenon is associated with the formation of trailing vortices (see Figure 39a) near the fin tips as the air from below tries to "curl up" around the tips. Depending on the fin tip shape, the distance between the resulting vortex cores may be less than the

actual span of the fins, leading to a reduction in effective span -- and therefore, to a reduction in effective aspect ratio. Figure 39b depicts several possible fin-tip shapes, with their changes in effective aspect ratio ΔR and the location of the vortex core in each case. Those shapes for which ΔR is positive or zero are most desirable, since they produce low induced drag. Of the shapes shown, this category would include numbers 1, 5, and 6. One shape not shown, but popular among designers of high-performance model rockets, is the elliptical fin. During the 1930's it was shown mathematically that, for airplane wings of moderate aspect ratio and without twist ("washin" or "washout" at the tips), an elliptical planform gives the least induced drag for a given lift. Elliptical or near-elliptical wing planforms were subsequently incorporated into several fighter planes of the World War II era, most famous among them being the Supermarine Spitfire of the English Royal Air Force. It is not known for certain whether the elliptical planform retains its advantage in the presence of a body tube of diameter commensurate with the fin span, and in fact the testing of model rocket fin planform shapes for induced drag is currently a pressing need which, it is hoped, advanced hobbyists will shortly fulfil. Nevertheless, the elliptical planform is currently preferred by a number of successful competition modelers.

5.2.3 Fin-Body Interference Drag at Angle of Attack

The subject of interference drag at angle of attack is prohibitively difficult to handle theoretically. Consequently, we shall rely entirely upon semiempirical determinations here.

The term "interference drag" refers to the increment in drag a complete configuration possesses over the sum of the drags of its separated, component parts. At the fin-body joints there is a joining and thickening of boundary layers, leading to increased drag in this region. Separation is a distinct possibility at such joints, and Stine (18) suggests the elimination of sharp corners by glue fillets to minimize this danger. Hoerner (9) has reported data indicating that interference drag is minimized when the fillet radius is between 4% and 8% of the fin chord at the root.

Reference (6) gives the following semiempirical expression for interference drag coefficient at angle of attack:

$$(146) \quad \Delta C_{D_i} = [K_{F(B)} + K_{B(F)} - 1] \frac{dC_L}{d\alpha} \frac{S_e}{S_m} \alpha^2$$

where

$$K_{F(B)} = \frac{\text{fin lift in the presence of the body}}{\text{fin lift alone}};$$

$$K_{B(F)} = \frac{\text{body lift in the presence of the fins}}{\text{fin lift alone}};$$

$\frac{dC_L}{d\alpha}$ is the lift-curve slope of the fin at $\alpha = 0$; and

S_e is the exposed fin planform area.

The functions $K_{F(B)}$ and $K_{B(F)}$ are both given in Figure 40.

We can now determine ΔC_{D_i} for our trial rocket. The total fin span b is 7.14 cm. and the body diameter d is 2.06 cm., so $d/b = .289$. This gives, from Figure 40, $K_{B(F)} = 0.44$ and $K_{F(B)} = 1.25$. Since only two fins are assumed to be producing

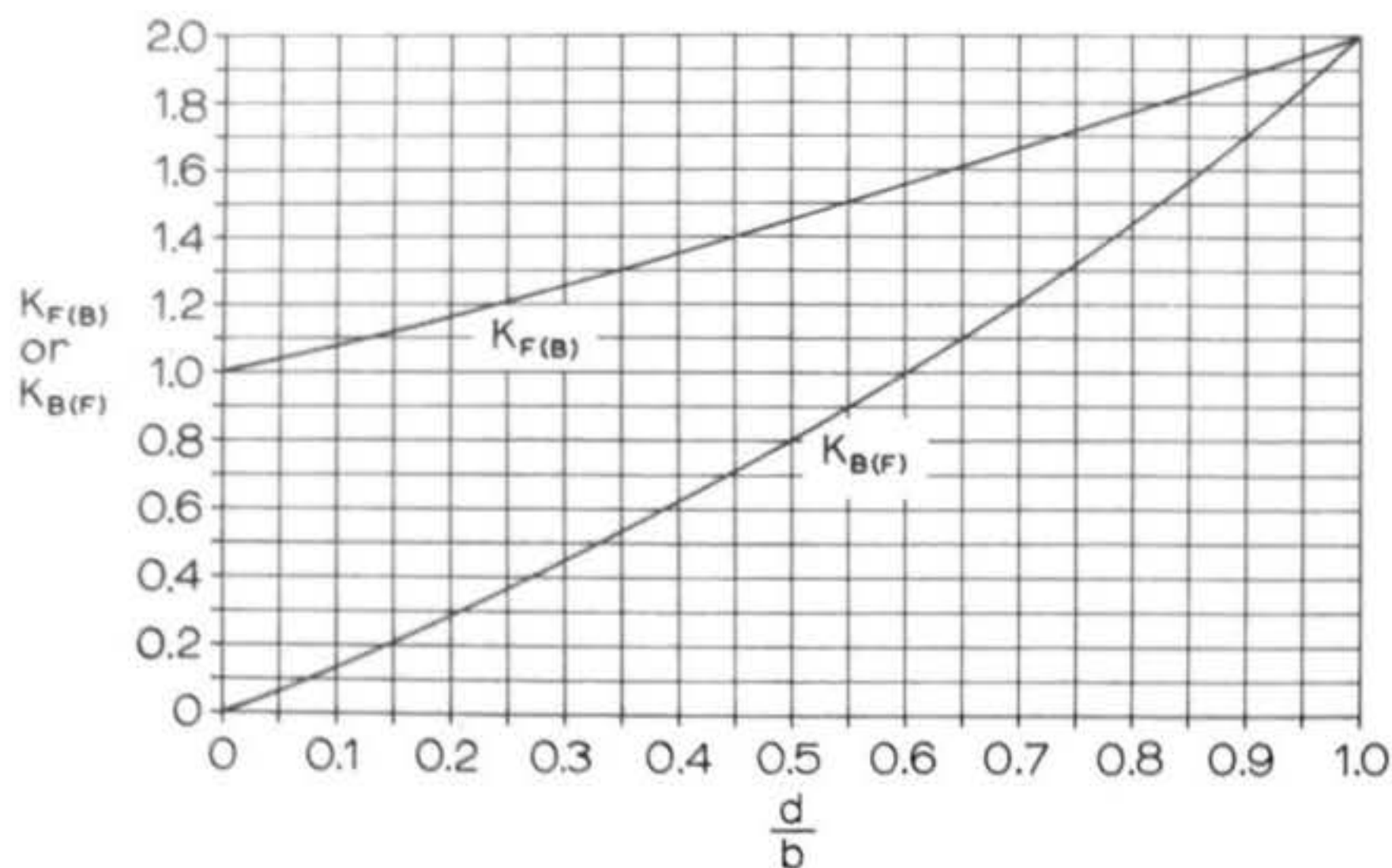


Figure 40: Fin-body interference coefficients for flight at nonzero angle of attack. d is the diameter of the body tube, while b is the span of a diametrically opposed pair of fins.

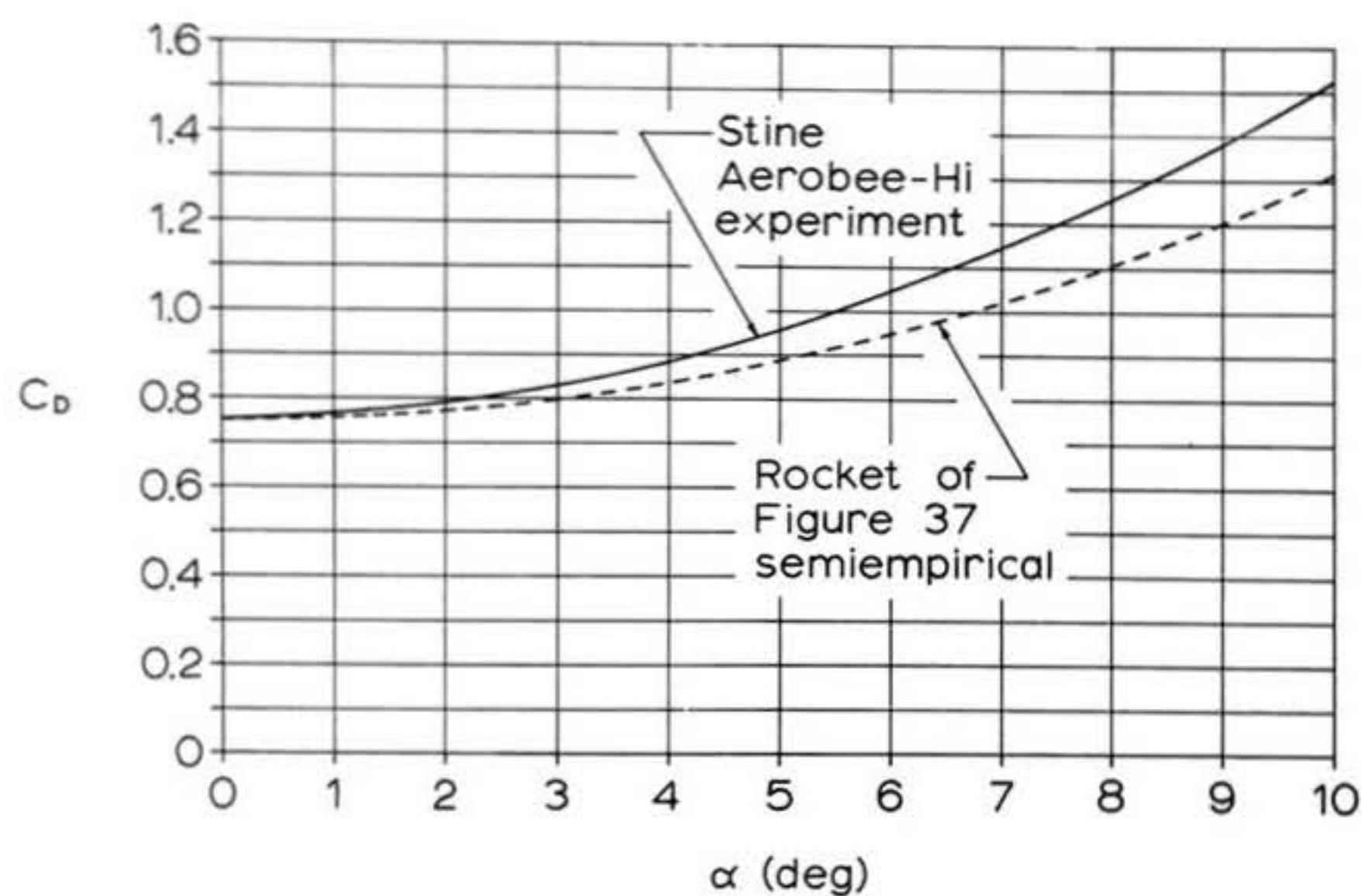


Figure 41: Increase in drag coefficient with angle of attack for the trial rocket of Figure 37 (semiempirical) and for a scale model Aerobee-Hi tested by G. Harry Stine, assuming the same drag coefficient for both rockets at zero angle of attack.

lift, $S_e = 12.95 \text{ cm.}^2$, and

$$S_m = \pi r^2 = 3.33 \text{ cm.}^2$$

$$\frac{dC_L}{d\alpha} = \frac{1}{.32} = 3.12$$

so that

$$(147) \quad \Delta C_{D_i} = (.44 + 1.25 - 1) 3.12 \frac{12.95}{3.33} \alpha^2 = 8.38 \alpha^2$$

coefficient

The interference drag ΔC_{D_i} due to angle of attack is thus of considerable magnitude; in fact, it is larger than the sum of $C_{DB}(\alpha)$ and C_{D1}' , as given by equations (144) and (145).

5.2.4 Total Drag Increase at Angle of Attack

If we now combine the results of 5.2.1, 5.2.2, and 5.2.3, we obtain an expression for the total drag increment $C_D(\alpha)$ due to angle of attack:

$$(148) \quad C_D(\alpha) = C_{Dg}(\alpha) + C_{D1}' + \Delta C_{D_i}$$

For our trial rocket, the result is

$$(149) \quad C_D(\alpha) = 16.83 \alpha^2 + 8.9 \alpha^3$$

This function, along with its constituent functions, is tabulated in Table 4 and is plotted in Figure 41. In order to compare equation (149) with the experimental data for G. Harry Stine's Aerobee-Hi, the trial rocket has been assumed to have the same zero-lift drag coefficient as the Aerobee-Hi (about 0.75). The trial vehicle would probably have a much lower zero-lift drag coefficient in actuality (unless its surface were very rough), but the assumption of equal zero-lift drag for the two vehicles makes it more convenient to compare their drag increments due to angle of attack. The agreement between the curves for the

TABLE 4

Angle of attack α (deg)	Angle of attack α (rad)	Body drag coefficient due to α :	Fin drag coefficient due to α :
		$C_{DB}(\alpha)$	C_{D1}
		$1.94\alpha^2 + 8.86\alpha^3$	$6.51\alpha^2$
0.5	.00873	.000	.000
1.0	.0175	.001	.002
2.0	.0349	.003	.008
3.0	.0524	.007	.018
4.0	.0698	.012	.031
5.0	.0873	.021	.050
6.0	.1047	.032	.072
7.0	.1222	.045	.097
8.0	.1396	.062	.127
9.0	.1571	.082	.161
10.0	.1745	.106	.198

Angle of attack α (deg)	Angle of attack α (rad)	Fin-body interference drag coefficient due to α :	Total drag coefficient due to α :
		ΔC_{Di}	$C_D(\alpha)$
		$8.38\alpha^2$	$16.83\alpha^2 + 8.9\alpha^3$
0.5	.00873	.001	.001
1.0	.0175	.003	.005
2.0	.0349	.010	.021
3.0	.0524	.023	.048
4.0	.0698	.041	.084
5.0	.0873	.063	.136
6.0	.1047	.092	.196
7.0	.1222	.125	.267
8.0	.1396	.163	.352
9.0	.1571	.208	.451
10.0	.1745	.255	.559

Table 4: Increase in drag coefficient with angle of attack for the trial rocket of Figure 37.

two vehicles is surprisingly close, considering the physical differences between the rockets and the simplifying assumptions made in the derivation of equation (149) -- a result which tends to confirm the validity of the semiempirical approach. It is, however, hoped that experiments will be performed in the near future on rockets similar to that of Figure 37 (with and without launch lug), to determine with greater precision the accuracy of this computational method.

One fact is clearly established in Figure 41: that the increase in drag at small angles of attack can be a sizeable portion of the zero-lift drag. For the Aerobee-Hi model, the drag coefficient is doubled at an incidence of ten degrees. Clearly, then, for maximum altitude performance, it is desirable to design a rocket such that all oscillations resulting from in-flight disturbances are damped out as quickly as possible.

We observe that equation (149) is dominated by the α^2 term over the entire range of angles of attack of interest in model rocketry; up to $\alpha = 5^\circ$, the α^3 term may be neglected with less than 5% error in the final result. With respect to determining the coefficient ϵ introduced in Chapter 1 and used in Chapter 4 to compute the effect of dynamic oscillations on altitude capability, however, the modeler will generally want to be conservative. A conservative determination of ϵ may be made by finding the value of α at which C_D is doubled over its zero-lift value, according to equation (148), and then determining the value of ϵ in the approximate function

$$(150) \quad C_D(\alpha) \cong \frac{2\epsilon}{\rho S_m} \alpha^2$$

such that the drag is again doubled at this same value of α . In the case of our trial rocket, the drag coefficient will be doubled over its zero lift value when $C_D(\alpha) = 0.75$. This occurs for $\alpha = 0.201$ radian, or about 11.5° . From equation (150) we find that the value of $\frac{2\epsilon}{\rho S_m}$ required to produce a $C_D(\alpha)$ of 0.75 at $\alpha = 0.201$ radian is 18.52, and this would determine the value of ϵ used in determining oscillation effects on altitude performance by the methods presented in Chapter 4. Equation (150) is conservative (that is, it slightly overestimates the drag) over the range of angles of attack between zero and that at which the drag is doubled -- and for the average model rocket, the α at which C_D is doubled marks the upper limit of the range of angles of attack of interest.

5.3 Drag Due to Rotation

A model rocket, rotating about its longitudinal -- or roll -- axis in flight, will experience an increase in drag due to the thickening of the boundary layer resulting from the circumferential velocity of the body tube surface. We shall denote this circumferential velocity component by u . This thickening of the boundary layer could conceivably cause separation on the forebody and fins, and an increased dead-air volume aft of the base, if u is sufficiently large.

The drag increase due to rotation may be estimated by examining Figure 42. The circumferential velocity is given by

$$(151) \quad u = \pi d n$$

where d is the diameter of the body and n is the number of

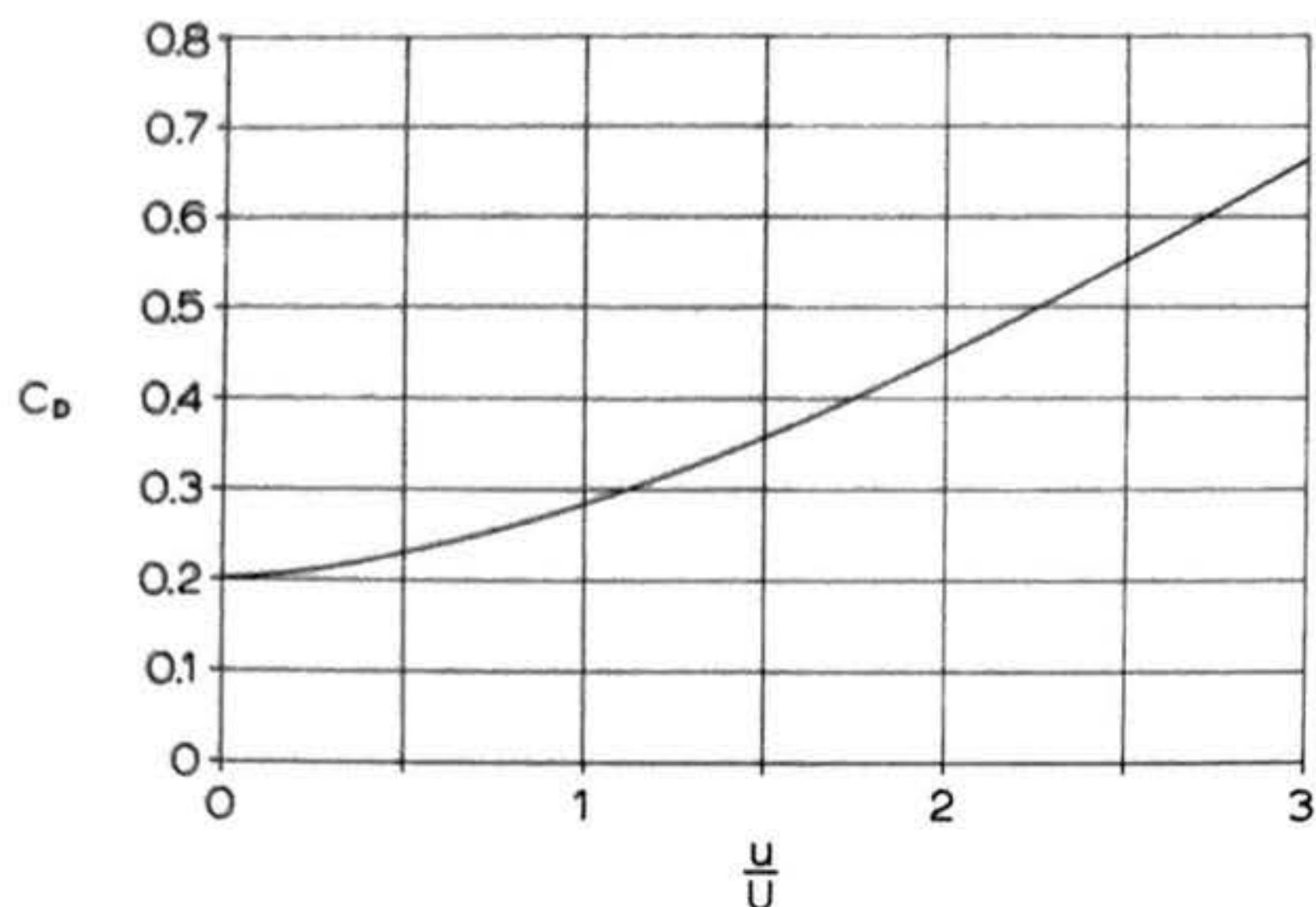


Figure 42: Increase in the drag coefficient of a finless projectile due to rotation (spinning) about the longitudinal axis. u is the tangential velocity of the projectile's surface due to the spin; U is the longitudinal free-stream velocity.

revolutions per second. If we assume that the trial rocket of our numerical example (diameter = 2.06 cm.) has been given a roll rate of 100 radians per second (15.9 revolutions/second) at an airspeed of 60 meters (6000 cm.) per second, we obtain

$$\frac{u}{U} = 0.0172$$

The effect of such small ratios of body tube circumferential velocity to vehicle airspeed -- ratios typical of model rockets -- is too small to be read from the curve of Figure 42. One may therefore conclude that, as far as the finless body is concerned, rotation does not exert a significant influence on model rocket drag.

The mechanism for inducing rotation in a model rocket purposefully is usually fin geometry -- that is, by canting the fins, giving them an asymmetrical section profile, or adding spinners. Of these three techniques, fin canting is the most commonly used. Since canting merely creates a permanent, artificially-induced angle of attack for the fins, the drag due to fin cant can be estimated using the methods of Chapter 2 and the results of Section 5.2.2 of the present chapter. According to equations (90), (115), (116), and (117) of Chapter 2, canting the fins of our trial rocket will give it a roll rate determined by

$$(152) \quad \omega_z = .1672 U \theta$$

For $\omega_z = 100$ radians/second at $U = 6000$ cm./sec., a fin cant angle θ almost exactly 0.1 radian is required (0.1 radian = 5.73°). Now the effective angle of attack of the fins is always less

than the cant angle, since the airflow itself is "canted" as seen by the rotating fins. To be more precise, the angle of attack varies with radius from the rocket's centerline according to

$$(153) \quad \alpha(r) = \theta - \frac{\omega_z r}{U}$$

For the simple, rectangular fins of our trial rocket, the average effective angle of attack can be used to determine the induced drag due to fin cant. The value of $\alpha(r)$ at the fin root is 0.0828, while the value at the tip is 0.0405. Since $\alpha(r)$ varies linearly with radial distance from the centerline, the average effective angle of attack $\bar{\alpha}$ is just

$$\bar{\alpha} = \frac{.0828 + .0405}{2} = .0617$$

In equation (145) the induced drag of two of the trial rocket's fins was found to be $6.24\alpha^2$. In the case of canted fins, all four fins are at the angle of attack $\bar{\alpha}$; equation (145) must therefore be doubled to give

$$(154) \quad (C_{D_i'})_{\text{cant}} \approx 12.5 \bar{\alpha}^2$$

For the computed $\bar{\alpha}$ of 0.0617, $(C_{D_i'})_c = .0475$. If the rocket's zero-incidence drag coefficient is .75 without fin cant, this means a 6.34% increase in C_{D_0} . If a spin rate double that used in the above calculations were desired, it would be necessary to incur four times this drag penalty, or an increase of 25.4% in C_{D_0} . These figures, together with the realization that they probably represent minimum values for the drag increase due to fin cant -- they do not account for increased fin-body interference --

indicate that, while the effects of rotation themselves may not be significant, the effects of the mechanism by which rotation is induced are considerable. Furthermore, there is an increasing danger of separation in the vicinity of the fin leading edges as the angle of cant is increased. Such separation could result in a gross magnification of pressure drag. While the angle of cant at which such phenomena become significant has not as yet been established with precision, it has been generally accepted for a number of years that cant angles greater than 15° produce reductions in performance so severe as to be detectable with the naked eye.

5.4 Drag Due to Surface Roughness in Turbulent Flow

In Section 3.5 we examined the critical height of roughness elements necessary to induce premature transition in the boundary layer from laminar to turbulent flow. Within the turbulent boundary layer which is prevalent over most of a model rocket at higher Reynolds numbers, roughness can affect the drag in another manner: if the individual roughness particles protrude above the thin laminar sublayer, they will have a viscous drag of their own. The turbulent skin-friction coefficient derived in Section 3 (equation 86) applies only to "hydraulically smooth" surfaces; that is, surfaces on which the grain size k of roughness particles is less than the thickness of the laminar sublayer.

The admissible height k_{adm} for roughness particles is defined as the maximum height of the particles which gives no increase in the drag compared with a smooth wall. A simple, conservative formula for determining k_{adm} for a flat plate is (15):

$$(155) \quad k_{adm} \leq 100 \frac{\nu}{U_\infty}$$

This relationship is accurate for Reynolds numbers below about 1×10^6 . It does not take into account the fact that the boundary-layer thickness increases with distance from the leading edge, and hence that k_{adm} is smaller upstream than downstream. Its use is justified, however, because it provides values of k_{adm} which are generally smaller than those obtained from the more precise expression (15)

$$(156) \quad k_{adm} < \frac{7 \nu}{U_\infty \sqrt{C_{fx}}}$$

where C_{fx} is the local skin-friction coefficient, given by $\frac{2 \tau_0}{\rho U_\infty^2}$. Equation (155) may thus be used for the entire range of model rocket Reynolds numbers without fear of obtaining values of k_{adm} which are too large.

If we let $U = 60$ meters/second, for instance, and $\nu = 1.495 \times 10^{-5}$ meter²/second, equation (155) yields

$$k_{adm} \leq 2.48 \times 10^{-5} \text{ meter} = 2.48 \times 10^{-3} \text{ cm.}$$

This result applies specifically to sand grains, for which equation (155) was empirically determined, but it can be used as an approximate guide for other forms of roughness. Hence, at a velocity typical of model rocket flight, the surface of the model downstream of the transition point may be regarded as hydraulically smooth if the size of distributed roughness grains does not exceed about 0.0025 cm. If this condition is satisfied, the smooth turbulent skin-friction coefficient of Section 3 may be used in calculations. It should be noted that the calculated

value of k_{adm} is considerably less than the roughness height required to induce premature transition as determined in Section 3.5. If the criterion of this section is satisfied, therefore, transition will not be induced prematurely.

Table 5 provides information on grain sizes in microns ($1 \text{ micron} = 1 \times 10^{-6} \text{ meter} = 1 \times 10^{-4} \text{ cm.}$) for various surfaces. It indicates that the finish on a model rocket should be about as smooth as that of paint on mass-produced aircraft, or better. Note that poorly-sprayed paint has a grain size of about 200 microns -- eight times our calculated k_{adm} . A rocket with such a poor finish will have a considerably higher skin-friction coefficient than one that is sufficiently well painted to be hydraulically smooth. The skin-friction coefficient of a surface having roughness elements sufficiently large that it cannot be considered hydraulically smooth may be found from the semi-empirical formula (15)

$$(157) \quad C_f = (1.89 + 1.62 \log \frac{l_b}{k})^{-2.5}$$

which is valid for values of $\frac{l_b}{k}$ between 10^2 and 10^6 , where l_b denotes the length of the body (or fin, as the case may be), and the notation "log" denotes the logarithm to the base 10. According to equation (157), a body 30 cm. in length having roughness particles of $k = 0.02 \text{ cm.}$ will exhibit a friction drag coefficient of

$$C_f = 7.63 \times 10^{-3}$$

The corresponding value for a hydraulically smooth body in turbulent flow is 4.5×10^{-3} , so in this instance roughness

TABLE 5

Type of surface	Approximate grain size k in microns
surfaces like that of a "mirror"	0
surface of average glass	0.1
finished and polished surfaces	0.5
aircraft-type sheet-metal surfaces	2
optimum paint-sprayed surfaces	5
planed wooden boards	15
paint in aircraft-mass production	20
bare steel plating	50
smooth cement surface	50
surface with asphalt-type coating	100
dip-galvanized metal surface	150
incorrectly sprayed aircraft paint	200
natural surface of cast iron	250
raw wooden boards	500
average concrete surface	1000

Table 5: Size of surface roughness elements for various surfaces.

increases the friction drag by about 70%.

Equation (157) applies only to surfaces which are completely rough; i.e., those for which the height of the roughness elements is everywhere greater than the thickness of the laminar sublayer. The degree of roughness of a given surface thus depends upon k/δ , the ratio of grain size to boundary-layer thickness. Since δ varies with Reynolds number, a given surface may appear rough or smooth, depending on the value of the free-stream velocity. If, for example, we examine a turbulent boundary layer over a surface at relatively low Reynolds numbers (around 5×10^5), the roughness elements may be completely submerged in the laminar sublayer, making the surface appear hydraulically smooth. As the velocity (and therefore the Reynolds number) increases, the boundary layer becomes thinner, and the roughness elements begin to protrude from the sublayer. This process is initiated near the nose, or leading edge, where the boundary layer is thinnest, and progresses downstream with increasing R . When a surface is in this "transition" state between a completely smooth and a completely rough appearance, its skin-friction coefficient will have a value intermediate between those determined from equations (86) and (157). Note that this process proceeds along a body in a direction opposite to that of laminar-to-turbulent boundary-layer transition, as described in Section 3.5.1.

Two final observations can be made regarding drag due to roughness. First, since equation (157) is independent of velocity, C_f is a constant for any given ratio $\frac{\ell_b}{k}$. In accordance with equation (18), it may then be concluded that

hydraulically rough surfaces obey the quadratic drag law exactly. Furthermore, equation (155) for k_{adm} is independent of body length; hence any two rockets travelling at the same velocity under identical atmospheric conditions have identical values of k_{adm} . The maximum velocity attained by a rocket determines the minimum value of k_{adm} . If this minimum grain size is not exceeded anywhere on the surface, the rocket may be regarded as hydraulically smooth throughout its flight, and the friction drag equations of Section 3 are applicable to the calculation of its drag coefficient.

6. Calculation of the Zero-Lift Drag of Simple Model Rockets

6.1 The United States Air Force Stability and Control Datcom Method

In the previous sections we have analyzed in detail the origin of drag forces on model rockets. Information of this nature is of interest in the design stage, when it is desired to minimize the drag on a vehicle whose size and shape are known to be subject to certain constraints arising from the purpose for which it is built, but whose precise, final form is yet to be determined. After the construction of the rocket is complete and it stands ready to launch, however, the modeler invariably finds himself asking, "Just how high will it go?". To answer this question one requires a knowledge of the overall drag coefficient of the model, which can generally be obtained in actual cases only through accurate wind-tunnel or drop tests. Since the facilities required for such tests are not available to the majority of model rocketeers, most of us must be content

with calculating fairly accurate C_D values from available semiempirical expressions.

This section presents and discusses one such semiempirical method, derived from the United States Air Force Stability and Control Datcom ("Datcom" standing for Data Compendium). The existence of this method was first brought to the author's attention through a short paper entitled "A Critical Examination of Model Rocket Drag for Use with Maximum Altitude Performance Charts", a work prepared by Dr. Gerald M. Gregorek of Ohio State University for presentation at the Eighth National Model Rocket Championships in 1966, and which subsequently received limited distribution to certain interested parties and local sections of the National Association of Rocketry. Through his compilation of this work, Dr. Gregorek deserves full credit for being the first to apply the Datcom method to model rockets.

The USAF Stability and Control Datcom is a large compilation of semiempirical expressions for evaluating the aerodynamic forces acting on aircraft and missiles in subsonic, supersonic, and hypersonic flight regimes. It is updated periodically to include new developments in the literature of aerodynamics. The formulae presented here are taken from the most recent edition available to the author at the time of writing (6). According to the Datcom, the zero-lift drag coefficient of a fin-body combination may be represented as

$$(158) \quad (C_{D_0})_{FB} = (C_{D_0})_F \frac{S_F}{S_m} + (C_{D_0})_B$$

where

S_F is the total planform area of all the fins;

S_m is the maximum body cross-sectional area;

$(C_{D_0})_F$ is the zero-lift drag coefficient of the fins as derived in Section 3.6, equation (108):

$$(159) \quad (C_{D_0})_F = 2(C_f)_F \left(1 + 2 \frac{t}{c} \right) \quad ; \text{ and}$$

$(C_{D_0})_B$ is the zero-lift drag coefficient of the body, which is further subdivided into the forebody drag and the base drag:

$$(160) \quad (C_{D_0})_B = (C_{D_f})_b + C_{D_b}$$

where

$$(161) \quad (C_{D_f})_b = (C_f)_b \left[1 + \frac{60}{(\ell_b/d_m)^3} + 0.0025 \left(\frac{\ell_b}{d_m} \right) \right] \frac{S_s}{S_m}$$

$$(162) \quad C_{D_b} = \frac{0.029 (d_b/d_m)^3}{\sqrt{(C_{D_f})_b}}$$

$(C_{D_0})_{FB}$ is based on the maximum body frontal area S_m . Figure 43 explains most of the notation pertaining to rocket geometry used in equations (159) through (162). Additional explanatory discussion may be found in Sections 6.1.1 and 6.1.2, where we shall examine in detail the calculation of $(C_{D_0})_F$ and $(C_{D_0})_B$, respectively.

6.1.1 Zero-Lift Drag Coefficient of the Fins

The Datcom expression for the drag coefficient of the fins at zero angle of attack is equation (159), which we repeat here for convenience:

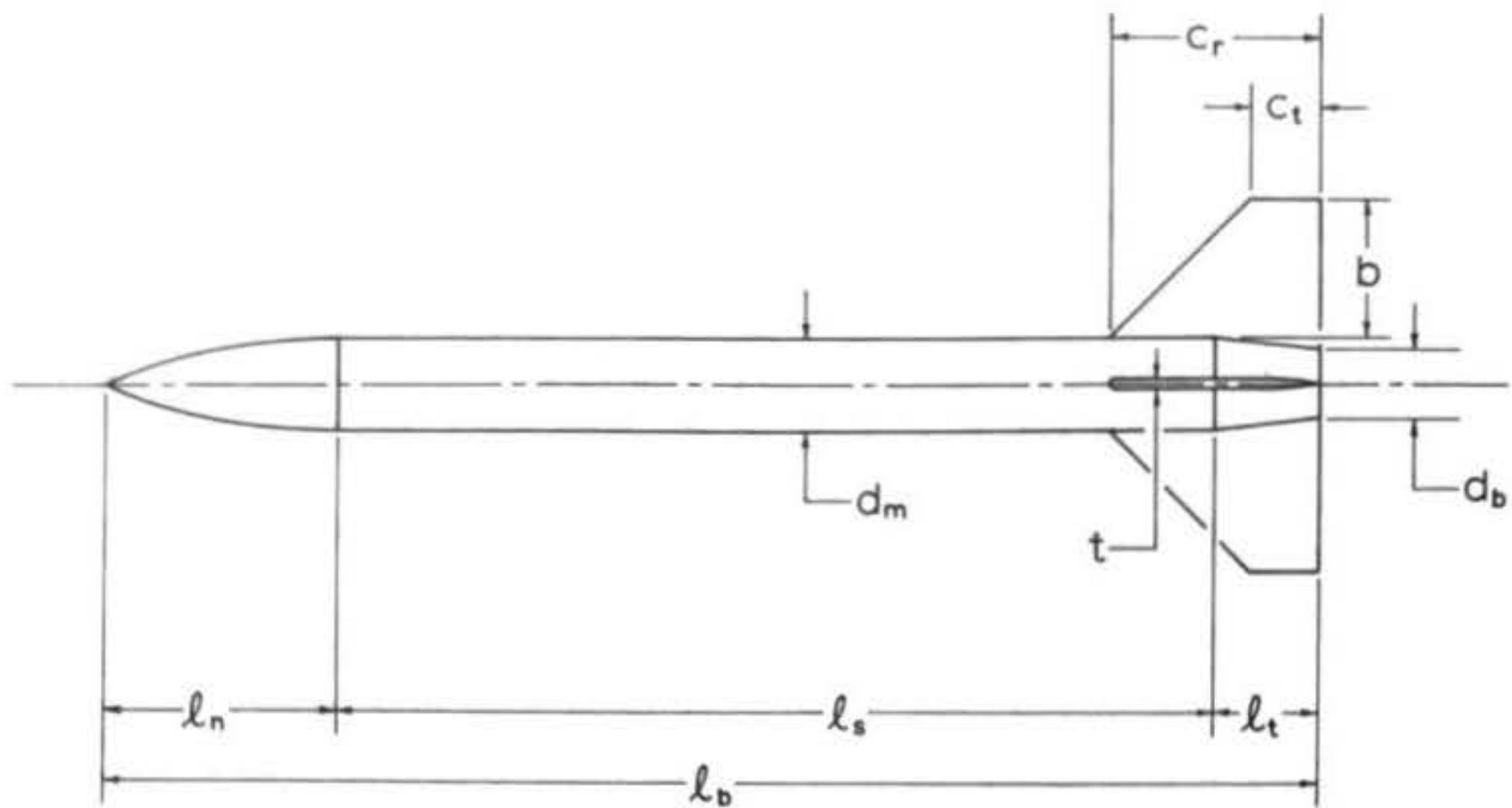


Figure 43: Notation used in the Datcom method for computing the drag of simple model rockets at zero angle of attack. Note that the variable b as used here refers to the span of a single fin, from root to tip; elsewhere in this chapter it usually refers to the span of a diametrically opposed pair of fins, tip to tip.

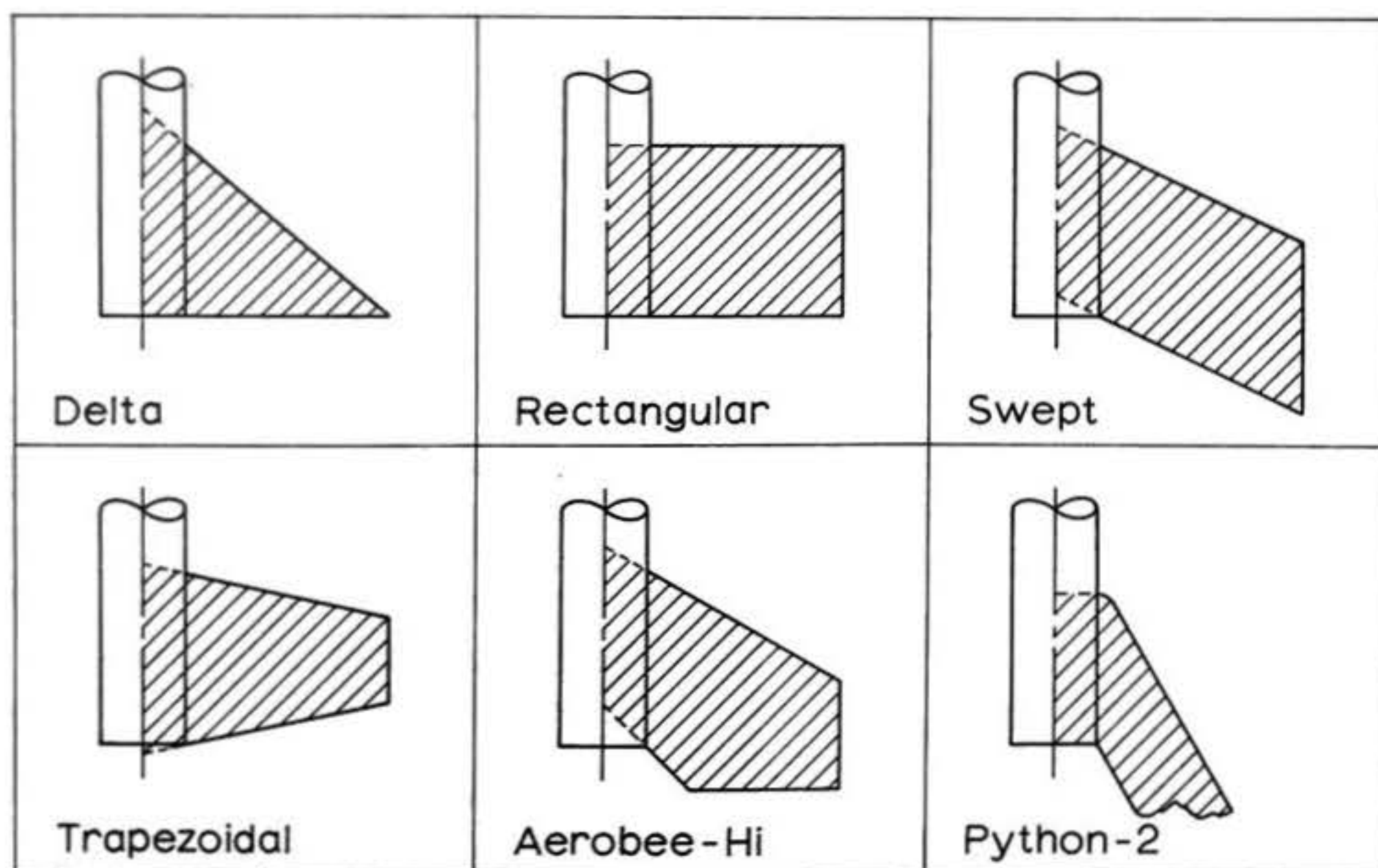


Figure 44: Obtaining the gross planform area of various fin shapes (shapes after G. Harry Stine).

$$(C_{D_0})_F = 2(C_f)_F \left(1 + 2\frac{t}{c}\right) \frac{S_F}{S_m}$$

where

t/c is the average streamwise thickness ratio of the fins;

$(C_f)_F$ is the flat-plate skin-friction coefficient of the fins;

S_F is the total fin planform area; and

S_m is the maximum body frontal, or cross-sectional, area.

In the interest of clarity, certain of these terms are explained in greater detail below:

For the purpose of these calculations, the planform area of a fin is considered to be the sum of its actual, exposed planform area and the planform area of its imaginary extension into the body tube. Figure 44 illustrates the procedure for obtaining this "gross area", denoted by $\tilde{\sigma}_F$, for a number of possible fin planforms. For most fins, $\tilde{\sigma}_F$ can be obtained by simply extending the leading and trailing edges until they intersect the body longitudinal axis. For shapes like that of the Python-2 (18), where the trailing edge intersects the body tube at a very shallow angle, it is better to extend straight lines from the leading and trailing edges of the root chord, parallel to the base, until they intersect the body centerline as shown. For a rocket with n identical fins, the total fin planform area S_F is equal to $n\tilde{\sigma}_F$.

Because S_F is greater than the exposed fin area S_E , we expect $(C_{D_0})_F$ as given by equation (159) to be an overestimate

of the true skin-friction drag. The difference between the overestimated and true values represents an approximation to the interference drag resulting from the juncture of the body and fins. C_{DI} , the interference drag coefficient, is then given by

$$(163) \quad C_{DI} = 2(C_f)_F \left(1 + 2 \frac{t}{c}\right) \frac{S_F - S_E}{S_m}$$

In the Datcom method, therefore, the skin-friction drag of the imaginary fin area within the body tube is taken to be the interference drag at zero angle of attack. It is apparent from our rather arbitrary means of determining the "hidden" fin area that we cannot expect any great precision in such a determination of C_{DI} . This is the best practical method currently available, however, since C_{DI} is an extremely difficult quantity to evaluate, whether theoretically or experimentally.

The thickness t of the fin can be represented for most purposes by the thickness of the original material from which the fin was constructed. Painstaking micrometer readings may look scientific, but they cannot improve the accuracy of an approximate method. The chord c used in these calculations is the average chord of the fin. For simple planforms, the expression

$$(164) \quad c = \frac{C_{root} + C_{tip}}{2}$$

can be used, while for more complicated shapes the determination can be made according to

$$(165) \quad c = \frac{\sigma_E}{b}$$

where σ_E denotes the exposed planform area of one fin and b is the fin span, or radial distance from root to tip.

The skin-friction coefficient of the fins, $(C_f)_F$, can be determined from the results of the preceding sections. Equation (63) may be used if the flow is completely laminar, while equation (101) applies in cases where transition occurs. Alternatively, the designer may choose to read the skin-friction coefficient from Figure 22 to save the work of making a calculation. The Reynolds number used in the determination of $(C_f)_F$ is based on the average fin chord: $R_c = \frac{U_\infty c}{\nu}$. Since the local chord may be considerably larger than this average value at certain locations on the fin, it is possible that transition will occur at lower velocities than predicted on the basis of R_c , and that the skin-friction coefficient will be underestimated when using equations (63) or (101), or Figure 22. Fortunately, the danger of this is not very great, as the flow over the fins is almost entirely laminar throughout the flight for all but a few model rockets, owing to the extremely high airspeeds and large chords necessary to effect transition on a model rocket fin. The implications of this problem will be further explored later on.

Equation (159) is valid for fins without separated flow at the leading or trailing edges; hence it is valid only for streamlined fins. At the time of writing there is no convenient, analytical method for estimating the effects of blunt leading and trailing edges on fin drag. This, however, is not a serious handicap, since no designer careful enough to apply analytical methods to his work will be inclined to permit a threefold drag increase on his rocket by neglecting the small job of sanding

its fins to the proper shape.

6.1.2 Zero-Lift Drag Coefficient of the Body

The Datcom expression for the drag coefficient of the body at zero angle of attack is

$$(166) \quad (C_{D_0})_B = (C_f)_B \left[1 + \frac{60}{(\ell_b/d_m)^3} + 0.0025 \left(\frac{\ell_b}{d_m} \right) \right] \frac{S_s}{S_m} + \frac{.029(d_b/d_m)^3}{\sqrt{(C_{Df})_b}}$$

where

$(C_{Df})_b$ is given by equation (161), and is also the first term in equation (166);

ℓ_b is the total length of the rocket body;

S_s is the total wetted surface area of the body, excluding the base;

S_m is the maximum frontal cross-sectional area of the body;

d_b is the diameter of the base; and

$(C_f)_B$ is the applicable skin-friction coefficient for the body.

Again, a more detailed explanation of these terms may prove useful in cases of practical application.

Strictly speaking, equation (166) is valid for bodies of revolution, a class of geometrical shapes to which most model rockets belong. The fineness ratio ℓ_b/d_m for several body configurations is defined in Figure 45. An excellent approximation to the drag coefficient of an object which is not a body

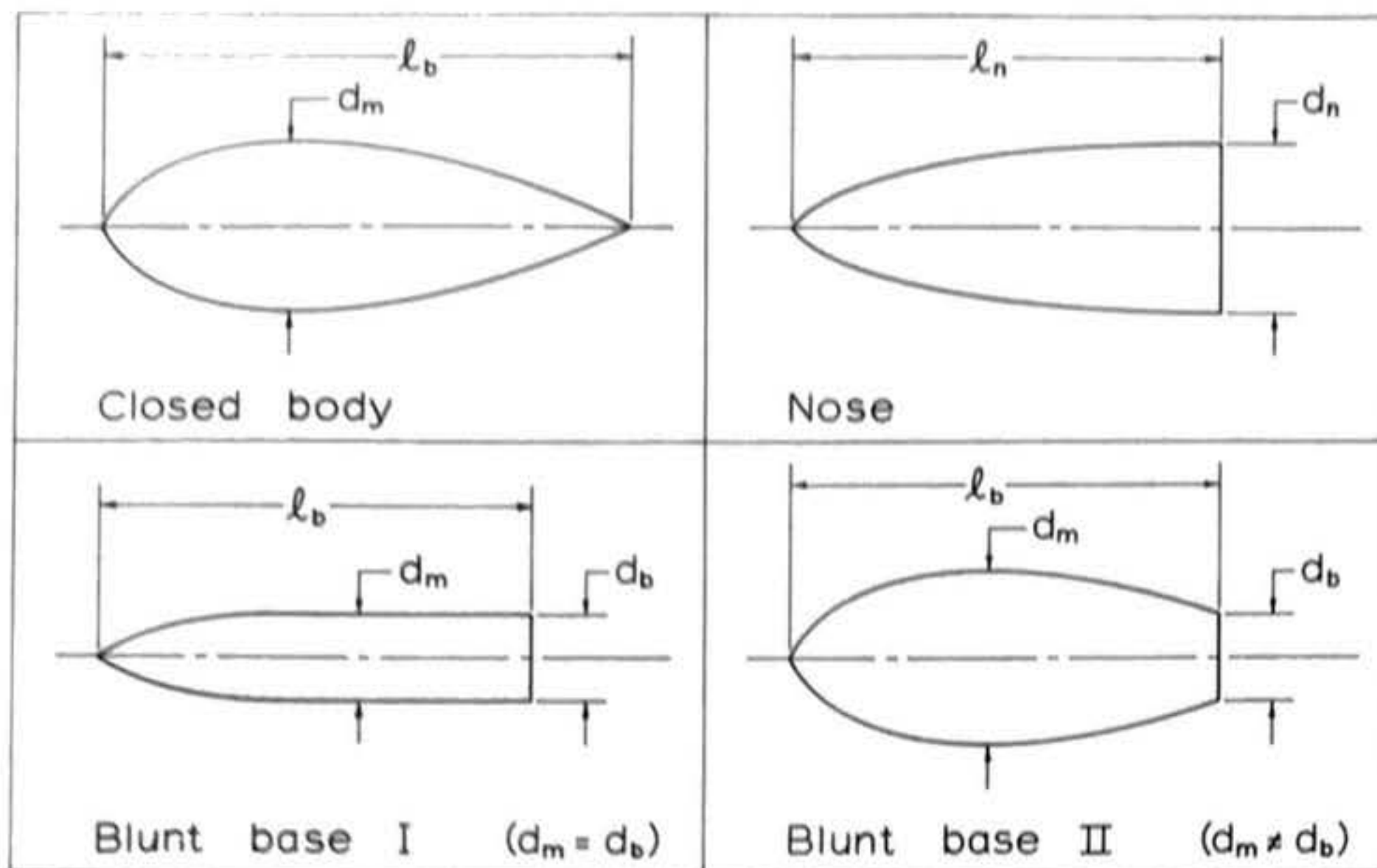


Figure 45: Definition of fineness ratio for various bodies of revolution. The fineness ratio of the nose is given by $\frac{l_n}{d_n}$; for the other three shapes the fineness ratio is defined as $\frac{l_b}{d_m}$.

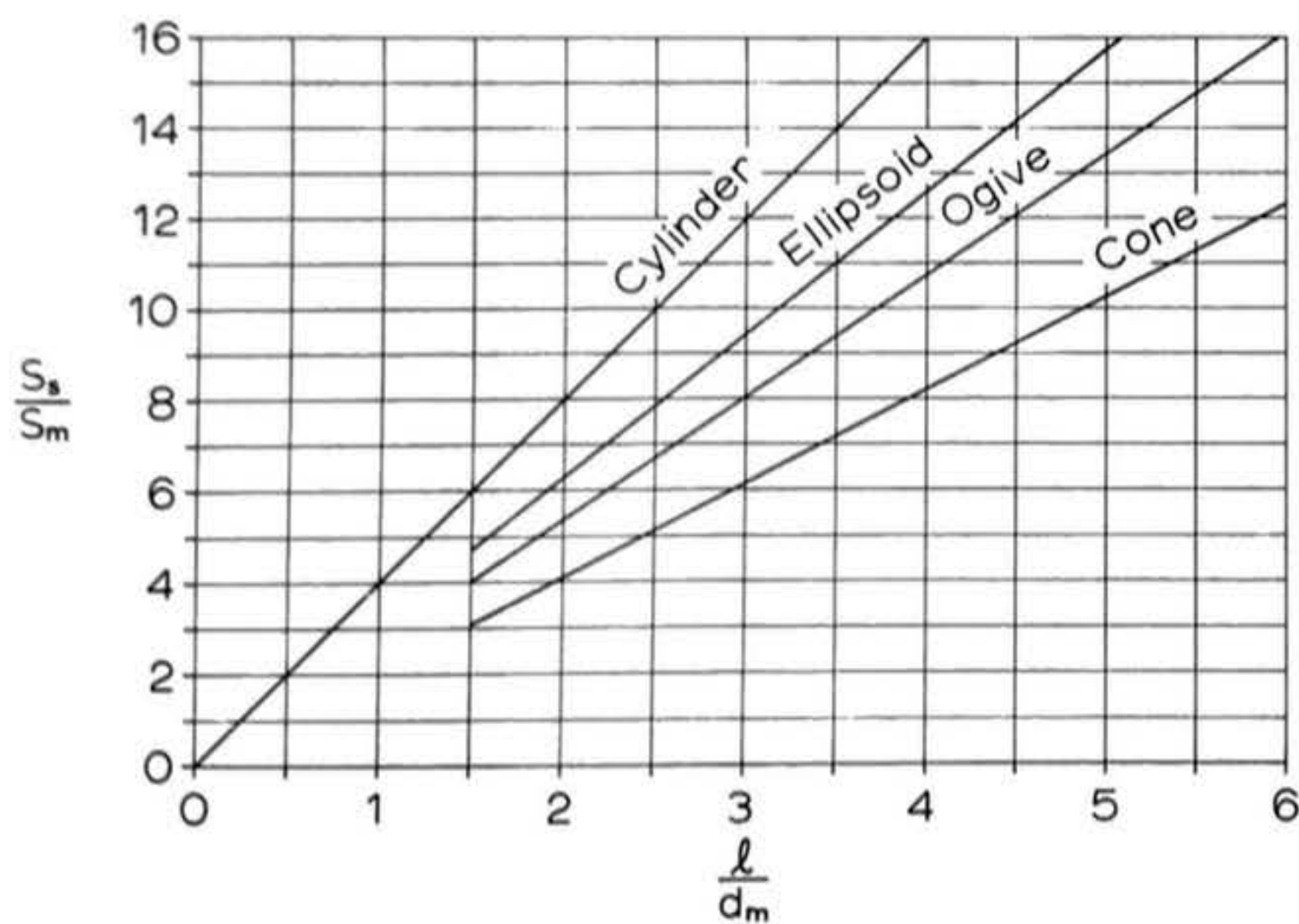


Figure 46: Ratio of surface area to maximum frontal area S_s/S_m as a function of fineness ratio λ/d_m for various component shapes. The functions for ellipsoids, cones, and ogives are approximate and are terminated at the lower limit of fineness ratio for which they give acceptable accuracy.

of revolution can, however, be computed by utilizing the equivalent diameter given by

$$(167) \quad d_{\text{equiv.}} = \sqrt{\frac{\text{cross-sectional area}}{0.7854}}$$

Such a procedure might be used, for instance, to determine the drag coefficient of a model rocket with an elliptical cross-section.

The wetted area of the body S_s is defined as the total surface area of the body in contact with the surrounding fluid, excluding in the case of a model rocket the area of the blunt base. Mathematically speaking, if $P(x)$ is the cross-section perimeter of the body at any station x (for this calculation x may be reckoned either forward from the base or aft from the nose),

$$(168) \quad S_s = \int_0^{l_b} P(x) dx$$

For a circular, cylindrical body tube $P(x)$ is a constant $P = \pi d_m$, and

$$(169) \quad (S_s)_{\text{cyl.}} = \pi d_m l_b$$

Since $(S_s)_{\text{cyl.}} = \pi r_m^2 = \pi \frac{d_m^2}{4}$, we then have

$$(170) \quad \left(\frac{S_s}{S_m}\right)_{\text{cyl.}} = \frac{\pi d_m l_b}{\pi d_m^2 / 4} = 4 \frac{l_b}{d_m}$$

In Figure 46 S_s/S_m is plotted as a function of component fineness ratio for the cylinder, as well as for ellipsoidal, conical, and tangent-ogive nose and afterbody shapes. The following equations may also be used to determine S_s/S_m for a variety of nosecone shapes:

$$(171a) \quad \left(\frac{S_s}{S_m}\right)_{\text{ELLIP.}} = 1 + \frac{2l/d_m}{\sqrt{1 - \frac{d_m^2}{4l^2}}} \sin^{-1} \sqrt{1 - \frac{d_m^2}{4l^2}}$$

$$(171b) \quad \left(\frac{S_s}{S_m}\right)_{\text{ELLIP.}} \approx (1 + \pi \frac{l}{d_m}) \quad \text{for } \frac{l}{d_m} \gg 1$$

$$(171c) \quad \left(\frac{S_s}{S_m}\right)_{\text{OGIVE}} \approx 2.67 \frac{l}{d_m} \quad \text{for } \frac{l}{d_m} > 1.5$$

$$(171d) \quad \left(\frac{S_s}{S_m}\right)_{\text{cone}} = 2\sqrt{\frac{1}{4} + (l/d_m)^2}$$

$$(171e) \quad \left(\frac{S_s}{S_m}\right)_{\text{cone}} \approx 2 \frac{l}{d_m} \quad \text{for } \frac{2l}{d_m} \gg 1$$

The above shapes, or combinations thereof, may be taken as good approximations to most model rocket nosecone shapes. The geometrical definitions of these shapes are illustrated in Figure 47. The ellipsoidal nose is constructed by first forming an ellipse (which is done by passing a plane through a cone at some angle less than a right angle to the cone axis, but greater than the half-angle of the cone itself), then dividing the ellipse about its minor axis, and finally revolving the remaining half-ellipse about its semimajor axis. As geometers know, parabolae and hyperbolae can also be constructed from the intersections of cones and planes; a parabola is formed by passing the plane through the cone at an angle to its axis equal to the cone half-angle, while a hyperbola results if the intersection occurs at a lesser angle. Paraboloidal and hyperboloidal nosecones can, of course, also be constructed, but they are not as good as ellipsoids because they do not become tangent to the body tube at their bases. Half the lateral section of a tangent-ogive nosecone is formed by the area bounded by a circle, a diameter of that circle, and a half-chord

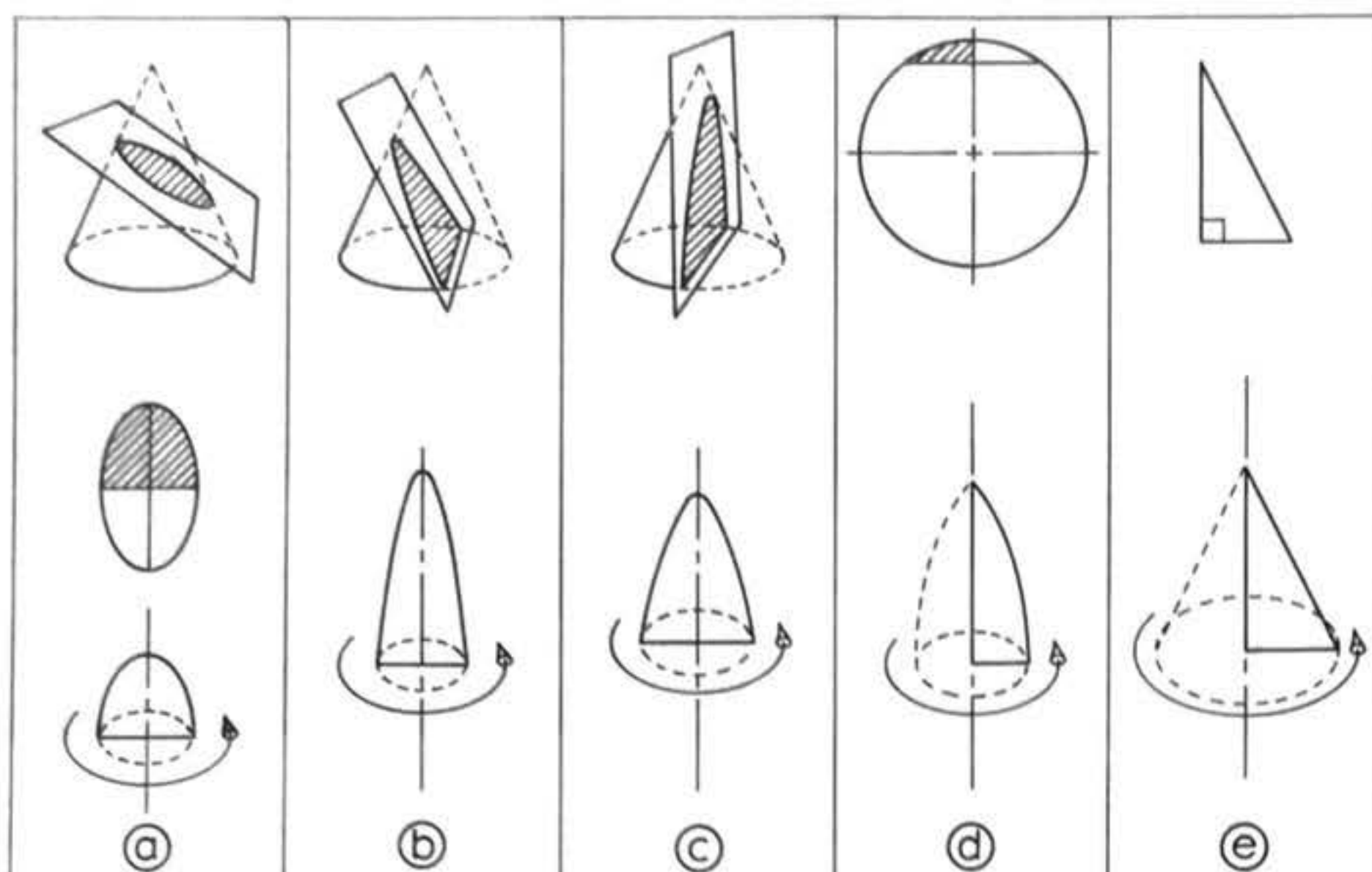


Figure 47: Geometrical definitions of common nose shapes. (a): An ellipse is formed by passing a plane through a cone at an angle to the cone axis greater than the cone's half-angle. The ellipse is divided along its minor axis and spun about its semimajor axis to form an ellipsoidal nose. (b): A parabola is formed by passing a plane through a cone at an angle equal to the half-angle of the cone and is then rotated to produce a paraboloidal nose. (c): A hyperbola is formed by passing a plane through a cone at an angle less than the cone half-angle and is rotated to produce a hyperboloidal nose. (d): A chord line is passed through a circle; the smaller segment thus formed is bisected by a radial line and the shaded half-segment is revolved about the chord line, forming a tangent ogive nose. (e): A right triangle is revolved about its altitude to form a conical nose.

of the circle perpendicular to the diameter. The familiar tangent ogive nose shape is generated by revolving this section about the chord line. The cone, simplest of the shapes, is generated by revolving a right triangle about its altitude. The cone suffers from the same shortcoming as the parabola and hyperbola in that the intersection of the nose with the body tube is not smooth. Its sharp point, however, gives it favorable drag characteristics in supersonic flight, as we shall see in Section 7.

When computing the ratio (S_s/S_m) for a boattail, account must be taken of the fact that the geometrical solid in whose shape the boattail has been made is truncated by the presence of the blunt base. For a conical boattail of maximum diameter d_m and base diameter d_b , the ratio of surface area to maximum cross-sectional area is given by

$$(172a) \quad \left(\frac{S_s}{S_m}\right)_{BOATTAIL} = \frac{2(d_m - d_b)\ell_T}{d_m^2} \sqrt{1 + \left(\frac{d_m - d_b}{2\ell_T}\right)^2}$$

$$(172b) \quad \left(\frac{S_s}{S_m}\right)_{BOATTAIL} \approx 2 \left(1 - \frac{d_b}{d_m}\right) \frac{\ell_T}{d_m} \quad \text{for } \frac{2\ell_T}{d_m - d_b} \gg 1$$

Equations (172a) and (172b) may also be used to approximate (S_s/S_m) for boattails made in the shape of truncated ellipsoids or ogives, as the exact formulae for these shapes are too complicated to be worth the gain in accuracy over (172a) and (172b) resulting from their use in practice.

If the body, nose, and boattail (if any) have the same maximum diameter, the overall ratio of surface area to maximum cross-sectional area can be expressed as

$$(173) \quad \frac{S_s}{S_m} = \left(\frac{S_s}{S_m}\right)_{NOSE} + \left(\frac{S_s}{S_m}\right)_{CYL} + \left(\frac{S_s}{S_m}\right)_{BOATTAIL}$$

The original Datcom method employs the turbulent skin-friction coefficient of the body for $(C_f)_B$ and the turbulent skin-friction coefficient of the fins for $(C_f)_F$ in all its calculations. This, presumably, is because the Datcom was devised for the purpose of providing drag coefficient predictions for full-scale aircraft and rockets. The Reynolds numbers of such vehicles are much higher than those commonly encountered in model rocketry. In the numerical example treated in Section 6.2, we shall begin the calculations by assuming completely turbulent flow over the rocket body and see how the estimate of the drag coefficient thus obtained compares with experimental values.

The body friction drag coefficient given in equation (161), which is also the first term on the right of equation (166), is of the form

$$(174) \quad (C_{Df})_b = (C_f)_B (1+a) \frac{S_s}{S_m}$$

The quantity a , which typically has a value of about 0.05, may be thought of as a three-dimensional correction to C_f as discussed in Section 3.6. The term $0.0025 \frac{l_b}{d_m}$, according to the Datcom, is the pressure-drag contribution of the body due to the effect of its "thickness", or cross-sectional area. In the Datcom method, therefore, the pressure drag of a streamlined body is reckoned for the purposes of practical calculation as part of its friction drag. The second -- i.e., base-drag -- term in equation (166) requires no further discussion here, as it was presented previously in Section 4.4.

6.2 The Datcom Method Applied to the Javelin Rocket

To illustrate the application of the equations presented in the preceding section, I shall perform the zero-lift drag coefficient calculation for a specific model rocket: the Javelin, a kit produced by the Centuri Engineering Company, and the same model for which Mercer has published experimentally-determined information on drag obtained through wind-tunnel tests. The availability of published data gives us a standard by which to measure the accuracy of the Datcom results. The Javelin, a simple, single-staged vehicle with a tangent-ogive nose, is shown in Figure 48.

I shall begin the calculation by making the following assumptions:

- (a) the angle of attack is zero;
- (b) the model has no launch lug;
- (c) the airspeed is 60 meters/second and $\rho = 1.495 \times 10^{-5}$ meter²/second;
- (d) the finish is hydraulically smooth at the given velocity;
- (e) the flow over the fins is completely laminar;
- (f) the flow over the body is completely turbulent; and
- (g) the flow does not separate from fins or body, except at the base.

The determination then proceeds as follows:

Step 1: forebody drag coefficient $(C_{Df})_b$

$$(C_{Df})_b = (C_f)_B \left[1 + \frac{60}{(l_b/d_m)^3} + 0.0025 \frac{l_b}{d_m} \right] \frac{S_s}{S_m}$$

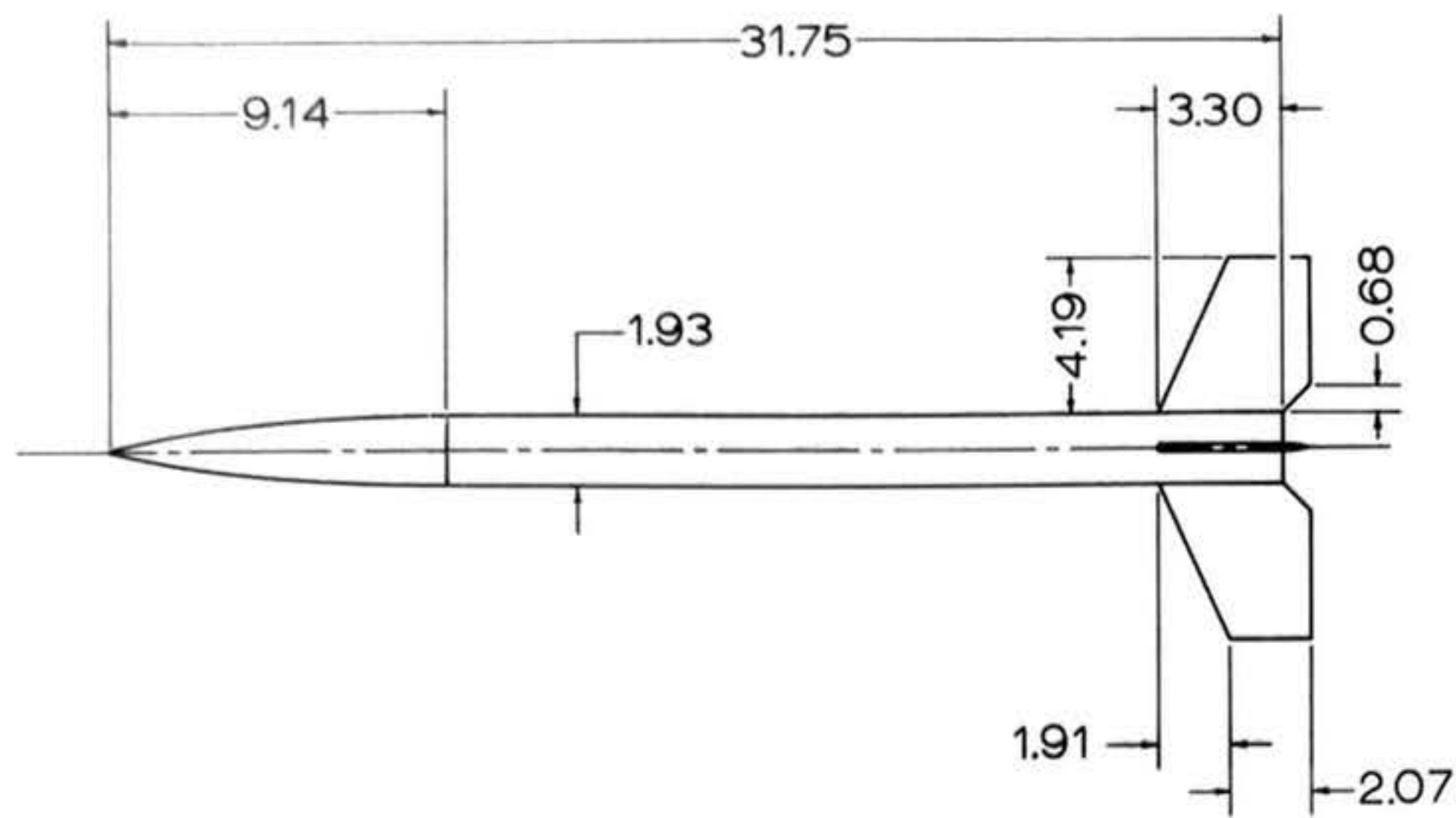


Figure 48: The Javelin rocket, produced in kit form by the Centuri Engineering Company of Phoenix, Arizona, shown with its stock BC-74 nosecone. All dimensions are given in centimeters.

Assume $(C_f)_B$ given by equation (86):

$$(C_f)_B = (C_f)_{turb} = \frac{.074}{(R_\ell)^{1/5}}$$

Since $\ell_b = 31.75$ cm. = 0.3175 meter, the Reynolds number based on body length is given by

$$R_\ell = \frac{60 \times .3175}{1.495 \times 10^{-5}} = 1.27 \times 10^6$$

Then the skin-friction coefficient of the body is

$$(C_f)_B = .00445$$

Since $\frac{\ell_b}{d_m} = \frac{31.75}{1.93} = 16.45$ we obtain

$$\left[1 + \frac{60}{(\ell_b/d_m)^3} + .0025 \frac{\ell_b}{d_m} \right] = 1 + .0135 + .0411 \approx 1.055$$

The ratio of wetted area to cross-sectional area is

$$\frac{S_s}{S_m} = \left(\frac{S_s}{S_m} \right)_{CYL} + \left(\frac{S_s}{S_m} \right)_{OGIVE}$$

For the cylindrical body we find from (170)

$$\left(\frac{S_s}{S_m} \right)_{CYL} = 4 \frac{\ell}{d_m} = \frac{22.61}{1.93} = 46.9$$

and for the ogival nose Figure 46 or equation (171c) gives

$$\left(\frac{S_s}{S_m} \right)_{OGIVE} \approx 2.7 \frac{\ell}{d_m} = 2.7 \frac{9.14}{1.93} = 12.8$$

So

$$\frac{S_s}{S_m} = 46.9 + 12.8 = 59.7$$

The forebody drag coefficient is thus

$$(C_D)_b = .00445 \times 1.055 \times 59.7 = 0.279$$

Step 2: base drag coefficient C_{D_b}

$$C_{D_b} = \frac{0.029(d_b/d_m)^3}{\sqrt{(C_{D_f})_b}}$$

From Step 1,

$$\sqrt{(C_{D_f})_b} = \sqrt{.279} = .528$$

and hence the base drag coefficient is

$$C_{D_b} = \frac{.029}{.528} = .055$$

Step 3: fin drag coefficient $(C_{D_f})_F$

$$(C_{D_f})_F = 2(C_f)_F \left(1 + 2 \frac{t}{c}\right) \frac{S_F}{S_m}$$

Assume $(C_f)_F$ given by equation (63):

$$(C_f)_F = (C_f)_{LAM.} = \frac{1.328}{\sqrt{R_c}}$$

The average fin chord is simply

$$c = \frac{3.97 + 2.07}{2} = 3.02 \text{ cm.} = .0302 \text{ meter}$$

Hence the Reynolds number for the fins is

$$R_c = \frac{60 \times .0302}{1.495 \times 10^{-5}} = 1.21 \times 10^5$$

which gives

$$(C_f)_F = \frac{1.328}{\sqrt{1.21 \times 10^5}} = .00382$$

Fins made of 3/32" balsa give $t = 0.238 \text{ cm.}$, so

$$\frac{t}{c} = \frac{.238}{.0302} = 0.079$$

The gross area σ_F of a single fin can be determined by resolving the Javelin fin into rectangles and right triangles, as shown in Figure 49b; this method simplifies the calculation of σ_F and, although it results in a slightly larger value than that obtained by the standard method (shown in Figure 49a), the difference is not very significant. Following Figure 49b, then,

$$\text{Area of region I} = \frac{1}{2} \times 1.90 \times 4.19 = 3.98 \text{ cm.}^2$$

$$\text{Area of region II} = 2.07 \times 4.19 = 8.68 \text{ cm.}^2$$

$$\text{Area of region III} = 3.21 \times 0.965 = 3.10 \text{ cm.}^2$$

$$\sigma_F = (3.98 + 8.68 + 3.10) \text{ cm.}^2 = 15.76 \text{ cm.}^2$$

Since the Javelin has four fins,

$$S_F = 4\sigma_F \approx 63 \text{ cm.}^2$$

The body frontal area is

$$S_m = \frac{\pi d_m^2}{4} = \frac{3.14 \times 1.93^2}{4} = 2.92 \text{ cm.}^2$$

and hence the fin drag coefficient is

$$(C_{D_0})_F = 2 \times .00382 \times 1.158 \times \frac{63}{2.92} = .190$$

Summing the results of steps 1, 2, and 3, we obtain the total zero-lift drag coefficient of the rocket:

$$(C_{D_0})_{FB} = .279 + .055 + .190 = .524$$

This value is about 25% greater than the drag coefficient measured by Mercer for the Javelin rocket with a Centuri BC-74 nosecone (see Figure 31).

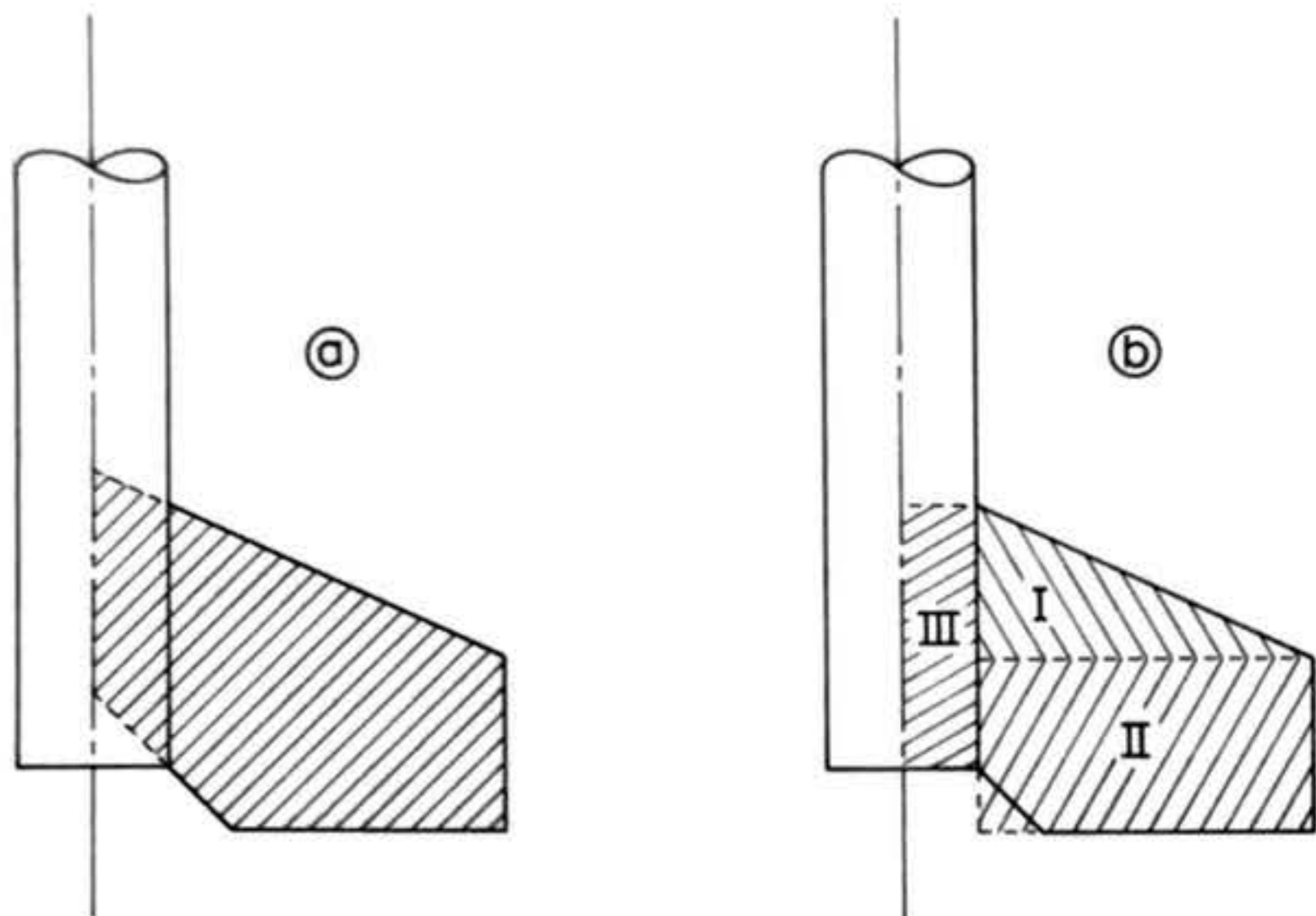


Figure 49: Standard and approximate methods of determining the gross fin planform area of the Javelin rocket. The approximate method (b) is preferred to the standard method (a) because it is more conservative; that is, it results in a larger value of σ_F .

Now suppose we see what happens if I rescind assumption (f) above and replace it with the more accurate assumption that the flow over the body is partly laminar and partly turbulent, with transition occurring at the critical Reynolds number $R_{crit} = 5 \times 10^5$.

Step 1: forebody drag coefficient $(C_{Df})_b$

The body skin-friction coefficient will now be given by equation (101):

$$(C_f)_B = \frac{0.074}{(R_\ell)^{1/5}} - \frac{B}{R_\ell}$$

From equation (100) we find $B = 1735$; since $R_\ell = 1.27 \times 10^6$,

$$(C_f)_B = .00445 - .00137 = .00308$$

The forebody drag coefficient then becomes

$$(C_{Df})_b = .00308 \times 1.055 \times 59.7 = .194$$

which is a reduction of 30.5% from its previous value of 0.279, or a reduction in the contribution to the overall drag coefficient by 0.085. This is due to the fact that, at these Reynolds numbers, the skin-friction coefficient for a laminar boundary layer is considerably lower than that for a turbulent boundary layer.

Step 2: base drag coefficient C_{Db}

Using the new value of $(C_{Df})_b$, we find the base drag coefficient to be

$$C_{Db} = \frac{0.029}{\sqrt{.194}} = .066$$

The base drag coefficient is thus increased by 20%, but since

it was a relatively small quantity to begin with the actual increase in drag coefficient due to this percentage increase is only 0.011.

Step 3: fin drag coefficient (C_{D_0})_F

Since R_c is less than the critical Reynolds number, laminar flow will be maintained on the fins. The fin drag coefficient thus remains unchanged from its previous value of 0.190.

Summing the contributions from Steps 1, 2, and 3 we obtain a new value for the total drag coefficient:

$$(C_{D_0})_{FB} = .194 + .066 + .190 = .450$$

This result is only about 7% greater than Mercer's measured value of 0.42 for the Javelin rocket. Actually, we have no right to expect any closer agreement with Mercer's data, both because a 7% error is within the measurement uncertainty of the type of equipment used in the wind-tunnel experiments and because the wind-tunnel tests were conducted at a much lower velocity than 60 meters/second, and hence a much lower Reynolds number than that on which the above calculations were based. An airspeed of 15 meters/second is representative of the test velocities produced by the type of wind tunnel used in the Mercer experiments. Suppose we then rescind assumption (c) above and replace it with the assumption that the airspeed is 15 meters/second. This gives $R_f = 3.175 \times 10^5$ and $R_c = 3.02 \times 10^4$. Both Reynolds numbers are subcritical, so the flow will remain entirely laminar over both body and fins.

Step 1: forebody drag coefficient $(C_{Df})_b$

The body skin-friction coefficient is given by

$$(C_f)_b = (C_f)_{LAM.} = \frac{1.328}{\sqrt{31.75 \times 10^4}} = .00154$$

so the forebody drag coefficient is

$$(C_{Df})_b = .00154 \times 1.055 \times 59.7 = .097$$

This represents a decrease of 0.097, or 50%, from the transition-flow value of $(C_{Df})_b$.

Step 2: base drag coefficient C_{Db}

$$C_{Db} = \frac{.029}{\sqrt{.097}} = .093$$

This is an increase of 0.028, or 41% over the transition-flow calculated value.

Step 3: fin drag coefficient $(C_{D0})_F$

The fin skin-friction coefficient is

$$(C_f)_F = \frac{1.328}{\sqrt{3.02 \times 10^4}} = .00765$$

$$\text{Then } (C_{D0})_F = 2 \times .00765 \times 1.158 \times \frac{63}{2.92} = .380$$

This is an increase of .190, or double the value calculated for 60 meters/second.

From these calculations we obtain an overall drag coefficient of

$$(C_{D0})_{FB} = .097 + .093 + .380 = .570$$

This is a substantial disagreement with the experimental result -- almost 36%. And yet the Mercer data should be closer to this value than to the other two values calculated, according to theory. Discrepancies of this kind can and often do arise, however, due to the airflow characteristics present in the test sections of many small, subsonic wind tunnels. Test facilities of this type are prone to have much more free-stream turbulence in the air moving through their test sections than is present in the open atmosphere. The effect of free-stream turbulence in wind-tunnel testing is to raise the effective Reynolds number of the test; i.e., to make the data look as if the Reynolds number were much higher than it actually is. One may thus conjecture that, although the Mercer tests may have been conducted at an airspeed closer to 15 than to 60 meters/second, free-stream turbulence in the wind tunnel made the drag coefficient appear as if the Reynolds number of the test had been closer to that produced by a 60 meter/second airspeed. If this were the case it would present model rocketeers with a rather paradoxical advantage, for it would mean that a turbulent, low-speed wind tunnel could produce drag coefficient data applicable to higher-speed model rocket flight in the open air. The difficulty with such an approach, of course, is that one cannot tell precisely what the effective Reynolds number of a test in a turbulent wind tunnel is, except by comparing the data with the semiempirical predictions of Datcom theory.

At a given Reynolds number, there are two major parameters which can be used to adjust the Datcom prediction of the drag coefficient of a given rocket: the critical Reynolds number

(and hence, the quantity B) and the decrease in base drag coefficient due to the presence of the fins. Since there are no data available to relate these effects quantitatively to either rocket geometry or flow conditions, such a process of adjustment must at present be considered pure guesswork. Variations in critical Reynolds number and base-drag reduction due to the fins could certainly be considered to account for the discrepancy between the prediction of our last calculation above and Mercer's experimental determination, but even if numerical estimates of these quantities are derived which, when used with the Datcom method, give an accurate value of $(C_{D_0})_{FB}$ for the Javelin rocket, there is no assurance that their use can be extended to other rocket configurations. The constant B, for example, almost certainly depends upon the individual rocket, so there will always be some error inherent in a general technique like the Datcom method. It can only be hoped that the variation of B from model to model is small enough so that the error is maintained within acceptable limits for model rocketry work -- say, about 10%.

In conclusion, it would appear that full adaptation of the Datcom method to the practical calculation of model rocket drag coefficients requires research to establish reasonably representative values of B for model rockets of different shapes, and to establish a semiempirical relationship between base drag and fin geometry and location, if this effect is indeed significant.

6.3 General Analysis of the Datcom Method

6.3.1 The General Configuration Rocket (GCR)

The preceding section was intended to familiarize the reader with the application of the Datcom method to a particular problem. In this section the drag coefficient equations will be cast into special forms, particularly applicable to model rockets, which will clarify the relationships between rocket geometry and drag. This general, nondimensional approach will be utilized to discover the behavior of the drag coefficient and the drag force with respect to changing Reynolds number in Sections 6.3.2 and 6.3.3.

We begin by listing in general form the functional dependence of the drag coefficients upon the variables of the Datcom equations (equations (158) through (162)):

$$(175) \quad (C_{Df})_b = G_1(B, R_L, \frac{l_b}{d_m}, \frac{S_s}{S_m})$$

$$(176) \quad C_{D_b} = G_2(B, R_L, \frac{l_b}{d_m}, \frac{S_s}{S_m}, \frac{d_b}{d_m})$$

$$(177) \quad (C_{D_o})_B = G_3(B, R_L, \frac{l_b}{d_m}, \frac{S_s}{S_m}, \frac{d_b}{d_m})$$

$$(178) \quad (C_{D_o})_F = G_4(B, R_c, \frac{t}{c}, \frac{S_F}{S_m})$$

$$(179) \quad (C_{D_o})_{FB} = G_5(B, R_L, \frac{l_b}{d_m}, \frac{S_s}{S_m}, \frac{d_b}{d_m}, R_c, \frac{t}{c}, \frac{S_F}{S_m})$$

where the right-hand sides of the equations are read as "G₁ of B, R_L, $\frac{l_b}{d_m}$, $\frac{S_s}{S_m}$ ", and so on. They are simply a form of mathematical shorthand to indicate that the drag coefficients depend on the quantities in parentheses on the right in some (as yet unspecified) fashion.

Theoretically, we could obtain a graphical relationship between any one of the above drag coefficients and one of its

variables by assigning constant values to all the other variables in the function. As a practical matter, however, this would not be very illuminating, as variables like S_S/S_m and S_F/S_m do not convey any concept of shape and are difficult to visualize. They can be converted to expressions involving only linear dimensions, though, if we assume specific shapes for the nosecone, fins, main body and boattail (if any) of the rocket.

For this reason, we adopt as the basis for the remainder of the analysis in this section the configuration shown in Figure 50: a rocket consisting of an ogive nosecone, a circular cylindrical body, rectangular fins, and a conical boattail. This class of vehicles will henceforth be referred to as the General Configuration Rocket (GCR), since by varying its proportions one can obtain reasonable approximations to the shape of many single-staged model rockets. It should be noted that the fins enter the Datcom equations only through their surface area S_F and the thickness ratio t/c ; hence no generality is lost by assuming rectangular fins for the GCR. The shape of the fins is important only in determining the drag and side force due to a nonzero angle of attack, whereas the Datcom equations presented here involve only the determination of the zero-lift drag coefficient. Furthermore, the GCR has no specific size until a numerical value for one of its linear dimensions is specified; the variations depicted in Figure 50 could be ten centimeters or one meter in length. This "nondimensionality" is the most valuable property of the GCR concept.

We can now write for the GCR,

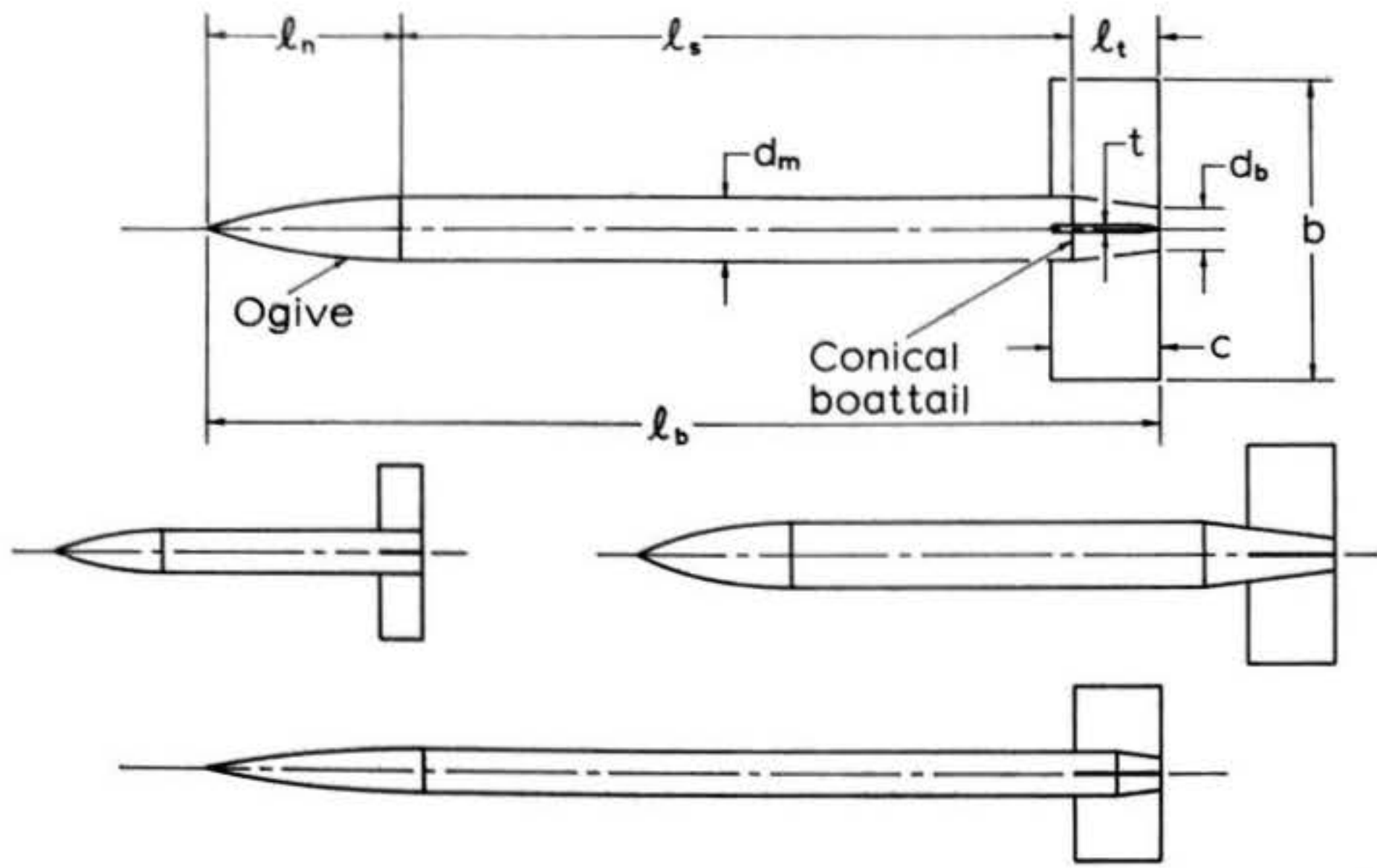


Figure 50: The General Configuration Rocket (GCR), shown with its nomenclature and three of its possible variations.

$$(180) \quad \left(\frac{S_s}{S_m}\right)_{GCR} = \left(\frac{S_s}{S_m}\right)_{OGIVE} + \left(\frac{S_s}{S_m}\right)_{CYL} + \left(\frac{S_s}{S_m}\right)_{BOATTAIL}$$

The approximate expression for the ogive nose is

$$(181) \quad \left(\frac{S_s}{S_m}\right)_{OGIVE} \approx 2.7 \frac{l_N}{d_m} \quad \left(\frac{l_N}{d_m} > 1.5\right)$$

and the exact equation for the cylindrical body is

$$(182) \quad \left(\frac{S_s}{S_m}\right)_{CYL} = 4 \frac{l_c}{d_m}$$

For the conical boattail,

$$(183a) \quad \left(\frac{S_s}{S_m}\right)_{BOATTAIL} = \frac{2(d_m - d_b)l_T}{d_m^2} \sqrt{1 + \left(\frac{d_m - d_b}{2l_T}\right)^2}$$

which, for any practical boattail, can be accurately approximated as

$$(183b) \quad \left(\frac{S_s}{S_m}\right)_{BOATTAIL} \approx 2 \left(1 - \frac{d_b}{d_m}\right) \frac{l_T}{d_m}$$

Hence,

$$(184) \quad \left(\frac{S_s}{S_m}\right)_{GCR} = 2.7 \frac{l_N}{d_m} + 4 \frac{l_s}{d_m} + 2 \left(1 - \frac{d_b}{d_m}\right) \frac{l_T}{d_m}$$

Equations (175), (176), and (177) can also be written

$$(185) \quad (C_{Df})_b = H_1 \left(B, R_l, \frac{d_b}{d_m}, \left\{ \frac{l_b}{d_m}, \frac{l_N}{d_m}, \frac{l_s}{d_m}, \frac{l_T}{d_m} \right\} \right)$$

$$(186) \quad C_{Db} = H_2 \left(B, R_l, \frac{d_b}{d_m}, \left\{ \frac{l_b}{d_m}, \frac{l_N}{d_m}, \frac{l_s}{d_m}, \frac{l_T}{d_m} \right\} \right)$$

$$(187) \quad (C_{D_o})_B = H_3 \left(B, R_l, \frac{d_b}{d_m}, \left\{ \frac{l_b}{d_m}, \frac{l_N}{d_m}, \frac{l_s}{d_m}, \frac{l_T}{d_m} \right\} \right)$$

where the letters H again just refer to the fact that the value of the quantity on the left-hand side of each equation depends upon the values of the quantities in parentheses on the right-hand side. The bracketed expression $\left\{ \frac{l_b}{d_m}, \frac{l_N}{d_m}, \frac{l_s}{d_m}, \frac{l_T}{d_m} \right\}$ means that only three of the four length-to-diameter ratios may be

chosen to specify the problem, since choosing values for any three determines the value of the fourth. This follows from the fact that

$$(188) \quad \frac{l_b}{d_m} = \frac{l_N}{d_m} + \frac{l_s}{d_m} + \frac{l_T}{d_m}$$

In a similar manner, S_F/S_m may be transformed:

$$(189) \quad S_F = 4\pi r_F = 4(c \frac{b}{2}) = 2cb$$

$$(190) \quad \frac{S_F}{S_m} = \frac{2cb}{\pi \frac{d_m^2}{4}} = \left(\frac{8}{\pi}\right)\left(\frac{c}{d_m}\right)\left(\frac{b}{d_m}\right)$$

Furthermore,

$$(191) \quad R_L = \frac{U_\infty l_b}{\nu} \quad \text{and} \quad R_c = \frac{U_\infty c}{\nu}$$

and R_c can therefore be eliminated by substituting

$$(192) \quad R_c = \left(\frac{c}{l_b}\right) R_L = \frac{(c/d_m)}{(l_b/d_m)} R_L$$

Consequently, equation (178) becomes

$$(193) \quad (C_{D_0})_F = H_4(B, R_L, \frac{l_b}{d_m}, \frac{t}{c}, \frac{c}{d_m}, \frac{b}{d_m})$$

The fin-body interference drag coefficient, which is one component of the fin drag coefficient, is given by

$$(194) \quad C_{DI} = 2(C_f)_F \left(1 + 2\frac{t}{c}\right) \frac{S_F - S_E}{S_m}$$

For the GCR, it is found that

$$(195) \quad \frac{S_F - S_E}{S_m} = \frac{4}{\pi} \left[\left(\frac{c}{d_m}\right)\left(\frac{d_b}{d_m}\right) + \left(\frac{c}{d_m}\right)^2 \left(\frac{d_m}{l_T}\right) \left(1 - \frac{d_b}{d_m}\right) \right]$$

so

$$(196) \quad C_{DI} = H_5(B, R_L, \frac{l_b}{d_m}, \frac{t}{c}, \frac{c}{d_m}, \frac{b}{d_m}, \frac{d_b}{d_m}, \frac{l_T}{d_m})$$

The total drag coefficient is then seen to exhibit the functional dependence

$$(197) \quad (C_{D_0})_{FB} = H_6 \left(B, R_\ell, \frac{d_b}{d_m}, \frac{t}{c}, \frac{c}{d_m}, \frac{b}{d_m}, \left\{ \frac{l_b}{d_m}, \frac{l_N}{d_m}, \frac{l_s}{d_m}, \frac{l_T}{d_m} \right\} \right)$$

Nine independent, dimensionless variables completely determine the overall drag coefficient and its various constituents, as seen in equations (185), (186), (187), (193), (196), and (197). Seven of these are strictly geometrical factors; the remaining two (B and R_ℓ) are related to the interaction of the rocket and the fluid through which it moves. This set of variables is not unique; for example, since

$$(198) \quad \left(\frac{t}{c} \right) \left(\frac{c}{d_m} \right) = \frac{t}{d_m}$$

any two of these three quantities may be used to replace t/c and c/d_m . Although each drag coefficient is a function of more variables than before (equations (175) through (179)), the problem has been simplified because there is a direct and visible relationship between $(C_{D_0})_{FB}$ and the pertinent factors of rocket geometry and vehicle-fluid interaction. The Datcom equations, expressed in terms of these 9 variables for the GCR, are as follows:

$$(199) \quad (C_{D_f})_b = \left[1 + \frac{60}{(l_b/d_m)^3} + .0025 \frac{l_b}{d_m} \right] \left[2.7 \frac{l_N}{d_m} + 4 \frac{l_s}{d_m} + 2 \left(1 - \frac{d_b}{d_m} \right) \frac{l_T}{d_m} \right] (C_f)_B$$

$$(200) \quad C_{D_b} = .029 \left(\frac{d_b}{d_m} \right)^3 / \sqrt{(C_{D_f})_b}$$

$$(201) \quad (C_{D_0})_F = \frac{16}{\pi} (C_f)_F \left(\frac{c}{d_m} \right) \left(\frac{b}{d_m} \right) \left(1 + 2 \frac{t}{c} \right)$$

$$(202) \quad C_{D_I} = \frac{8}{\pi} (C_f)_F \left(1 + 2 \frac{t}{c} \right) \left[\left(\frac{c}{d_m} \right) \left(\frac{d_b}{d_m} \right) + \left(\frac{c}{d_m} \right)^2 \left(\frac{d_m}{l_T} \right) \left(1 - \frac{d_b}{d_m} \right) \right]$$

where

$$(203a) \quad (C_f)_B = \frac{1.328}{\sqrt{R_\ell}} \quad (R_\ell < R_{crit})$$

$$(203b) \quad (C_f)_B = \frac{0.074}{(R_\ell)^{1/5}} - \frac{B}{R_\ell} \quad (R_\ell \geq R_{crit})$$

$$(204a) \quad (C_f)_F = \sqrt{\frac{l_b}{c}} - \frac{1.328}{\sqrt{R_\ell}} \quad (R_\ell < R_{crit})$$

$$(204b) \quad (C_f)_F = \left(\frac{l_b}{c}\right)^{1/5} \frac{0.074}{(R_\ell)^{1/5}} - \left(\frac{l_b}{c}\right) \frac{B}{R_\ell} \quad (R_\ell \geq R_{crit})$$

and the overall zero-lift drag coefficient is given by

$$(205) \quad (C_{D_0})_{FB} = (C_{Df})_b + C_{Db} + (C_{D0})_F$$

It is now a relatively straightforward matter to produce graphs depicting the behavior of any of the above drag coefficients as one of its parameters is varied. Some of these relationships will be more useful than others; it does not seem productive, for example, to determine the effect of the nose fineness ratio on the base drag coefficient. To illustrate such an analysis, we instead consider the far more important relationship between drag coefficient and Reynolds number -- which, for a rocket of given length, translates directly into a relationship between drag coefficient and airspeed.

6.3.2 Dependence of the Drag Coefficient on Reynolds Number for the General Configuration Rocket

The Reynolds number R_ℓ is itself a function of three variables, U_∞ , l_b , and ν . If the relationship between drag coefficient and R_ℓ is known, therefore, this relationship can be used to determine C_D as a function of velocity by assuming numerical values for the 8 other quantities in the Datcom

equations:

$$(206) \quad C_D = f(U_\infty) \quad \left(\frac{l_b}{\nu} = \text{constant} \right)$$

A knowledge of this function is essential for accurate performance calculations. In particular, an assurance that C_D does not vary greatly over the expected velocity range encountered by a given model in flight is required before a constant C_D can be used in the performance calculations for that model with a high degree of confidence. To determine the variation of C_D with R_ℓ for a particular example of the GCR (denoted GCR-x) the following values were assigned to the 8 variables:

$$\frac{d_b}{d_m} = .8 \quad \frac{l_T}{d_m} = 3 \quad \frac{l_N}{d_m} = 3.5 \quad \frac{l_s}{d_m} = 11.5$$

$$\frac{t}{c} = .02 \quad \frac{c}{d_m} = 1.75 \quad \frac{b}{d_m} = 5 \quad B = 1735 \quad (R_{\text{crit}} = 5 \times 10^5)$$

The overall fineness ratio l_b/d_m is thus 18, making the GCR-x a fairly slender model. Substituting these values into equations (199) through (204), we obtain

$$\left. \begin{aligned} (C_{D_f})_b &= 82.8(C_f)_B \\ C_{D_b} &= \frac{.0149}{\sqrt{(C_{D_f})_b}} \end{aligned} \right\} (C_{D_f})_b + C_{D_b} = (C_{D_o})_B$$

$$C_{D_I} = 4.25(C_f)_F$$

$$(C_{D_o})_F = 46.4(C_f)_F$$

where

$$(C_f)_B = \frac{1.328}{\sqrt{R_\ell}} \quad (R_\ell = \frac{U_\infty l_b}{\nu} < 5 \times 10^5)$$

$$(C_f)_B = \frac{0.074}{(R_\ell)^{1/6}} - \frac{1735}{R_\ell} \quad (R_\ell \geq 5 \times 10^5)$$

$$(C_f)_F = \frac{4.25}{\sqrt{R_\ell}} \quad (R_\ell < 5.14 \times 10^6)$$

$$(C_f)_F = \frac{0.118}{(R_\ell)^{1/5}} - \frac{17,900}{R_\ell} \quad (R_\ell \geq 5.14 \times 10^6)$$

and the overall zero-lift drag coefficient is therefore

$$(C_{D_0})_{FB} = 82.8(C_f)_B + \frac{.0149}{\sqrt{82.8(C_f)_B}} + 46.4(C_f)_F$$

The results obtained for Reynolds numbers between 1×10^4 and 1×10^7 are summarized in Table 6 and presented graphically in Figure 51. The total drag coefficient $(C_{D_0})_{FB}$ has a very interesting shape which exhibits three main phases.

At Reynolds numbers less than 5×10^5 the flow over the entire rocket is laminar and Phase I behavior of the total drag coefficient is observed. At small Reynolds numbers, $(C_{D_0})_{FB}$ is extremely large, achieving a value of 3.08 for $R_\ell = 1 \times 10^4$. This behavior is expected, as the boundary layer thickens with decreasing Reynolds number and viscous forces play a much greater role in the flow behavior than is the case at higher Reynolds numbers. For a model rocket of 30 centimeters length, a Reynolds number of 10^4 corresponds to an airspeed of only about 0.6 meter/second. A well-designed model rocket does not leave its launcher with a velocity much less than 9 meters/second, so the behavior of the drag coefficient at such low Reynolds numbers is not of much interest in model rocket flight calculations.

At Reynolds numbers between 5×10^5 and 5×10^6 the rocket is operating in Phase 2 flight. When the critical Reynolds number $R_\ell = 5 \times 10^5$ is attained, a region of turbulence begins to grow from the model's base forward. This is reflected in an increase in the body drag coefficient $(C_{D_0})_B$ with increasing Reynolds number. Simultaneously, however, there is pure laminar

TABLE 6

R_e	C_{D0}	$(C_{D0})_B$	$(C_{D0})_F$	$(C_{D0})_{FB}$
1×10^4	.014	1.114	1.970	3.080
5×10^4	.021	.513	.883	1.396
7×10^4	.023	.438	.748	1.186
1×10^5	.025	.373	.627	1.000
1.5×10^5	.028	.312	.510	.822
2×10^5	.030	.276	.441	.717
3×10^5	.033	.233	.359	.592
4×10^5	.036	.210	.312	.522
5×10^5	.038	.194	.279	.473
6×10^5	.034	.223	.255	.478
7×10^5	.033	.242	.236	.478
8×10^5	.031	.257	.221	.478
9×10^5	.031	.266	.208	.474
1×10^6	.030	.272	.197	.469
1.25×10^6	.030	.284	.176	.460
1.5×10^6	.029	.289	.161	.450
2×10^6	.029	.293	.139	.432
3×10^6	.029	.292	.112	.404
4×10^6	.029	.287	.098	.385
5×10^6	.030	.281	.089	.370
6×10^6	.030	.276	.102	.378
8×10^6	.031	.268	.122	.390
1×10^7	.031	.261	.135	.396

Table 6: Drag coefficient of the GCR-X rocket at various Reynolds numbers.

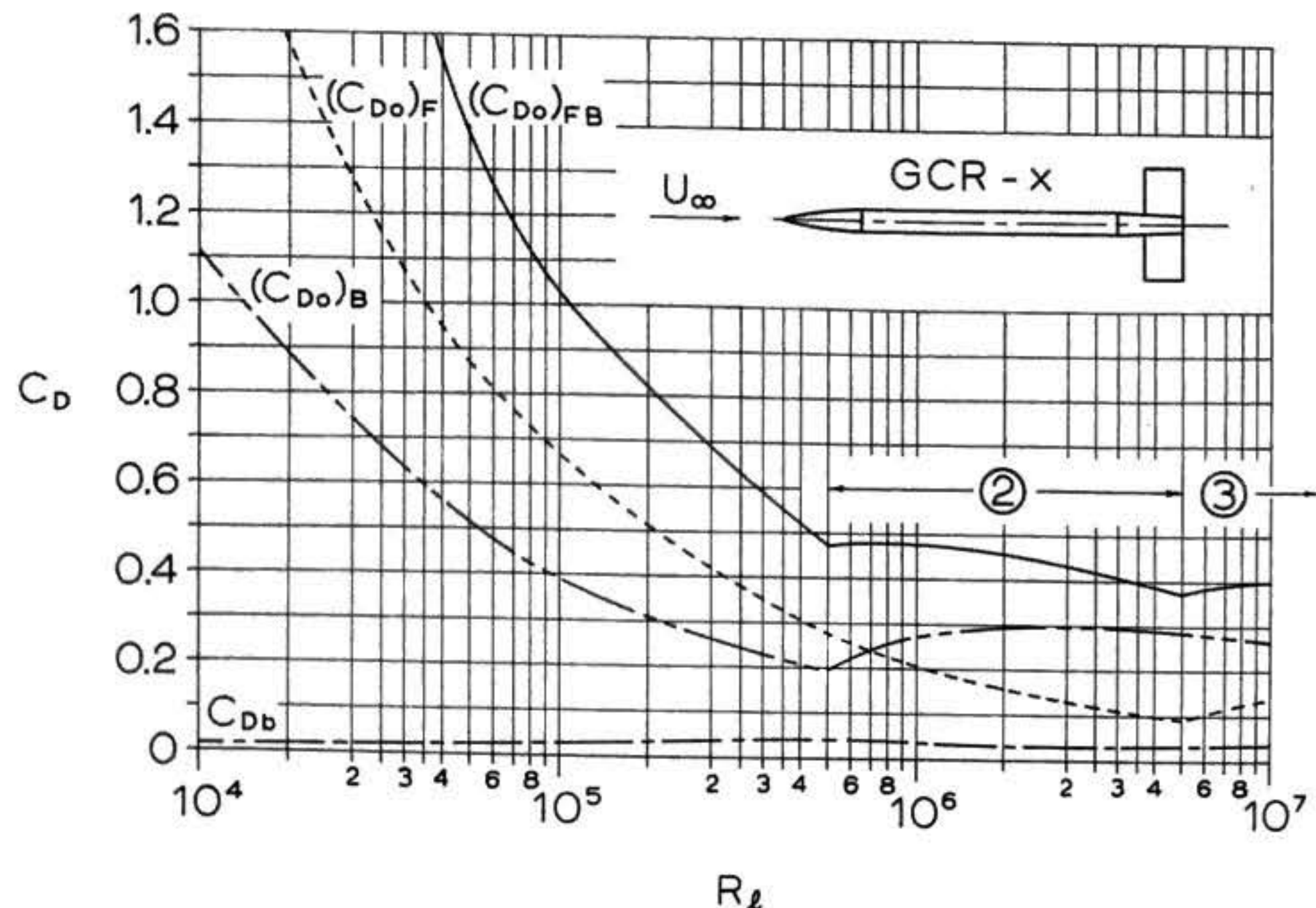


Figure 51: Variation of $(C_{D_o})_{FB}$ with Reynolds number for the GCR-x rocket. Also shown are the constituent drag functions $(C_{D_o})_B$ and $(C_{D_o})_F$ and the base drag coefficient C_{Db} . At Reynolds numbers below 5×10^5 the flow over the entire rocket is laminar. Between 5×10^5 and 5×10^6 (region (2) on the graph) transition to turbulent flow occurs partway down the body but the flow over the fins is laminar. Above a Reynolds number of 5×10^6 transition to turbulent flow occurs partway back on the fins as well (region (3) on the graph). Region (2) is referred to as the body transition zone; region (3) is called the fin transition zone.

flow over the fins, and from equation (204a) it is seen that $(C_{D_0})_F$ will decrease with increasing Reynolds number. The net effect of these two opposing trends is to hold $(C_{D_0})_{FB}$ virtually constant in this phase, denoted the body transition zone on the graph of Figure 51. $(C_{D_0})_B$ does not increase indefinitely, however, as it too is subject to opposing phenomena. From $R_\ell = 5 \times 10^5$ to $R_\ell = 2 \times 10^6$, the increase in skin-friction drag due to the growing turbulent region on the body is greater than the decrease experienced in both the laminar and turbulent regions due to the inverse variation of $(C_f)_B$ with R_ℓ (see equations (203a) and (203b)); thus $(C_{D_0})_B$ increases. At $R_\ell = 2.5 \times 10^6$, however, the body is mostly turbulent and the important effect becomes the reduction in $(C_f)_B$ with increasing Reynolds number. Hence, in the upper range of the body transition zone, both $(C_{D_0})_B$ and $(C_{D_0})_F$ are decreasing, and $(C_{D_0})_{FB}$ decreases with them. Phase 2 is the flight regime of greatest interest to the model rocketeer, as most model rocket flight occurs in this range of Reynolds numbers. A 30-centimeter-long rocket is in Phase 2 flight whenever its velocity is between about 30 and 300 meters/second.

At a Reynolds number of 5.14×10^6 , the fins of the GCR-x experience the development of a turbulent boundary layer beginning near the trailing edge and the rocket enters Phase 3 flight. In this phase the behavior of $(C_{D_0})_F$ is completely analogous to that of $(C_{D_0})_B$ in Phase 2. If Figure 51 were extended to higher Reynolds numbers, $(C_{D_0})_F$ would be seen to attain a peak and then decrease again. In essence, the roles of $(C_{D_0})_B$ and $(C_{D_0})_F$ are reversed in Phases 2 and 3 with respect to their

effects on $(C_{D_0})_{FB}$. Phase 3, labeled the fin transition zone in Figure 51, is rarely attained in model rocket flight, due to limitations on engine power and the rapidly increasing magnitude of the drag force at the velocities required to produce these high Reynolds numbers. Of course, rockets with very large fin chords, comparable to the rocket length ℓ_b , will attain phase 3 at comparatively low Reynolds numbers -- but this is an uncommon occurrence. The effects of compressibility generally become noticeable in Phase 3, or even in the upper range of Phase 2, so our analysis is not completely valid for these high-velocity regimes.

The base drag coefficient is essentially constant over the entire spectrum of Reynolds numbers, attaining its maximum value when $(C_{D_0})_B$ attains its minimum value -- which occurs at $R_\ell = 5 \times 10^5$. It is a relatively insignificant contribution to $(C_{D_0})_{FB}$ at low Reynolds numbers, but in Phase 2 or Phase 3 flight it represents about 7% of the total drag coefficient.

Although the curves of Figure 51 were determined from specific values for the Datcom variables, their general behavior will not be altered by changes in the values of these variables. For example, an increase in $\frac{\ell_N}{d_m}$, $\frac{\ell_s}{d_m}$, or $\frac{\ell_T}{d_m}$, or any combination of these three, while the original values of all the other variables are maintained, will widen the body transition zone, as transition on the fins will now occur at a higher value of R_ℓ (although R_{crit} remains unchanged). Furthermore, $(C_{D_0})_B$ and $(C_{D_0})_{FB}$ will be shifted slightly upwards, while C_{Db} will be decreased everywhere. Figure 51 thus presents the correct shape of the drag coefficient vs. Reynolds number curves for

any model rocket which can be represented (even approximately) by some variation of the GCR. This category includes a great many slender ($\frac{l_b}{d_m} \geq 5$) single-staged model rockets.

To determine the drag coefficient as a function of velocity U_∞ , it is required to know only the values of ν and l_b . While ν does vary somewhat with altitude as discussed in Section 2.1, one may reasonably assume a constant value of $\nu = 1.495 \times 10^{-5}$ meter²/second, giving

$$(207) \quad U_\infty = \frac{1.495 \times 10^{-5}}{l_b} R_e$$

Multiplying the abscissa R_e of Figure 51 by $\frac{1.495 \times 10^{-5}}{l_b}$ converts the Reynolds number axis to a velocity axis, measured in meters/second. For a rocket of 30 centimeters length,

$$U_\infty = 4.975 \times 10^{-5} R_e$$

The body transition zone will then begin at an airspeed of 24.9 meters/second, and if the rocket has the same geometric proportions as the GCR-x, fin transition begins at 256 meters/second.

In general, obtaining a plot of drag coefficient versus Reynolds number, as in Figure 51, requires a considerable amount of calculation. This work cannot be avoided if maximum accuracy is desired, as for theoretical predictions of altitude. As the following section will show, however, it is possible to choose a single value of the drag coefficient (C_{D_0})_{FB} which, if used in performance calculations, yields a good approximation to the "exact" behavior predicted by the Datcom method.

6.3.3 Dependence of the Drag Force on Reynolds Number for the General Configuration Rocket

The drag force D is expressed in terms of the drag coefficient as

$$(208) \quad D = \frac{1}{2} \rho U_{\infty}^2 C_D S_m$$

To eliminate S_m and U_{∞} , we write

$$S_m = \frac{\pi d_m^2}{4}$$

and

$$U_{\infty}^2 = \frac{R_e^2 \nu^2}{l_b^2}$$

Then

$$D = \frac{1}{2} \rho \left(\frac{R_e^2 \nu^2}{l_b^2} \right) C_D \left(\frac{\pi d_m^2}{4} \right)$$

and finally

$$(209) \quad D = \left[\frac{(\pi/8) \rho \nu^2}{(l_b/d_m)^2} \right] C_D R_e^2$$

Since C_D is known as a function of R_e from a plot like that of Figure 51, compiled from Datcom calculations, it is possible to determine the behavior of the drag force as a function of R_e using equation (209). Assuming $\nu = 1.495 \times 10^{-5}$ meter²/second and $\rho = 1.225$ kilograms/meter³ (sea-level atmosphere), and $\frac{l_b}{d_m} = 18$ as for the GCR-X, we have

$$(210) \quad D = 3.33 \times 10^{-13} C_D R_e^2$$

for the drag force in newtons.

The column headed D_e in Table 7 summarizes the results

TABLE 7

R	D _e (N)	D _a (N)	Percent error
1 x 10 ⁴	1.03 x 10 ⁻⁴	1.57 x 10 ⁻⁵	-84.6
5 x 10 ⁴	1.16 x 10 ⁻³	3.94 x 10 ⁻⁴	-66.2
7 x 10 ⁴	1.94 x 10 ⁻³	7.70 x 10 ⁻⁴	-60.1
1 x 10 ⁵	3.33 x 10 ⁻³	1.57 x 10 ⁻³	-52.6
1.5 x 10 ⁵	6.18 x 10 ⁻³	3.53 x 10 ⁻³	-42.7
2 x 10 ⁵	9.55 x 10 ⁻³	6.31 x 10 ⁻³	-33.9
3 x 10 ⁵	1.77 x 10 ⁻²	1.42 x 10 ⁻²	-20.0
4 x 10 ⁵	2.77 x 10 ⁻²	2.51 x 10 ⁻²	-9.4
5 x 10 ⁵	3.94 x 10 ⁻²	3.94 x 10 ⁻²	0.0
6 x 10 ⁵	5.74 x 10 ⁻²	5.65 x 10 ⁻²	-1.5
7 x 10 ⁵	7.80 x 10 ⁻²	7.70 x 10 ⁻²	-1.1
8 x 10 ⁵	1.02 x 10 ⁻¹	1.01 x 10 ⁻¹	-1.3
9 x 10 ⁵	1.28 x 10 ⁻¹	1.27 x 10 ⁻¹	-0.2
1 x 10 ⁶	1.56 x 10 ⁻¹	1.57 x 10 ⁻¹	0.9
1.25 x 10 ⁶	2.39 x 10 ⁻¹	2.46 x 10 ⁻¹	2.9
1.5 x 10 ⁶	3.39 x 10 ⁻¹	3.53 x 10 ⁻¹	4.2
1.75 x 10 ⁶	4.50 x 10 ⁻¹	4.82 x 10 ⁻¹	7.0
2 x 10 ⁶	5.82 x 10 ⁻¹	6.31 x 10 ⁻¹	8.4
2.2 x 10 ⁶	6.89 x 10 ⁻¹	7.63 x 10 ⁻¹	10.8
2.4 x 10 ⁶	8.05 x 10 ⁻¹	9.09 x 10 ⁻¹	12.4
3 x 10 ⁶	1.21	1.42	17.3
4 x 10 ⁶	2.05	2.51	22.8
5 x 10 ⁶	3.07	3.94	28.0
6 x 10 ⁶	4.45	5.65	27.1
8 x 10 ⁶	8.31	10.1	21.0
1 x 10 ⁷	13.2	15.7	19.6

Table 7: Comparison of the "exact" drag force in newtons on the GCR-X rocket, calculated using the variable drag coefficient obtained from the Datcom equations, with the approximate drag force calculated on the assumption of $(C_{D0})_{FB} = 0.473$ at various Reynolds numbers.

obtained from equation (210) over the Reynolds number range 1×10^4 through 1×10^7 . For Reynolds numbers up to about 1×10^5 , the drag force is very small compared with either the rocket weight (very few model rockets weigh less than 0.25 newton at liftoff) or the thrust levels commonly encountered in model rocket engines. The drag force is so minute in this flight regime that in the graphical representation of the data shown in Figure 52, no distinction between values of the drag force predicted by equation (210) and by the assumption of a constant C_D can be seen.

The reason for this behavior is that, although $(C_{D0})_{FB}$ is very large for values of $R\ell$ less than 10^5 , the quadratic dependence of the drag force on the Reynolds number drives D downwards as $R\ell$ decreases. Since the laminar skin-friction coefficient is inversely proportional to the square root of $R\ell$, $(C_{D0})_{FB}$ cannot increase rapidly enough to offset this effect.

As the Reynolds number increases into the body transition zone, the drag force climbs rapidly, experiencing a tenfold increase between $R\ell = 6 \times 10^5$ and $R\ell = 2 \times 10^6$. Plotted along with the "exact" function D_e in Figure 52 is an approximating function for the drag D_a , derived from equation (210) by assuming the drag coefficient to be constant over the entire Reynolds number range. The value I have elected to choose for this constant is the value of $(C_{D0})_{FB}$ at the initiation of Phase 2 flight, or $R\ell = 5 \times 10^5$. From Table 6 we read this as $(C_{D0})_{FB} = 0.473$, so

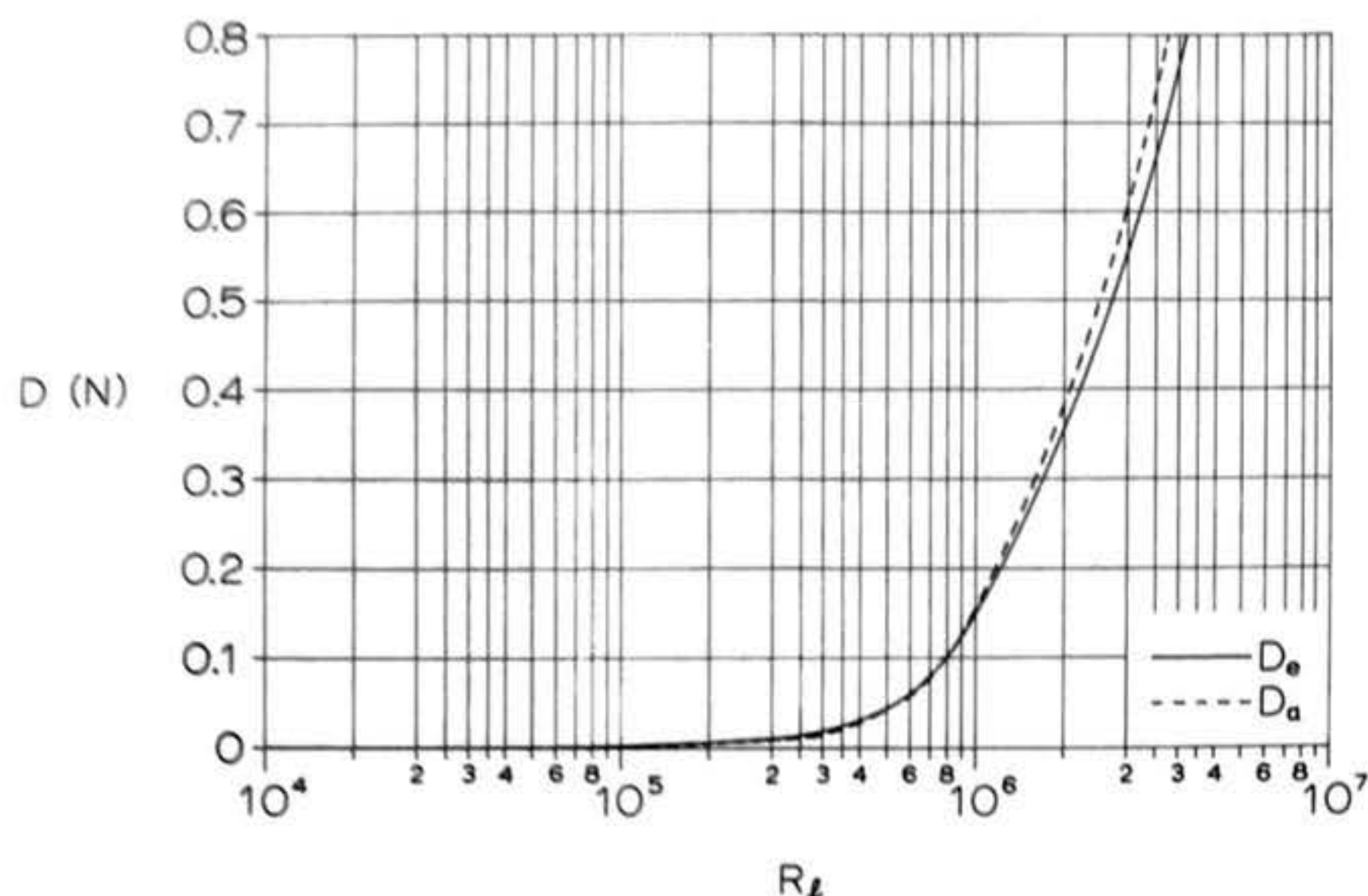


Figure 52: Variation of drag force in newtons with Reynolds number for the GCR-x rocket. D_e is the "exact" drag obtained using the variable drag coefficient computed by the Datcom method; D_a is the approximate drag obtained by taking $(C_{D0})_{FB}$ as 0.473.

$$(211) \quad D = 1.58 \times 10^{-13} R_\ell^2$$

gives the approximate drag force in newtons.

From inspection of Table 7, it may be seen that this function approximates D_e quite closely over the range of Reynolds numbers of interest in model rocket flight, deviating less than 10% from the exact function for Reynolds numbers between 4×10^5 and 2.2×10^6 . Furthermore, although the percentage error is large below $R_\ell = 4 \times 10^5$ (as C_D attains large values in the exact calculation), the absolute magnitude of the drag force is so small that these deviations are insignificant in the calculation of model rocket performance. It is not necessary to know whether the drag force is 1/1000 of a newton or 2/1000 of a newton when the thrust and weight of the vehicle are both three or four orders of magnitude greater than these values.

At higher Reynolds numbers -- that is, R_ℓ greater than 5×10^5 -- D_a represents a good approximation to the actual drag force because, as we saw in Figure 51, the drag coefficient is very nearly constant in the body transition zone. The value of $(C_{D0})_{FB}$ at $R_\ell = 5 \times 10^5$ was chosen as the approximate, constant C_D for the calculations on which Table 7 and Figure 52 are based for two major reasons: first, because $R_\ell = 5 \times 10^5$ may be considered to represent the onset of body transition for all model rockets, regardless of configuration; and second, because the exact magnitude of the drag is obtainable from this value of C_D to within 10% up to Reynolds numbers in the neighborhood of 2.2×10^6 , very nearly the practical limit of R_ℓ .

encountered during the flight of small- to moderate-sized model rockets.

This result can be stated in the form of a semiempirical rule: for single-staged model rockets not expected to exceed a Reynolds number of about 3×10^6 in flight, the assumption of a constant C_D with a value equal to that attained at $R\varrho = 5 \times 10^5$ yields acceptable estimates of performance when used in closed-form altitude calculations requiring the assumption of a constant C_D .

The Reynolds number axis of Figure 52, like that of Figure 51, can be converted to a velocity axis by applying the coordinate transformation given in equation (207).

7. Model Rocket Drag at Transonic and Supersonic Speeds

7.1 Limits on the Applicability of Incompressible Analysis

As stated in Section 2.1.1, the results of the analyses and semiempirical treatments contained in the first six sections of this chapter can be assumed accurate on an *a priori* basis only if the compression of the atmosphere due to the airspeed of the model is relatively slight. The reader may also recall from this discussion that the analytical criterion of "sufficiently slight" compression corresponds to a Mach number M of less than 0.316, where

$$(212) \quad M = \frac{U_\infty}{c}$$

and c is the speed with which sound waves travel through the air: the so-called "speed of sound".

Strictly speaking, the Mach number associated with a given

airspeed varies with atmospheric conditions, since c itself varies with atmospheric composition and temperature. In this connection you may again wish to consult Figure 4, which shows the variation of sound speed with altitude for the United States standard atmosphere. The dependence of c upon local temperature is given by

$$(213) \quad C = C_{\text{std}} \sqrt{\frac{T}{T_{\text{std}}}}$$

where T_{std} is the standard atmospheric temperature at the altitude in question and T is the actual temperature at that altitude at the time in question, and where the temperatures must be measured on one of the absolute scales, Rankine or Kelvin. It is found from Figure 4 and equation (213), however, that the speed of sound varies only slightly -- a few percent at most -- over the range of temperatures for which it is practical to launch model rockets and over the range of altitudes present-day models can achieve. It is therefore reasonable to assume that c remains constant at its sea-level standard value of about 340 meters/second for all calculations of interest to model rocketeers. The maximum airspeed at which the results obtained from incompressible-flow theory can be considered analytically valid is therefore approximately 107 meters/second.

Above this speed the influence of compressibility on the flow about the rocket makes its presence known through a number of phenomena. The air in the vicinity of the stagnation points at the tip of the nose and the leading edges of the fins, as well as the air within the boundary layer, increases noticeably in density. The boundary layer thickens and its velocity

profile becomes altered. The fins behave as if their aspect ratio were lower than ^A which is geometrically the case. A precise, analytical description of the effects of each of these phenomena upon the overall drag of the model would fill a book by itself. It is not our purpose to present such a treatment here, as the mathematics involved are quite a bit more complex than those by which we have been able to treat incompressible flow. Furthermore, only a small portion of the vast literature that has grown up around the study of compressible fluid flow is of appreciable interest to model rocketeers. What is of interest to us as designers of high-performance model rockets is the experimentally-observed fact that the overall drag coefficient of a finned body of revolution, such as a model rocket, does not exhibit any appreciable deviation from the value predicted by incompressible flow theory at Mach numbers below 0.9. It is Nature's gift to the designer that the various compressibility phenomena interact in such a manner as to make this true. Although the results of incompressible flow theory are not analytically valid above $M = 0.316$, therefore, they are numerically accurate up to $M = 0.9$ and may thus be used without modification in closed-form performance calculations. In short, the effects of compressibility on the drag coefficient of a model rocket are negligible at airspeeds up to approximately 306 meters/second.

7.2 Drag Divergence

As a model rocket approaches "Mach one" -- the speed of sound -- regions form near the nose tip and the fin leading

edges in which the air is highly compressed over a relatively short distance. In a similar manner, regions form near the fin trailing edges and the body tube base in which the air expands again to fill the partial void left by the rocket's passage. This behavior is associated with the fact that the speed of sound in a fluid is the speed with which fluid elements can transmit information to one another. As a body travelling through the fluid approaches the sonic velocity the fluid directly in front of it cannot "inform" the fluid further upstream that the body is approaching in time for the upstream fluid elements to move smoothly aside to let the body pass (as they do in subsonic flight). The upstream elements therefore "pile up" on one another and become crushed, or compressed, against the nose tip and the fin leading edges of a model rocket entering the transonic flight regime. Once the model has passed by, the compressed fluid elements endeavor to return to their original volume, thus undergoing a rapid expansion.

At a Mach number of 1.0 the region of compression at the nose becomes a thin surface normal to the longitudinal axis of the rocket, called a normal shock. As M increases above 1.0 the compression region becomes conical, with the cone half-angle decreasing as the Mach number increases: a three-dimensional oblique shock. The surface bounded by the oblique shock trailing from the nose of a supersonically-flying body of revolution is called the Mach cone; in cases of horizontally-flying airplanes this cone may intersect the ground, causing observers to hear the so-called sonic boom. In addition, any sound produced by the body itself can only be heard within the Mach cone; to an

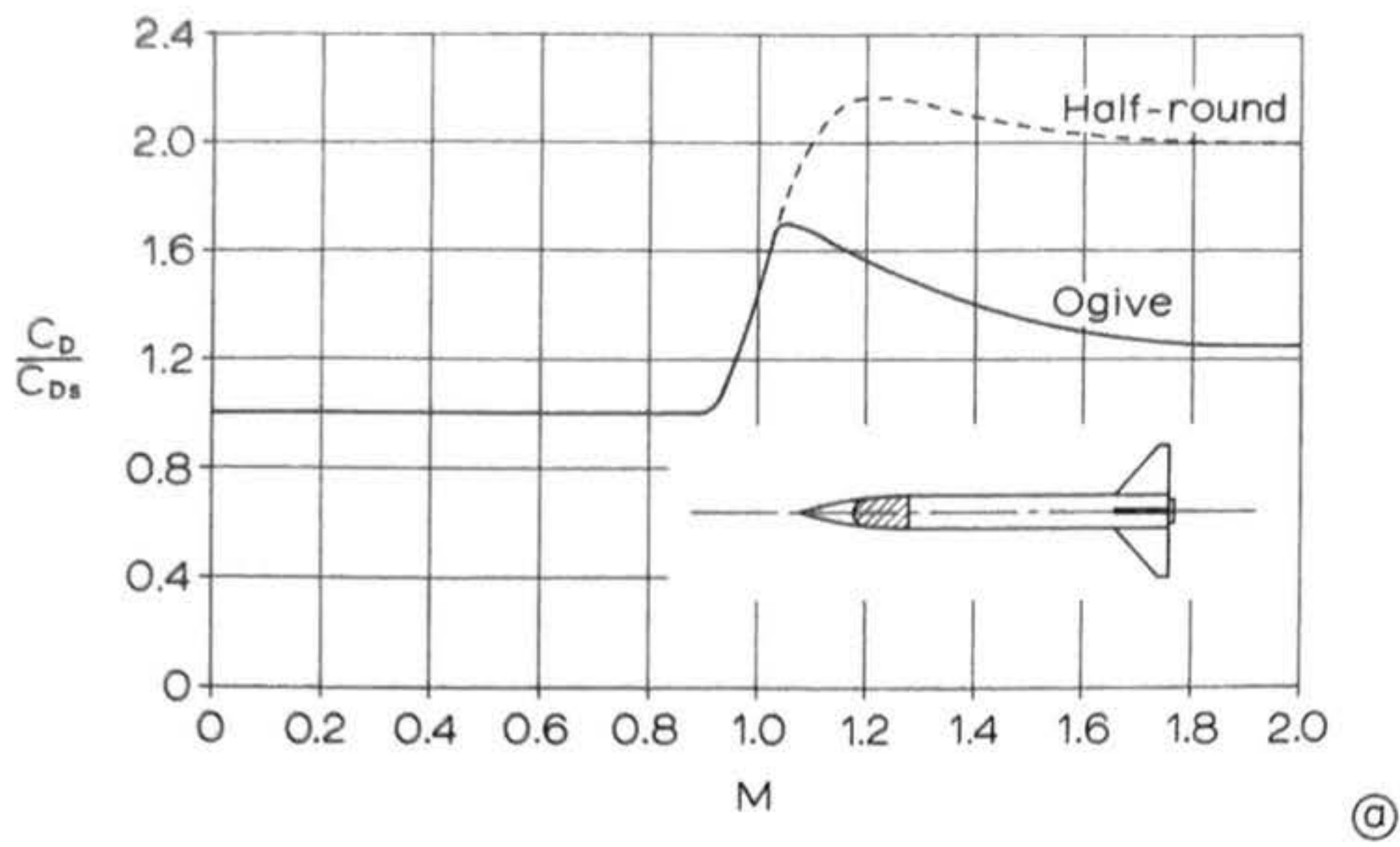
observer outside the cone the vehicle appears to be flying in perfect silence. For this reason a supersonic airplane can only be heard after it has already passed overhead, and an observer on the ground must "lead" the sound (i.e., look ahead of it) in order to see the aircraft. The expansion of the atmosphere into the region behind a model rocket in supersonic flight occurs with a very rapid decrease in density, exhibiting a characteristic flow pattern known as the Prandtl-Meyer expansion fan.

Now the importance of these phenomena to model rocket drag is that the air which passes through the shock and expansion pattern surrounding the model is not returned completely to its original state once the rocket has gone by. The shock/expansion system causes a certain amount of momentum to be transferred from the model to the airstream over and above the quantity that would be transferred under subsonic conditions. The drag coefficient of a model rocket in transonic and supersonic flight is therefore greater than its subsonic drag coefficient. Typically, C_D increases rapidly as Mach 1.0 is approached, reaches a peak at slightly above the sonic velocity, and declines again toward a value that is somewhat greater than the subsonic drag coefficient as the Mach number increases toward 2.0. The rapid increase experienced in the transonic regime, between $M = 0.9$ and the Mach number at which the peak C_D occurs, is called drag divergence. The existence of drag divergence is one reason that it was common to call Mach one "the sound barrier" before the rocket-powered Bell X-1 airplane first exceeded it in 1947, and for some years thereafter. Drag divergence also

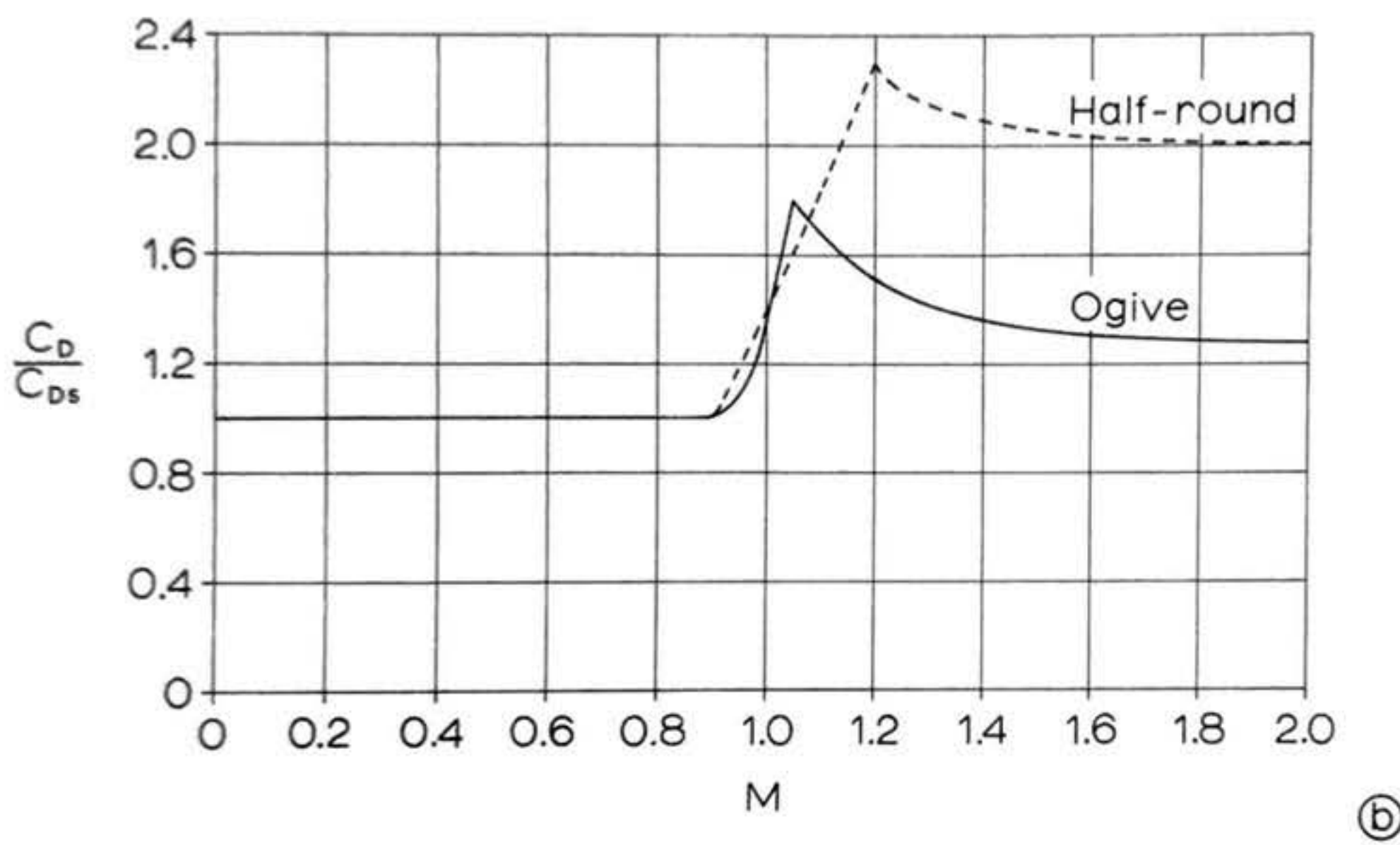
means that it is extremely difficult for small vehicles of limited total impulse, such as model rockets, to exceed Mach one. Only our very highest-performance designs can accomplish this feat, and then only when powered by the highest-thrust model rocket engines available -- types B14, F67, F100, and so on -- and even then resort must often be had to multiple staging.

7.3 Semiempirical Determination of Transonic and Supersonic Drag Coefficients

The mathematical complexity associated with the analysis of compressible fluid flow about a finned body of revolution is too great to permit the practical calculation of transonic and supersonic drag coefficients directly from first principles. As was the case for subsonic flight, we must have recourse to semiempirical formulae based on experimental data in order to obtain values of C_D for use in model rocket performance calculations. Hoerner (9) presents drag coefficient data for a number of small fin-body combinations tested at transonic and supersonic velocities. As shown in Figure 53a, the test results fall into two distinct categories: one containing rockets having sharp (ogival or conical) noses, and one comprised of models having rounded nose shapes. For the sharp-nosed rockets the drag coefficient C_D rises to 1.7 times its subsonic value (denoted C_{Ds}) at $M = 1.05$ and then declines again to about $1.27 C_{Ds}$ as M approaches 2.0. The round-nosed configuration is more severely affected by compressibility: its C_D peaks at $2.17 C_{Ds}$ at $M = 1.2$ and falls back only as far as $2.0 C_{Ds}$ for M approaching



(a)



(b)

Figure 53: Variation of drag coefficient with Mach number for finned bodies of revolution. (a): Experimentally determined behavior of the drag coefficient of the rocket pictured, using both ogive and half-round noses. (b): Analytical functions described in equations (214) and (215) that approximate the experimental behavior to within 10%.

2.0. The difference in behavior between the two configuration classes is due to a fundamental difference in nature between the shock associated with a sharp nose and the shock generated by a rounded nose. The oblique shock produced by a sharp nose in supersonic flight is an attached shock; i.e., the shock appears to be shed directly from the point of the nose like a cone suspended on a pencil point. The shock due to a rounded nose, on the other hand, it itself rounded at its forward extremity and is detached: it "stands off" slightly ahead of the front surface of the nose itself. Figure 54 illustrates the difference in structure between the two shock patterns, and also the shock/expansion pattern observed in the neighborhood of the base of a blunt-based body of revolution. As there is appreciably greater momentum transfer associated with the detached than with the attached shock, the rounded-nose configurations have higher drag coefficients at transonic and supersonic velocities.

It is mathematically possible to construct formulae for the drag coefficients which will represent the curves of Figure 53a to a very high order of precision. Such a procedure is not really worth the trouble, though, since the data presented in Figure 53a are only approximate (in fact, the curves above Mach 1.5 are based on extrapolation) and their applicability to a wide range of model rocket configurations has not been established. If one takes the liberty of initially assuming a high-performance rocket configuration (which in itself is justified by the fact that only the highest-performance model rockets are in fact capable of exceeding Mach one), however, it should prove possible

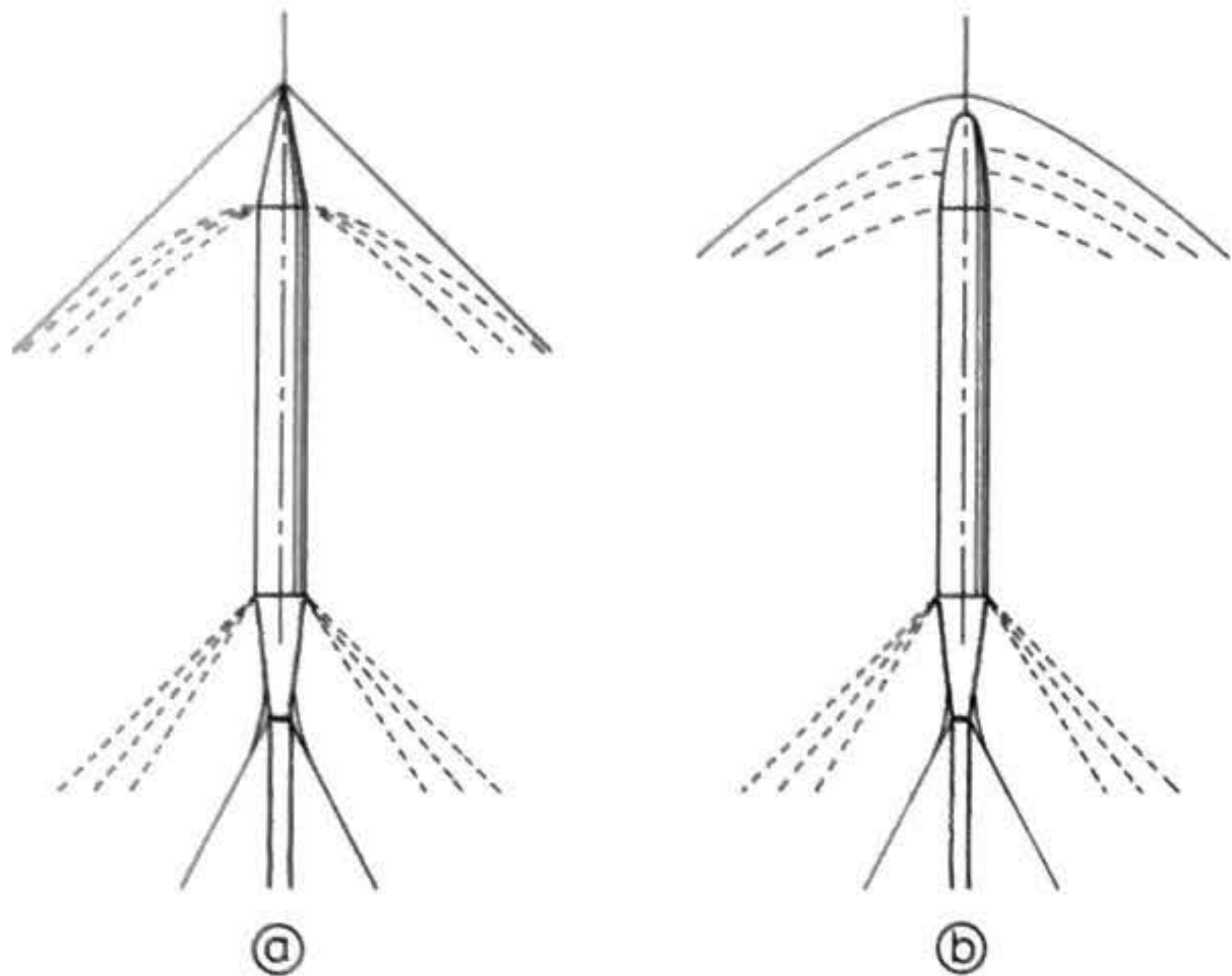


Figure 54: Shock and expansion patterns about sharp-nosed and blunt-nosed bodies of revolution. Solid lines indicate shocks and compression waves; dotted lines indicate expansion waves or fans; wavy lines delineate the wakes of the bodies. The conical nose produces an attached shock (a) which results in a lower drag than the detached shock (b) formed in front of the rounded nose.

to construct approximating functions that are relatively simple, yet will represent C_D with reasonable accuracy over the Mach number range of interest to the hobbyist.

One possible choice for such a function assumes a rise in C_D given by a power function in Mach number, followed by a decline given by an exponential in Mach number. Such a representation is referred to as piecewise smooth, since the graph obtained from such a set of formulae is a smooth curve everywhere except at the point at which the first formula leaves off and the second begins -- where there is a sharp "peak". It will be found that a reasonably accurate set of approximating functions of this type for sharp-nosed vehicles is given by

$$(214a) \quad \frac{C_D}{C_{D_s}} = 1.0 + 35.5 (M - 0.9)^2 \quad (0.9 \leq M \leq 1.05)$$

$$(214b) \quad \frac{C_D}{C_{D_s}} = 1.27 + 0.53 e^{-5.2(M-1.05)} \quad (1.05 \leq M \leq 2.0)$$

and that a similar set for round-nosed rockets may be written

$$(215a) \quad \frac{C_D}{C_{D_s}} = 1.0 + 4.88 (M - 0.9)^{1.1} \quad (0.9 \leq M \leq 1.2)$$

$$(215b) \quad \frac{C_D}{C_{D_s}} = 2.0 + 0.3 e^{-5.75(M-1.2)} \quad (1.2 \leq M \leq 2.0)$$

These approximating functions are displayed in Figure 53b and compared with the experimental data curves in Table 8. Inspection of Table 8 reveals that even these relatively simple functions predict C_D values within 10% of those determined by experiment over the Mach number range 0.9 through 2.0.

I cannot emphasize strongly enough, however, that you should not regard equations (214) and (215) as having any valid basis in mathematical physics, or as having a precision anywhere

TABLE 8

Ogive Nose

M	$\left[\frac{C_D}{C_{Ds}} \right]_e$	$\left[\frac{C_D}{C_{Ds}} \right]_a$	Percent error
0.90	1.00	1.000	0.00
0.95	1.17	1.089	-6.92
1.00	1.43	1.355	-5.25
1.05	1.70	1.800	5.56
1.10	1.67	1.680	0.60
1.20	1.57	1.513	-3.63
1.40	1.40	1.356	-3.14
1.60	1.30	1.300	0.00
1.80	1.27	1.281	0.84
2.00	1.27	1.274	0.31

Half-Round Nose

M	$\left[\frac{C_D}{C_{Ds}} \right]_e$	$\left[\frac{C_D}{C_{Ds}} \right]_a$	Percent error
0.90	1.00	1.000	0.00
0.95	1.17	1.182	1.03
1.00	1.43	1.389	-2.86
1.05	1.76	1.610	-8.50
1.10	2.00	1.830	-8.50
1.20	2.17	2.300	6.00
1.40	2.10	2.095	-0.24
1.60	2.03	2.030	0.00
1.80	2.00	2.010	0.48
2.00	2.00	2.003	0.15

Table 8: Comparison of the analytical drag divergence functions $(C_D/C_{Ds})_a$ given in equations (214) and (215) with the experimentally observed drag divergence functions $(C_D/C_{Ds})_e$ for rockets with ogive and half-round noses at Mach numbers between 0.9 and 2.0.

near that of the Datcom equations for subsonic flight. The tenuous nature of the connection between the experimental data and the actual flight of model rockets, and the extent to which I have extrapolated the data curves, is such that the best that can be said of equations (214) and (215) is that they represent reasonable suggestions of the behavior of model rocket drag coefficients at transonic and supersonic speeds. They are to be used with the understanding that they are tentative and with the provision that they are acceptable for use only until better approximations are available. At present, however, they may be considered accurate enough for design study and altitude prediction work.

Finally, the reader should realize that the behavior of the drag coefficient at these high velocities presents us with a fundamental analytical difficulty in carrying out performance calculations. Since C_D in this flight regime is a strongly-varying function of Mach number, and hence of velocity, a constant, average value of C_D cannot be used in computing altitude performance. This precludes the use of any of the closed-form, analytical altitude-performance equations presented in Chapter 4 and makes the use of computerized interval methods essential in calculating the performance of any model rocket that is expected to enter the transonic and/or supersonic range of velocities at any time during its flight.

8. Experimental Determination of Drag Coefficients

All the material presented thus far in this chapter has dealt with the theoretical or semiempirical prediction of

model rocket drag coefficients. In order to determine the accuracy of the drag coefficient values obtained from such predictive calculations it is necessary to compare them to results obtained by experimental measurement. In addition, there exist designs whose shape is too complicated to permit the use of any of the analytical methods discussed in the preceding sections (the reader will recall, for instance, that even the presence of a mere launch lug forced us to use a tentative and highly speculative semiempirical rule to account for its effect). We therefore conclude this chapter with a brief discussion of three basic experimental techniques which may be used to determine the drag coefficient of any model rocket.

8.1 Wind Tunnel and Balance System

The most common experimental technique presently in use for determining drag coefficients, whether of model rockets or any other objects, is the wind-tunnel test. I will assume that readers of this volume already have some knowledge of wind tunnels, balances, and testing procedure; for the topic of wind-tunnel testing itself is a very broad one and would require far too lengthy a discussion for us to include it here. Those interested may find explanations of the various types of tunnels and balance systems, as well as information of use in designing and building wind tunnels, in an excellent book on the subject called Wind Tunnel Testing, by Alan Pope, published by John Wiley and Sons of New York in several editions over the last twenty years.

Plate 6 shows a small wind tunnel and balance system capable of testing model rockets at airspeeds up to about 19

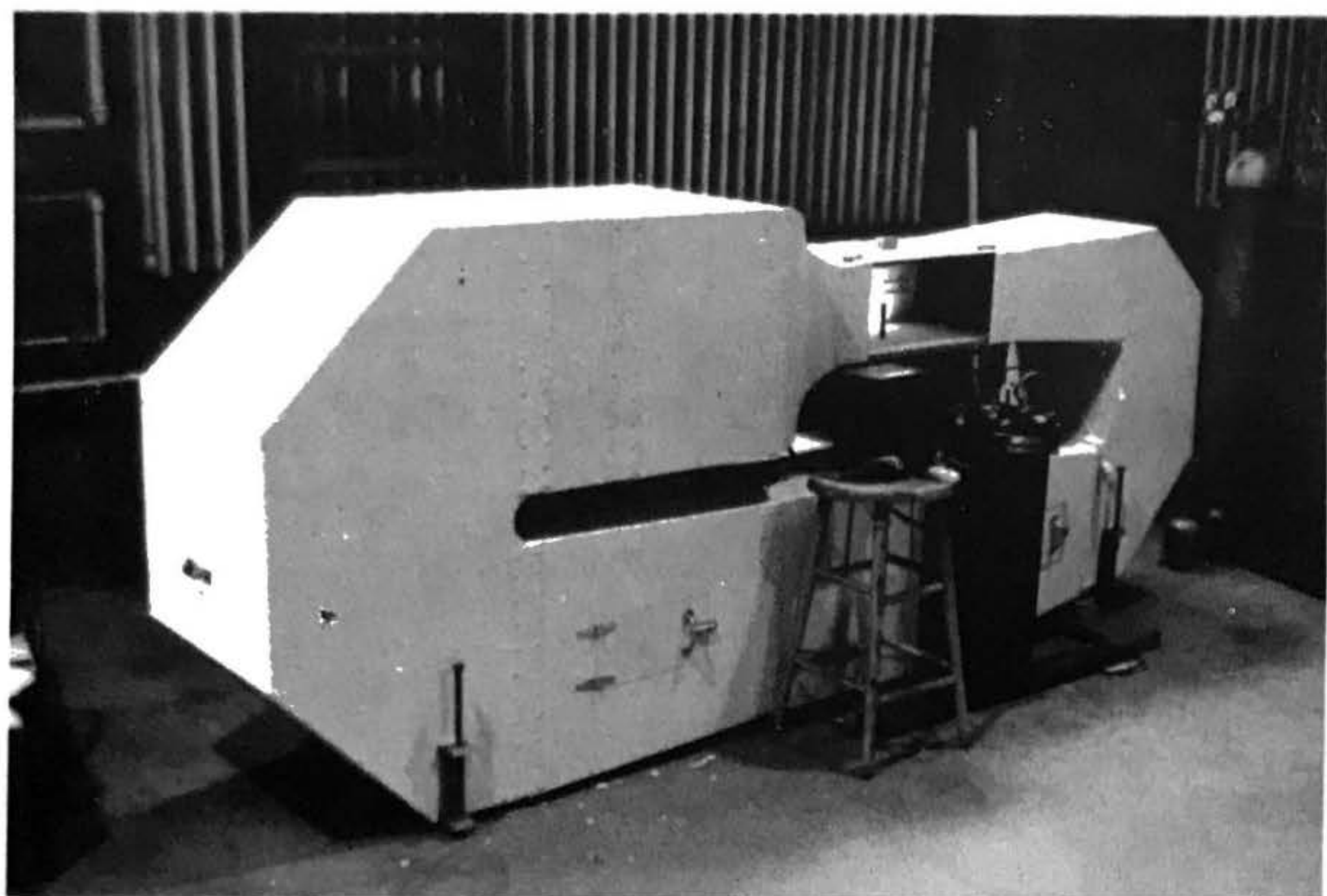


Plate 6: A small wind tunnel that can be used to measure the drag coefficient of a model rocket.

meters/second. The particular version illustrated is a return-flow tunnel of the "single-return" variety, in which the air circulates clockwise through the closed, doughnut-like duct system. It can be constructed, complete with variable-speed drive, for several hundred dollars and represents a type that can be afforded by some of the larger model rocket clubs and NAR Sections. A somewhat similar (but larger) design was used by Mark Mercer for his drag experiments. One can also construct much simpler, "open-circuit" tunnels in which the air is drawn through an intake, passes through the test section, and is expelled through a "diffuser", or exhaust. In designing any wind tunnel the greatest care must be exercised to prevent, insofar as is possible, turbulence in the airstream which passes through the test section. If too much turbulence is present the tunnel airflow will not accurately duplicate the conditions existing in free flight and the experimental results may not be accurate. Most wind tunnels thus far constructed by model rocketeers are in fact known to suffer from this problem. Another difficulty encountered by hobbyists attempting to design home-built wind tunnels involves velocity: the test-section airspeed must be high enough to provide reasonably good dynamic similarity (a Reynolds number not too different from those encountered in flight); yet, for a given test section cross-sectional area, the motor power required increases approximately as the cube of the desired airspeed! In short, the design and construction of a wind tunnel that can provide high-quality drag data is not a project to be taken lightly: it will make considerable demands on a modeler's time, skill, and finances.

Assuming that one has a wind tunnel and balance system (or access to one, as in a university), however, the drag coefficient of any model mounted on the balance can be determined by reading the drag directly from the balance indicator. The drag reading obtained must be corrected for tare (the drag of the balance support arm itself), aerodynamic interference between the model and the balance arm, and the effect of the test section walls on the airflow pattern about the model. Pope's text outlines the techniques for accomplishing these corrections with a high degree of precision (this is, however, a rather tedious task and many hobbyists prefer simply to subtract the tare drag from the total drag reading, a procedure which still permits determinations of C_D to within 5% in most cases). The drag coefficient is then found from the corrected drag using the equation

$$(216) \quad C_D = \frac{D}{\frac{1}{2} \rho S_m U^2}$$

where the test-section velocity U is that which has been measured on the velocity-indicating manometer. In a good wind tunnel the airspeed can be varied from zero to the maximum of which the tunnel is capable at will, by using an electrical or hydraulic control.

The performance calculations of Chapter 4 use a drag parameter k , given by

$$(217) \quad k = \frac{1}{2} \rho S_m C_D$$

rather than the drag coefficient C_D explicitly, in determining velocity and altitude. This drag parameter can be determined

from the corrected drag as just

$$(218) \quad k = \frac{D}{U^2}$$

8.2 Vertical Wind Tunnel

A number of prominent modelers have suggested the construction of a vertical wind tunnel; that is, one in which the test-section airstream travels directly upward. Such a design has the advantage of not requiring a balance system, since the airspeed can be adjusted until the model is suspended motionless in the center of the test section. The drag is then just equal in magnitude to the model's weight:

$$(219) \quad D = k U^2 = mg$$

so

$$(220) \quad k = \frac{mg}{U^2}$$

where m is the mass of the model and g is the acceleration of gravity. In MKS (meter-kilogram-second) units, m is given in kilograms and g is 9.8 meters/second². The drag coefficient, if desired, can be extracted from the drag parameter using the relation

$$(221) \quad C_D = \frac{k}{\frac{1}{2} \rho S_m}$$

The vertical tunnel concept does have some drawbacks. For one thing, fairly high velocities -- 50 to 75 meters/second or even more -- will be required to make the drag of a high-performance model rocket equal its weight. The required velocity can be

reduced by constructing a light test model and leaving out the engine, but the vertical wind tunnel will still need quite a lot more power than a standard, horizontal design using a balance. There may also be problems in maintaining the model's position within the test section, and the testing technique can only determine drag at a zero angle of attack.

8.3 Vertical Drop Test

It has also been noted that the drag parameter of a model can be determined without a wind tunnel, by measuring the time taken by the model to fall a specified distance when released from rest in a nose-down attitude. The relationship between the time of fall and the drag parameter can be determined by solving the differential equation of the rocket's motion, which is just Newton's second law for an object of constant mass:

$$(222) \quad \vec{F} = m \vec{a} = m \frac{d\vec{U}}{dt}$$

Where \vec{F} is the vector sum of the forces acting on the object and \vec{a} is its acceleration. If we adopt the convention that force, acceleration, velocity, and displacement are all to be considered positive downward we have for the falling rocket

$$(223) \quad m \frac{dU}{dt} = mg - k U^2$$

This equation can be solved for time as a function of velocity:

$$(224) \quad t = \int_0^v \frac{du}{g - \frac{k}{m} u^2}$$

The integral on the right-hand side of (224) is known to have the form

$$(225) \quad t = \sqrt{\frac{m}{gk}} \tanh^{-1} \left[U \sqrt{\frac{k}{mg}} \right]$$

from which, by algebraic manipulation and the use of inverse functions, we obtain

$$(226) \quad U = \sqrt{\frac{mg}{k}} \tanh \left[t \sqrt{\frac{gk}{m}} \right]$$

Since the hyperbolic tangent function approaches 1.0 for time approaching infinity, the terminal velocity of the falling model is seen to be $\sqrt{\frac{mg}{k}}$ -- the same velocity required to suspend the model motionless in the vertical wind tunnel.

Letting the displacement, or distance fallen, be denoted by x , and recognizing that $U = dx/dt$, we have

$$\frac{dU}{dt} = \frac{dU}{dx} \frac{dx}{dt} = U \frac{dU}{dx}$$

Then equation (223) can be written

$$(227) \quad mU \frac{dU}{dx} = mg - kU^2$$

and solved for x as follows:

$$(228) \quad x = \int_0^U \frac{U dU}{g - \frac{k}{m} U^2}$$

performing the integration, we have

$$(229) \quad x = -\frac{m}{2k} \ln \left[1 - \frac{k}{mg} U^2 \right]$$

Note that the argument of the natural logarithm function is always less than one; hence the logarithm itself is a negative number and x is a positive quantity, as it should be, indicating downward displacement. By substituting the right-hand side of equation (226) for U we obtain the desired functional relationship

between displacement and time:

$$(230) \quad x = -\frac{m}{2k} \ln \left[1 - \tanh^2 \left(t \sqrt{\frac{gk}{m}} \right) \right]$$

Again, x will be found positive for all positive values of t .

Equation (230) can be used in conjunction with computerized calculation methods to compile graphs which display time as a function of the variable (k/m) for various values of the "drop distance" x . One such "drop chart" is shown in Figure 55. Inspection of the chart reveals that a fairly sizeable drop distance is required to enable the determination of (k/m) , and hence k , to a reasonable accuracy, since the velocity must be allowed to increase to the point at which drag has a significant influence on the model's behavior. The minimum distance needed for an accurate determination decreases as (k/m) increases, but something on the order of 10 meters seems to be the limit for any reasonable test model -- even if it is of lightweight construction and dropped without its engine. This means that a tower or building of some sort must be used for drop testing, and that the model must be cushioned at the end of its fall to avoid damage. Not all models can be tested in this manner; no amount of cushioning, for instance, can protect a model of the Saturn-V. The drop test, like the vertical wind tunnel, is suitable only for determining the drag parameter at a zero angle of attack -- but it also eliminates the need for a balance system and has the added advantage that the test takes place in the open air, so that there are no tunnel wall effects.

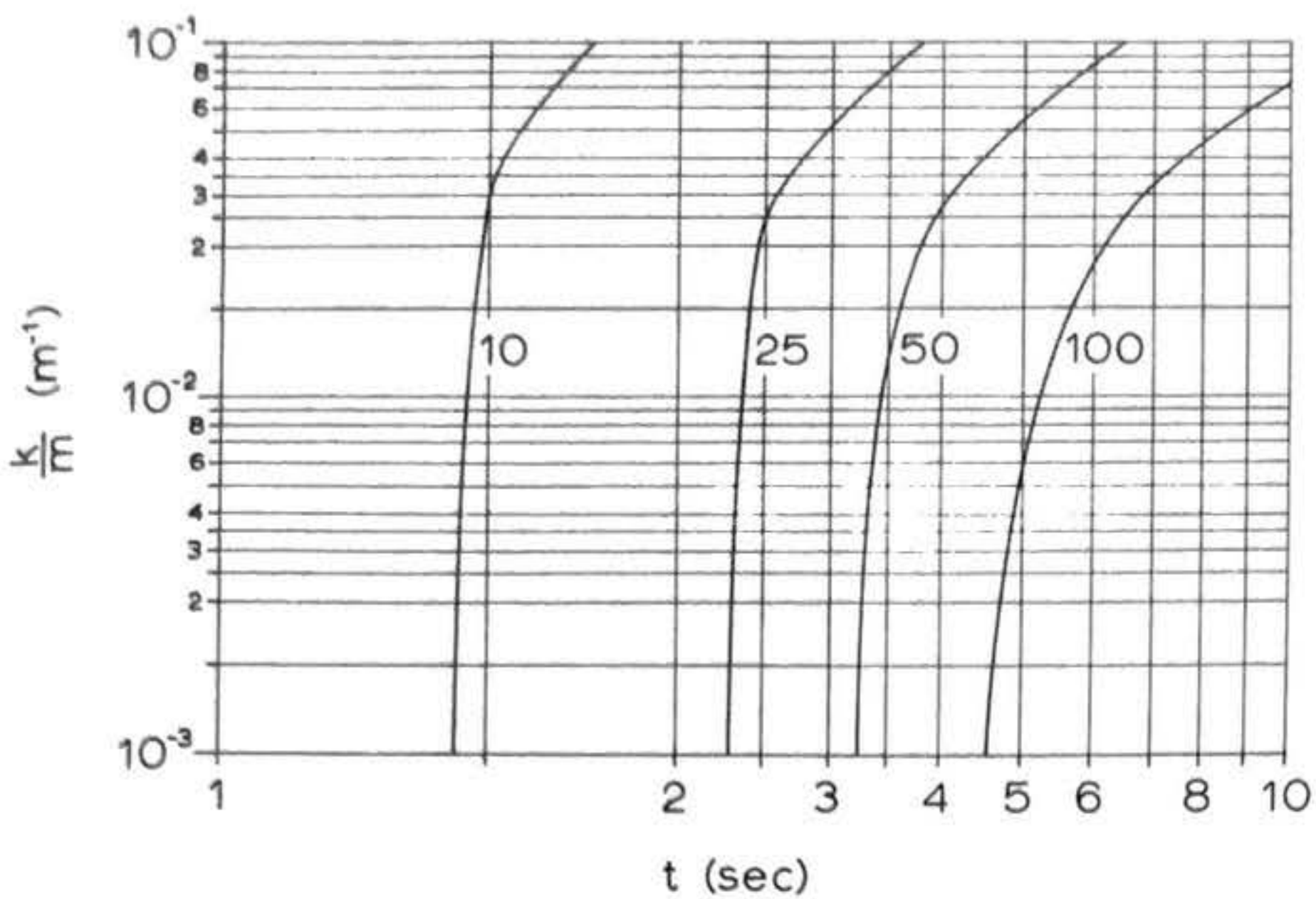


Figure 55: A "drop chart" of the type that might be used in determining the drag parameter k of a model rocket from vertical drop tests. Curves are presented for drop distances of 10, 25, 50, and 100 meters. The curves flatten at the top because k/m becomes great enough for the rocket to attain its terminal velocity within the specified drop distance, after which the drop time becomes roughly proportional to $\sqrt{\frac{k}{m}}$. For the smaller drop distances accurate determinations of k cannot be made without extremely accurate timing devices.

8.4 Conclusion

The relative merits of the three experimental techniques described above can only be properly judged at such time as all three have been tried in practice and developed to the highest level of effectiveness of which it is reasonable to believe they are capable. It is our hope that, in the near future, each of them will be tried and that an extensive experimental literature will be generated within the hobby as a result, for only a large body of reliable experimental data can permit us to verify or improve upon the techniques herein described for the analytical prediction of model rocket drag.

REFERENCES

1. Gregorek, Dr. Gerald M., A Critical Examination of Model Rocket Drag for Use With Maximum Altitude Performance Charts (photocopy of original document received by the author in 1967).
2. Barrowman, James, Calculating the Center of Pressure of a Model Rocket, Centuri Engineering Company Technical Information Report TIR-33, 1968.
3. Braslow, Albert L., and Knox, Eugene C., Simplified Method for Determination of Critical Height of Distributed Roughness Particles for Boundary-Layer Transition at Mach Numbers from 0 to 5, NACA Technical Note 4363, September 1958.
4. Brazzel, Charles E. and Henderson, James H., An Empirical Technique for Estimating Power-On Base Drag of Bodies-of-Revolution With a Single Jet Exhaust, AGARD CP-10, September 1966.
5. Compton, William B. III, Effects on Base Drag of Recessing the Bases of Conical Afterbodies at Subsonic and Transonic Speeds, NASA TN D-4821, October 1968.
6. Ellison, D.E., and Malthan, L.V., principal investigators, United States Air Force Stability and Control Datcom, Douglas Aircraft Company, Inc., October 1960, revised July 1963, Prepared under contract for the Flight Control Division, Air Force Flight Dynamics Laboratory, Wright-Patterson Air Force Base, Ohio.
7. Davis, L. Jr., Follin, James W. Jr., and Blitzer, Leon, The Exterior Ballistics of Rockets, D. Van Nostrand Company, Inc., Princeton, New Jersey, 1958.
8. Durand, Frederick W. (Ed.), Aerodynamic Theory: A General Review of Progress, Volumes I - VI, Dover Publications, Inc., New York, 1963 (unabridged republication of 1936 work).
9. Hoerner, Sighard F., Fluid-Dynamic Drag, published by the author, 148 Busteed Drive, Midland Park, New Jersey, 1958.
10. Malewicki, Douglas, Model Rocket Altitude Performance, Centuri Engineering Company Technical Information Report TIR-100, 1968.
11. Mayo, Edward E., Newtonian Aerodynamics for Tangent Ogive Bodies of Revolution, NASA TN D-3337, March 1966.

12. Prandtl, L., and Tietjens, O.G., Applied Hydro- and Aeromechanics, Dover Publications, Inc., New York, 1957 (unabridged republication of 1934 work).
13. Prandtl, L., and Tietjens, O.G., Fundamentals of Hydro- and Aeromechanics, Dover Publications, Inc., New York, 1957 (unabridged republication of 1934 work).
14. Nielsen, Jack N., Missile Aerodynamics, McGraw-Hill Book Company, Inc., New York, 1960.
15. Schlichting, Hermann, Boundary Layer Theory, 4th Edition, McGraw-Hill Book Company, Inc., New York, 1960.
16. Sedney, R., Review of Base Drag, AGARD CP-10, September 1966.
17. Shapiro, Ascher H., Shape and Flow: The Fluid Dynamics of Drag, Science Study Series, Doubleday and Company, Inc., Garden City, New York, 1961.
18. Stine, G. Harry, Handbook of Model Rocketry, Follett Publishing Company, Chicago, 1965.
19. United States Standard Atmosphere, 1962.
20. Malewicki, Douglas, "Drag Coefficient Measurements", in Model Rocketry, April 1970, Model Rocketry, Inc., Cambridge, Massachusetts, 1970.

CHAPTER 4

ELEMENTS OF TRAJECTORY ANALYSIS

George J. Caporaso



SYMBOLS

<u>Symbol</u>	<u>Meaning</u>
A, B	dummy variables used in trigonometric identities
A_f	amplitude of sinusoidal forcing
A_r	reference area
A_0	value of A_f at an airspeed of 1 meter/second
A_1, A_2	coefficients used in Riccati solution
C_D	coefficient of drag
C_1	corrective moment coefficient
C_2	damping moment coefficient
D	drag
\vec{E}	vector sum of all externally applied forces
F	average thrust
\vec{F}	force
$F(t)$	thrust as a function of time
F_m	maximum thrust
F_n	average thrust of nth stage motor
F_p	component of thrust perpendicular to trajectory
F_s	sustainer thrust
F_t	component of thrust tangent to trajectory
F_2	average thrust of second stage motor
H	function of thrust, mass, and drag parameter used in writing Riccati solution
H_x	strength of yaw impulse
H_y	strength of pitch impulse

<u>Symbol</u>	<u>Meaning</u>
I_L	longitudinal moment of inertia
I_R	radial moment of inertia
I_{sp}	specific impulse
I_t	total impulse
M_x	strength of step moment in yaw
M_y	strength of step moment in pitch
\vec{a}	acceleration
c	magnitude of exhaust velocity
\vec{c}	exhaust velocity
$d()/dt$	derivative of () with respect to time
e	base of the Napierian logarithm system, numerically equal to approximately 2.718
$f(\alpha)$	function of angle of attack
$f_x(t)$	yaw forcing function
$f_y(t)$	pitch forcing function
g	acceleration of gravity
k	parameter of drag at zero angle of attack
k_n	drag parameter of nth stage carrying all subsequent stages atop it
k_2	drag parameter of second stage
m	mass; <u>also</u> average mass
$m(t)$	mass as a function of time
m_b	burnout mass
m_f	mass of propellant charge
m_n	mass of nth stage carrying all subsequent stages atop it
m_o	initial mass
m_1	average mass of first stage carrying all subsequent stages atop it

<u>Symbol</u>	<u>Meaning</u>
m_2	average mass of second stage
\dot{m}	mass flow rate (alternate notation)
dm_e	differential of expelled mass
dm_e/dt	mass flow rate
\vec{p}	momentum
$d\vec{p}$	differential change in momentum
$d\vec{p}_E$	differential change in momentum due to the action of externally applied forces
$d\vec{p}_e$	differential quantity of momentum added to the exhaust stream by the rocket motor
t	time
t_b	burning time
t_c	coasting time
t_m	time at which maximum thrust occurs
t_n	burning time of nth stage rocket motor
t_o	time at which in-flight disturbance begins to act
t_s	time at which sustainer thrust begins
t_1	first stage burning time
t_2	second stage burning time
dt	differential of time
Δt	time increment
u	variable of transformation used in Riccati analysis
v	magnitude of velocity
\vec{v}	velocity
v_b	burnout velocity
v_n	burnout velocity of nth stage

<u>Symbol</u>	<u>Meaning</u>
v_x	horizontal component of velocity
v_y	vertical component of velocity
v_1	burnout velocity of first stage
v_2	burnout velocity of second stage
dv	differential change in velocity
Δv	change in velocity
Δv_a	actual velocity increment
Δv_t	drag-free velocity increment
x	horizontal coordinate, range
x_b	range at burnout
Δx	increment of range
\dot{x}	horizontal component of velocity (alternate notation)
$\Delta \dot{x}_a$	actual increment in horizontal velocity component
$\Delta \dot{x}_t$	drag-free increment in horizontal velocity component
y	vertical coordinate, altitude
y_b	burnout altitude
y_c	coasted altitude increment
y_n	altitude increment gained during nth stage burn
y_1	first stage burnout altitude
y_2	altitude increment gained during second stage burn
Δy	increment in altitude
\dot{y}	vertical velocity component (alternate notation)
$\Delta \dot{y}_a$	actual vertical velocity increment
$\Delta \dot{y}_t$	drag-free vertical velocity increment
α	angle of attack

<u>Symbol</u>	<u>Meaning</u>
$\alpha(t)$	angle of attack as a function of time
α_x	yaw angle
$\alpha_x(t)$	yaw angle as a function of time
α_{x0}	yaw angle at time t_0
$\Delta\alpha_x$	increment in yaw angle
α_y	pitch angle
$\alpha_y(t)$	pitch angle as a function of time
α_{y0}	pitch angle at time t_0
$\Delta\alpha_y$	increment in pitch angle
γ	average rate of mass expulsion
ϵ	parameter of drag due to angle of attack
ζ	damping ratio
θ	angle between tangent to trajectory and local vertical
θ_0	angle between direction of launch and local vertical
ρ	density of the atmosphere
ω	angular frequency in radians per second
ω_{cres}	coupled resonant angular frequency
ω_f	angular frequency of sinusoidal forcing
ω_n	natural frequency
ω_x	yaw rate
ω_{x0}	yaw rate at time t_0
$\Delta\omega_x$	increment in yaw rate
ω_y	pitch rate
ω_{y0}	pitch rate at time t_0
$\Delta\omega_y$	increment in pitch rate

<u>Symbol</u>	<u>Meaning</u>
ω_z	roll rate
ω_{z0}	roll rate at an airspeed of 1 meter/second
ω_0	value of ω_z at an airspeed of 1 meter/second
(\cdot)	derivative of () with respect to time (alternate notation)
($\cdot\cdot$)	second derivative of () with respect to time (alternate notation)
$\int [] d()$	integral of [] with respect to ()

ELEMENTS OF TRAJECTORY ANALYSIS

Introduction

The interest of model rocketeers in determining the flight paths that their models will follow, once launched, dates back to the earliest days of the hobby itself. Questions of trajectory analysis, and particularly the question of altitude capability determination, antedate all other topics in the literature of model rocketry.

The first technical report issued by the then-infant National Association of Rocketry (#TR-1, first printed in 1958), entitled "Basic Model Rocket Flight Calculations" and written by former NAR President G. Harry Stine, described a simple technique for computing the burnout velocity, burnout altitude, and maximum altitude of a model rocket under the assumptions of zero drag and a perfectly vertical flight path. The effect of drag in this treatment was allowed for by observing that a typical model rocket attains only 40 to 60 percent of the altitude calculated under the drag-free assumption. The report also contained drag data obtained from testing a model Aerobee-Hi in the subsonic wind tunnel of the United States Air Force Academy, as well as a brief discussion of the effects of nonvertical launch on a model's trajectory.

Stine observed that, to take the effects of drag into account more accurately, it would be necessary either to apply

the techniques of integral calculus or to divide the time of flight into small intervals (a tenth of a second or less each) during which the velocity of the model, and hence the drag on it, could be assumed constant. With the mass of the model approximated by a constant in each interval computable from the rate of mass expulsion, the simplified form of Newton's second law ($\vec{F} = m\vec{a}$) could then be applied to determine the acceleration, velocity, and altitude of the rocket at any time during the flight. The interval method was discussed in greater detail in Stine's Handbook of Model Rocketry, whose first edition appeared in 1965.

During the period 1958 through 1964 the interval method was virtually the only analytical tool available to model rocketeers who wished to take the effects of drag and mass variation accurately into account in computing model rocket flight paths. This technique can be quite accurate if the intervals used are sufficiently small; it provides, in fact, an exact solution "in the limit" as the intervals become vanishingly small. Unfortunately, as the size of the intervals decreases the number of intervals required to describe the entire flight increases, so that a modeler desiring a really high order of accuracy in his trajectory calculations would find himself faced with the task of performing hundreds -- or even thousands -- of calculations. Such a procedure involves a prohibitive amount of drudgery for a human being, but it is well suited to automatic computing machines that can perform the thousands of relatively simple calculations required in a matter of only a few seconds for any given rocket.

The step-by-step results obtained for the vertical upward flight of a typical model rocket as determined by an IBM 1620 computing system appeared in the first edition of the Handbook of Model Rocketry and served well to illustrate the accuracy attainable with the interval method.

Still, the user of the interval technique must either perform many hours of calculations himself or have access to and the ability to use an electronic computer for each case he desires to analyze. Since most model rocketeers do not have free access to computers or a knowledge of how to use them, this constitutes an essential practical shortcoming of the technique.

Efforts on the part of advanced model rocketeers to overcome this difficulty by using the techniques of integral calculus to derive closed-form analytical solutions (i.e., single algebraic formulae) for the burnout velocity, burnout altitude, maximum altitude, and flight path of a model rocket began about 1964, and during the period 1964-1965 Leonard G. Fehskens and Douglas J. Malewicki, working independently, succeeded in obtaining such solutions for vertical flight. Malewicki subsequently prepared his results for publication in graphical form, and they appear as technical reports published by two of the large model rocket manufacturers: Estes Industries, Inc., of Penrose, Colorado, and the Centuri Engineering Company of Phoenix, Arizona.

The present author began investigating the problems of model rocket trajectory analysis in the fall of 1965. A

number of different solutions to the equations of vertical motion were obtained between 1965 and 1968, some of the earlier work in this period being done in collaboration with Fehskens and with William P. Bengen. In this chapter I have taken the liberty of presenting all the most important results obtained during the 1965-1968 period, as well as those derived during the actual preparation of this book, both for historical completeness and because I believe the multiplicity of approaches will enhance the reader's physical insight into the problems involved. Most of the material contained in the present chapter was formally prepared for publication during 1968 and 1969, and it was during this period that the investigations into the behavior of model rockets in nonvertical flight and into the importance of altitude reduction due to dynamic oscillations were begun.

The equations describing the point-mass motion of a model rocket along its flight path, like many of the equations in this book, are differential equations and as such require either calculus or numerical techniques for their solution. As in the previous chapters, it is possible to facilitate the solutions to some extent through the use of linearization approximations, and such approximations have been used wherever they are consistent with the desired accuracy. It will be found, however, that the equations of motion contain an essential nonlinearity due to the quadratic dependence of aerodynamic drag upon velocity. The presence of this nonlinearity increases the difficulty and mathematical complexity of the solutions, necessitating the use of such techniques as the change of variable and estimation.

and truncation of integrals. All approximations and other techniques used during the derivation of solutions will be identified in the text as they are used, for the information of those advanced rocketeers who have a special interest in the mathematics involved. As has been our policy throughout the book, however, special emphasis will also be placed on the algebraic results obtained from the calculus derivations, for the practical use of modelers who are not so mathematically inclined.

1. The General Differential Equations of Motion

The general differential equations of motion for a free, ballistic rocket follow directly from the fundamental principle of classical mechanics: Newton's second law of motion. It is well to acquire a good intuitive, physical understanding of this principle before launching into the mathematical complexities involved in obtaining particular solutions to the equations of motion. I have therefore taken the liberty of presenting the following detailed derivation of Newton's second law as applied to rocket-propelled bodies:

Consider a rocket as shown in Figure 1a, at some instant of time which we shall denote as t . At this time the rocket has a mass $m(t)$ (read "m as a function of t" or simply "m of t", meaning that the mass of the rocket varies with time) and a (vector) velocity \vec{v} with respect to an observer stationary on the ground -- and therefore a vector momentum given by

$$(1) \quad \vec{p} = m(t) \vec{v}$$

The rocket will, in general, also be acted upon by a number of externally-applied forces, whose vector sum we shall denote by \vec{E} .

Now suppose we wait for some very short interval of time dt (which mathematicians call a differential of time; an interval of "infinitesimal" or "vanishingly small" duration) and observe our rocket again at time $t + dt$, when the rocket appears as in Figure 1b. We shall find that a number of changes have occurred during the interval despite its extreme brevity. For one thing, the rocket's velocity has changed by a differential increment $d\vec{v}$, so its velocity is now $\vec{v} + d\vec{v}$. For another, a differential quantity of mass dm_e has been expelled from the motor nozzle during dt , decreasing the vehicle mass to $m(t) - dm_e$. The rocket's vector momentum at time $t + dt$ is therefore

$$(2) \quad \vec{p} + d\vec{p} = [m(t) - dm_e] (\vec{v} + d\vec{v}) \\ = m(t)\vec{v} - \vec{v}dm_e + m(t)d\vec{v} - dm_e d\vec{v}$$

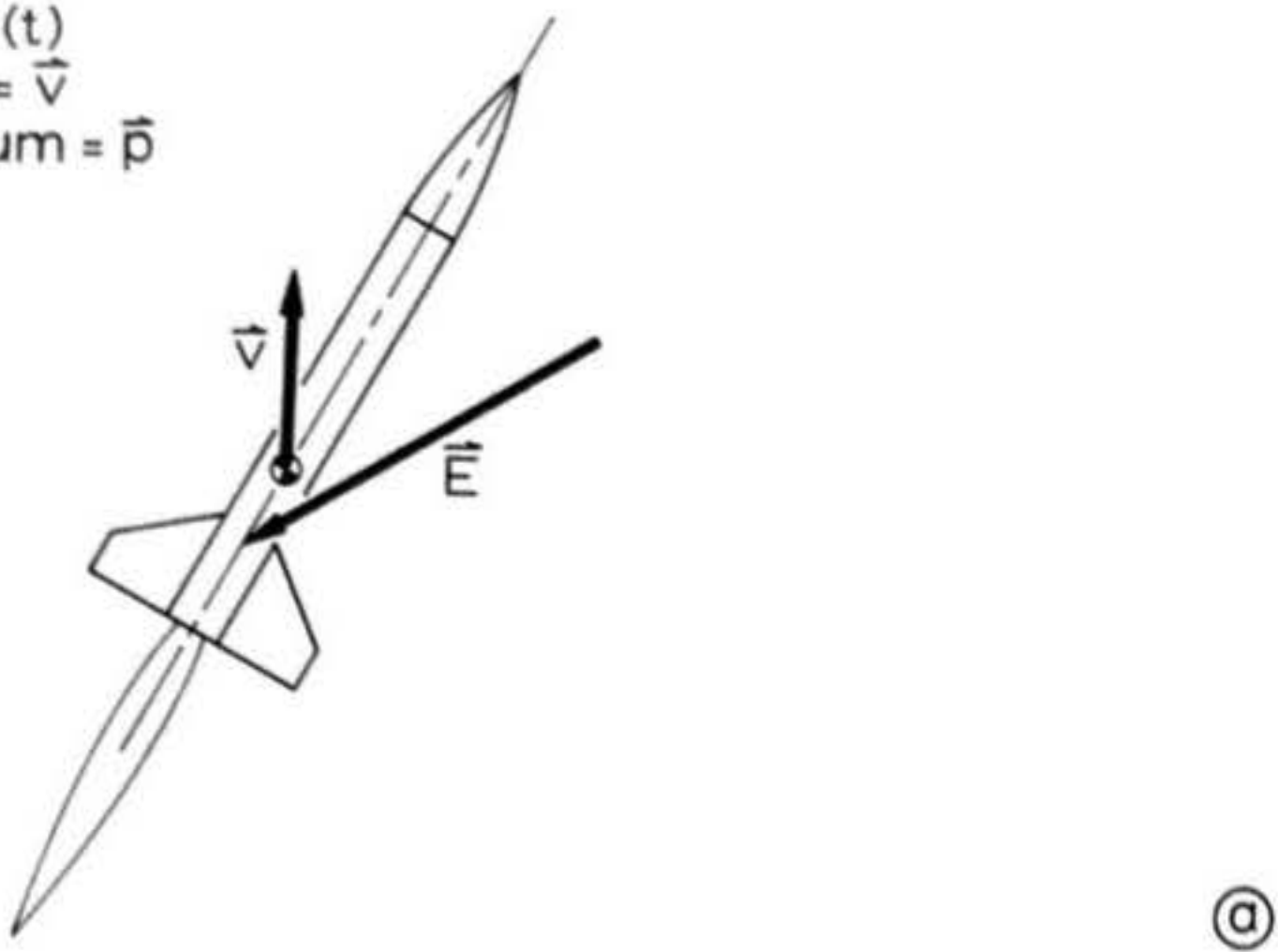
Subtracting equation (1) from (2), we find that the rocket has acquired a differential increment of momentum given by

$$d\vec{p} = m(t)d\vec{v} - \vec{v}dm_e - dm_e d\vec{v}$$

The term $dm_e d\vec{v}$ involves a product of two differential quantities and is of negligible magnitude compared to the other terms; it may therefore be discarded without loss of accuracy, resulting in

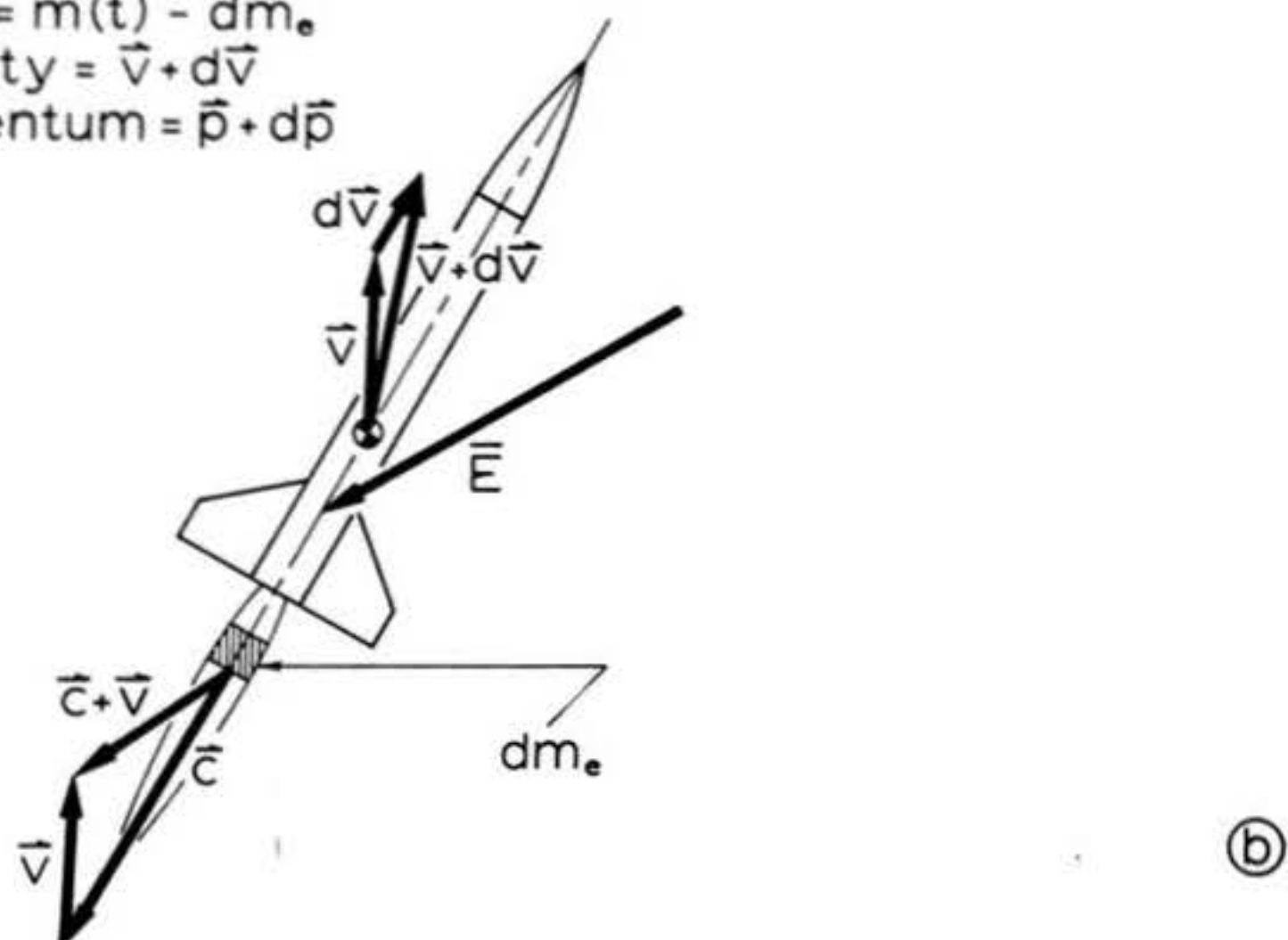
$$(3) \quad d\vec{p} = m(t)d\vec{v} - \vec{v}dm_e$$

Time = t
Rocket mass = $m(t)$
Rocket velocity = \vec{v}
Rocket momentum = \vec{p}



(a)

Time = $t + dt$
Rocket mass = $m(t) - dm_e$
Rocket velocity = $\vec{v} + d\vec{v}$
Rocket momentum = $\vec{p} + d\vec{p}$



(b)

Figure 1: Model rocket in flight, with its engine thrusting and under the influence of externally-applied forces. Panel (a) shows the rocket at time t ; (b) shows it a short time later at time $t + dt$.

Now according to classical mechanics, momentum is conserved; that is, the total momentum of the system consisting of the rocket and all its surroundings must remain constant. This being the case, the momentum increment $d\vec{p}$ must have had some quantitatively identifiable sources outside the rocket airframe itself -- and the sum total of the momentum increments contributed by these sources must precisely equal $d\vec{p}$. There are in fact two such sources in the case of the rocket: the momentum flux due to the exhaust and the action of the externally-applied forces.

As we have already noted, the rocket motor has expelled a mass increment dm_e during the interval dt . It has, moreover, expelled this mass at a high velocity -- the exhaust velocity \vec{c} with respect to the rocket, which is a velocity $(\vec{c} + \vec{v})$ with respect to our hypothetical observer standing stationary on the ground. An increment of momentum

$$(4) \quad d\vec{p}_e = (\vec{c} + \vec{v}) dm_e$$

has therefore been transferred from the rocket to the exhaust stream by the expulsion of mass from the rocket nozzle: $d\vec{p}_e$ as given by (4) has been added to the exhaust stream and subtracted from the rocket.

The vector sum of all the externally applied forces, \vec{E} , acting over the interval dt , produces an impulse $\vec{E} dt$. This impulse is equal to the momentum increment imparted by the externally applied forces to the rocket. We may then write

$$(5) \quad d\vec{p}_E = \vec{E} dt$$

Now $d\vec{p}_E$ has been added to the rocket during dt , while $d\vec{p}_e$ has been subtracted from it, and the sum total of the two effects is precisely equal to the total momentum change experienced by the rocket during the interval. That is,

$$d\vec{p} = d\vec{p}_E - d\vec{p}_e$$

or

$$(6) \quad m(t)d\vec{v} - \vec{v}dm_e = \vec{E}dt - (\vec{c} + \vec{v})dm_e$$

Collecting terms and dividing by dt , we obtain the general, vector differential equation of motion for a rocket under thrust and subject to externally-applied forces as

$$(7) \quad m(t)\frac{d\vec{v}}{dt} = -\vec{c}\frac{dm_e}{dt} + \vec{E}$$

The term $-\vec{c}(dm_e/dt)$ is just the thrust of the rocket motor as it would be measured in a static test stand. Since the exhaust velocity \vec{c} is directed backward along the longitudinal axis of the rocket it is vectorially negative with respect to \vec{v} . And since the rate of mass expulsion has been expressed as the positive mass-flow rate dm_e/dt , equivalent to \dot{m} as used by professional rocket engineers, the thrust is a positive force tending to increase \vec{v} -- which, as practical rocketeers, we already know from experience. The thrust can be denoted by the single symbol $\vec{F}(t)$, so we can write

$$(8) \quad m(t)\frac{d\vec{v}}{dt} = \vec{F}(t) + \vec{E}$$

Both the engine thrust and the externally-applied forces will be referred to as flight forces, as per the notation of Chapter 1,

in the following discussion. The externally-applied flight forces whose vector sum is here represented by \mathbf{E} will be resolved into two components: weight and aerodynamic resistance, or drag.

1.1 Mathematical Representation of the Flight Forces

The various forces acting on a model rocket in flight were described in Chapter 1. We now proceed to represent these forces as explicit functions of time, angle of attack, mass, and so on. Once these representations have been constructed the general, componentized differential equations of motion can be formed explicitly according to the general law expressed in equation (8).

The first of the flight forces to be considered will be

the thrust of the engine. The thrust is usually a rather complicated function of time, whose general form may be expressed by the functional notation $F(t)$, and in a properly designed model whose engine is functioning normally is directed along the longitudinal principal axis (centerline) of the rocket. Disturbances due to winds, misaligned fins, asymmetries, and other factors as discussed in Chapter 2 will cause the longitudinal axis of the vehicle to deviate from the tangent to the trajectory at the point of interest -- that is, such disturbances will cause the model to develop an angle of attack. Such a rigid-body rotation will thus produce components of thrust in other than the intended direction of flight, and in particular will reduce the effective thrust in the direction of the trajectory according to

$$(9) \quad F_t = F(t) \cos \alpha$$

$$(10) \quad F_p = F(t) \sin \alpha$$

where the subscripts t and p denote thrust components tangential and perpendicular to the trajectory at the point of interest, respectively, α is a generalized angle of pitch or yaw (or both), and $F(t)$ is the thrust of the engine expressed explicitly as a function of time.

Also of importance in determining the trajectory is the weight of the vehicle. The weight of a model rocket is always a function of time, as the quantity of propellant expended during the engine burning phase continuously decreases the rocket's weight. The weight vector always points in the negative vertical

(downward) direction, and may be denoted simply by $m(t)g$, where $m(t)$ is the model's mass as a function of time and g is the acceleration of the Earth's gravity field.

Perhaps the most interesting of the flight forces, and also the most difficult to handle analytically, is aerodynamic drag. As described in Chapter 3, it is a function of the model's velocity, its shape and size, the smoothness of its finish, and so on. For purposes of analytical convenience the net effect of all these various influences will be accounted for by expressing the drag force as kv^2 , as was done in Chapter 1, where the lumped parameter k is a function of Reynolds number, atmospheric density, shape, etc. The drag force is subject to the same perturbing influences as the thrust, namely the rigid-body rotations which change the cross-sectional frontal area and effective shape of the model, resulting in an increase in drag with angle of attack. The total drag force on a model flying at an angle of attack can thus be characterized as

$$(11) \quad D = (k + \epsilon f(\alpha))v^2$$

where ϵ is some constant and $f(\alpha)$ is some function of the angle of attack.

The flight forces just considered are referred to as external forces; that is, they represent net forces acting on the rocket's center of mass (for all practical purposes the center of mass is identical to the center of gravity, or C.G.). These forces interact with, and are thus said to be coupled to, the detailed dynamic moments which cause the rigid-body motions

discussed in Chapter 2. The rigid-body rotations, however, do not affect the motion of the C.G. directly; they can only influence it through their interaction with the external forces. This interaction, as discussed in Chapter 1, occurs through the increase in drag and the side force associated with changes in the angle of attack. Hence, it is sufficient to consider the forces already discussed in order to obtain a suitable representation of the rocket's point-mass motion, as we have already accounted for the interaction of the rigid-body rotations with the external forces in the terms previously considered. The increase in drag with angle of attack has already been expressed in equation (11). Side force, as can be deduced from the treatments in Chapter 2, is an oscillatory phenomenon of extremely short duration in any one transverse direction for any reasonably well-designed model rocket. It can therefore be disregarded under the same rationale by which the effects of lateral translation were neglected in Chapter 2.

1.2 Selection of the Coordinate System and Formation of the General Differential Equations of Motion

In order to write down the differential equations of motion, one must first select a suitable coordinate system with respect to which the different components of the model's motion will be taken. An exact description of the trajectory of any flying body would require taking into account the curvature and rotation rate of the Earth; spherical polar coordinates would thus seem a likely choice. A model rocket, however, never attains altitudes sufficiently great to warrant considerations of planetary

curvature and rotation in the computation of its flight path, so we might just as well select a rectilinear, Cartesian coordinate system as our reference frame. Such a coordinate frame will be used for all subsequent analysis in this chapter. In addition, the horizontal Cartesian axis will be taken to lie in the plane of the rocket's trajectory, so only one horizontal coordinate need be used. The horizontal axis will be referred to as the x -axis; the vertical axis will be called the y -axis.

The differential equations of motion can then be formed along the two mutually perpendicular axes, yielding a horizontal, or x -component of motion and a vertical, or y -component of motion:

$$(12) \quad m(t) \frac{dv_y}{dt} = F_t \cos \theta - m(t)g - [k + \epsilon f(\alpha)] v^2 \cos \theta$$

$$(13) \quad m(t) \frac{dv_x}{dt} = F_t \sin \theta - [k + \epsilon f(\alpha)] v^2 \sin \theta$$

where θ is the value of the angle between the tangent to the trajectory and the y -axis at the instant of time under consideration. Figure 2 illustrates this componentization of the rocket's motion. The cosine and sine in terms of the velocity v along the trajectory and the vertical and horizontal components of v , which may be written as \dot{y} and \dot{x} , respectively, are

$$(14) \quad \cos \theta = \frac{\dot{y}}{v}$$

$$(15) \quad \sin \theta = \frac{\dot{x}}{v}$$

The placing of a dot over a variable is one of the standard calculus notations for denoting the variable's time derivative; the notation \dot{x} is thus a shorthand way of writing dx/dt , and so on. Similarly, multiple dots are used

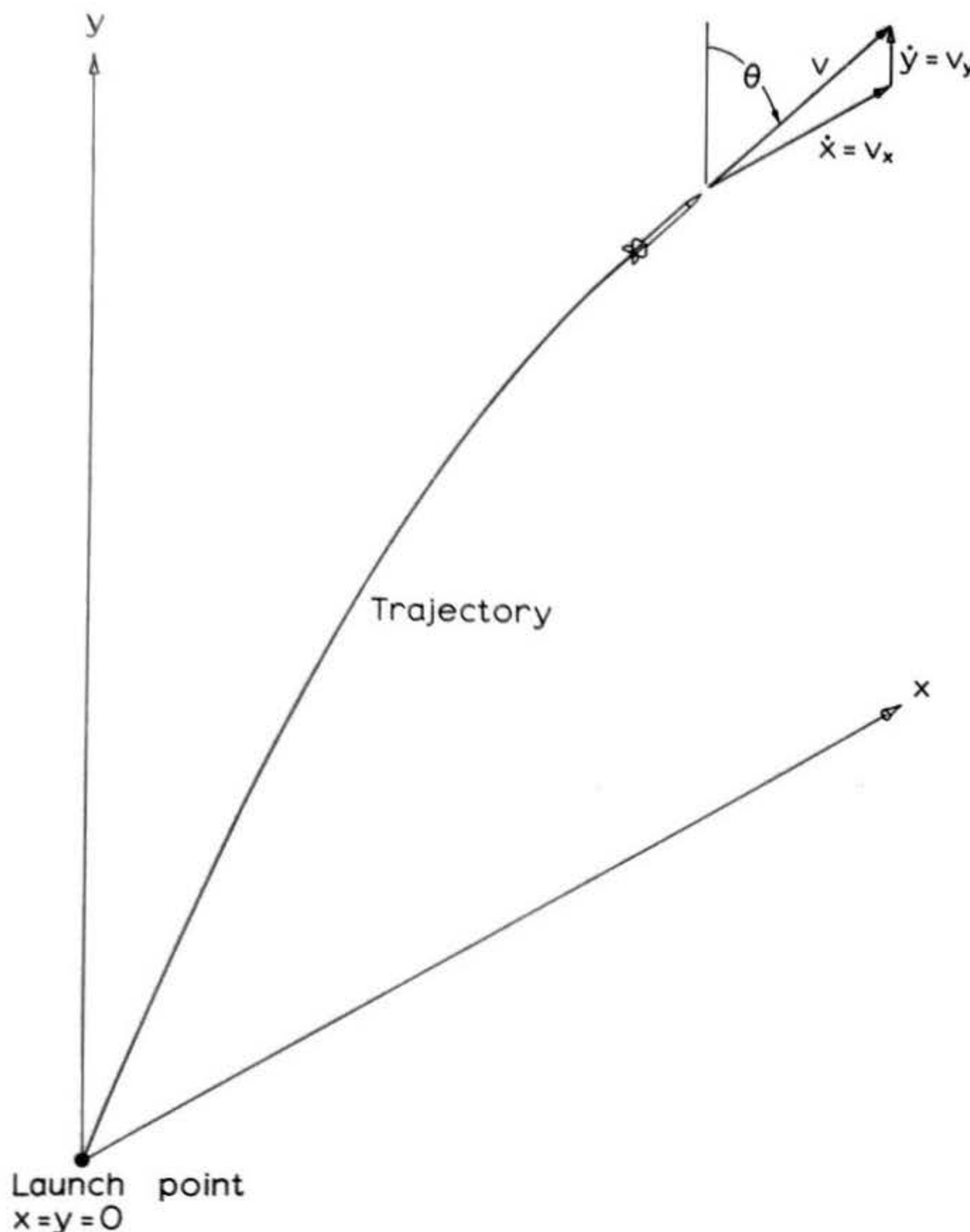


Figure 2: Resolution of a model rocket's flight path, or trajectory, along rectangular Cartesian coordinates. The horizontal distance x travelled from the launch point is the range; the vertical distance y travelled from the launch point is the altitude of the model.

to denote multiple differentiations with respect to time; hence \ddot{x} is equivalent to d^2x/dt^2 , etc. The dot shorthand for time differentiation will be used extensively throughout the treatments of this chapter, as it saves considerable writing when the formulae being discussed become longer and more complicated than those for which the conventional notation for the derivatives would be convenient.

Substituting (9), (10), (14) and (15) into (12) and (13) results in general differential equations of motion in the form

$$(16) \quad m(t) \frac{dv_y}{dt} = F(t) \cos \alpha (\dot{y}/v) - m(t)g - [k + \epsilon f(\alpha)] v \dot{y}$$

$$(17) \quad m(t) \frac{dv_x}{dt} = F(t) \cos \alpha (\dot{x}/v) - [k + \epsilon f(\alpha)] v \dot{x}$$

It must be noted here that the generalized angle of attack α is assumed to be decoupled from the rest of the terms in the equations. That is, any rigid-body rotational oscillations of the model are assumed to be rapid in comparison to the rate at which the model's velocity is changing and the effects of pitch or yaw on the rocket's velocity are, to a first-order approximation, decoupled from the actual determination of the pitching and yawing angles.

2. The Non-Oscillating Rocket: Solutions for Vehicles Launched Vertically

2.1 The Specialized Differential Equation for the Vertical Case

In attempting to solve equations (16) and (17) we will introduce certain physical and mathematical approximations

that will enable the modeler to obtain solutions for a number of specific, idealized cases. Once these solutions are obtained, they will be modified to account for the varying angle of attack produced by rigid-body motion (that is, pitching and yawing oscillations). For most of the cases under consideration, it will be found possible to obtain closed-form solutions to (16) and (17) while maintaining a high order of accuracy.

The simplest idealizations of (16) and (17) that are consistent with the accurate representation of an actual model rocket flight involve the assumptions that

- (a) The rocket is launched vertically and maintains a purely vertical direction throughout the course of its flight;
- (b) The angle of attack is zero; that is, the rocket does not oscillate; and
- (c) The mass of the rocket remains constant at the average of the initial mass and the burnout mass.

With these approximations, equation (17) becomes identically zero and equation (16) may be written in the form

$$(18) \quad m \frac{dv}{dt} = F(t) - mg - kv^2$$

where it is to be understood that v is identical to v_y in all cases of purely vertical flight. Even this greatly simplified equation cannot be solved exactly in closed form. One can, however, obtain excellent approximations by any of the procedures described in the following sections.

2.1.1 Fehskens-Malewicki Solution

This method consists of replacing $F(t)$ by the average value of the thrust over the burn time and solving the resulting equation by a method known to mathematicians as separation of variables. This technique involves rearranging the differential equation algebraically so that the dependent variable -- velocity in this case -- appears on one side of the equation and the independent variable -- time -- appears on the other:

$$(19a) \quad \frac{m dv}{F - mg - kv^2} = dt$$

Equation (19a) can then be integrated to yield the value of the burnout velocity as follows:

$$(19b) \quad \int_0^{v_b} \frac{m dv}{F - mg - kv^2} = \int_0^{t_b} dt$$

Upon performing the integrations one obtains

$$(20) \quad v_b = \sqrt{\frac{F-mg}{k}} \tanh \left[\frac{t_b}{m} \sqrt{k(F-mg)} \right]$$

where F denotes the average thrust, v_b is the burnout velocity, and t_b is the engine burn time. Equation (20) was first obtained by Leonard G. Fehskens and later, independently, by Douglas J. Malewicki. Both researchers also performed an additional integration with respect to time to obtain the burnout altitude, y_b , in the form

$$(21) \quad y_b = \frac{m}{k} \ln \left[\cosh \left(\frac{t_b}{m} \sqrt{k(F-mg)} \right) \right]$$

In equations (20) and (21) the notations $\tanh(\)$, $\ln(\)$, and $\cosh(\)$ refer to the hyperbolic tangent, natural logarithm, and hyperbolic cosine functions of the parenthesized quantity,

respectively. These functions, like the natural trigonometric functions, have been tabulated and may be found in any good book of mathematical tables and formulae. In order to use such tables, as with the natural trigonometric functions, it is necessary to compute the numerical value of the parenthesized quantity, or argument, of the function beforehand. The numerical value of the argument is then located in the table and matched with the corresponding value of the desired function.

2.1.2 Caporaso-Bengen Solution

A second approximate procedure for calculating the burnout velocity and burnout altitude consists in trying to integrate (18) directly with respect to time. In this method the actual, time-varying value of $F(t)$ can be used but the integral of v^2 with respect to time must be approximated:

$$(22) \quad \int_0^{t_b} m \frac{dv}{dt} dt = \int_0^{t_b} F(t) dt - \int_0^{t_b} mg dt - \int_0^{t_b} kv^2 dt$$

The left-hand side of (22) becomes the burnout velocity times the average mass. The thrust integral just yields the total impulse of the engine, irrespective of the particular functional form of $F(t)$, and the weight term is just the product of the average weight mg and the burn time t_b . The drag integral, however, must be computed by considering v^2 as its equivalent form $v(dy/dt)$ and applying the following rule of integral calculus:

$$(23) \quad \int_0^{t_b} k v \frac{dy}{dt} dt = k y v \Big|_{0,0}^{t_b, v_b} - k \int_0^{t_b} y \frac{dv}{dt} dt$$

The first term on the right of (23) is just the product kyv taken

at $v = v_b$ and $y = y_b$, minus the product kyv taken at $v = 0$ and $y = 0$ -- or simply $ky_b v_b$. The second term, however, cannot in general be integrated. The integral on the left side of (23) is therefore truncated by disregarding the second term on the right to obtain a first approximation. The approximate solution of (22) then becomes

$$(24) \quad mv_b = I_t - mg t_b - ky_b v_b$$

where I_t denotes the total impulse of the motor. Equation (24) can then be integrated again if one replaces the velocities, times, and altitudes by "dummy" running variables to avoid confusing their running values with their end-point values.

Upon completion of the integration one obtains

$$(25) \quad my_b = \int_0^{t_b} \left[\int_0^t F(t) dt \right] dt - mg \frac{t_b^2}{2} - \frac{ky_b^2}{2}$$

where you should note that, once the drag integral (23) has been truncated to obtain (24), no further truncation is required to obtain (25). It can be seen that, while the burnout velocity does not depend on the exact functional form of the thrust, the burnout altitude does. In particular, if we approximate $F(t)$ by a constant, average value F as in equations (19), (25) becomes

$$(26) \quad my_b = F \frac{t_b^2}{2} - mg \frac{t_b^2}{2} - \frac{ky_b^2}{2}$$

which, when solved algebraically for y_b , yields

$$(27) \quad y_b = \frac{-m + \sqrt{m^2 + kt_b^2(F-mg)}}{k}$$

Upon substituting (27) into (24) and solving for v_b one obtains

$$(28) \quad v_b = \frac{I_t - mg t_b}{\sqrt{m^2 + k t_b^2 (F - mg)}}$$

This alternative approximate approach was first used by William P. Bengen and the present author shortly after Fehskens had derived equations (20) and (21).

2.1.3 Caporaso-Riccati Solution

A third solution to equation (18) can be obtained by recognizing (18) as a form of what mathematicians call the Riccati equation. The method of Riccati can then be applied to solve (18) as follows:

Suppose we introduce the transformation of variables

$$v = \frac{m}{k} \frac{\dot{u}}{u}$$

and substitute $\frac{m}{k} \frac{\dot{u}}{u}$ for v everywhere in (18). The result will be a second-order linear differential equation for the unknown function u :

$$(29) \quad \frac{m^2}{k} \left[\frac{\ddot{u}}{u} - \left(\frac{\dot{u}}{u} \right)^2 \right] + \frac{m^2}{k} \left(\frac{\dot{u}}{u} \right)^2 = F(t) - mg$$

Combining terms, we have

$$(30) \quad \frac{m}{k} \frac{\ddot{u}}{u} = \frac{F(t) - mg}{m}$$

Upon multiplication of both sides by u and a little rearrangement, a linear, second-order differential equation for u with one time-varying coefficient is obtained:

$$(31) \quad \frac{m}{k} \ddot{u} - \left[\frac{F(t) - mg}{m} \right] u = 0$$

Thus far, it has not been necessary to make any approximations; one can obtain equation (31) using the full, general functional form of $F(t)$. In fact, the Riccati technique would even have permitted the use of the time-varying mass $m(t)$ instead of the average value m .

Equation (31), however, is impossible to solve in closed form unless it is simplified in some manner. It will possess a relatively simple and rather well-known solution if all the coefficients of the various derivatives of u are constants. In order to obtain and investigate this solution we shall, in addition to approximating $m(t)$ by the average mass m , consider $F(t)$ to be F , the average value of the thrust over the burn time. Under these assumptions (31) has a solution familiar to students of mathematics and the sciences, namely the exponential solution

$$(32) \quad u = A_1 e^{Ht} + A_2 e^{-Ht}$$

where e is the base of the natural, or Napierian, system of logarithms and H has the following form:

$$(33) \quad H = \frac{1}{m} \sqrt{k(F - mg)}$$

The constants A_1 and A_2 must be determined from the initial conditions that both the velocity and the altitude of the model are zero at $t = 0$. Constructing v from u according to the variable transformation $v = \frac{m}{k} \frac{\dot{u}}{u}$ results in

$$(34) \quad v = \frac{m}{k} \left[\frac{A_1 H e^{Ht} - A_2 H e^{-Ht}}{A_1 e^{Ht} + A_2 e^{-Ht}} \right]$$

Imposing the initial condition that the velocity is zero at $t = 0$ forces the numerator of (34) to vanish for this value of time:

$$A_1 H - A_2 H = 0$$

so that

$$(35) \quad A_1 = A_2$$

When A_1 is substituted for A_2 everywhere in (34) it cancels in division, leaving us with

$$(36) \quad v = H \frac{m}{k} \left[\frac{e^{Ht} - e^{-Ht}}{e^{Ht} + e^{-Ht}} \right]$$

Now it is known that

$$(37) \quad \frac{e^{Ht} - e^{-Ht}}{e^{Ht} + e^{-Ht}} = \tanh(Ht)$$

for this is just the exponential definition of the hyperbolic tangent. The burnout velocity can then be obtained by setting $t = t_b$ and substituting the right-hand side of equation (33) for H :

$$(38) \quad v_b = \sqrt{\frac{F-mg}{k}} \tanh \left[\frac{t_b}{m} \sqrt{k(F-mg)} \right]$$

The altitude is determined by integrating the expression for the velocity with respect to time. When this is done it is found that the resulting equation identically satisfies the condition that the altitude be zero at $t = 0$, and that the burnout altitude is given by

$$(39) \quad y_b = \frac{m}{k} \ln \left[\cosh \left(\frac{t_b}{m} \sqrt{k(F-mg)} \right) \right]$$

Equations (38) and (39) are seen to be identical to equations (20) and (21). The Riccati technique is thus an alternative procedure by which one can obtain the Fehskens-Malewicki solution.

Equation (39) concludes this section's treatment of model rocket trajectory analysis, which has been restricted to the determination of the burnout velocity and burnout altitude of non-oscillating, single-staged model rockets flying straight upward. For the benefit of those readers who have found the mathematical derivations burdensome or impossible to follow, I shall complete the section with a summary of the important results and explicit instructions on how to apply them.

To use the Fehskens-Malewicki method, compute the burnout velocity using equation (20) and the burnout altitude using equation (21).

To use the Caporaso-Bengen method, compute the burnout velocity by using equation (28) and the burnout altitude according to equation (27).

To use the Caporaso-Riccati method, compute the burnout velocity and burnout altitude according to equations (38) and (39), respectively -- although, since these equations are identical to those of the Fehskens-Malewicki method, there is no real reason to consider them distinct from the results obtained by Fehskens and Malewicki.

2.2 Extension of the Solutions to Multistaged Vehicles

The problem of computing the burnout velocity and altitude of the upper stages of a multistaged model rocket is somewhat

more difficult than that of computing the burnout velocity and altitude of a single-staged model. In each case the differential equations of motion have precisely the same form; in fact, the general forms of the solutions are also identical. The crucial difference between the single-stage and multistage solutions lies in the choice of initial conditions and limits of integration. The problem essentially reduces to one of choosing the correct limits in the indefinite integral solutions thus far derived.

As will be shown in Section 2.5, the approximations derived in Section 2.1 are quite accurate and compare very well with each other, as well as with computer solutions obtained by interval methods (which are, in the limit of vanishingly small intervals, exact). Since extending the methods of Section 2.1 to multistaged vehicles is algebraically laborious, we shall first want to choose the easiest approximation to handle analytically. Such a choice is perfectly justified, as all the approximations are more than sufficiently accurate for model rocketry purposes.

2.2.1 Extended Caporaso-Bengen Solution

The most logical choice in this respect would seem to be the Caporaso-Bengen method used in deriving equations (27) and (28), since it not only is analytically simple, but also affords the greatest physical insight into the problem of choosing the limits of integration. In extending this method we shall first apply equation (22) to a two-staged model, modifying the limits of integration for the calculation of the second-stage burnout velocity and burnout altitude. The following notation will be used:

$y_1 = y_b$ = burnout altitude of first stage

$v_1 = v_b$ = burnout velocity of first stage

v_2 = burnout velocity of second stage

y_2 = altitude gained during the burning time of the second-stage engine (not the total second-stage burnout altitude)

m_1 = average mass of first and second stages together

m_2 = average mass of second stage alone

k_2 = second-stage drag parameter

t_2 = burning time of second-stage engine

$t_1 = t_b$ = burning time of first-stage engine

To better conceptualize the reasons for the choice of limits to be made in the following derivation, suppose we consider the rocket just after the burnout of the first stage, in the infinitesimal time interval before the second stage ignites. The second stage has already jettisoned the first through the action of the propellant-wall blow-through function of the first-stage engine (which also ignites the second-stage engine), but the second-stage engine has not been lit long enough to have developed any measurable thrust. The upper stage will have aerodynamic drag on it equal to the square of the first-stage burnout velocity times the second-stage drag parameter; i.e., the drag will equal $k_2 v_1^2$. The weight of the second stage is the only other force acting on the model and, if the second-stage engine did not ignite, would (in conjunction with the drag) begin to decrease its upward momentum.

The second stage now fires and contributes to the vehicle a quantity of momentum equal to its total impulse. Thus, after the burnout of the first stage, the momentum of the rocket is

changed only by the forces acting on it during the second-stage burning time and we may write

$$(40) \quad \int_{t_1}^{t_1+t_2} m_2 \frac{dv}{dt} dt = \int_{t_1}^{t_1+t_2} F_2(t) dt - \int_{t_1}^{t_1+t_2} m_2 g dt - \int_{t_1}^{t_1+t_2} k_2 v^2 dt$$

The value of the integral on the left taken between the indicated limits is just $m_2(v_2 - v_1)$. It is now necessary to make the same truncation approximation as was made in equation (23), and to supply the proper limits of integration for making such an approximation. Here we are integrating the drag from a nonzero quantity up through its second-stage burnout value; we are attempting to find the drag integral only over the second-stage burning time. Now it is a well-known property of integrals that they obey the following additive relationship with respect to their limits of integration:

$$(41) \quad \int_0^\alpha f(x) dx = \int_0^\beta f(x) dx + \int_\beta^\alpha f(x) dx$$

where x , in this case, represents any independent variable (not the horizontal coordinate to be used in our later investigation of nonvertical trajectories), and $f(x)$ represents any function of that variable. In the present case, we desire the solution for the component integral over the last interval:

$$(42) \quad \int_\beta^\alpha f(x) dx = \int_0^\alpha f(x) dx - \int_0^\beta f(x) dx$$

Replacing the dummy function $f(x)$ by v^2 and the dummy variable x by t , we have

$$(43) \quad \int_{t_1}^{t_1+t_2} v^2 dt = \int_0^{t_1+t_2} v^2 dt - \int_0^{t_1} v^2 dt$$

and using the same truncation procedure as in (23),

$$(44) \quad \int_{t_1}^{t_1+t_2} v^2 dt = (y_1 + y_2)v_2 - y_1 v_1$$

It is essential to note here that we are integrating the drag as it would have been if the drag parameter k had been k₂ throughout the flight. The reason for this is that, at the instant after first-stage burnout and jettison, the drag is $k_2 v_1^2$ and k_1 should have nothing at all to do with the integral of the drag during the second-stage burn, except insofar as it has played a role in determining v_1 (which is already known).

The drag integral must be evaluated in this manner, since there is considerable analytical difficulty involved in matching the drag of the rocket just before and just after burnout and jettison of the first stage without assuming that the drag parameter has been k_2 up to that point. Substituting the approximation (44) into (40) and evaluating the other integrals subject to the approximations of constant average thrust and mass. we obtain

$$(45) \quad m_2 v_2 - m_2 v_1 = F_2 t_2 - m_2 g t_2 - k_2 [(y_1 + y_2)v_2 - y_1 v_1]$$

which can be solved to give v_2 in the form

$$(46) \quad v_2 = \frac{t_2(F_2 - m_2 g) + m_2 v_1 + k_2 y_1 v_1}{m_2 + k_2(y_1 + y_2)}$$

Proceeding as in the single-stage case, we integrate (45) to obtain a solution for y_2 :

$$(47) \quad m_2 y_2 - m_2 v_1 t_2 = \frac{t_2^2}{2}(F_2 - m_2 g) - k_2 y_1 y_2 - k_2 \frac{y_2^2}{2} + k_2 y_1 v_1 t_2$$

You should note at this point that all quantities relating to the first-stage burnout values v_1 and y_1 are to be treated as constants and not to be integrated as their respective functions. The first-stage burnout velocity and altitude are assumed to be already known, having been computed by treating the model as if it were single-staged and applying the methods of Section 2.1.

Equation (47) can then be solved for y_2 , yielding

$$(48) \quad y_2 = \frac{-(m_2 + k_2 y_1) + \sqrt{(m_2 + k_2 y_1)^2 + 2k_2 t_2 \left[\frac{t_2}{2}(F_2 - m_2 g) + (k_2 y_1 v_1 - m_2 v_1) \right]}}{k_2}$$

Substituting (48) into (46) gives the second-stage burnout velocity as

$$(49) \quad v_2 = \frac{t_2(F_2 - m_2 g) + m_2 v_1 + k_2 y_1 v_1}{\sqrt{(m_2 + k_2 y_1)^2 + 2k_2 t_2 \left[\frac{t_2}{2}(F_2 - m_2 g) + (k_2 y_1 v_1 - m_2 v_1) \right]}}$$

As a check on (48) and (49), suppose we let y_1 and v_1 both be zero; we should then get back equations (27) and (28) for a single-staged rocket with $k = k_2$, $F = F_2$, $t_b = t_2$, and $m = m_2$. It is readily seen that setting y_1 and v_1 to zero does indeed reduce the above equations to a form identical to (27) and (28).

The generalization of the burnout velocity and altitude increment equations to rockets of three or more stages is now fairly simple. In the case of a three-staged rocket, for example, the first-stage burnout velocity and altitude are calculated using the methods of Section 2.1; the second-stage burnout velocity and the altitude increment gained during the second-stage burn are then calculated by (48) and (49), and the third-stage altitude increment and burnout velocity are found using the same method by which (48) and (49) were derived.

In more general terms, the burnout velocity of the nth stage of a multistaged rocket is given by

$$(50) \quad v_n = \frac{t_n(F_n - m_n g) + m_n v_{n-1} + k_n y_{n-1} v_{n-1}}{\sqrt{[m_n + k_n(y_1 + \dots + y_{n-1})]^2 + 2k_n t_n \left\{ \frac{t_n}{2}(F_n - m_n g) + [k_n(y_1 + \dots + y_{n-1})v_{n-1} - m_n v_{n-1}] \right\}}}$$

and the altitude increment gained between burnout of the (n-1)th stage and the nth-stage burnout is

$$(51) \quad y_n = \frac{-[m_n + k_n(y_1 + \dots + y_{n-1})]}{k_n} + \frac{\sqrt{[m_n + k_n(y_1 + \dots + y_{n-1})]^2 + 2k_n t_n \left\{ \frac{t_n}{2}(F_n - m_n g) + [k_n(y_1 + \dots + y_{n-1})v_{n-1} - m_n v_{n-1}] \right\}}}{k_n}$$

where F_n and t_n are the average thrust and burning time of the nth-stage engine, k_n is the drag parameter of the nth stage plus all subsequent stages, and m_n is the average mass of the nth stage with all subsequent stages carried atop it.

I have presented equations (50) and (51), which are applicable to a model rocket of any number of stages, in the interest of analytical completeness and generality. The reader should bear in mind, however, that the construction of rockets having more than three stages is a risky and ill-advised undertaking. The probability that all stages will fire successfully decreases alarmingly as the number of stages increases. Multistaged model rockets, moreover, have been observed to suffer more from "weathercocking" -- the tendency of the model, when launched, to fly directly into the wind -- than single-staged vehicles. Weathercocking, plus transient disturbances due to the staging process itself, has even been known to cause the upper stages of multistaged model rockets to fire in a nose-down attitude! For these reasons, the United States Model Rocket Sporting Code

of the National Association of Rocketry prohibits the launching of any model rocket having more than three operable stages in NAR-sanctioned competition.

2.2.2 Extended Fehskens-Malewicki Solution

The Fehskens-Malewicki technique can be extended to multi-staged model rockets by appropriately altering the limits between which the integral (19b) is evaluated. Using the same notation as in Section 2.2.1 for a two-staged model, one obtains the integral in the form

$$(52) \int_{v_1}^{v_2} \frac{m_2 dv}{F_2 - m_2 g - k_2 v^2} = \int_{t_1}^{t_1 + t_2} dt$$

Performing the indicated integration, we have

$$(53) \frac{m_2}{\sqrt{k_2(F_2 - m_2 g)}} \tanh^{-1} \left[v \sqrt{\frac{k_2}{F_2 - m_2 g}} \right]_{v_1}^{v_2}$$

which, when expanded, yields

$$(54) \tanh^{-1} \left(v_2 \sqrt{\frac{k_2}{F_2 - m_2 g}} \right) - \tanh^{-1} \left(v_1 \sqrt{\frac{k_2}{F_2 - m_2 g}} \right) = \frac{t_2}{m_2} \sqrt{k_2(F_2 - m_2 g)}$$

Solving equation (54) for v_2 , we obtain

$$(55) v_2 = \sqrt{\frac{F_2 - m_2 g}{k_2}} \tanh \left[\frac{t_2}{m_2} \sqrt{k_2(F_2 - m_2 g)} + \tanh^{-1} \left(v_1 \sqrt{\frac{k_2}{F_2 - m_2 g}} \right) \right]$$

Now the upper limit of integration on the left of (52) could have been taken as v , the velocity of the second stage at any time t during its burn, while the upper limit on the right of (52) could accordingly have been taken as t , where it is understood that t is a value of time that is greater than or equal to t_1 and less than or equal to $t_1 + t_2$. The resulting expression for v is entirely analogous to (55), but gives the second-stage

velocity as a function of time:

$$(56) \quad v = \sqrt{\frac{F_2 - m_2 g}{k_2}} \tanh \left[\frac{t - t_1}{m_2} \sqrt{k_2(F_2 - m_2 g)} + \tanh^{-1} \left(v_1 \sqrt{\frac{k_2}{F_2 - m_2 g}} \right) \right]$$

The altitude increment gained during the second-stage burn can then be determined by integrating (56) from $t = t_1$ to $t = t_1 + t_2$:

$$(57) \quad y_2 = \frac{m_2}{k_2} \ln \left[\frac{\cosh \left[\frac{t_2}{m_2} \sqrt{k_2(F_2 - m_2 g)} + \tanh^{-1} \left(v_1 \sqrt{\frac{k_2}{F_2 - m_2 g}} \right) \right]}{\cosh \left[\tanh^{-1} \left(v_1 \sqrt{\frac{k_2}{F_2 - m_2 g}} \right) \right]} \right]$$

and through the use of the well-known identity

$$\cosh(A+B) = \cosh(A)\cosh(B) + \sinh(A)\sinh(B)$$

where A and B represent any two quantities, (57) may be cast into the simpler form

$$(58) \quad y_2 = \frac{m_2}{k_2} \ln \left[\cosh \left(\frac{t_2}{m_2} \sqrt{k_2(F_2 - m_2 g)} \right) + v_1 \sqrt{\frac{k_2}{F_2 - m_2 g}} \sinh \left(\frac{t_2}{m_2} \sqrt{k_2(F_2 - m_2 g)} \right) \right]$$

The burnout velocity and altitude increment equations can be generalized to any number of stages, as was done in the case of the Caporaso-Bengen solution. It will be found that the burnout velocity of the nth stage of a multistaged model rocket (carrying all subsequent stages atop it) is given by

$$(59) \quad v_n = \sqrt{\frac{F_n - m_n g}{k_n}} \tanh \left[\frac{t_n}{m_n} \sqrt{k_n(F_n - m_n g)} + \tanh^{-1} \left(v_{n-1} \sqrt{\frac{k_n}{F_n - m_n g}} \right) \right]$$

while the altitude increment gained between the burnout of the $(n-1)$ th stage and the burnout of the nth stage is

$$(60) \quad y_n = \frac{m_n}{k_n} \ln \left[\cosh \left(\frac{t_n}{m_n} \sqrt{k_n(F_n - m_n g)} \right) + v_{n-1} \sqrt{\frac{k_n}{F_n - m_n g}} \sinh \left(\frac{t_n}{m_n} \sqrt{k_n(F_n - m_n g)} \right) \right]$$

The equations obtained through the application of the Caroraso-Riccati method are, as in the case of single-staged rockets, identical to those derived by the Rehskens-Malewicki method. Consequently, I shall not present their step-by-step development here.

The qualitative features of the multistage solutions developed in this section are all similar to those of the corresponding single-stage solutions. For instance, it can be seen from equations (49) and (55) that, as the burn time becomes very long, the burnout velocity tends toward the terminal velocity of the stage; i.e., toward that velocity at which drag and weight exactly counterbalance thrust and no further increase in velocity is possible. At the same time, the t_2^2 term dominates the radicand in equation (48) and the argument of the natural logarithm function in (58) approaches a pure exponential, so that the resulting burnout altitude increment becomes almost directly proportional to burn time -- corresponding to the model's having reached a constant (terminal) velocity. Upon inspection, both the single-stage solutions and the multistage solutions for rockets of three or more stages will also be found to exhibit this property. As in the case of a single-staged rocket, the terminal velocity of an upper stage with all subsequent stages atop it depends upon the relative magnitudes of the thrust, weight, and drag parameter. A curious consequence of this fact

is that the burnout velocity of an upper stage can be less than the first-stage burnout velocity. This can happen, for instance, in a two-staged rocket where a high-thrust engine is used for the first stage and a low-thrust engine for the second. Under these conditions the burnout velocity of the upper stage approaches the terminal velocity from above rather than from below. In the mid-1960's a number of model rockets were constructed for the purpose of "breaking the sound barrier"; that is, exceeding the 340-meter-per-second velocity of sound in sea-level air. Since most of these vehicles relied on low-thrust sustainer stages atop high-thrust boosters, almost all of them failed in their objective: the sustainer stage actually slowed down after burnout of the booster stages!

Equation (60) completes the analysis of this section, which has been directed toward the determination of the burnout velocity and burning-phase altitude increment of the upper stages of multistaged model rockets in non-oscillating, purely vertical flight. Again, for the benefit of readers not mathematically inclined, I shall conclude with a summary of explicit instructions for applying the results obtained.

To use the extended Caporaso-Bengen method for a two-staged model, calculate v_2 using equation (49) and y_2 using equation (48). For the n th stage of a multistaged rocket use equation (50) for v_n , (51) for y_n .

To use the extended Fehskens-Malewicki method for a two-staged rocket, compute v_2 by equation (55) and y_2 by equation (58). In analyzing the n th stage of a multistaged rocket, use equation (59) for v_n and equation (60) for y_n .

2.3 Solutions for a Non-Oscillating Rocket in the Coasting Phase

The analyses of Sections 2.1 and 2.2 have been directed toward the determination of the burnout altitude and burnout velocity of a vertically-launched model rocket that does not experience any changes in angle of attack due to rigid-body rotations. The burning phase, however, tells only half the story of a rocket's flight. After expending its propellant charge the model continues to coast upward for a considerable distance until the momentum associated with its burnout velocity is reduced to zero by the action of gravity and aerodynamic drag, at which time the apex, or highest point in the flight, occurs. In fact, as those who have seen model rockets in flight doubtless know, the coasted altitude increment is usually considerably greater than the burnout altitude. In this section the differential equation of point-mass motion will be solved to yield the two quantities of primary importance to a knowledge of the coasting phase of a rocket's flight: the coasted altitude increment and the time interval between the burnout of the uppermost stage and the flight apex.

After the burnout of the last stage, the vertical differential equation of motion becomes

$$(61) \quad m(t) \frac{dv}{dt} = -m(t)g - kv^2$$

As we did for the burning-phase analyses, we shall make the approximation that the mass of the rocket remains constant throughout the coasting phase of flight. The only change in mass that does in fact occur after burnout is the slight mass

loss due to the burning of the delay train, or time delay charge, in the engine. For all practical purposes this mass loss is negligible, so that $m(t)$ can be approximated by the burnout mass m_b and equation (61) becomes

$$(62) \quad m_b \frac{dv}{dt} = -m_b g - kv^2$$

This relation may be rearranged to solve for t as a function of v . Using the fact that the model's velocity is reduced to zero at flight apex, one can then obtain the coasting time between burnout and apex by solving

$$(63) \quad \int_{v_b}^0 \frac{m_b dv}{-m_b g - kv^2} = \int_0^{t_c} dt$$

which yields

$$(64) \quad t_c = \sqrt{\frac{m_b}{gk}} \tan^{-1} \left[v_b \sqrt{\frac{k}{m_b g}} \right]$$

Equation (62) can also be solved for the coasted altitude increment by introducing the following transformation of variables:

$$(65) \quad \frac{dv}{dt} = \frac{dv}{dy} \frac{dy}{dt} = v \frac{dv}{dy}$$

When (65) is substituted into (62) and the resulting equation is solved for y as a function of v we obtain

$$(66) \quad \int_{v_b}^0 \frac{v dv}{m_b g + kv^2} = \int_0^{y_c} -\frac{dy}{m_b}$$

When integrated, (66) yields the coasted altitude increment y_c as

$$(67) \quad y_c = \frac{m_b}{2k} \ln \left[\frac{kv_b^2}{m_b g} + 1 \right]$$

The total altitude at apex is then just the sum of y_c and the burnout altitude increments of all the stages, while the

total time elapsed from liftoff to apex is the sum of t_c and the burning times of all the stages. When using equation (64) to calculate the coasting time and equation (67) to calculate the coasted altitude increment of the uppermost stage of a multistaged rocket, it is important to note that the burnout mass, burnout velocity, and drag parameter of that stage must be used for m_b , v_b , and k , respectively. Figure 3 illustrates by example the synthesis of burning-phase and coasting-phase solutions to obtain the overall performance and flight-time characteristics of a three-staged model rocket.

2.4 Numerical Methods for the Digital Computation of Altitude Performance

The preceding sections have described methods which can be used by the model rocketeer to give accurate predictions of his vehicle's altitude capability with relatively little actual calculation. By this I certainly do not mean to imply that the reader should find the solutions trivial to work; indeed, until you have had some practice with them it is to be expected that you may find them somewhat difficult to handle. But a human being who applies himself with a reasonable amount of diligence can work them out in fairly short order -- and this fact alone indicates that there is little actual calculation involved, considering the difficulty of the problem. The methods developed in Sections 2.1 through 2.3 are, moreover, excellent approximations to the exact solution of the differential equation of vertical motion, equation (12), with α and θ both equal to zero. If a more precise determination of the flight performance than that

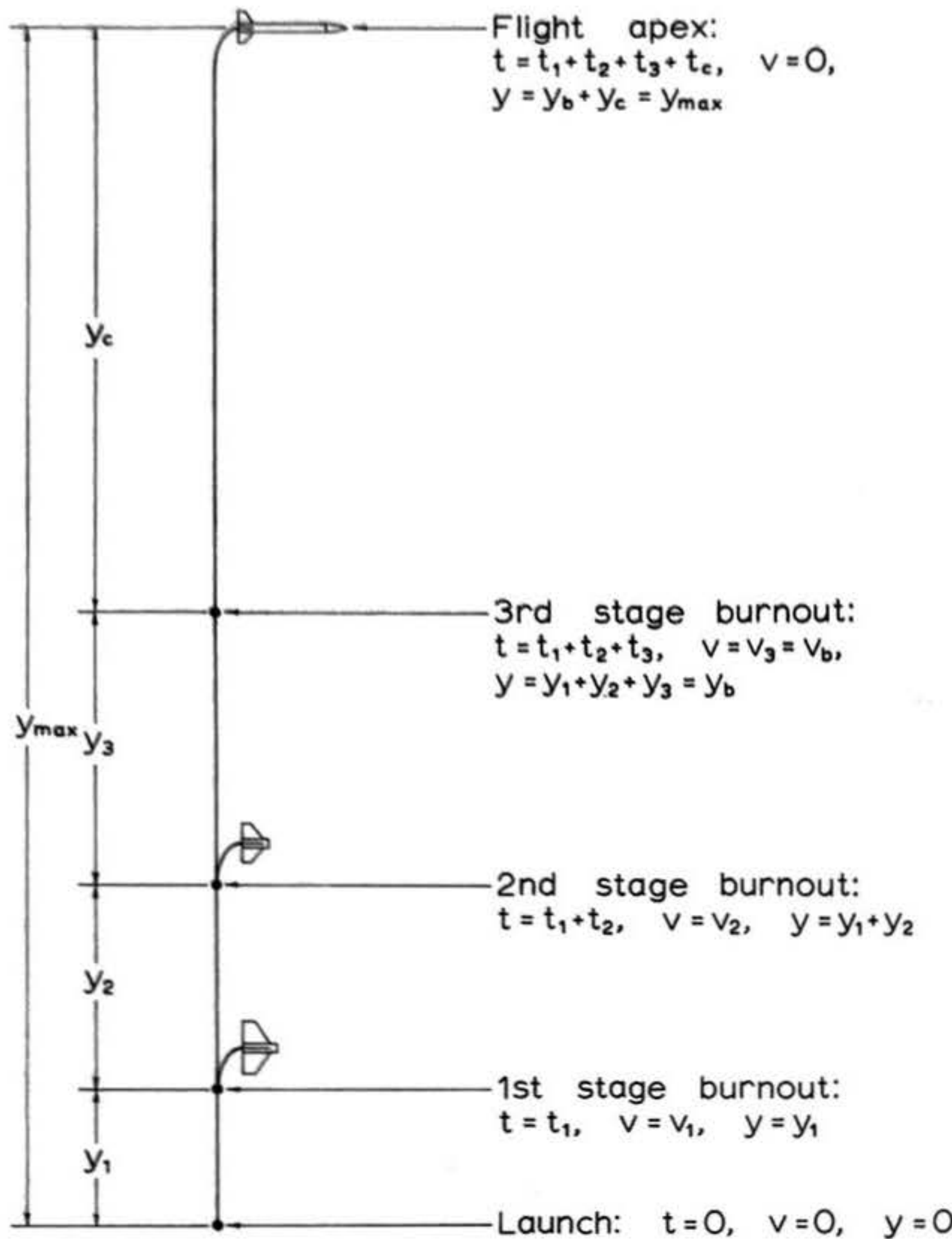


Figure 3: Assembly of burning-phase and coasting-phase solutions to obtain the total altitude and time to flight apex of a three-staged model rocket.

possible using the preceding methods is desired, (12) can be solved to any desired accuracy -- but, since such a solution requires the use of numerical methods involving a far greater amount of calculation than the closed-form approximations, it becomes necessary to program the problem for solution on an automatic, digital computer. This section will present two such methods, as well as some supplementary material on engine thrust and mass functions.

Before we can obtain an accurate solution to the differential equation of motion, we require an accurate knowledge of the thrust-vs.-time and mass-vs.-time curves for the rocket in question. This usually means closed-form, analytic expressions for these curves, for although such curves can be represented by tables which are read by the machine at any desired value of time most modelers who have used computers find the tabular representation awkward and inconvenient in practice. For a rocket engine, as was shown in Chapter 1, we have the following relationship between thrust and mass loss:

$$(68) \quad F(t) = c \frac{dm_e}{dt}$$

where c is the exhaust velocity of the combustion products and dm_e/dt is the mass flow rate at which the combustion products are being expelled from the nozzle. For the great majority of model rocket engines, the exhaust velocity does not vary greatly during the burn time and can be approximated by its average value, which in turn can be calculated from the motor's specific impulse according to

$$(69) \quad c = g I_{sp}$$

so that it is a simple matter to obtain dm_e/dt from (68) once the analytic function representing the variation of thrust with time is known. This, in turn, is fairly easily determined since all manufacturers of model rocket engines give rather accurate data on the total impulse, maximum thrust, average thrust, burn time, and general shape of the thrust-time curve of each type they produce. The rate at which the mass of the rocket changes during the burning phase of flight is just equal to $-dm_e/dt$, since the loss of combustion products through the nozzle is the only source of mass variation in virtually all model rockets.

It will be recalled that typical thrust-time curves for model rocket engines were discussed in detail in Chapter 1, and that these curves fall into three basic categories:

- (a) The curves of end-burning engines (most engines in NAR classes $\frac{1}{2}A$ through C), which are characterized by relatively long burning times and relatively low, constant thrust except for a "starting peak" at ignition;
- (b) The curve of the NAR type B14 engine, characterized by a rapid rise in thrust, an equally rapid decay in thrust, and a short burning time; and
- (c) The curves of many engines in NAR classes D through F, whose conical-port grain geometries result in a thrust peak just before burnout, a

relatively high average thrust, and a burn time intermediate between categories (a) and (b) above.

The overwhelming majority of model rocket engines in common use are of the end-burning type where the approximation of constant thrust is usually acceptable, and the mass expulsion rate may be regarded as nearly constant throughout the burning time. The mass of a rocket using such an engine, as a function of time, can then be written as

$$(70) \quad m(t) = m_0 - \gamma t$$

where m_0 is the rocket's mass at the instant of ignition and

$$(71) \quad \gamma = \frac{m_f}{t_b}$$

where m_f is the mass of the propellant charge and t_b is the burning time.

The thrust-time and mass-time curves of any engine type, end-burning or not, may be represented by approximating the thrust-time curve by a closed-form, analytic function which satisfies the following basic criteria:

- (a) The total impulse of the mathematical representation chosen must equal the actual total impulse of the engine; i.e., if $F(t)$ is the mathematical representation,

$$(72) \quad I_t = \int_0^{t_b} F(t) dt$$

- (b) The burning time of the mathematical representation must equal the actual burning time of the engine;

- (c) The maximum thrust of the mathematical representation must equal the actual peak thrust of the engine; and
- (d) The mathematical representation must equal the actual thrust of the engine at several points on the thrust-time curve or must be of the same general shape as the actual thrust-time curve, depending on the degree of accuracy desired.

To approximate the actual thrust function, one may use a Fourier sine or cosine series, a polynomial fit, or a combination of the two. Model rocket engines of any given type do exhibit a certain amount of variation from one production article to the next, however, and it is not generally worthwhile to insist on too high a degree of precision when constructing mathematical models of thrust-time curves -- at least from the standpoint of practical design. In fact, it turns out that the thrust-time curve of almost any model rocket engine can be adequately approximated by a piecewise-linear representation of the form

$$(73a) \quad F(t) = F_m \frac{t}{t_m} \quad (0 \leq t \leq t_m)$$

$$(73b) \quad F(t) = F_m - \frac{t - t_m}{t_s - t_m} (F_m - F_s) \quad (t_m \leq t \leq t_s)$$

$$(73c) \quad F(t) = F_s \quad (t_s \leq t \leq t_b)$$

where F_m = maximum thrust

F_s = sustainer thrust

t_m = time of occurrence of maximum thrust, and

t_s = time of onset of sustainer thrust

The corresponding functions for representing the model's mass as a function of time are

$$(74a) \quad m(t) = m_0 - F_m \frac{t^2}{2ctm} \quad (0 \leq t \leq t_m)$$

$$(74b) \quad m(t) = m_0 - \frac{F_m}{c} \left(t - \frac{t_m}{2} \right) + (F_m - F_s) \frac{(t - t_m)^2}{2c(ts - t_m)} \quad (t_m \leq t \leq t_s)$$

$$(74c) \quad m(t) = m_0 - \frac{F_m ts}{2c} - \frac{F_s(ts - t_m)}{2c} - \frac{F_s}{c}(t - t_s) \quad (t_s \leq t \leq t_b)$$

and the total impulse of the engine is given by

$$(75) \quad I_t = F_m \frac{t_s}{2} + F_s \left(t_b - \frac{t_m}{2} - \frac{t_s}{2} \right)$$

The reader will recognize the notation used in equations (73) through (75) as referring specifically to the end-burning engine with its characteristic initial thrust spike and clearly identifiable sustainer thrust level; I repeat, however, that virtually any existing engine's characteristics can be fairly well represented by this scheme. To approximate the thrust-time curve of a core-burning motor like the Bl4, for instance, one would set t_s equal to t_b and F_s equal to zero. With t_s and F_s thus fixed it is no longer possible to satisfy our condition (c) above, but the error in F_m is insufficient to significantly affect performance calculations. In the case of the Bl4, for instance, F_m turns out to be 28.6 newtons, just over 10% less than the nominal test value of 32 newtons -- a representation that is certainly accurate enough for any calculations likely to be of interest to the practical rocketeer. Figure 4 illustrates by example the application of the piecewise-linear method in approximating the thrust-time curve of a typical model rocket engine.

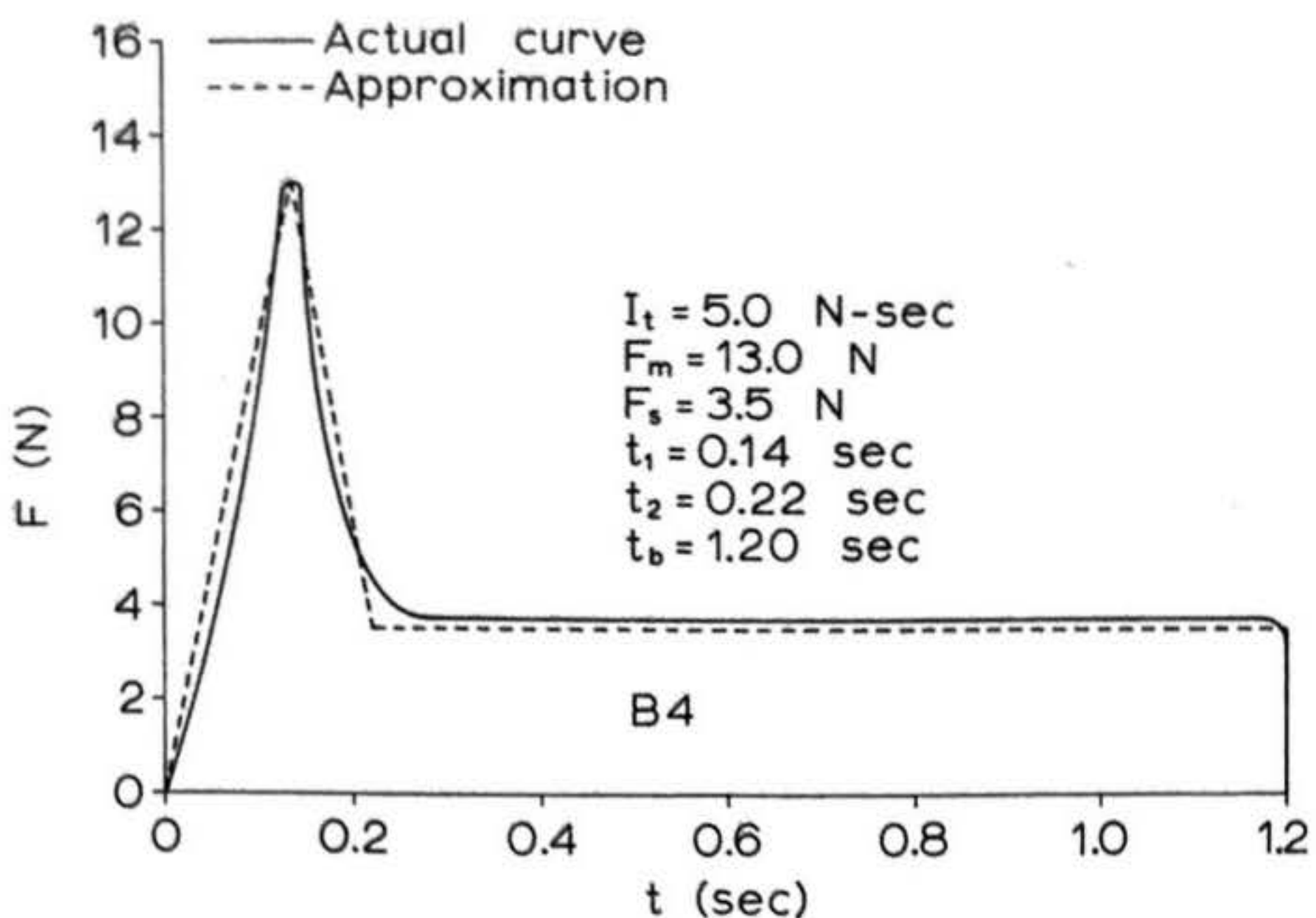


Figure 4: Approximating the thrust-time curve of a typical model rocket engine by a piecewise-linear fit. The parameters used in constructing an approximation to the thrust-time curve of the NAR Type B4 engine are shown along with the actual and approximate thrust-time curves.

We now proceed to the discussion of actual iteration schemes for solving the differential equation of vertical motion. At this stage in the development we can assume that all the functions and parameters of the model and its rocket engine are known. The first iteration procedure consists of determining the

theoretical velocity increment without drag over a small interval of time, adding this theoretical increment to the velocity in the last interval, and determining the drag from the sum thus obtained. The drag is then substituted back into the original force equation and the actual velocity increment is computed from the equation thus generated. The method works well for 0.1-second intervals, but intervals of 0.01 second are easily used on a digital computer and will yield greater accuracy. This method of computation is outlined below:

$$(76) \Delta v_t = \Delta t [F(t) - m(t)g] / m(t)$$

$$(77) \text{Drag} = k(v + \Delta v_t)^2$$

$$(78) \Delta v_a = \Delta t [F(t) - m(t)g - k(v + \Delta v_t)^2] / m(t)$$

$$(79) \Delta y = \Delta t [v + \Delta v_a / 2]$$

$$(80) v = v + \Delta v_a$$

$$(81) y = y + \Delta y$$

$$(82) t = t + \Delta t$$

where Δv_t = drag-free velocity increment,

Δv_a = actual velocity increment, and

Δt = time interval between calculations

The procedure is repeated in a "loop", or iterative fashion, with the time incremented according to (82) used to determine $F(t)$ and $m(t)$ for the subsequent calculations (76) through (81), until the running time t in (82) is equal to the burning time; the program must then enter the next-stage burning phase or the

coasting phase. If you are not used to working with computers the calculations (81) and (82) may not seem like very reasonable equations; after all, how can a quantity be equal to itself plus another quantity, unless the other quantity is itself zero? The answer is that "equations" (81) and (82) are not equations at all; they are what computer programmers call arithmetic assignment statements: instructions to the computer to replace the value on the left with the value on the right of the "equals" sign. The effect of such a notation, when used with an electronic computer, is that at the end of the nth iteration the machine calculates "new" or "present" values of v, y, and t for use in the first part of the (n + 1)th iteration and then "forgets" the "old" or "former" values used in the first part of the nth iteration.

If one assumes that the mass remains

constant during the coasting phase of flight, then equations (64) and (67) are the exact solution to the differential equation of motion and no improvement in accuracy can be obtained through the use of computer interval solution methods; in fact, the computer solution will be an approximation to (64) and (67). If it is desired to take the extremely slight mass loss due to the burning of the delay train into account through the use of a mass-time curve, the iterations are basically the same as those used during the burning phase. The only change that occurs is the disappearance of $F(t)$ from the formulae, unless it is also desired to account for the small fraction of a newton of thrust produced by the burning of the time delay charge. In the latter case there is no difference whatsoever in the form of the computational formulae.

A second method, more easily set up on a digital computer, is one which also requires an extremely small time interval between iterations for good accuracy. The basic difference between this method and the previous one is that it relies upon the calculation of the drag in the nth interval of time from the velocity during the (n-1)th interval. The operation of the method is as follows:

$$(83) \quad \Delta v = \Delta t [F(t) - m(t)g - kv^2] / m(t)$$

$$(84) \quad \Delta y = \Delta t (v + \Delta v / 2)$$

$$(85) \quad v = v + \Delta v$$

$$(86) \quad y = y + \Delta y$$

$$(87) \quad t = t + \Delta t$$

Although this technique requires the use of very small intervals for convergence, it will converge in the limit as $\Delta t \rightarrow 0$ since the iteration formulae then approach the original differential equation. This can be seen by observing that, as the time interval approaches zero, the Δ 's go over to their infinitesimal counterparts; that is, differentials, or d's, and (83) becomes

$$(88) \quad dv = dt [F(t) - m(t)g - kv^2] / m(t)$$

which, upon rearranging terms, yields

$$(89) \quad m(t) \frac{dv}{dt} = F(t) - m(t)g - kv^2$$

which in turn is just the original differential equation of vertical motion (12) for the case in which α and θ are both uniformly zero. Intervals of 0.001 second, when used with this method, will generate results which are, for all practical purposes, exact solutions. The generalization of the method to the coasting phase or a second burning phase is entirely analogous to the generalization of the first method.

2.5 Validity of the Approximate Methods Compared to Numerical Solutions by the Interval Method

The latter computational method discussed in Section 2.4 has been used to determine the accuracy of the closed-form approximate solutions derived in Section 2.1. Five engine types were considered: the B14, B4, D4, F100, and F7. These engines, together with the selection of masses and drag parameters used in the calculations, represent every extreme and all ranges

of mass, drag parameter, thrust, and burning time of interest in the field of model rocketry. For each engine, the minimum and maximum values of the drag parameter k that can reasonably be expected of a rocket powered by that particular engine type were ascertained. Twenty values of liftoff mass, spanning the practical range of mass to be expected of rockets powered by each type of engine, were then selected and values of v_b , y_b , and y_{max} computed by the second iterative method discussed in the previous section for each of the forty combinations of mass and drag parameter associated with each engine. These computations were carried out on an IBM 360/65 computing system using variable mass-time and thrust-time functions and time intervals of 0.001 second. Corresponding results were then obtained using the Fehskens-Malewicki and Caporaso-Bengen methods and compared to the interval-method values. The percentage errors incurred by the use of the approximate methods, as determined by this comparison, are shown in the accompanying graphs, Figures 5 through 9. It can be seen that the approximate techniques are well within the limits of accuracy required for model rocketry purposes for all ranges of input data. The accuracy of the approximations is, in fact, well within the operational scatter range associated with normal variations in thrust-time characteristics among model rocket engines of the same type. The total impulse of any one model rocket engine of a given type may vary as much as 10% from the nominal total impulse of that engine type. Since the maximum error incurred through the use of either of the approximate methods is less than the variation in performance produced by this total-impulse

Figures 5 - 5.9:

Figures 5 through 9 show the percentage errors incurred in burnout velocity, burnout altitude, and total maximum altitude through the use of the approximate Fehskens-Malewicki and Caporaso-Bengen solutions for vertical model rocket flight. Error analyses for each of the five engine types considered were performed using two values of the drag parameter k : the minimum value considered possible for a rocket powered by the engine under consideration and the maximum value considered feasible for a successful rocket flight with the engine under consideration. The former value is referred to as k_{\min} in the figures and corresponds to a drag coefficient of roughly 0.3 in a rocket whose body tube is glove-fit to the engine under consideration. The latter value is referred to as k_{\max} in the figures and is approximately 40 times k_{\min} . k_{\max} may be thought of as corresponding to a drag coefficient of roughly 2.5 in a rocket whose body is approximately 2.2 times the diameter of the engine casing. Both values of k are computed on the assumption of standard sea-level atmospheric density. Values of the drag parameter and other pertinent data useful in interpreting Figures 5 through 9 are listed below:

Figure number	Engine type	Casing diameter (mm)	k_{\min} (kg/m)	k_{\max} (kg/m)
5	B14	18	.00005	.002
6	B4	18	.00005	.002
7	D4	21	.00007	.0027
8	F100	27	.00012	.0045
9	F7	27	.00012	.0045

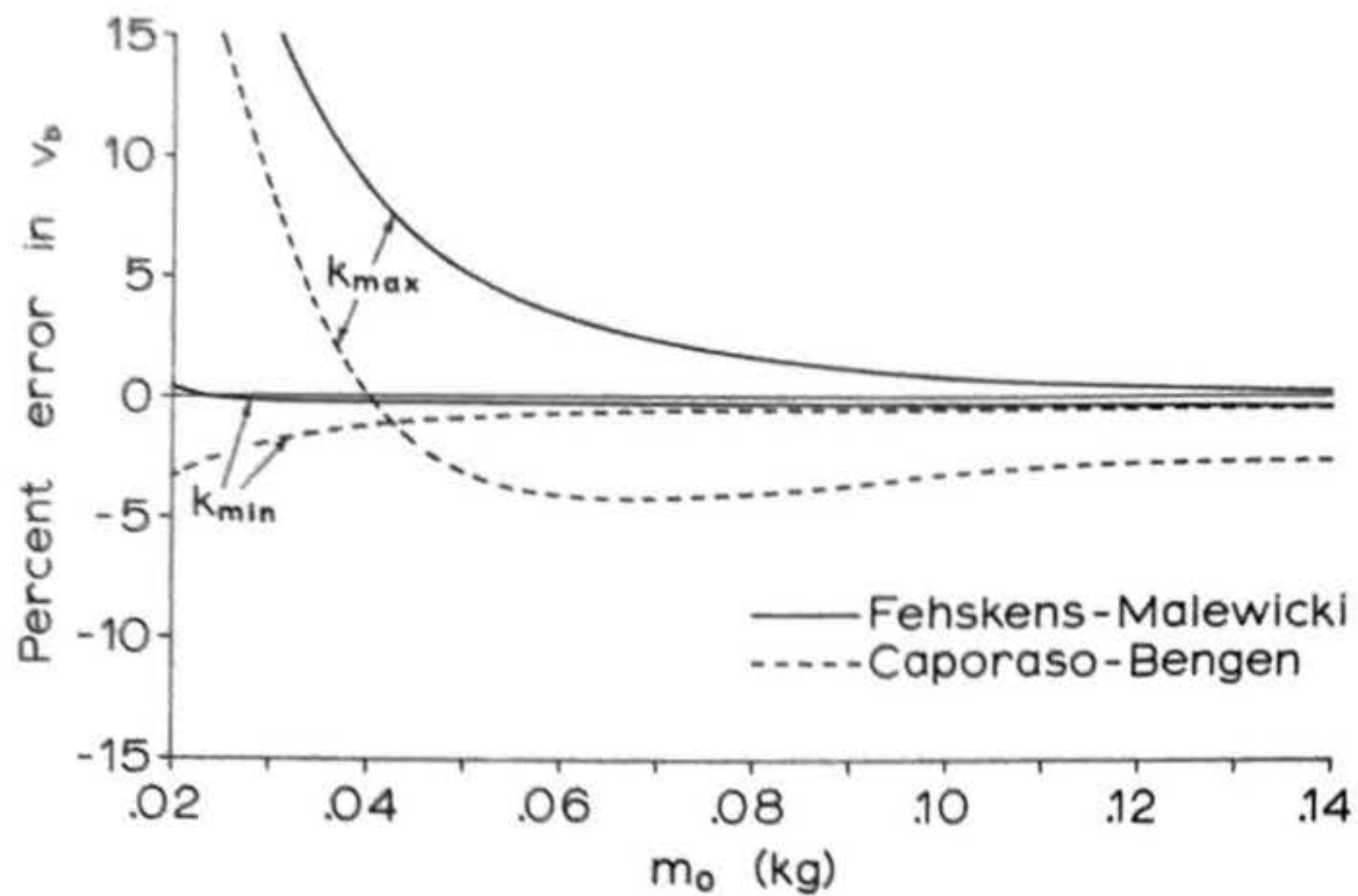


Figure 5(a): Burnout velocity error of approximate methods for vertical flight; models using Type Bl4 engine.

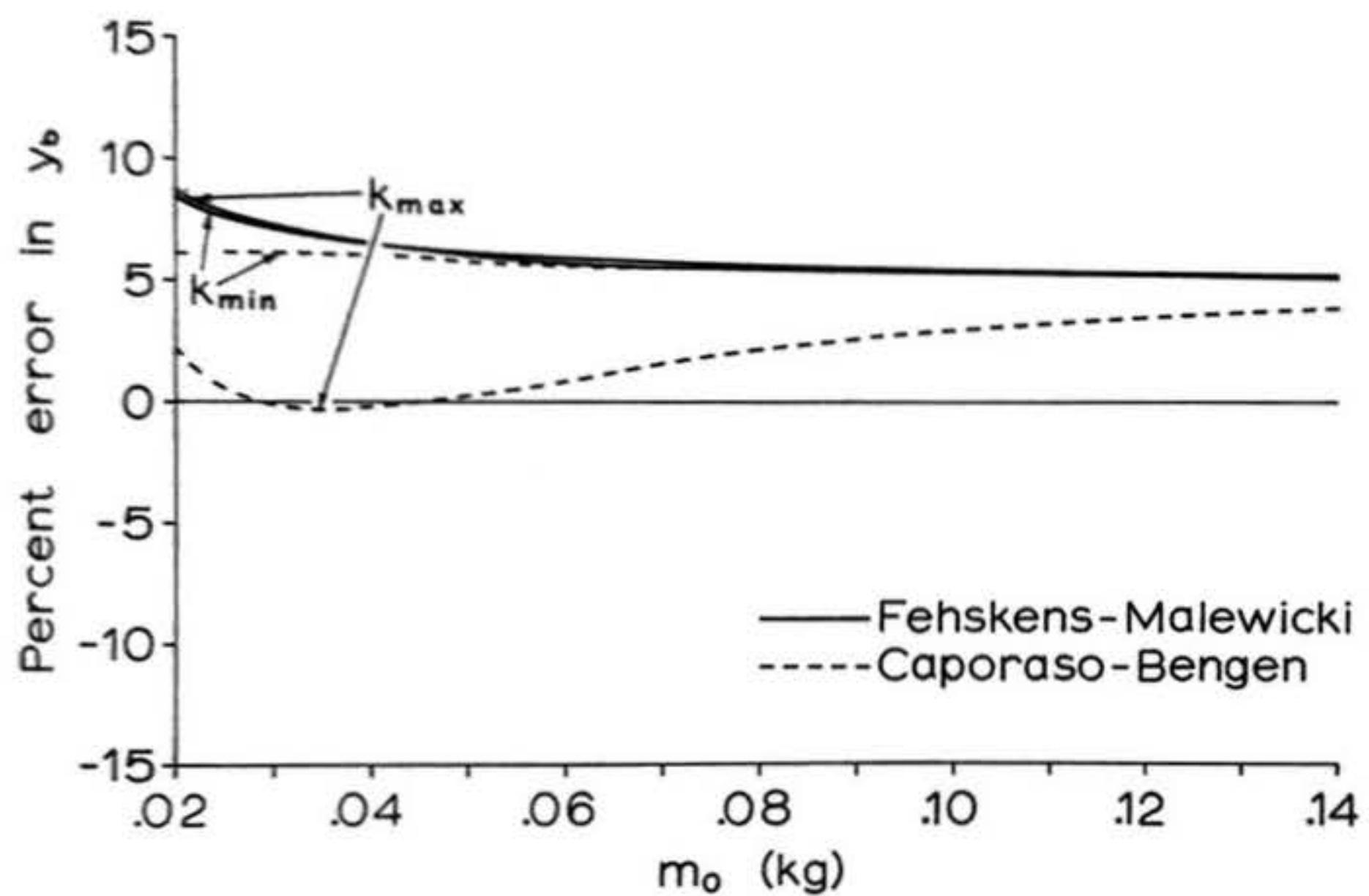


Figure 5(b): Burnout altitude error of approximate methods for vertical flight; models using Type Bl4 engine.

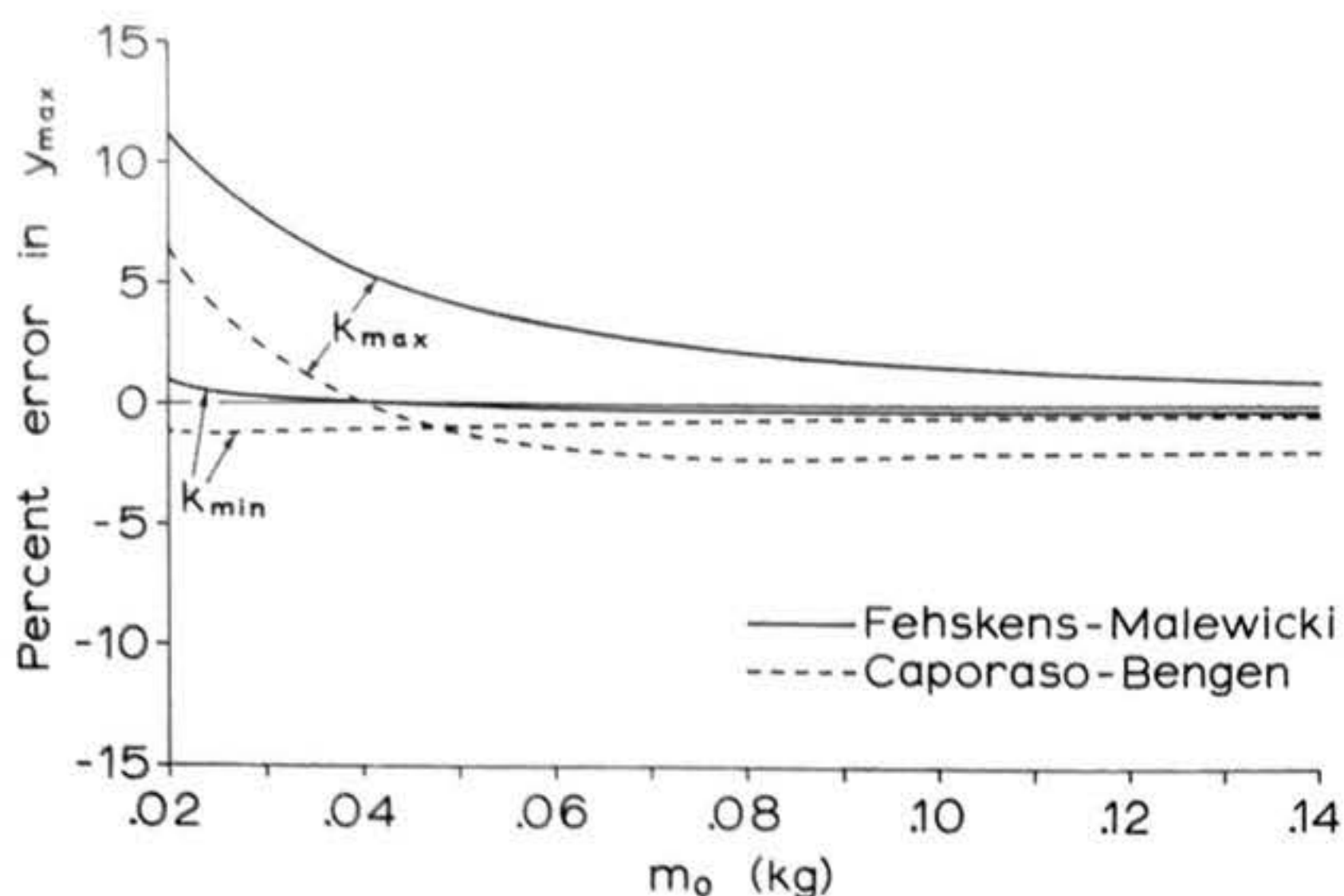


Figure 5(c): Maximum altitude error of approximate methods for vertical flight; models using Type B14 engine.

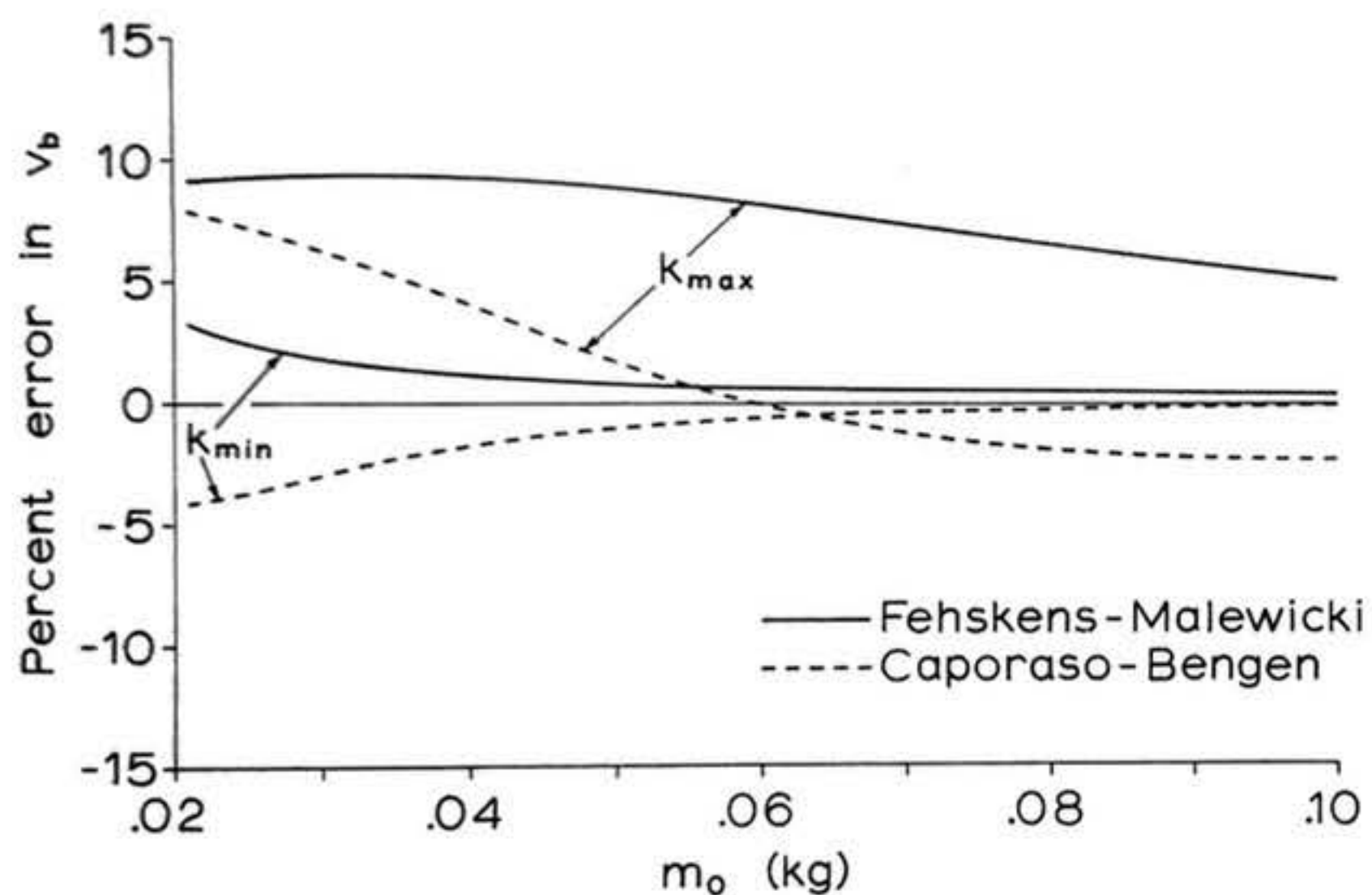


Figure 6(a): Burnout velocity error of approximate methods for vertical flight; models using Type B4 engine.

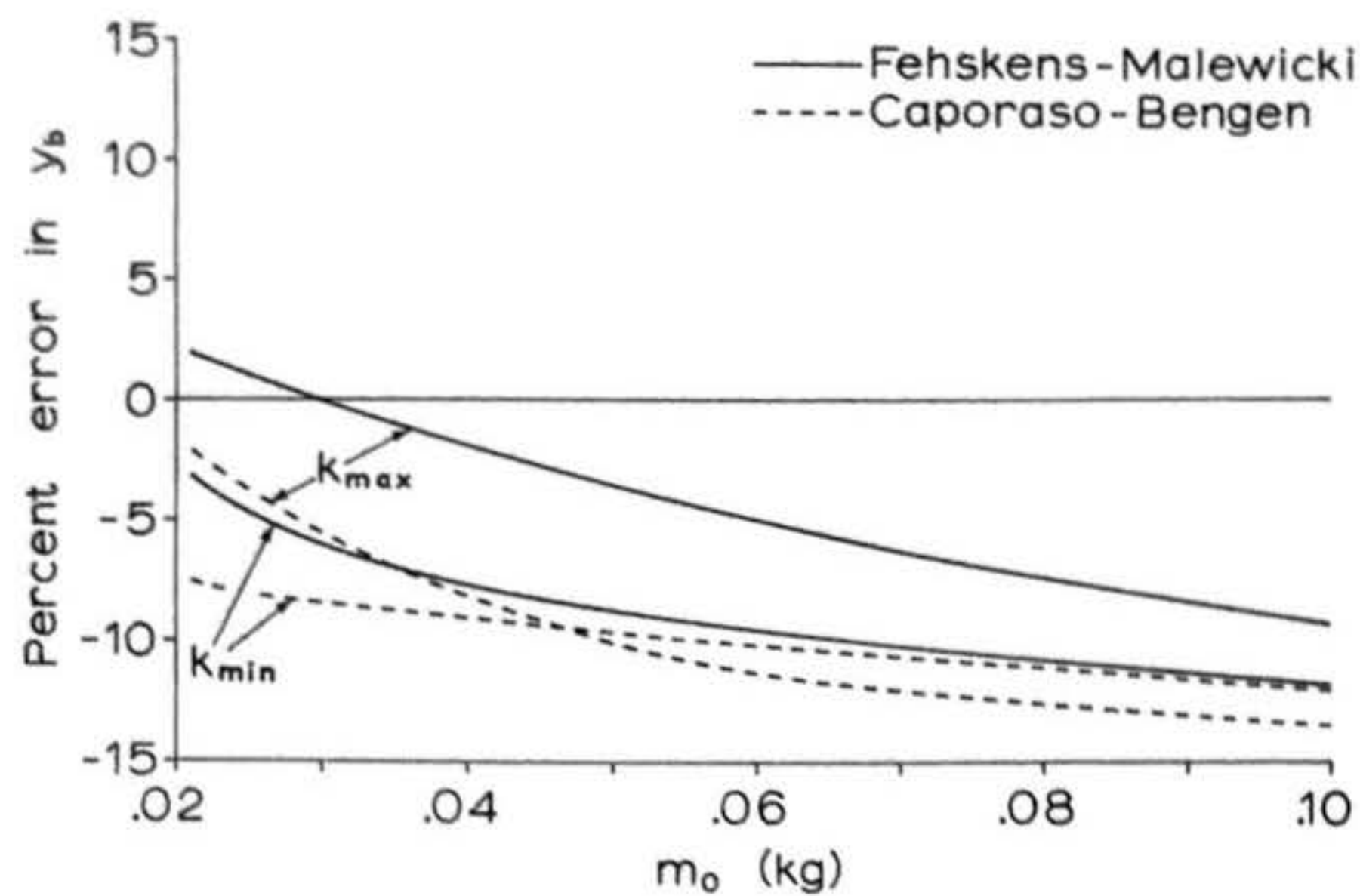


Figure 6(b): Burnout altitude error of approximate methods for vertical flight; models using Type B4 engine.

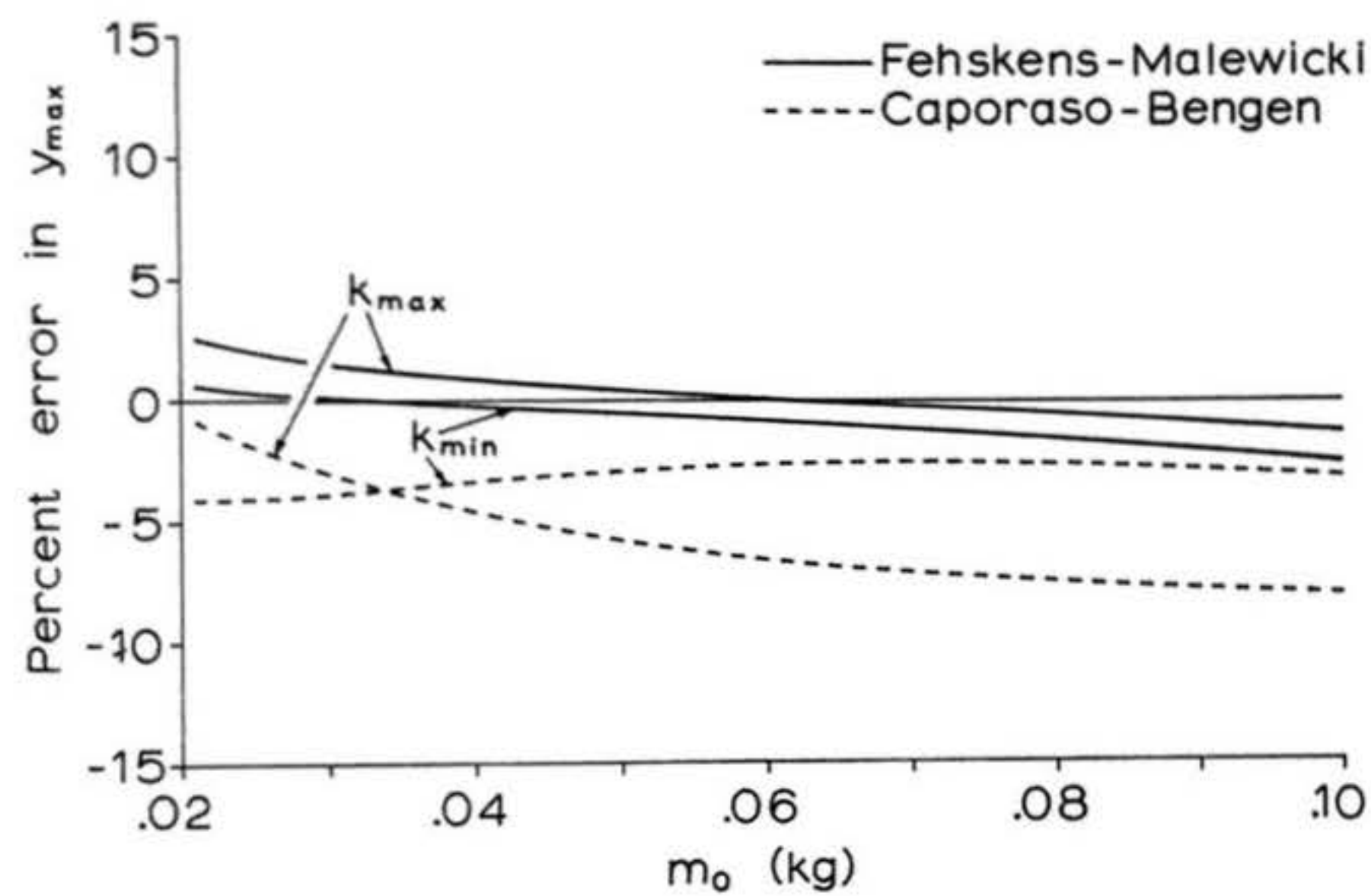


Figure 6(c): Maximum altitude error of approximate methods for vertical flight; models using Type B4 engine.

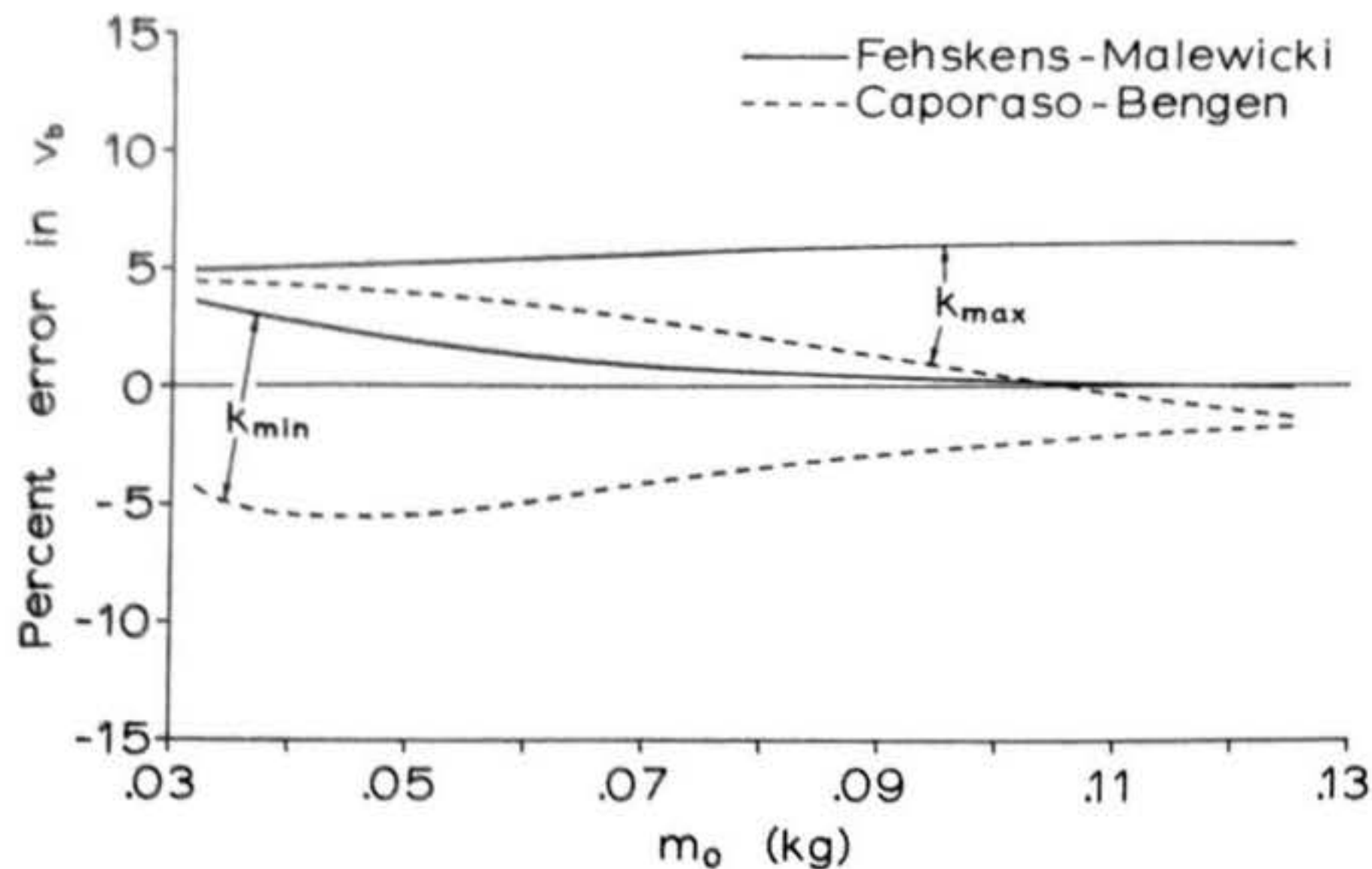


Figure 7(a): Burnout velocity error of approximate methods for vertical flight; models using Type D4 engine.

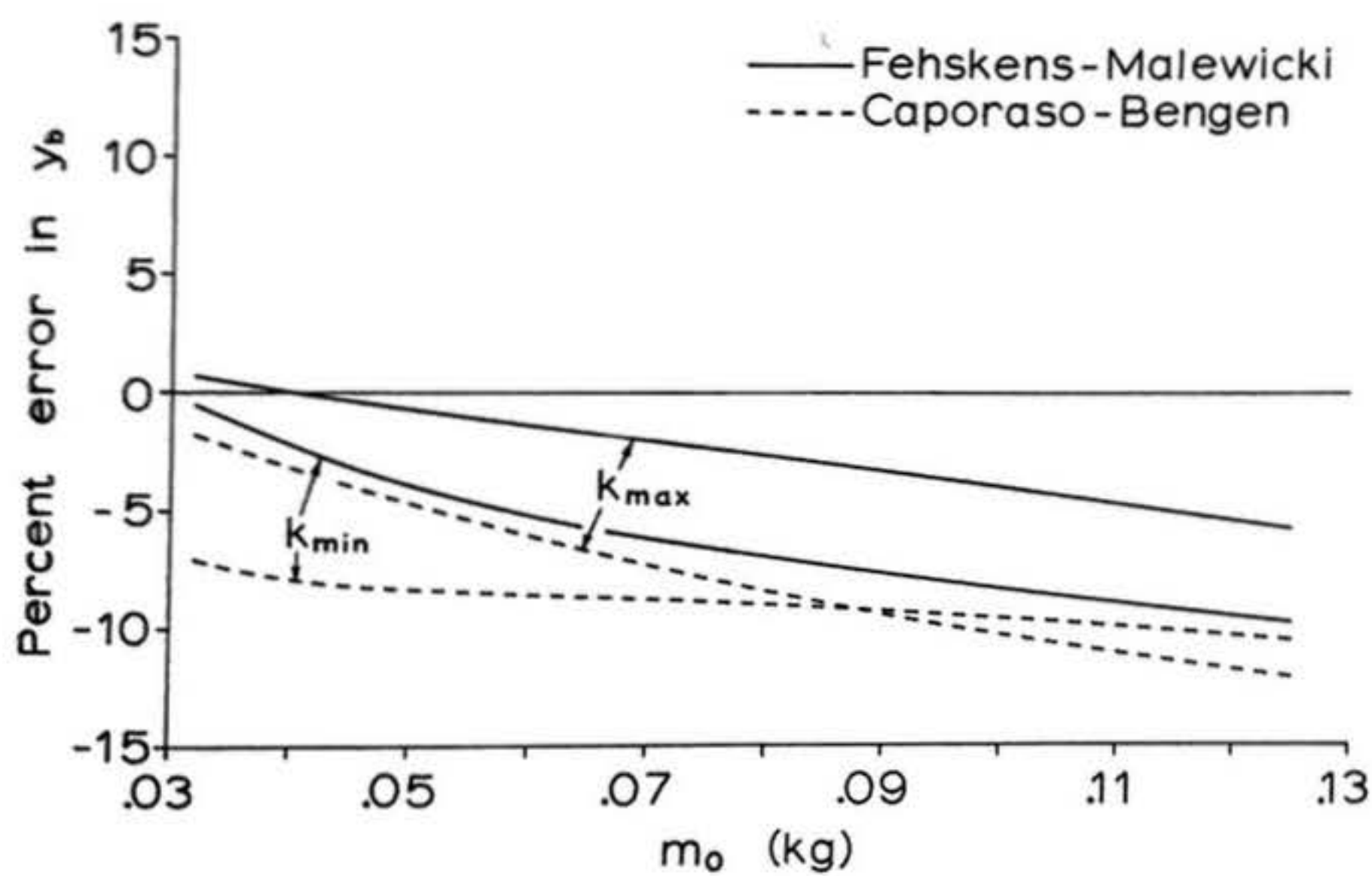


Figure 7(b): Burnout altitude error of approximate methods for vertical flight; models using Type D4 engine.

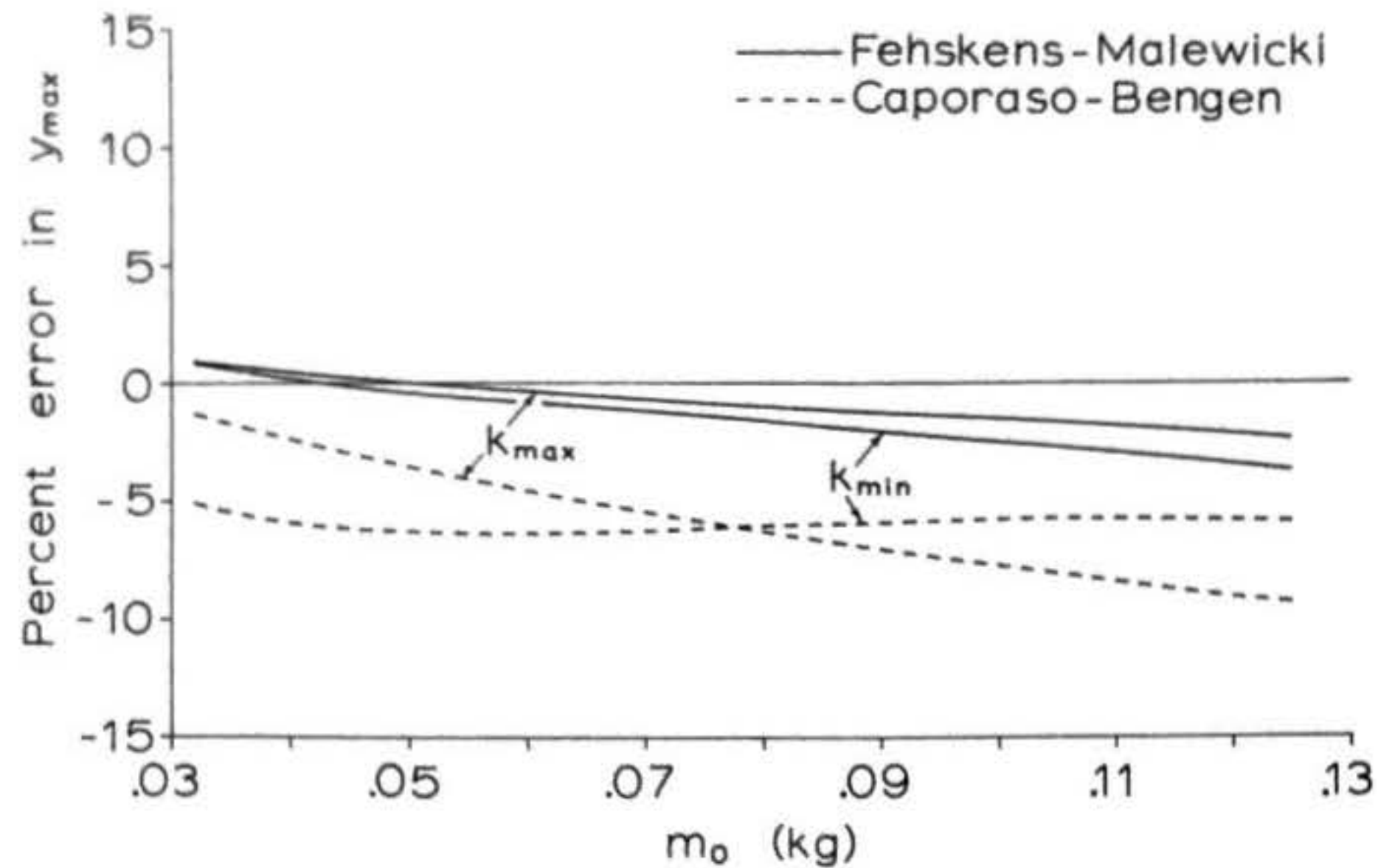


Figure 7(c): Maximum altitude error of approximate methods for vertical flight; models using Type D4 engine.

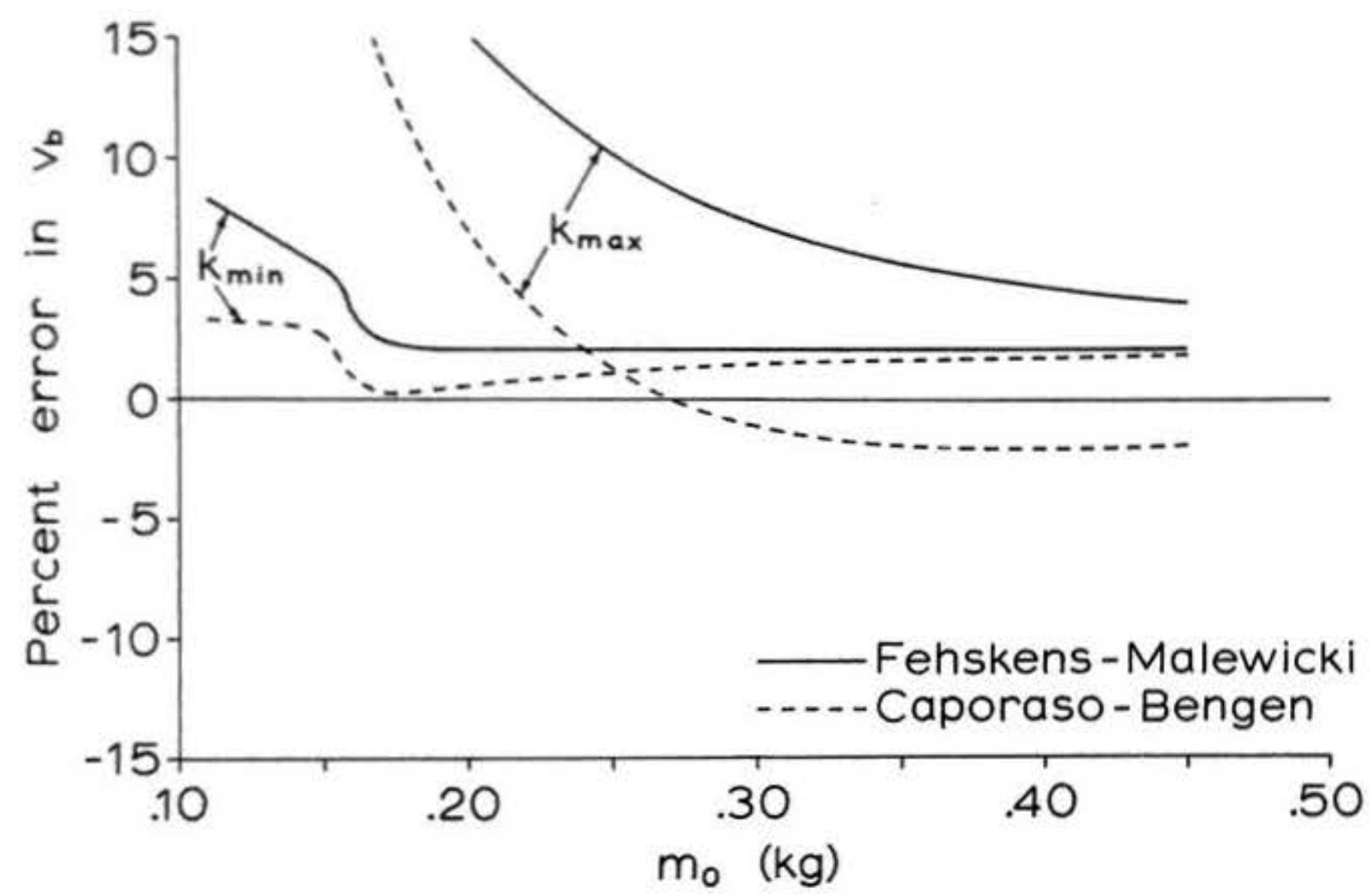


Figure 8(a): Burnout velocity error of approximate methods for vertical flight; models using Type F100 engine. An additional error is incurred for values of m_0 below 0.17 kg due to transonic drag divergence, in the k_{\min} cases.

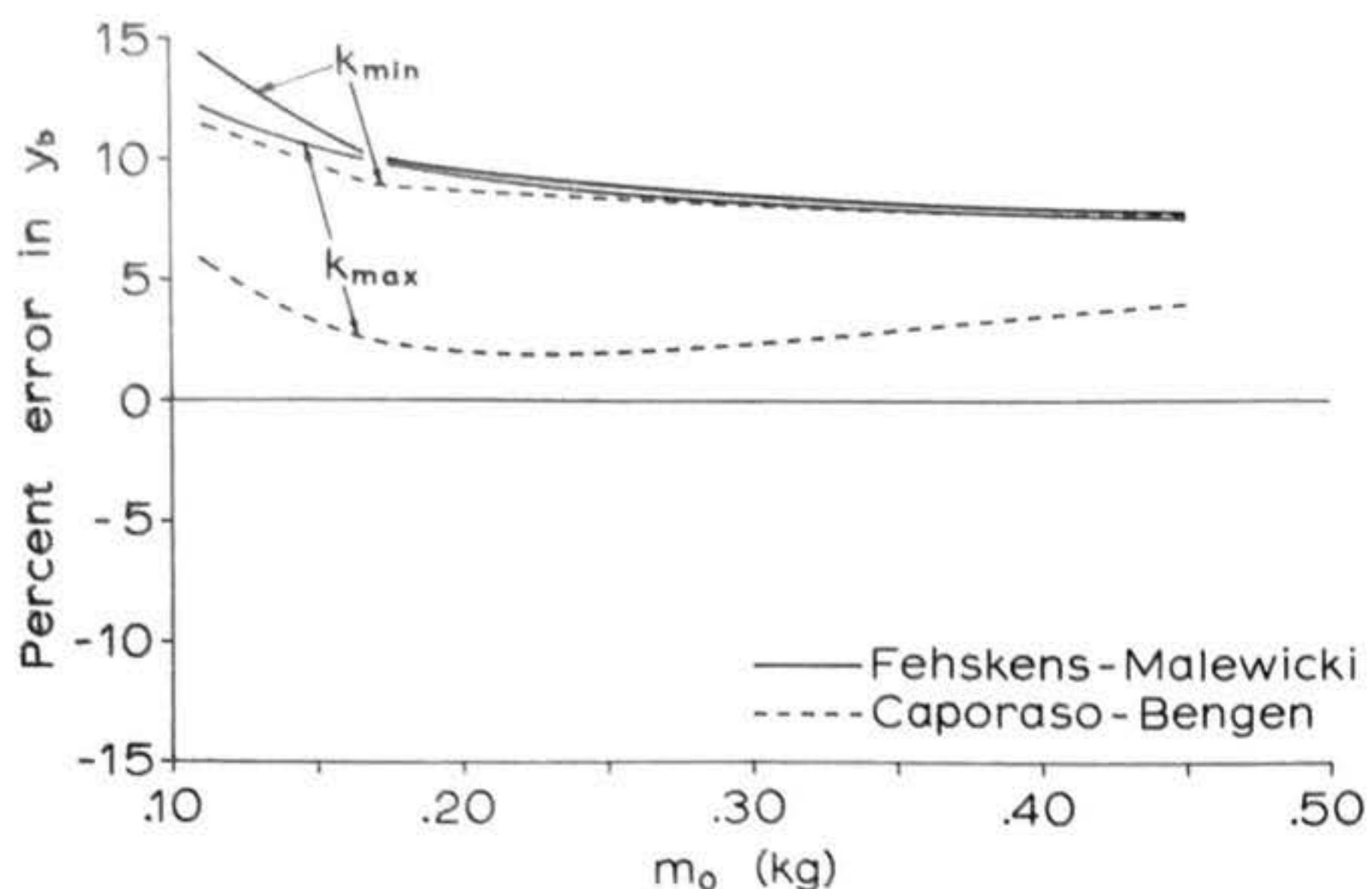


Figure 8(b): Burnout altitude error of approximate methods for vertical flight; models using Type F100 engine. An additional error is incurred for values of m_0 below 0.17 kg due to transonic drag divergence, in the k_{\min} cases.

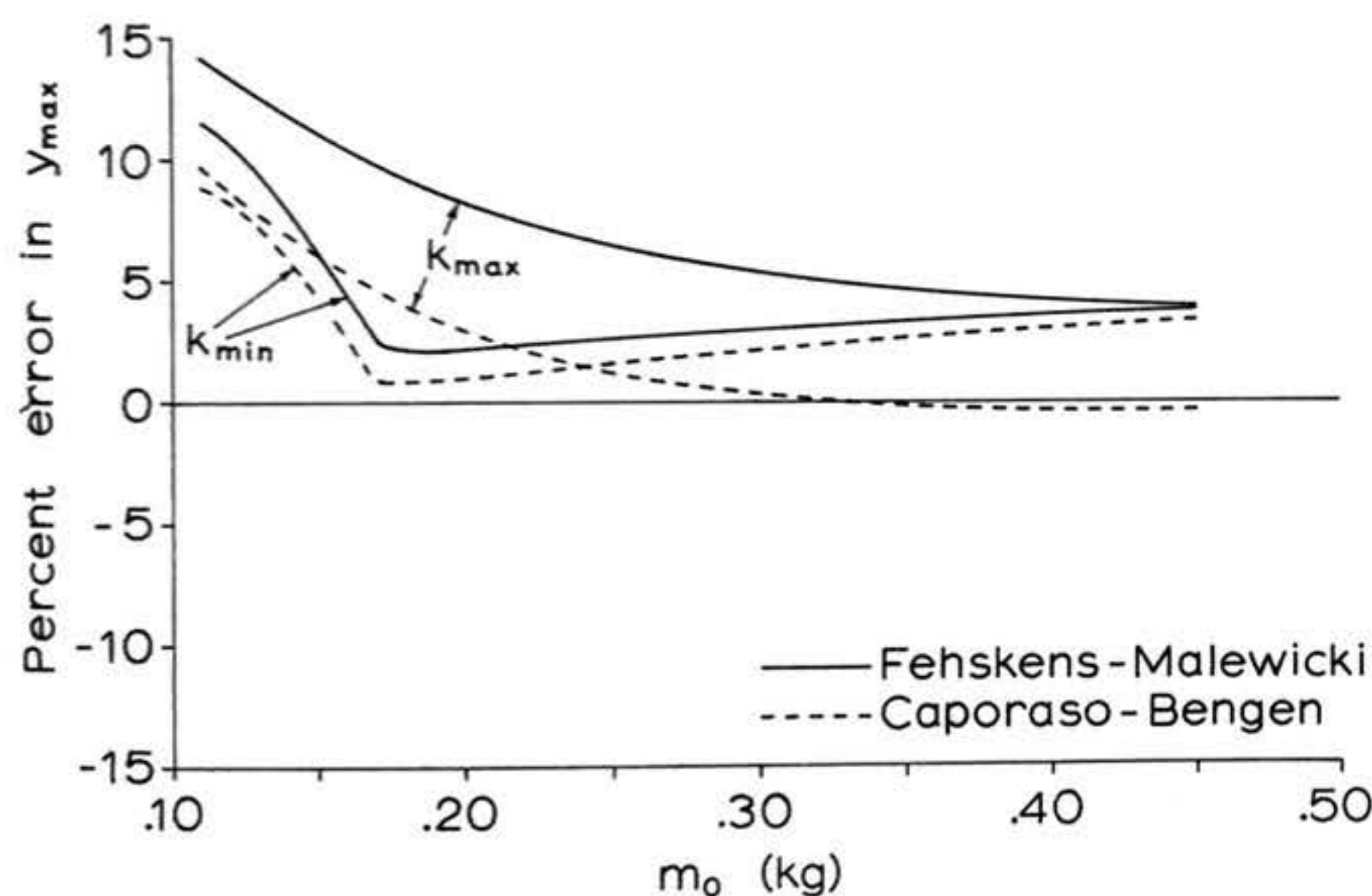


Figure 8(c): Maximum altitude error of approximate methods for vertical flight; models using Type F100 engine. An additional error is incurred for values of m_0 below 0.17 kg due to transonic drag divergence, in the k_{\min} cases.

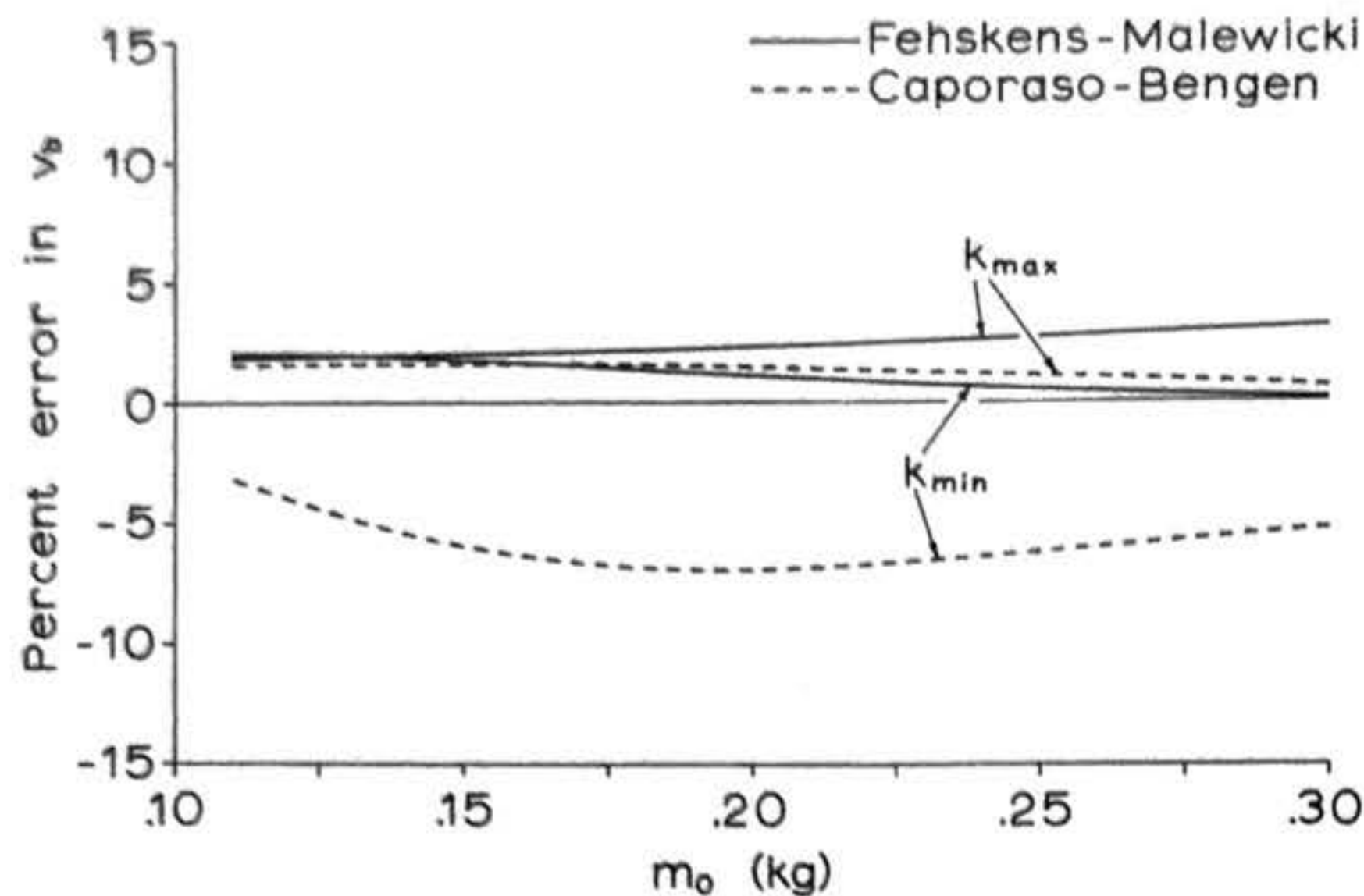


Figure 9(a): Burnout velocity error of approximate methods for vertical flight; models using Type F7 engine.

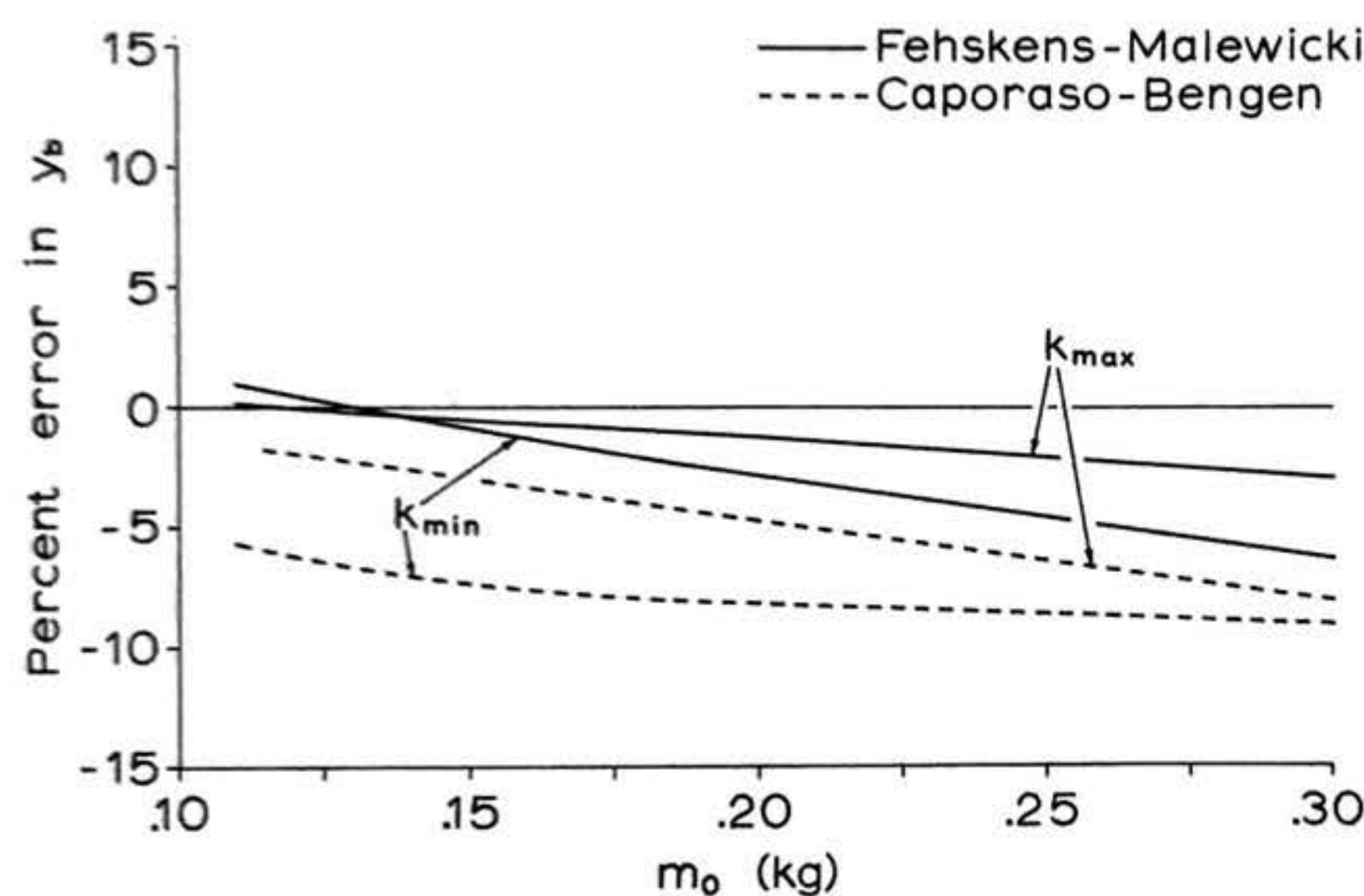


Figure 9(b): Burnout altitude error of approximate methods for vertical flight; models using Type F7 engine.

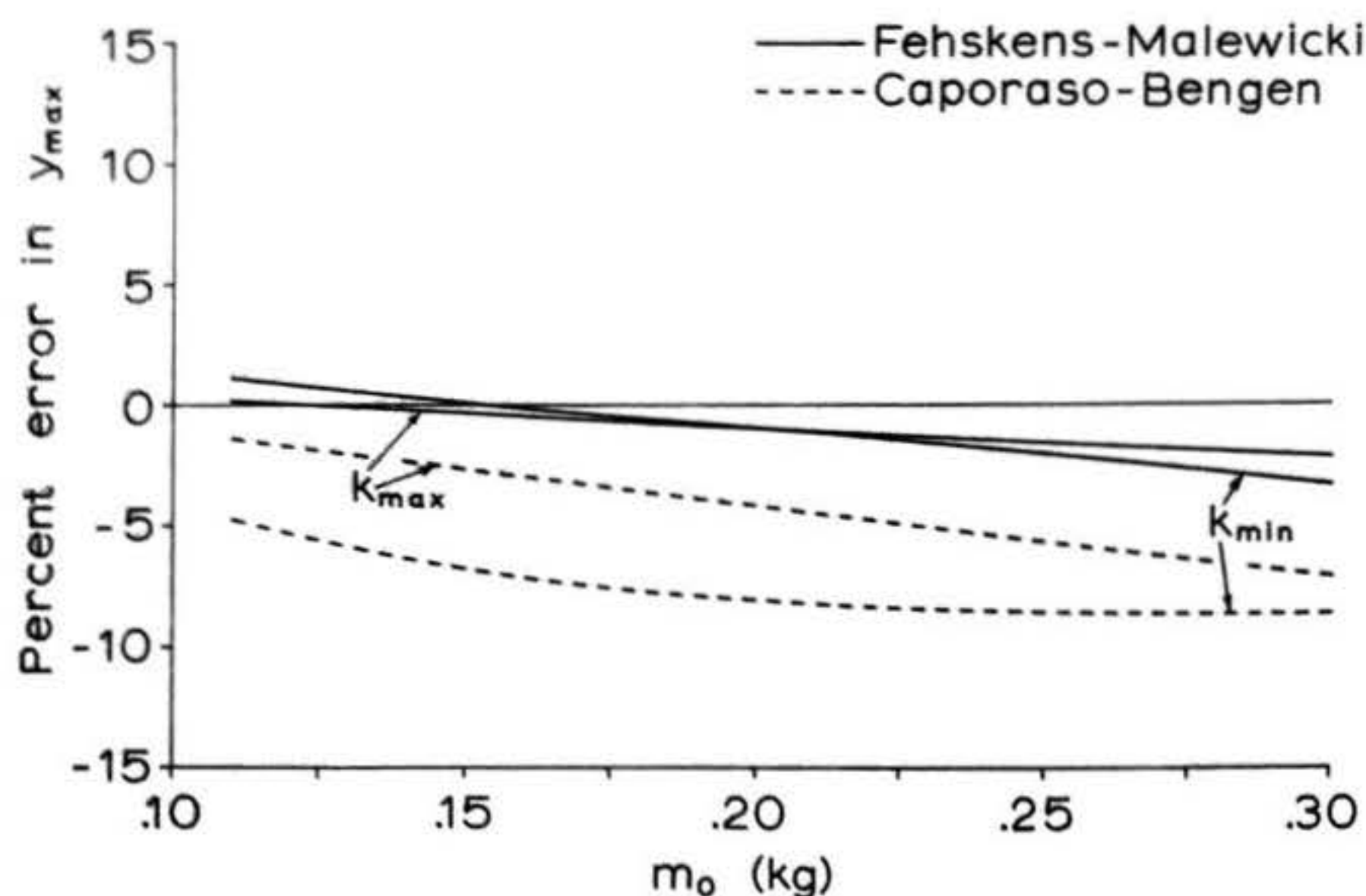


Figure 9(c): Maximum altitude error of approximate methods for vertical flight; models using Type F7 engine.

scatter, we may conclude that the closed-form, analytical solutions developed in Section 2.1 produce results that are as accurate as we shall ever need for the purpose of designing model rockets.

3. The Non-Oscillating Rocket: Solutions for Vehicles Launched at Any Angle from the Vertical

3.1 The Differential Equations of Motion

As stated in Section 1, the general differential equations of motion for the vertical and horizontal components of a model rocket's motion in flight are, respectively,

$$(16) \quad m(t) \frac{dv_y}{dt} = F(t) \frac{\dot{y}}{v} \cos\alpha - m(t)g - [k + \epsilon f(\alpha)] v \dot{y} \quad \text{and}$$

$$(17) \quad m(t) \frac{dv_x}{dt} = F(t) \frac{\dot{x}}{v} \cos\alpha - [k + \epsilon f(\alpha)] v \dot{x}$$

Under the assumption that the model does not oscillate, or experience rigid-body rotations, during its flight (16) and (17) reduce to

$$(90) \quad m(t) \frac{dv_y}{dt} = F(t) \frac{\dot{y}}{v} - m(t)g - kv \dot{y}$$

$$(91) \quad m(t) \frac{dv_x}{dt} = F(t) \frac{\dot{x}}{v} - kv \dot{x}$$

3.2 Numerical Methods for the Digital Computation of Nonvertical Trajectories

In Section 2 of this chapter we were able to determine closed-form, approximate solutions to the equations of motion that were sufficiently accurate, simple, and general for practical use. In the case of equations (90) and (91) we shall not be

so fortunate. Extensive investigation on the part of several researchers has failed to reveal any closed-form, approximate, analytical solution to (90) and (91) which is sufficiently accurate (even) for hobby purposes and still sufficiently easy to work by hand to offer a perceptible advantage over computer interval techniques. The solutions of this section will therefore be based on numerical techniques analogous to those of Section 2.4, intended primarily for use with automatic computing machinery. One can also carry out such iterative calculations by hand, of course, but those who wish to do so must necessarily accept either a considerable amount of work or the degradation in accuracy concomitant with the use of coarser time intervals.

The generalization of either of the computation schemes of Section 2.4 to nonvertical flight is a relatively simple matter of separating the motion of the rocket into its vertical and horizontal components. Once this has been done, a single "loop", or iteration, of the theoretical-velocity-increment method appears in the following form:

$$(92) \quad \Delta \dot{y}_t = \frac{\Delta t [F(t) \frac{\dot{y}}{v} - m(t)g]}{m(t)}$$

$$(93) \quad \Delta \dot{x}_t = \frac{\Delta t [F(t) \frac{\dot{x}}{v}]}{m(t)}$$

$$(94) \quad v_t = \sqrt{(\dot{x} + \Delta \dot{x}_t)^2 + (\dot{y} + \Delta \dot{y}_t)^2}$$

$$(95) \quad \text{Drag} = k v_t^2$$

$$(96) \quad \Delta \dot{y}_a = \frac{\Delta t [F(t) \frac{\dot{y}}{v} - m(t)g - k v_t^2 \frac{\dot{y}}{v}]}{m(t)}$$

$$(97) \quad \Delta \dot{x}_a = \frac{\Delta t [F(t) \frac{\dot{x}}{v} - k v_t^2 \frac{\dot{x}}{v}]}{m(t)}$$

$$(98) \quad \Delta y = \Delta t \left[\dot{y} + \frac{\Delta \dot{y}_a}{2} \right]$$

$$(99) \quad \Delta x = \Delta t \left[\dot{x} + \frac{\Delta \dot{x}_a}{2} \right]$$

$$(100) \quad y = y + \Delta y$$

$$(101) \quad x = x + \Delta x$$

$$(102) \quad \dot{y} = \dot{y} + \Delta \dot{y}_a$$

$$(103) \quad \dot{x} = \dot{x} + \Delta \dot{x}_a$$

$$(104) \quad v = \sqrt{(\dot{x})^2 + (\dot{y})^2}$$

$$(105) \quad t = t + \Delta t$$

where $\Delta \dot{x}_t$ = drag-free "theoretical" horizontal velocity increment

$\Delta \dot{y}_t$ = drag-free vertical velocity increment

$\Delta \dot{x}_a$ = actual horizontal velocity increment

$\Delta \dot{y}_a$ = actual vertical velocity increment

and the other variables are as in Section 2.4.

Likewise, the drag-from-prior-velocity method -- the second technique of Section 2.4 -- generalizes to nonvertical flight according to the set of equations presented below:

$$(106) \quad \Delta \dot{y} = \frac{\Delta t [F(t) \frac{\dot{y}}{v} - m(t)g - kv\dot{y}]}{m(t)}$$

$$(107) \quad \Delta \dot{x} = \frac{\Delta t [F(t) \frac{\dot{x}}{v} - kv\dot{x}]}{m(t)}$$

$$(108) \quad \Delta y = \Delta t \left[\dot{y} + \frac{\Delta \dot{y}}{2} \right]$$

$$(109) \quad \Delta x = \Delta t \left[\dot{x} + \frac{\Delta \dot{x}}{2} \right]$$

$$(110) \quad \dot{y} = \dot{y} + \Delta \dot{y}$$

$$(111) \quad \dot{x} = \dot{x} + \Delta \dot{x}$$

$$(112) \quad v = \sqrt{(\dot{x})^2 + (\dot{y})^2}$$

$$(113) \quad y = y + \Delta y$$

$$(114) \quad x = x + \Delta x$$

$$(115) \quad t = t + \Delta t$$

In order to begin calculations from zero velocity on the ground it is necessary to simulate the presence of the launch rod for the first meter or so of motion by using a slightly different set of equations that assumes a fixed trajectory angle equal to the initial angle of launch θ_0 . Such a scheme suitable for use with the method of theoretical velocity increments is

$$(116) \quad \Delta v_t = \frac{\Delta t [F(t) - m(t)g \cos \theta_0]}{m(t)}$$

$$(117) \quad \text{Drag} = k(v + \Delta v_t)^2$$

$$(118) \quad \Delta v_a = \frac{\Delta t [F(t) - m(t)g \cos \theta_0 - k(v + \Delta v_t)^2]}{m(t)}$$

$$(119) \quad \Delta y = \Delta t [v + \frac{\Delta v_a}{2}] \cos \theta_0$$

$$(120) \quad \Delta x = \Delta t [v + \frac{\Delta v_a}{2}] \sin \theta_0$$

$$(121) \quad v = v + \Delta v_a$$

$$(122) \quad y = y + \Delta y$$

$$(123) \quad x = x + \Delta x$$

$$(124) \quad t = t + \Delta t$$

while the launch phase of a nonvertical flight may be represented using the method of drag from prior velocity as

$$(125) \quad \Delta v = \frac{\Delta t [F(t) - m(t)g \cos \theta_0 - kv^2]}{m(t)}$$

$$(126) \quad \Delta y = \Delta t [v + \frac{\Delta v}{2}] \cos \theta_0$$

$$(127) \quad \Delta x = \Delta t [v + \frac{\Delta v}{2}] \sin \theta_0$$

$$(128) \quad v = v + \Delta v$$

$$(129) \quad y = y + \Delta y$$

$$(130) \quad x = x + \Delta x$$

$$(131) \quad t = t + \Delta t$$

As was the case with the vertical solutions, both the computing schemes presented herein can be extended to multistaged vehicles and to the coasting phase of flight by altering the thrust and mass functions appropriately at staging or at burnout. Again, the latter method requires a smaller time interval than the former for good accuracy; 0.1 or 0.01 second may be used with the first method, while .001 second is recommended for use with the second. The thrust and mass functions to be used with either of the above methods are the same as those described in Section 2.4; they do not, therefore, require any further discussion here.

3.3 Examples of Nonvertical Model Rocket Trajectories

The second of the numerical methods discussed in Section 3.2 has been employed to calculate a number of representative nonvertical model rocket flight paths. The same five engine

types used in Section 2.5 were considered; i.e., the B14, B4, D4, F100, and F7. Due to the vast quantity of data that would have to be generated to account for a full range of variation in each and every parameter relevant to nonvertical flight, the calculations were restricted to certain cases deemed to be of particular interest or illustrative value in practical model rocketry.

The decision was first made to perform all burning-phase calculations under the assumption of an initial launch angle of 30° to the vertical, this being the greatest deviation from vertical launch permitted by the Safety Code of the National Association of Rocketry, as well as by most of the laws governing the practice of model rocketry. The initial angle θ_0 of 30° thus represents the most severe condition of nonverticality possible within the rules of the hobby.

Three cases were then computed for each engine: one representing the best-performing rocket, one representing a typical rocket, and one representing the worst-performing rocket considered possible for that engine. For the first case, an initial mass m_0 equal to the mass of the engine alone and a drag parameter k corresponding to a drag coefficient of about 0.3 in sea-level air with a body tube glove-fit to the engine were used. For the second, both quantities were slightly more than doubled; for the third, a value of m_0 equal to the manufacturer's maximum recommended liftoff weight and a value of k approximately 40 times that of the first case were used. An exception was made in the case of the F100 engine, where the maximum value of m_0 was taken as 453 grams (0.453 Kg), this being the maximum legal liftoff

mass for model rockets in the United States.

The results of the calculations are displayed in Figures 10 through 14. As one would expect, the influence of a nonvertical launch on subsequent flight behavior and altitude performance is least severe for cases involving short-burning-time engines. As the burn time increases, the flight paths are seen to develop considerable burning-phase curvature. The low thrust and 9-second burning time of the type F7 engine makes a nonvertical launch a very risky proposition indeed, particularly in cases of medium- or heavy-weight rockets; the high drag and weight case of Figure 14, in fact, results in catastrophic behavior -- a dive into the ground under power, more commonly and colloquially called a "power prang". You should note, when examining Figures 10 through 14, that all trajectories have been continued until impact with the ground is predicted, as if there were no parachute ejection or other recovery system activation. Times in seconds from launch have been marked on the curves to enable the reader to predict the position of the rocket at recovery system activation for any given time delay. Needless to say, safety considerations require the selection of a delay time such that the rocket does not strike the ground before the recovery system activates -- a rule which applies to all model rocket flights, whether vertical or not.

The behavior in nonvertical flight of models using long-burning engines bears some further discussion because of its safety implications. The severe change in trajectory angle experienced during the burning phase of flight by models using long-burning engines is due to a phenomenon known to professional rocketry as the "gravity turn", a term which describes the following

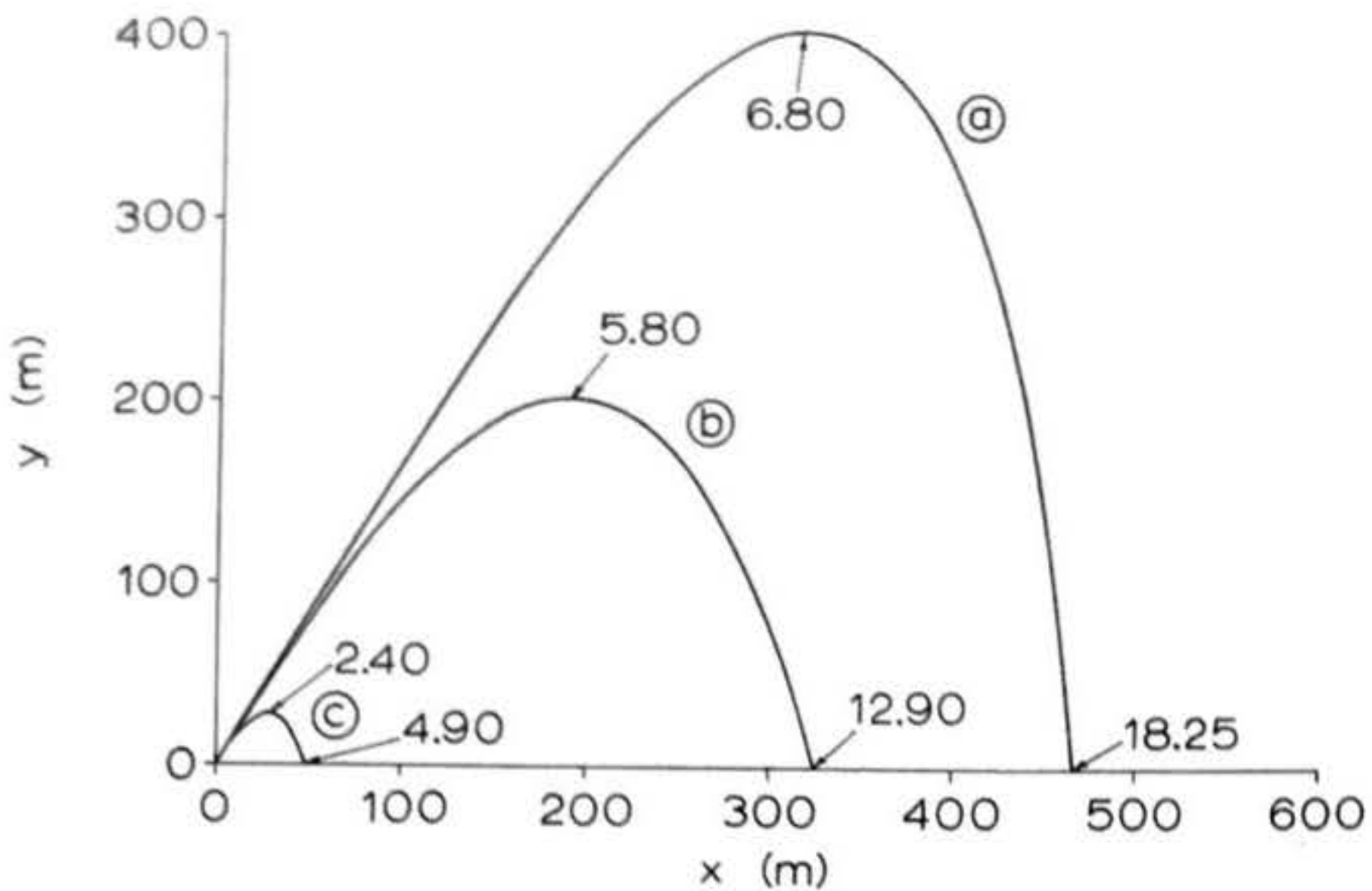


Figure 10: Non-vertical trajectories for 30° launch angle; models using Type Bl4 engine. Curve (a): $m_0 = .020$ kg, $k = .00005$ kg/m; burnout range x_b is 23 m, burnout altitude y_b is 40 m. Curve (b): $m_0 = .050$ kg, $k = .00012$ kg/m; $x_b = 9$ m, $y_b = 15$ m. Curve (c): $m_0 = .140$ kg, $k = .002$ kg/m; $x_b = 3$ m, $y_b = 5$ m. The engine burning time is 0.35 second. The time of flight apex, and the time of predicted impact on the ground if there were no recovery system activation, in seconds, are marked on the curves.

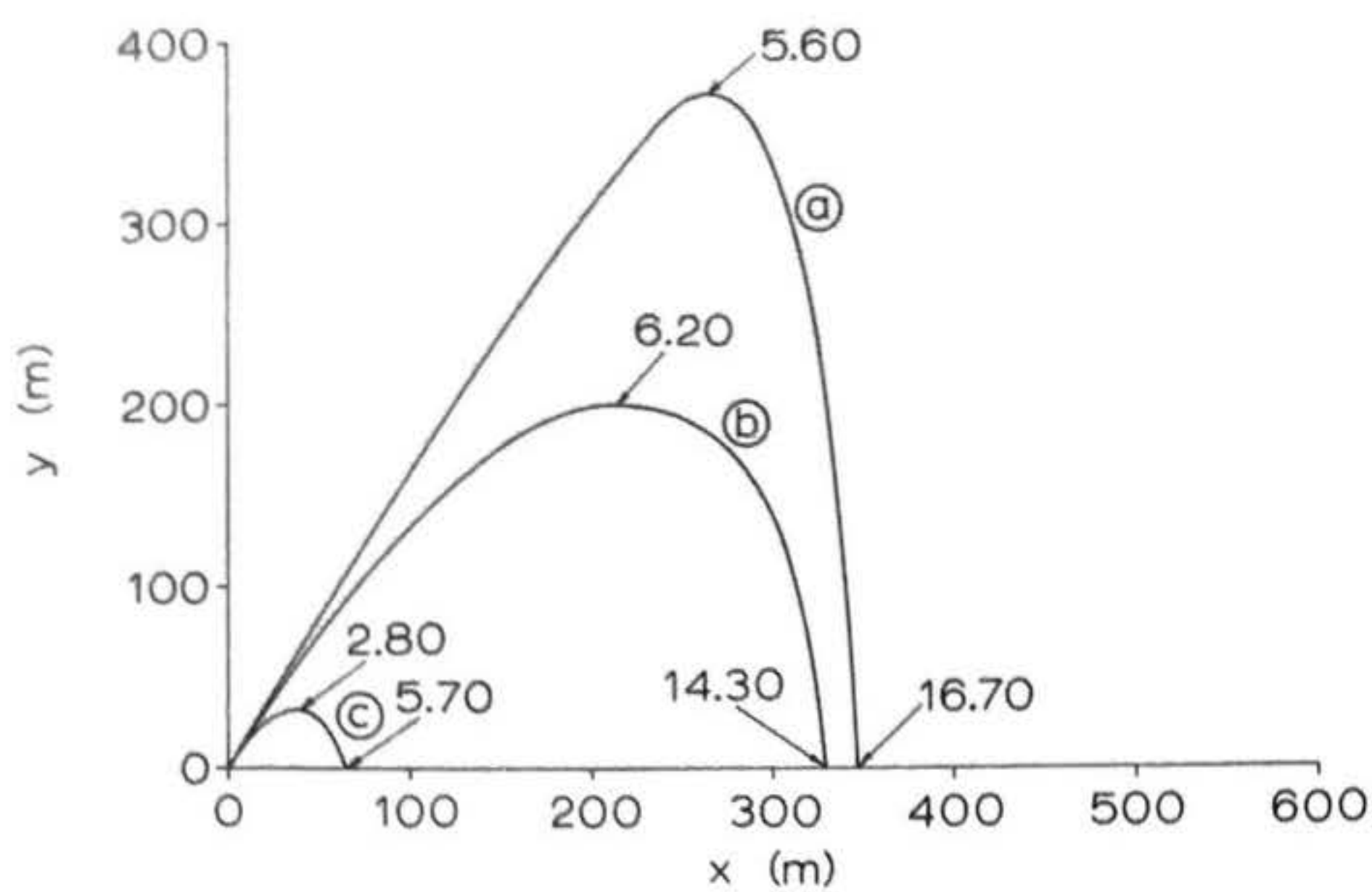


Figure 11: Non-vertical trajectories for 30° launch angle; models using Type B4 engine. Curve (a): $m_0 = .021$ kg, $k = .00005$ kg/m; $x_b = 82$ m, $y_b = 131$ m. Curve (b): $m_0 = .050$ kg, $k = .00012$ kg/m; $x_b = 35$ m, $y_b = 51$ m. Curve (c): $m_0 = .100$ kg, $k = .002$ kg/m; $x_b = 15$ m, $y_b = 19$ m. The engine burning time is 1.20 sec.

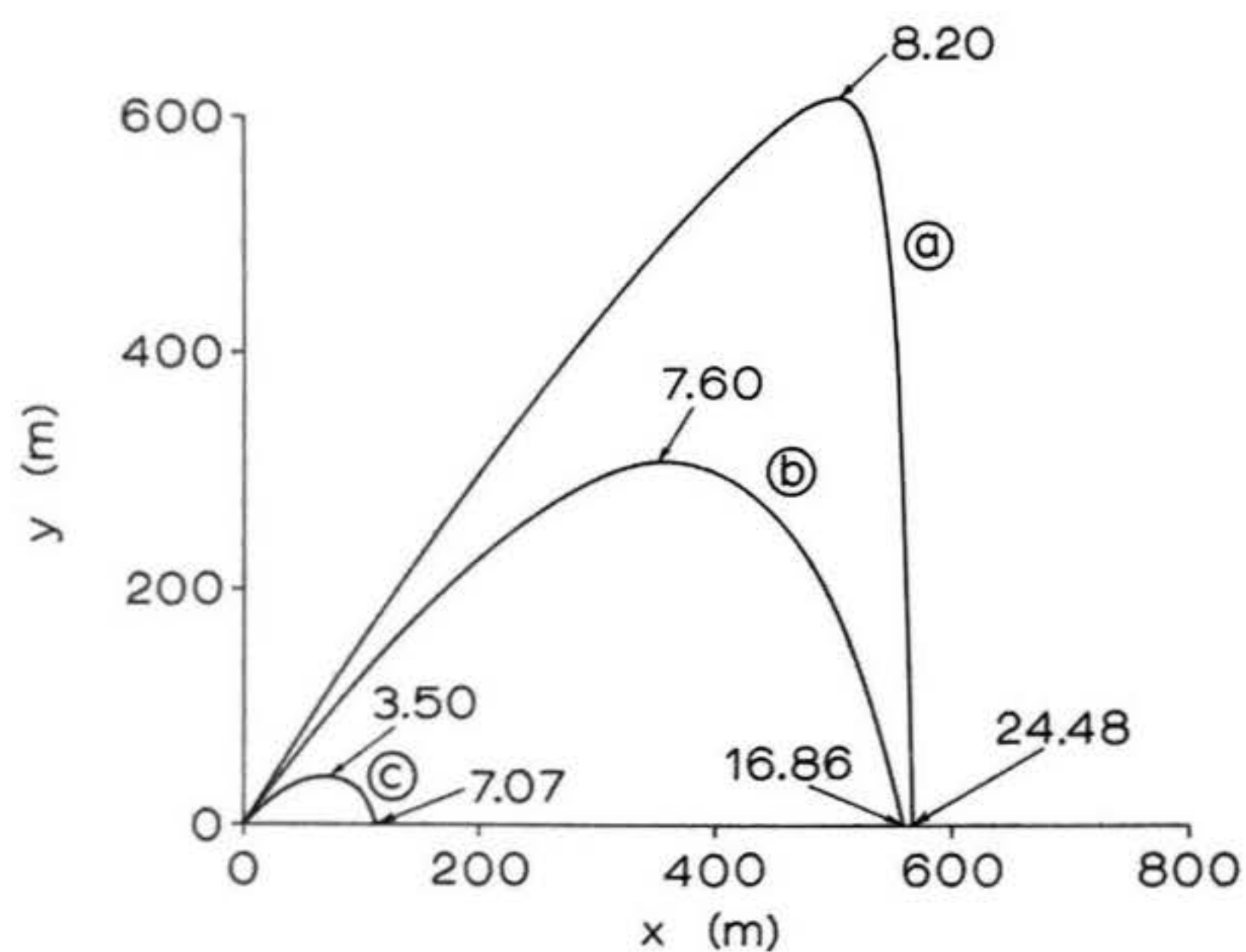


Figure 12: Non-vertical trajectories for 30° launch angle; models using Type D4 engine. Curve (a): $m_0 = .032$ kg, $k = .00007$ kg/m; $x_b = 236$ m, $y_b = 342$ m. Curve (b): $m_0 = .065$ kg, $k = .00017$ kg/m; $x_b = 133$ m, $y_b = 160$ m. Curve (c): $m_0 = .125$ kg, $k = .0027$ kg/m; $x_b = 57$ m, $y_b = 38$ m. The engine burning time is 2.90 sec.

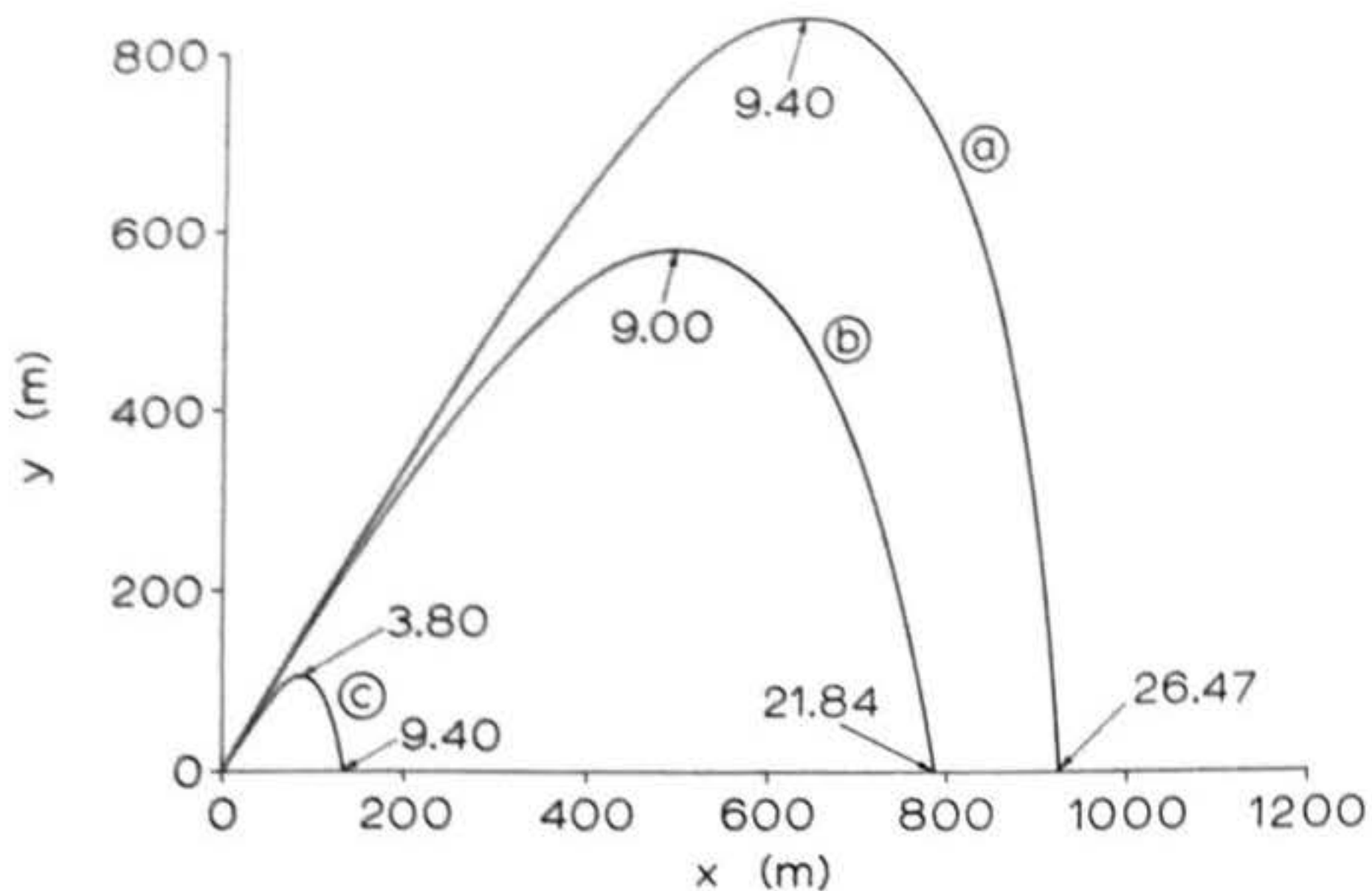


Figure 13: Non-vertical trajectories for 30° launch angle; models using Type F100 engine. Curve (a): $m_0 = .110$ kg, $k = .00012$ kg/m; $x_b = 61$ m, $y_b = 103$ m. Curve (b): $m_0 = .230$ kg, $k = .0003$ kg/m; $x_b = 28$ m, $y_b = 47$ m. Curve (c): $m_0 = .453$ kg, $k = .0045$ kg/m; $x_b = 13$ m, $y_b = 21$ m. The engine burning time is 0.50 sec.

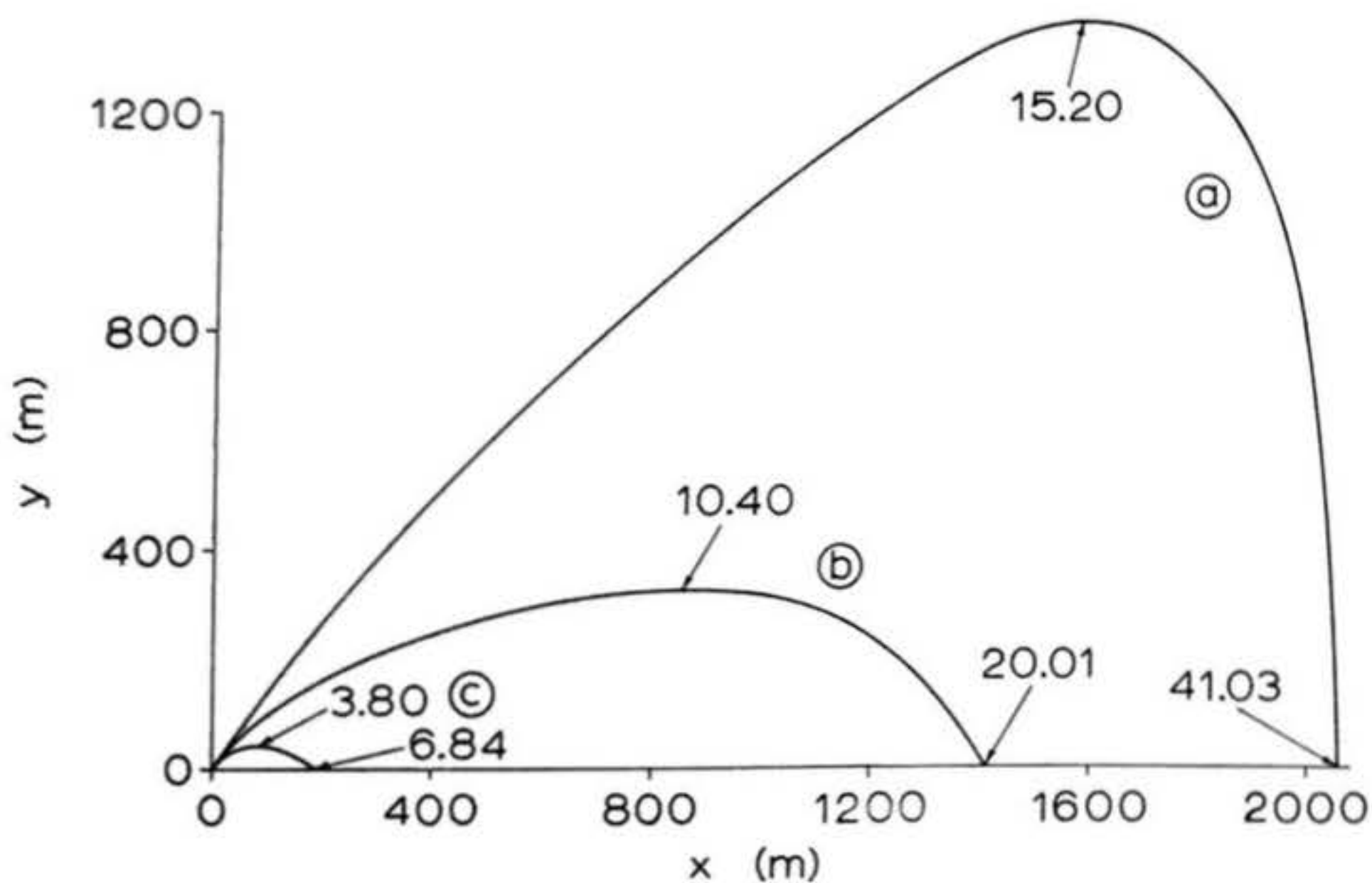


Figure 14: Non-vertical trajectories for 30° launch angle; models using Type F7 engine. Curve (a): $m_0 = .110$ kg, $k = .00012$ kg/m; $x_b = 1050$ m, $y_b = 1079$ m. Curve (b): $m_0 = .230$ kg, $k = .0003$ kg/m; $x_b = 696$ m, $y_b = 311$ m. Curve (c): $m_0 = .300$ kg, $k = .0045$ kg/m; the model impacts on the ground under power 6.84 seconds after liftoff. The engine burning time is 9.00 sec.

sequence of events:

In a rocket whose trajectory initially makes some angle θ_0 with the local vertical there is a component of gravity $g \sin \theta_0$ normal (i.e., perpendicular) to the instantaneous direction of flight, and which therefore tends to cause the subsequent flight path to curve further away from the vertical. When this happens θ becomes greater than θ_0 , causing the quantity $g \sin \theta$ to increase. Also, since the vertical component of thrust is given by $F(t) \cos \theta$, the effective thrust in the vertical direction is decreased. Both these effects cause the trajectory to curve even further away from the vertical, a process which is illustrated in Figure 15 -- and which, for a low-thrust, long-burning engine, may eventuate in a power-on impact.

In professional aerospace engineering, the gravity turn is an intentional maneuver performed for the purpose of helping to change a booster vehicle's course so as to enable a satellite to be injected into its orbit in a direction that is more or less parallel to a line tangent to the Earth's surface. In model rocketry, however, the gravity turn is an undesirable effect and even a potential safety hazard in cases of long-burning engines or multistaged vehicles. A great many three-staged model rockets, and even some two-staged designs, are so adversely affected by gravity turning that their topmost stages are often observed to be travelling nearly horizontally or even downward under thrust before burnout of the last-stage engine occurs -- a fact mentioned earlier in connection with safety limitations on the number of stages a model may have. The same is true of many single-staged models using the low-thrust, long-burning

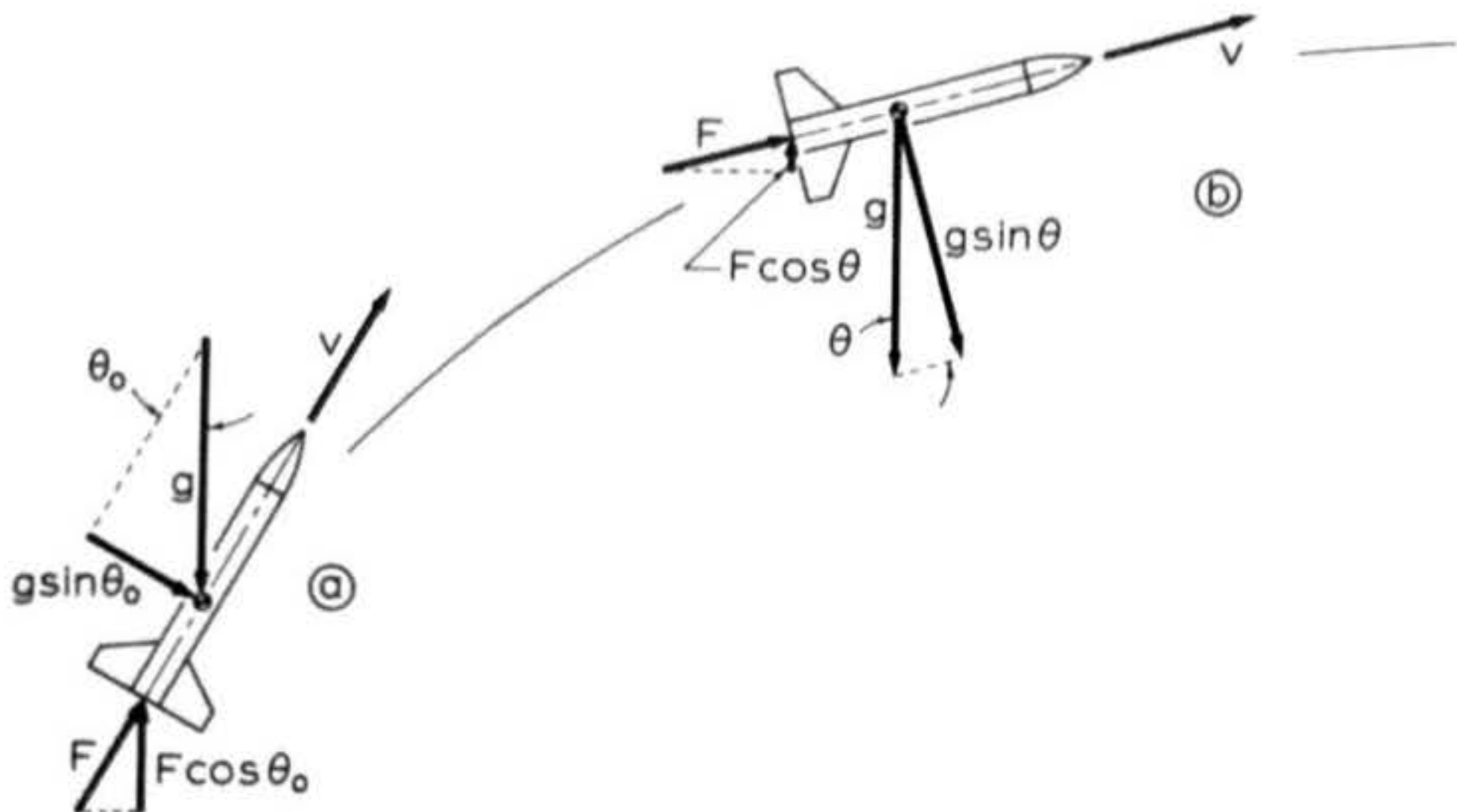


Figure 15: Rocket undergoing a gravity turn. In (a) the rocket is subjected to a component of gravity perpendicular to its instantaneous velocity vector, and which therefore tends to bend its flight path further away from the vertical. Also, since it is already flying at an angle θ_0 to the vertical, not all of its thrust F is effective against gravity. The rocket therefore tips over to position (b), in which there is an even greater component of gravity perpendicular to its instantaneous velocity vector, and in which even less of its thrust is effective against gravity -- thus causing the turn to continue.

E or F engines such as the F7. In the past, modelers have tended to build such vehicles somewhat too heavy for their intended engines and/or with excessive positive static stability margins. The latter characteristic often makes vertical flight impossible even when a vertical launch is attempted, since even a light breeze will cause the slowly-ascending model to "weathercock", or turn upwind, as soon as it leaves the launcher -- thereby creating the nonzero θ_0 required for the beginning of a sometimes-disastrous gravity turn. The reader will recall that the dangers of weathercocking and gravity-turning have caused models of more than three stages to be prohibited under the N.A.R. Sporting Code. Similarly, the dangers of gravity-turning and high-speed horizontal flight at low altitudes are responsible for the regulations prohibiting the launching of model rockets at angles greater than 30° away from the vertical.

Those readers who are familiar with the elementary physics equations for the calculation of projectile motion under drag-free conditions will notice a fundamental difference between those portions of the curves of Figures 10 through 14 lying above the burnout points and those that would result if k were assumed to be zero. The trajectory of a drag-free, constant-mass projectile, neglecting the Earth's curvature, will be in the shape of an inverted parabola -- which is to say that, if there were no drag, the portions of the trajectories above the burnout points would be symmetrical about a vertical line drawn through the flight apex. In cases of nonzero drag, however, this symmetry is lost; the trajectory falls off more steeply after the flight apex, giving the flight path the appearance of being compressed

in the x-direction, or "humped over", in the later stages of flight. A trajectory computed for finite drag will also lie entirely below (or "inside") the zero-drag flight path.

The asymmetry, as can be seen from the figures, becomes more pronounced as the ratio k/m_b increases. The term "whiffle-ball effect", derived from the similarity of this behavior to the flight of a whiffle ball or ping-pong ball, has sometimes been used informally to describe this phenomenon.

4. Coupling of Dynamic Oscillations to the Trajectory Equations

Having obtained satisfactory solutions to all aspects of point-mass model rocket flight behavior under the assumption of a uniformly zero angle of attack, we are now in a position to consider the effects of the rigid-body motion discussed in Chapter 2 in the calculation of altitude capability.

It would be senseless -- and well-nigh impossible -- to attempt to present equations for the detailed calculation of a rocket's altitude performance under conditions of completely general in-flight disturbances because of the virtually infinite variety of forcing functions which may cause oscillations of the vehicle. The winds at different altitudes have different speeds and directions, which moreover change from moment to moment; it is therefore not possible for a modeler to know precisely the wind profile his vehicle will encounter in any given flight. Impulsive forcing due to launch departure and staging effects, and the precise nature of the forcing due to slight propulsive malfunctions such as solid-particle ejection, are also impossible to predict with any precision. Because of these uncertainties in the nature of the disturbances encountered in flight, a detailed method for the precise calculation of the maximum altitude attained by a rocket subjected to completely general forcing functions would be useless. It is a far more

meaningful and fruitful task to solve for the reduction in altitude caused by several standard and well-defined forcing functions, with the object of revealing the structural and aerodynamic characteristics of the vehicle that contribute to the reduction in altitude, thereby facilitating the design of rockets which are least affected by in-flight disturbances. It is to this purpose that the solutions of this section will be directed. Derivations of the solutions will be carried out for a set of standard forcing functions which form the basis for all possible rigid-body rotative disturbances encountered in model rocket flight, which is to say that any possible forcing function can be synthesized from some combination of this set of standard disturbances.

4.1 The Differential Equations of Motion with Perturbation Terms

In Section 1.2 we wrote down the general differential equations of motion which included perturbation terms due to increases in drag and the reduction of effective thrust due to pitching and yawing of the vehicle. Later in this section we shall attempt the solution of these equations. First, however, a review of the assumptions which led to the formation of the vertical equation of motion (16) is in order. It is important to remember that equation (16) is not the exact differential equation of vertical motion; it is an approximation. The dynamic analysis of Chapter 2 is valid only provided that the model's C.G. does not move laterally too much during any given disturbance. In actuality, the momentary deflections of an oscillating rocket will cause it to head in a direction

that is not tangent to the intended direction of flight and the C.G. will move slightly to the side before the angle of attack passes through zero on its way toward the opposite extreme of the oscillation. This effect will contribute to the reduction in altitude caused by the disturbance and will appear as an additional term not originally included in equation (16). The treatments of this section will, however, be restricted to cases for which the dynamic analyses of Chapter 2 are valid. It will therefore be assumed that the model's frequency of oscillation is sufficiently high, and its amplitude sufficiently small, that the oscillatory horizontal translations of the C.G. are negligibly slight. Such an assumption is justified, since (as was shown in Chapter 2) a too-low oscillation frequency or a critically-damped or overdamped response is incompatible with dynamically stable flight.

It will thus be assumed that the rocket's C.G. is travelling in a purely vertical direction and develops no lateral components of velocity. Under such an assumption, equation (16) becomes an exact description of the rocket's vertical motion. We are then free to consider the method by which we will solve (16).

Since a stable rocket will, as shown in Chapter 2, practically never experience pitch or yaw angles exceeding 12° , it is possible to expand some of the terms of equation (16) containing functions of $\alpha(t)$ as factors, in powers of $\alpha(t)$, where $\alpha(t)$ is the generalized yaw-pitch angle which equals

$$(132) \quad \alpha(t) = \sqrt{[\alpha_x(t)]^2 + [\alpha_y(t)]^2}$$

and $\alpha_x(t)$ and $\alpha_y(t)$ are the yaw and pitch angles of the model

as functions of time.

As stated in Chapter 1 and confirmed in greater detail in Chapter 3, the function $f(\alpha)$ appearing in (16) can be represented to a high order of accuracy by a quadratic function in $\alpha(t)$, so that the approximate drag as a function of the angle of attack can be written as

$$(133) \quad \text{Drag} = (k + \epsilon \alpha^2) v^2$$

where the determination of the constants k and ϵ has been discussed in Chapters 1 and 3, and α is just $\alpha(t)$, the generalized angle of attack. It is also possible to replace $\cos(\alpha)$ by its power series expansion

$$(134) \quad \cos(\alpha) = 1 - \frac{\alpha^2}{2} + \frac{\alpha^4}{4} - \dots$$

and to truncate the expansion after its α^2 term, since α will never exceed 0.2 radian for cases amenable to analysis by the methods of Chapter 2:

$$(135) \quad \cos(\alpha) \approx 1 - \frac{\alpha^2}{2}$$

Equation (16) may then be written as

$$(136) \quad m(t) \frac{dv}{dt} = F(t) \left[1 - \frac{\alpha^2}{2} \right] - m(t) g - (k + \epsilon \alpha^2) v^2$$

where the y subscript has been discarded as unnecessary due to the fact that we are here considering cases of vertical flight only.

Despite the simplifying approximations made to obtain it, equation (136) is sufficiently complicated that no practical, closed-form solution to it has yet been found. As in Section 3,

therefore, we shall have to resort to numerical solutions obtained by incremental methods similar to those of Section 2.4. While it is not possible to visualize the sensitive parameters influencing a model's behavior as concisely when such computer-oriented techniques are used as it would be if an accurate and reasonably simple closed-form solution were available, it will be found that one can gain by example some feeling for the effects of various disturbances on the altitude capability of representative model rockets. Such numerical data, interpreted in the light of the analytical results of Chapter 2, enable us to fulfill our stated purpose of extracting criteria of use in designing models which possess maximum resistance to in-flight perturbations.

4.2 A Numerical Method for the Digital Computation of Altitude Performance in Cases of Oscillating Rockets

Like the vertical equation of motion for non-oscillating rockets, equation (136) can be solved to any desired accuracy using numerical techniques in which the differential time dt is replaced by a finite interval Δt . In order to obtain solutions for rockets undergoing rigid-body oscillations, however, it is necessary to add some additional computing steps derived from Euler's dynamical equations -- equations (14) of Chapter 2. Listed below is the computational procedure for completing a single iterative loop analogous to the drag-from-prior-velocity method of Section 2.4:

$$(137) \quad \Delta v = \Delta t \left\{ F(t) \left[1 - \frac{\alpha^2}{2} \right] - m(t)g - (k + \epsilon \alpha^2) v^2 \right\} / m(t)$$

$$(138) \quad \Delta y = \Delta t \left(v + \frac{\Delta v}{2} \right)$$

$$(139) \quad v = v + \Delta v$$

$$(140) \quad y = y + \Delta y$$

(141) calculate c_1

(142) calculate c_2

(143) calculate or input ω_z

$$(144) \quad \Delta \omega_x = \Delta t [f_x(t) - c_2 \omega_x - c_1 \alpha_x - I_R \omega_y \omega_z] / I_L$$

$$(145) \quad \Delta \omega_y = \Delta t [f_y(t) - c_2 \omega_y - c_1 \alpha_y + I_R \omega_x \omega_z] / I_L$$

$$(146) \quad \Delta \alpha_x = \Delta t \left[\omega_x + \frac{\Delta \omega_x}{2} \right]$$

$$(147) \quad \Delta \alpha_y = \Delta t \left[\omega_y + \frac{\Delta \omega_y}{2} \right]$$

$$(148) \quad \omega_x = \omega_x + \Delta \omega_x$$

$$(149) \quad \omega_y = \omega_y + \Delta \omega_y$$

$$(150) \quad \alpha_x = \alpha_x + \Delta \alpha_x$$

$$(151) \quad \alpha_y = \alpha_y + \Delta \alpha_y$$

$$(152) \quad \alpha = \sqrt{\alpha_x^2 + \alpha_y^2}$$

$$(153) \quad t = t + \Delta t$$

Again, as in Section 2.4, expressions such as (175) are not equations as we understand them, but arithmetic assignment statements which instruct the computer to replace the "old" or "former" value of a variable with its "new" or "present" value. The notation of

Chapter 2 has been used for all the expressions involving rigid-body dynamics: subscripts x and y do not refer to the Cartesian axes used in the general equations of nonvertical motion, but rather to the pitch and yaw axes of the vehicle; ω denotes angular velocity; α denotes angular displacement or angle of attack; the $f(t)$ are forcing functions or perturbing moments that may vary with time; C_1 is the corrective moment coefficient; C_2 is the damping moment coefficient; I_L is the longitudinal moment of inertia; and I_R is the radial moment of inertia.

You should note that equations (144) and (145) are approximate in that they assume constant, average values for I_L and I_R (the moments of inertia actually change slightly as the propellant is expended). Exact, time-varying values could be used -- as could the exact expressions for thrust reduction and drag increase due to angle of attack -- but the increase in accuracy obtained thereby is not worth the consequent increase in complexity. The computer is going to have to perform the calculations (137) through (153) a great many times, so even a slight time saving in a few steps of the loop can add up to worthwhile savings in time and expense over the full course of a computer "run".

Steps (141), (142), and (143) require the use of formulae developed in Chapter 2. Specifically, C_1 is proportional to the square of the velocity according to the relation expressed in equation (95) of Chapter 2, while C_2 depends on both the velocity and the motor characteristics as given in equations (97) through (101) of that chapter. In cases where the roll rate ω_z is induced by canted fins it may be calculated from equations (115) through (117) of Chapter 2; if induced by other means it must be determined

by a formula appropriate to the method of roll forcing. If the assumption of zero roll rate is to be made the value $\omega_x = 0$ must be input (or you can write a special program for use with non-rolling rockets only, in which the equations assume ω_x equal to zero).

As you can determine by working a few numerical examples, the angular velocities -- called pitch, yaw, and roll rates by engineers -- can become quite high for model rockets near burnout velocity. The method of theoretical velocity increments presented in Section 2.4 therefore loses its computational advantage over the drag-from-prior-velocity method when applied to cases of oscillating rockets. That advantage consisted of a tolerance for relatively large time increments while maintaining good accuracy, and it is lost when oscillating rockets are considered because short intervals are required for an accurate determination of the angle of attack. The modification of the theoretical-velocity-increment method for oscillating vehicles will not, therefore, be presented here. For best results, Δt as used in (137) through (153) should be of the order of 0.001 second -- and it is unlikely that the theoretical-velocity-increment method would tolerate much more than this. For hand calculations it is of course impractical to attempt the use of Δt 's less than 0.1 second. Those who perform such calculations should not, therefore, expect too much in the way of accuracy from the procedure detailed above.

4.3 Solutions for Standard Forcing Functions

In order to apply the method of Section 4.2 in computing

the altitude performance of a model rocket perturbed by one of the standard forcing functions described in Chapter 2 it is necessary to select specific functional forms for $f_x(t)$ and $f_y(t)$ and specific initial values for ω_x , ω_y , α_x , and α_y . The remainder of this section will present such formulae and values for use in determining the effects of a homogeneous response and of responses to each of the standard forcing functions considered in Chapter 2. Our treatment will be restricted to single-staged models (although the method of Section 4.2 is completely general and can be applied to rockets of any number of stages), since all information of design interest to model rocketeers concerning dynamic response is obtainable from the study of single-stage cases.

4.3.1 Homogeneous Response for General Initial Conditions

When one is primarily concerned with the behavior of a model once it has been placed in a given state of angular displacement and angular velocity, without regard to the precise nature of the disturbance that caused it to assume that state, it is best to compute the homogeneous response resulting from the initial conditions that have been assumed. For such a calculation we assume that, prior to some time t_0 after liftoff, the vehicle has been flying vertically straight and true. For values of t less than t_0 , therefore,

$$\left. \begin{array}{l} (154a) \quad \alpha_x = \alpha_y = 0 \\ (154b) \quad \omega_x = \omega_y = 0 \\ (156c) \quad f_x(t) = f_y(t) = 0 \end{array} \right\} t < t_0$$

Equations (154) are said to specify the rocket's state prior to t_0 as rotationally quiescent; it follows that the iterative procedure described in Section 4.2 produces values of v and y identical to those obtained by the methods of Section 2.4 for all values of t up through t_0 .

In the instant before t_0 , it is assumed that some unspecified occurrence disturbs the rocket from a straight-and-true attitude, leaving it with nonzero angular displacements and velocities as follows:

$$\left. \begin{array}{l} (155a) \quad \alpha_x = \alpha_{x0} \\ (155b) \quad \alpha_y = \alpha_{y0} \\ (155c) \quad \omega_x = \omega_{x0} \\ (155d) \quad \omega_y = \omega_{y0} \end{array} \right\} t = t_0$$

where the zero-subscripted quantities are the initial values of angular displacement and velocity to be considered. These values must be chosen by the person performing the calculation and are arbitrary except for the restriction that they cannot be so large as to cause the model to have an angle of attack greater than 0.2 radian at any time during the subsequent oscillation. Since a homogeneous response is defined as a response for which there is no forcing function, the yaw and pitch forcing remain uniformly zero for all values of time, after as well as before t_0 :

$$(156) \quad f_x(t) = f_y(t) = 0 \quad (t \geq t_0)$$

Computations of this kind may be performed for either zero or nonzero roll rate. In either case, no generality will be lost

and the response behavior will be more easily interpreted if you assume nonzero initial angular displacement and angular velocity about one axis only; it is merely for the sake of completeness that I have taken into account both the pitch and the yaw axis in setting initial conditions.

4.3.2 Step Response

In order to compute the response of a model to step forcing that suddenly arises at some time t_0 into the flight we again assume that the rocket is in a rotationally quiescent state for all time prior to t_0 ; equations (154) thus remain valid for this problem. At the moment the step forcing begins the model will still be in an undisturbed state, so the initial conditions are

$$(157a) \quad \begin{cases} \alpha_x = \alpha_y = 0 \\ \omega_x = \omega_y = 0 \end{cases} \quad t = t_0$$

The forcing functions, however, become nonzero at this instant and persist as long as the step is assumed to last -- i.e., until some time t_1 at which the forcing "steps down" again to zero (or until flight apex occurs, which is equivalent to setting t_1 equal to the duration of the upward flight). Then

$$(158a) \quad f_x(t) = M_x \quad \left. \right\} \quad t_0 \leq t \leq t_1$$

where M_x and M_y are the disturbing torques, or moments, about the yaw and pitch axes, respectively, and

$$(159) \quad f_x(t) = f_y(t) = 0 \quad (t \geq t_1)$$

In cases of non-spinning rockets where the step forcing is due to slight aerodynamic asymmetries, the strength of the perturbing moments will vary as the square of the airspeed. Where the step arises from a uniform horizontal wind the magnitudes of M_x and M_y will be constant throughout the time during which the wind is blowing.

It is important to note that step forcing is not an accurate representation of the action of a horizontal wind upon the model except for relatively short times -- on the order of a few tenths of a second for most model rockets. You may remember from the discussion of step responses in Chapter 2 that true step forcing applied for a sufficiently long time causes the vehicle to assume an angle of attack equal to M/C_l , where M is the disturbing moment. A horizontal wind, however, adds vectorially to the model's airspeed and changes the direction in which the rocket must fly to be at zero angle of attack; its long-term effect is therefore to make the model tip over into a nonvertical trajectory (we as model rocketeers are used to referring to this as weathercocking), lowering its altitude by this means as well as by the decreased effective thrust and increased drag due to the oscillatory response. The steady angle of attack predicted by the step-response treatment produces a considerable overestimate of the aerodynamic drag on the perturbed rocket, though, and this drag overestimate nearly always more than compensates for the failure to consider the nonverticality of the flight path. For this reason it is acceptable to use step forcing to simulate horizontal wind effects in making performance degradation estimates despite the admitted analytical inaccuracy of the technique.

In making step response calculations you may choose M_x and M_y arbitrarily, subject only to the restriction that they be small enough to make sure the rocket will not exceed an angle of attack of 0.2 radian at any time during the response. It admittedly takes some numerical experimentation to establish such upper bounds, but the work is unavoidable if the validity of Chapter 2's dynamic analyses is to be guaranteed. By reasoning similar to that of Section 4.3.1 it may be concluded that no information regarding the response will be lost if one of the disturbing torques is considered to be zero; this is true whether or not the rocket is spinning.

4.3.3 Impulse Response

In order to determine a model's response to impulsive forcing occurring at the instant t_0 after liftoff we again assume the quiescent prior rotational state specified by equations (189). The effect of the impulse, as discussed in Chapter 2, will then be to produce a homogeneous response for time greater than t_0 with the following specialized set of initial conditions:

$$\left. \begin{array}{l} (160a) \quad \alpha_x = \alpha_y = 0 \\ (160b) \quad \omega_x = \frac{H_x}{I_L} \\ (160c) \quad \omega_y = \frac{H_y}{I_L} \end{array} \right\} t=t_0$$

where H_x and H_y are the components of the impulse about the yaw and pitch axes, respectively.

Because of the unique nature of impulsive forcing (the impulse is a mathematical idealization involving the assumption of an infinite disturbing moment applied for an infinitesimal time period),

an impulse response must be computed by setting the yaw and pitch forcing functions to zero for all time:

$$(161) \quad f_x(t) = f_y(t) = 0$$

Actually, $f_x(t)$ and $f_y(t)$ are both effectively infinite at the time t_0 , but the results of this have already been taken into account in equations (195).

Again, any values for H_x and H_y -- including zero for either one -- will be acceptable as long as these values do not cause the overall angle of attack to exceed 0.2 radian during the subsequent response.

4.3.4 Response to Sinusoidal Forcing

Although a wide variety of sinusoidal disturbances could be hypothesized for cases of both rolling and non-rolling rockets, the model rocketeer will find that all the information relating to sinusoidal forcing that is of interest in designing high-performance models can be obtained by analyzing two specialized cases:

- (a) Sinusoidal forcing of a non-rolling rocket about one axis only, in which the amplitude of the forcing varies as the square of the airspeed and its frequency varies directly with the airspeed; and
- (b) Sinusoidal forcing of a rolling rocket in which the sinusoidal nature of the forcing is due to the roll rate itself, so that sinusoidal moments exist about the pitch and yaw axes of angular

frequency equal to the roll rate and of amplitude proportional to the square of the airspeed.

A disturbance of the first type may be characterized by the following set of forcing functions:

$$(162a) \quad f_x(t) = A_f \sin \omega_f t$$

$$(162b) \quad f_y(t) = 0$$

where the disturbance has been assumed to occur about the yaw axis. The proportionality of the forcing amplitude A_f and the forcing frequency ω_f to the rocket's velocity can be expressed as

$$(163a) \quad A_f = A_0 v^2 \quad \text{and}$$

$$(163b) \quad \omega_f = \omega_0 v$$

where A_0 and ω_0 are constants of proportionality which may be thought of as the values of A_f and ω_f at an airspeed of one meter per second.

A disturbance of the second type exhibits forcing functions of the form

$$(164a) \quad f_x(t) = A_f \sin \omega_z t$$

$$(164b) \quad f_y(t) = A_f \cos \omega_z t$$

Since spin in model rockets is almost invariably induced by aerodynamic means, the roll rate may be considered linearly proportional to velocity for most cases of interest. The same sort of proportionality scheme used for the non-rolling case can then be used

here:

$$(165a) \quad A_f = A_0 v^2$$

$$(165b) \quad \omega_z = \omega_{z0} v$$

Equation (200a) applies whether the disturbance is due to aerodynamic or to inertial causes, since the strength of the aerodynamic perturbation is proportional to the square of the airspeed and that of the inertial perturbation is proportional to the square of the roll rate, which in turn varies directly with airspeed.

Both types of perturbations are assumed to arise immediately upon liftoff and to persist throughout the flight, as such a mathematical model most accurately represents the actual behavior of sinusoidal forcing in the vast majority of cases of interest. Calculations should therefore be started at $t = 0$ with rotationally quiescent initial conditions:

$$(166a) \quad \alpha_x = \alpha_y = 0 \quad \left. \right\} t = 0$$

$$(166b) \quad \omega_x = \omega_y = 0 \quad \left. \right\}$$

It should be noted that the calculations presented here differ somewhat from the analyses of Chapter 2's Sections 3.1.4 and 3.2.4 in that we are considering the complete response to sinusoidal forcing rather than the steady-state response only; our numerical calculations will therefore pick up so-called starting transients which are not considered in the discussion of Chapter 2. The basic character of the response will not, however, be greatly altered and it is very nearly correct to

consider the method of this section the numerical equivalent to the closed-form analyses of Chapter 2.

4.4 The Effect of Dynamic Oscillations on the Altitude Performance of a Typical Model Rocket

In order to give the reader some "feel" for the magnitude of the performance degradations resulting from the various in-flight disturbances that cause pitching and yawing oscillations in model rockets, this section will present the results of sample calculations based on representative disturbances encountered by a typical model rocket. The trial rocket illustrated in Figure 37 of Chapter 3 was chosen as a representative design; reasonable values of inertial and propulsive characteristics were then supplied which, in addition to the drag parameters and normal force coefficients computable from the model's geometry, permitted a complete characterization of the vehicle for computational purposes. A complete list of the vehicle parameters used in solving the coupled equations of motion by the incremental method of Section 4.2 appears in Table 1.

Table 2 summarizes the results of calculations performed for various cases of input disturbances. Although these results admittedly apply only to the particular rocket described in Table 1, they do -- in combination with the discussion of Chapter 2 -- permit us to draw certain conclusions of general interest and applicability to model rocket design.

Since the drag increase due to angle of attack is proportional both to the square of α and to the square of the airspeed, for instance, it follows that a transient disturbance producing a given maximum angle of attack will reduce a model's overall

TABLE 1

Characteristic	Value
Liftoff mass	40 g = 0.04 kg
Burnout mass	31.67 g = 0.03167 kg
Engine thrust	4.0 N (average)
Burning time	1.20 sec
Propellant mass	8.33 g = .00833 kg
Static stability margin	2.06 cm = 1.0 caliber
C_L	$396v^2$ dyn-cm for v in m/sec
C_{2A}	$242v$ dyn-cm-sec for v in m/sec
C_{2R}	661 dyn-cm-sec (average)
I_L	3640 g-cm 2 (average)
I_R	42.4 g-cm 2 (average)
ζ	0.101 neglecting jet damping
ζ_c	0.1004 neglecting jet damping
ω_{res}	$0.327v$ rad/sec for v in m/sec
ω_{cres}	$0.325v$ rad/sec for v in m/sec
$(C_D)_FB$	0.45 without fin cant
Fin cant angle for $\omega_z = \omega_{cres}$	0.01945 rad = 1.11°
Fin cant angle for $\omega_z = 10\omega_{cres}$	0.1945 rad = 11.1°
k	0.92×10^{-4} kg/m without fin cant 0.924×10^{-4} kg/m with 1.11° cant 1.288×10^{-4} kg/m with 11.1° cant
ϵ	37.8×10^{-4} (kg/m)/rad 2

Table 1: Ballistic and dynamic characteristics of the rocket shown in Figure 37 of Chapter 3.

TABLE 2

Description of disturbance or response	ω_z (rad/sec)	t_o (sec)	α_{\max} (rad)
No disturbance	0	----	0.000
Homogeneous response to $\alpha_{x_0} = 0.2$ rad	0	0.1	0.200
Homogeneous response to $\alpha_{x_0} = 0.2$ rad	0	1.2	0.200
Step of intensity $39.6v^2$ dyn-cm	0	0.1	0.155
Step of intensity $51.0v^2$ dyn-cm	0	0.1	0.200
Step of intensity $39.6v^2$ dyn-cm	0	1.2	0.177
Step of intensity $45.0v^2$ dyn-cm	0	1.2	0.200
Impulse of strength 2510 dyn-cm-sec	0	0.1	0.062
Impulse of strength 8080 dyn-cm-sec	0	0.1	0.200
Impulse of strength $26,600$ dyn-cm-sec	0	1.2	0.175
Impulse of strength $30,400$ dyn-cm-sec	0	1.2	0.200
Sinusoidal forcing of $A_f = 15.9v^2$, $\omega_f = \omega_{res}$	0	0.1	0.143
Sinusoidal forcing of $A_f = 26.7v^2$, $\omega_f = \omega_{res}$	0	0.1	0.200
Homogeneous response to $\alpha_{x_0} = 0.2$ rad	$3.25v$	0.1	0.200
Homogeneous response to $\alpha_{x_0} = 0.2$ rad	$3.25v$	1.2	0.200
Step of intensity $39.6v^2$ dyn-cm	$3.25v$	0.1	0.155
Step of intensity $51.0v^2$ dyn-cm	$3.25v$	0.1	0.200

TABLE 2 (continued)

Description of disturbance or response	ω_z (rad/sec)	t_0 (sec)	α_{\max} (rad)
Step of intensity $39.6v^2$ dyn-cm	3.25v	1.2	0.176
Step of intensity $45.0v^2$ dyn-cm	3.25v	1.2	0.200
Impulse of strength 2510 dyn-cm-sec	3.25v	0.1	0.062
Impulse of strength 8080 dyn-cm-sec	3.25v	0.1	0.200
Impulse of strength 26,600 dyn-cm-sec	3.25v	1.2	0.175
Impulse of strength 30,400 dyn-cm-sec	3.25v	1.2	0.200
Coupled sinusoidal forcing of $A_f = 15.9v^2$, $\omega_z = \omega_{cres}$	0.325v	0.1	0.141
Coupled sinusoidal forcing of $A_f = 26.7v^2$, $\omega_z = \omega_{cres}$	0.325v	0.1	0.220
Coupled sinusoidal forcing of $A_f = 23.8v^2$, $\omega_z = \omega_{cres}$	0.325v	0.1	0.200

Table 2: The effect of various disturbances on the performance of the rocket shown in Figure 37 of Chapter 3. In all cases where disturbances or roll rates are velocity-dependent the velocity is given in meters per second, and the amplitudes of sinusoidal forcing functions are given in dyn-cm. t_0 is the time at which the disturbance begins; α_{\max} is the maximum angle of attack produced by the disturbance.

TABLE 2

v_b (m/sec)	y_b (m)	t_c (sec)	y_c (m)	y_{max} (m)	Percent reduction in y_{max}
111.4	78.1	6.46	265.5	343.6	0.00
110.3	76.9	6.44	262.8	339.6	1.17
111.4	78.1	6.35	254.3	332.4	3.26
105.3	75.7	5.67	211.0	286.7	16.58
101.7	74.2	5.28	186.1	260.3	24.25
111.4	78.1	5.75	220.4	298.4	13.16
111.4	78.1	5.59	210.3	288.4	16.08
111.3	77.9	6.46	265.2	343.1	0.15
109.9	76.7	6.43	261.9	338.6	1.46
111.4	78.1	6.35	254.7	332.8	3.14
111.4	78.1	6.32	251.5	329.5	4.10
111.1	77.9	6.33	257.8	335.7	2.30
110.5	77.6	6.08	242.9	320.5	6.72
105.0	74.9	5.68	211.2	286.1	16.74
106.0	76.0	5.60	204.6	280.6	18.34
100.6	73.8	5.13	176.9	250.7	27.05
97.4	72.5	4.84	159.1	231.6	32.60

TABLE 2 (continued)

v_b (m/sec)	y_b (m)	t_c (sec)	y_c (m)	y_{max} (m)	Percent reduction in y_{max}
106.0	76.1	5.20	183.8	259.8	24.39
106.0	76.1	5.08	176.8	252.9	26.41
105.9	75.9	5.69	212.9	288.8	15.95
104.7	74.7	5.67	210.6	285.4	16.95
106.0	76.1	5.61	205.0	281.0	18.23
106.0	76.1	5.58	202.5	278.6	18.92
110.7	77.7	6.19	249.5	327.2	4.78
109.7	77.1	5.83	228.3	305.4	11.12
110.0	77.3	5.93	234.4	311.7	9.29

altitude capability more when it occurs near burnout (when the velocity is high) than near liftoff (when the velocity is low). Because the corrective moment coefficient C_l increases as the square of the airspeed, however, a much stronger disturbance is required to produce a given maximum angle of attack near burnout than near liftoff -- and a disturbance of a given strength occurring near burnout will produce a reduction in performance roughly equivalent to that resulting from a disturbance of the same strength occurring near liftoff. The quadratic dependence of drag upon angle of attack also means that a disturbance of a given type occurring at a given time after liftoff will produce a performance degradation roughly proportional to the square of its strength.

Given a set of in-flight disturbances of different types, all of which arise at the same time into the flight and produce identical values of the maximum angle of attack in response, the severity of the resulting performance degradations may be ranked according to the type of forcing function involved as follows:

- (a) impulse (least severe)
- (b) step of constant intensity
- (c) sinusoid
- (d) step of intensity proportional to v^2 (most severe)

A rocket that is spinning about its longitudinal axis will have a greater drag at zero angle of attack than will the same vehicle if constructed so as not to roll. That the drag increase associated with fitting a model with angled "spin fins" can be considerable has already been shown by the analysis of Section

5.3 of Chapter 3. If, however (as has been noted by Thomas McKim), the product of I_R and ω_z is great enough to cause the angular momentum about the longitudinal axis to be very large, the maximum angle of attack due to a transient disturbance of a given strength will be significantly reduced over what it would have been without roll. During much of the response, therefore, the overall drag of the rolling rocket may be less than the drag associated with the same vehicle built so as not to spin. The response will, however, also persist for a longer time than it would in the case of zero roll rate because the inverse time constant of the slower mode of oscillation is reduced as the product $I_R \omega_z$ is increased. Both effects are due to the fact that the presence of angular momentum about the roll axis causes the model to act as if it had a larger longitudinal moment of inertia than its actual value of I_L and thereby decreases the amplitude, frequency, and decay rate of the response. Model rockets which are well designed to begin with almost always suffer, rather than benefit, from the use of spin since the reduction in maximum angle of attack due to any given disturbance is more than offset by the increased duration of the transient response and the increase in drag at zero angle of attack associated with spinning the model by aerodynamic means. There are a few exceptions to this rule; for example, the use of spin fins and/or spin motors in the first stage of a heavy, multi-staged model that might otherwise suffer excessively from step or impulse forcing during its relatively slow liftoff. In most cases where the incorporation of spin into a design improves its performance, however, it will be found that it is because the design has not been optimized in the non-spinning configuration.

Finally, the ability of a given model to resist a disturbance of a given type can be evaluated from the following brief summary of the results of Chapter 2:

- (a) Resistance to step forcing increases with an increasing corrective moment coefficient C_1 ;
- (b) Resistance to impulsive forcing increases with an increase in the product $I_L \omega$, where
$$\omega = \sqrt{\frac{C_1}{I_L} - \frac{C_2^2}{4I_L^2}} ; \text{ and}$$
- (c) Resistance to sinusoidal forcing increases with an increase in the product $C_1 \zeta \sqrt{1 - \zeta^2}$, where $\zeta = \frac{C_2}{2\sqrt{C_1 I_L}}$.

The effect of a nonzero roll rate is to increase the apparent value of the longitudinal moment of inertia, thereby lessening the angular frequency of the slower pitch and yaw oscillation modes and decreasing the effective damping.

5. Recapitulation and Qualitative Features of the Analytical Results

Now that the methods of Chapters 2 and 3, and the present chapter, have placed at our disposal methods for predicting the dynamic behavior, drag, and altitude capability of any model rocket we may turn our attention to the qualitative features of the results obtained in order to ascertain the relative importance of each characteristic, or parameter, of the vehicle to its overall altitude performance. The flight dynamics and aerodynamics chapters each presented criteria for good design practice in relation to their own subject matter. This section will attempt to integrate those criteria with some that are basic to

the ballistic characteristics of model rockets and to arrive at some fundamental, unified design rules.

5.1 Bengen's Maxima

If one were to construct a graph of total altitude as a function of initial mass for various values of the drag constant k, given a specific model rocket engine type, a curious effect would be noticed: there is an optimum, nonzero weight that gives maximum altitude performance. If the model is either heavier or lighter than the optimum weight, its altitude capability will be less than it would be at the optimum. The existence of such optimum points was first noted by Bengen in 1965. Malewicki, working independently, published explicit examples of graphs displaying the altitude maxima in 1966 as model rocket manufacturer's reports. It is also true, as you can see from the sample plot presented in Figure 19, that the optimum weight decreases as the value of k decreases until, in the limit as k approaches zero, the optimum weight also approaches zero. It is actually possible, for most values of k to which practical model rockets can be built, to build a rocket that is too light for maximum altitude performance! It is a remarkable coincidence, as noted by Stine in his Handbook of Model Rocketry even prior to Bengen and Malewicki, that many model rockets just happen to be constructed near the ballistically optimum point.

The effect which produces Bengen's maxima can be explained qualitatively in the following manner. A typical model rocket gains most of its altitude during the coasted portion of the flight. The coasted altitude increment depends heavily upon two things (other than the deceleration due to gravity, which is

constant for all model rockets): the burnout momentum and the drag due to the burnout velocity. It actually depends analytically on the burnout mass, the burnout velocity, and the drag parameter k . If the vehicle is extremely light, its burnout velocity will be large since the burnout velocity increases monotonically with decreasing weight (i.e., the burnout velocity always increases as the weight decreases). The low weight, however, will prevent the burnout momentum from being very large. The drag, on the other hand, will be extremely high due to its quadratic dependence on velocity. As a result, the momentum of the rocket is dissipated, or used up, very rapidly and the coasted altitude is disappointingly low. This is the same effect that insures that a whiffle ball or ping-pong ball cannot travel very far regardless of how hard it is hit. The extreme limit of this behavior would be the example of a feather being shot out of a cannon: the muzzle velocity is tremendous but the momentum of the feather is almost instantly overcome by its large drag.

If we now have a rocket that is very heavy, its burnout velocity will be relatively low. Its large mass, however, insures that its burnout momentum will be about the same as that of the lighter rocket (actually, with the exception of the momentum lost to drag and gravity during the burning phase, the two rockets will have identical values of burnout momentum; this must be true since the total impulse of the engine is just the total momentum change imparted to the rocket by its engine). The low burnout velocity insures that aerodynamic drag will dissipate the burnout momentum much more slowly than is the case for the light rocket. The deceleration of gravity, however, will dissipate

the burnout momentum at a rate much greater than in the case of the light rocket -- and again the altitude performance suffers.

Thus, the optimum liftoff mass lies somewhere between the two extremes. Since the methods of Section 2 of this chapter have given us closed-form, algebraic solutions for altitude performance in cases of vertical flight, it is theoretically possible to obtain a closed-form expression for the ballistically optimum liftoff mass. When one attempts this in practice, however, it is found that the resulting expression is far more complicated than the original total altitude function and requires a prohibitive amount of time and effort to solve in any given case. While such an expression satisfies the letter of the definition, "closed-form solution", it literally covers pages when written out; it does not satisfy the intent of the definition as used in this book, which requires a practical closed-form solution to be quicker and easier to use than numerical or graphical methods from which the same result could be obtained.

The most convenient method yet found for determining the optimum liftoff mass of a model rocket is to consult a graph of the kind described at the beginning of this section. Sets of such plots are currently available from Estes Industries, Incorporated of Penrose, Colorado as Technical Report TR-10, Altitude Prediction Charts; and from the Centuri Engineering Company of Phoenix, Arizona as Technical Information Report TIR-100, Model Rocket Altitude Performance. Ambitious modelers can prepare their own charts for engine types not listed in these reports, using the methods of Section 2 except in very high-performance cases, where numerical interval methods must be used due to drag

divergence at transonic speeds. It is also suggested that calculations be restricted to values of liftoff mass greater than the mass of the loaded engine alone (which is the least possible mass of any actual model) and that values of k be kept above a reasonable minimum associated with the lowest possible drag coefficient to which a model rocket can, as a practical matter, be designed.

5.2 Model Rocket Design Optimization

With the sum total of the information presented throughout this volume ready to our hand, we are now in a position to formulate a general design procedure which, if adhered to, will enable the model rocketeer to formulate designs which are optimized from the standpoint of the altitude they are capable of achieving with the specific model rocket engine for which they are designed to be flown. It is important to remember that our criterion of optimization is altitude capability alone. The material presented in this book, properly applied, permits the synthesis of rocket designs that may be considered "superior", or even "best", for applications depending solely upon maximum altitude achieved. Examples of such applications are micrometeorological sounding and the National Association of Rocketry's altitude and payload competition events. There exist applications in the field of model rocketry, however, for which the rocket with the greatest altitude capability is not necessarily the best one. Examples that come immediately to mind in this category are the NAR parachute, boost/glider, and rocket glider duration events, in which the model's altitude capability must be balanced against the need for a parachute or aerodynamic surfaces large enough to insure a

slow descent and a good probability of the descending model's being caught by thermals. With the caution that our optimization techniques are valid only for models in which altitude capability is the sole criterion of excellence, then, we present the following design optimization procedure.

5.2.1 Initial Design Definition

Given the purpose for which your model is to be used and the model rocket engine with which it is to be flown, make a rough sketch of your first impression of what it should look like. Refine the sketch as necessary, adding dimensions (the dimensions are, of course, approximate and may be changed later as necessary). Simplicity is the rule at this stage in the design: avoid all unnecessary complication of shape and arrangement. A way-out, Buck Rogers design may make a fine sport, demonstration, or display model, but it will rarely if ever come out looking very good when judged solely on the basis of its altitude capability. Also avoid unnecessary size, making the design as compact as possible consistent with adequate provisions for a good, reliable recovery system and any payload that is to be carried.

5.2.2 Drag Coefficient

Using the techniques presented in Section 6 of Chapter 3, estimate the coefficient of drag of your model at a zero angle of attack. You should be somewhat conservative regarding your assumptions of skin-friction drag at this point, both to allow for small imperfections encountered in finishing the model and to allow for the deterioration of the rocket's surface that will occur from flight to flight. In designing model rockets for

maximum altitude performance the lowest possible drag coefficient is desirable, and to this end you should not hesitate to experiment with variations on the initial design formulated in Section 5.2.1. Avoid the use of launch lugs on high-performance models if at all possible by launching from a low-friction tower or closed-breech mechanism, or at least try to incorporate a "pop-off" or "shuck-off" lug design if a lugless launching device is not available. Remember that, if you do use a fixed launch lug system, you will probably have to accept an increment in drag coefficient (ΔC_D)_{lug} on the order of 0.25 as given in Section 4.3.3 of Chapter 3. Since it is sometimes possible to design model rockets with values of C_D less than 0.4, provided no launch lug is present, you can see that the presence of a fixed lug exacts a considerable penalty in terms of altitude performance.

5.2.3 Weight Optimization

Use the first-estimate value of C_D obtained in Section 5.2.2 to compute the drag parameter k (it will be recalled that k is equal to $\frac{1}{2}\rho C_D A_r$, where A_r is the reference cross-sectional area and ρ is the density of the atmosphere). If you will be launching from a site considerably above sea level, or if your model will reach an extremely great altitude (of which you have a rough idea), be sure to adjust your value of ρ from its sea-level value of 1.225 kilograms per cubic meter. Remember that k , for use with charts such as Figure 16, must be computed using MKS units. If you have a single-staged, single-engined model you may then use a Malewicki chart (as plots such as Figure 16 have come to be called) to select the optimum weight for your rocket directly by locating Bengen's maximum for that particular value of k .

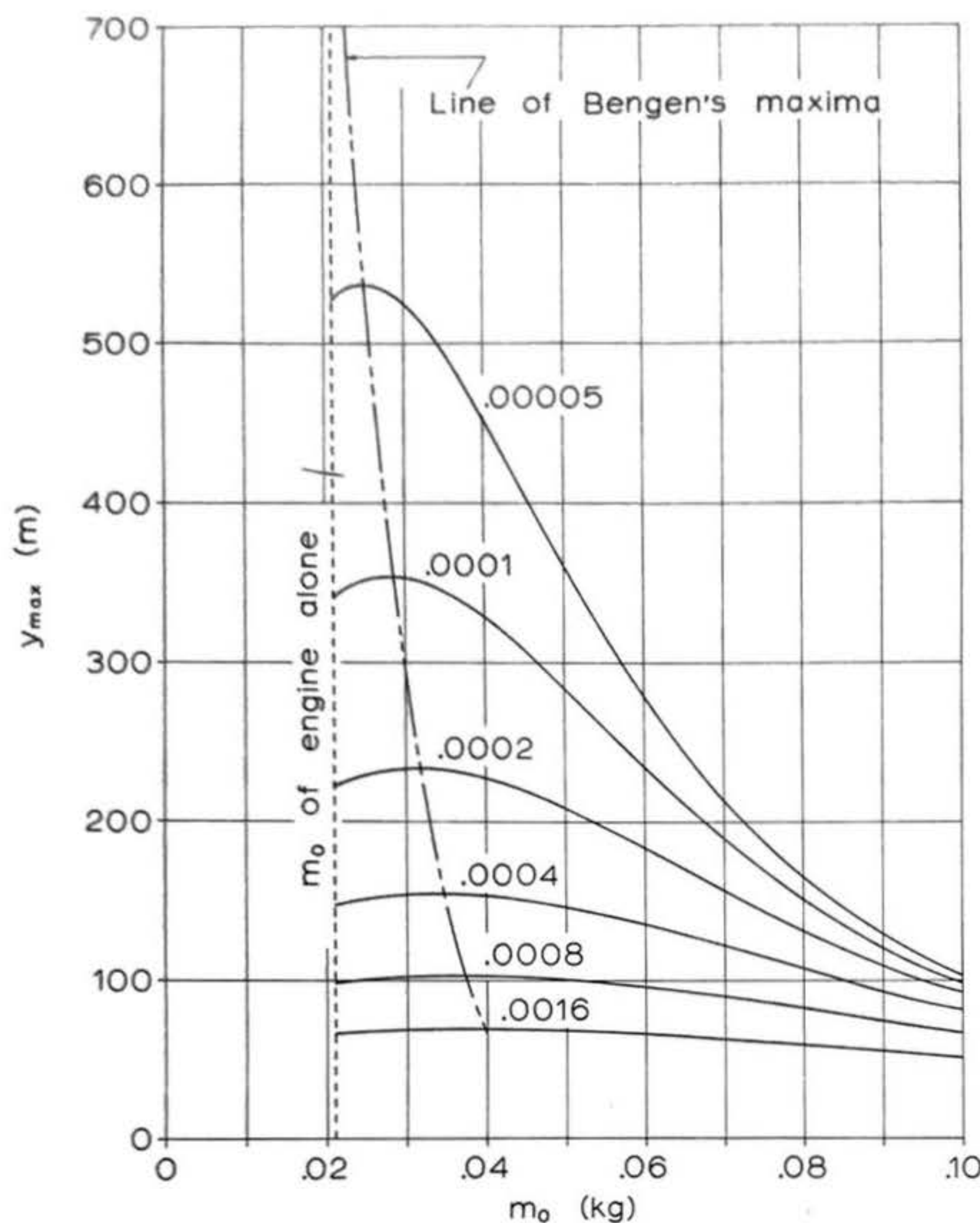


Figure 16: Maximum altitude attained in vertical flight vs. liftoff mass for models using the Type B4 engine; an example of Bengen's maxima. Curves have been plotted for models having several values of the drag parameter k ; the k values, in kg/m , have been noted on the curves. Since the line on which all Bengen's maxima lie is to the right of the line representing the initial mass of the engine itself (for all values of k to which model rockets can actually be built), Bengen's maxima are practical considerations that must be taken into account when designing model rockets for maximum altitude performance. Graphs of this type were first compiled by Douglas J. Malewicki and are therefore called "Malewicki charts".

If you are using clustering or staging, some numerical experimentation with different values of liftoff mass using the methods described in Section 2 will be required. For some rockets having very low values of k , it may not be possible to achieve the optimum weight (for instance, when the weight of the payload and engine alone are found to total more than the optimum). In such cases, the model must simply be built as light as practicable consistent with adequate structural strength. For rockets to which weight must be added to optimize the liftoff mass, adding nose weight is usually best since this permits adequate stability to be attained with smaller fins than would otherwise be the case, and thus lessens drag.

5.2.4 Dynamic Stability Optimization

Determine the values of the dynamic parameters C_1 , C_2 , I_L , and I_R for your tentative design according to the methods presented in Section 5 of Chapter 2. Adjust these values by altering the mass distribution, length, fin size, fin shape, and fin placement as necessary to obtain a static stability margin of about one caliber or slightly more, a damping ratio ζ between 0.05 and 0.3, and a desirable value of the natural frequency ω_n . We would suggest, based on experience to date, that the most desirable natural frequencies for vehicles of model rocket size lie between 0.002v and 0.01v, where v is the airspeed of the model given in centimeters per second (remember that CGS units are used throughout Chapter 2). The equivalent limits for airspeeds given in meters per second are 0.2v and 1.0v. A lower value usually means the longitudinal moment of inertia is too great for the corrective moment coefficient, so that the model cannot respond

to the moments applied by its fins with sufficient rapidity for safe and stable flight at average, present-day launch departure velocities. A higher value usually means the longitudinal moment of inertia is too low, so the model is easily disturbed, or that the corrective moment coefficient is too large, usually indicating too-large fins that cause excessive drag. If you wish to use a roll rate to reduce horizontal dispersion, check to insure that it is not too near the coupled resonant frequency ω_{cres} . You may also wish to check the roll rates induced by various assumed slight fin misalignments to guard against the possibility of resonance due to unintentional roll.

5.2.5 Reduction of Drag at Angle of Attack

Consistent with the requirements of the preceding steps, attempt to select or refine the fin design such that the increase in drag with angle of attack is minimized. Since, for any given value of k , the reduction in altitude performance due to dynamic oscillations depends strongly on the ratio of ϵ to k , a model with a relatively small value of this ratio has an advantage over one with a larger value (provided the two vehicles have identical resistance to in-flight disturbances). Elliptical fins are often used to help here, since it is known that an airplane wing that is not twisted and has a moderate aspect ratio will have the lowest induced drag due to lift if its planform is elliptical.

5.2.6 Philosophy of Design and Flight

You have no doubt noticed that the procedures outlined in each of the Sections 5.2.1 through 5.2.5 tend to alter the design of the model from what it was at the previous stage of the procedure.

The possibility thus exists that optimization of the design at any given stage, using information from the previous stage, may to a certain extent invalidate the figures taken from the previous stage. To "home in" on an optimum design to an arbitrary degree of precision it is therefore generally necessary to perform several design iterations; that is, to go through the process outlined in Sections 5.2.1 through 5.2.5 several times, using the status of the design from the previous iteration, or "pass", to perform the next iteration. A great deal of this is done in professional industry, but the modeler can, at his option, choose the number and precision of his iterations at will, depending on how precise he desires his optimization to be. For many purposes, of course, a bare minimum of analysis, not even using all the methods and procedures outlined in this book, will suffice to produce a reasonably good design. For contest work, however, or record-setting attempts and scientific payload lofting, many rocketeers will want to take full advantage of the most advanced and painstaking analytical methods of design available.

No matter how careful the design of his vehicle has been, however, there exist certain conditions encountered at the launch site which may sometimes force the modeler to depart from strictly altitude-optimized design to achieve the desired results in actual operation. If a strong horizontal wind exists at the time of launch, for instance, a model designed for a low-thrust, long-burning engine will often achieve a higher altitude if launched with a high-thrust, short-burning engine of identical specific impulse, since it will not then have time to respond completely to the horizontal wind encounter during the burning phase of flight.

An example would be the substitution of a B14 engine in a model optimized for a B4, in case of strong winds at the launch site. There also exist instances in which it is wise for the modeler to render his design deliberately off-optimum in order to remain below cloud cover or within the capabilities of limited tracking facilities. Such cases, however, are entirely a matter of the rocketeer's intuition and expertise gained through experience and we do not see fit to discuss them in a book devoted strictly to the optimization of the actual altitude capability of model rockets.

In closing, the authors of this volume would like to state that it is not their intention to end all questions of model rocket design with the material presented herein. To the best of our knowledge and belief based on experience to date, the techniques and information presented in this book form a valid framework within which each model rocketeer can construct his own philosophy of altitude optimization. A great deal remains to be said, however, for the value of intuition and experience, and much experimental and analytical research remains to be done in model rocketry, a field that is at once a science, a sport, a hobby, and a fine art.

REFERENCES

1. Malewicki, Douglas, Model Rocket Altitude Performance, Centuri Engineering Company Technical Information Report TIR-100, Phoenix, 1968.
2. Martin, William T., and Reissner, Eric, Elementary Differential Equations, Second Edition, Addison-Wesley Publishing Company, Inc., Reading, Massachusetts, 1961.
3. Stine, G. Harry, "Basic Model Rocket Flight Calculations", National Association of Rocketry Technical Report #1, New York, 1958.
4. Stine, G. Harry, Handbook of Model Rocketry, First Edition, Follett Publishing Company, Chicago, 1965.
5. Thomas, George B. Jr., Calculus and Analytic Geometry, Third Edition, Addison-Wesley Publishing Company, Inc., Reading, Massachusetts, 1960.

APPENDIXES



APPENDIX A
CORRESPONDENCE BETWEEN METRIC AND ENGLISH UNITS

1. Centimeter-Gram-Second (CGS) to English Units

1 gram (g.) = .0353 ounce-mass

= .0022 pound-mass

= 6.84×10^{-5} slug

1 dyne (dn.) = 2.248×10^{-6} pound-force

1 centimeter (cm.) = .0328 foot

= .3937 inch

2. Meter-Kilogram-Second (MKS) to English Units

1 kilogram (Kg.) = 35.27 ounce-mass

= 2.204 pound-mass

= .0684 slug

1 newton (nt.) = .2248 pound-force

1 meter (m.) = 3.28 feet

= 39.37 inches

APPENDIX B

PHYSICAL CONSTANTS AND PARAMETERS

mean sea-level acceleration of gravity (g)	= 32.173 feet/(second 2) = 9.806 meters/(second 2) = 980.6 centimeters/(second 2)
sea-level density of standard atmosphere (ρ)	= 1.225 kilogram/(meter 3) = .001225 gram/(centimeter 3) = .002377 slug/(foot 3)
sea-level pressure of standard atmosphere (p)	= 101,325 newtons/(meter 2) = 1,013,250 dynes/(centimeter 2) = 14.696 pounds/(inch 2) = 2115 pounds/(foot 2)
sea-level coefficient of viscosity for standard atmosphere (μ)	= 1.789×10^{-5} Kg./(m.-sec.) = 1.789×10^{-4} g./(cm.-sec.) = 3.725×10^{-7} slug/(ft.-sec.)
sea-level kinematic viscosity for standard atmosphere (ν)	= 1.4607×10^{-5} meter 2 /second = 1.4607×10^{-1} centimeter 2 /sec = 1.571×10^{-4} foot 2 /second

sea-level temperature of standard atmosphere (T)	= 288.16° K
	= 15.0° C
	= 518.69° R
	= 59.09° F
sea-level speed of sound in standard atmosphere (c)	= 340.3 meters/second
	= 34,030 centimeters/second
	= 1118 feet/second

APPENDIX C

CORRESPONDENCE BETWEEN SCIENTIFIC AND DECIMAL NOTATION

<u>Scientific Notation</u>	<u>Decimal Notation</u>
10^{-8}	0.00000001
10^{-7}	0.0000001
10^{-6}	0.000001
10^{-5}	0.00001
10^{-4}	0.0001
10^{-3}	0.001
10^{-2}	0.01
10^{-1}	0.1
10^0	1
10^1	10
10^2	100
10^3	1000
10^4	10,000
10^5	100,000
10^6	1,000,000
10^7	10,000,000
10^8	100,000,000

APPENDIX D

A WORD ABOUT THE NATIONAL ASSOCIATION OF ROCKETRY

In the course of this book a number of references have been made to the National Association of Rocketry (NAR). The NAR is the most important organization devoted to the advancement of model rocket activity, protecting and promoting the cause of safe, properly regulated model rocketry since 1957. The NAR is a nonprofit organization and as such cannot "lobby", but it can and has provided expert testimony when called upon to do so in a number of instances where model rocketry might well have been effectively banned, had not such testimony been given. In connection with this "recognized authority" status, the NAR is in constant liaison with the Federal Aviation Agency, the Food and Drug Administration, the National Fire Protection Association, the United States Air Force, and the Civil Air Patrol. The NAR also maintains close contact with the Hobby Industry Association of America to encourage the continued production and distribution of high-quality products of use in the hobby. The NAR Standards and Testing Committee is the only nationally-recognized agency competent to grant safety and/or contest certification to model rocket engine types, and in many states an engine type must bear NAR safety certification to be legally used.

The NAR is affiliated with the National Aeronautic Association, the United States representative to the Federation Aeronautique Internationale in Paris. The FAI is the internationally-recognized authority governing all forms of competition in spaceflight,

aviation, soaring, parachuting, and aeromodelling; the NAR therefore conducts the only internationally-recognized program of model rocket competition in the United States and is the only organization competent to certify U.S. national model rocket performance records and to file world performance records established in the United States with the FAI. One must, in effect, be a member of the NAR to establish an officially recognized model rocket performance record.

The NAR also maintains a system for the dissemination of useful information among its membership. Through its affiliation with the Hobby Industry Association of America, NAR is kept aware of all model rocket manufacturing activity currently in progress in the United States and has been instrumental in putting interested members in touch with a wide range of manufacturers and additional sources of model rocketry literature and information.

The authors, NAR members themselves, highly recommend NAR membership to anyone whose interest in the rocket hobby is more than passing. Membership applications and additional literature can be obtained by writing to the National Association of Rocketry, Box 178, McLean, Virginia 22101.

Figure Credits

Chapter 2

Figure 10 (After G.K. Mandell, Model Rocketry Magazine, Oct. 1968, by permission of Model Rocketry, Inc.)

Figure 11 (After Mandell, Model Rocketry, Oct. 1968, by permission of Model Rocketry, Inc.)

Figure 12 (After Mandell, Model Rocketry, Oct. 1968, by permission of Model Rocketry, Inc.)

Figure 13 (After Mandell, Model Rocketry, Oct. 1968, by permission of Model Rocketry, Inc.)

Figure 14 (After Mandell, Model Rocketry, Oct. 1968, by permission of Model Rocketry, Inc.)

Figure 15 (After Mandell, Model Rocketry, Oct. 1968, by permission of Model Rocketry, Inc.)

Figure 16 (After Mandell, Model Rocketry, Oct. 1968, by permission of Model Rocketry, Inc.)

Figure 17 (After Mandell, Model Rocketry, Oct. 1968, by permission of Model Rocketry, Inc.)

Figure 18 (After Mandell, Model Rocketry, Oct. 1968, by permission of Model Rocketry, Inc.)

Figure 19 (After Mandell, Model Rocketry, Oct. 1968, by permission of Model Rocketry, Inc.)

Figure 20 (After Mandell, Model Rocketry, Oct. 1968, by permission of Model Rocketry, Inc.)

Figure 21 (After Mandell, Model Rocketry, Oct. 1968, by permission of Model Rocketry, Inc.)

Figure 22 (After Mandell, Model Rocketry, Oct. 1968, by permission of Model Rocketry, Inc.)

Figure 23 (After Mandell, Model Rocketry, Oct. 1968, by permission of Model Rocketry, Inc.)

Figure 24 (After Mandell, Model Rocketry, Oct. 1968, by permission of Model Rocketry, Inc.)

Figure 25 (After Mandell, Model Rocketry, Oct. 1968, by permission of Model Rocketry, Inc.)

Figure 26 (After Mandell, Model Rocketry, Nov. 1968, by permission of Model Rocketry, Inc.)

Figure 27 (After Mandell, Model Rocketry, Nov. 1968, by permission of Model Rocketry, Inc.)

Figure 28 (After Mandell, Model Rocketry, Nov. 1968, by permission of Model Rocketry, Inc.)

Figure 29 (After Mandell, Model Rocketry, Nov. 1968, by permission of Model Rocketry, Inc.)

Figure 30 (After Mandell, Model Rocketry, Nov. 1968, by permission of Model Rocketry, Inc.)

Figure 31 (After Mandell, Model Rocketry, Nov. 1968, by permission of Model Rocketry, Inc.)

Figure 32 (After J.S. Barrowman, by permission of the author*)

*This notation refers to material drawn from two sources: The Practical Calculation of the Aerodynamic Characteristics of Slender Finned Vehicles, M.S.A.E. Thesis, March 1967, and "Calculating the Center of Pressure of a Rocket", NASA/Goddard Space Flight Center information pamphlet, both by James S. Barrowman. I also wish to acknowledge, however, that similar material appears in Centuri Engineering Company Technical Information Report TIR-33, "Calculating the Center of Pressure of a Model Rocket", by James S. Barrowman and edited by Douglas J. Malewicki, copyright © 1968 by Space Graphics Division of Centuri Engineering Company, Inc.

Figure 33 (After J.S. Barrowman, by permission of the author)

Figure 34 (After J.S. Barrowman, by permission of the author)

Figure 35 (After J.S. Barrowman, by permission of the author)

Figure 36 (After J.S. Barrowman, by permission of the author)

Figure 37 (After Mandell, Model Rocketry, Jan. 1969, by permission of Model Rocketry, Inc.)

Figure 38 (After Mandell, Model Rocketry, Jan. 1969, by permission of Model Rocketry, Inc.)

Figure 39 (After Mandell, Model Rocketry, Jan. 1969 by permission of Model Rocketry, Inc.)

Figure 40 (After Mandell, Model Rocketry, Jan. 1969, by permission of Model Rocketry, Inc.)

Figure 41 (After Mandell, Model Rocketry, Jan. 1969, by permission of Model Rocketry, Inc.)

Figure 42 (After Mandell, Model Rocketry, Jan. 1969, by permission of Model Rocketry, Inc.)

Figure 43 (After Mandell, Model Rocketry, Apr. 1969, by permission of Model Rocketry, Inc.)

Figure 44 (After Mandell, Model Rocketry, Feb. 1969, by permission of Model Rocketry, Inc.)

Figure 45 (After Mandell, Model Rocketry, Feb. 1969, by permission of Model Rocketry, Inc.)

Figure 46 (After Mandell, Model Rocketry, Feb. 1969, by permission of Model Rocketry, Inc.)

Figure 47 (After Mandell, Model Rocketry, Feb. 1969, by permission of Model Rocketry, Inc.)

Figure 48 (After Mandell, Model Rocketry, Mar. 1969, by permission of Model Rocketry, Inc.)

Figure 49 (After Mandell, Model Rocketry, Mar. 1969, by permission of Model Rocketry, Inc.)

Figure 50 (After Mandell, Model Rocketry, Mar. 1969, by permission of Model Rocketry, Inc.)

Figure 51 (After Mandell, Model Rocketry, Mar. 1969, by permission of Model Rocketry, Inc.)

Plate 1 (Prints by J. Nickerson from motion pictures by G. Mandell)

Chapter 3

Figure 2 (After U.S. Standard Atmosphere, 1962)

Figure 3 (After U.S. Standard Atmosphere, 1962)

Figure 4 (After U.S. Standard Atmosphere, 1962)

Figure 6 (After H. Schlichting)

Figure 7 (After U.S. Standard Atmosphere, 1962)

Figure 8 (After U.S. Standard Atmosphere, 1962)

Figure 9 (After H. Schlichting)

Figure 13 (After H. Schlichting, Boundary Layer Theory, copyright © 1968 by McGraw-Hill, Inc., Sixth Edition, by permission of McGraw-Hill Book Company)

Figure 14 (After H. Schlichting, Boundary Layer Theory, copyright © 1968 by McGraw-Hill, Inc., Sixth Edition, by permission of McGraw-Hill Book Company)

Figure 15 (After H. Schlichting, Boundary Layer Theory, copyright © 1968 by McGraw-Hill, Inc., Sixth Edition, by permission of McGraw-Hill Book Company)

Figure 16 (After H. Schlichting, Boundary Layer Theory, copyright © 1968 by McGraw-Hill, Inc., Sixth Edition, by permission of McGraw-Hill Book Company)

Figure 17 (After H. Schlichting, Boundary Layer Theory, copyright © 1968 by McGraw-Hill, Inc., Sixth Edition, by permission of McGraw-Hill Book Company)

Figure 19 (After NACA TN 4363)

Figure 20 (After NACA TN 4363)

Figure 21 (After NACA TN 4363)

Figure 23 (After H. Schlichting)

Figure 24 (After Dr. S.F. Hoerner, Fluid Dynamic Drag, published by the author 1965, by permission of Mrs. S.F. Hoerner*)

*Fluid Dynamic Drag is distributed by Hoerner Fluid Dynamics, 2 King Lane, Greenbriar, Brick Town, New Jersey 08723.

Figure 25 (After Dr. S.F. Hoerner, Fluid Dynamic Drag, published by the author 1965, by permission of Mrs. S.F. Hoerner)

Figure 26 (After H. Schlichting, Boundary Layer Theory, copyright © 1968 by McGraw-Hill, Inc., Sixth Edition, by permission of McGraw-Hill Book Company)

Figure 27 (After L. Prandl and O.G. Tietjens, Applied Hydro- and Aeromechanics, Dover Publications, Inc., New York, by permission of the publisher)

Figure 28 (After L. Prandl and O.G. Tietjens, Applied Hydro- and Aeromechanics, Dover Publications, Inc., New York, by permission of the publisher)

Figure 29 (After Dr. S.F. Hoerner, Fluid Dynamic Drag, published by the author 1965, by permission of Mrs. S.F. Hoerner)

Figure 30 (After Dr. S.F. Hoerner, Fluid Dynamic Drag, published by the author 1965, by permission of Mrs. S.F. Hoerner)

Figure 31 (After Douglas J. Malewicki, "Model Rocket Altitude Performance", Centuri Engineering Company Technical Information Report TIR-100, by permission of Centuri Engineering Company)

Figure 32 (After G. Harry Stine, Handbook of Model Rocketry, copyright © 1970, 1967, 1965 by G. Harry Stine, by permission of Follett Publishing Company)

Figure 34 (After Dr. S.F. Hoerner, Fluid Dynamic Drag, published by the author 1965, by permission of Mrs. S.F. Hoerner)

Figure 35 (After U.S.A.F. Stability and Control Datcom)

Figure 36 (After U.S.A.F. Stability and Control Datcom)

Figure 39 (After Dr. S.F. Hoerner, Fluid Dynamic Drag, published by the author 1965, by permission of Mrs. S.F. Hoerner)

Figure 40 (After U.S.A.F. Stability and Control Datcom)

Figure 41 (Aerobee experimental data after G.H. Stine)

Figure 42 (After Dr. S.F. Hoerner, Fluid Dynamic Drag, published by the author 1965, by permission of Mrs. S.F. Hoerner)

Figure 44 (fin shapes after G.H. Stine)

Figure 46 (After U.S.A.F. Stability and Control Datcom)

Figure 48 (After James S. Barrowman, "Calculating the Center of Pressure of a Model Rocket", Edited by Douglas J. Malewicki, Centuri Engineering Company Technical Information Report TIR-33, by permission of Centuri Engineering Company)

Figure 53 (After Dr. S.F. Hoerner, Fluid Dynamic Drag, published by the author 1965, by permission of Mrs. S.F. Hoerner)

Figure 54 (After Dr. S.F. Hoerner, Fluid Dynamic Drag, published by the author 1965, by permission of Mrs. S.F. Hoerner)

Plate 1 (From Shape and Flow, by Ascher Shapiro, copyright © 1961 by Educational Services, Incorporated. Reprinted by permission of Doubleday and Company, Inc.)

Plate 2 (From Applied Hydro- and Aeromechanics, by L. Prandl and O.G. Tietjens, Dover Publications, Inc., New York. Reprinted by permission of the publisher.)

Plate 3 (From Boundary Layer Theory, by H. Schlichting, copyright © 1968 by McGraw-Hill, Inc., Sixth Edition. Used by permission of McGraw-Hill Book Company.)

Plate 4 (From Applied Hydro- and Aeromechanics, by L. Prandl and O.G. Tietjens, Dover Publications, Inc., New York. Reprinted by permission of the publisher.)

Plate 5 (From Applied Hydro- and Aeromechanics, by L. Prandl and O.G. Tietjens, Dover Publications, Inc., New York. Reprinted by permission of the publisher.)

Plate 6 (Photo by G. Mandell)

Table 1 (From Boundary Layer Theory, by H. Schlichting, copyright © 1968 by McGraw-Hill, Inc., Sixth Edition. Used by permission of McGraw-Hill Book Company.)

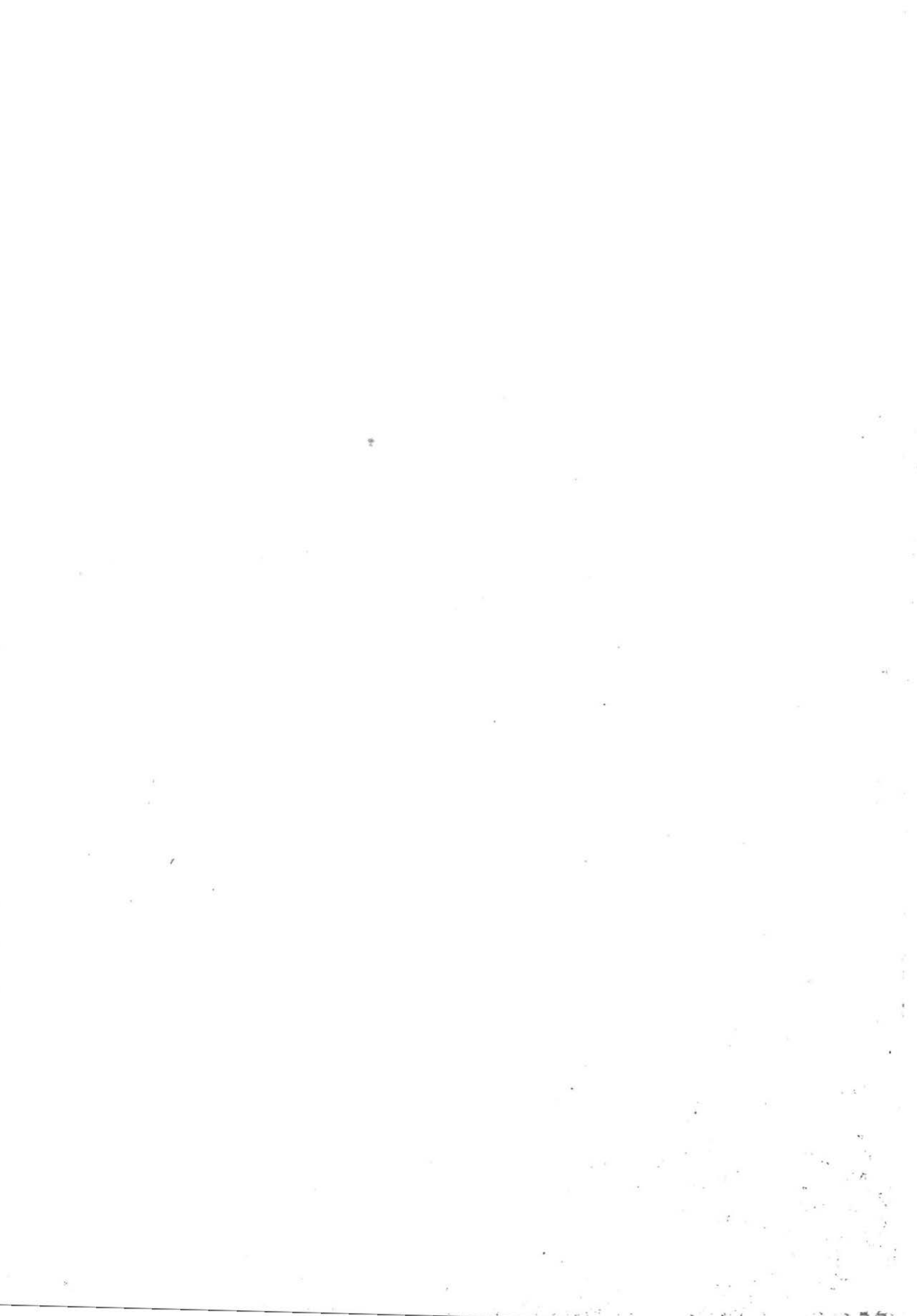
Table 5 (From Fluid Dynamic Drag, by Dr. S.F. Hoerner, published by the author in 1965. Reprinted by permission of Mrs. S.F. Hoerner.)

Table 8 (Experimental data after Dr. S.F. Hoerner, Fluid Dynamic Drag, published by the author in 1965. Used by permission of Mrs. S.F. Hoerner.)

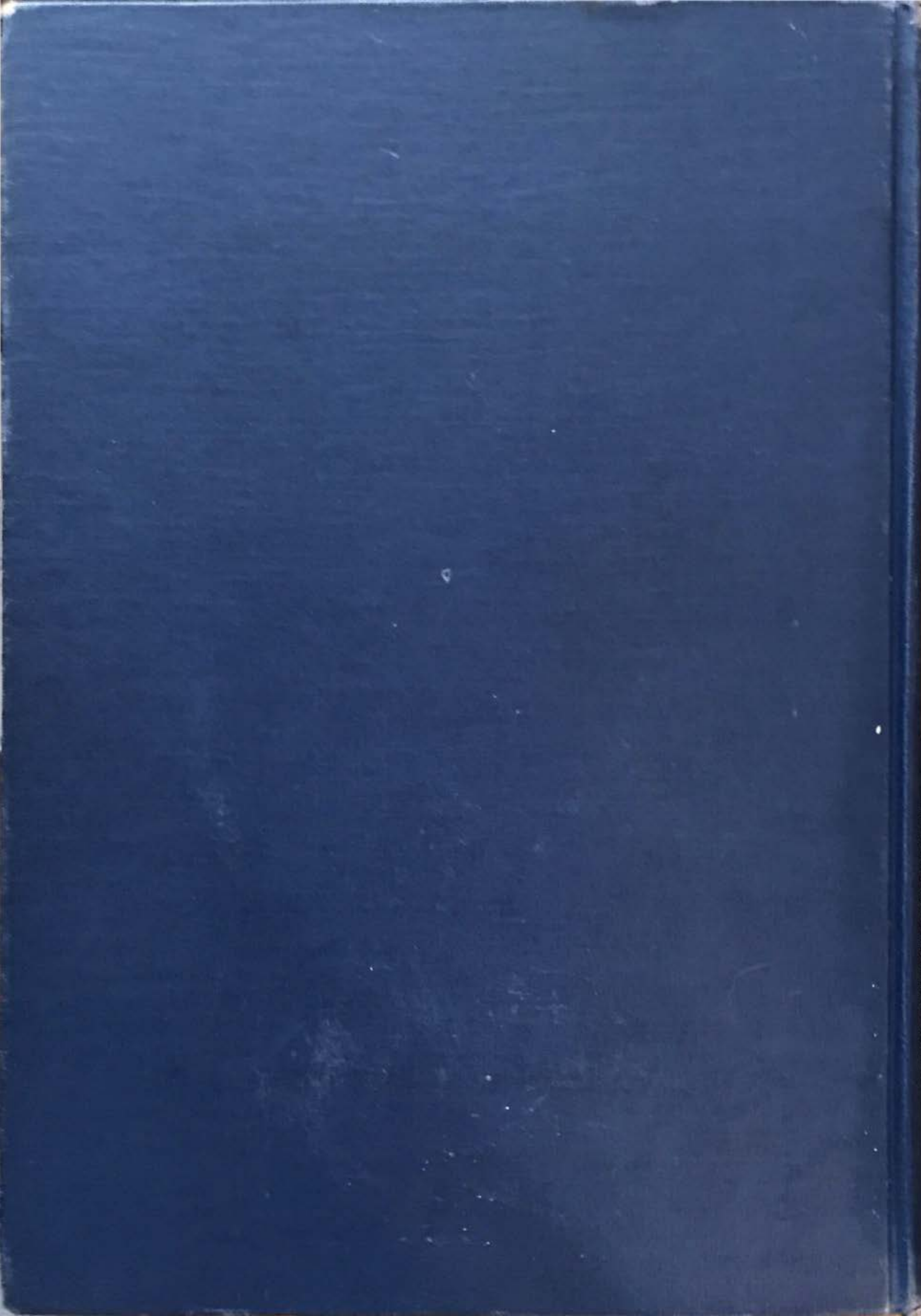












ERATTA

TOPICS IN ADVANCED MODEL ROCKETRY

by Gordon K. Mandell, George J. Caporaso, and William P. Bengen
(Cambridge, Massachusetts: The MIT Press, 1973)

Page vii, line 2 from bottom should read:
model rocket industry; the proliferation of annual conventions.

Page 5, line 3, should read:
 $\sum()$ sum of all ()

Page 108, last line of figure caption, should read:
 $\propto \omega$ as if encased in very thick glue or tar,

Page 113, Equation (30) should read:

$$(30) \propto x = Ae^{-Dt} \sin(\omega t + \varphi) + \frac{M_s}{C_1}$$

Page 144 and 145, The A, B, and C in the last two equations on page 144 and the first two equations on page 145 should be:
A', B', and C'

Page 268, line 3 should read:
 \vec{n} unit normal vector

Page 270, the last line should read
 ∞ infinity

Page 342, line 15 should read:
forces due to rotation of the body, and whether or not heat

Page 364, the second complete sentence should read:
In accordance with Bernoulli's equation, there is a decrease in static pressure between A and B, and a corresponding increase along the downstream surface from B to C.

Page 382, line 1 should read:
(from left to right in the diagram) the drag coefficient shows a corresponding increase.

Page 401, line 15 should read:
is usually small compared to that due to the mechanism which

Page 480, line 8 should read:
nose, on the other hand, is itself rounded at its forward

Page 534, the last term under the radical in equation (51) should have a righthand brace to the right of the bracket after v_{n-1} , i.e.:

$$y_n = \frac{-[m_n + k_n(y_1 + \dots + y_{n-1})]}{k_n} + \sqrt{\frac{[m_n + k_n(y_1 + \dots + y_{n-1})]^2 + 2k_n t_n \left\{ \frac{t_n}{2}(F_n - m_n g) + [k_n(y_1 + \dots + y_{n-1})v_{n-1} - m_n v_{n-1}] \right\}}{k_n}}$$

Page 583, line 4 from the bottom, should read:

Again, as in Section 2.4, expressions such as (139) are not equations

Page 590, line 3 of Section 4.3.3 should read:

quiescent prior rotational state specified by equations (154).

Page 591, line 6 should read:

account in equations (160).